Quantification of surface protonic conduction in porous oxides

Xinwei Sun

Dissertation for the Degree of Philosophiae Doctor

Department of Chemistry
Faculty of Mathematics and Natural Sciences

UNIVERSITY OF OSLO

January / 2023

Series of dissertations submitted to the
Faculty of Mathematics and Natural Sciences, University of Oslo
No. 2604

ISSN 1501-7710

Cover: UiO.
Print production: Graphics Center, University of Oslo.

Preface

This dissertation – written in the form of a monography with appendices - is submitted in partial fulfilment of the requirements for the degree of Philosophiae Doctor (PhD) at the Department of Chemistry, Faculty of Mathematics and Natural Science, University of Oslo, Norway. The doctoral scholarship has been funded by MoZEES – a Norwegian Centre for Environment-friendly Energy Research (FME), co-sponsored by the Research Council of Norway (project #257653) and 40 partners from research, industry and public sectors during the period of September 2018 to November 2021. This work has also received funding from the project "Surface protonics for oxide-based electrochemical energy devices" (SUPROX, #280868) within the ENERGIX program financed by the Research Council of Norway during the period of December 2021 to November 2022.

Support from the Norwegian Centre for Transmission Electron Microscopy (NORTEM, #197405) and the iCSI project financed by the Research Council of Norway (#237922) is also acknowledged. The work presented here was carried out at the Centre for Materials Science and Nanotechnology (SMN) in the Group for Electrochemistry under the supervision of Professor Truls Norby as main supervisor and Dr. Athanasios Chatzitakis (UiO) and Dr. Marie-Laure Fontaine (SINTEF Industry) as co-supervisors.

Acknowledgements

First of all, I would like to express my heartfelt and deepest gratitude to my main supervisor Professor Truls Norby. Thank you for your always supporting, for your constant encouragement, and our frequent discussions, on top of that, your invaluable and tireless help with this thesis and the appended articles. You have taught me more than you perhaps realize. This thesis would not have been the same without your interest, guides, and efforts, it may never have been realized.

Sincerest thanks go to my co-supervisors, Chatzitakis ("Sakis") and Marie-Laure for your generous and professional guidance. I am grateful to Sakis for all your inputs, feedbacks and assistance, and being available whenever I needed. It is my great pleasure to have you as a co-supervisor.

A big thank you to the SUPROX gang at SINTEF Industry for the many fruitful discussions during the morning meetings, especially Dr. Per Martin Rørvik and Dr. Einar Vøllestad for all the constructive tips and helpful advices. I am grateful to Dr. Annett Thøgersen for performing the TEM-EELS experiments, and data analysis, and not least Dr. Sebastian Prodinger for conducting the water sorption measurements.

I would like to take this opportunity to express my sincere thanks to Professor Donglin Han and Jie Gu from University of Soochow, China, for the smooth collaboration. A warm thanks to Jie for conducting part of the experimental work in one of the appended articles in China.

I am indebted to many friends and colleagues at the Group for Electrochemistry for providing the fantastic collaborative working environment, and all the valuable discussions along the way, and not to mention for reminding me that there is a life outside the lab as well.

Above all, I am tremendously thankful for my beloved parents and grandparents, for your love, motivation, patience, guidance, always believing in me and supporting me throughout this endeavour. The dissertation is devoted to my loving family.

Xinwei Sun
January 2023

Summary

The research leading up to this thesis has provided a fundamental and methodological framework for parameterisation of the thermodynamics and kinetics involved in surface protonic conduction of porous oxide ceramics, specifically ZrO_2 and CeO_2.

The discovery of a dual time constant from the impedance spectra in porous oxides is believed to reflect surface conduction over the curved surface of the porous microstructure, specifically, conduction over the concave regions (neck) with small capacitance of the gas phase over the gap and convex regions (grain) with higher capacitance due to the dielectric solid phase.

A novel nomenclature for defect surface species is introduced, which allows us to operate with standard states, statistical thermodynamics, and configurational entropies through equilibrium coefficients. It connects further to diffusional transport theory and eventually preexponentials for protonic surface conductance in the adsorbed water layers. In the present work, the surface conductance by protons is considered in terms of various proton migration routes, including jumps between the oxide ions on the surface (denoted the -*s* mechanism), between the surface and adsorbed (chemisorbed) species (-*sa*), between adsorbed species (-*a*), between water molecules in the first physisorbed layer (-*ph1*), and in the liquid-like physisorbed layer (-*ph2*). It was further assumed that all jumps take place between two neighbouring oxide ions, so that the preexponentials of the diffusivity and hence charge mobility can be taken as the same for all mechanisms.

A brick layer model (BLM) is developed, which enables us to link the predicted preexponentials of surface protonic conductance to those of the measured conductivities of the porous ceramic samples. ZrO_2 and CeO_2 as well as anatase TiO_2 from a preceding work serve as model systems for the validation of the proposed models, which appear distinctly different based on the different hydrophilicities of these oxides. For the first time, the widely differing behaviours of surface protonic conductivity from chemisorbed and physisorbed water layers on porous oxides of different microstructures have been fully mapped and parameterised over large ranges of temperature, p_{H_2O}, and hence relative humidity (*RH)*. The BLM has been shown to enable order-of-magnitude discrimination between models for surface protonic conduction for actual samples of porous oxide ceramics.

In the chemisorbed water layer at the highest temperatures investigated, the surface protonic conductivity decreases with decreasing temperature, attributed to favourable chemisorption of water that is dissociated to protons strongly bonded to surface oxide ions, having high enthalpies of mobility of 50-80 kJ/mol. The model is supported by the $p_{H_2O}^{1/2}$ dependence of surface protonic conductivity under these conditions.

At intermediate temperatures (200-300°C), less faceted ZrO_2 and (101)-dominated TiO_2 show considerable conductivity across a shallow minimum in common with CeO_2, which we for the first time have given a plausible interpretation in terms of chemisorption with partial dissociation to protons migrating between surface oxide ions and adsorbed species. The enthalpy of proton mobility is in this case smaller, assigned to the involvement of more loosely bonded adsorbed species, e.g. 35 kJ/mol for CeO_2.

Below 200°C, the thickness of the adsorbed water layer increases with further decreasing temperatures and increasing *RH*, evidenced by increased surface protonic conductivity. ZrO_2 and anatase TiO_2 appears to have more physisorbed water and more protonic conduction from this layer as compared to CeO_2. Migration of protons between adsorbed species in the first physisorbed layer (in ZrO_2) have low enthalpies of 17-25 kJ/mol, reasonably just a bit larger than that of bulk liquid water (12 kJ/mol). An additional strong increase in conductivity is observed for TiO_2 as *RH* surpasses 60%, assigned to liquid-like physisorbed water, which was not observed for the other oxides.

CeO_2 appears more hydrophobic, and the physisorbed water did not appear until near room temperature. An observed $p_{H_2O}^{3/2}$ dependence of surface protonic conductivity indicates proton transport between the loosely bonded adsorbed species within the chemisorbed layer, with an estimated enthalpy of proton mobility of 17 kJ/mol, similar to what is traditionally assigned to transport in the physisorbed layer in other more hydrophilic oxides such as TiO_2 and ZrO_2, where probably the two mechanisms contribute together. The levelling off in conductivity of CeO_2 at the highest *RH* near RT was ascribed to saturation to full coverage of the chemisorbed layer without much contribution from conduction in the physisorbed water on the hydrophobic surface.

The findings and models developed in the present work contribute to the understanding and control of surface protonic conduction in porous oxide ceramics, which is believed to play an important role in electrochemical cells (as electrolytes, electrodes, or fillers in membranes), humidity sensors, heterogeneous catalysis, and not least photocatalysis.

Sammendrag

Forskningen som har ledet frem til denne avhandlingen har gitt et grunnleggende og metodisk rammeverk for parameterisering av termodynamikken og kinetikken involvert i protonisk overflateledning av porøse keramiske oksider, spesielt ZrO_2 og CeO_2.

Oppdagelsen av en dobbel tidskonstant fra impedansspektrene i porøse oksider ser ut til å reflektere overflateledning over den buede overflaten av porøse mikrostrukturer, med andre ord ledning over de konkave områdene (kornhals) med liten kapasitans i gassfasen og de konvekse områdene (korn) med høyere kapasitans i den dielektriske fastfasen.

En ny nomenklatur for defekte species i overflater er introdusert, som muliggjør definisjon av standardtilstander, bruk av statistisk termodynamikk og konfigurasjonelle entropier gjennom likevektskoeffisienter. Den kobles videre til teori for diffusjon og migrasjon og til slutt preeksponentielle for protonisk overflatekonduktans i de adsorberte vannlagene. I dette arbeidet ble overflatekonduktansen vurdert i forhold til forskjellige migrasjonsruter for protoner, som inkluderer hopp mellom oksidioner på overflaten (betegnet –*s*-mekanismen), mellom overflate og adsorberte (kjemisorberte) species (-*sa*), mellom adsorberte species (-*a*), mellom vannmolekyler i det første fysisorberte laget (-*ph1*), og i det væske-lignende fysisorberte laget (-*ph2*). Det ble videre antatt at alle hoppene finner sted mellom to nabooksidioner, slik at den preeksponentielle til diffusiviteten og dermed ladningsmobiliteten kan antas lik for alle mekanismene.

En såkalt «brick layer model» (BLM) ble utviklet, som gjør oss i stand til å koble de forutsagte preeksponentielle for de protoniske overflatekonduktansene til eksperimentelle resultater basert på ledningsevnemålinger i de porøse keramiske prøvene. ZrO_2 og CeO_2 samt anatas TiO_2 fra et tidligere arbeid ble brukt som modellsystemer for validering av de foreslåtte modellene, som fremstår som tydelig forskjellige basert på forskjellige hydrofilisiteter til disse oksidene. For første gang har den vidt forskjellige oppførselen til protonisk overflateledningsevne fra kjemisorberte og fysisorberte vannlag i porøse oksider med forskjellige mikrostrukturer blitt fullstendig kartlagt og parameterisert over store områder av temperatur, p_{H_2O} og dermed relativ fuktighet. BLM har vist seg å muliggjøre diskriminering i størrelsesorden mellom modeller for protonisk overflateledning i porøse keramiske oksider.

I det kjemisorberte vannlaget ved de høyeste undersøkte temperaturene, avtok den protoniske overflateledningsevnen med synkende temperaturer tilskrevet kjemisorpsjon av vann som dissosierer til protoner sterkt bundet til overflateoksidioner, med høye mobilitetsentalpier på 50-80 kJ/mol. Modellen støttes av en $p_{H_2O}^{1/2}$ -avhengighet for den protoniske overflateledningsevne under disse forholdene.

Ved intermediære temperaturer (200-300°C) viste de mindre fasetterte ZrO_2 prøvene og (101)-dominert TiO_2 høy ledningsevne til felles med CeO_2, som vi for første gang har gitt en mulig tolkning i forhold til kjemisorpsjon med partiell dissosiasjon til protoner som migrerer mellom overflateoksidioner og adsorberte species. Entalpiene for protonmobilitet er i dette tilfellet betydelig mindre, tilordnet involvering av mer løst bundne adsorberte species, f. eks. 35 kJ/mol for CeO_2.

Under 200°C øker tykkelsen på det adsorberte vannlaget med ytterligere synkende temperaturer og økende relativ fuktighet, som førte til økende protonisk overflateledningsevne. ZrO_2 og anatas TiO_2 ser ut til å ha mer fysisorbert vann og mer protonledning fra dette laget sammenlignet med CeO_2. Migrering av protoner mellom adsorberte species i det første fysisorberte laget (i ZrO_2) har lave entalpier på 17-25 kJ/mol, litt større enn i flytende vann (12 kJ/mol). En ytterligere stigning i ledningsevnen var observert for TiO_2 når relativ fuktighet oversteg 60%, tildelt det væske-lignende fysisorberte vannet, som ikke ble observert for de andre oksidene.

CeO_2 virker mer hydrofobt, og det fysisorberte vannet opptrådte bare nær romtemperatur. En observert $p_{H_2O}^{3/2}$ -avhengighet av den protoniske overflateledningsevnen indikerte protontransport mellom løsere adsorberte species i det kjemisorberte laget, med en estimert entalpi for protonmobilitet på 17 kJ/mol, noe som samsvarte godt med det som tradisjonelt tilordnes transport i det fysisorberte laget i andre mer hydrofile oksider som TiO_2 og ZrO_2, hvor sannsynligvis de to mekanismene bidrar sammen. Utjevning i overflateledningsevnen til CeO_2 ved høyeste relative fuktighet tilskrevet metning til full dekning av det kjemisorberte laget uten mye bidrag for protonledning i det fysisorberte vannet på den hydrofobe overflaten.

Oppdagelsene og modellene som er utviklet i dette arbeidet bidrar til forståelse og kontroll av protonisk overflateledning i porøse keramiske oksider, som kan spille en viktig rolle i elektrokjemiske celler (som elektrolytt, elektroder eller oksid-«filler» i membraner), fuktighetssensorer, heterogen katalyse, og ikke minst fotokatalyse.

Contents

Preface ..... **iii**

Acknowledgements iii

Summary ..... **v**

Sammendrag ..... **vii**

1 Introduction **1**

1.1 Hydrogen in energy transition 1
1.2 Solid-state ionic conductors – An overview 2
1.3 Progress towards high-temperature PEM materials 4
1.4 Surface protonics of porous nanoscopic ceramics 8
1.5 Aims, objectives and the structure of the thesis 11

2 Water on ceramic surfaces: Thermodynamics and transport **13**

2.1 Hydrogenation of the (sub)surface 13
2.2 Chemisorption and physisorption 14
2.3 Interaction of water with oxide surfaces 15
2.4 Surface protonic conduction in adsorbed water 18
2.5 Nomenclature 21
2.6 Molecular and dissociative chemisorption 22
2.7 Physisorption 38

3 A brick layer model for surface protonic conduction **47**

3.1 Conductivity of porous materials 47
3.2 A more general brick layer model (BLM) 49
3.3 Common features and general comments 53

4 Surface protonic conduction in porous monolinic ZrO_2 ..... **55**

4.1 Introduction 55
4.2 Experimental 56
4.3 Results 58
4.4 Models and quantitative interpretation 66
4.5 Discussion and conclusions for ZrO_2 72

5 Surface protonic conduction of CeO_2 ..... **75**

5.1 Introduction 75

5.2 Experimental 76
5.3 Results and discussion 79
5.4 Modelling the surface protonic conductivity 90
5.5 Protonic conduction in physisorbed water 95
5.6 Conclusions on CeO_2 97

6 Further results, summarising discussions and outlook 99

6.1 Specific surface area and pore size 99
6.2 Evaluation of specific surface area: BET vs BLM 102
6.3 Concentration of adsorbed water by thermogravimetry 103
6.4 Migration and conductivity 113
6.5 Implications for applications and future research 117

7 Conclusions 123

References 125

Appendices 139

Appendix I 141

List of symbols and abbreviations

Applendix II 145

Quantifiable models for surface protonic conductivity in porous oxides – case of monoclinic ZrO_2

Appendix III 173

Surface protonic conductivity in chemisorbed water in porous nanoscopic CeO_2

Appendix IV 213

In-situ electron loss spectroscopy reveals surface dehydrogenation of hydrated ceria nanoparticles at elevated temperatures

Appendix V 223

Composite membranes for high temperature PEM fuel cells and electrolysers: A critical review

1 Introduction

1.1 Hydrogen in energy transition

The environmental and ecological challenges presented by the rapid depletion of fossil fuels and global climate change have stimulated extensive research for development of sustainable, environment-friendly energy technologies and solutions during the last decades. In this regard, the conversion between chemical energy and electricity generated from renewable sources (e.g. solar, wind, hydropower) through the use of electrolysers and fuel cells is of prime importance. In view of this, hydrogen plays a predominant role as an energy carrier. As suggested in Figure 1, hydrogen is an efficient and zero-carbon energy carrier that can help tackle various critical energy challenges to reduce greenhouse gas (GHG) emissions for our sustainable future societies.[1-4]

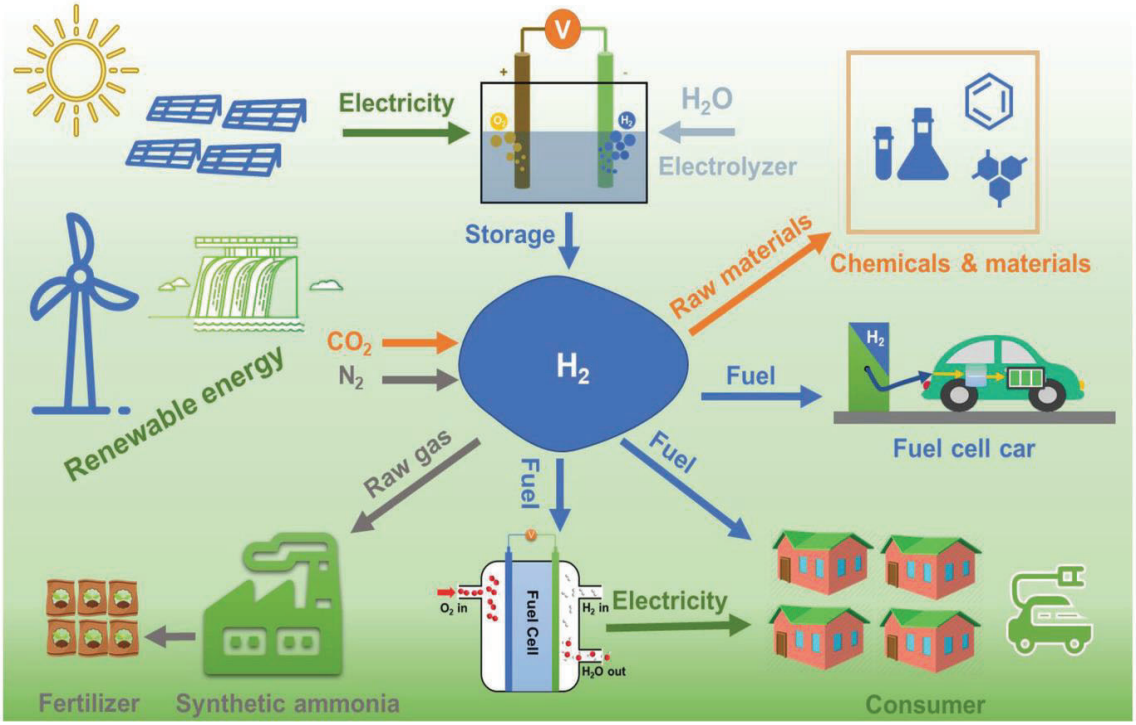

Figure 1 A sustainable energy economy based on hydrogen. Copyright © 2020 WILEY-VCH Verlag GmbH & Co. KGaA, Weinheim.[5]

Up to today, hydrogen production still relies on fossil fuels such as natural gas steam reforming and coal gasification, due to their lower cost.[6-8] The production of low-emission hydrogen accounts for less than 1 % of global hydrogen production in 2021.[9] Currently, the different technologies are at different stages of development. For the production of hydrogen through electrolysis, the commercial electrolysers are dominated by alkaline electrolysers (AEs)

because of their higher durability due to an exchangeable electrolyte and the fact that they can operate with lower amounts of noble-metal based catalysts.[10-12] One of the world leading manufacturers of alkaline electrolysers and hydrogen generators is Nel Hydrogen in Norway.[3] Hydrogen production through polymer electrolyte membrane electrolysers (PEMEs) is also commercially available.[13] In comparison to AEs, PEMEs offer certain advantages such as higher efficiency, operation at higher current densities, rapid start-up and shutdown, and simplicity.[14-16] The use of a thin polymer membrane (typical 100–200 µm) results in low ohmic losses, while still allowing high pressures. However, the need of electrocatalysts containing precious metals (notably the extremely scarce Ir), and expensive materials for membrane and bipolar plates make hydrogen production by PEMEs less cost-competitive compared to AEs.[17]

Hydrogen fuel cells have developed significantly over the past decades. At present, the main technologies are based on phosphoric acid fuel cells (PAFCs), polymer electrolyte membrane fuel cells (PEMFCs), and molten carbonate fuel cells (MCFCs).[18, 19] In terms of fuels, the low-temperature fuel cells such as PAFCs and PEMFCs all require high purity hydrogen to maintain stable performance. If other fuels (e.g. natural gas) are to be used, a fuel processor must be added to first covert the fuel into hydrogen, which adds to the cost and complexity of installation and operation. As for practical applications, the transport sector is one of the major contributors of global GHG emissions.[18, 20] Significant efforts have hence been dedicated to hydrogen fuel cells as an alternative for internal combustion engine (ICE), with PEMFCs being the most mature and promising technology. Nonetheless, for fuel cells to be widely implemented in transport applications, critical issues that must be addressed are reliability, durability, and manufacturing cost, along with the development of cost-effective H_2 production, distribution, and storage systems.[21-23]

Phosphoric acid, alkaline, and molten carbonate electrochemical cells utilize liquid electrolytes (aqueous H_3PO_4, KOH or molten salt, respectively), which can be corrosive, and do not allow operation at differential pressures. Unwanted permeation of gases can occur, resulting in reduced overall efficiency.[17] Other low- and high-temperature electrochemical devices use solid electrolytes, which can be either proton conductors or oxide ion conductors depending on the type of cells. Compared to liquid electrolytes, all-solid cell configurations reduce corrosion and electrolyte management problems, enable a more compact design, and operation at differential pressures.[17] Therefore, electrochemical cells based on solid electrolytes have received great attention during the past decades. In the following section, an overview of existing solid-state ionic conductors will be given.

1.2 Solid-state ionic conductors – An overview

The performance of electrochemical devices depends crucially on the properties of their component materials, and central to all is the electrolyte through its contribution to the ohmic resistance. Solid oxide fuel cells (SOFCs) and solid oxide electrolysers (SOEs) that typically operate at 800-1000°C use oxide ion conductors as a solid-state electrolyte, represented by

yttria-stabilized zirconia (YSZ), gadolinium- or samarium-doped ceria (GDC, SDC), as well as Sr- and Mg-doped lanthanum gallate (LSGM).[24] Despite the high energy conversion efficiency of SOFCs and SOEs, fuel flexibility and low environmental impact, such high operating temperature requires long start up time, and imposes materials degradation problems.[25, 26] In order to reduce the materials and sealing costs, prolong the lifetime and improve efficiency of the cell system, the operating temperature must be lowered.[27]

As we lower operating temperatures into the intermediate temperature (IT) region of 400-700°C (IT-SOFCs and IT-SOEs), the electrolyte resistance increases significantly. Strategies to overcome this problem include reducing the electrolyte thickness or using alternative electrolyte materials. A growing interest has been driven towards high-temperature proton-conducting ceramics (HT-PCCs) based on perovskite-type materials, taking the advantage of their relatively low activation energy for proton conduction.[28-31] PCC electrolytes also prevent fuel dilution, an issue faced by oxide ion conductors.[32] Therefore, such cells are also called proton ceramic fuel cells (PCFCs) and proton ceramic electrolysers (PCEs). Considering hydrocarbon fuels (*i.e.,* methane), PCEs with HT-PCC electrolytes allow the production of H_2 and other valuable hydrocarbons (e.g. C_2H_4, C_2H_6) through methane dehydrogenation without the generation of H_2O, CO and CO_2.[33] Tremendous efforts have been dedicated to couple the high proton conductivity of $BaCeO_3$-based proton conductors (10^{-2} S/cm at 600°C [28, 34]) and the good chemical stability of $BaZrO_3$-based proton conductors [29, 35] in a single proton-conducting electrolyte. Fabbri *et al.* [33] provides a nice summary of the $BaCe_{1-x-y}Zr_xM_yO_{3-\delta}$ (where M = Y, Nd, Gd, Sc) chemical composition series that provides the best compromises of chemical stability and proton conductivity. More recently, Ni *et al.* [27] demonstrates an electrolyte of a Na_xCoO_2/CeO_2 composite, showing a conductivity of 0.1-0.3 S/cm at 370-520°C. A fuel cell operated with this electrolyte of 400 μm thick achieved peak powder densities of 1000 mW/cm^2 at 520°C, better than the benchmark PCFCs with a thin film perovskite electrolyte.

Even lower operating temperatures (< 400°C) reduce the cell system cost further owing to the wider choice of materials for interconnectors and seals, and ease thermal cycling from ambient to operating temperatures.[36] This makes conventional PEMFCs operated below 100°C favorable for portable power generation and transport applications over SOFCs, although high-purity hydrogen is required. PEM technology and proton conducting polymers are discussed separately in **Section 1.3**.

Apart from this, low-temperature protonic conduction has been reported for solid acids. A fuel cell made of a $CsHSO_4$ electrolyte membrane operating at 150-160°C in H_2/O_2 atmosphere have been demonstrated, showing an open circuit voltage of 1.11 V and current densities of 44 mA/cm^2 at short circuit.[37] A proton-conductive electrolyte based on a CsH_2PO_4/SiP_2O_7 composite showed a conductivity of 44 mS/cm at 266°C.[38] Several other phosphate-type materials also showed protonic conductivity comparable to that of Nafion polymers under humidified conditions.[39, 40]

In addition, protonic conduction becomes prominent also due to proton migration in adsorbed and dissociated water layers on the internal surfaces of nano-grained porous ceramics such as

TiO_2, CeO_2, SDC, YSZ and $La_2Ce_2O_7$, even if the bulk property involves negligible protonic conductivity.[41] Enhanced conductivity is observed under humidified conditions at intermediate and low temperatures, even at room temperature. This phenomenon is called *surface protonics*, which we will be described in **Section 1.4**.

A key parameter in charactering the performance of electrolyte materials is their conductivity. Figure 2 shows a summary of the typical ionic conductivities *vs* temperatures of common solid-state ionic conductors, including oxide ion conductors and proton-conducting ceramics of high- and low-temperature categories. The conductivity required for PEMs for transportation applications according to the U.S. Department of Energy (DOE) is also indicated (R_{areal} < 0.02 Ωcm^2 at 120°C).[42, 43]

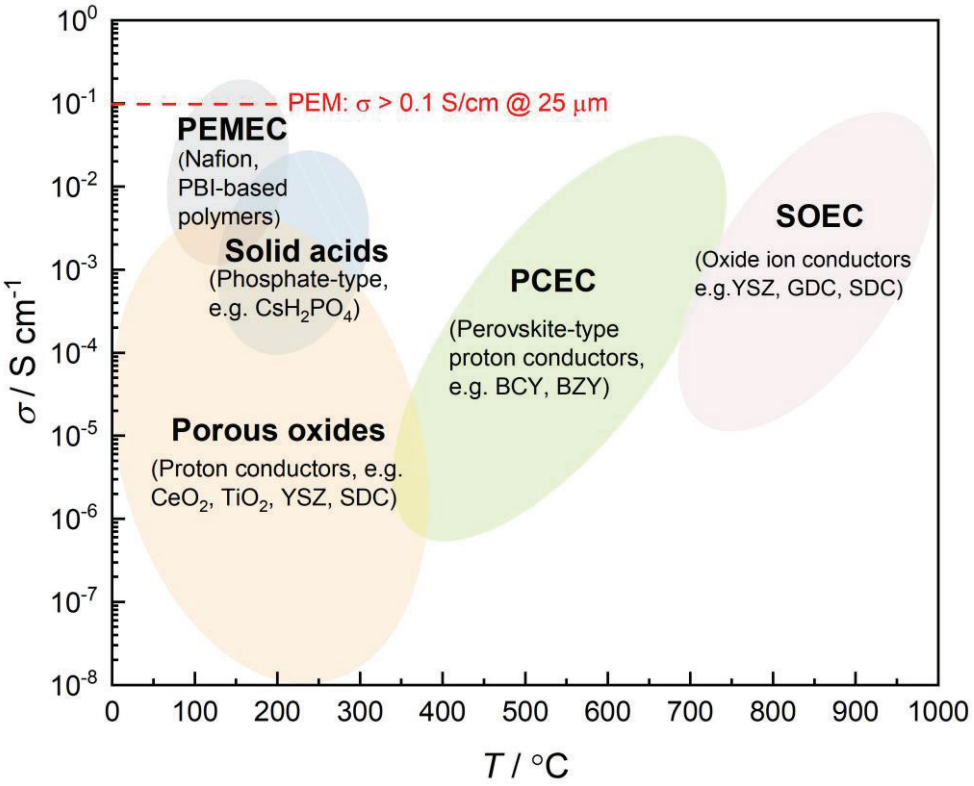

Figure 2 Conductivity ranges of different solid-state ionic conductors as a function of temperature for electrochemical cells ("EC" in the plot) of various types. Conductivity data are estimated based on refences (for illustration only).[24, 33, 37, 41] The conductivity required for PEMs to be used in transportation applications is indicated (showing by the red dashed line).

1.3 Progress towards high-temperature PEM materials

In order to meet the future global energy demand, it is necessary to develop energy efficient water electrolysis systems. In this context, PEM can be a key enabling technology. As mentioned in **Section 1.1**, PEM fuel cells are catching up, expanding its area of application into sectors that require large energy quantities, in particular, fuel cell electric vehicles (FCEVs),[42, 44] and heavy-duty vehicles (HDVs).[45]

As shown in Figure 3, the core component of PEM electrochemical cells is the membrane electrode assembly (MEA), which consists of a solid-state proton-conductive electrolyte (SPE) sandwiched between two porous, electronically conducting catalytic electrodes, and more openly porous transport layer (PTL). The SPE ensures conduction of protonic charge carriers (hydrated H_3O^+) between the electrodes, and at the same time it must not conduct electrons (or electronic current), also being impermeable to inlet gases (H_2 and O_2). One electrode operates under reducing conditions, exposed to H_2 and water vapour. It is always negative, whether running as an anode in the fuel cell or a cathode in an electrolyser, and we refer to it as a *negatrode*.[46] Similarly, the other electrode is positive, operating in oxidising conditions in O_2 and water vapour as a cathode in fuel cell or anode in electrolyser, and we will refer to it as a *positrode*. Each of the electrodes comprises a catalyst layer (CL), where the electrocatalysts are dispersed on a nanoporous support. Developing electrocatalysts is of great importance to promote charge transfer kinetics.[47] Recent progress of replacing noble-metal electrocatalysts with earth-abundant catalysts (EACs) for the oxygen evolution reaction (OER) and hydrogen evolution reaction (HER) in PEM electrolysers is reviewed by Sun *et al.* [48].

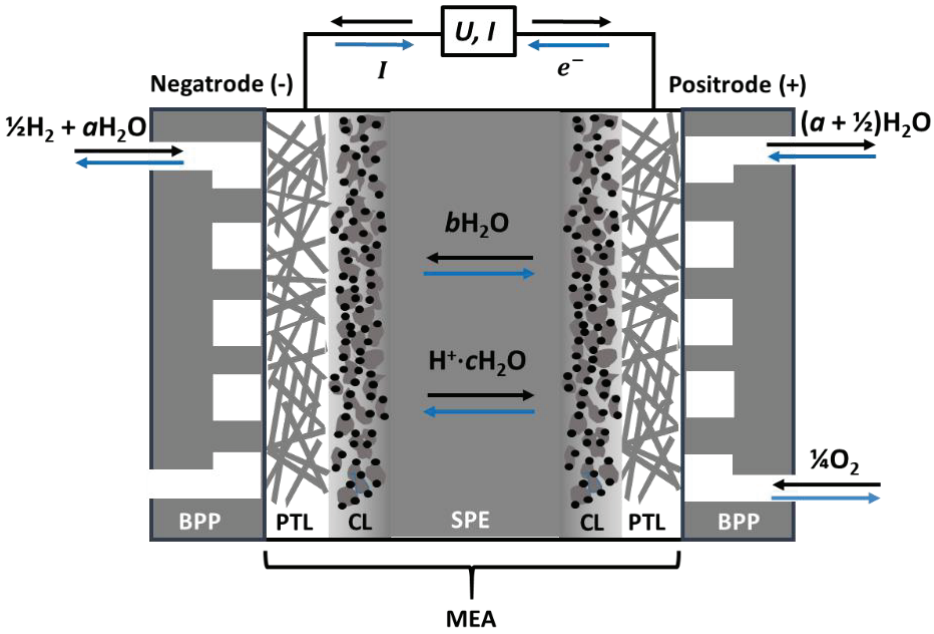

Figure 3 Schematic of PEM electrochemical cells – fuel cells (black upper arrows) and electrolysers (blue lower arrows). Protons hydrated with c bonded and electro-osmotically dragged H_2O molecules migrate through the solid polymer electrolyte (SPE), the water supplied by b back-diffusing water, and a water supplied in a feed gas, so that a + b = c. BPP: bipolar plate gas manifold, PTL: Porous transport layer, CL: catalyst layer, SPE: solid polymer electrolyte, MEA: membrane electrode assembly. Copyright @ 2019 MDPI Membranes.[46]

1.3.1 Water management issues

The operation conditions of conventional low-temperature PEMs (LT-PEMs) are restricted to 80-90°C and high relative humidity (*RH* ~ 80%) to maintain reasonable protonic conductivity.

State-of-the-art LT-PEMs are based on perfluorosulfonic acid ionomers, represented by Nafion® (DuPont), which consists of a polytetrafluoroethylene (PTFE) backbone and sulfonated side chain.[49] At relatively high *RH*, transport of hydrated protons (H_3O^+) take place through liquid-like water channels that form as a result of nanophase separation of the hydrophilic (acid ionic group, usually -SO_3H) and the hydrophobic PTFE backbone of the polymer. This implies that the reactant gases should be of high relative humidity. However, if the net content of liquid water is oversaturated, water may condense and partially block the gas flowing path and the pores of the catalyst, hence reducing the active sites on the catalyst surface.

Nevertheless, industry often requests more rigorous operating temperature to improve mass transport, avoid catalyst poisoning and electrode flooding, increase efficiency, and further reduce the cost and complexity of the system. When above 100°C, Nafion membranes show drastic decline in protonic conductivity. Therefore, alternative membranes exhibiting comparable conductivity to that of Nafion at elevated temperatures and lower *RH* are needed as the water management system would otherwise grow unacceptably large. In this context, non-fluorinated PEMs that are based on aromatic heterocyclic polymers such as those of the family of polybenzimidazole (PBI)[50-52] and polyether-ether-ketone (PEEK)[53, 54] emerged due to their exceptional mechanical properties, thermal stability and conductivity at higher temperature after acid doping, and not least lower cost. The Advent PBI-based (formerly BASF P1100W membrane) MEA have shown protonic conductivity up to 0.1 S/cm in the absence of water, with a proven lifetime of 20,000 h at operation temperature between 120-180°C.[55] Protons in such hydrocarbon polymers are conducted as free protons via Brønsted acid sites on the polymer backbone. In general, higher acid doping levels lead to higher protonic conductivity, but at the cost of deterioration in mechanical strength of the polymer due to the "plasticizing effect" of the acid.[56, 57] The long-term stability of these polymers is also compromised, leading to significantly decreased cell performance at such temperatures. In addition, acid leaching can also corrode metal interconnections.[58]

1.3.2 The role of ceramic fillers in polymer-ceramic composites

Nevertheless, as shown in Figure 4, the "conductivity gap" between the upper temperature limit for Nafion-based membranes and the lower temperature for acid-doped PBI still exists.[42] Considerable efforts have been made to overcome some of the above-mentioned problems, and to further bring the operating temperature of PEMs closer to the technical targets of 120°C for practical applications.[59] One approach is to incorporate ceramics fillers such as hygroscopic inorganic oxides, solid acids, metal organic frameworks and carbon materials into the polymer matrix so as to make polymer-ceramic composites. We did a literature review regarding composite membranes covering polymer systems of Nafion, PA-PBI and SPEEK for PEM applications, and discussed their significance. We also touched upon composites of mixed proton-electron conducting composites that are of interest for development of the catalyst layer.[46] The paper is further appended to the thesis in **Appendix V**.

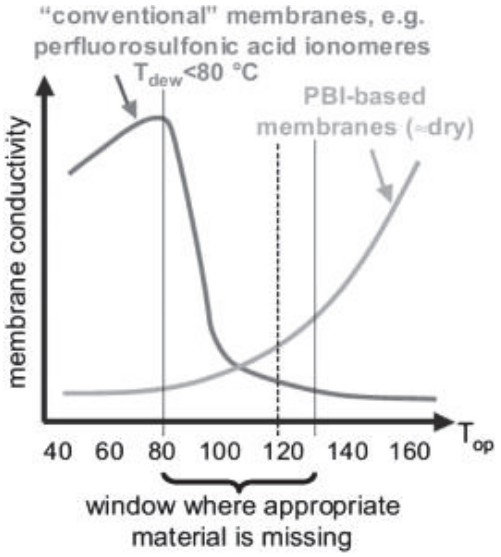

Figure 4 Membrane conductivity based on perfluorosulfonic acid (PFSA) ionomers and PBI-based membranes, displaying the conductivity gap from 80 to 130°C. Copyright © 2004 WILEY-VCH Verlag GmbH & Co. KGaA, Weinheim.[42]

Such filler particles are claimed to show improved protonic conductivity, mechanical and thermal stability of the polymers and better water/acid-retaining properties over a wider range of temperatures.[60, 61] We found that the incorporation of metal oxide fillers maintains the water content in Nafion up to 130°C, but showed no significant improvement in protonic conductivity.[62] Nafion-MOF composites showed enhanced protonic conductivity at higher temperatures and lower *RH*, owing to the interconnected microporous networks of MOFs that can facilitate proton conduction.[63, 64] In general, acid-doped PBI composites exhibit the specific conductivities of Nafion at 150°C and above, yet show poor conductivity below 100°C. Above all, very few reports provide credible explanation to the interaction mechanism between the filler and the polymer matrix. PEMFC testing are also lacking from the majority of the studies, while they are crucial to assess the compatibility, stability and lifetime of such composite membranes.

Most research works to date have been focusing on enhancing the performance of the composite membranes, while the proton conduction mechanisms in water channels are far less studied and understood. The absence of experimental studies regarding why ceramic fillers would work or not work in such composite membranes highlights a major knowledge gap in the literature. Some refer to the use of nanoparticles of oxide ceramics as introduced in **Section 1.2**, all of which are recently understood to merely adsorb water on their surfaces and exhibit surface protonic conduction in adsorbed water layers. This encourages us to study the water adsorption and protonic conduction in typical ceramic oxide fillers for PEM electrolytes, which may contribute to the understanding of the effect of filler particles in such polymer-ceramic composite membranes under wet conditions at low temperatures.

1.4 Surface protonics of porous nanoscopic ceramics

Initially, it was commonly accepted that most of the proton-conducting ceramics rely on protons within the crystalline structure. For instance, MH_nXO_4-type solid acids (where M = monovalent cation, X = S, Se, P, As, and n = 1,2) are said to undergo a "superprotonic conductivity".[65] On the other hand, YSZ, a material known to be a pure oxide ion conductor for use as a solid electrolyte in high-temperature SOFCs and SOEs (see also **Section 1.2**) has been shown to exhibit considerable protonic conductivity in nanocrystalline form at low temperatures for the first time in 2006.[66] The protonic conductivity of YSZ with an average grain size of 17 nm measured at 30°C was comparable to that of the oxide ion conductivity of the microcrystalline YSZ measured at around 400°C.[67] Apparently, nanomaterials show enhanced surface properties different from the bulk. Since the first discovery, extensive research has been carried out on nanostructured low-temperature proton conducting ceramics, in particular, on fluorite-type oxides.

The origin of the observed protonic conductivity in such materials has been disputed. Some reports proposed that the high density of grain boundaries in these nanocrystalline materials are exclusively responsible for the protonic conduction (e.g. through the space charge layer),[68-72] but Shirpour *et al.* [73] raised doubt about this as the proton mobility in the crystal lattice of simple oxides along the grain boundary would be too low to justify the measured conductivity. The suggestion of proton conduction along grain boundaries was later also disapproved by Tande *et al.* [74] and by Scherrer *et al.* [75] through measurements of YSZ thin films deposited by different methods so as to vary their porosity, grain size, and shape. Gregori *et al.* [76] observed enhanced protonic conductivity from a nanocrystalline porous ceria thin film below 300°C in wet atmosphere, which was not observed for the dense nanocrystalline sample. Sm-doped CeO_2 samples prepared at 300°C under 6 GPa by using a high-pressure apparatus result in a relative density of 85 to 93%, showing protonic conductivity of the order 10^{-7} and 10^{-8} S/cm at 50°C under pH_2O of 0.026 atm.[77] Tredici *et al.* [78] demonstrated the presence of a considerable fraction of residue open nanoporosity in nanometric TiO_2 despite a high relative density of 95% prepared by a high-pressure field assisted sintering (HP-FAST) process. These results indicate that the open porosity is in charge of the enhanced low-temperature conductivity, rather than the high density of grain boundaries.

Nowadays, it is commonly accepted that the triple-grain junctions in some studies were open enough that it can be treated as transport via adsorbed water layers. In other words, proton conduction can take place via water molecules and hydroxyls adsorbed on the inner surface of percolating nanopores, what we today call *surface protonics*. Figure 5 shows a simple illustration of the concept of surface proton conduction in nanograined materials (Figure 5 b) compared to the conventional HT-PCCs (e.g. doped $BaCeO_3$), where the protonic conductivity is determined by the number of oxygen vacancies in the bulk since protons are incorporated into the materials (Figure 5 a).

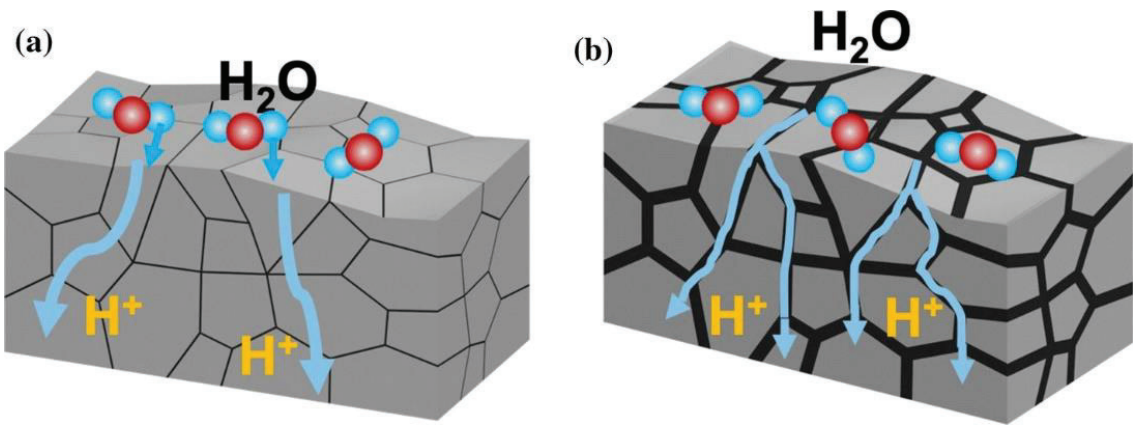

Figure 5 Proton conduction a) through a bulk material (e.g. HT-PCCs), b) via interfacial water layers in nanograined materials. Copyright © 2019 Springer.[41]

The conduction of protons is generally explained in terms of Grotthuss and vehicle mechanisms. In the case of Grotthuss transport, a proton jumps through the hydrogen bond network of water molecules, involving continuously breaking and forming of hydrogen bonds. In the vehicle case, the proton diffuses as part of protonated molecules (e.g. H_3O^+) and the diffusion of H_2O allows net transport of protons, common for proton conduction in liquid water.[79, 80]

Figure 6 schematically depicts the proton conduction pathways proposed to date, covering proton transport within the bulk (route 1), along the grain boundaries (route 2), and in the adsorbed water layers of the ceramic (routes 3 and 4). More recently, Stub *et al.* [81, 82] and Manabe *et al.* [83] reported the presence of two time constants from impedance spectra of porous sintered YSZ and CeO_2 with capacitances being consistent with the bulk and grain boundary response, respectively. It was then suggested that proton conduction within the adsorbed water layer (route 4 in Figure 6) can be subdivided further into transport on the surface above the grain (*intragrain*) and on the surface over the grain boundary (*intergrain*). Miyoshi *et al.* [84, 85] showed that the room temperature protonic conductivity of YSZ increased by 3 orders of magnitude when reducing the grain size from 100 to 13 nm, while the concentration of Y_2O_3 did not have a significant effect on the protonic conductivity. The authors attributed the protonic conductivity to water adsorbed at the grain boundaries and surfaces.

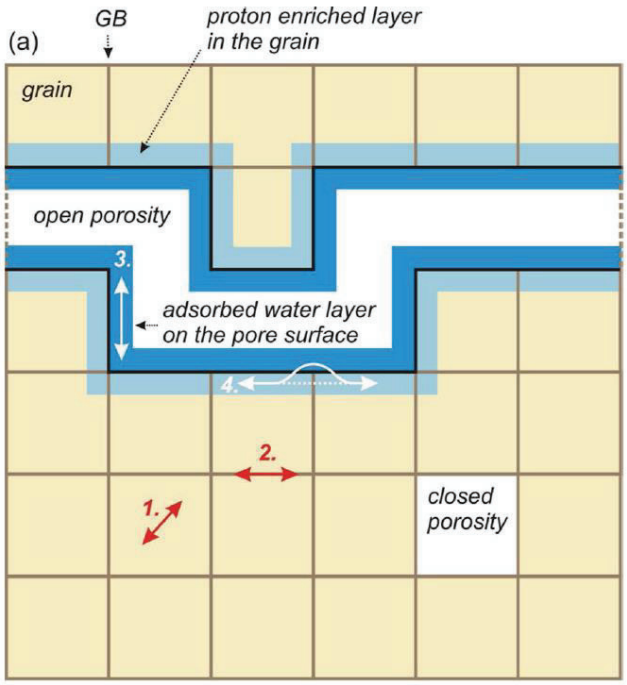

Figure 6 Schematic 2D illustration of the pathways of proton transport 1) in the bulk, 2) along the grain boundaries, 3) along the water layer adsorbed on the walls of the open pores (subsurface region), 4) in a layer of adsorbed water. Copyright © 2013 WILEY-VCH Verlag GmbH & Co. KGaA, Weinheim.[76]

Several techniques have been used for the preparation of nanocrystalline proton conductors, including high-pressure room-temperature compaction, hot pressing, spark plasma sintering, high-pressure field-assisted sintering, spray pyrolysis, chemical vapor deposition, pulsed laser deposition, laser irradiation, and powder sintering. Miyoshi *et al.* [85] provided a nice summary of the reported conductivity of nanostructured fluorite-type oxides (see Figure 6 b in the reference). However, different processing techniques give rise to different nanostructures (e.g. grain size and porosity), crystallinities (amorphous *vs* crystallite), structural phases (e.g. cubic, hexagonal) and crystallographic orientations, resulting in distinct discrepancies in protonic conductivity even for one chemical composition. Due to this complexity, the interpretation and comparison of the results are not straightforward. The important question that remains is how these parameters affects the degree of protonation, and thereby the overall protonic conductivity of the material.

Surface protonics enables humidity sensors involving the use of ceramic, semiconducting and polymer materials [86-89] and give rise to protonic conduction that in combination with various airborne contamination decreases the performance of electrical insulators.[90] Moreover, surface protonics has been shown to occur on heterogeneous catalysts under an applied electric field, with enhanced catalytic activity.[91, 92] It makes low-temperature catalytic reactions possible for hydrogen production and ammonia synthesis.[93-95] In this respect, CeO_2 is of particular importance as a catalyst. Water adsorption and surface protonic conduction on CeO_2 has been characterised and measured,[73, 76, 96, 97] but it exhibits a complex surface chemistry with slow equilibria and considerable hysteresis.[98, 99]

Porous nanograined ceramics with surface protonic conductivity have received interest as potential electrolyte materials in fuel cells and electrolysers. Both highly hydrophilic nanoporous anatase membranes[100, 101] and highly dense nanometric TiO_2 [78] exhibited protonic conductivity over a broad range of temperatures between 400°C and room temperature not much lower than typical conductivities of conventional polymeric membranes. The comparable protonic conductivity, high hydrophilicity, and lower cost of nanouporous simple oxides make them potential substitutes for Nafion as proton conducting membrane materials at low temperatures. Sgabanikia *et al*. [102] reported that the incorporation of nanosized $La_2Ce_2O_7$ in a PBI membrane increases the hydrophilicity of the polymer and alters the hydrophilic/hydrophobic character of the composite membrane. Columnar thin films of CeO_2 with well-aligned pore structure showed four times higher protonic conductivity than that of the nanograined CeO_2 sintered pellets examined under identical conditions.[103] It implies that the protonic conductivity can be improved further by optimising the microstructure, in this case by transport of protons through water adsorbed on the columnar film surface, while overcoming the issue of low thermal stability of polymer materials.

Kim *et al.* [104] demonstrated water concentration cells using dense nanostructured YSZ (8 mol% yttria-doped zirconia) and SDC (20 mol% samaria-doped ceria) as electrolytes, with one electrode exposed to wet air, and the other electrode immersed in deionized water. The cell showed an electromotive force (emf) of about 110 mV and 220 mV at room temperature for the YSZ and SDC cells, respectively. In contrast, the emf was nearly zero when the cell was exposed to dry air, indicating proton conduction within the nanostructured oxides. Recently, a new type of glucose fuel cell has been demonstrated based on freestanding porous and dense CeO_2 membranes as proton-conducting electrolyte, integrated with a silicon chip.[105] The porous CeO_2 film is comprised of a dense bottom of 20 nm to avoid fuel crossover, and a disordered top microstructure with the purposes of 1) enhancing the overall protonic conductivity by surface protonic conduction, 2) reducing the mechanical stress in the membrane. In contrast to polymer-based electrolyte, the ceramic-electrolyte glucose fuel cell remained stable through the high-temperature sterilization process, and can be directly integrated into bioelectronics devices and implants. Inspired by PEMs, Xu *et al.* [106] demonstrated a solid-state photoelectrochemical (SSPEC) cell for gas phase water splitting under simulated solar illumination for hydrogen production. The mechanism of operation was discussed in view of surface protonic conduction, which requires a porous photoanode for charge transfer to the electrode-electrolyte interface and transport of proton to the electrolyte, and a polymer proton-conducting membrane (e.g. Nafion) that transport protons in the adsorbed water layers. The relative humidity, hence, the amount of adsorbed water appears to be central for the use of TiO_2 as photocatalysts,[107, 108] as well as the hydrogen production rate.[109]

1.5 Aims, objectives and the structure of the thesis

The **primary objective** of the PhD project for this thesis is to investigate systematically the surface protonic conductivity of highly porous oxide ceramics under controlled conditions such

as temperature and pH_2O. Due to the key role of ionic MO_2 oxides such as TiO_2, ZrO_2, and CeO_2 in many established and emerging technologies as stated above, and to keep the system simple and consistent, nanocrystalline porous sintered oxides of undoped ZrO_2 and CeO_2 with well-defined microstructure are used as the model systems in this work.

Understanding the surface properties of these oxides, and their interaction with adsorbed entities such as water is of key interest in several technological areas. In principle, the in-plane protonic conductance of a layer of adsorbed water with well-defined geometries can be estimated from the concentration and charge mobility of protons. The **secondary objective** is to elucidate and calculate the surface conductance based on the fundamentals of thermodynamics of adsorption and dissociation of water, and proton migration. Then, the next question is naturally how we from such a surface conductance can make a prediction of the macroscopic (measured) conductivity of a porous material with predominant surface conduction. With the model systems investigated in this work, the overall goal is thus to develop a credible model that may be used for conversion between the surface conductance and sample conductivity, applicable to other porous oxides and ceramics as well. In this thesis, a brick layer model (BLM) is developed and applied to meet this objective. This will gain deeper understanding of the many types of processes involving surfaces and provide first indications for which types of adsorption and surface transport predominate the protonic conductivity under what conditions.

This thesis is structured into 7 chapters, written in the form of a monograph, that cooperatively address the primary and secondary objectives. The thermodynamics of adsorption and dissociation of water and the kinetics of protonic diffusion and migration, leading up to conduction central for this work, are treated in depth in **Chapter 2**. **Chapter 3** introduces the concept of a brick layer model, which connects the conductance of an adsorbed water layer to the measured macroscopic surface protonic conductivity of openly porous materials. ZrO_2 and CeO_2 serve as model systems for validation of the proposed models, and the measurements and interpretations are presented in **Chapters 4** and **5**, respectively. **Chapter 6** presents some additional findings on porous oxides in general, relevant for this thesis, following an overarching final summarising discussion, providing new insights for future research. The overall conclusions are given in **Chapter 7**. A comprehensive list of symbols and abbreviations is provided at the end of the thesis in **Appdendix I**. For ease of reading, papers with further details are provided as **Appendices II-V**, with their own independent reference lists.

2 Water on ceramic surfaces: Thermodynamics and transport

The theoretical analysis of surface protonic conduction in porous oxides in this thesis is treated in this chapter. I shall be starting with the phenomenon of surface hydrogenation of oxides, which is believed to play a role in adsorption of water on oxides. This is followed by some general concepts of adsorption, the structure of water layers on oxides, and properties of oxide surfaces which are germane to discussion of protonic conduction in porous oxides. Thereafter, the essential definitions and clarifications of conductivity contributions will be addressed, before moving on to the adsorption theory and defect equilibrium thermodynamics, which in combination with various proton diffusion and transport mechanisms leads to full expressions for protonic conductance in adsorbed water layers on porous materials. For convenience, a nomenclature for surface species and transport mechanisms will be established with respect to this.

2.1 Hydrogenation of the (sub)surface

The driving force behind many surface processes is lowering of the surface free energy of the system. For this reason, many oxides are often covered by hydrocarbons or water as they lower the surface energy of the oxide surfaces.[110, 111] Apart from this, another way of lowering the surface energy of oxides is through a hydrogenation process.[112, 113] With hydrogenation, we mean adsorption and dissociation of hydrogen (e.g. from water molecules) on the surface of an oxide, which can occur spontaneously under ambient conditions.[112] With CeO_2 as an example, surface hydrogenation of CeO_2 can for instance be written as

$$CeO_2 + \tfrac{1}{2}H_2(g) \rightleftarrows CeOOH \qquad \text{Eq. 1}$$

$$CeO_2 + \tfrac{1}{2}H_2O(g) \rightleftarrows CeOOH + \tfrac{1}{4}O_2(g) \qquad \text{Eq. 2}$$

Or in defect-chemical notation, the latter case (Eq. 2) can be written as

$$Ce_{Ce}^{x} + O_O^{x} + \tfrac{1}{2}H_2O(g) \rightleftarrows Ce_{Ce}^{/} + OH_O^{\bullet} + \tfrac{1}{4}O_2(g) \qquad \text{Eq. 3}$$

where Ce_{Ce}^{x} and $Ce_{Ce}^{/}$ represent Ce^{4+} and Ce^{3+}, respectively, and O_O^{x} and $OH_O^{\bullet}$ represent oxide and hydroxide ions, respectively.

Our recent study by *in situ* electron energy loss spectroscopy (EELS) of CeO_2 nanoparticles in transition electron microscopy (TEM) showing that Ce^{3+} in a surface layer oxidises to Ce^{4+}

during heating in vacuum, which we may assign to dehydrogenation (reversed Eq. 1) and formation of a reduced oxyhydroxide, a process that requires diffusion of hydrogen only.[114]

This phenomenon may be expected to be significant for oxides with reducible cations, possibly at relatively high temperatures, and may affect subsequent chemisorption and physisorption of water. I therefore refer to the work on CeO_2 for further discussion in **Chapter 5**. It is, otherwise, not the prime focus of the work presented here, and we leave it for the most part to further dedicated studies (See **Chapter 6** Further results, summarising discussions and outlook).

2.2 Chemisorption and physisorption

When a gas molecule (adsorbate) collides with a solid (adsorbent), it may lose energy to the solid through inelastic collision. Under the condition of low energy loss, the gas molecule may leave the surface. However, if the energy loss is larger than a critical amount, the gas molecule become trapped (adsorbed) at the surface, which open new possibilities. One should note the difference between a*b*sorption *vs* a*d*sorption, where in the former, the molecule becomes an integrated part of the material, while the latter indicates that the molecule binds to the surface of the material. In this thesis, we shall deal with a*d*sorption only.

Adsorption is almost invariably an exothermic process. The adsorbate loses translational and vibrational energy, decreasing the entropy of the molecule, and $-T\Delta S$ of the reaction becomes positive. In order for $\Delta G = \Delta H - T\Delta S$ to become negative, ΔH is thus negative (that is, the process is exothermic). Figure 7 illustrates the adsorption state for a diatomic molecule X_2 approaching a surface (coming from the right-hand side of the diagram). The molecules at the solid–vapor interface have a higher potential energy than the molecules in the bulk phase because of attractive forces between the molecules. Consequently, the molecules are "pulled down" (showing negative potential energy) due to the asymmetrical forces at the surface. Typically, an incoming molecule first feels the weak van der Waals interactions in which the electronic structure of the adsorbate molecules is largely unaffected except for induced dipoles, *i.e.,* physisorbs to the surface associated with a shallow minimum far from the surface. Physisorption (an abbreviation of "physical adsorption") is always a non-activated process, but useful for gas uptake. The energy released when a molecule is physisorbed is of the same magnitude as the enthalpy of condensation, which is indicated as ΔH_{phys} in the figure.

If the molecule can further rearrange its electronic configuration by formation of new orbitals between adsorbate and adsorbent, a proper chemical bond to the surface may take place. It is called associative chemisorption because the molecule still holds together, and it may be non-activated or weakly activated as indicated in the figure. If the adsorbate molecule by dissociation (breaking of bonds) into atoms can approach closer to the surface and the sum of bonds is stronger than those of the associated molecule and its adsorption forces, we get a deeper energy well for dissociative adsorption of the two atoms. Because of the need to break the molecular bond of X_2 into 2X, there will now be a significant activation barrier (E_a in the figure) to reach dissociative adsorption – it is always activated. If the energy required to form the

chemisorbed state from the physisorbed is larger than $-\Delta H_{phys}$, then the energy needed for desorbing the chemisorbed atoms is indicated as E_d in the figure. Nonetheless, chemisorption energy depends much on the orientation of the molecules with respect to the atoms in the surface, accordingly, the real potential is much more complicated than the simplified representation shown here.

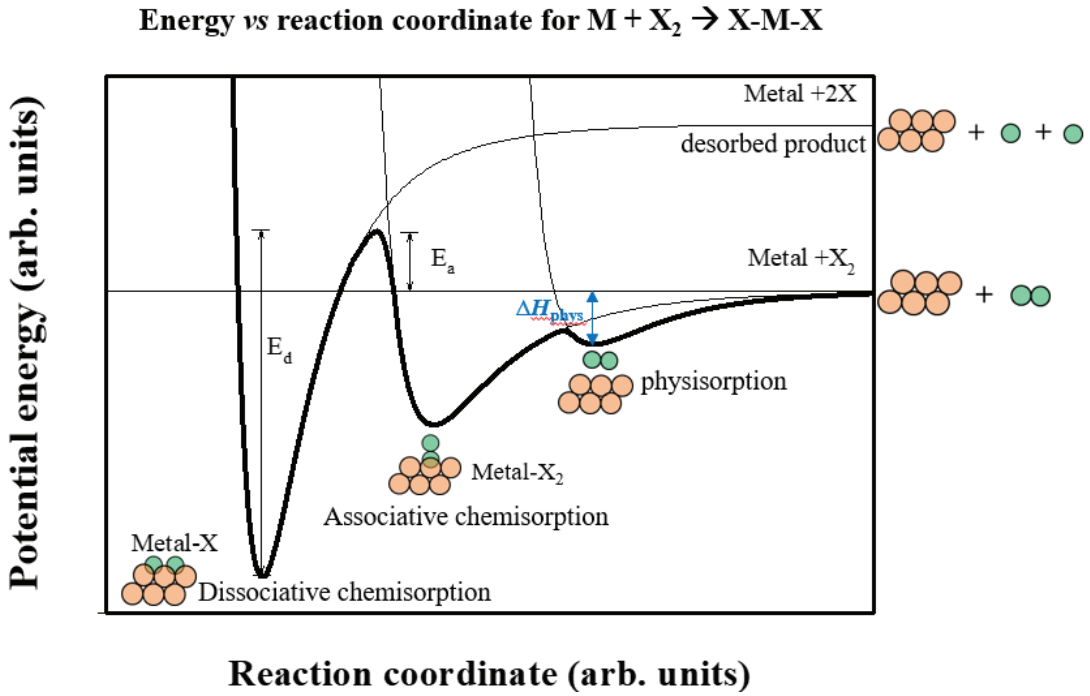

Figure 7 Potential energy diagram for a diatomic molecule X_2 that approaches a surface, in this case denoted a metal M. Adsorption would run from right to left, while desorption would run from left to right. The three curves represent total energy of dissociatively chemisorbed M-X, associatively chemisorbed M-X_2, and physisorbed M+X_2 as a function of reaction coordinate, which may also represent distance from the surface. Each curve has a reference non-bonded energy to the far right (obviously higher for 2X than for X_2), a decrease with decreasing distance due to bonding, and a sharp increase at short distances due to steric repulsion. The transitions between states form activation energy barriers, the important ones being E_a and E_d for dissociative adsorption and desorption, respectively. Modified based on Fig. 6.34 in ref. [111].

2.3 Interaction of water with oxide surfaces

The previous section has set the stage for describing the essentials of what happens when an adsorbate approaches a surface (exemplified by a metal). Since this thesis targets water molecules as adsorbate and ionic oxides as adsorbent, I will therefore in the following limit the discussion to the adsorption of water on the surface of oxides. Oxide surfaces are intrinsically complex as they vary in ionicity and acidity/basicity and form a variety of surfaces and terminations. Defects in various forms may prevalent, which adds to their complexity, all making them challenging to classify and describe uniformly. However, oxides are still by far the most studied in terms of adsorption of water.

2.3.1 Water layer structure on oxide surfaces

We start however with the simplest possible description of homogeneous adsorption of water on ideal oxide surfaces. The ionic or polar covalent nature of oxides possesses acid-base, or donor-acceptor character. The bulk structure of a metal oxide is best described as M_aO_b, where the surfaces contain cation (M_s) and oxide ion (O_s) behaving as Lewis acid and base sites, respectively. This means, the oxide ions (O^{2-}) can donate electrons to a metal cation (electron acceptor), which can form a bond with the oxygen lone pairs in the H_2O molecule. As a result, H_2O molecules may chemisorb with the oxygen atom of the H_2O molecule (O_w) bonding to the surface metal M_s forming M_s-OH_2. The acidity (pull on electrons) of the M_s cation makes M_s-OH_2 a Brønsted acid that can donate protons to a surface oxide atom O_s, and hence give rise to proton conduction. The dissociation (protolysis) of M_s-OH_2 hence leads to the formation of an adsorbed hydroxyl group M-OH^- and a surface hydroxyl group OH_s^-. This means that H_2O may chemisorbs both molecularly and dissociatively on M_aO_b: M-OH_2, M-OH^- and bridging M-(O_sH^+)-M sites coexist, as indicated by the circles in Figure 8.

Further incoming H_2O molecules are physisorbed via H-bonding to the chemisorbed layer. The amount of physisorbed water depend strongly on the relative humidity (*RH*).[81] At *RH* up to 30% there is around one physisorbed layer, and because of its hydrogen bonds with the rigid chemisorbed layer, the two layers form altogether an "ice-like" structure. As *RH* increases above 30%, the physisorbed water layer grows further, the outermost layers change gradually from "ice-like" to "liquid-like", and above 60%, the majority outermost part of the physisorbed water layers are randomly oriented and behaves fully "liquid-like". In this layer, the mobility of protons is enhanced significantly, resulting in much higher protonic conductivity. The overall picture of the water structure on oxide surfaces are schematically depicted in Figure 8.

What has been said so far points towards the important concept of the wettability of water on a surface. The establishment of equilibrium of water on a surface is given by the interfacial energies, or surface tensions, given by Young's equation.[115] In brief, surfaces that form a contact angle below 90° are termed hydrophilic. Water tends to spread on a surface to maximise the solid-liquid interactions. In contrast, surfaces that form a contact angle above 90° are termed hydrophobic, the cohesive forces within water outcompetes the adhesion to the surface, thus spreading is hindered.[116] For simplicity, we consider here only ideal solid surfaces that are perfectly clean and chemically homogeneous with a single contact angle, and disregard contribution from contact angle hysteresis due to surface roughness and/or contaminations.

A natural consequence of the above is that, in general, all simple and smooth oxide surfaces will be hydrophilic, since liquid water (not shown in Figure 8) will share interface with liquid-like water adsorbed on the solid oxide surface that it is in equilibrium with. Exceptions from this hence point at unusual surface compositions or geometries, such as hydrophobic CeO_2 nanostructures, which we will come back to in **Chapter 5**.

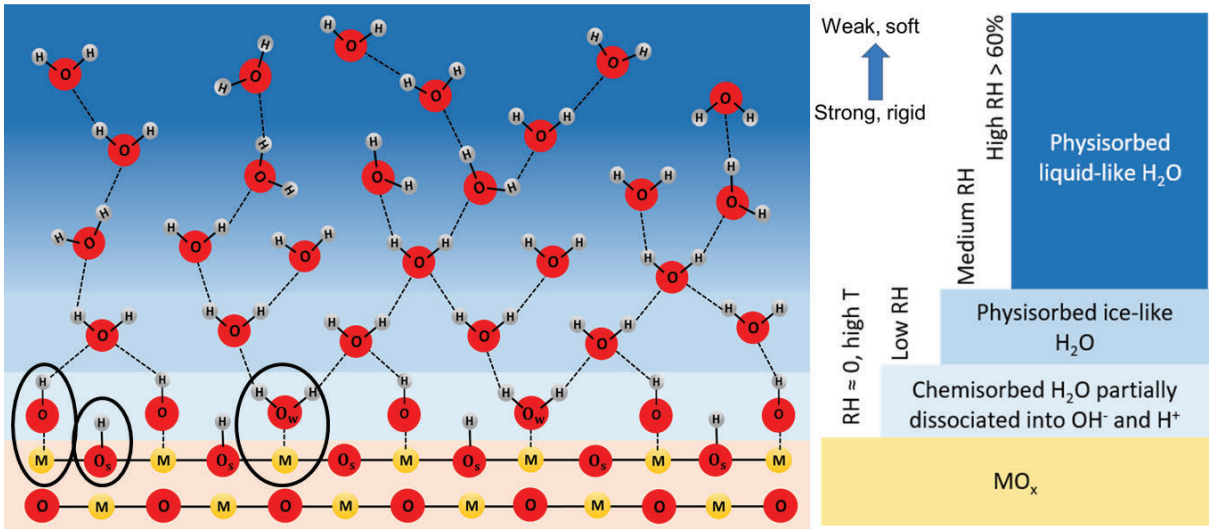

Figure 8 Water layer structure on an ionic oxide MO_x. At low *RH* (< 30%), the water layer consists of one chemisorbed (strongly bonded) layer that is partly dissociated into adsorbed (M-OH^-) and surface hydroxide ions (O_s-H^+), represented by the circles in the figure. A strongly hydrogen-bonded "ice-like" physisorbed water monolayer forms at *RH* ~ 30%. As *RH* increases further, a few more water layers add, considered essentially "liquid-like" at *RH* > 60%.

2.3.2 Structure and termination of oxide surfaces

Water adsorption and dissociation on oxide surfaces are highly correlated to 1) coordination environment of surface atoms, 2) redox properties of the oxide, and 3) oxidation state of the surface.[117] While redox property is mainly a matter of the choice of cations, the coordination of surface atoms (concentration and strength of the terminating acidic cation sites) can be controlled by the preparation procedure for samples which allow different surface facets to be formed. Our recent work on porous sintered nanocrystalline TiO_2 materials fabricated under conditions that favour different crystal facets reveal that the water adsorption behaviour and surface protonic conduction differ largely for the same material for different surface terminations.[118] The H_2O-TiO_2 interactions have been elucidated by means of *in situ* Fourier transform infrared (FT-IR) spectroscopy under controlled temperature and atmosphere. The type of coordination of the oxygen atoms (terminal *vs* bridging oxygen as shown in Figure 8) results in different wavenumber of the O-H stretching vibration, allow differentiation of the adsorption state of water (*i.e.,* molecular or dissociative) on the TiO_2 surface.

As shown in Figure 9 (a), water chemisorbs dissociatively on the (001) and (100) facets of anatase TiO_2, but molecularly on the (101) facet, attributed to the different coordination degrees of surface atoms and their geometric arrangements. Similar conclusions have been drawn from computational studies, suggesting molecular chemisorption of water on the most common (101) surface of anatase TiO_2, and partial dissociation on the (001) surface depending on coverage.[119-121] Nonetheless, the presence of oxygen vacancies on the (101) surface facilitates water dissociation to form hydroxyls.[122] Moreover, as revealed in Figure 9 (b), the exposed crystal facets and different chemisorption states show characteristic differences in their measured

surface protonic conductivities – well pronounced in their temperature dependencies. Specifically, the subsequent physisorbed water layer (below 200°C) is more rigidly bonded and solid (*i.e.,* ice-like) on (001) and (100) facets, but more loosely bonded on (101) facet due to the lack of rigid hydroxyl groups to bond to.

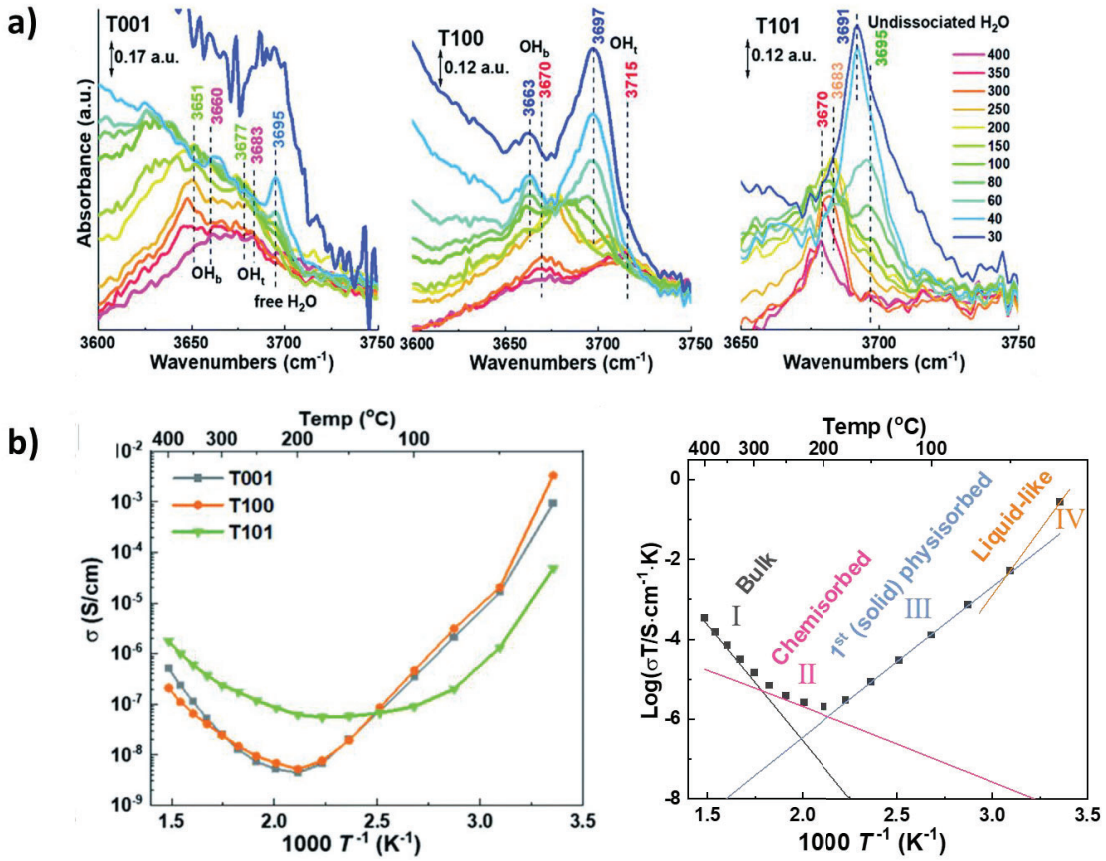

Figure 9 a) The high wavenumber range of *in situ* FTIR spectra of water adsorption on T001, T100 and T101 anatase TiO_2 samples at different temperatures (in °C) upon progressive water vapour removal, b) the total conductivity of TiO_2 samples with predominance of three crystal facets measured at p_{H_2O} = 0.026 bar in ambient air. Copyright © 2022 Royal Society of Chemistry.[118]

2.4 Surface protonic conduction in adsorbed water

Until now, we have seen that water molecules may adsorb on the internal surface of ionic oxides, forming water layers that enables protonic conduction. The surface conductivity can in principle be calculated based on the mobility and surface concentration of charge carriers, or via the conductance of the water layer with a certain thickness. In this section, definitions and clarifications of conductivity contributions and considerations of geometrical factors for surface conduction in porous materials will be discussed. Charge mobility of protons shall be estimated. Existing theory about transport mechanisms will be reviewed.

2.4.1 Conductivity in the adsorbed layer and surface conductance

The macroscopic (measured) conductivity of a porous ceramic σ_M can be taken to have bulk and surface contributions

$$\sigma_M = \sigma_{M,b} + \sigma_{M,s} \quad \text{Eq. 4}$$

The macroscopic bulk conductivity ($\sigma_{M,b}$) may be electronic or ionic. The macroscopic surface conductivity ($\sigma_{M,s}$) in wet atmosphere is obtained after subtraction of the bulk conductivity from the total conductivity, and may have contributions from native ions and electrons in addition to protons. The latter, *i.e.,* macroscopic surface protonic conductivity (σ_{M,s,H^+}) may be taken to arise from migration in the sub(surface) itself (as pointed out in **Section 2.1**) and in adsorbed water layers, namely, chemisorbed, first ice-like physisorbed, and further liquid-like physisorbed water layers

$$\sigma_{M,s,H^+} = \sigma_{M,sub,H^+} + \sigma_{M,ch,H^+} + \sigma_{M,ph1,H^+} + \sigma_{M,ph2,H^+} \quad \text{Eq. 5}$$

In reality, the distinction between different surface and adsorbed layers may not be sharp, and there will be overlapping contributions. In our treatment, we will for the most part treat conduction in the adsorbed layers, and we will furthermore not differentiate between them: we will for consideration of measured conductivity consider the water layers as one, with a certain thickness and a certain in-plane conductance, as the next important section will clarify further.

Geometry, conductance and conductivity

For a particular charge carrier of any kind, the volume conductivity, σ_i, is given as the product of charge, mobility and concentration, *i.e.,* $\sigma_i = z_i F u_i c_i$. For protons, the corresponding surface layer volume conductivity is

$$\sigma_{s,H^+} = F u_{H^+} c_{H^+} \quad \text{Eq. 6}$$

where u_{H^+} is the charge mobility of protons and c_{H^+} (in mol/cm^3) is the average volume concentration of protons in the water layer.

The macroscopic surface protonic conductivity (σ_{M,s,H^+}) of porous ceramics may be related to the volume conductivity, σ_{s,H^+}, for protons in an adsorbed water layer along an appropriate geometric model. For this, we need the surface protonic conductance, G_{s,H^+} (with unit Siemens, S). It is the in-plane conductance of a square area of a surface layer with thickness *t*, and width = length = *w*. It is independent of the width *w* and length *l* of the square, since they are equal and cancel.

The surface protonic conductance G_{s,H^+} is then proportional to the protonic surface layer volume conductivity σ_{s,H^+} via

$$G_{s,H^+} = \sigma_{s,H^+} \frac{w}{l} t \overset{w=l}{=} \sigma_{s,H^+} t = F u_{H^+} c_{H^+} t = F u_{H^+} \gamma_{H^+} \quad \text{Eq. 7}$$

where we have also replaced the protonic surface layer volume concentration c_{H^+} with surface concentration γ_{H^+} (in mol/cm^2) and layer thickness t in $c_{H^+} = \gamma_{H^+} / t$. As stated above, we here treat the surface layer as one, and we have deliberately used subscript s to distinguish conductance and conductivity of the surface layer from other geometries, while we have omitted the superscript s for concentration and mobility terms to avoid build-up of too many subscripts later on.

2.4.2 Charge mobility of protons

We now consider the diffusivity and charge mobility of protons. Since the proton is a defect on oxide surfaces, its random diffusivity D_{H^+} is in the classic approximation we will use here a simple activated function, multiplied by the chance X_O that the oxide ion it jumps to is available to accept the proton

$$D_{H^+} = X_O D_{H^+0} \exp\left(\frac{-\Delta H_{m,H^+}}{RT}\right) \quad \text{Eq. 8}$$

where X_O is the fractional occupancy of any oxide-ion containing species, O^{2-}, OH^-, or H_2O, that can accept a proton, depending on the mechanism.

The preexponential of proton diffusivity is given by

$$D_{H^+0} = A s^2 \omega_0 \cdot \exp(\tfrac{\Delta S_m}{R}) \quad \text{Eq. 9}$$

where A is a geometrical factor of the order of unity, s is the jump distance, ω_0 is the vibrational attempt frequency, and ΔS_m is the entropy of the energy barrier. The proton always jumps from its host oxide ion to a nearest one, so we may take the effective jump distance to be 2.8 ≈ 3 Å. The vibrational attempt frequency ω_0 is in practice that of the oxide ion host, of the order of 10^{12} /s (not the 10^{13} /s of the proton itself). With this, we get $D_{H^+0} \approx 1 \cdot 10^{-3}$ cm^2/s as an order of magnitude estimate of preexponentials, irrespective of mechanism or host system.

The charge mobility of protons u_{H^+} and proton diffusivity D_{H^+} are further linked through the Nernst-Einstein relation $u = zeB = \frac{ze}{kT} D = \frac{zE}{RT} D$ as

$$u_{H^+} = \frac{F}{RT} D_{H^+} = X_O \frac{F}{RT} D_{H^+0} \exp\left(\frac{-\Delta H_{m,H^+}}{RT}\right) = X_O \frac{1}{T} u_{H^+0} \exp\left(\frac{-\Delta H_{m,H^+}}{RT}\right) \quad \text{Eq. 10}$$

where $u_{H^+0} = \frac{F}{R} D_{H^+0}$. Taken $D_{H^+0} \approx 1 \cdot 10^{-3}$ cm^2/s as derived above, we yield $u_{H^+0} \approx 10$ cm^{2}K/Vs. $\Delta H_{m,H^+}$ is the enthalpy of proton mobility.

The enthalpy of proton mobility $\Delta H_{m,H^+}$ of porous oxides is still unknown. On the other hand, measuring the temperature dependence of conductivity at constant relative humidity (*RH*) result in an activation enthalpy reflecting the sum of the dissociation enthalpy (*i.e.,* defect formation) and mobility enthalpy. At given *RH*, the concentration of water is considered more or less equal (based on the BET isotherm as we will see later in **Section 2.7.1**), in other words, the water coverage is constant. Stub *et al.* [81] measured the conductivity of YSZ at constant *RH* in the region of physisorption, and revealed ΔH_{RH} around 43-34 kJ/mol at *RH* of 20–60%. Colomer [100, 101] studied the temperature dependence of proton conductivity (from 25-80°C) of nanoporous anatase TiO_2 thin films at different *RH* and found the activation enthalpies to be 36 kJ/mol at *RH* of 33%, and 33 kJ/mol at *RH* of 58%.

2.5 Nomenclature

2.5.1 Surface species

In the following, I will derive the thermodynamics of adsorption and dissociation on an oxide M_aO_b, with the aim to obtain the area-specific concentration of protons and combine it with charge mobility to get conductance and conductivity. For this sake, I will define and use structural surface sites and adsorbed species as defects, so that we can apply statistical thermodynamics and diffusional transport theory. I will use a Kröger-Vink compatible notation for surface chemistry in which superscripts ^{x}, $^/$, and $^\bullet$ denote, respectively, neutral, negative, and positive effective charges compared to the charge of the clean, "perfect" surface. For compatibility with other binary oxides, I furthermore choose to denote cations by the general symbol *M*, so that *M* denotes the cation in the binary oxides, and surface cation and oxide ion sites are hence denoted M_s and O_s.

2.5.2 Adsorption, dissociation, and transport

I further introduce subscripts of three levels to identify processes and their thermodynamic and kinetic parameters. First level subscripts contain a letter denoting **a**dsorption, **d**issociation, and **m**igration, while second level subscripts have a first letter denoting **c**hemisorbed (*vs.* **p**hysisorbed), a second letter denoting **m**olecular *vs.* **d**issociative, a third letter denoting whether the dissociated proton goes to the **s**urface oxide ion or the **a**dsorbed water molecule, and – following a dash – one or two letters stating the transport of protons, including migration of

protons between oxide ions in the surface layer (**–s**), between a surface oxide ion and an adsorbed hydroxide ion (**–sa**), or between water and an ionised species in the adsorbed layer (**–a**). A comprehensive list of symbols and abbreviations is provided in **Appendix I**.

2.6 Molecular and dissociative chemisorption

I start by predicting the behaviour of surface protonic conductivity in the chemisorbed layer, which dominates typically in wet atmospheres at high temperatures down to around 200°C.

2.6.1 Thermodynamics and concentration of water

2.6.1.1 Thermodynamics of molecular chemisorption

H_2O adsorbs first on a surface M^{4+} cation, but it may not easily dissociate protons H^+ to surface oxide ions O^{2-} or to other water molecules. The lack of dissociation, *i.e.,* an endothermic dissociation enthalpy, leaves the overall chemisorption weak (only modestly exothermic adsorption enthalpy, dominated by unfavourable entropy) and leaves the layer covered by molecular H_2O. Molecular (associative) chemisorption of water ("cm") is in our nomenclature written as

$$M_{M_s}^{x} + \mathrm{H_2O}(g) \rightleftharpoons M_{M_s}\mathrm{OH}_2^{x} \qquad \text{Eq. 11}$$

where M denotes the cation in binary oxides. Surface cation and oxide ion sites are denoted M_s and O_s, respectively.

The equilibrium coefficient (adsorption coefficient) for Eq. 11 can be expressed as per

$$K_{\mathrm{a_{cm}}} = \frac{X_{M_{M_s}\mathrm{OH}_2^{x}}}{X_{M_{M_s}^{x}} \frac{p_{\mathrm{H_2O}(g)}}{p^0}} = \frac{\gamma_{M_{M_s}\mathrm{OH}_2^{x}}}{\gamma_{M_{M_s}^{x}} \frac{p_{H_2O}}{p^0}} = \exp\left(\frac{\Delta S^0_{\mathrm{a_{cm}}}}{R}\right)\exp\left(\frac{-\Delta H^0_{\mathrm{a_{cm}}}}{RT}\right) \qquad \text{Eq. 12}$$

where X denotes fractional occupancy (which ideally corresponds to activity and also to surface site coverage), R is gas constant, p is partial pressure, and γ is surface concentration, $\Delta S^0_{\mathrm{a_{cm}}}$ and $\Delta H^0_{\mathrm{a_{cm}}}$ are the standard entropy and enthalpy change of chemisorption, respectively.

In general, molecular chemisorption is exothermic and the standard enthalpy of chemisorption hence predictably negative. Calorimetric approaches have been extensively used for the determination of the standard enthalpy of molecular chemisorption on pure and doped compounds, in addition to calculations using density functional theory.[96, 123-127] The structural inhomogeneity of oxide surfaces causes considerable variations in adsorption enthalpies, which in general becomes less exothermic with increasing water coverage.

On the other hand, the standard entropy change $\Delta S^0_{a_{cm}}$ plays a major role and represents a considerable uncertainty. Such adsorption has predictable negative standard entropy given by loss of one mole of gas, empirically within -120 ± 20 J/molK.[128] Condensation of water vapor to liquid water has a standard entropy change of -109 J/molK at 100°C.[129] It decreases strongly with temperature, e.g. to -44 J/molK at 300°C, which is relevant for chemisorption temperature range. Nevertheless, the entropy of condensation to ice is larger than to water (-144 *vs* -118 J/molK at RT) and the entropy of molecular adsorption to hydroxylated α-Fe_2O_3, *i.e.,* physisorption, has been reported to be -138 J/molK.[130, 131] Differences in entropy may also arise from polymorphism, as evidenced for monoclinic and yttria-stabilized cubic ZrO_2.[132, 133] For the sake of convenience, we will hence in this thesis for the most part use the -109 J/molK for the entropy of condensation to water at 100°C as an estimate of $\Delta S^0_{a_{cm}}$. This implies uncertainties of several orders of magnitude in our calculations of conductances, yet helps to differentiate different proton transport models – this will be treated later in **Section 2.6.3**. With $\Delta S^0_{a_{cm}} \approx$ -109 J/molK, the preexponential of equilibrium coefficient becomes $K^0_{a_{cm}} = \exp\left(\frac{\Delta S^0_{a_{cm}}}{R}\right) = 2.0 \cdot 10^{-6}$.

2.6.1.2 Concentration of adsorbed water

The concentration of adsorbed water according to the molecular chemisorption model follows normal adsorption isotherms, *i.e.,* the Langmuir isotherms, which holds under the assumptions of no interaction between adsorbed water molecules and that the surface is uniform.[134, 135] The Langmuir adsorption isotherm is represented by Eq. 12, which can be rearranged to

$$\gamma_{M_{M_s}OH_2^x} = \frac{K_{a_{cm}} \frac{p_{H_2O}}{p^0}}{1 + K_{a_{cm}} \frac{p_{H_2O}}{p^0}} \gamma_{M_s} \qquad \text{Eq. 13}$$

where cation surface site balance requires $\gamma_{M_s} = \gamma_{M_{M_s}OH_2^x} + \gamma_{M^x_{M_s}}$, and $K_{a_{cm}}$ can be expressed in terms of T, $\Delta S^0_{a_{cm}}$ and $\Delta H^0_{a_{cm}}$ given by Eq. 12.

At low coverage (high T, low p_{H_2O} and RH), we have $\gamma_{M_{M_s}OH_2^x} << \gamma_{M^x_{M_s}} \approx \gamma_{M_s}$. Eq. 13 thus simplifies to

$$\gamma_{M_{M_s}OH_2^x} \approx \gamma_{M_s} K_{a_{cm}} \frac{p_{H_2O}}{p^0} \qquad \text{Eq. 14}$$

so that the coverage would be proportional to p_{H_2O} (and hence RH at constant T), but involves the enthalpy of adsorption providing a temperature dependence at constant p_{H_2O}.

At relatively high *RH* (low *T*), the molecular chemisorbed layer may reach complete coverage

$$\gamma_{M_{M_s}\mathrm{OH}_2^x} = \gamma_{M_s} = \text{constant} \qquad \text{Eq. 15}$$

hence independent of both T and $p_{\mathrm{H_2O}}$ (*RH*). As an estimate of average cation surface concentration and hence adsorption sites we use 5 H_2O per nm^2 as an ideal monolayer coverage,[126] *i.e.*, γ_{M_s} = 5 /nm^2 = 8·10^{-10} mol/cm^2.

Figure 10 illustrates the relative coverage of water $X_{M_{M_s}\mathrm{OH}_2^x}$ as a function of inverse temperature (Figure 10 a) and as a function of $p_{\mathrm{H_2O}}$ (Figure 10 b) according to Eq. 13 with $\Delta S^0_{\mathrm{a_{cm}}}$ = -109 J/molK, and $\Delta H^0_{\mathrm{a_{cm}}}$ = -74 kJ/mol for YSZ,[127] as compared to existing literature values (dashed lines). Raz *et al.* [136] first adopted $\Delta H^0_{\mathrm{a_{cm}}}$ = -100 kJ/mol with $\frac{1}{p_{\mathrm{H_2O}} K^0_{\mathrm{a_{cm}}}}$ = 2.0·10^5 and $\Delta H^0_{\mathrm{a_{cm}}}$ = -200 kJ/mol with $\frac{1}{p_{\mathrm{H_2O}} K^0_{\mathrm{a_{cm}}}}$ = 8.0·10^9. In their case, the preexponentials $K^0_{\mathrm{a_{cm}}}$ were adjusted to keep the change in both cases in the vicinity of 600°C. More recently, Stub *et al.* [137] used $\Delta H^0_{\mathrm{a_{cm}}}$ of -74 kJ/mol for YSZ and $\Delta S^0_{\mathrm{a_{cm}}}$ = -87 J/molK in order to have a fully covered chemisorbed layer around 250°C.

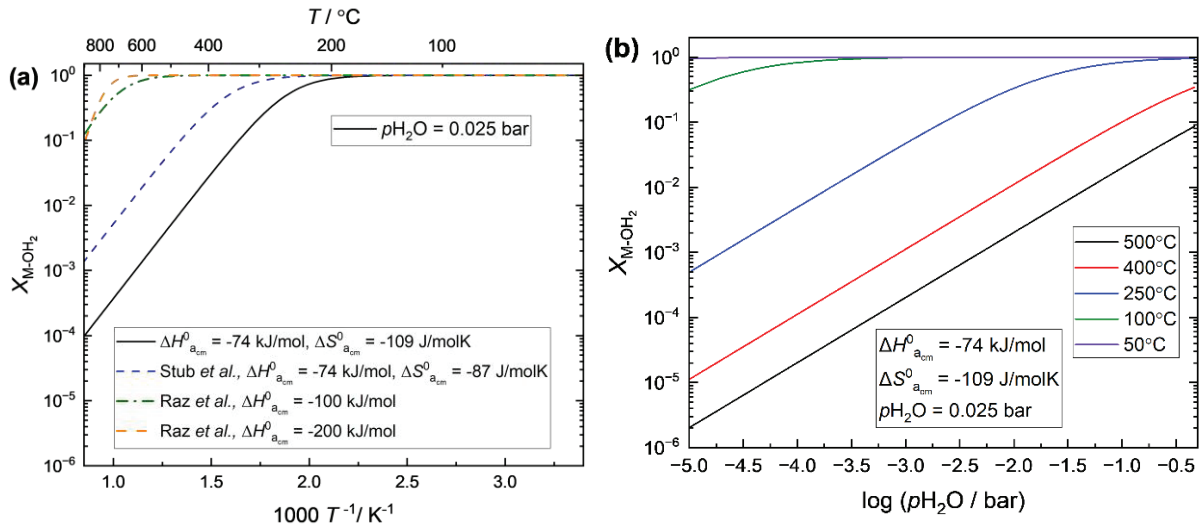

Figure 10 Langmuir adsorption for molecular chemisorption represented as (a) relative coverage $X_{M_{M_s}\mathrm{OH}_2^x}$ *vs* 1/*T* at $p_{\mathrm{H_2O}}$ = 0.025 bar with $\Delta H^0_{\mathrm{a_{cm}}}$ = -74 kJ/mol and $\Delta S^0_{\mathrm{a_{cm}}}$ = -109 J/molK (black line) as compared to literature values (dashed lines) given in ref. [136, 137], (b) relative coverage $X_{M_{M_s}\mathrm{OH}_2^x}$ *vs* $p_{\mathrm{H_2O}}$ at different temperatures.

2.6.1.3 Thermodynamics of dissociative chemisorption

Molecular chemisorption with dissociation to surface oxide ions

The adsorbed H_2O may dissociate into an adsorbed OH^- and a proton on a surface oxide ion forming surface hydroxide ion OH^- according to

$$M_{M_s}\mathrm{OH}_2^{\mathrm{x}} + \mathrm{O}_{\mathrm{O}_s}^{\mathrm{x}} \rightleftharpoons M_{M_s}\mathrm{OH}^{/} + \mathrm{OH}_{\mathrm{O}_s}^{\bullet} \qquad \text{Eq. 16}$$

with equilibrium coefficient

$$K_{\mathrm{d_{cs}}} = \frac{X_{M_{M_s}\mathrm{OH}^{/}} X_{\mathrm{OH}_{\mathrm{O}_s}^{\bullet}}}{X_{M_{M_s}\mathrm{OH}_2^{\mathrm{x}}} X_{\mathrm{O}_{\mathrm{O}_s}^{\mathrm{x}}}} = \frac{\gamma_{M_{M_s}\mathrm{OH}^{/}} \gamma_{\mathrm{OH}_{\mathrm{O}_s}^{\bullet}}}{\gamma_{M_{M_s}\mathrm{OH}_2^{\mathrm{x}}} \gamma_{\mathrm{O}_{\mathrm{O}_s}^{\mathrm{x}}}} = \exp\left(\frac{\Delta S_{\mathrm{d_{cs}}}^0}{R}\right)\exp\left(\frac{-\Delta H_{\mathrm{d_{cs}}}^0}{RT}\right) \qquad \text{Eq. 17}$$

The standard entropy change is unknown, but should be modest since no gas molecules are involved. The large negative dissociation entropy of liquid water – caused by hydration of ions - need not apply here, since there is no hydration. We will hence assume $\Delta S_{\mathrm{d_{cs}}}^0 = 0$ J/molK. The enthalpy of dissociation to surface, $\Delta H_{\mathrm{d_{cs}}}^0$, is expectedly positive.

Dissociative chemisorption

Dissociation of protons onto surface oxide ions may be sufficiently favourable to dissociate all adsorbed molecules in what is termed dissociative chemisorption ("*cds*"), which we may write without the molecular intermediate directly as the sum of the reactions in Eq. 11 and Eq. 16

$$M_{M_s}^{\mathrm{x}} + \mathrm{O}_{\mathrm{O}_s}^{\mathrm{x}} + \mathrm{H_2O}(g) \rightleftharpoons M_{M_s}\mathrm{OH}^{/} + \mathrm{OH}_{\mathrm{O}_s}^{\bullet} \qquad \text{Eq. 18}$$

The equilibrium coefficient is then (from now on omitting the stage of site fractions)

$$K_{\mathrm{a_{cds}}} = K_{\mathrm{a_{cm}}} K_{\mathrm{d_{cs}}} = \frac{\gamma_{M_{M_s}\mathrm{OH}^{/}} \gamma_{\mathrm{OH}_{\mathrm{O}_s}^{\bullet}}}{\gamma_{M_{M_s}^{\mathrm{x}}} \gamma_{\mathrm{O}_{\mathrm{O}_s}^{\mathrm{x}}} \frac{p_{\mathrm{H_2O}}}{p^0}} = \exp\left(\frac{\Delta S_{\mathrm{a_{cds}}}^0}{R}\right)\exp\left(\frac{-\Delta H_{\mathrm{a_{cds}}}^0}{RT}\right) \qquad \text{Eq. 19}$$

where the standard entropy and enthalpy changes are sums of those for molecular chemisorption and dissociation: $\Delta S_{\mathrm{a_{cds}}}^0 = \Delta S_{\mathrm{a_{cm}}}^0 + \Delta S_{\mathrm{d_{cs}}}^0$ and $\Delta H_{\mathrm{a_{cds}}}^0 = \Delta H_{\mathrm{a_{cm}}}^0 + \Delta H_{\mathrm{d_{cs}}}^0$. Here, $\Delta S_{\mathrm{a_{cds}}}^0$ is taken to be -109 + 0 = -109 J/molK.

Regardless of whether we have weak dissociation and hence molecular chemisorption ("*cm*") or dissociative chemisorption ("*cd*"), the simplified electroneutrality condition is given as

$$\gamma_{\mathrm{OH}_{\mathrm{O}_s}^{\bullet}} = \gamma_{M_{M_s}\mathrm{OH}^{/}} \qquad \text{Eq. 20}$$

Insertion into Eq. 19 yields

$$\gamma_{\mathrm{OH}^{\bullet}_{\mathrm{O}_s}} = \gamma_{M_{M_s}\mathrm{OH}^{/}} = \sqrt{K_{\mathrm{a_{cds}}}\gamma_{M^{\mathrm{x}}_{M_s}}\gamma_{\mathrm{O}^{\mathrm{x}}_{\mathrm{O}_s}}\frac{p_{\mathrm{H_2O}}}{p^0}} \qquad \text{Eq. 21}$$

where cation surface site balance follows $\gamma_{M_s} = \gamma_{M_{M_s}\mathrm{OH}^{/}} + \gamma_{M^{\mathrm{x}}_{M_s}}$, oxide surface site balance requires $\gamma_{\mathrm{O}_s} = \gamma_{\mathrm{O}^{\mathrm{x}}_{\mathrm{O}_s}} + \gamma_{\mathrm{OH}^{\bullet}_{\mathrm{O}_s}}$.

In $M\mathrm{O}_2$ oxides where $\gamma_{\mathrm{O}_s} = 2\gamma_{M_s}$, the concentration of dissociatively chemisorbed water is written as

$$\gamma_{\mathrm{OH}^{\bullet}_{\mathrm{O}_s}} = \gamma_{M_{M_s}\mathrm{OH}^{/}} = \frac{-3K_{\mathrm{a_{cds}}}\frac{p_{\mathrm{H_2O}}}{p^0}\gamma_{M_s} \pm \sqrt{(3K_{\mathrm{a_{cds}}}\frac{p_{\mathrm{H_2O}}}{p^0}\gamma_{M_s})^2 + 8(1-K_{\mathrm{a_{cds}}}\frac{p_{\mathrm{H_2O}}}{p^0})K_{\mathrm{a_{cds}}}\frac{p_{\mathrm{H_2O}}}{p^0}\gamma^2_{M_{M_s}\mathrm{OH}^{/}}\gamma^2_{\gamma_{M_s}}}}{2(1-K_{\mathrm{a_{cds}}}\frac{p_{\mathrm{H_2O}}}{p^0})} \qquad \text{Eq. 22}$$

At low coverage, applying $\gamma_{M^{\mathrm{x}}_{M_s}} \approx \gamma_{M_s}$ and $\gamma_{\mathrm{O}^{\mathrm{x}}_{\mathrm{O}_s}} \approx \gamma_{\mathrm{O}_s} = 2\gamma_{M_s}$, we get

$$\gamma_{\mathrm{OH}^{\bullet}_{\mathrm{O}_s}} = \gamma_{M_{M_s}\mathrm{OH}^{/}} = \gamma_{M_s}\sqrt{2K_{\mathrm{a_{cds}}}\frac{p_{\mathrm{H_2O}}}{p^0}} \qquad \text{Eq. 23}$$

As can be seen, the coverage will follow a $p^{1/2}_{\mathrm{H_2O}}$ dependence in this case. This indicates that dissociation will still be strong, even though the overall chemisorption is weak.

We may consider the strongly dissociative chemisorption by Eq. 18 as a case where we may reach full coverage and obtain

$$\gamma_{\mathrm{OH}^{\bullet}_{\mathrm{O}_s}} = \gamma_{M_{M_s}\mathrm{OH}^{/}} = \gamma_{M_s} = \text{constant} \qquad \text{Eq. 24}$$

Molecular chemisorption with dissociation to adsorbed water molecules

Chemisorbed $\mathrm{H_2O}$ may also dissociate within the molecular layer into adsorbed $\mathrm{OH^-}$ ions and adsorbed $\mathrm{H_3O^+}$ ions as treated by Raz *et al.* [136] In our nomenclature it is written as

$$2M_{M_s}\mathrm{OH}^{\mathrm{x}}_2 \rightleftharpoons M_{M_s}\mathrm{OH}^{/} + M_{M_s}\mathrm{OH}^{\bullet}_3 \qquad \text{Eq. 25}$$

and the corresponding equilibrium coefficient can then be written as

$$K_{\mathrm{d_{ca}}} = \frac{X_{M_{M_s}\mathrm{OH}^{/}}X_{M_{M_s}\mathrm{OH}^{\bullet}_3}}{X^2_{M_{M_s}\mathrm{OH}^{\mathrm{x}}_2}} = \frac{\gamma_{M_{M_s}\mathrm{OH}^{/}}\gamma_{M_{M_s}\mathrm{OH}^{\bullet}_3}}{\gamma^2_{M_{M_s}\mathrm{OH}^{\mathrm{x}}_2}} = \exp\left(\frac{\Delta S^0_{\mathrm{d_{ca}}}}{R}\right)\exp\left(\frac{-\Delta H^0_{\mathrm{d_{ca}}}}{RT}\right) \qquad \text{Eq. 26}$$

Assuming that this dissociation has again a negligible standard entropy $\Delta S^0_{\mathrm{d_{ca}}} = 0$ J/molK, while the enthalpy should be higher than for dissociation to surface oxygen.

The total electroneutrality condition now becomes

$$\gamma_{\mathrm{OH}^{\bullet}_{\mathrm{O_s}}} + \gamma_{M_{M_s}\mathrm{OH}^{\bullet}_{3}} = \gamma_{M_{M_s}\mathrm{OH}^{/}} \qquad \text{Eq. 27}$$

If dissociation to the surface oxide ions dominates and Eq. 23 applies, insertion into Eq. 26 yields the concentration of minority hydronium ions, but this plays no role, as proton transport in the chemisorbed layer then will take place mainly between the majority adsorbed hydroxide ions and water molecules.

If instead dissociation within the chemisorbed layer dominates, electroneutrality simplifies to

$$\gamma_{M_{M_s}\mathrm{OH}^{\bullet}_{3}} = \gamma_{M_{M_s}\mathrm{OH}^{/}} \qquad \text{Eq. 28}$$

and cation surface site balance requires $\gamma_{M^{\mathrm{x}}_{M_s}} + \gamma_{M_{M_s}\mathrm{OH}^{\mathrm{x}}_{2}} + \gamma_{M_{M_s}\mathrm{OH}^{/}} + \gamma_{M_{M_s}\mathrm{OH}^{\bullet}_{3}} = \gamma_{M_s}$, and oxide surface site balance requires $\gamma_{\mathrm{O}^{\mathrm{x}}_{\mathrm{O_s}}} + \gamma_{\mathrm{OH}^{\bullet}_{\mathrm{O_s}}} = \gamma_{\mathrm{O_s}}$.

In the following, we assume that dissociation in the molecular layer must remain incomplete. With low coverage and limited dissociation, $\gamma_{M^{\mathrm{x}}_{M_s}} \approx \gamma_{M_s} >> \gamma_{M_{M_s}\mathrm{OH}^{\mathrm{x}}_{2}} >> \gamma_{M_{M_s}\mathrm{OH}^{/}} + \gamma_{M_{M_s}\mathrm{OH}^{\bullet}_{3}}$. We can insert and simplify to get the concentration of the dissociated species

$$K_{\mathrm{d_{ca}}} = \frac{\gamma^2_{M_{M_s}\mathrm{OH}^{/}}}{\left(K_{\mathrm{a_{cm}}}\gamma_{M_s}\dfrac{p_{\mathrm{H_2O}}}{p^0}\right)^2} \quad \Rightarrow \quad \gamma_{M_{M_s}\mathrm{OH}^{\bullet}_{3}} = \gamma_{M_{M_s}\mathrm{OH}^{/}} = \gamma_{M_s} K_{\mathrm{a_{cm}}}\sqrt{K_{\mathrm{d_{ca}}}}\frac{p_{\mathrm{H_2O}}}{p^0} \qquad \text{Eq. 29}$$

At full coverage within the molecular chemisorbed layer, and that dissociation within this layer is weak, the cation surface site balance becomes $\gamma_{M_{M_s}\mathrm{OH}^{\mathrm{x}}_{2}} \approx \gamma_{M_s}$, and we can insert and simplify to get the temperature dependence of the dissociated species

$$K_{\mathrm{d_{ca}}} = \frac{\gamma^2_{M_{M_s}\mathrm{OH}^{/}}}{\gamma^2_{M_s}} \quad \Rightarrow \quad \gamma_{M_{M_s}\mathrm{OH}^{\bullet}_{3}} = \gamma_{M_{M_s}\mathrm{OH}^{/}} = \gamma_{M_s}\sqrt{K_{\mathrm{d_{ca}}}} \qquad \text{Eq. 30}$$

As summarized in Table 1, in all cases of molecular chemisorption following Eq. 11 and Eq. 12, measurements of water adsorption and coverage (for instance by sorption and TG measurements) will reflect the amount of molecular water given by Eq. 14 in the low coverage region with a $p^1_{\mathrm{H_2O}}$ dependence, and Eq. 15 in the high coverage cases (*i.e.,* independent of $p_{\mathrm{H_2O}}$). In the case of dissociative adsorption, on the other hand, following Eq. 18, adsorption and coverage are determined by the dissociated charged species and have a $p^{1/2}_{\mathrm{H_2O}}$ dependence (Eq. 23). As we shall see later, conduction always follows the dissociated species and may have the same or other $p_{\mathrm{H_2O}}$ dependences. When the models reach full coverage, the $p_{\mathrm{H_2O}}$

dependences always disappear, both for total water contents and for dissociated species by conductance.

Table 1 Derived p_{H_2O} dependences of water adsorption and coverage based on the thermodynamics of adsorption and dissociation in cases of low and full coverage.

***n* in $p_{H_2O}^n$ at**	**Low coverage**	**Full coverage**
Molecular chemisorption, "***cm***"	1	0
Dissociative chemisorption, "***cd***"	1/2	0

2.6.2 Protonic conduction in chemisorbed water

In order to evaluate conduction, some simplified cases of proton migration are taken. In the following reactions, the proton jumps from the first to the second species (see also schematic illustrations below).

Migration of protons between surface hydroxide and oxide ions, with charge mobility $u_{H^+_s}$:

$$OH^{\bullet}_{O_s} + O^{x}_{O_s} \rightleftharpoons O^{x}_{O_s} + OH^{\bullet}_{O_s} \qquad \text{Eq. 31}$$

Migration between surface and adsorbed hydroxide ions (reverse and forward dissociation), with charge mobility $u_{H^+_{sa}}$:

$$OH^{\bullet}_{O_s} + M_{M_s}OH^{/} \rightleftharpoons O^{x}_{O_s} + M_{M_s}OH^{x}_{2} \qquad \text{Eq. 32}$$

Migration in the adsorbed layer between water molecules and hydroxide ions, with charge mobility $u_{H^+_a}$:

$$M_{M_s}OH^{x}_{2} + M_{M_s}OH^{/} \rightleftharpoons M_{M_s}OH^{/} + M_{M_s}OH^{x}_{2} \qquad \text{Eq. 33}$$

Migration between hydroxonium ions and water molecules, assumed to have numerically the same charge mobility $u_{H^+_a}$:

$$M_{M_s}OH^{\bullet}_{3} + M_{M_s}OH^{x}_{2} \rightleftharpoons M_{M_s}OH^{x}_{2} + M_{M_s}OH^{\bullet}_{3} \qquad \text{Eq. 34}$$

It should be noted that all these mobilities will be treated according to analysis of $u_{H^+_s}$ introduced in **Section 2.4.2**. They hence have the same preexponentials, $u_{H^+_s0}$, but different activation energies. Generally speaking, the activation energies decrease, and mobilities hence increase, as we go from the protons on the rigid surface, via jumps between the surface and the adsorbed layer, to jumps between adsorbed and hence more vibrant species.

2.6.3 Models for surface protonic conduction in the chemisorbed water layer

I will now move on to derive expressions for surface protonic conduction based on the thermodynamics and different proton transport pathways introduced in the preceding sections. In the following, the "forth level" in our nomenclature (**Section 2.5.2**) showing proton migration following a dash (–s, –sa, –a) comes in.

The mechanisms that describe surface protonic conductivity in porous oxides are furthermore schematically depicted as they are coupled with the thermodynamics that determines carrier and jump site concentrations to obtain surface conductances. In order to demonstrate the structure of oxide surfaces, all the schematics has been generalized with the (111) surface of CeO_2 for illustrative purposes.

Proton migration between surface oxide ions: cms-s and cds-s

A schematic illustration of the *cms-s* and *cds-s* models for adsorption, dissociation and proton migration at various water coverage is provided in Figure 11.

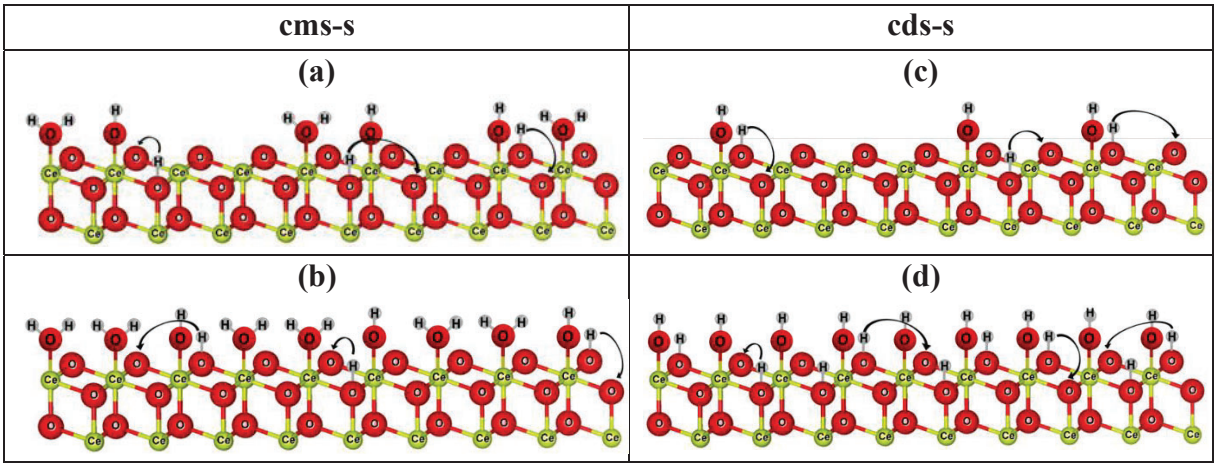

Figure 11 Schematic illustration of the "*cms-s*" model on the (111) surface of CeO_2 at low coverage (a) and at full coverage of molecular water with low dissociation (b), "*cds-s*" model at low coverage (c) and at full coverage of dissociatively chemisorbed water (d). The arrows show the protonic migration.

The proton on surface oxide in the $OH^{\bullet}_{O_s}$ defect may migrate by jumping to other surface oxide ions. The surface protonic conductance according to Eq. 7 is denoted as:

$$G_{s,H^+_{cds\text{-}s}} = G_{s,H^+_{cms\text{-}s}} = F\gamma_{OH^{\bullet}_{O_s}} u_{H^+_s} = F\gamma_{OH^{\bullet}_{O_s}} X_{O^x_{O_s}} u_{H^+0} \frac{1}{T} \exp\left(\frac{-\Delta H_{m,H^+_s}}{RT}\right) \qquad \text{Eq. 35}$$

In the case of low coverage (Figure 11 a and c), unprotonated surface oxide ions are generally available, $X_{O^x_{O_s}} \approx 1$, so that we by inserting Eq. 23 get

$$G_{\mathrm{s,H^+_{cms\text{-}s}}} = F\gamma_{M_s}\sqrt{2K_{\mathrm{a_{cds}}}\frac{p_{\mathrm{H_2O}}}{p^0}}u_{\mathrm{H^+0}}\frac{1}{T}\exp\left(\frac{-\Delta H_{\mathrm{m,H^+_s}}}{RT}\right) \qquad \text{Eq. 36}$$

which we may express as

$$G_{\mathrm{s,H^+_{cms\text{-}s}}} = G_{\mathrm{s,H^+_{cms\text{-}s}0}}\frac{1}{T}\exp\left(\frac{-\left(\frac{1}{2}\Delta H^0_{\mathrm{a_{cm}}} + \frac{1}{2}\Delta H^0_{\mathrm{d_{cs}}} + \Delta H_{\mathrm{m,H^+_s}}\right)}{RT}\right) \qquad \text{Eq. 37}$$

In this case, the apparent activation enthalpy of conductance should be interpreted according to $\Delta H_{\mathrm{c_{cms\text{-}s}}} = \Delta H_{\mathrm{c_{cds\text{-}s}}} = \frac{1}{2}\Delta H^0_{\mathrm{a_{cm}}} + \frac{1}{2}\Delta H^0_{\mathrm{d_{cs}}} + \Delta H_{\mathrm{m,H^+_s}}$.

The preexponential of surface protonic conductance is given by

$$G_{\mathrm{s,H^+_{cms\text{-}s}0}} = G^0_{\mathrm{s,H^+_{cms\text{-}s}0}}\sqrt{\frac{p_{\mathrm{H_2O}}}{p^0}} = \sqrt{2}F\gamma_{M_s}\exp\left(\frac{\frac{1}{2}\Delta S^0_{\mathrm{a_{cm}}} + \frac{1}{2}\Delta S^0_{\mathrm{d_{cs}}}}{R}\right)u_{\mathrm{H^+0}}\sqrt{\frac{p_{\mathrm{H_2O}}}{p^0}} \qquad \text{Eq. 38}$$

where $G^0_{\mathrm{s,H^+_{cms\text{-}s}0}}$ is the standard preexponential of surface protonic conductance at $p_{\mathrm{H_2O}}$ = 1 bar. $G^0_{\mathrm{s,H^+_{chm}0}}$ is hence the most fundamental parameter specific for a surface and a particular adsorption and transport model. To derive such a fundamental parameter is only meaningful once a model is chosen, so that the $p_{\mathrm{H_2O}}$ dependency is clear.

The $G^0_{\mathrm{s,H^+_{cms\text{-}s}0}}$ is furthermore predicted using the estimates made above, $\Delta S^0_{\mathrm{a_{cm}}}$ = -109 J/molK, $\Delta S^0_{\mathrm{d_{cs}}}$ = 0 J/molK, $\gamma_{M_s} \approx 5$ /nm^2 = 8·10^{-10} mol/cm^2, and $u_{\mathrm{H^+0}} \approx 10$ cm^{2}K/Vs. As a result, $G^0_{\mathrm{s,H^+_{cms\text{-}s}0}}$ turns out as 1.6·10^{-6} SK at $p_{\mathrm{H_2O}}$ = 1 bar.

We note that for low coverage and proton migration on surface oxide ions, the above applies to surface protonic conduction regardless of whether the chemisorbed water remains mainly molecular or mainly dissociated, applying to models *cms-s* and *cds-s*.

However, the measurement of the amount of adsorbed water follows either the dominant molecular species H_2O with a $p^1_{\mathrm{H_2O}}$ dependence (different from the conductance) or the dominant dissociated species with a $p^{1/2}_{\mathrm{H_2O}}$ dependence (same as conductance), see $p_{\mathrm{H_2O}}$ dependences for total concentration of adsorbed water in Table 1 *vs* those for conductance in Table 2 (below).

At full coverage of molecularly chemisorbed water (Figure 11 b), by sufficiently low *T* and high $p_{\mathrm{H_2O}}$ and *RH*, we have instead

$$\gamma_{M_{M_s}\mathrm{OH}_2^{\mathrm{x}}} = \gamma_{M_s} >> \gamma_{M_{M_s}\mathrm{OH}^{/}} = \gamma_{\mathrm{OH}^{\bullet}_{\mathrm{O}_s}} = \sqrt{\gamma_{M_s}\gamma_{\mathrm{O}^{\mathrm{x}}_{\mathrm{O}_s}} K_{\mathrm{d_{cs}}}} \qquad \text{Eq. 39}$$

We may assume $\gamma_{\mathrm{O}^{\mathrm{x}}_{\mathrm{O}_s}} = \gamma_{\mathrm{O}_s} = 2\gamma_{M_s}$ so that the surface protonic conductance becomes

$$G_{\mathrm{s,H^+_{cms\text{-}s}}} = F\gamma_{M_s}\sqrt{2K_{\mathrm{d_{cms}}}}\,u_{\mathrm{H^+0}}\frac{1}{T}\exp\left(\frac{-\Delta H_{\mathrm{m,H^+_s}}}{RT}\right) = G_{\mathrm{s,H^+_{cms\text{-}s}0}}\frac{1}{T}\exp\left(\frac{-\left(\frac{1}{2}\Delta H^0_{\mathrm{d_{cs}}} + \Delta H_{\mathrm{m,H^+_s}}\right)}{RT}\right) \qquad \text{Eq. 40}$$

with preexponential of surface protonic conductance

$$G_{\mathrm{s,H^+_{cms\text{-}s}0}} = G^0_{\mathrm{s,H^+_{cms\text{-}s}0}} = \sqrt{2}F\gamma_{M_s}\exp\left(\frac{\Delta S^0_{\mathrm{d_{cs}}}}{2R}\right)u_{\mathrm{H^+0}} \qquad \text{Eq. 41}$$

In this case, the concentration of dissociated protons is independent of $p_{\mathrm{H_2O}}$, and the temperature dependence is attributable to the enthalpies of dissociation and mobility, *i.e.,* $\Delta H_{\mathrm{c_{cms\text{-}s}}} = \frac{1}{2}\Delta H^0_{\mathrm{d_{cs}}} + \Delta H_{\mathrm{m,H^+_s}}$. With parameters as before, we now get $G_{\mathrm{s,H^+_{cms\text{-}s}0}} = G^0_{\mathrm{s,H^+_{cms\text{-}s}0}} \approx 1{\cdot}10^{-3}$ SK.

At full coverage of dissociatively chemisorbed water (Figure 11 d), we will have

$$\gamma_{M_{M_s}\mathrm{OH}^{/}} = \gamma_{\mathrm{OH}^{\bullet}_{\mathrm{O}_s}} = \gamma_{M_s} \qquad \text{Eq. 42}$$

If migration of dissociated protons takes place by jumps between surface oxide host sites, we may now assume an average occupancy of $X_{\mathrm{O}^{\mathrm{x}}_{\mathrm{O}_s}} = 0.5$ since half of them are occupied with dissociated protons. The surface protonic conductance given in Eq. 35 then becomes

$$G_{\mathrm{s,H^+_{cds\text{-}s}}} = \frac{F}{2}\gamma_{M_s}u_{\mathrm{H^+0}}\frac{1}{T}\exp\left(\frac{-\Delta H_{\mathrm{m,H^+_s}}}{RT}\right) = G_{\mathrm{s,H^+_{cds\text{-}s}0}}\frac{1}{T}\exp\left(\frac{-\Delta H_{\mathrm{m,H^+_s}}}{RT}\right) \qquad \text{Eq. 43}$$

with preexponential of surface protonic conductance given by

$$G_{\mathrm{s,H^+_{cds\text{-}s}0}} = G^0_{\mathrm{s,H^+_{cds\text{-}s}0}} = \frac{F}{2}\gamma_{M_s}u_{\mathrm{H^+0}} \qquad \text{Eq. 44}$$

In this case, the concentration of dissociated protons is independent of temperature and $p_{\mathrm{H_2O}}$, and the temperature dependence is attributable to the mobility of protons alone. With the same assumptions as before, we get $G_{\mathrm{s,H^+_{cds\text{-}s}0}} = G^0_{\mathrm{s,H^+_{cds\text{-}s}0}} \approx 4{\cdot}10^{-4}$ SK. Moreover, the enthalpy will in this case reflect proton mobility only.

Proton migration between surface oxide ions and adsorbed hydroxide ions: cms-sa and cds-sa

Let us now analyse the contribution from protons jumping between the $OH^{\bullet}_{O_s}$ and $M_{M_s}OH^{/}$ defects formed in the dissociation, schematically depicted in Figure 12.

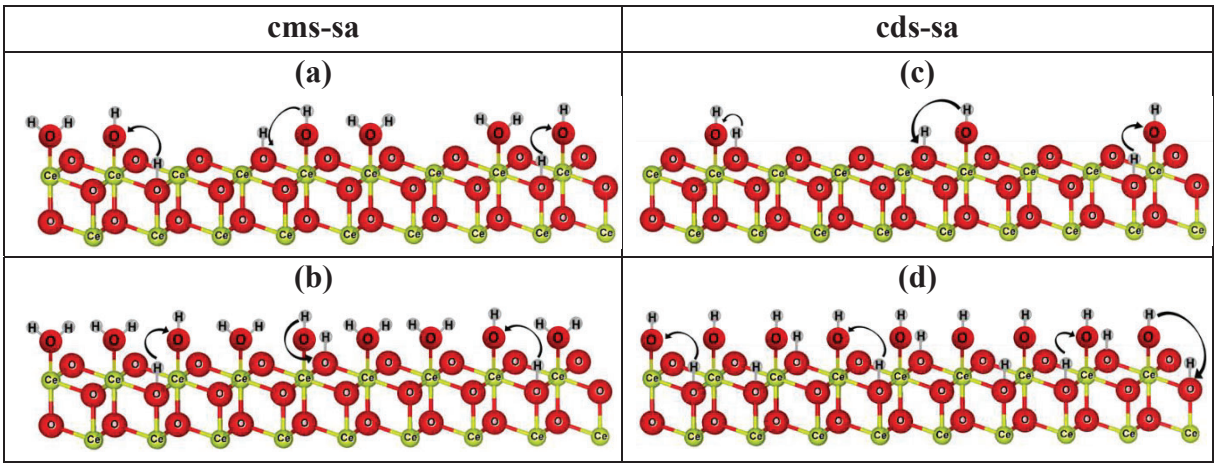

Figure 12 Schematic illustration of the "*cms-sa*" model on the (111) surface of CeO_2 at low coverage (a) and full coverage of molecular water with low dissociation (b), "*cds-sa*" model at low coverage (c) and at full coverage of dissociatively chemisorbed water (d). The arrows show the protonic migration.

The surface protonic conductance along this can be expressed in terms of the surface protons and will then be proportional to the site fraction of available dissociated adsorbed hydroxide ions

$$G_{s,H^+_{cds\text{-}sa}} = G_{s,H^+_{cms\text{-}sa}} = F\gamma_{OH^{\bullet}_{O_s}} u_{H^+_{sa}} = F\gamma_{OH^{\bullet}_{O_s}} X_{M_{M_s}OH^{/}} u_{H^+0} \frac{1}{T} \exp\left(\frac{-\Delta H_{m,H^+_{sa}}}{RT}\right) \quad \text{Eq. 45}$$

By assuming low coverage (Figure 12 a and c) and inserting Eq. 23, we get

$$G_{s,H^+_{cms\text{-}sa}} = 2FK_{a_{cm}} K_{d_{cs}} \gamma_{M_s} \frac{p_{H_2O}}{p^0} u_{H^+0} \frac{1}{T} \exp\left(\frac{-\Delta H_{m,H^+_{sa}}}{RT}\right) \quad \text{Eq. 46}$$

and hence

$$G_{s,H^+_{cms\text{-}sa}} = G_{s,H^+_{cms\text{-}sa}0} \frac{1}{T} \exp\left(\frac{-\left(\Delta H^0_{a_{cm}} + \Delta H^0_{d_{cs}} + \Delta H_{m,H^+_{sa}}\right)}{RT}\right) \quad \text{Eq. 47}$$

with $\Delta H_{c_{cms\text{-}sa}} = \Delta H^0_{a_{cm}} + \Delta H^0_{d_{cs}} + \Delta H_{m,H^+_{sa}}$.

The corresponding preexponential of surface protonic conductance is

$$G_{\mathrm{s,H^+_{cms\text{-}sa}}\,0} = G^0_{\mathrm{s,H^+_{cms\text{-}sa}}\,0}\frac{p_{\mathrm{H_2O}}}{p^0} = 2F\gamma_{M_\mathrm{s}}\exp\left(\frac{\Delta S^0_{\mathrm{a_{cm}}} + \Delta S^0_{\mathrm{d_{cs}}}}{R}\right)u_{\mathrm{H^+}0}\frac{p_{\mathrm{H_2O}}}{p^0} \qquad \text{Eq. 48}$$

With assumptions like before, we get $G^0_{\mathrm{s,H^+_{cms\text{-}sa}}\,0} \approx 3\cdot10^{-9}$ SK.

At full coverage, $\gamma_{M_{M_\mathrm{s}}\mathrm{OH}^\mathrm{x}_2} \approx \gamma_{M_\mathrm{s}}$, but still low dissociation ($\gamma_{\mathrm{O}^\mathrm{x}_{\mathrm{O_s}}} \approx \gamma_{\mathrm{O_s}} = 2\gamma_{M_\mathrm{s}}$), as illustrated by Figure 12 b, combination with Eq. 17 yields for the conductance

$$G_{\mathrm{s,H^+_{cms\text{-}sa}}} = F\gamma_{\mathrm{OH^\bullet_{O_s}}}\frac{\gamma_{M_{M_\mathrm{s}}\mathrm{OH}^/}}{\gamma_{M_\mathrm{s}}}u_{\mathrm{H^+}0}\frac{1}{T}\exp\left(\frac{-\Delta H_{\mathrm{m,H^+_{sa}}}}{RT}\right) = 2F\gamma_{M_\mathrm{s}}K_{\mathrm{d_{cs}}}u_{\mathrm{H^+}0}\frac{1}{T}\exp\left(\frac{-\Delta H_{\mathrm{m,H^+_{sa}}}}{RT}\right) \qquad \text{Eq. 49}$$

and hence

$$G_{\mathrm{s,H^+_{cms\text{-}sa}}} = G_{\mathrm{s,H^+_{cms\text{-}sa}}\,0}\frac{1}{T}\exp\left(\frac{-\left(\Delta H^0_{\mathrm{d_{cs}}} + \Delta H_{\mathrm{m,H^+_{sa}}}\right)}{RT}\right) \qquad \text{Eq. 50}$$

with preexponential of surface protonic conductance

$$G_{\mathrm{s,H^+_{cms\text{-}sa}}\,0} = G^0_{\mathrm{s,H^+_{cms\text{-}sa}}\,0} = 2F\gamma_{M_\mathrm{s}}\exp\left(\frac{\Delta S^0_{\mathrm{d_{cs}}}}{R}\right)u_{\mathrm{H^+}0} \qquad \text{Eq. 51}$$

Here, we estimate $G_{\mathrm{s,H^+_{cms\text{-}sa}}\,0} = G^0_{\mathrm{s,H^+_{cms\text{-}sa}}\,0} \approx 1.5\cdot10^{-3}$ SK.

At full coverage but now high dissociation (Figure 12 d), we have $\gamma_{\mathrm{OH^\bullet_{O_s}}} = \gamma_{M_{M_\mathrm{s}}\mathrm{OH}^/} \approx \gamma_{M_\mathrm{s}}$ which yields for the conductance

$$G_{\mathrm{s,H^+_{cds\text{-}sa}}} = F\gamma_{\mathrm{OH^\bullet_{O_s}}}\frac{\gamma_{M_{M_\mathrm{s}}\mathrm{OH}^/}}{\gamma_{M_\mathrm{s}}}u_{\mathrm{H^+}0}\frac{1}{T}\exp\left(\frac{-\Delta H_{\mathrm{m,H^+_{sa}}}}{RT}\right) = F\gamma_{M_\mathrm{s}}u_{\mathrm{H^+}0}\frac{1}{T}\exp\left(\frac{-\Delta H_{\mathrm{m,H^+_{sa}}}}{RT}\right) \qquad \text{Eq. 52}$$

and hence

$$G_{\mathrm{s,H^+_{cds\text{-}sa}}} = G_{\mathrm{s,H^+_{cds\text{-}sa}}\,0}\frac{1}{T}\exp\left(\frac{-\Delta H_{\mathrm{m,H^+_{sa}}}}{RT}\right) \qquad \text{Eq. 53}$$

with preexponential of surface protonic conductance

$$G_{\mathrm{s,H^+_{cds\text{-}sa}}\,0} = G^0_{\mathrm{s,H^+_{cds\text{-}sa}}\,0} = F\gamma_{M_\mathrm{s}}u_{\mathrm{H^+}0} \qquad \text{Eq. 54}$$

Here, we estimate $G_{\mathrm{s,H^+_{cds\text{-}sa}}\,0} = G^0_{\mathrm{s,H^+_{cds\text{-}sa}}\,0} \approx 8\cdot10^{-4}$ SK.

Proton migration between adsorbed water molecules and hydroxide ions: cms-a and cds-a

Schematic illustrations of the *cms-a* and *cds-a* models at low and full coverage are displayed in Figure 13.

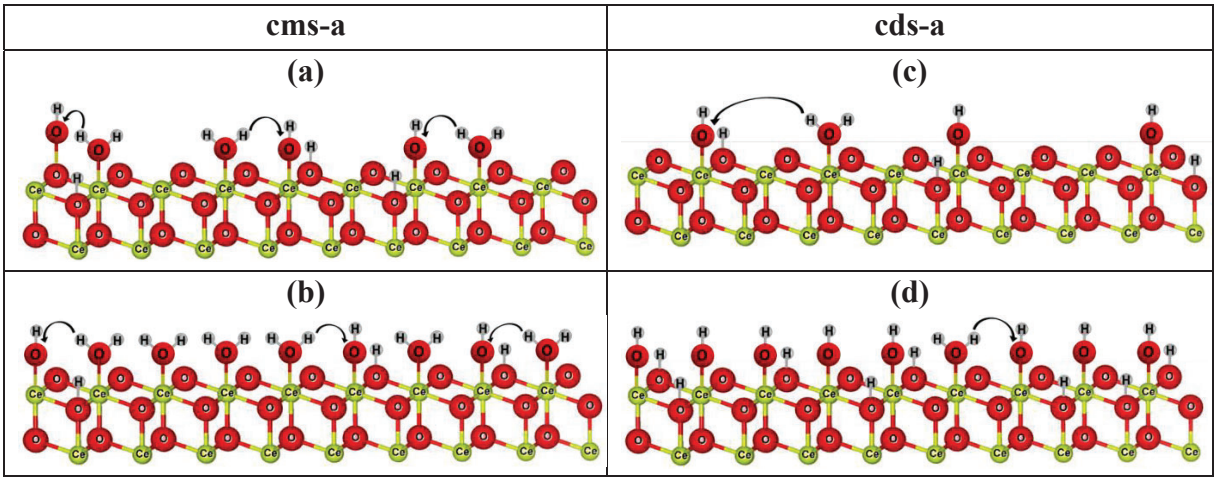

Figure 13 Schematic illustration of the "cms-a" model on the (111) surface of CeO_2 at low coverage (a) and full coverage of molecular water and low dissociation (b), "cds-a" model at low coverage (c) and full coverage with high dissociation of chemisorbed water (d). The arrows show the protonic migration.

The surface conductance based on Eq. 33 can be written

$$G_{\mathrm{s,H^+_{cds\text{-}a}}} = G_{\mathrm{s,H^+_{cms\text{-}a}}} = F\gamma_{M_{M_s}\mathrm{OH}_2^{\mathrm{x}}} u_{\mathrm{H^+_a}} = F\gamma_{M_{M_s}\mathrm{OH}_2^{\mathrm{x}}} \frac{\gamma_{M_{M_s}\mathrm{OH}^{/}}}{\gamma_{M_s}} u_{\mathrm{H^+}0} \frac{1}{T} \exp\left(\frac{-\Delta H_{\mathrm{m,H^+_a}}}{RT}\right) \qquad \text{Eq. 55}$$

which, under assumption of low coverage (Figure 13 a and c) by combination with Eq. 12 and Eq. 23 yields

$$G_{\mathrm{s,H^+_{cms\text{-}a}}} = F\gamma_{M_s} K_{\mathrm{a_{cm}}} \sqrt{2K_{\mathrm{a_{cs}}}} \left(\frac{p_{\mathrm{H_2O}}}{p^0}\right)^{3/2} u_{\mathrm{H^+}0} \frac{1}{T} \exp\left(\frac{-\Delta H_{\mathrm{m,H^+_a}}}{RT}\right) \qquad \text{Eq. 56}$$

We rewrite this as

$$G_{\mathrm{s,H^+_{cms\text{-}a}}} = G_{\mathrm{s,H^+_{cms\text{-}a}}0} \frac{1}{T} \exp\left(\frac{-\Delta H_{\mathrm{cms\text{-}a}}}{RT}\right) = G_{\mathrm{s,H^+_{cms\text{-}a}}0} \frac{1}{T} \exp\left(\frac{-\left(\Delta H^0_{\mathrm{a_{cm}}} + \frac{1}{2}\Delta H^0_{\mathrm{a_{cs}}} + \Delta H_{\mathrm{m,H^+_a}}\right)}{RT}\right) \qquad \text{Eq. 57}$$

with $\Delta H_{\mathrm{c_{cms\text{-}a}}} = \Delta H^0_{\mathrm{a_{cm}}} + \frac{1}{2}\Delta H^0_{\mathrm{a_{cs}}} + \Delta H_{\mathrm{m,H^+_a}} = \frac{3}{2}\Delta H^0_{\mathrm{a_{cm}}} + \frac{1}{2}\Delta H^0_{\mathrm{d_{cs}}} + \Delta H_{\mathrm{m,H^+_a}}$.

The preexponential of surface protonic conductance is given by

$$G_{\mathrm{s,H^+_{cms\text{-}a}}0} = G^0_{\mathrm{s,H^+_{cms\text{-}a}}0} \left(\frac{p_{\mathrm{H_2O}}}{p^0}\right)^{3/2} = \sqrt{2}F\gamma_{M_s} \exp\left(\frac{\frac{3}{2}\Delta S^0_{\mathrm{a_{cm}}} + \frac{1}{2}\Delta S^0_{\mathrm{d_{cs}}}}{R}\right) u_{\mathrm{H^+}0} \left(\frac{p_{\mathrm{H_2O}}}{p^0}\right)^{3/2} \qquad \text{Eq. 58}$$

With assumptions as before, we obtain $G^0_{\mathrm{s,H^+_{chm\text{-}a}}0} \approx 3\cdot10^{-12}$ SK.

At full coverage, $\gamma_{M_{M_s}\mathrm{OH_2^x}} \approx \gamma_{M_s}$, and low dissociation ($\gamma_{\mathrm{O_s}} \approx 2\gamma_{M_s}$), as illustrated in Figure 13 b, combination with Eq. 17 yields for the conductance

$$G_{\mathrm{s,H^+_{cms\text{-}a}}} = F\gamma_{M_{M_s}\mathrm{OH_2^x}} u_{\mathrm{H^+_a}} = F\gamma_{M_s}\sqrt{2K_{\mathrm{d_{cs}}}}\,u_{\mathrm{H^+}0}\frac{1}{T}\exp\left(\frac{-\Delta H_{\mathrm{m,H^+_a}}}{RT}\right) \qquad \text{Eq. 59}$$

which can be rewrite as

$$G_{\mathrm{s,H^+_{cms\text{-}a}}} = G_{\mathrm{s,H^+_{cms\text{-}a}}0}\frac{1}{T}\exp\left(\frac{-\Delta H_{\mathrm{cms\text{-}a}}}{RT}\right) = G_{\mathrm{s,H^+_{cms\text{-}a}}0}\frac{1}{T}\exp\left(\frac{-\left(\frac{1}{2}\Delta H^0_{\mathrm{d_{cs}}} + \Delta H_{\mathrm{m,H^+_a}}\right)}{RT}\right) \qquad \text{Eq. 60}$$

with $\Delta H_{\mathrm{c_{cms\text{-}a}}} = \frac{1}{2}\Delta H^0_{\mathrm{d_{cs}}} + \Delta H_{\mathrm{m,H^+_a}}$.

The preexponential of surface protonic conductance becomes

$$G_{\mathrm{s,H^+_{cms\text{-}a}}0} = G^0_{\mathrm{s,H^+_{cms\text{-}a}}0} = \sqrt{2}F\gamma_{M_s}\exp\left(\frac{\frac{1}{2}\Delta S^0_{\mathrm{d_{cs}}}}{R}\right)u_{\mathrm{H^+}0} \qquad \text{Eq. 61}$$

with $G_{\mathrm{s,H^+_{cms\text{-}a}}0} = G^0_{\mathrm{s,H^+_{cms\text{-}a}}0}$ coming out as $1.1\cdot10^{-3}$ SK.

At full coverage and high dissociation (Figure 13 d), we have $\gamma_{\mathrm{OH^\bullet_O}} = \gamma_{M_{M_s}\mathrm{OH'}} \approx \gamma_{M_s}$. Combination with Eq. 17 yields for the conductance in the adsorbed layer

$$G_{\mathrm{s,H^+_{cds\text{-}a}}} = \frac{F\gamma_{M_s}}{K_{\mathrm{d_{cs}}}}u_{\mathrm{H^+}0}\frac{1}{T}\exp\left(\frac{-\Delta H_{\mathrm{m,H^+_a}}}{RT}\right) \qquad \text{Eq. 62}$$

which we rewrite as

$$G_{\mathrm{s,H^+_{cds\text{-}a}}} = G_{\mathrm{s,H^+_{cds\text{-}a}}0}\frac{1}{T}\exp\left(\frac{-\Delta H_{\mathrm{c_{cms\text{-}a}}}}{RT}\right) = G_{\mathrm{s,H^+_{cms\text{-}a}}0}\frac{1}{T}\exp\left(\frac{-\left(-\Delta H^0_{\mathrm{d_{cs}}} + \Delta H_{\mathrm{m,H^+_a}}\right)}{RT}\right) \qquad \text{Eq. 63}$$

where $\Delta H_{\mathrm{c_{cds\text{-}a}}} = -\Delta H^0_{\mathrm{d_{cs}}} + \Delta H_{\mathrm{m,H^+_a}}$ and preexponential

$$G_{\mathrm{s,H^+_{cds\text{-}a}}0} = G^0_{\mathrm{s,H^+_{cds\text{-}a}}0} = F\gamma_{M_s}\exp\left(\frac{-\Delta S^0_{\mathrm{d_{cs}}}}{R}\right)u_{\mathrm{H^+}0} \qquad \text{Eq. 64}$$

coming out as $G_{\mathrm{s,H^+_{cds\text{-}a}}0} = G^0_{\mathrm{s,H^+_{cds\text{-}a}}0} = 8\cdot10^{-4}$ SK.

Proton migration between dissociated species within the chemisorbed layer: cma-a

The *cma-a* model is schematically shown in Figure 14.

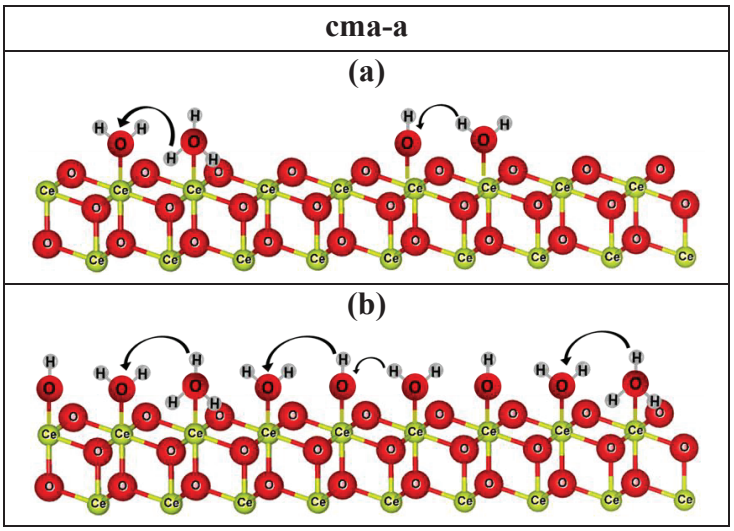

Figure 14 Schematic illustration of the "cma-a" model on the (111) surface of CeO_2 at low (a) and full coverage (b). The arrows show the protonic migration.

If dissociation within the chemisorbed layer (Eq. 25) dominates, the electroneutrality and concentrations are determined by Eq. 28 and Eq. 29, respectively. This corresponds to the model suggested by Raz *et al.* [136] but as stated above, it cannot prevail because dissociation in the water layer should be weaker than to the surface oxide ions. Nevertheless, I will provide a derivation of the conductance under molecular and dissociative dominance for reference.

In estimating the surface conductance based on this model, it is assumed that jumps of protons from dissociated protons H_3O^+ to H_2O and jumps from H_2O to dissociated OH^- contribute equally

$$G_{s,H^+_{cma\text{-}a}} = F(\gamma_{M_{M_s}OH_3^\bullet} u_{H^+_a} + \gamma_{M_{M_s}OH^/} u_{H^+_a}) = 2F\gamma_{M_{M_s}OH_3^\bullet} u_{H^+_a} \qquad \text{Eq. 65}$$

The charge mobility of the charged defects contains the chance that a proton in an H_3O^+ group finds an adjacent water molecule to jump to, or that a water molecule is there to offer a proton to jump to OH^-. Hence, it becomes

$$G_{s,H^+_{cma\text{-}a}} = 2F\gamma_{M_{M_s}OH_3^\bullet} \frac{\gamma_{M_{M_s}OH_2^x}}{\gamma_{M_s}} u_{H^+0} \frac{1}{T} \exp\left(\frac{-\Delta H_{m,H^+_a}}{RT}\right) \qquad \text{Eq. 66}$$

which for low coverage (Figure 14 a) and combination with Eq. 12 and Eq. 29 yields

$$G_{s,H^+_{cma\text{-}a}} = 2F\gamma_{M_s} K^2_{a_{cm}} \sqrt{K_{d_{ca}}} \left(\frac{p_{H_2O}}{p^0}\right)^2 u_{H^+0} \frac{1}{T} \exp\left(\frac{-\Delta H_{m,H^+_a}}{RT}\right) \qquad \text{Eq. 67}$$

We rewrite this as

$$G_{s,H^+_{cma\text{-}a}} = G_{s,H^+_{cma\text{-}a}0}\frac{1}{T}\exp\left(\frac{-\Delta H}{RT}\right) = G_{s,H^+_{cma\text{-}a}0}\frac{1}{T}\exp\left(\frac{-\left(2\Delta H^0_{a_{cm}} + \frac{1}{2}\Delta H^0_{d_{ca}} + \Delta H_{m,H^+_a}\right)}{RT}\right) \quad \text{Eq. 68}$$

where $\Delta H_{c_{cma\text{-}a}} = 2\Delta H^0_{a_{cm}} + \frac{1}{2}\Delta H^0_{d_{ca}} + \Delta H_{m,H^+_a}$, and the preexponential becomes

$$G_{s,H^+_{cma\text{-}a}0} = G^0_{s,H^+_{cma\text{-}a}0}\left(\frac{p_{H_2O}}{p^0}\right)^2 = 2F\gamma_{M_s}\exp\left(\frac{2\Delta S^0_{a_{cm}} + \frac{1}{2}\Delta S^0_{d_{ca}}}{R}\right)u_{H^+0}\left(\frac{p_{H_2O}}{p^0}\right)^2 \quad \text{Eq. 69}$$

By using assumptions as above, with the standard entropy change of dissociation in the chemisorbed layer $\Delta S^0_{d_{cma}}$ negligible, we get $G^0_{s,H^+_{cma\text{-}a}0} \approx 6\cdot10^{-15}$ SK.

At full coverage (Figure 14 b), the *cma-a* model gives

$$G_{s,H^+_{cma\text{-}a}} = 2F\gamma_{M_sOH^x_2:}\frac{\gamma_{M_sOH^x_2}}{\gamma_{M_s}}u_{H^+0}\frac{1}{T}\exp\left(\frac{-\Delta H_{m,H^+_a}}{RT}\right) = 2F\gamma_{M_s}\sqrt{K_{d_{ca}}}u_{H^+0}\frac{1}{T}\exp\left(\frac{-\Delta H_{m,H^+_a}}{RT}\right) \quad \text{Eq. 70}$$

We rewrite this as

$$G_{s,H^+_{cma\text{-}a}} = G_{s,H^+_{cma\text{-}a}0}\frac{1}{T}\exp\left(\frac{-\Delta H}{RT}\right) = G_{s,H^+_{cma\text{-}a}0}\frac{1}{T}\exp\left(\frac{-\left(\frac{1}{2}\Delta H^0_{d_{ca}} + \Delta H_{m,H^+_a}\right)}{RT}\right) \quad \text{Eq. 71}$$

with preexponential of surface protonic conductance given by

$$G_{s,H^+_{cma\text{-}a}0} = G^0_{s,H^+_{cma\text{-}a}0} = 2F\gamma_{M_s}\exp\left(\frac{\frac{1}{2}\Delta S^0_{d_{ca}}}{R}\right)u_{H^+0} \quad \text{Eq. 72}$$

With the same assumptions as before, we obtain $G^0_{s,H^+_{cma\text{-}a}0} = G_{s,H^+_{cma\text{-}a}0} \approx 1.5\cdot10^{-3}$ SK. Here, we do not consider the possibility of full dissociation in the adsorbed layer (no *cda-a* model).

Table 2 further summarizes the derived p_{H_2O} dependencies for surface protonic conduction within chemisorbed water layer on porous MO_2 oxides in general along with the predicted standard preexponential of surface protonic conductance at p_{H_2O} = 1 bar. As mentioned, the p_{H_2O} dependence of surface protonic conductance under low coverage is the same for molecular and dissociated water when the transport mechanism is the same, e.g. *cms-s* and *cds-s*, which is different from that of the p_{H_2O} dependences of concentration of adsorbed water shown in Table 1.

Table 2 Summary of the derived p_{H_2O} dependences and predicted standard preexponential of surface protonic conductance G^0_{s,H^+0} at p_{H_2O} = 1 bar within the chemisorbed water layer according to the models of adsorption, dissociation and proton migration in the cases of low and high water coverage.

Model **Parameter**	**cms-s** **cds-s**	**cms-sa** **cds-sa**	**cms-a** **cds-a**	**cma-a**	**cms-s**	**cds-s**	**cms-sa**	**cds-sa**	**cms-a**	**cds-a**	**cma-a**
n in $G_{s,H^+0} \propto p^n_{H_2O}$	1/2	1	3/2	2	0 (Full coverage)						
G^0_{s,H^+0} (SK), p_{H_2O} = 1 bar	$2\cdot10^{-6}$	$3\cdot10^{-9}$	$3\cdot10^{-12}$	$6\cdot10^{-15}$	$1\cdot10^{-3}$	$4\cdot10^{-4}$	$1.5\cdot10^{-3}$	$8\cdot10^{-4}$	$1\cdot10^{-3}$	$8\cdot10^{-4}$	$1.5\cdot10^{-3}$

2.7 Physisorption

2.7.1 Physisorption and surface coverage

As *RH* increases by increasing p_{H_2O} and/or lower temperature, the conductivities of the samples start to increase, attributed to the effect of water molecules physisorbed on top of the chemisorbed water.

Physisorption starts with a structured, relatively rigid (ice-like) first molecular layer, which in our nomenclature is written as

$$v_{H_2O_{ph1}} + H_2O(g) = H_2O_{H_2O_{ph1}} \qquad \text{Eq. 73}$$

with equilibrium coefficient

$$K_{ph1} = \frac{\gamma_{H_2O_{H_2O_{ph1}}}}{(\gamma_{H_2O_{ph1}} - \gamma_{H_2O_{H_2O_{ph1}}})\frac{p_{H_2O}}{p^0}} = \exp\left(\frac{\Delta S^0_{ph1}}{R}\right)\exp\left(\frac{-\Delta H^0_{ph1}}{RT}\right) \qquad \text{Eq. 74}$$

The standard enthalpy of physisorption starts out a bit more exothermic than condensation into liquid water due to the stronger hydrogen bonds to the chemisorbed layer, and becomes less exothermic and eventually reaches the heat of condensation of water, which is -44.0 kJ/mol H_2O at RT and decreasing with increasing temperature, e.g. -40.7 kJ/mol H_2O at 100°C.

The coverage of physisorbed waters is described by the BET (Brunauer Emmett Teller) isotherm, which holds for multilayer adsorption, and fits experimental observations well over a certain range of pressure.[138] BET physisorption experiments are commonly employed to determine the macroscopic surface area and the volume of an adsorbent.

The BET equation is defined as

$$\frac{\gamma_{H_2O_{H_2O_{ph1}}}}{\gamma_{H_2O_{ph1}}} = \frac{v}{v_m} = \frac{c_{BET}\dfrac{p_{H_2O}}{p_{ce}}}{\left(1-\dfrac{p_{H_2O}}{p_{ce}}\right)\left(1+(c_{BET}-1)\dfrac{p_{H_2O}}{p_{ce}}\right)} = \frac{c_{BET}\cdot RH}{(1-RH)(1+(c_{BET}-1)RH)} \qquad \text{Eq. 75}$$

where v is the total volume of the adsorbed water, v_m is the volume corresponding to monolayer coverage such that v/v_m gives the surface coverage that can exceed unity for multilayer coverage, p_{H_2O} is the partial pressure of water, p_{ce} is the condensation-evaporation equilibrium water partial pressure, $RH = \frac{p_{H_2O}}{p_{ce}}$, and c_{BET} is the so-called BET constant, which is approximated by

$$c_{BET} \cong \exp\left(\frac{|E_1| - |E_L|}{RT}\right) \qquad \text{Eq. 76}$$

where E_1 is the heat of adsorption for the first layer and E_L for the second and higher layers. E_L is usually more or less equal to the heat of condensation of liquid water, -44 kJ/mol at RT, and -40.7 kJ/mol at 100°C. Here, when the chemisorbed layer is treated separately and we deal only with the physisorbed layers, the energy difference between the first and second physisorbed water layer is expected to be small, but still non-zero. In our paper in ref. [139] where we treated the entire derivation for physisorbed water layers, the c_{BET} in Eq. 33 was provided by actual negative enthalpies for condensation, so that a typical estimate is E_1 - E_L = -4 kJ/mol. For the calculation of the c_{BET} the way it enters the BET equation, the absolute values of the enthalpies should be used, such that $|E_1|$ - $|E_L|$ = 4 kJ/mol. It must be noted that very often in literatures, for instance in ref. [136], E_1 and E_L are given by their magnitudes, *i.e.*, absolute values, without using the absolute symbol.

The equilibrium partial pressure of water p_{ce} is a strong function of temperature, which can be expressed for instance by the Arden Buck equation.[140] Alternatively, p_{ce} can be expressed by the thermodynamics of vaporisation or condensation as

$$\frac{p_{ce}}{p^0} = \frac{1}{K_{ce}} = \frac{1}{\exp\left(\dfrac{\Delta S^0_{ce}}{R}\right)\exp\left(\dfrac{-\Delta H^0_{ce}}{RT}\right)} \qquad \text{Eq. 77}$$

At 25°C (RT), we have approximate thermodynamic parameters of condensation of $\Delta S^0_{ce,298.15}$ = -118.9 J/molK and $\Delta H^0_{ce,298.15}$ = -44.0 kJ/mol, while at 100°C, we have $\Delta S^0_{ce,373.15}$ = -109.0 J/molK and $\Delta H^0_{ce,373.15}$ = -40.7 kJ/mol.[129]

In our nomenclature, the coverage for the first ice-like physisorbed layer can be obtained by rearranging Eq. 74 into

$$X_{\mathrm{H_2O}_{\mathrm{H_2O_{ph1}}}} = \frac{\gamma_{\mathrm{H_2O}_{\mathrm{H_2O_{ph1}}}}}{\gamma_{\mathrm{H_2O}_{\mathrm{ph1}}}} = \frac{v}{v_m} = \frac{K_{\mathrm{ph1}} \dfrac{p_{H_2O}}{p^0}}{1 + K_{\mathrm{ph1}} \dfrac{p_{H_2O}}{p^0}} \qquad \text{Eq. 78}$$

where K_{ph1} is given by Eq. 74 – a function of $\Delta S^0_{\mathrm{ph1}}$, $\Delta H^0_{\mathrm{ph1}}$ and T. It is seen that the Langmuir equation for molecular chemisorption applies to each physisorbed water layer.

In the following, we will use an estimate that the standard enthalpy of physisorption for the first physisorbed layer around 100°C will be $\Delta H^0_{\mathrm{ph1}}$ ≈ -(40.7 + 4) kJ/mol ≈ -45 kJ/mol, which is very close to that of water physisorbed on SnO_2 [141] and SiO_2 surface [142] with $\Delta H^0_{\mathrm{ph1}}$ of -47 to -48 kJ/mol. $\Delta S^0_{\mathrm{ph1}}$ was assumed as -109 J/molK as before, which is the entropy of condensation to water at 100°C.

In the low coverage region of the first physisorbed layer, Eq. 74 and Eq. 75 can be simplified to yield the coverage as

$$X_{\mathrm{H_2O}_{\mathrm{H_2O_{ph1}}}} = \frac{\gamma_{\mathrm{H_2O}_{\mathrm{H_2O_{ph1}}}}}{\gamma_{\mathrm{H_2O}_{\mathrm{ph1}}}} = \frac{v}{v_m} = c_{\mathrm{BET}} \frac{p_{\mathrm{H_2O}}}{p_{\mathrm{ce}}} = c_{\mathrm{BET}} RH = \frac{p_{\mathrm{H_2O}}}{p^0} K_{\mathrm{ph1}} = \frac{p_{\mathrm{H_2O}}}{p^0} \exp\left(\frac{\Delta S^0_{\mathrm{ph1}}}{R}\right) \exp\left(\frac{-\Delta H^0_{\mathrm{ph1}}}{RT}\right) \qquad \text{Eq. 79}$$

We express this in many ways and by many parameters to stress its significance and simplicity. Here, $\Delta S^0_{\mathrm{ph1}}$ and $\Delta H^0_{\mathrm{ph1}}$ are temperature dependent parameters for the first physisorbed layer, expressing the temperature dependency of $c_{\mathrm{BET}}/p_{\mathrm{ce}}$. They are close to those of condensation to bulk water, enhanced by the extra few kJ/mol of exothermic enthalpy because of the extra hydrogen bonds for the first layer bonding to the chemisorbed layer underneath. Eq. 78 is an alternative representation of Eq. 75 and Eq. 76, more useful for our purpose. It reveals that apart from the modest effect of c_{BET}, a constant RH yields a constant coverage.

Figure 15 illustrates the coverage of physisorbed water as a function of temperature at $p_{\mathrm{H_2O}}$ = 0.02 bar when the BET equation (Eq. 75) and the alternative representation given in Eq. 78 were applied. In the former case, $|E_1|$ - $|E_{\mathrm{L}}|$ with typical values of 0, 2 and 4 kJ/mol were employed. For the calculation of RH, the equilibrium partial pressure of water p_{ce} was evaluated both by the Arden Buck equation [140] (solid lines) and via K_{ce} given in Eq. 77 (dashed lines). The coverage described by both methods show negligible difference at the selected c_{BET} at 150°C and below. The first physisorbed monolayer (black horizontal dashed line) is achieved

only around 29–37°C at p_{H_2O} = 0.02 bar, depending on the c_{BET}. In addition, the surface coverage obtained from Eq. 78 describing the coverage up to the first ice-like physisorbed layer is represented by the light blue dotted symbols. It follows that of the BET equation in the case of $|E_1|$ - $|E_L|$ = 4 kJ/mol towards around 60°C at p_{H_2O} = 0.02 bar. At even lower temperatures (see also the inset of the figure), the coverage given by Eq. 78 levels off, reflecting a filling up of the physisorbed monolayer.

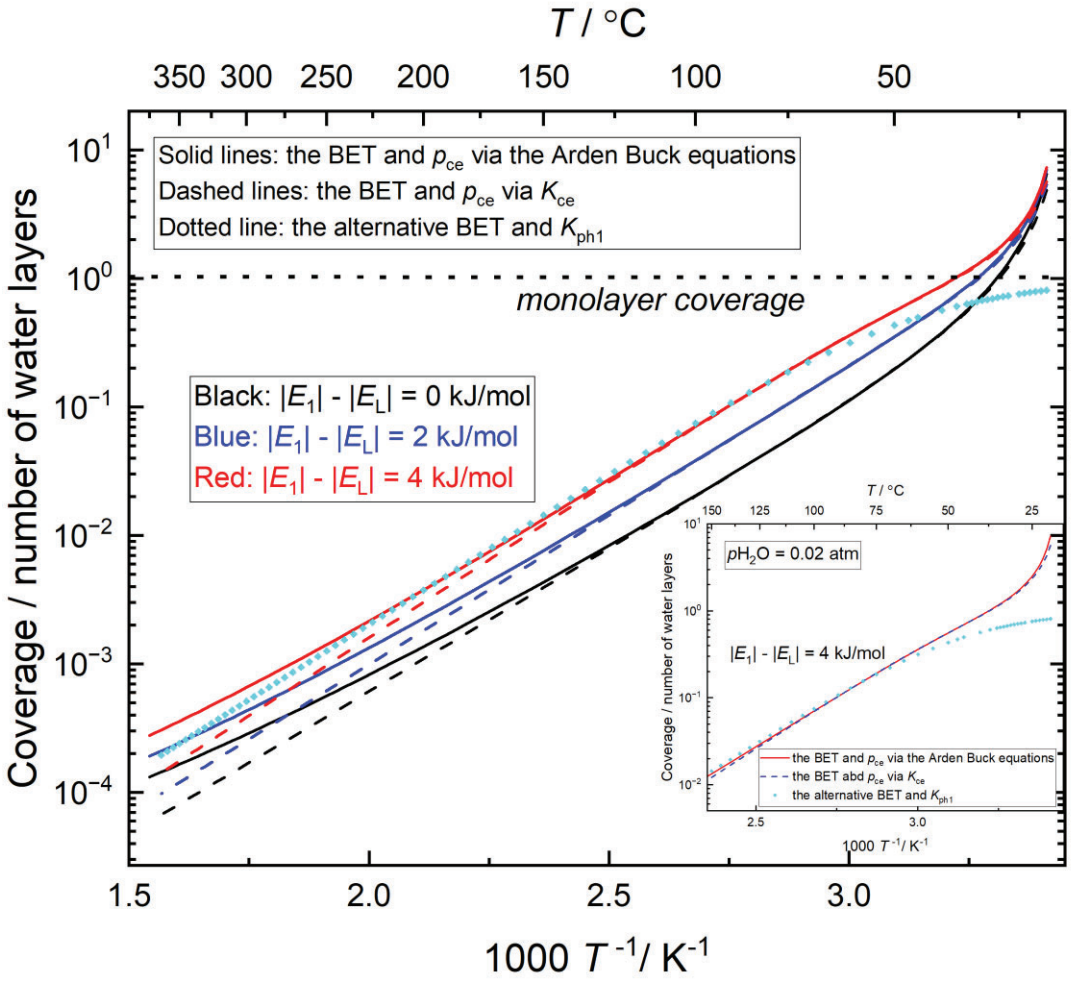

Figure 15 Theoretical surface coverage in number of water layers as a function of temperature at p_{H_2O} = 0.02 bar according to the BET equation (Eq. 75) and the alternative equation shown in Eq. 78. The BET equation was exemplified by $|E_1|$ - $|E_L|$ = 0 kJ/mol (black), 2 kJ/mol (dark blue) and 4 kJ/mol (red). The equilibrium water vapor pressure p_{ce} was calculated based on the Arden Buck equation (solid lines) as well as via the K_{ce} (Eq. 77) with ΔS^0_{ce} ≈ -114 J/molK and ΔH^0_{ce} ≈ -42.5 kJ/mol (dashed lines), *i.e.,* the average value between RT and 100°C. In the alternative BET equation, the dotted light blue symbols were drawn based on ΔS^0_{ph1} ≈ -109 J/molK and ΔH^0_{ph1} ≈ -45 kJ/mol. The inset of the figure shows the close-ups of the low-temperature part of the curves, with $|E_1|$ - $|E_L|$ = 4 kJ/mol when BET was used.

2.7.2 Models for protonic conduction in the 1st physisorbed water layer

Dissociation of physisorbed water have different possibilities. In this thesis, I will consider and evaluate two of them.

Dissociation from chemisorbed to physisorbed water: chm-ph1

In one possibility, it is assumed that chemisorbed water molecules dissociate protons to the first physisorbed water layer forming H_3O^+, as schematically displayed in Figure 16.

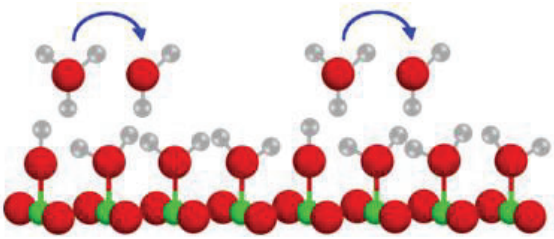

Figure 16 Partial coverage of 1st physisorbed layer with protons dissociated from a fully covered chemisorbed layer underneath with limited dissociation.

In this case, we have

$$M_{M_s}\mathrm{OH}_2^{\mathrm{x}} + \mathrm{H_2O}_{\mathrm{H_2O_{ph1}}} \rightleftharpoons M_{M_s}\mathrm{OH}^{/} + \mathrm{H_3O}^{\bullet}_{\mathrm{H_2O_{ph1}}} \qquad \text{Eq. 80}$$

with equilibrium constant

$$K_{\mathrm{d_{chm\text{-}ph1}}} = \frac{X_{M_{M_s}\mathrm{OH}^{/}} X_{\mathrm{H_3O}^{\bullet}_{\mathrm{H_2O_{ph1}}}}}{X_{M_{M_s}\mathrm{OH}_2^{\mathrm{x}}} X_{\mathrm{H_2O}_{\mathrm{H_2O_{ph1}}}}} = \frac{\gamma_{M_{M_s}\mathrm{OH}^{/}} \gamma_{\mathrm{H_3O}^{\bullet}_{\mathrm{H_2O_{ph1}}}}}{\gamma_{M_{M_s}\mathrm{OH}_2^{\mathrm{x}}} \gamma_{\mathrm{H_2O}_{\mathrm{H_2O_{ph1}}}}} = \exp\left(\frac{\Delta S^0_{\mathrm{d_{chm\text{-}ph1}}}}{R}\right)\exp\left(\frac{-\Delta H^0_{\mathrm{d_{chm\text{-}ph1}}}}{RT}\right) \qquad \text{Eq. 81}$$

If this dominates, the following electroneutrality applies

$$\gamma_{M_{M_s}\mathrm{OH}^{/}} = \gamma_{\mathrm{H_3O}^{\bullet}_{\mathrm{H_2O_{ph1}}}} \qquad \text{Eq. 82}$$

Moreover, cation surface site balance assuming full coverage in the chemisorbed layer and low dissociation $\gamma_{M_{M_s}\mathrm{OH}_2^{\mathrm{x}}} \approx \gamma_{M_s}$ allows us to insert, combine with physisorption thermodynamics and obtain

$$K_{\mathrm{d_{chm\text{-}ph1}}} = \frac{\gamma_{M_{M_s}\mathrm{OH}^{/}} \gamma_{\mathrm{H_3O}^{\bullet}_{\mathrm{H_2O_{ph1}}}}}{\gamma_{M_s} \gamma_{\mathrm{H_2O}_{\mathrm{H_2O_{ph1}}}}} = \frac{\gamma^2_{\mathrm{H_3O}^{\bullet}_{\mathrm{H_2O_{ph1}}}}}{\gamma_{M_s} \gamma_{\mathrm{H_2O}_{\mathrm{ph1}}} \frac{p_{\mathrm{H_2O}}}{p^0} K_{\mathrm{ph1}}} \qquad \text{Eq. 83}$$

which is rearranged into

$$\gamma_{H_3O^{\bullet}_{H_2O_{ph1}}} = \sqrt{K_{d_{chm\text{-}ph1}} \gamma_{M_s} \gamma_{H_2O_{ph1}} \frac{p_{H_2O}}{p^0} K_{ph1}} \qquad \text{Eq. 84}$$

The surface protonic conductance in the 1st physisorbed layer will by this model be

$$G_{s,H^+_{chm\text{-}ph1}} = F \gamma_{H_3O^{\bullet}_{H_2O_{ph1}}} u_{H_3O^{\bullet}_{H_2O_{ph1}}} = F \sqrt{K_{d_{chm\text{-}ph1}} \gamma_{M_s} \gamma_{H_2O_{ph1}}} \left(\frac{p_{H_2O}}{p^0} K_{ph1} \right)^{3/2} u_{H^+0} \frac{1}{T} \exp\left(\frac{-\Delta H_{m,H^+_{chm\text{-}ph1}}}{RT} \right) \qquad \text{Eq. 85}$$

which we may write

$$G_{s,H^+_{chm\text{-}ph1}} = G_{s,H^+_{chm\text{-}ph1}0} \frac{1}{T} \exp\left(\frac{-(\frac{3}{2}\Delta H^0_{ph1} + \frac{1}{2}\Delta H^0_{d_{chm\text{-}ph1}} + \Delta H_{m,H^+_{chm\text{-}ph1}})}{RT} \right) \qquad \text{Eq. 86}$$

with $\Delta H_{c_{chm\text{-}ph1}} = \frac{3}{2}\Delta H^0_{ph1} + \frac{1}{2}\Delta H^0_{d_{chm\text{-}ph1}} + \Delta H_{m,H^+_{chm\text{-}ph1}}$, and preexponential

$$G_{s,H^+_{chm\text{-}ph1}0} = G^0_{s,H^+_{chm\text{-}ph1}0} \left(\frac{p_{H_2O}}{p^0} \right)^{3/2} = F \sqrt{\gamma_{M_s} \gamma_{H_2O_{ph1}}} \exp\left(\frac{\frac{3}{2}\Delta S^0_{ph1} + \frac{1}{2}\Delta S^0_{d_{chm\text{-}ph1}}}{R} \right) u_{H^+0} \left(\frac{p_{H_2O}}{p^0} \right)^{3/2} \qquad \text{Eq. 87}$$

If u_{H^+0} is still of the order of magnitude as before, namely 10 cm^{2}K/Vs, and that the standard entropy of physisorption $\Delta S^0_{ph1} \approx$ -109 J/molK, and that of dissociation is negligible, we obtain $G^0_{s,H^+_{chm\text{-}ph1}0} \approx 2.3 \cdot 10^{-12}$ SK.

Dissociation within physisorbed water: ph1

In the other case, we assume instead that the chemisorbed water is already fully dissociated to surface protons, and that dissociation to the physisorbed layer must originate from physisorbed water molecules themselves, as illustrated in Figure 17.

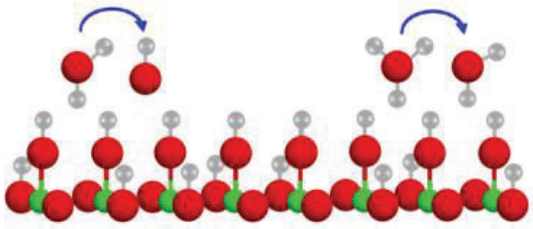

Figure 17 Partial coverage of the first physisorbed layer with weak dissociation over a fully dissociated chemisorbed water layer underneath.

In our nomenclature it is written

$$2H_2O_{H_2O_{ph1}} \rightleftharpoons OH'_{H_2O_{ph1}} + H_3O^{\bullet}_{H_2O_{ph1}} \qquad \text{Eq. 88}$$

with equilibrium constant

$$K_{\mathrm{d_{ph1}}} = \frac{X_{\mathrm{OH'_{H_2O_{ph1}}}} X_{\mathrm{H_3O^{\bullet}_{H_2O_{ph1}}}}}{X^2_{\mathrm{H_2O_{H_2O_{ph1}}}}} = \frac{\gamma_{\mathrm{OH'_{H_2O_{ph1}}}} \gamma_{\mathrm{H_3O^{\bullet}_{H_2O_{ph1}}}}}{\gamma^2_{\mathrm{H_2O_{H_2O_{ph1}}}}} = \exp\left(\frac{\Delta S^0_{\mathrm{d_{ph1}}}}{R}\right)\exp\left(\frac{-\Delta H^0_{\mathrm{d_{ph1}}}}{RT}\right) \qquad \text{Eq. 89}$$

If this dominates, the electroneutrality follows

$$\gamma_{\mathrm{OH'_{H_2O_{ph1}}}} = \gamma_{\mathrm{H_3O^{\bullet}_{H_2O_{ph1}}}} \qquad \text{Eq. 90}$$

Under the assumption of low coverage and low degree of dissociation of the physisorbed layer, and that the surface concentration of physisorption sites is the same as for chemisorption, $\gamma_{\mathrm{H_2O_{ph1}}} \approx \gamma_{M_s}$, we may insert and combine with physisorption thermodynamics to get

$$K_{\mathrm{d_{ph1}}} = \frac{\gamma^2_{\mathrm{H_3O^{\bullet}_{H_2O_{ph1}}}}}{\gamma^2_{\mathrm{H_2O_{H_2O_{ph1}}}}} = \frac{\gamma^2_{\mathrm{H_3O^{\bullet}_{H_2O_{ph1}}}}}{\left(\gamma_{M_s}\frac{p_{\mathrm{H_2O}}}{p^0}K_{\mathrm{ph1}}\right)^2} \quad \Rightarrow \quad \gamma_{\mathrm{H_3O^{\bullet}_{H_2O_{ph1}}}} = \sqrt{K_{\mathrm{d_{ph1}}}}\,\gamma_{M_s}\frac{p_{\mathrm{H_2O}}}{p^0}K_{\mathrm{ph1}} \qquad \text{Eq. 91}$$

The surface protonic conductance in the 1st physisorbed layer will by this model, assuming contributions of jumps from both H_3O^+ to H_2O and from H_2O to OH^-, be

$$G_{\mathrm{s,H^+_{ph1}}} = 2F\gamma_{\mathrm{H_3O^{\bullet}_{H_2O_{ph1}}}} u_{\mathrm{H_3O^{\bullet}_{H_2O_{ph1}}}} = 2F\sqrt{K_{\mathrm{d_{ph1}}}}\,\gamma_{M_s}\left(\frac{p_{\mathrm{H_2O}}}{p^0}K_{\mathrm{ph1}}\right)^2 u_{\mathrm{H^+0}}\frac{1}{T}\exp\left(\frac{-\Delta H_{\mathrm{m,H^+_{ph1}}}}{RT}\right) \qquad \text{Eq. 92}$$

The surface protonic conductance from this process is then

$$G_{\mathrm{s,H^+_{ph1}}} = 2G_{\mathrm{s,H^+_{ph1}0}}\frac{1}{T}\exp\left(\frac{-(2\Delta H^0_{\mathrm{ph1}} + \frac{1}{2}\Delta H^0_{\mathrm{d_{ph1}}} + \Delta H_{\mathrm{m,H^+_{ph1}}})}{RT}\right) \qquad \text{Eq. 93}$$

where $\Delta H_{\mathrm{c_{ph1}}} = 2\Delta H^0_{\mathrm{ph1}} + \frac{1}{2}\Delta H^0_{\mathrm{d_{ph1}}} + \Delta H_{\mathrm{m,H^+_{ph1}}}$, and the preexponential

$$G_{\mathrm{s,H^+_{ph1}0}} = G^0_{\mathrm{s,H^+_{ph1}0}}\left(\frac{p_{\mathrm{H_2O}}}{p^0}\right)^2 = 2F\gamma_{M_s}\exp\left(\frac{2\Delta S^0_{\mathrm{ph1}} + \frac{1}{2}\Delta S^0_{\mathrm{d_{ph1}}}}{R}\right)u_{\mathrm{H^+0}}\left(\frac{p_{\mathrm{H_2O}}}{p^0}\right)^2 \qquad \text{Eq. 94}$$

Under the same assumptions as above, we obtain $G^0_{\mathrm{s,H^+_{ph1}0}} \approx 6\cdot10^{-15}$ SK.

2.7.3 Protonic conduction in liquid-like physisorbed water layers

While approaching room temperature and with *RH* surpasses 0.6, the ice-like physisorbed layer becomes thicker and expectedly evolves into multilayers, with characteristics similar to that of bulk liquid water.

$$H_2O(g) = H_2O_{ph2} \qquad \text{Eq. 95}$$

As we move from the first ice-like to the next, liquid-like physisorbed waters, the transport of proton changes from structural diffusion (Grotthuss mechanism) to a vehicular mode as hydrated ions (H_3O^+). Such a change in proton transport mechanism is evidenced by the disappearance of the isotope effect.[143] Experimentally, Miyoshi *et al.* [85] showed that the ratio $\sigma(H_2O)/\sigma(D_2O)$ of YSZ was around 2 above 60°C indicating that Grotthuss hopping was dominating, and that the isotope effect almost disappears as *RH* exceeds 0.6 at lower temperatures suggesting the change to vehicular transport. Similar ratios of protonic over deuteronic conductivity in H_2O and D_2O atmospheres has been reported for anatase TiO_2.[118]

Nevertheless, the temperature dependence of surface protonic conductivities varies considerably among materials. For some porous nanoscopic oxides, e.g. YSZ [81, 85] and TiO_2, [118, 144] a sharp increase in proton conductivity has been observed at constant p_{H_2O} at close to RT, ascribed to the high vehicular mobility of protons in the liquid-like physisorbed water layer approaching that of bulk water (3.62×10^{-3} cm^2K/Vs at RT [145]) with an activation enthalpy of 11.29 kJ/mol.[146] It is worth mentioning that the dramatic increase in conductivity might be suppressed for certain oxides such as CeO_2 as a result of hydrophobicity and possible restructuring of the surface, and maybe also involve changes in surface composition (degree of hydrogenation as discussed in **Section 2.1**). I therefore refer to **Chapter 5** for further discussion.

3 A brick layer model for surface protonic conduction

In this chapter, the measured macroscopic conductivity of a porous material with predominant surface conduction will be linked to the surface layer conductance derived in **Chapter 2** through a brick layer model (BLM) of the ceramic microstructure. The model is derived on basis of grains and pores of similar sizes and will be most applicable for sintered powder compacts and porous ceramics. In the last part of this chapter, we shall see that the proposed BLM also relates the specific surface area to the microstructure factor ψ of the BLM.

3.1 Conductivity of porous materials

As mentioned in **Section 2.4.1**, the macroscopic conductivity, σ_M, of a porous material can be connected to the volume conductivity of the water layers, which is in turn related to the surface volume conductance, G_s. The latter is the in-plane conductance of a square area of a surface layer with a certain thickness.

With this, the macroscopic conductivity of the porous material can then be related to its surface conductance via a factor that we shall denote ψ (psi), which has unit of 1/m or 1/cm:

$$\sigma_M = \psi G_s \qquad \text{Eq. 96}$$

ψ will depend on the geometry and percolation of surface pathways, derived from the density, grain and pore sizes, and texture. We will come back to this in **Section 3.2**.

3.1.1 Materials with columnar or structural pores

Before I dive into porous ceramic materials with randomly organised grains and pores as in compacts and sinters, let us first consider ideally columnar ("c") materials, in which pores are parallel and infinitely open. These may be one-dimensional (1D) or three-dimensional (3D) if a surface conductance can be defined in those structural pores.

1D columnar porosity

For conduction on surfaces in the direction of the columnar pores, simple geometric considerations regardless of the cross-sectional shape of the pore shows that the macroscopic surface conductivity σ_M of the porous material is directly proportional to the volume-specific surface area A_v of the columnar pores, with units of, e.g. m^2/m^3 or cm^2/cm^3:

$$\sigma_{M,c} = \psi_c G_s = A_v G_s \qquad \text{Eq. 97}$$

For square columns, each pore column has a circumference of $4w_c$ and depth d_g through the layer and hence conductance $4w_cG_s/d_g$. Each grain contributes one such corner column and the total conductance through an entire layer is proportional to the number of grains $(1/d_g)^2$ and hence $(4w_cG_s/d_g)(1/d_g)^2 = 4w_cG_s/d_g^3$. The conductance and hence conductivity through the unit cube is then $\sigma_{M,c} = (4w_cG_s/d_g^3)/(1/d_g) = 4w_cG_s/d_g^2 = \psi_cG_s$. The volume specific surface area (of the cube) is $A_v = 4w_c/d_g^2 = \psi_c$.

The volume of pores in the unit volume, hence the relative porosity, is $p_r = w_c^2/d_g^2$. We can then let $\psi_c = 4w_c/d_g^2 = 4p_r/w_c = 4(1\text{-}\rho_r)/w_c$. We may introduce a unit-less factor $\Psi_c = \psi_c w_c = 4(1\text{-}\rho_r)$ for columnar porosity, and express the macroscopic materials conductivity in the direction of the columnar pores by the surface conductance and pore width and distance (grain size), relative porosity or density, unit-less geometry factor, or geometry factor

$$\sigma_{M,c} = \frac{4w_c}{d_g^2}G_s = \frac{4p_r}{w_c}G_s = \frac{4(1-\rho_r)}{w_c}G_s = \frac{\Psi_c}{w_c}G_s = \psi_c G_s = A_v G_s \qquad \text{Eq. 98}$$

It should be noted that "ρ" is used for density, and "p" is used for porosity. Here, ρ_r is the relative density, p_r is the relative porosity of the material, hence: $\rho_r = 1\text{-}p_r$.

3D structural porosity

Now, we add the volume of similarly penetrating pore columns in the two orthogonal directions. For small pores, they will to a first approximation not contribute to or obstruct conduction in the pores in the conducting direction. The porosity is to a first approximation 3 times that of the 1D case, *i.e.*, $p_r = 3w_c^2/d_g^2$. Hence, the relationship between conductivity and porosity is affected with the same factor, and we get $\psi_c = 4w_c/d_g^2 = (4/3)p_r/w_c = (4/3)(1\text{-}\rho_r)/w_c$, and for this case $\Psi_c = (4/3)(1\text{-}\rho_r)$. Overall, the macroscopic materials conductivity for a case of open columnar porosity in the dimensions is

$$\sigma_{M,c} = \frac{4w_c}{d_g^2}G_s = \frac{4p_r}{3w_c}G_s = \frac{4(1-\rho_r)}{3w_c}G_s = \frac{\Psi_c}{w_c}G_s = \psi_c G_s \qquad \text{Eq. 99}$$

If the material is isotropic (cubic) and has open columnar porosity in all three directions, it does not matter in which direction the conductivity is measured due to the contributions from columns as they come into the driving electrical field.

This model may be appropriate for microporous materials such as zeolites and metal-organic frameworks (MOFs) if the pores are large enough that a surface conductance can be defined in their structural pores. In reality, such materials are difficult to prepare as dense films or bulk samples and may normally comprise inter-grain porosity like we will treat next in addition to the intra-grain structural porosity.

3.1.2 Porous materials

For sintered powder compacts and porous ceramics, we may apply geometric models to predict the macroscopic conductivity from the grain size, porosity, and surface conductivity.

Existing brick layer model

The concept of a brick layer model (BLM) comes from analysis of grain boundary impedance in ceramics.[147] The literature offers also treatises of conducting interfaces [148] between grains and grains covered with a second phase that offers parallel admittance and series impedance,[149] both with some but not enough relevance to be further referred to here.

Stub *et al.* [81, 82] treated surface protonic conduction quantitatively based on own measurements, standard models for adsorption, and transport terms for YSZ developed by Raz *et al.* [136]. Gregori *et al.* [76] proposed a BLM for estimation of the surface protonic conductivity of less porous ceramics, and to our knowledge that is the work with the closest relevance to ours on porous materials. Based on measurements of conductivity of dense films and porous ceramic samples of ceria under wet and dry atmospheres, they proposed a model considering proton transport via grain or grain boundary in the ceramic bulk, and in the subsurface region of pores or on the adsorbed water layer above its surface, see Figure 6 (route 1-4) in **Section 1.4**.

According to the model, the macroscopic conductivity, σ_M, can be estimated from the pore size, volume fraction of the open porosity, thickness and bulk conductivity of adsorbed water layer

$$\sigma_M = \beta\varphi_p\Omega a\sigma_{\infty,L} = \frac{4}{d}\varphi_p a\sigma_{\infty,L} = \frac{4}{d}\varphi_p G_s \qquad \text{Eq. 100}$$

where $\beta = 2/3$ in a brick layer model, φ_p is the open porosity volume fraction, $\Omega = 6/d$ is the surface to volume fraction of a pore of size d, and a and $\sigma_{\infty,L}$ are the thickness and volume conductivity of the water layer, respectively. The rightmost expression inserts our surface layer conductance $G_s = a\,\sigma_{\infty,L}$, and inspection shows that it thereby has become equivalent to our 1D columnar model in Eq. 98. The model comprises a simple proportionality to open porosity and is unsuited for larger porosities in materials with randomly organised porosity like compacted or sintered ceramics. This was also emphasised by the authors who applied it qualitatively to account for measured surface protonic conductivity in relatively dense samples with low porosities, given that the protonic mobility in the adsorbed water was similar to that of the self-diffusion of H_3O^+ in water (~ $8\cdot10^{-3}$ cm^2/Vs at 200°C).

3.2 A more general brick layer model (BLM)

The growing understanding for surface protonic conduction have led us to propose a new porous brick layer model more generally applicable, especially for highly porous compacted and sintered samples.

Let us start by dividing the volume of a porous material with equal size d_g of grains and pores into cubic bricks of the same size d_g so that there are $1/d_g$ bricks in each unit length direction and $1/d_g^2$ per cross-sectional unit area, and $1/d_g^3$ bricks per unit volume. Figure 18 illustrates the cross-sectional planes with different porosities. Surfaces may be counted as belonging to grains or pores. We arbitrarily choose to count surfaces as belonging to grains. The chance that a brick is a grain is proportional to the relative density ρ_r, and hence also related to the relative porosity p_r of the material: $\rho_r = 1 - p_r$.

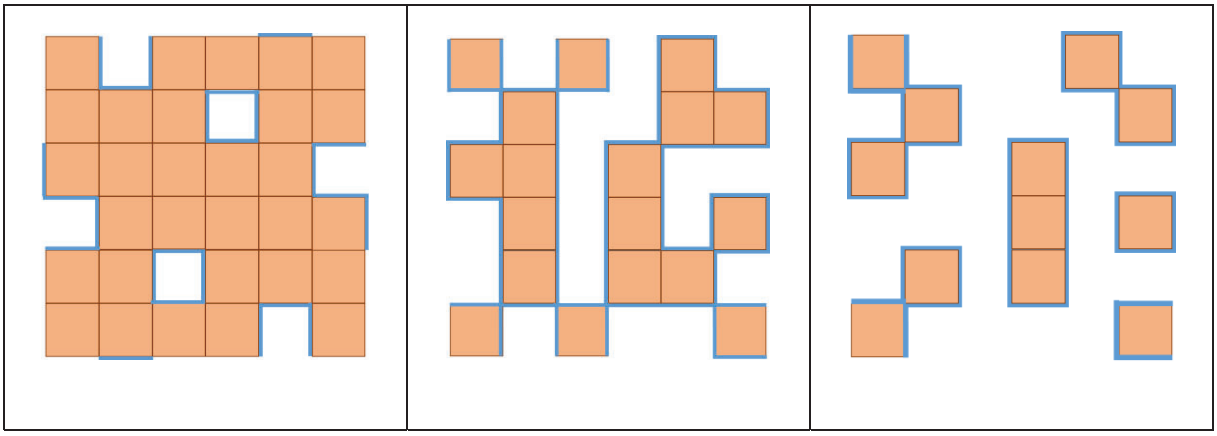

Figure 18 Schematic single layers of 6 x 6 brick "random" porous microstructures viewed from above, into the direction of conduction through the plane of the image. Coloured bricks are grains, grain boundaries are the thin lines between them. Surfaces with adsorbed water are thick blue lines. Surfaces are drawn at the outer boundaries only where they would appear by expanding the same pattern in all four directions of the plane (in this way drawn differently than in the figure in the supplementary information of our paper on ZrO_2.[139]) Densities are 5/6 (≈ 83%, left), 1/2 (50%, middle), and 1/3 (≈ 33%, right). Statistical numbers of conducting through-plane surfaces of the 6 x 6 brick layer according to the developed model (Eq. 101, in this case with $d_g = 1/6$) are, respectively, 20, 36, and 32, while the actual numbers in a repeating matrix of these "random" examples of a small number of bricks are, respectively, 24, 47, and 40. The difference to the model is assigned to the human rather than statistical selection of the microstructure.

In the direction of conduction, 4 of the 6 sides (2/3) of a grain can contribute a conducting surface, and only if the neighbouring brick is a pore. For unit area of a single layer of bricks, the number of grain side surfaces is thus

$$n_{sL} = \frac{4\rho_r p_r}{d_g^2} = \frac{4\rho_r(1-\rho_r)}{d_g^2} \qquad \text{Eq. 101}$$

This is a simple function that goes through a maximum value at 50% relative density for which each brick contributes on average one conducting surface, *i.e.,* 2 per grain. The conductance through one layer is obtained by multiplying with the surface conductance of the side sheet:

$$G_{sL} = G_s n_{sL} = G_s \frac{4\rho_r p_r}{d_g^2} = G_s \frac{4\rho_r(1-\rho_r)}{d_g^2} \qquad \text{Eq. 102}$$

Now, we apply the simplest possible consideration of percolation, *i.e.,* the chance that a surface coincides directly with a new surface in the next layer. We take this to be the same that an interface is a surface, namely, as before, $\rho_r\, p_r = \rho_r(1\text{-}\rho_r)$. Hence, the area specific number of connected conducting surfaces through one layer that percolates to the next is reduced to

$$n_{\mathrm{sLp1}} = \frac{4\rho_r^2 p_r^2}{d_g^2} = \frac{4\rho_r^2(1-\rho_r)^2}{d_g^2} \qquad \text{Eq. 103}$$

and the conductance through this one layer is then correspondingly

$$G_{\mathrm{sLp1}} = G_s n_{\mathrm{sLp1}} = G_s \frac{4\rho_r^2 p_r^2}{d_g^2} = G_s \frac{4\rho_r^2(1-\rho_r)^2}{d_g^2} \qquad \text{Eq. 104}$$

We might continue like this, making the straight percolating conduction path ever rarer, but orthogonal surfaces will immediately start to connect the ones we consider, and increase the conducting pathways. A numerical simulation of this could be useful, but the brick model is simply a rough estimation. Generally, the power that the density and porosity are raised to, 1 and 2 in the above cases, can be a variable ξ (xi):

$$G_{\mathrm{sLp1}} = G_s n_{\mathrm{sLp1}} = G_s \frac{4(\rho_r p_r)^{\xi}}{d_g^2} = G_s \frac{4(\rho_r(1-\rho_r))^{\xi}}{d_g^2} \qquad \text{Eq. 105}$$

As suggested by Sun *et al.,* [139] ξ can be taken as 1-2 for materials of regular and equal shapes of grains and pores and densities around 50%, while low porosities and certain non-isotropic pore structures may have ξ above 2.

A unit volume will have a conductance divided by the number of layers of grains, *i.e.,* $1/d_g$, so that the macroscopic specific conductivity σ_M becomes

$$\sigma_M = \frac{G_{\mathrm{sLp1}}}{\frac{1}{d_g}} = G_{\mathrm{sLp1}} d_g = G_s \frac{4\rho_r^{\xi} p_r^{\xi}}{d_g} = G_s \frac{4\rho_r^{\xi}(1-\rho_r)^{\xi}}{d_g} = \psi G_s \qquad \text{Eq. 106}$$

In this formula, we recognise that the essential parameters are the conductance G_s of the surface layer, the relative density (or porosity) and the grain (and pore) size d_g. The percolation coefficient ξ expectedly in the range 1-2 plays an additional, but modest role.

The surface protonic conductivity of a simple porous material according to this model is inversely proportional to the grain size and has a maximum at 50% relative density of $\sigma_M = G_s/d_g$ for $\xi = 1$ and $0.25 G_s/d_g$ for $\xi = 2$.

Figure 19 shows plots of the unit-less factor Ψ as a function of relative density for the BLM with ξ = 1, 1.5, and 2, compared with values for 1D and 3D columnar porosity mentioned earlier. The figure also shows ψ (the ratio between materials conductivity and surface conductance) for the case of grain and pore sizes of 100 nm. The columnar models are limited mathematically and realistically to high relative densities. The BLM handles in principle any

relative densities between 0 to 1, and to some extent closed porosity if $\xi > 1$, as can be seen from the concave shape of the conductivity curve near full density for $\xi = 1.5$ and 2. In considering square bricks it underestimates conductivity by not allowing conduction along facets connecting otherwise unconnected grain sides. The BLM and the model proposed by Gregori *et al.* [76] model coincide well for $\xi = 1$ (full percolation) at low porosities, while the BLM continues to handle the situation also as the porosity gets high.

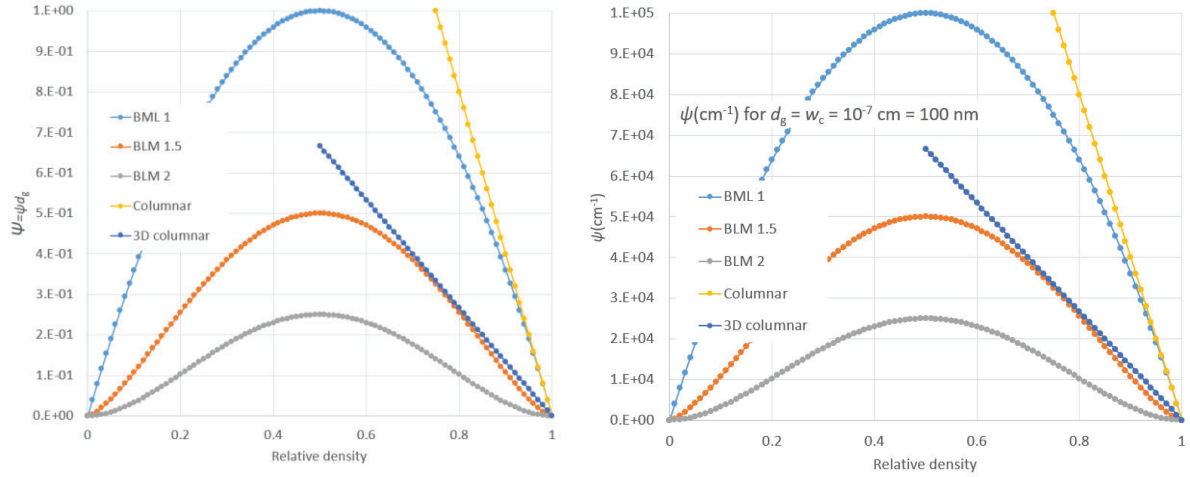

Figure 19 Left: Unit-less geometrical factor $\Psi = \psi d_g$ for the BLM for porous materials and $\Psi_c = \psi_c w_c$ for columnar porosity models, as a function of relative density. Right: Corresponding values of ψ and ψ_c for the case of 100 nm grain and pore sizes. The numbers for the BLM are calculated with percolation powers of $\xi = 1$, 1.5, and 2. The regular 1D columnar model coincides with that of Gregori *et al.* [76].

3.2.1 Estimation of specific surface area

The BLM also allows estimates of the volume-specific surface area A_v of a porous material of the category we deal with here. In each layer there are 6 sides to each cube provided that the cube is a grain, and its neighbour (in all 6 directions) is a pore. The total number of surface sides per unit area of a single layer of bricks is then

$$n_{6sL} = \frac{6\rho_r p_r}{d_g^2} = \frac{6\rho_r(1-\rho_r)}{d_g^2} \qquad \text{Eq. 107}$$

The number of surface sides in a unit volume will be that of one layer multiplied with the number of layers of grains, *i.e.,* $1/d_g$;

$$n_{vs} = \frac{n_{6sL}}{d_g} = \frac{6\rho_r(1-\rho_r)}{d_g^3} \qquad \text{Eq. 108}$$

The volumetric specific surface area A_v is then obtained by multiplying with the area of each side

$$A_{\mathrm{v}} = n_{vs} d_g^2 = \frac{6\rho_r(1-\rho_r)}{d_g} \qquad \text{Eq. 109}$$

Inserting this, we get

$$\psi = \frac{4\rho_r^{\xi}(1-\rho_r)^{\xi}}{d_g} = \rho_r^{\xi-1}(1-\rho_r)^{\xi-1}\frac{4\rho_r(1-\rho_r)}{d_g} = \rho_r^{\xi-1}(1-\rho_r)^{\xi-1}\frac{2}{3}A_{\mathrm{v}} \qquad \text{Eq. 110}$$

and in the simplest assumption of $\xi = 1$, we obtain simply

$$\psi = \frac{2}{3}A_{\mathrm{v}} \qquad \text{Eq. 111}$$

We may further convert volumetric specific surface area A_{v} to gravimetric specific surface area A_{g} by

$$A_{\mathrm{g}} = \frac{A_{\mathrm{v}}}{\rho_{\mathrm{p}}} = \frac{A_{\mathrm{v}}}{\rho_{\mathrm{r}}\rho_{\mathrm{s}}} \qquad \text{Eq. 112}$$

where ρ_{p} and ρ_{r} are, respectively, the density and relative density of the porous material, and ρ_{s} is the theoretical density of the dense material.

We may also convert to molar specific surface area A_{m} by

$$A_{\mathrm{m}} = A_{\mathrm{g}} M_{\mathrm{m}} = \frac{A_{\mathrm{v}} M_{\mathrm{m}}}{\rho_{\mathrm{r}}\rho_{\mathrm{s}}} \qquad \text{Eq. 113}$$

where M_{m} is the molar mass of the material.

3.3 Common features and general comments

It must be said that the simple models shown here should only be seen as a very first approximation. Nevertheless, they show a few important trends: Firstly, the sample conductivity is for all models proportional to the surface layer conductivity, and in turn by the specific surface layer conductivity and its thickness. Secondly, it is inversely proportional to the grain and pore size. Lastly, it is a function of the relative density. From the geometry of porous ceramics, the macroscopic materials conductivities are expected to have shallow peaks around 50% density at values corresponding to order of magnitude of $\sigma_{\mathrm{M}} = G_{\mathrm{s}}/d_{\mathrm{g}}$, *i.e.,* the surface layer conductance divided by the grain or pore size.

At this stage, there are to our knowledge no systematic experimental studies of surface conduction for a material over a large range of density and/or grain or pore size that would be able to test the validity of the proposed BLM. Such studies would be much welcomed, and for now we must use the model with precaution.

4 Surface protonic conduction in porous monolinic ZrO_2

With the models for proton conduction in chemisorbed and physisorbed water on porous oxides derived in **Chapter 2**, and a brick layer model that links the predicted surface conductance to the sample conductivity presented in **Chapter 3**, we are now ready to verify the proposed models. In this respect, nanoscopic binary oxides such as TiO_2, ZrO_2, and CeO_2 with or without doping are most commonly studied, modelled, and applied in surface protonics (see **Section 1.4**), and will serve as our generalised or explicit model materials too in this thesis. In this chapter, the surface protonic conductivity of porous monoclinic ZrO_2 sintered at temperatures in the range 700-1100°C yielding relative densities of around 60% and grain sizes of approximately 160 nm has been studied with electrochemical impedance spectroscopy as a function of temperature, supported by thermogravimetry of adsorption. The appearance of two high-frequency time responses in the impedance spectra is briefly discussed, which our samples have in common with most porous materials with surface protonic conduction. The present chapter forms the basis of the paper in ref. [139].

4.1 Introduction

The surfaces of nano-grained ZrO_2-based oxides exhibit characteristic water adsorption properties. Much of our present knowledge on adsorption of water and property of ZrO_2 surfaces stems from studies of undoped ZrO_2,[126, 150-153] and Y-stabilised ZrO_2 (YSZ).[68, 75, 81, 82, 127, 136, 154] Monoclinic, cubic and tetragonal ZrO_2 differs in e.g. surface hydroxyl species and acid-base properties.[155, 156] Undoped ZrO_2 is monoclinic up to high temperatures [157] and has gained interest both as a catalyst support and as a catalyst on its own. The surfaces of monoclinic ZrO_2 show a preferred termination along the (111) plane after sintering at high temperatures.[158] To our knowledge, surface protonic conductivity has not been reported for porous monoclinic ZrO_2 and only scarcely from the perspective of volume conduction in undoped ZrO_2 with relatively high density and coarse microstructure.[159]

The present study investigates the surface protonic conductivity in adsorbed water layers in nano-grained porous monoclinic ZrO_2, with focus on validation of the models for adsorption, dissociation, and migration presented in **Chapter 2** and which were developed along with this experimental study. The effects of sintering temperature and hence small differences in microstructure and degree of faceting of the surfaces are evaluated. The results are interpreted according to the model in terms of activation enthalpies and preexponentials of protonic conduction in adsorbed water layers, supported by the observed isothermal p_{H_2O} dependences.

4.2 Experimental

In order to prepare ZrO_2 ceramic pellets, ZrO_2 powder (99.99% metal basis except Hf, CAS no. 1314-23-4, Aladdin Industrial Corporation, China) and binder (a mixture of polyvinyl, glycerol, ethanol and DI water) were mixed in the weight ratio of 7:1 and pressed into disks with diameter of 12.7 mm and thickness of approx. 2.0 mm under a pressure of 760 MPa. They were sintered for 24 h at 600, 700, 800, 900, 1000, or 1100°C, with a heating and cooling ramp rate of 5°C/min. Samples sintered at 600°C were of insufficient mechanical strength for conductivity measurements, and only samples sintered at 700-1100°C were characterised further and are denoted ST700-ST1100 accordingly, see Table 3.

Powder XRD patterns were collected by a Bruker D8 Advance Diffractometer (Laguna Hills, CA, USA) with Cu *Kα* radiation (λ = 1.5418 Å). Microstructures were observed by SEM with a Hitachi SU 8010 Boerne (Hitachi, Tokyo, Japan).

Thermogravimetric data were acquired with a Netzsch STA (simultaneous thermal analyser) Jupiter® 449 *F3* (GmbH, Germany) on the ST700 and ST1000, representing samples sintered at low and high temperatures, respectively, in addition to the pristine ZrO_2 powder using corundum crucibles (Al_2O_3). Samples were first degassed during heating to temperatures right below the sintering temperatures, *i.e.,* 650°C (ST700) or 900°C (ST1000) at 3 K/min using bottle-dry 99.999% N_2 as both carrier and protective gas, and further held at the given temperature for 2 h to ensure complete dehydration. Then, the uptake of water was measured by flowing wet (p_{H_2O} = 0.02 bar) N_2 over the samples during stepwise cooling to 26°C. The water uptake was obtained after subtraction of the background measurements in dry N_2 gas carried out under otherwise identical conditions.

For the electrical measurements, silver paste (SOFCMAN, China) was painted on both sides of the pellets, and heat-treated at 800°C in ambient atmosphere for 2 h to burn off the organic residuals in the paste, except for the sample sintered at 700°C for which the heat-treatment was made at 600°C. The pellets were mounted in a ProboStat™ (NORECS, Norway) sample holder with a standard 4-wire 2-electrode configuration. The ProboStat™ base unit chassis was connected to instrument ground to reduce noise and eliminate parasitic parallel conduction. The gas atmosphere was flowing Ar (99.999%) either bottle-dry or wetted to $p_{H_2O} \approx 0.03$ bar by bubbling through de-ionized (DI) water at room temperature or by a HumiStat gas-mixer and humidifier (NORECS, Norway). The standard HumiStat consists of the humidifier itself and the heated gas supply line. It has inputs for gases A and B (which can be mixed simultaneously if needed), and input for liquid C (*i.e.,* DI water). A built-in temperature controller uses PID algorithm, on a thermocouple feedback from the heated gas line to regulate the powder to the gas line. Here, the temperature was selected high enough to ensure that water is vaporized. The heated gas line has Swagelok tube fitting connects at each end for connection to the ProboStat™ sample holder. The HumiStat software allows selection of gases with specific partial pressures.

Figure 20 shows the HumiStat gas-mixer and the major components of the ProboStat™ measurement cell. The ProboStat™ cell temperature was controlled by a thermocouple placed next to the sample inside the cell and a PID regulator (Eurotherm 2216). Based on previous experiences from logging of temperature, the thermal fluctuations were less than 0.1°C. This setup allows for different types of electrical measurements in a variety of atmospheres, temperatures and relative humidities.

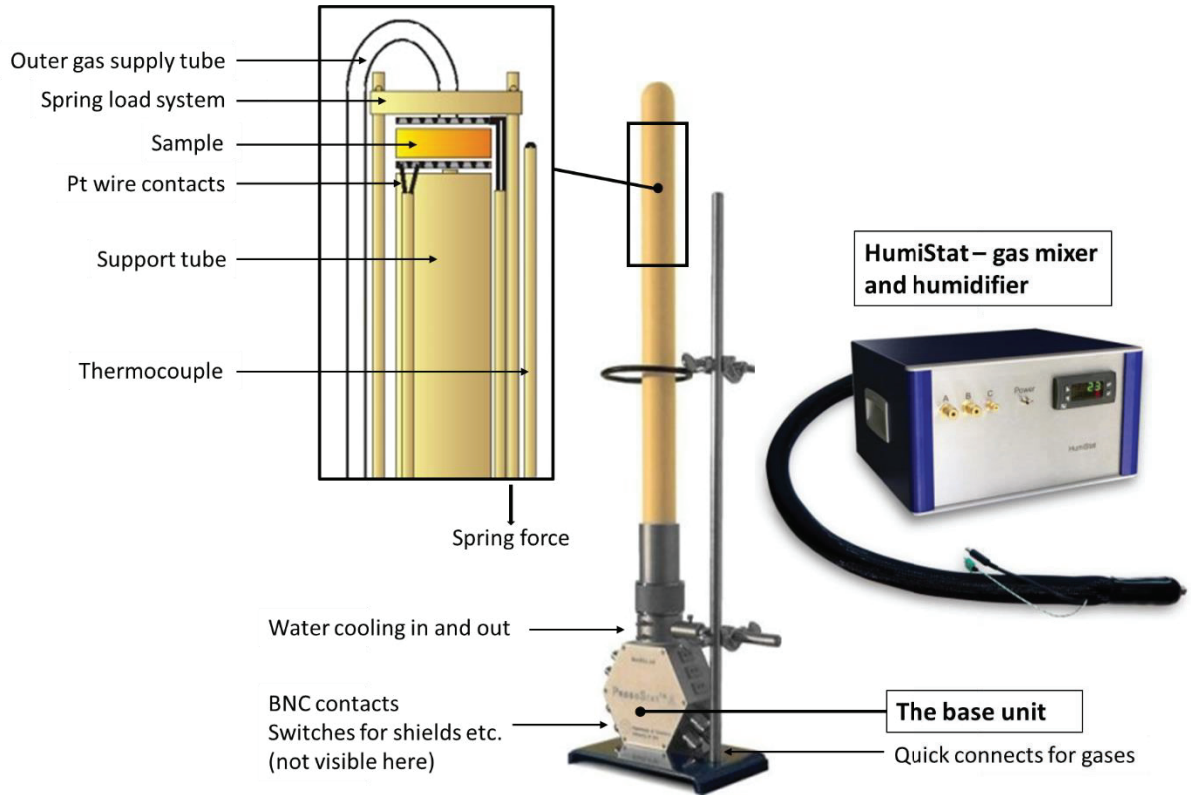

Figure 20 ProboStat system and details for the upper part of the cell where the sample is mounted in the 4-wire 2-electrode configuration, and the HumiStat gas-mixer and humidifier. Pictures and figures: NORECS, Norway (www.norecs.no)

Impedance spectroscopy was used to study the ionic conductivity of nanocrystalline oxides. It allows differentiating transport processes characterized by different time constants, e.g. geometric and grain boundaries. The impedance $Z(\omega)$ can be expressed by its real (Z') and imaginary (Z'') components

$$Z(\omega) = Z' + iZ'' = R + iX \qquad \text{Eq. 114}$$

where R and X are resistance and reactance, respectively. A plot of R against X over a given frequency range is called the Nyquist plot of the impedance data.

The Nyquist plots obtained from the porous samples were fitted to an equivalent circuit that reflects the different transport processes. The choose of equivalent circuits for fitting impedance responses of porous oxides will be discussed in **Section 4.3.3.2**.

AC impedance spectra were collected in the range 1 MHz – 1 Hz at 0.7 V rms applied voltage with a CHI604E electrochemical workstation (Shanghai Chenhua Instruments Ltd., Shanghai, China) or at 3 V rms with a Solartron SI 1260 frequency response analyser (Solartron Analytical, Farnborough, UK). It was controlled that both instruments yielded equivalent impedance spectra. Moreover, each spectrum was recorded twice until no change in spectra was observed to ensure reproducibility. The results were analysed with ZView software (Scribner Associates, Inc. NC, USA). The electrical conductivity of each porous sample is calculated from its resistance, thickness, and electrode area.

4.3 Results

4.3.1 Microstructure characterisation

The geometrical dimensions after sintering were close to those of the green bodies, *i.e.,* little sintering takes place. From the dimensions and weight, the relative densities were calculated to vary only between 60% and 70% for the samples sintered at 700 and 1100°C, respectively, see Table 3.

Table 3 Sample notation with sintering and microstructural parameters. The factor ψ is the ratio between the macroscopic conductivity for the porous sample and the grain surface conductance according to the brick layer model (BLM) introduced in **Section 3.2** (Eq. 106 with $\xi = 1$). Also, volumetric, gravimetric, and molar specific surface areas are estimated to first approximation based on **Section 3.2.1**.

Sample	**ST700**	**ST800**	**ST900**	**ST1000**	**ST1100**
Sintering temperature, °C	700	800	900	1000	1100
Relative density, %	60	60	60	65	70
Average grain size from SEM, nm	150	150	160	170	190
ψ, 1/cm (Eq. 106 with $\xi = 1$)	$6.4 \cdot 10^4$	$6.4 \cdot 10^4$	$6.0 \cdot 10^4$	$5.4 \cdot 10^4$	$4.4 \cdot 10^4$
A_v, cm^2/cm^3	$9.6 \cdot 10^4$	$9.6 \cdot 10^4$	$9.0 \cdot 10^4$	$8.1 \cdot 10^4$	$6.6 \cdot 10^4$
A_g, cm^2/g	$2.7 \cdot 10^4$	$2.7 \cdot 10^4$	$2.6 \cdot 10^4$	$2.1 \cdot 10^4$	$1.6 \cdot 10^4$
A_M, cm^2/mol	$3.4 \cdot 10^6$	$3.4 \cdot 10^6$	$3.2 \cdot 10^6$	$2.6 \cdot 10^6$	$2.0 \cdot 10^6$

Figure 21 shows the XRD results for the precursor powder and powder grinded off the sintered samples. They all correspond to the monoclinic polymorph of ZrO_2. Analyses of the main peaks shows that the full width at half maximum (FWHM) values are close, indicating from the Debye-Scherrer formula average crystallite sizes around 50 nm.[160]

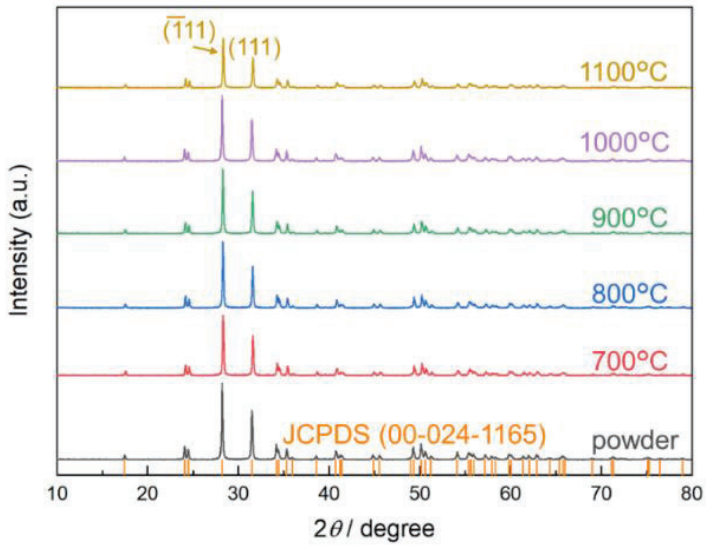

Figure 21 X-ray diffractograms for the ZrO_2 powder and samples sintered at the given temperatures, compared with peak locations for the monoclinic ZrO_2 structure (JCPDS).

Figure 22 shows SEM images of the precursor powder and sintered samples, revealing the openly porous microstructure in agreement with the densities from the geometry and weight. From statistical analyses of the images, we estimate average grain sizes of 150 nm for the precursor powder and 150-190 nm for the ST700-ST1100 samples. Hence, both sintering and grain growth are modest at the sintering temperatures applied here.

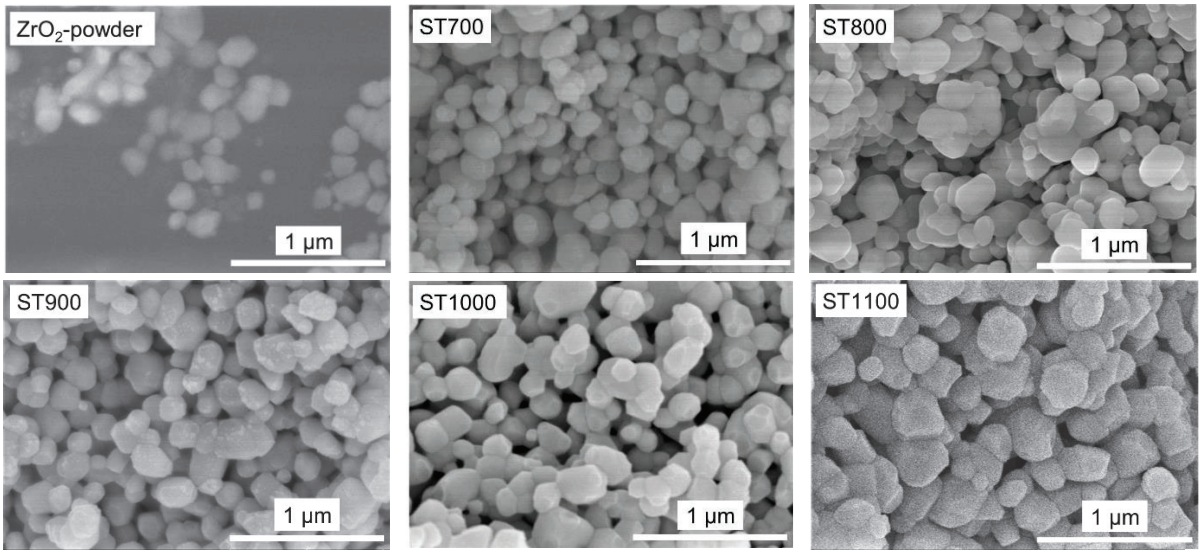

Figure 22 SEM images of the precursor powder and fracture surfaces of the sintered samples.

Closer inspection of the grains suggests no differences in aspect ratio and modest differences in connectivity (necks). However, while the mostly spherical shape of the precursor particles has been retained in the samples sintered at the lowest temperatures (below 900°C), the particles of samples sintered at higher temperatures show more faceted surfaces, a distribution over normal (100), (110), and (111) surfaces (in cubic framework) as the regular aspect of the crystallite is maintained.

4.3.2 Thermogravimetry (TG)

Figure 23 shows the TG result in terms of amount of water (chemisorbed and physisorbed) adsorbed on the pristine ZrO_2 powder and on the ST700 and ST1000, with area specific coverage calculated based on the estimates of specific surface areas (**Section 3.2.1**) listed in Table 3. The uptake of chemisorbed water saturates towards 200°C at around 4-5 H_2O molecules/nm^2, which is considered a monolayer.[126] We note that the coverage is not yet complete at 400°C for the ST700 sample, suggesting relatively weak and hence molecular chemisorption, while the ST1000 sample achieves the same coverage at somewhat higher temperature, indicating stronger chemisorption on its more developed (faceted) surfaces.

Physisorption sets in below 200°C, and a first physisorbed layer is complete around 80°C for the sintered samples. Qualitatively, the water uptake modelled as a sum of a completed chemisorbed layer and physisorbed layers yields adsorption enthalpies similar to that of condensation to liquid water,[136] as expected. The total water uptake corresponds well to one reported in the literature, when its surface area of 80 m^2/g a factor of 4 higher than in our samples is taken into account.[161]

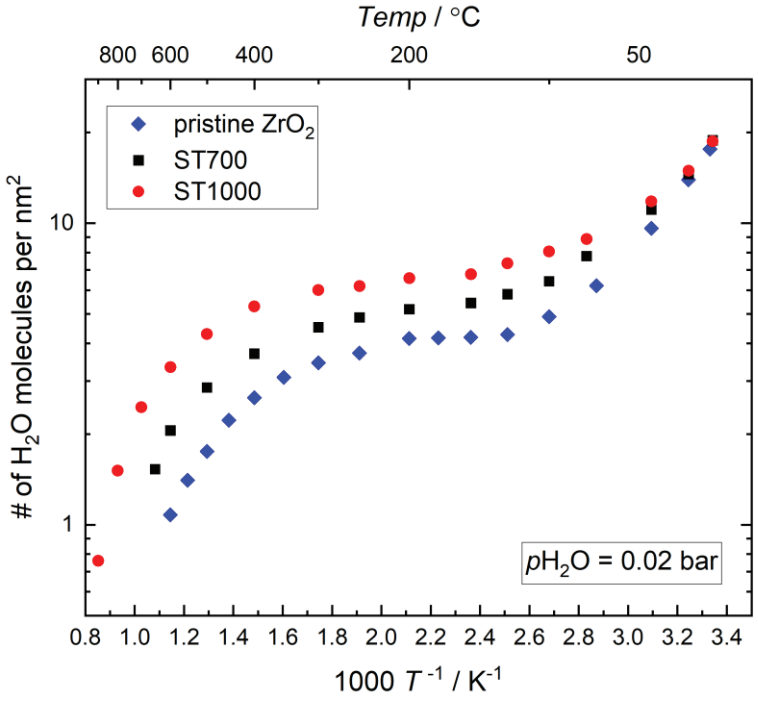

Figure 23 The area specific uptake of water obtained from TG analysis for the pristine powder and the sintered samples (ST700 and ST1000) in wet (p_{H_2O} = 0.02 bar) N_2 *vs* 1/*T*.

4.3.3 Electrical properties

4.3.3.1 Impedance spectroscopy

Representative impedance spectra of the sintered samples are displayed in Figure 24. All samples exhibited two overlapping semicircles in the high frequency domain, with capacitances in the lower and higher end of the 10^{-11} F range, irrespective of sintering and measurement temperature or atmosphere (dry or wet). Similar duality has been reported for porous YSZ, but with bigger differences in capacitance, suggested to reflect *intra-grain* protonic transport over grain surfaces affiliated with low capacitance and *inter-grain* protonic transport over resistive grain boundaries affiliated with higher capacitance.[82]

The two responses are present also in dry atmospheres at the highest measurement temperatures (Figure 24 e and f). This reflects that also the native, non-protonic conduction is dominated by surface transport, which is reasonable in these fine-grained porous samples. At the highest measurement temperatures, there is an additional response at the lowest frequencies, with characteristic capacitances of order of magnitude 10^{-8} F, both in wet and dry atmospheres. This may be a grain boundary impedance like reported by Stub *et al.* [82] for YSZ, but it may also be an electrode response: The contact area between the adsorbed water layer and the metal electrode is small compared with a normal solid electrolyte, hence the normal capacitance of 10^{-6} F for samples of this size attributed to the double layer in parallel with charge transfer may be reduced by orders of magnitude and be what we observe.

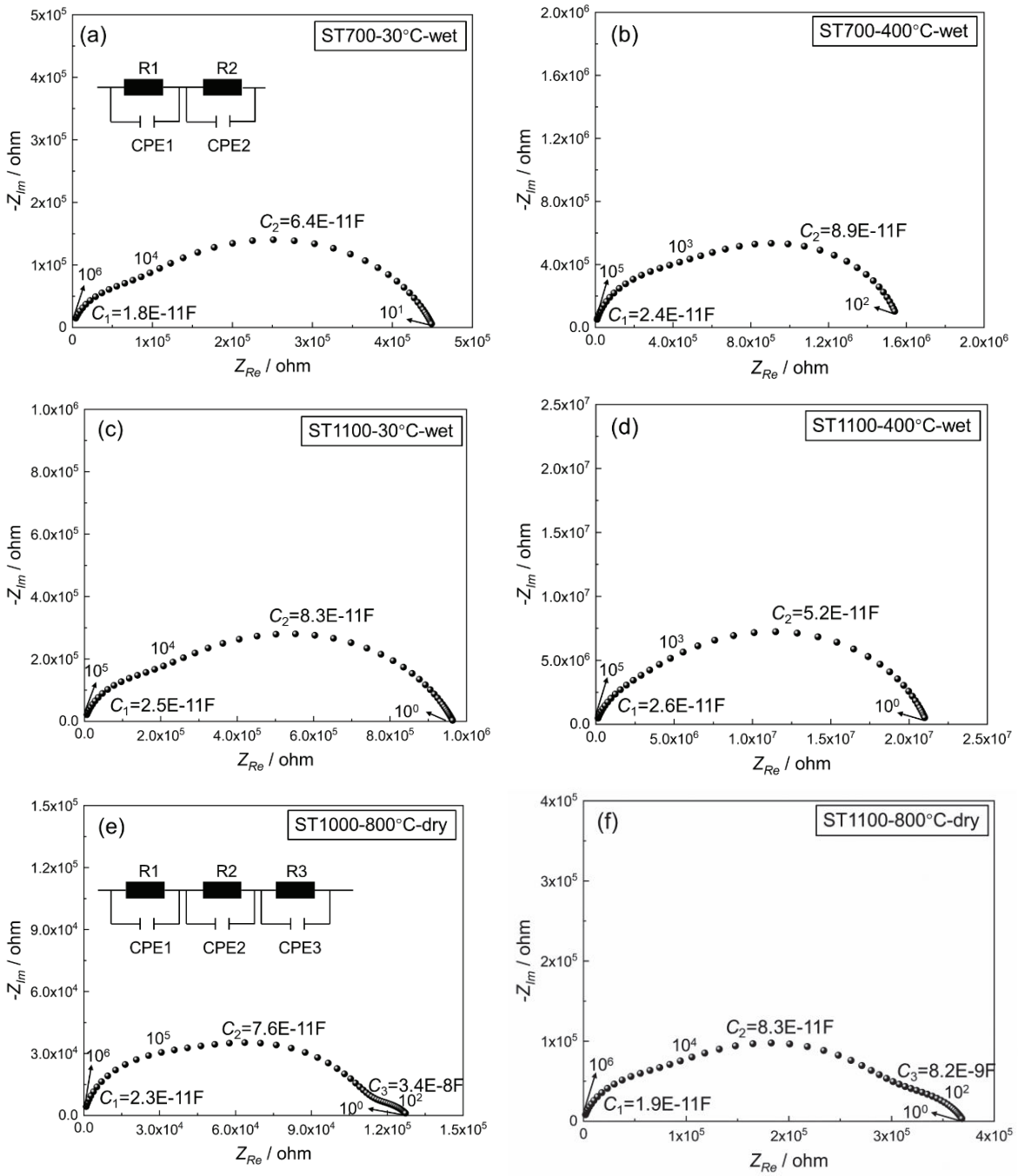

Figure 24 Impedance spectra ($-Z_{\mathrm{im}}$ vs Z_{Re} in ohms) as measured at 30°C (a and c), 400°C (b and d) in wet ($p_{\mathrm{H_2O}}$ = 0.03 bar) Ar and at 800°C (e and f) in dry Ar for the samples sintered at 700°C (a and b), 1000°C (e), and 1100°C (c, d, f). The equivalent circuit used to model the data was either $(R_1Q_1)(R_2Q_2)$ in wet (exemplified in a) or $(R_1Q_1)(R_2Q_2)(R_3Q_3)$ in dry (exemplified in e). Numbers along the curve show the AC frequencies. Characteristic capacitances for the two or three responses are indicated (these include the parasitic capacitance of the ProboStat™ cell, which in the configuration used amounts to a few pF).

4.3.3.2 Origin of the two high-frequency responses

The presence of two high-frequency responses and small bulk-like capacitances in these samples could be attempted rationalised as due to intersecting grain boundaries or part of the electrode impedance. However, the high-temperature spectra in this study shows that the two high-frequency responses are well separated from the third response at lower frequencies that may be grain boundaries or electrodes. Moreover, the omnipresence of these dual time constants for all samples and conditions in this work and other studies of surface conduction in porous ceramics suggests that a more intrinsic phenomenon is at play.

Consider first two electrodes connected to a porous sample with no conductivity. It will have a dielectric response corresponding to the effective dielectric constant $\varepsilon_e = \varepsilon_{re}\varepsilon_0$ given by those of the gas phase (approximated by that of vacuum) and the ceramic phase, to a first approximation weighted by the relative density:

$$\varepsilon_{re} = 1 + (\varepsilon_r - 1)\rho_r \quad \text{and} \quad \varepsilon_e = \varepsilon_0(1 + (\varepsilon_r - 1)\rho_r) \qquad \text{Eq. 115}$$

For bulk monoclinic ZrO_2, the relative dielectric constant is approximately 20,[162] so that with 60% relative density, we will have $\varepsilon_{re} \approx 12$ and $\varepsilon_e \approx 10^{-10}$ F/m = 10^{-12} F/cm. Our samples with thickness 0.20 cm and electrode area 1.27 cm^2 would be expected to exhibit a geometric capacitance of $C_{geom} \approx 6 \cdot 10^{-12}$ F. With the addition of parasitic cell capacitance, this corresponds acceptably to the smallest capacitance responses in Figure 24.

If conduction would take place in the bulk of the grains, or along parallel surfaces, the response will be given by a simple circuit of the conductance and the capacitance in parallel, yielding a single bulk-like semicircle in a Nyquist plot. However, if the surface is curved, it will have convex features, like rounded and edged grains, and concave features, like grain necks. When the current passes over a convex feature, it will have a longer way to go in the conductive surface layer, but the parallel capacitance through the dielectric material of the grain gives this part of the transport a higher ratio between the parallel capacitance and the conductance compared to the average sample. In contrast, passing a concave part offers little capacitance from the gas phase there. Hence, the sample response would break up into a $(R_{cave}C_{cave})(R_{cvex}C_{cvex})$ type circuit, where the first part attributed to the concave features has low capacitance and high-frequency response, and the second one attributed to convex features has higher capacitance and a lower-frequency response. As an alternative, one may assign the geometric capacitance C_{geom} in parallel over a series connection of the concave part resistance and the parallel $(R_{cvex}C_{cvex})$ element: $(C_{geom}(R_{cave}(R_{cvex}C_{cvex})))$. In reality, parameters are even more complicated to predict and analyse and may be expected to be dispersed due to variations in real microstructures. Hence, a very first step in this direction is to assign constant phase elements Q_{cvex} instead of C_{cvex} and use circuit $(C_{geom}(R_{cave}(R_{cvex}Q_{cvex})))$.

In this work, we take the sum of resistances of the two high-frequency responses to represent the total resistance of the surface transport, *i.e.,* $R_{tot} = R_{cave} + R_{cvex}$.

4.3.3.3 Temperature dependence of conductivities

The temperature dependencies of the electrical conductivity for all samples are shown in Figure 25 (a). In bottle-dry atmospheres at the highest measurement temperatures (open-symbols), the measured conductivities were similar for all samples, with activation energies of around 100 kJ/mol, attributable to inherent conduction by oxide ions in gross agreement with literature data for bulk conductivity of monoclinic ZrO_2.[159, 163] We attribute it to native conductivity of the sample, dominated by surface transport based on the above-mentioned interpretation of the impedance spectra (*i.e.,* overlapping high-frequency semicircles) in dry atmospheres. The conductivities in wet atmosphere generally behave like typical surface protonic isobars with considerable conductivities at high temperatures, a minimum at around 200°C, and conductivities increasing with decreasing temperature towards room temperature. Another ST800 sample measured in wet O_2 (not shown on the plot) revealed qualitatively the same conductivities and temperature dependencies as ST800 and the other samples measured in wet Ar, suggesting that the oxygen partial pressure plays no significant role for ZrO_2.

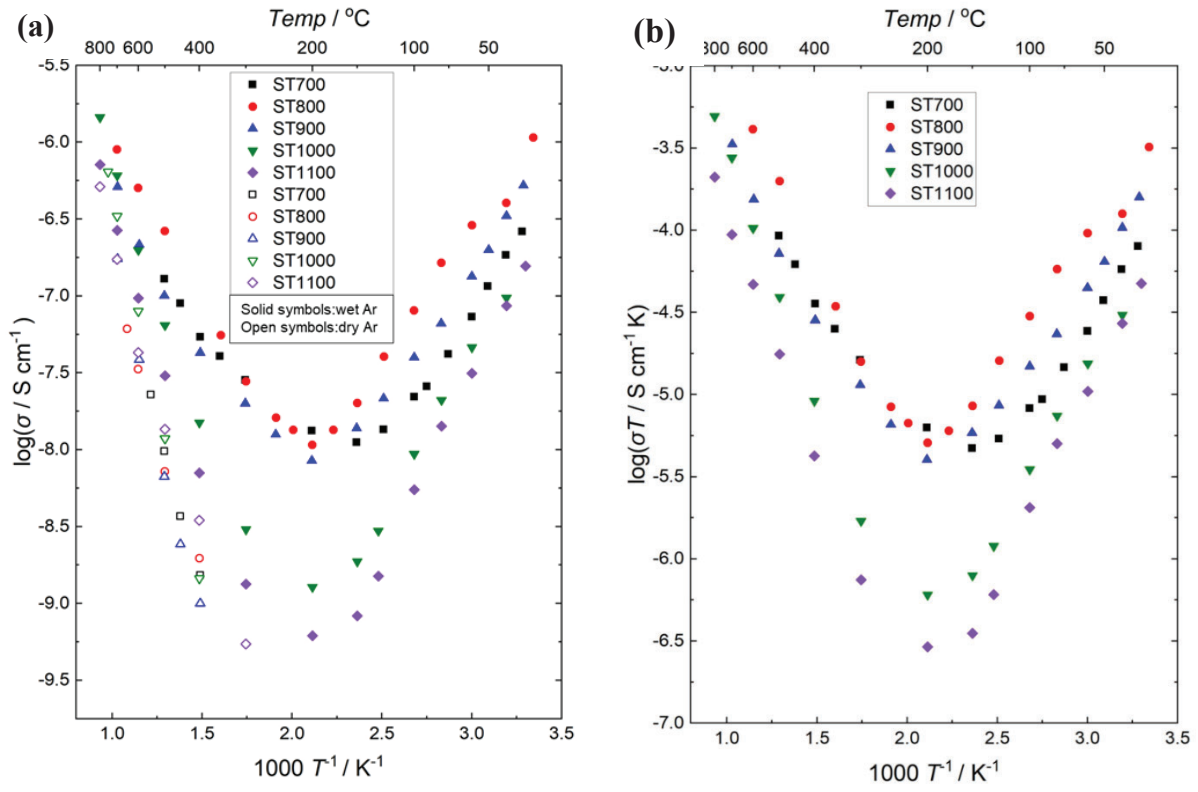

Figure 25 (a) Plot of logσ *vs* 1/T in wet (p_{H_2O} = 0.03 bar) or bottle-dry Ar for samples sintered at different temperatures shown in the legend, (b) Plot of log(σT) *vs* 1/T measured in wet Ar after subtraction of the native conductivities in dry Ar, as explained in the text.

Figure 25 (b) displays the surface protonic conductivities obtained in wet Ar after subtraction of the native conductivity, plotted as log(σT) *vs* 1/T. The activation enthalpies and preexponentials were further extracted from the plot, and listed in Table 4.

Above 200°C are typical of conduction in the chemisorbed water layer, which according to adsorption thermodynamics of ZrO_2 [126] should approach full coverage below 400°C at p_{H_2O} = 0.03 bar. The activation enthalpies in this region are approaching 60 kJ/mol for ST1000 and ST1100, which is comparable to the enthalpy of mobility of protons in lattices of MO_2 oxides, e.g. 58 kJ/mol for polycrystalline rutile TiO_2,[164] and 43 kJ/mol as an estimate for 50% La-doped CeO_2.[165] With lower sintering temperatures, the enthalpies decrease to around 30 kJ/mol for ST700, and conductivities are higher reflecting that the enthalpy of mobility is lower and/or the exothermic adsorption is at play, *i.e.,* the layer is not complete and still filling up with decreasing temperature for these samples, in agreement with the TG results, and to be discussed further later.

Below 150°C, a strong increase in conductivity is observed as a first molecular physisorbed water layer starts to build on top of the chemisorbed layer, providing easier transfer of protons. The activation enthalpies are now found to be in the range -40 to -20 kJ/mol. This is qualitatively dominated by the exothermic enthalpy of condensation of water vapour, and we shall quantify it when we discuss models for transport in this layer later.

As the physisorbed layer builds, it expectedly gets more liquid-like and the physisorption enthalpy approaches that of pure liquid water. This gives rise to an additional strong increase in the surface protonic conductivity in many porous ceramics when approaching RT and *RH* surpasses 60%.[81, 118, 144] For our monoclinic ZrO_2 samples however, there is no such secondary increase in conductivity. This is similar to undoped CeO_2 [166] and Gd-doped CeO_2.[70] As our data do not extensively explore the region at $RH > 60\%$, we refrain from analysing that region further and it is not part of Table 4.

Table 4 Preexponentials and activation enthalpies of the macroscopic conductivity of the porous ZrO_2 samples fitted from $\log(\sigma T)$ *vs* $1/T$ plots in Figure 25 (b).

Conditions	**Type of conduction**	**Sample** / **Parameter**	**ST700**	**ST800**	**ST900**	**ST1000**	**ST1100**
High *T*, dry	Native conductivity	$\sigma_{M\,0}$, SK/cm	$2{\cdot}10^{1}$	$1{\cdot}10^{1}$	$1{\cdot}10^{2}$	$1{\cdot}10^{2}$	$7{\cdot}10^{1}$
		ΔH, kJ/mol	95	92	109	105	104
High *T*, wet	Surface protonic, chemisorbed	$\sigma_{M\,0}$, SK/cm	$5{\cdot}10^{-3}$	$1{\cdot}10^{-1}$	$2{\cdot}10^{-2}$	$4{\cdot}10^{-1}$	$1{\cdot}10^{-1}$
		ΔH, kJ/mol	27	41	34	58	57
Low *T*, wet	Surface protonic, 1st physisorbed	$\sigma_{M\,0}$, SK/cm	$6{\cdot}10^{-9}$	$1{\cdot}10^{-9}$	$5{\cdot}10^{-9}$	$7{\cdot}10^{-12}$	$4{\cdot}10^{-13}$
		ΔH, kJ/mol	-22	-32	-25	-40	-47

4.3.3.4 Isothermal pH_2O dependencies

Figure 26 shows the p_{H_2O} dependence of surface protonic conductivity obtained for the ST700 sample recorded at 400 and 100°C, reflecting the chemisorbed and first physisorbed water layer, respectively. A close to $p_{H_2O}^{1/2}$ dependency is revealed at 400°C, in agreement with results for 4 mol% Y_2O_3-stabilised ZrO_2 (4YSZ) at 250-400°C [84] and for undoped CeO_2 at 400°C.[166] This may be interpreted to reflect weak molecular and hence incomplete chemisorbed layer with only partial dissociation to conduct protons. At 100°C, we obtained close to a $p_{H_2O}^{3/2}$ dependency. We will discuss models that may rationalise it below.

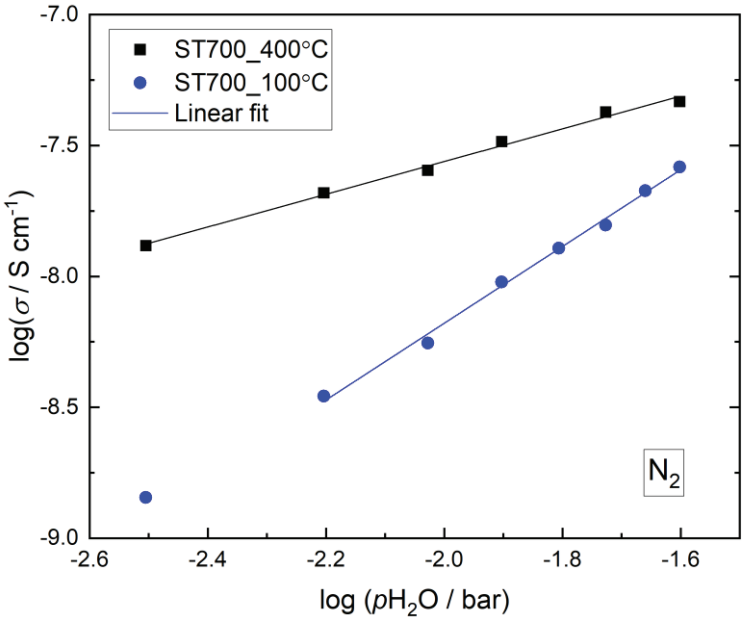

Figure 26 p_{H_2O} dependence of surface protonic conductivity for ST700 at 400 and 100°C recorded in N_2 gas, representing the chemisorbed and physisorbed region, respectively.

4.4 Models and quantitative interpretation

As shown in Table 4, the ZrO_2 samples behave differently in terms of activation enthalpy and preexponentials of surface conduction. In the following, a theoretical analysis of these parameters is provided based on the different models for adsorption, dissociation and protonic migration (**Chapter 2**). As we shall see, the preexponentials (G_0 and/or σ_0) are quantitatively assessable on order-of-magnitude level to discriminate models via the brick layer model (BLM, see **Chapter 3**). Furthermore, the mobility of protons in the different water layers will be estimated. As mentioned, please refer to **Appendix I** for a full list of symbols and abbreviations.

Under the experimental conditions, the bulk conductivity of ZrO_2 ($\sigma_{M,b}$) is due to native oxide ion transport, and while it appears that this is negligible, the macroscopic surface conductivity

($\sigma_{M,s}$) also has a contribution from oxide ions in addition to protonic conduction. With this, Eq. 4 (**Section 2.4.1**) for the case of ZrO_2 can be written as

$$\sigma_M = \sigma_{M,b} + \sigma_{M,s} \approx \sigma_{M,s,O^{2-}} + \sigma_{M,s,H^+} \qquad \text{Eq. 116}$$

After subtraction from the inherent surface oxide ion conductivity in dry atmosphere, Figure 25 b) represents $\sigma_M = \sigma_{M,s,H^+}$, with contributions from the chemisorbed and physisorbed water layers in accordance with Eq. 5.

We may make an order-of-magnitude approximation to the macroscopic conductivity σ_M of a porous material from the surface conductance G_s according to the BLM. In this work, we hence estimate the macroscopic sample surface protonic conductivity from

$$\sigma_{M,s,H^+} \approx \frac{4\rho_r^{\xi}(1-\rho_r)^{\xi}}{d_g} G_{s,H^+} = \psi G_{s,H^+} \qquad \text{Eq. 117}$$

The factor ψ calculated on this basis is listed for our samples in Table 3.

4.4.1 Chemisorbed layer

We start by attempting to predict the level and behaviour of surface protonic conductivity in the chemisorbed layer, which dominates typically in wet atmospheres at high temperatures down to around 200°C. Two chemisorption models that are shown to be applicable to ZrO_2 sintered at low and high temperatures, respectively, will be discussed. Another model based on dissociation to and migration between adsorbed water molecules ("*cma-a*" model, see illustration in Figure 14) was also evaluated, however, it has a predicted preexponential orders of magnitude away from experimental values, hence is ruled out and for the sake of simplicity not discussed further here. Table 5 summarizes the two models of relevance with the derived p_{H_2O} dependences along with the predicted estimates of preexponentials (G_0 and σ_0) under the experimental conditions. In the same table, values for ST700 and ST1100 from curve-fitting, representing samples sintered at low and high temperatures, representatively, are included for comparison purpose. The standard preexponentials G^0_{s,H^+0} is repeated in Table 5 for completeness.

Table 5. Derived p_{H_2O} dependences and predicted preexponentials for two quantifiable chemisorption models describe surface protonic conductivity in porous ZrO_2, compared with experimental values of the same parameters for ST700 and ST1100. The preexponentials are rounded off to one significant digit, but the realistic predictive power is much less accurate, rather within 1-2 orders of magnitude due to the many assumptions mainly in adsorption thermodynamics and transport parameters.

	Derived values according to the models		**Experimental values**	
Model notation / Sample name	*cms-s* / *cds-s* (low coverage)	*cds-s* (full coverage)	ST700	ST1100
p_{H_2O} dependency, n in $p_{H_2O}^n$	0.5	0	0.6	-
G^0_{s,H^+0}(SK), p_{H_2O} = 1 bar	$2\cdot10^{-6}$	$4\cdot10^{-4}$		
G_{s,H^+0}(SK), p_{H_2O} = 0.03 bar	$3\cdot10^{-7}$	$4\cdot10^{-4}$	$8\cdot10^{-8}$	$2\cdot10^{-6}$
σ_{M,s,H^+0} (SK/cm), p_{H_2O} = 0.03 bar, $\psi = 6\cdot10^4$ /cm	$2\cdot10^{-2}$	$2\cdot10^{1}$	$5\cdot10^{-3}$	$1\cdot10^{-1}$

4.4.1.1 Molecular chemisorption

A previous *in situ* FTIR study supports the non-dissociative mechanism of water chemisorption on monoclinic ZrO_2 between RT and 1173 K over a pressure range of 10^{-5}–24 mbar, in contrast to highly hydroxylated YSZ and Y_2O_3.[154] Room temperature IR measurements on high surface area ZrO_2 after annealing at 873 K reveal a single broad peak at 3690 cm^{-1}, attributed to the O-H stretch mode of H_2O molecules, in addition to a characteristic molecular water band at ~1630 cm^{-1} due to H-O-H bending.[161] *Ab initio* molecular dynamics calculations suggest that while only dissociative adsorption is observed on tetragonal ZrO_2(110) surfaces,[167] both undissociated and dissociated water species coexist on the two most stable surfaces of monoclinic ZrO_2, *i.e.,* (101) and (111) surfaces.[152]

These experimental and computational studies suggest the possibility that H_2O molecules may first chemisorb on a surface M^{4+} cation, following Eq. 11. As shown in Table 5, the samples sintered at the lowest temperatures (e.g. ST700) can be rationalised by the model for low coverage of chemisorbed water with limited dissociation to other surface oxide ions according to Eq. 16 and Eq. 17, and further proton migration between surface oxide ions (*i.e.,* "*cms-s*"and "*cds-s*" model, Figure 11 a and c), thereby providing protonic conductivity.

The surface protonic conductance ($G_{s,H^+_{cms\text{-}s}}$) then follows Eq. 36, with the corresponding preexponential ($G_{s,H^+_{cms\text{-}s}0}$) given by Eq. 38. In order to estimate $G_{s,H^+_{chm\text{-}s}0}$, considering that the concentration of surface oxide adsorption sites in ZrO_2 is twice that of cation sites, *i.e.,* $\gamma_{O_s} = 2\gamma_{M_s}$, and other parameters the same as those applied when predicting $G^0_{s,H^+_{chm}0}$ at p_{H_2O} =

1 bar (Table 2), namely, $\Delta S^0_{a_{cm}}$ = -109 J/molK, $\Delta S^0_{d_{cm}}$ = 0 J/molK, $\gamma_{M_s} \approx 5$ /nm^2 = 8·10^{-10} mol/cm^2, and $u_{H^+0} \approx 10$ cm^{2}K/Vs as derived in Section 2.4.2, we get $G_{s,H^+_{chm\text{-}s}0} \approx 3\cdot10^{-7}$ SK at p_{H_2O} = 0.03 bar. By applying the BLM: $\sigma_{M,s,H^+_{cms\text{-}s}0} = \psi G_{s,H^+_{cms\text{-}s}0}$ and values of ψ from Table 3, we get predicted preexponentials for macroscopic surface protonic conductivity $\sigma_{M,s,H^+_{chm\text{-}s}0} \approx 2\cdot10^{-2}$ SK/cm at p_{H_2O} = 0.03 bar for samples sintered at relatively low temperatures.

Sample ST700 has a measured preexponential of macroscopic conductivity of around 5·10^{-3} SK/cm (Table 4 and also Table 5), *i.e.,* within an order of magnitude of the prediction, suggesting that low coverage of chemisorbed water (molecular or dissociative) with weak dissociation to protons transported along surface oxide ions may apply for the surface protonic conductivity at temperatures above 200°C for samples sintered at the lowest temperature. The model further proposes a proportionality to $p^{1/2}_{H_2O}$ of surface protonic conduction, which is in line with the experimental results obtained for the ST700 sample at 400°C (Figure 26).

We suggest that this may apply also to other oxides where similar behaviour is observed, and is a result of surfaces that are relatively amorphous or rounded (*vs* faceted) or has terminations where dissociation is unfavourable. While the transfer of a proton to a surface oxide ion is not very favourable, the transfer between oxide ions may be correspondingly easier.

Activation enethaly for surface protonic conduction can be as low as 0.15 eV.[168] In this case, the experimental activation enthalpy of around 27 kJ/mol (listed in Table 4) should be interpreted according to $\Delta H_{c_{cms\text{-}s}} = \Delta H_{c_{cds\text{-}s}} = \frac{1}{2}\Delta H^0_{a_{cm}} + \frac{1}{2}\Delta H^0_{d_{cs}} + \Delta H_{m,H^+_s}$, as shown in Eq. 37. The standard enthalpy of molecular chemisorption has been determined calorimetrically as $\Delta H^0_{a_{cm}}$ = -76±5 kJ/mol for YSZ relatively independent of Y content.[127] If we adopt the dissociation enthalpy of $\Delta H^0_{d_{cs}}$ = 22.1 kJ/mol from ref. [169] used by Raz *et al.* [136] for YSZ, we get an enthalpy for mobility of protons along surface oxide ions of $\Delta H_{m,H^+_s}$ = 54 kJ/mol.

4.4.1.2 Dissociative chemisorption

As indicated in Table 5, comparison between the experimental vs predicted σ_{M,s,H^+0} suggest that samples sintered at higher temperatures (e.g. ST1100) may follow Eq. 18 for a fully covered dissociated chemisorbed water layer, with migration of dissociated protons by jumping between surface oxide ions (*i.e.,* "*cds-s*" model, Figure 11 d). The electroneutrality and assumption of full coverage leads to Eq. 42 as explained earlier.

In this case, the surface protonic conductance $G_{s,H^+_{cds\text{-}s}}$ follows Eq. 43 with preexponential $G_{s,H^+_{cds\text{-}s}0}$ given by Eq. 44. With the same assumptions and parameters as before, this yields

$G_{s,H^+_{cds\text{-}s}0} = G^0_{s,H^+_{cds\text{-}s}0} \approx 4 \cdot 10^{-4}$ SK, and $\sigma_{M,s,H^+_{chd}0} \approx 20$ SK/cm via the BLM, to be compared with the corresponding experimental preexponentials (Table 4) for the chemisorbed layer of 0.1-0.4 SK/cm for the samples sintered at the highest temperatures. The two orders of magnitude difference may be ascribed to the many approximations along the way, but may also mean that the assumptions of the model comprising fully covering and dissociated chemisorbed water are not fully met. Moreover, if the current model applies, the isothermal p_{H_2O} dependence of conductivity will disappear for full coverage as can be seen from Eq. 44, yet the p_{H_2O} dependence remains to be verified in this work.

Following this model, we may further assign the activation enthalpies of up to 60 kJ/mol observed for ST1000 and ST1100 to the diffusion barrier for protons migrating (see Eq. 43) between oxide ions on the faceted surfaces of monoclinic ZrO_2 covered with dissociatively chemisorbed water. The aforementioned comparison to the enthalpy of mobility of protons of 58 kJ/mol for polycrystalline rutile TiO_2 [164] and 43 kJ/mol as an estimate for 50% La-doped CeO_2 [165] is reasonable if the concentration of carriers is constant as in a fully covered chemisorbed layer, which based on TG (Figure 23) seems reasonable for the samples sintered at the highest temperatures.

The samples sintered at intermediate temperatures show preexponentials and enthalpies between those sintered at the lowest and highest temperatures, and we may expect that they (or in fact all samples) have mixed presence of surface areas with molecular and dissociated chemisorption.

4.4.2 The first physisorbed water layer

At lower temperatures and higher *RH*, the conductivities of the samples increase with decreasing temperatures. This is may be assigned to the formation of physisorbed water layers on top of the chemisorbed water layer. Protonic conduction in the first physisorbed water layer is evaluated based on the two models treated in **Section 2.7.2**. Similar to chemisorption, the predicted estimates of preexponentials and p_{H_2O} dependencies for surface protonic conduction in the 1st physisorbed layer of water to be compared with the experimental values for ST700 and ST1100, and summarized in Table 6. It can be seen that the two proposed models appear to apply for the samples sintered at low and high temperatures, respectively.

Table 6. Derived p_{H_2O} dependencies and predicted preexponentials for the two models of protonic surface transport in the 1st physisorbed water layer, for the case of conditions and microstructures in this paper, compared with experimental values of the same parameters for ST700 and ST1100.

	Derived values according to the models		**Experimental values**	
Model notation / Sample name	*chm-ph1*	*ph1*	ST700	ST1100
p_{H_2O} dependency, n in $p_{H_2O}^n$	1.5	2	1.5	-
G^0_{s,H^+0} (SK), p_{H_2O} = 1 bar	$2\cdot10^{-12}$	$6\cdot10^{-15}$		
G_{s,H^+0} (SK), p_{H_2O} = 0.03 bar	$1\cdot10^{-14}$	$6\cdot10^{-18}$	$9\cdot10^{-14}$	$6\cdot10^{-18}$
σ_{M,s,H^+0} (SK/cm), p_{H_2O} = 0.03 bar, $\psi = 6\cdot10^4$ /cm	$7\cdot10^{-10}$	$3\cdot10^{-13}$	$6\cdot10^{-9}$	$4\cdot10^{-13}$

4.4.2.1 Dissociation from chemisorbed to physisorbed water

In the case where the chemisorbed molecular water layer is fully covered, associated with limited dissociation to the physisorbed layer forming H_3O^+ according to Eq. 80 (schematically displayed in Figure 16), the surface protonic conductance $G_{s,H^+_{chm\text{-}ph1}}$ and its preexponential $G_{s,H^+_{chm\text{-}ph1}0}$ follows Eq. 85 and Eq. 87, respectively ("*chm-ph1*" model).

Assuming that the parameters for chemisorption also applies to physisorption, *i.e.*, $u_{H^+0} \approx 10$ cm^{2}K/Vs, $\Delta S^0_{ph1} \approx$ -109 J/molK, $\Delta S^0_{d_{chm\text{-}ph1}}$ is negligible, we obtain $G_{s,H^+_{chm\text{-}ph1}0} \approx 1.2\cdot10^{-14}$ SK at p_{H_2O} = 0.03 bar. By applying the BLM $\sigma_{M,s,H^+_{chm\text{-}ph1}0} = \psi G_{s,H^+_{chm\text{-}ph1}0}$ with $\psi = 6\cdot10^4$ /cm, $\sigma_{M,s,H^+_{chm\text{-}ph1}0}$ comes out as $7\cdot10^{-10}$ SK/cm. If we assign a negative standard entropy to dissociation, like a small part of what it is in liquid water, the preexponentials decrease further. This is in rough agreement with the experimentally observed preexponentials of conductivity in the 1st physisorbed layer for the samples sintered at the lowest temperatures (~10^{-9} SK/cm for ST700, see Table 4 and/or Table 5).

The corresponding apparent activation enthalpies of around -30 kJ/mol should according to this model follow $\Delta H_{c_{chm\text{-}ph1}} = \frac{3}{2}\Delta H^0_{ph1} + \frac{1}{2}\Delta H^0_{d_{chm\text{-}ph1}} + \Delta H_{m,H^+_{chm\text{-}ph1}}$ as indicated in Eq. 86. Taking $\Delta H^0_{ph1} \approx$ -45 kJ/mol as explained earlier (**Section 2.7.1**), $\Delta H^0_{d_{chm\text{-}ph1}}$ as that in water at 100°C of +42 kJ/mol as a first estimate, the activation enthalpy of proton mobility $\Delta H_{m,H^+_{chm\text{-}ph1}}$ ≈ +17 kJ/mol, credible in being just somewhat higher than that in liquid water of 12 kJ/mol.

Furthermore, ZrO_2 ST700 revealed an approximate $p_{H_2O}^{3/2}$ dependence of conductivity in the physisorbed region (Figure 26), in agreement with the predicted results from the current model, suggesting that dissociated protons may come from the chemisorbed water layer underneath.

4.4.2.2 Dissociation within physisorbed water

In the other "*ph1*" model, it is assumed that the physisorbed water molecules dissociates protons within the same physisorbed layer because the chemisorbed water underneath is already fully dissociated (Eq. 88), as schematically illustrated in Figure 17. The surface protonic conductance $G_{s,H^+_{ph1}}$ from this process then follows Eq. 92, with preexponentials $G_{s,H^+_{ph1}0}$ given by Eq. 94. Under the same assumptions as above, we obtain $G_{s,H^+_{ph1}0} \approx 6 \cdot 10^{-18}$ SK, and $\sigma_{M,s,H^+_{ph1}0}$ around $3.4 \cdot 10^{-13}$ SK/cm via the BLM, possibly somewhat lower if the entropy of dissociation is negative like in liquid water. This corresponds well with the experimentally observed preexponentials for the samples sintered at the highest temperatures, see Table 4 and also Table 5 for the ST1100 sample. Furthermore, there is a $p_{H_2O}^2$ -dependence of conductivity of this model *vs* a $p_{H_2O}^{3/2}$ -dependence of the preceding p_{H_2O} one, which remains to be confirmed for the ST1100.

As suggested by Eq. 93, the apparent activation enthalpies approaching -50 kJ/mol are to compare with the 2 times the estimated standard adsorption enthalpy of -45 kJ/mol plus half the dissociation enthalpy which as a first estimate may be taken as that in liquid water at 100°C of +42 kJ/mol ($\Delta H_{c_{ph1}} = 2\Delta H^0_{ph1} + \frac{1}{2}\Delta H^0_{d_{ph1}} + \Delta H_{m,H^+_{ph1}}$), leaving the enthalpy of proton mobility at $\Delta H_{m,H^+_{ph1}} \approx 19$ kJ/mol, again a credible assessment. The difference to the preceding model is the expected effect of half the adsorption enthalpy.

For the sake of completion, we mention here that the expected even stronger increase in conductivity due to the formation of the liquid-like physisorbed layer as temperature decreases further (see **Section 2.7.3**) was not evidenced in this study of monoclinic ZrO_2.

4.5 Discussion and conclusions for ZrO_2

Our impedance spectrometric study of the surface protonic conductivity *vs* temperature of porous undoped monoclinic ZrO_2 sintered at five different temperatures has allowed us to forward the first set of models for interpretation and parameterisation of surface protonic conduction. The observed dual time constants in the high frequency part of the impedance spectra in concomitance with capacitances in the geometric (bulk) range were suggested to represent capacitances over concave and convex surface paths of porous microstructures.

The surface protonic conduction of ZrO_2 has been interpreted in terms of migration in chemisorbed and physisorbed water in order to rationalise the two opposite temperature

dependences. As we shall see in the next chapter, CeO_2 may rationalise a similar behaviour using chemisorbed water only. No doubt, future studies will build on the advances made in this thesis, and provide more nuanced total analyses.

The measured preexponentials of macroscopic surface protonic conductivity σ_{M,s,H^+0} of porous ZrO_2 were connected to predicted values from credible models of preexponentials of surface protonic conductance G_{s,H^+0} via the brick layer model (BLM).

The surface protonic conductivity of ZrO_2 in wet atmospheres above 200°C is attributed to transport of protons dissociated from the chemisorbed water monolayer and migrating on surface oxide ions. Samples sintered at relatively low temperatures show preexponentials and an observed $p_{H_2O}^{1/2}$ dependence of surface protonic conductivity suggesting weak chemisorption and dissociation to protons migrating between surface oxide ions, apparently a result of less faceted surfaces. The small activation enthalpies of around 30 kJ/mol can be understood as a combination of incomplete exothermic molecular adsorption, unfavourable endothermic dissociation, and relatively easy mobility of protons on surface oxide ions.

Higher sintering temperatures lead to correspondingly higher preexponentials due to better developed facets, expected for more complete dissociative chemisorption maybe driven by a more exothermic dissociation to surface oxide ions, corresponding to the "*cds-s*" model at full coverage. The higher activation enthalpy of conductivity of up to 58 kJ/mol can in this case be interpreted as that of mobility of protons on surface oxide ions only. The well-faceted surfaces are relaxed by protons that bond strongly and are hard to move, while the random surfaces have less affinity for protons, allowing those that are there to move more easily.

The surface protonic conductivity in wet atmospheres below around 150°C and down to around 50°C can be attributed to the first physisorbed water monolayer. The steep rise in conductivity with increasing coverage of this layer then must imply that the mobility of protons has a lower activation enthalpy than on the oxide surface. Indeed, the derived enthalpies of mobility go from those typical of solid-state proton mobility in the chemisorbed water layer towards those typical of liquid water in the first physisorbed water layer.

The samples sintered at low temperatures have preexponentials and a $p_{H_2O}^{3/2}$ dependence of conductance suggested to follow the "*chm-ph1*" model, namely, weak molecular chemisorption with physisorbed water that dissociates protons from the chemisorbed water underneath.

For samples sintered at high temperatures, they seem to have dissociation from the physisorbed water itself ("*ph1*" model). This may reflect that the strongly dissociated chemisorbed water on the high temperature sintered samples has no more protons to offer, they have all gone to the oxide surface, where they are immobile due to their high activation enthalpy and the lower temperature. Hence, the conduction in the physisorbed layer can only arise from dissociation within the same layer. The measured activation enthalpies fit to the models if physisorption is

assumed to have an enthalpy of -45 kJ/mol, dissociation has +42 kJ/mol like in water at the corresponding temperature, and proton mobility has around 18 kJ/mol, as said, close to that in liquid water.

All in all, it is believed that the difference between samples of ZrO_2 sintered at low and high temperatures is related to crystallisation and faceting from a more amorphous state of the surface.

5 Surface protonic conduction of CeO_2

This chapter provides another experimental work to quantitatively relate the surface layer conductance to the measured conductivity of porous sintered nanoscopic CeO_2 samples. *In situ* electron energy loss spectroscopy and thermogravimetry confirms surface hydrogenation from Ce^{4+} to Ce^{3+} under ambient conditions. The hydrophobic behaviour of CeO_2 revealed by water sorption measurements in combination with a hydrogenated CeO_2 surface provides a plausible explanation for the relatively low protonic conductivity at near room temperature. The paper on surface protonics of CeO_2 along with the in-depth characterization of CeO_2 nanoparticles can be found in ref. [166] and ref. [114], respectively.

5.1 Introduction

Ceria (CeO_2) takes on a cubic fluorite structure irrespective of temperature, and is remarkably unreactive with bases and acids such as H_2O and CO_2 and most acidic metal oxides. It has a well-understood defect structure dominated by understoichiometry ($CeO_{2-\delta}$; oxygen vacancies and charge compensating electrons representing Ce^{3+}). Lower-valent acceptor impurities or deliberate doping with for instance Gd^{3+} or Sm^{3+} to form gadolinia- or samaria-doped ceria (GDC, SDC) enhance the concentration of oxygen vacancies and suppress electrons, making the material a good oxide ion conductor for use as a solid-state electrolyte in solid oxide fuel cells (SOFCs).[104, 170, 171] The oxygen vacancies in bulk ceria have unfavourable hydration thermodynamics and there is hence no reliable report of significant hydration or proton conductivity in regularly acceptor-doped bulk ceria, and only a hardly measurable hydrogen permeability.[172] It has recently been shown that doping with 50% La^{3+} to form $Ce_{0.5}La_{0.5}O_{1.75}$ (or "$Ce_2La_2O_7$") leads to some hydration, but this is attributed to the affinity of protons to oxide ions fully coordinated by basic La^{3+} ions.[165]

Porous CeO_2 exhibits surface protonic conductivity in chemisorbed water down to around 200°C, similar to other MO_2 oxides. Below this, an increase with decreasing temperature is traditionally attributed to conduction in physisorbed water, [73, 76, 173] but in the case of CeO_2, we shall see that it for a large part arises from chemisorbed water alone.

Runnerstrom *et al.* [174] found that CeO_2 and TiO_2 thin films with grain sizes well below 10 nm exhibit more pronounced protonic conductivity across the minimum at intermediate temperatures (100-350°C) than more well-crystallised samples. This tendency is observed also for certain facets of surfaces on TiO_2 [118] and for poorly crystallised ZrO_2.[139] Dependences on oxygen activity and morphology led the authors to suggest that oxygen vacancies promote dissociative adsorption of water and resulting in higher protonic conductivity. Simons *et al.* [99]

studied CeO_2 thin films and found that hydration of CeO_2 is a slow process, while adsorption along surfaces and through open pores is fast.

An important application of nano- or microcrystalline ceria is as catalyst or support for noble metal nanoparticles in chemical industry and combustion engine exhaust catalyst systems.[91, 175] Its catalytic activity suggests that CeO_2 surfaces deviate from the simplicity of bulk cubic CeO_2.[176, 177] In other words, the surface oxides might be the catalytically active phase in reactions rather than the adsorbed oxygen in the bulk. This may comprise enhanced understoichiometry and n-type conductivity as well as hydration. On-going density functional theory (DFT) calculations show strong tendency of hydration of reduced CeO_2 surfaces, meaning that the surfaces may be seen as reduced oxyhydroxides formed according to hydrogenation reactions like Eq. 1 or Eq. 2 proposed in **Section 2.1**.

While the surface chemistry of CeO_2 is important and much studied and reviewed, [98, 178, 179] the adsorption of water and resulting surface protonic transport are far from well understood. Here we contribute a study of adsorption of water and dissociation and migration of protons in adsorbed water on the internal surfaces of nanoscopic porous CeO_2 ceramics. The results are interpreted in terms of the theoretical framework in **Chapter 2** and the BLM in **Chapter 3**. The combined used of thermogravimetry and conductivity *vs* T and p_{H_2O} suggests that hydrogenation of the surface must be taken into account and that transport in the chemisorbed layer covers a wider range of temperature than hitherto realised, with an extended set of models for this. Physisorption is supressed due to the hydrophobicity of CeO_2 that, in turn, arises from the hydrogenated surface.

5.2 Experimental

5.2.1 Materials and preparation

Ceria nanopowder (CeO_2, < 50 nm particle size, 99.95% trace rare earth metals basis, SKU no. 700290, Sigma Aldrich) was cold-pressed at ~ 65 MPa, followed by sintering at 550 or 750°C in air with a dwell time of 8 h into disks with approximate dimensions of 20 mm diameter and 2 mm thickness. The sintered samples are hereafter denoted CeO_2-550 and CeO_2-750. The resulting relative densities of the disks were about 50% (CeO_2-550) and 62% (CeO_2-750), calculated from their mass and geometry and nominal density of stoichiometric CeO_2 of 7.22 g/cm^3.[180]

5.2.2 Characterization

The microstructure and porosity of the samples were analysed by scanning electron microscopy (SEM, Hitachi SU8230). Powder X-ray diffraction with a Bruker D8 Discover diffractometer with CuKα_1 radiation (λ = 1.5406 Å, Bragg-Brentano mode) was used to verify the structure and examine the crystallite size.

The as-received (*i.e.,* pristine) ceria nanopowders (< 25 nm particle size, Sigma Aldrich) were analysed by a probe corrected and monochromated FEI Titan G2 60-300 microscope operated at 300 kV, using high resolution scanning transmission electron microscopy (STEM), electron energy-loss spectroscopy (EELS) with a Gatan imaging filter and detector, and Super-X energy dispersive spectroscopy (EDS). Electron beam current of less than 0.1 nA was used to ensure minimal beam damage. The EELS spectra were acquired using dual EELS spectrum image (SI). This means, we acquire a low loss EELS spectrum with the zero-loss peak together with the core-loss EELS spectrum of the Ce-$M_{4,5}$ peak, and using the zero-loss peak as the referencing peak. The post-acquisition data processing was performed using Digital Micrograph (Gatan Inc. and CasaXPS) for peak fitting analysis. *In situ* heating was performed with temperature steps of 0.05° per second, for then to wait about 10 min (before taking the EELS spectra) to avoid drift due to heating. EELS spectra were acquired with either a 0.25 eV/ch dispersion (collection semi-angle 12 mrad and convergence semi-angle 21 mrad), or with a 0.1 eV/ch dispersion (collection semi-angle 100 mrad and convergence semi-angle 30 mrad).

Nitrogen sorption measurements were performed on a BELSORP mini II instrument (MicrotracBEL Corp., Japan) at 77 K to determine the gravimetric specific surface area (A_g), and the pore size distribution of the materials. In each experiment, approximately 200 mg of material was weighed into a quartz cell. The samples were pre-treated by annealing under dynamic vacuum for 2 h at 150°C. The total surface area was extracted from the nitrogen adsorption isotherms via the Brunauer–Emmett–Teller (BET) method.[181] Non-local density functional theory (NLDFT) calculations of the pore size distribution were performed using the commercial BELMaster software (MicrotracBEL Corp., Japan). The Grand Canonical Monte Carlo (GCMC) calculation method was applied on the adsorption branch using the nitrogen physisorption data collected at 77 K, assuming a slit pore model.

Water sorption measurements were performed at 25°C using a BELSORP Max physisorption instrument (MicrotracBEL Corp., Japan) to determine the maximum water capacity.[182] The measurements took place in the relative humidity (*RH*) range: $0 < RH < 0.9$, with p_{ce} being the condensation equilibrium partial pressure of H_2O at 25°C. In each experiment, approximately 200 mg of material was weighed into a quartz cell and pre-treated with annealing under dynamic vacuum for 2 h at 150°C *in situ* to avoid exposure to atmospheric humidity. The number of physisorbed H_2O molecules per unit surface is calculated from Eq. 118, where wt.% is the gravimetric adsorption, N_A is Avogadro's number, MW_{gas} is the molecular weight of the adsorbed gas (H_2O), and A_g is the gravimetric specific surface area from BET analysis.

$$\frac{N_{molecule}}{nm^2} = \frac{N_A \cdot wt.\%}{10^{20} \cdot MW_{gas} \cdot A_g} \qquad \text{Eq. 118}$$

Thermogravimetry (TG) was carried out using a 449 *F3* Jupiter® thermal analyser (Netzsch GmbH, Germany) on the pristine CeO_2 powder and sintered samples under bottle-dry or wet N_2 (99.999%) purge gases. The sintered samples were crushed coarsely to fit into the sample holder, while retaining its microstructure. The samples were heated to 550°C at 3 K/min in

bottle-dry N_2 at a flow rate of 40 mL/min, thereafter held at the given temperature for at least 2 h to eliminate adsorbed water and organic residue from the sample surface. The p_{H_2O} dependence of water adsorption was measured at 400, 100, 50 and 30°C. The temperature dependence was conducted as follows: After fully dehydrating at 550°C as described above, the samples were equilibrated at p_{H_2O} = 0.02 bar at 550°C and measured during stepwise cooling to 25°C – the weight increase reflects the total content of hydrogen as well as both chemisorbed and physisorbed water. Background measurements in bottle-dry N_2 were carried out under otherwise identical conditions and used for background subtraction, with the dry-to-wet step at 550°C as a starting point, given that water uptake in dry atmosphere at 550°C is zero. Figure 27 shows the results from a typical isobaric measurement on CeO_2 samples, where distinct steps in relative mass change were obtained upon hydration, corrected for other effects such as non-stoichiometry by running an equivalent experiment in dry atmosphere.

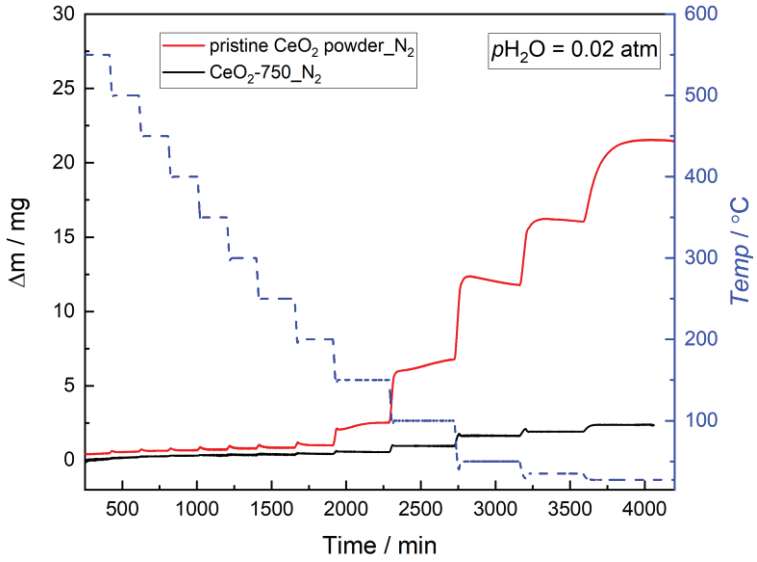

Figure 27 Amount of water adsorbed on the pristine CeO_2 (red line) and CeO_2-750 (black line) *vs* time in response to the stepwise cooling (blue dashed line) after dry curve subtraction at p_{H_2O} = 0.02 bar.

For electrical characterization, symmetrical circular Ag paste electrodes of 10 mm diameter were painted on both faces of the sintered pellets. Electrical conductivity was measured via Pt mesh and four Pt wire contacts by electrochemical impedance spectroscopy (EIS) in a ProboStat™ sample holder cell (NORECS, Norway), see **Section 4.2** for details. The atmosphere was a flow of bottle-dry or wet (p_{H_2O} = 0.025 bar) N_2 (99.999%), O_2 (99.5% or 99.999%) or air, or N_2 with variable p_{H_2O} controlled by a HumiStat gas-mixer and humidifier (NORECS, Norway). Impedance spectra (10 MHz – 10 mHz, 100-500 mV RMS) were recorded using a Novocontrol alpha-A spectrometer coupled with a ZG4 interface. Impedance data were analysed and modelled with ZView™ software (Scribner Associates Inc.). Conductivities of the porous samples were calculated based on their thickness and electrode area, without correction for the porosity.

5.3 Results and discussion

5.3.1 Microstructural characterization

Figure 28 presents SEM images of the CeO_2-550 and CeO_2-750 samples, showing average grain sizes of approximately 40 and 90 nm, respectively. The shape of the particles of the CeO_2-550 sample remains rounded, similar to the pristine powder, but evolved to more faceted surfaces upon sintering at 750°C.

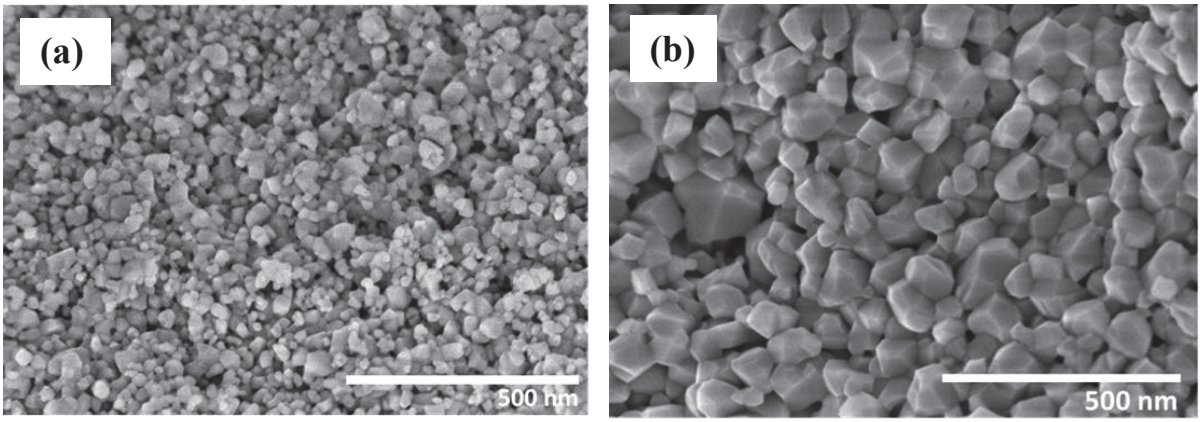

Figure 28 SEM images of the (a) CeO_2-550 and (b) CeO_2-750 samples.

Figure 29 shows the X-ray diffractograms of the CeO_2 starting powder and the sintered samples show cubic fluorite structure with space group *Fm*-3*m* and lattice parameters $a = b = c = 5.411$ Å (COD_9009008). The grain sizes obtained from Scherrer analysis were 21 and 62 nm for CeO_2-550 and CeO_2-750, respectively, while they were 20 and 80 nm from Rietveld analysis, in rough agreement with those from SEM images, which we have used in subsequent quantitative analyses. From weight and geometry, sintering at 550 and 750°C resulted in relative densities of around 50 and 62%, respectively, in agreement with the SEM images.

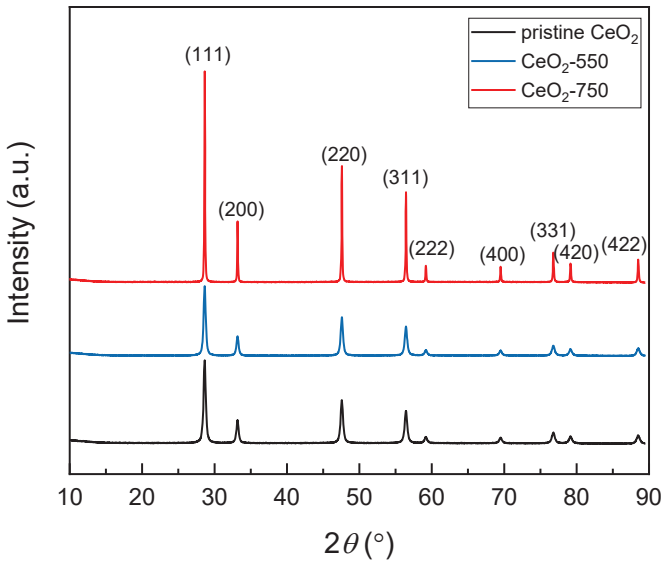

Figure 29 X-ray diffractograms of the CeO_2 starting powder and the corresponding sintered samples.

5.3.2 *In situ* scanning transmission electron microscopy with electron energy loss spectroscopy (STEM-EELS)

Figure 30 (A-B) shows the EELS spectra of the pristine CeO_2 nanoparticle, from the whole particle and from the particle surface, and the corresponding STEM image with element mapping (Figure 30 C) at 25, 200 and 400°C, where most of the changes in composition were found to occur. The Ce-M_5 and Ce-M_4 peaks of Ce^{3+} are located at energy losses of 880.1 eV and 898 eV respectively, with an energy separation of 17.9 ± 0.2 eV. For the Ce^{4+} component, the Ce-M_5 peak is located at 881.4 eV and Ce-M_4 peak at 899.6 eV, with an energy separation of 18.2 ± 0.2 eV. Intensity ratios of the M_5 to M_4 white lines (I_{M5}/ I_{M4}) of Ce^{3+} was found to be 1.3, while for Ce^{4+} the intensity difference is 0.8. A variation in-between these two numbers can be related to a change in the oxidation state.

Energy loss mapping of the integrated EELS signal of the Ce^{4+} and Ce^{3+} peaks presented in Figure 30 (C) shows that at 25°C, the particle contains a mix of both Ce^{3+} (red) and Ce^{4+} (blue). During heating, the majority of the Ce^{3+} in the bulk particle transform into Ce^{4+}, while the transformation at the surface is not as quick, resulting in a layer of Ce^{3+} at the surface.

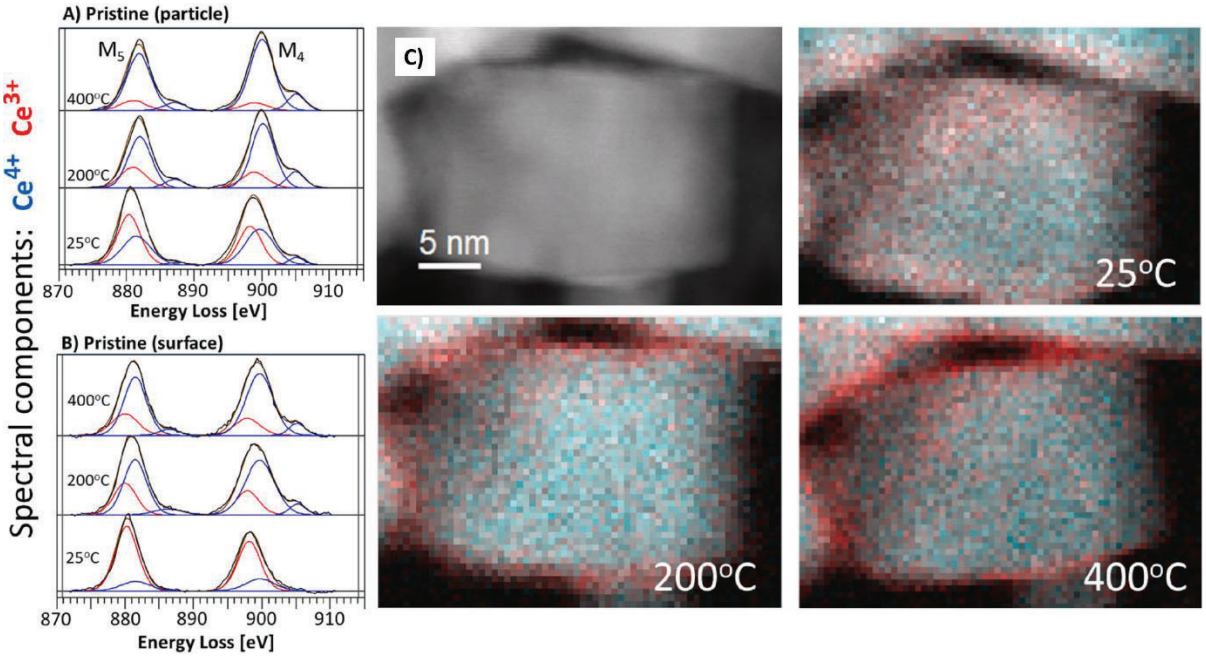

Figure 30 EELS spectra of the Ce-$M_{4,5}$ peaks from the whole particle (A) and at the surface of the pristine ceria particle (B), where the component of Ce^{4+} is shown in blue, Ce^{3+} in red, and the black is the experimental spectra. (C) STEM image of a pristine ceria particle and EELS mapping of the Ce^{3+} (red) and Ce^{4+} (blue) peaks at selected temperatures.

The percentages of Ce^{3+} at the given temperatures, as well as the estimated oxidation state based on the white line ratios M_5/M_4 of the EELS spectra are summarized in Table 7. At 25°C, the pristine particle contains 53% Ce^{3+} in the whole particle, and 80% Ce^{3+} at the surface. During heating in high vacuum, the EELS Ce-$M_{4,5}$ peak moves to higher energy loss, and the white

line intensity ratio shifts to a clear Ce^{4+} signature. At 400°C, the particle contains only 13% Ce^{3+}, and 31% Ce^{3+} at the surface layer.

Table 7 Amount of Ce^{3+} present in the pristine ceria particle with the mean oxidation state (ox. state) calculated based on the white line ratio.

Temperature	Particle Ce^{3+}		Surface Ce^{3+}	
°C	%	Ox. state	%	Ox. state
25	53	+3.3	80	+3.0
200	26	+3.6	24	+3.4
400	13	+3.8	31	+3.6

EELS results indicate that the pristine ceria prior to analysis has a high amount of Ce^{3+} at the surface of the particles, which transforms into Ce^{4+} when heating in vacuum. This is surprising because heating in high vacuum should normally not lead to further oxidation. If the reoxidation to Ce^{4+} was due to annihilation of oxygen vacancies, it would require uptake of oxygen (which is not available in high vacuum) and lower temperatures (due to the negative entropy change of gas uptake). However, the results can be rationalized if the surface layer is an oxyhydroxide (based on the known stability of rare earth (III) oxyhydroxides) that we for simplicity represent as CeOOH, and not a reduced oxide such as Ce_2O_3. Dehydrogenation of a hydroxide (e.g. according to Eq. 1 or Eq. 2) yields hydrogen release, which is natural in the TEM vacuum, and it increases with temperature due to the positive entropy change of gas release. The growth of this subsurface layer stops as soon as the surface attains bulk properties and/or the two space charge layers in the CeOOH layer meet.

The existence of a subsurface layer of CeOOH on CeO_2 surfaces explains many observations, behaviours, and properties of CeO_2, e.g. redox and catalytic behaviour as well as protons found on the surface, but not bulk. The reasons why the surface phase has not been observed earlier may stem from the fact that it has the same oxygen content and a similar structure as the host CeO_2, and is very thin, requiring the use of *in situ* heating instruments like TEM.

5.3.3 Nitrogen and water sorption measurements

N_2 adsorption-desorption of all CeO_2 samples display characteristic type II isotherms, as shown in Figure 31 (a).[183] The hysteresis loops are associated with capillary condensation of N_2 in mesopore structures. Sintering at 750°C reduced the number of mesopores as shown from the pore size distributions (Barrett-Joyner-Halenda (BJH) analyses) of the BET analyses (Figure 31 b), shifting the average pore size from 10 for the CeO_2-550 sample to around 20 nm for the CeO_2-750 sample.

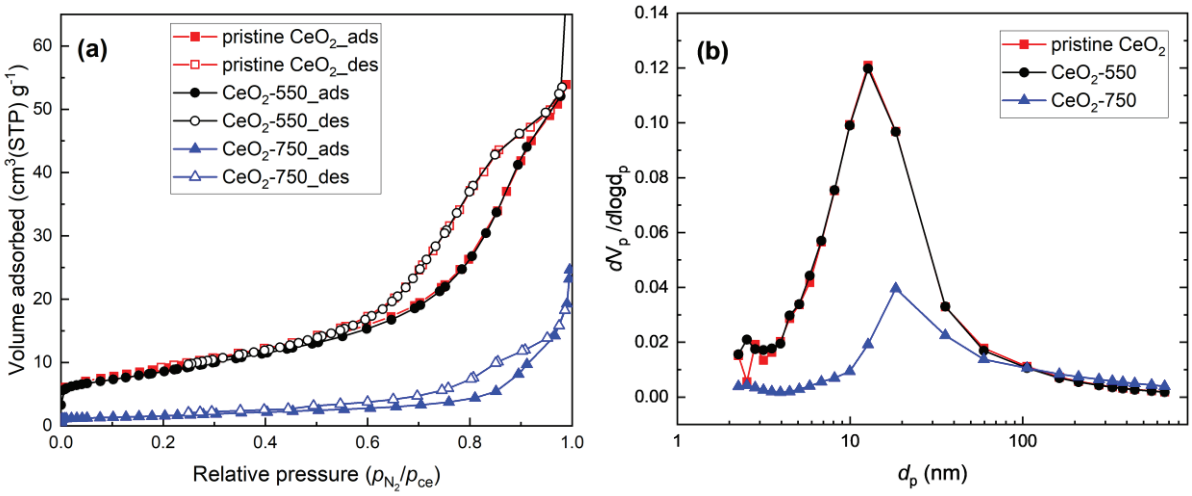

Figure 31 (a) N_2 adsorption-desorption isotherms of the CeO_2 samples, (b) the corresponding pore size distribution (BJH method).

BET analyses of the pristine CeO_2, CeO_2-550, and CeO_2-750 provide gravimetric specific surface area (A_g) of $3.2 \cdot 10^5$, $3.1 \cdot 10^5$ and $5.9 \cdot 10^4$ cm^2/g, respectively (Table 8) and average pore size of 13, 14, and 20 nm, which is again characteristic of mesoporous structures. The volume specific surface area (A_v) is also included in Table 8, calculated as the product of the A_g and the density of the porous sample. The results reflect the modest increases in grain size and relative density by sintering at 750°C *vs* 550°C, while the surface area for adsorption varies by a factor of 5, probably due to elimination of sub-granular and surface defects.

Table 8 Sorption parameters from N_2 adsorption isotherms at 77 K and water adsorption data at 298 K.

Samples	Specific surface area[§]		Total pore volume[§]	Average pore size (BJH)[§]	α (RH at 50% of H_2O uptake at $RH = 0.9$)	Water capacity[§§]
	A_g (cm^2/g)	A_v (cm^2/cm^3)	(cm^3/g)	(nm)		(cm^3/g)
Pristine CeO_2	$3.2 \cdot 10^5$	n.a.	$1.1 \cdot 10^{-1}$	13	0.78	53
CeO_2-550	$3.1 \cdot 10^5$	$1.1 \cdot 10^6$	$1.0 \cdot 10^{-1}$	14	0.79	55
CeO_2-750	$5.9 \cdot 10^4$	$2.6 \cdot 10^5$	$3.5 \cdot 10^{-2}$	20	0.82	10

[§] Estimated from N_2 adsorption isotherms at 77 K; [§§] From H_2O adsorption data at 298 K at $RH = 0.9$.

Water sorption measurements were performed at 25°C for all samples, exhibiting type II isotherms similar to the N_2 adsorption. The number of adsorbed H_2O molecules normalised for BET surface area via Eq. 118 is shown in Figure 32 at $0 < RH < 0.9$, and is remarkably equal for all three samples. The surface coverage is also shown, on basis of 5 H_2O per nm^2 as monolayer coverage.[126] A first layer of chemisorbed water appears to be in place already at low RH in agreement with calorimetric adsorption measurements on various oxides.[96, 126, 127] However, saturation appears to be reached only at closer to two monolayers. As indicated by

TG results later on, part of this may reflect subsurface hydrogenation that gives an overestimate of what is interpreted as chemisorbed water.

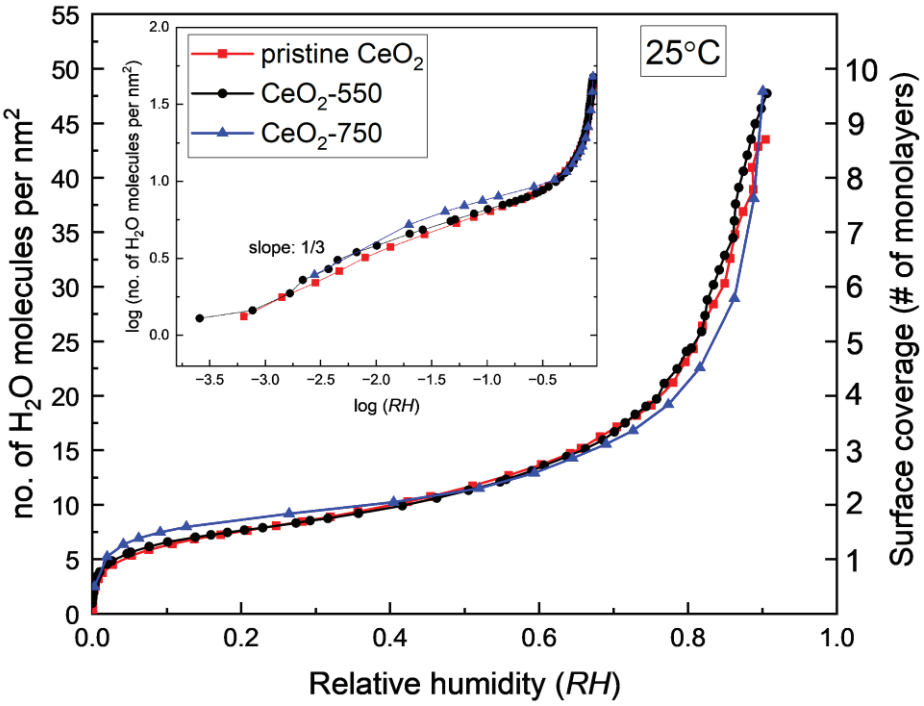

Figure 32 Number of adsorbed water molecules per nm^2 as a function of relative humidity (*RH*) calculated from water sorption isotherms at 25°C. The right-hand axis shows the same data in number of layers of water, under the assumption of a monolayer coverage of 5 H_2O per nm^2. The inset shows a double-logarithmic plot of the data, suggesting approximately a $p_{H_2O}^{1/3}$ dependence in the low *RH* part.

The double-logarithmic insert in Figure 32 displays a slope around 1/3 at low *RH*. This shows that adsorption is far from molecular (slope of 1) and instead suggests that each water molecule dissociates into 2, 3, or 4 species (slopes of ½, 1/3, or ¼, respectively). Based on the TG results to follow, we believe this reflects a combination of subsurface hydrogenation to protons and electrons with a $p_{H_2O}^{1/4}$ dependence and dissociative chemisorption with a $p_{H_2O}^{1/2}$ dependence.

Figure 32 further shows that major uptake of physisorbed water beyond the chemisorbed layer occurs in our material only at unusually high *RH*, reflecting stronger adsorbate-adsorbate (H_2O-H_2O) interaction than adsorbate-adsorbent (H_2O-CeO_2) interaction. The α parameter (*RH* at which we reach half of the total water capacity, taken here to be at *RH* = 0.9) is a qualitative indication of surface hydrophobicity.[184] It was extracted from the water sorption data and listed in Table 8 and show that all CeO_2 samples can be considered as hydrophobic by having high α values of 0.78–0.82. Hydrophobicity is demonstrated for low-index CeO_2 surfaces by DFT calculations.[185] The intrinsic hydrophobicity of CeO_2 surfaces is a property it has in common with other rare-earth(*RE*) oxides (RE_2O_3).[186] We note that this may be connected with the general stability of *RE*OOH oxyhydroxides and hence tendency of RE_2O_3 forming a *RE*OOH-like surface by hydration, like CeO_2 may form CeOOH by hydrogenation.

The total volume of water adsorbed at *RH* of 0.9, commonly taken as the water adsorption capacity, can serve as a measure of sample porosity.[187] As seen in Table 8, it is indeed proportional to the BET surface area. The results indicate that at a *RH* of 0.9 there will be around 10 monolayers of water with a total thickness of close to 3 nm based on a monolayer thickness of 2.82 Å.[188]

5.3.4 Thermogravimetry

Figure 33 shows isothermal p_{H_2O} dependences of water uptake measured by TG. If in Figure 33 (a) we attribute the weight increase at 400°C to H_2O, the water layer is still far from being complete assuming a monolayer coverage as 5 H_2O per nm^2 as stated above. A close to a $p_{H_2O}^{1/4}$ dependence is observed for both samples at 400°C. STEM-EELS (**Section 5.3.2**) suggests that CeO_2 surfaces have a nm-thick CeOOH-like subsurface layer, in line with other findings of Ce^{3+} in CeO_2 nanoparticles.[96, 189] If that is the case, the TG results at 400°C may be better interpreted in terms of weight of uptake of H_2 instead of H_2O. Although it is reasonable *per se* and from the STEM-EELS that the hydrogen is dissolved in the subsurface, we may still express the uptake as a surface concentration, *i.e.,* number of H_2 per nm^2 surface (filled symbols in the figure).

If Eq. 3 provides the dominant charged defects, but at low concentrations, we obtain

$$[OH_O^{\bullet}] = [Ce_{Ce}^{/}] = K_H^{1/4} p_{H_2O}^{1/4} p_{O_2}^{-1/8} \qquad \text{Eq. 119}$$

where K_H is the equilibrium coefficient of the reaction. The qualitative fit with the observed $p_{H_2O}^{1/4}$ dependence supports our suggestion that the weight increase at 400°C is dominated by reduction of the subsurface, and not by adsorption of water.

Figure 33 (b) shows the p_{H_2O} dependence of water uptake at 100, 50, and 30°C. At 100°C, the weight change represents filling up of a yet far from complete chemisorbed water layer, with an overall $p_{H_2O}^{1/2}$ dependence – showing that the chemisorption is mainly dissociative. At 50°C and 30°C, the lower p_{H_2O} dependence may represent a beginning completion of the chemisorbed layer, while physisorbed water comes on at the highest p_{H_2O} at 30°C (*RH* > 50%), giving rise to what appears to approach a $p_{H_2O}^{1}$ dependence (molecular physisorption).

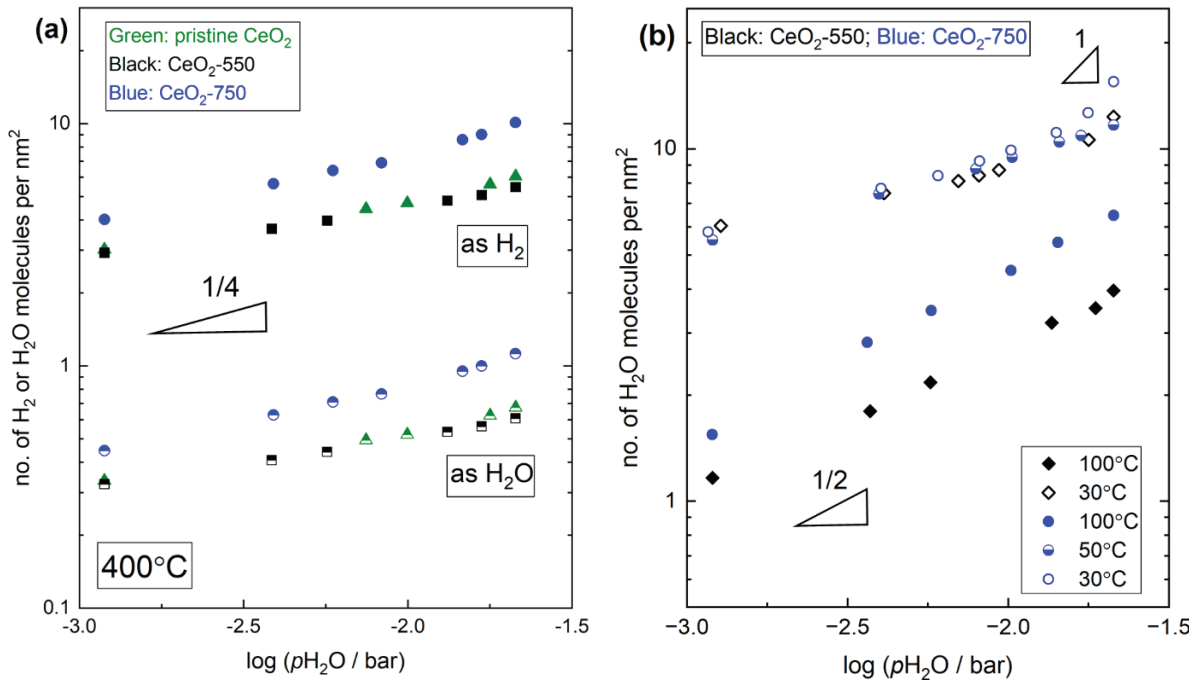

Figure 33 Area specific adsorption in CeO_2 samples as a function of p_{H_2O} in N_2 represented as number of H_2 or H_2O per nm^2 measured at (a) 400°C and at (b) 100, 50, and 30°C.

Recall the thermodynamics derived in **Chapter 2**, if chemisorbed water remains undissociated, the mass gain would show a $p_{H_2O}^{1}$ dependence at low coverage (Eq. 14), while if it is predominantly dissociated, a $p_{H_2O}^{1/2}$ dependence is obtained (Eq. 21). If the overall process saturates at complete coverage, the mass of the chemisorbed layer will become constant, independent of p_{H_2O}, irrespective of the degree of dissociation.

Figure 34 displays the area-specific water uptake by TG, obtained by using the A_g from BET analysis. The mass gain upon cooling from 550°C appears to level off towards 200°C corresponding to around 0.8 H_2O per nm^2 for the pristine CeO_2 powder and the CeO_2-550 sample and around 2 H_2O per nm^2 for CeO_2-750. Such low coverage supports the finding that what we see in this region is not chemisorption of water, but saturation of the CeOOH-like subsurface layer as a result of hydrogenation of CeO_2 from water vapour. Recalculated, the apparent levels of 0.8 and 2 H_2O per nm^2 correspond then instead to 7 and 18 H_2 (or 14 and 36 H) per nm^2, meaning that the layer of "CeOOH" with Ce^{3+} and H^+ goes 4-8 unit cells down if each Ce takes one electron.

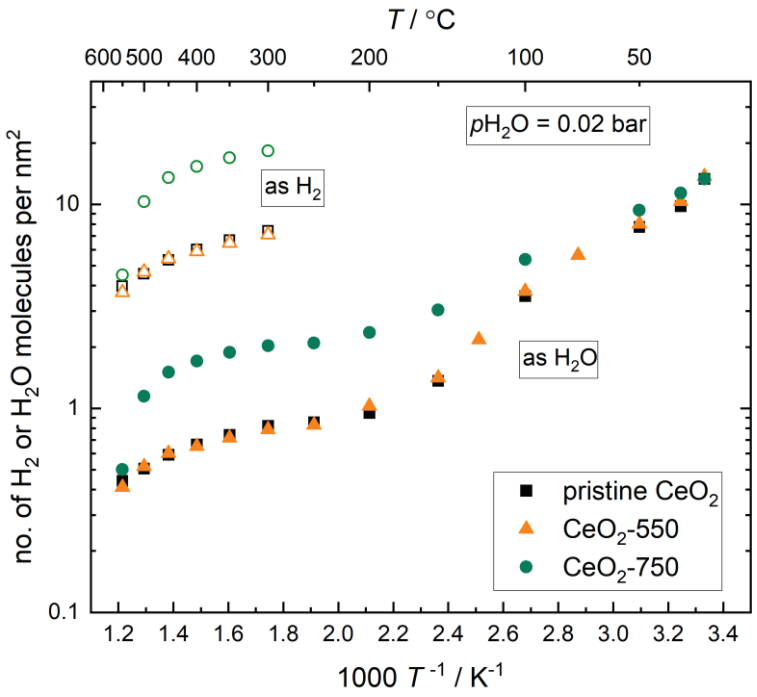

Figure 34 Area-specific uptake from water by TG interpreted as number of H_2 or H_2O per nm^2 for the CeO_2 samples in the range 550-25°C in wet (p_{H_2O} = 0.02 bar) N_2 atmosphere.

The stronger increase in water adsorption below 200°C then reflects chemisorbed water. After subtraction of the mass from the CeOOH-like layer, the data in the range 200-100°C have enthalpies around -40 kJ/mol. If this is molecular chemisorption, we expect from Eq. 14 an enthalpy corresponding to $\Delta H^0_{a_{cm}}$. The observed $p^{1/2}_{H_2O}$ dependences at 100°C suggest predominantly dissociative chemisorption, the enthalpy is then $\Delta H^0_{a_{cds}} = \Delta H^0_{a_{cm}} + \Delta H^0_{d_{cs}}$. Existing literature suggests that $\Delta H^0_{a_{cm}}$ = -60 kJ/mol (for both nanocrystalline and microcrystalline CeO_2 for the same water coverage) based on calorimetry measurements [96] and first-principles calculations,[190, 191] and we may take $\Delta H^0_{d_{cs}} \approx$ 20 kJ/mol as a round-off estimate based on the dissociation enthalpy 22 kJ/mol of water adsorbed on YSZ.[169] The enthalpies of $\Delta H^0_{a_{cds}}$ is hence expected as around -40 kJ/mol for the dissociated case, in good agreement with what we got, changing towards $\Delta H^0_{a_{cm}} \approx$ -60 kJ/mol as it turns molecular with decreasing T and increasing p_{H_2O}.

Towards 50°C, the curves in Figure 34 display a tendency of levelling out at around 10 H_2O per nm^2, in agreement with the curve at the same temperature in Figure 33 (b), which we attribute to saturation at full coverage of the chemisorbed layer. On further approach to RT and the highest *RH*, there is a new increase in mass gain as physisorbed water comes on, visible in both Figure 33 (b) and Figure 34.

5.3.5 Electrical conductivity

5.3.5.1 *Effects of atmosphere and temperature*

The conductivities of CeO_2-550 and CeO_2-750 have been measured *vs* temperature below their sintering temperatures. The main features of the electrical conductivity involve native non-protonic conductivity at the highest temperatures and surface protonic conductivity in adsorbed water with characteristic temperature dependences. Nevertheless, the surface protonic conductivity of CeO_2 reveals in our experience more complex behaviours than for other oxides, comprising slow, hysteretic, or irreversible effects of atmosphere (O_2 or air *vs* N_2), and what is believed to be surface restructuring and hydrophobicity of water adsorption at near ambient temperatures and high relative humidities. We note that some of these effects may be attributable to changes in the "CeOOH"-like subsurface layer, which only requires transport of protons and electrons and may take place at low temperatures. Furthermore, one may also expect that minor gas phase components (e.g. hydrocarbons, CO_2) may compete with water.[110] We here proceed to report and interpret results taken with long equilibration times under N_2 atmospheres, which represent the most reproducible and systematic behaviours.

5.3.5.2 *Temperature dependences*

Figure 35 (a) shows the Arrhenius plots of the conductivity (σ) of both CeO_2 samples, measured in bottle-dry and wet (p_{H_2O} = 0.025 bar) N_2. Under nominally dry conditions, the conductivity is significant and measurable only at the highest temperatures. It follows Arrhenius behaviour, with apparent activation enthalpies of around 80 kJ/mol. This is low compared to that of the conductivity of many bulk and porous nanoceria materials attributed to oxide ion conduction,[76, 99, 192] but comparable to what is expected for n-type electronic conduction of CeO_2 [73] (e.g. 0.77 eV for nanocrystalline CeO_2 thin film [174]). Knauth *et al.* [193] measured the p_{O_2} dependence of conductance of CeO_2 nanopowder and of coarsened powder, which gave rise to a $p_{O_2}^{-1/6}$ dependence, similar to those of PLD thin films.[194]

In this work, the lack of an electrode impedance in impedance spectra at high temperatures in dry atmospheres (Figure 35 b) correspondingly suggest that this conduction is electronic (assumingly n-type), but the lower resistance in wet than in dry atmosphere is typical of protonic contribution. The presence of dual time constants in impedance spectra further suggests that it is surface conduction, similar to what is reported for porous monoclinic ZrO_2 (Figure 24). At intermediate temperatures (Figure 35 c), three distinct processes were recognized from the impedance plots. The capacitance of the third response observed below 400°C under wet conditions is of the order of 10^{-7}-10^{-6} F/cm^2, typical of an electrode contribution, which becomes blocking at the lowest temperatures.

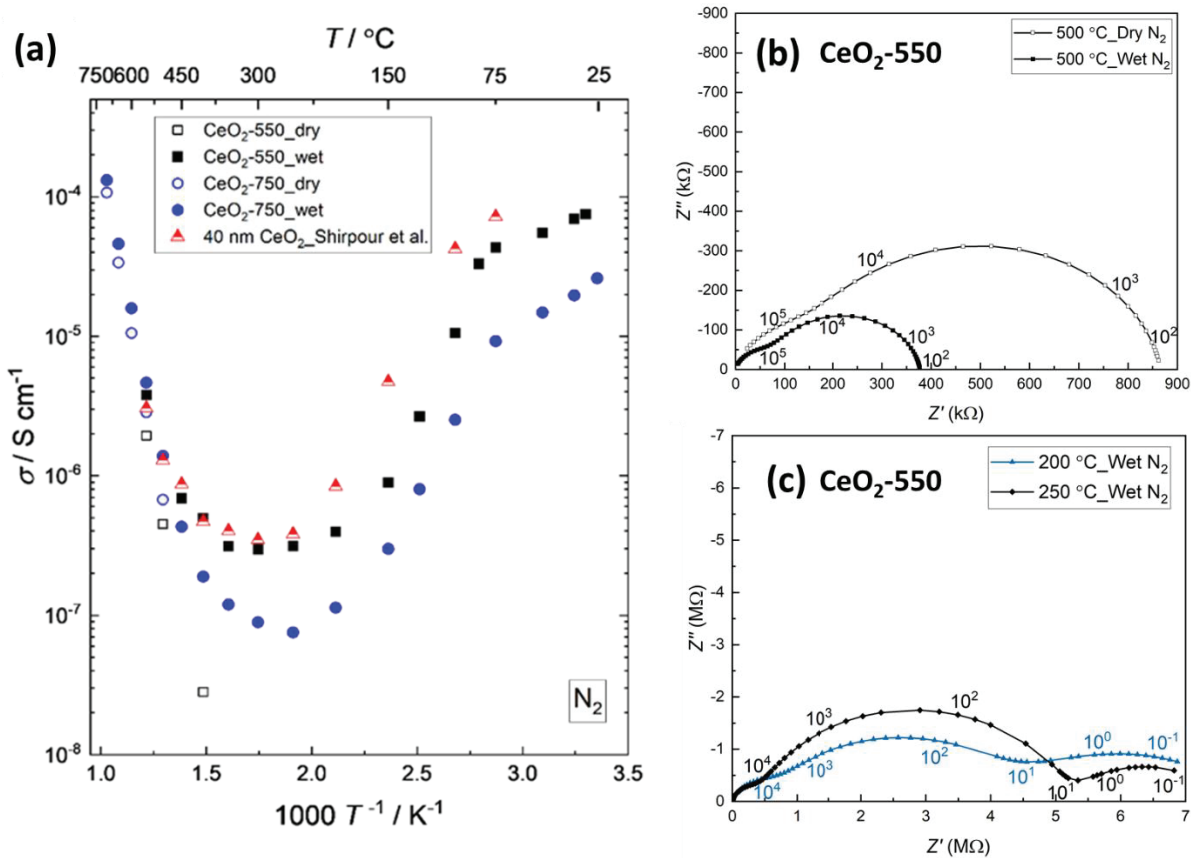

Figure 35 (a) Plot of σ *vs* $1/T$ for CeO_2-550 and CeO_2-750 in dry (open symbols) and wet (p_{H_2O} = 0.025 bar, solid symbols) N_2. Protonic conductivity reported by Shirpour *et al.* [73] for nanocrystalline undoped CeO_2 is shown for comparison. Representative Nyquist impedance plots for the porous CeO_2-550 sample recorded in N_2 atmosphere at (b) 500°C, (c) intermediate temperatures. Numerical labels show the AC frequencies.

Figure 36 further shows the conductivity of our CeO_2 samples after subtraction of the native apparently electronic conductivity measured in dry atmosphere. At temperatures above 500°C, this may be attributed to electrons in the hydrogenated (CeOOH-like) layer, with a high activation energy. This deserves further study, but is beyond the scope of this work.

Below 500°C, the impedance spectra show – as said above – that we have increasingly dominant surface protonic conduction, with a contribution with positive apparent activation enthalpy attributed to transport in the chemisorbed layer in the range 500–300°C. In the temperature range 300-200°C, the conductivity levels out, like in previous studies on nanocrystalline CeO_2 [70, 73, 103] formerly not having a plausible interpretation.

Below 200°C, the conductivity increases with decreasing temperature, while as temperature passes below 100°C and *RH* surpasses ~ 6%, the conductivity increases less steeply. These have commonly been attributed to solid- and liquid-like physisorbed water. The TG results showed however that the low-temperature (high *RH*) regions may need re-interpretation in the case of CeO_2: The region 200 – 100°C is in fact mainly filling up with chemisorbed water, the first (solid-like) physisorbed water comes on only well below 100°C, and liquid-like physisorbed

water maybe never contributes much to conduction on CeO_2 surfaces due to their hydrophobicity as revealed from the water sorption data (Figure 32).

In the following, I will evaluate these assessments by comparing their p_{H_2O} dependences, temperature dependences (enthalpies) and preexponentials with models introduced before. These partly coincide with and partly go beyond those presented in our preceding work on ZrO_2 in **Chapter 4** and ref. [139].

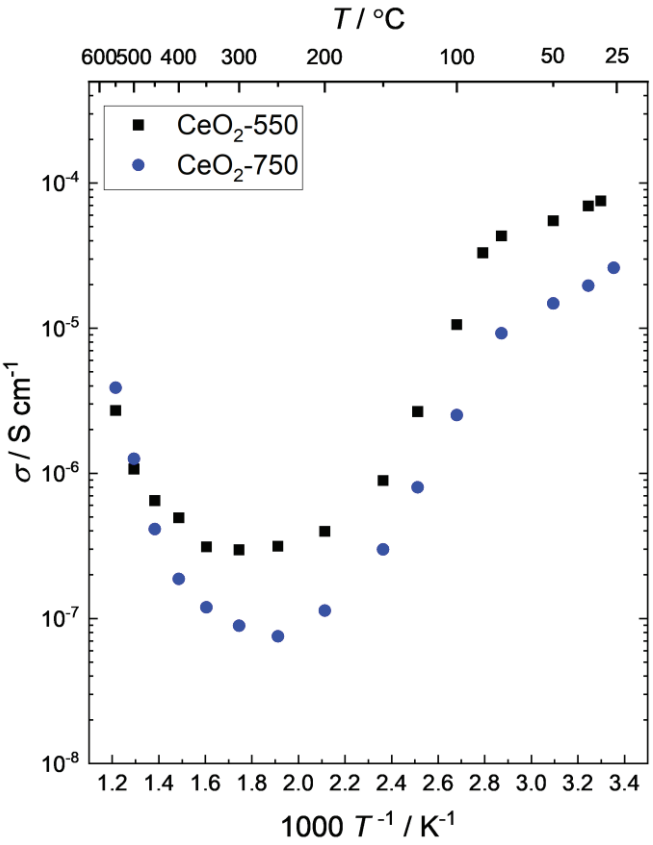

Figure 36 Plot of σ *vs* $1/T$ for surface protonic conductivity of CeO_2-550 and CeO_2-750 obtained from wet N_2 atmosphere after subtraction of the dry conductivity.

5.3.5.3 Isothermal conductivity vs pH2O

Figure 37 shows the isothermal p_{H_2O} dependences of the surface protonic conductivity of the two CeO_2 samples. At 400°C (Figure 37 a), we have close to a $p_{H_2O}^{1/2}$ dependence of surface protonic conductivity, steepening a bit towards a slope of 1 towards the highest pressure (0.025 bar), coinciding with a report by Manabe *et al.* [83] of a $p_{H_2O}^{1}$ dependence in the range p_{H_2O} = 0.026 – 0.2 bar of conductivity over grain surfaces (σ_{intra}) in porous CeO_2 at 400°C. Studies of $Zr_{1-x}Y_xO_{2-x/2}$ (x = 0.04, 4YSZ) showed a $p_{H_2O}^{1/2}$ dependence of surface protonic conductivity at 400–250°C,[84] and so did $Ce_{0.9}Gd_{0.1}O_{2-\delta}$ at 200°C,[97] and $La_2Ce_2O_7$ at 550–250°C.[195] The $p_{H_2O}^{1/2}$

dependence shows that each adsorbed H_2O molecule splits in two charged species to facilitate protonic transport in chemisorbed water.

At 100°C, Figure 37 (b) shows higher slopes reflecting close to $p_{H_2O}^{3/2}$ dependences of conductivity, suggesting involvement of multiple H_2O molecules in the protonic transport step. In the previous work on ZrO_2, we proposed models for surface protonic conduction in the first physisorbed layer with $p_{H_2O}^{3/2}$ and $p_{H_2O}^{2}$ dependences, but based on the TG results for CeO_2 here, we have only chemisorption under these conditions, and we shall derive and parameterise extended models for conductance in the chemisorbed layer that yield similar predictions.

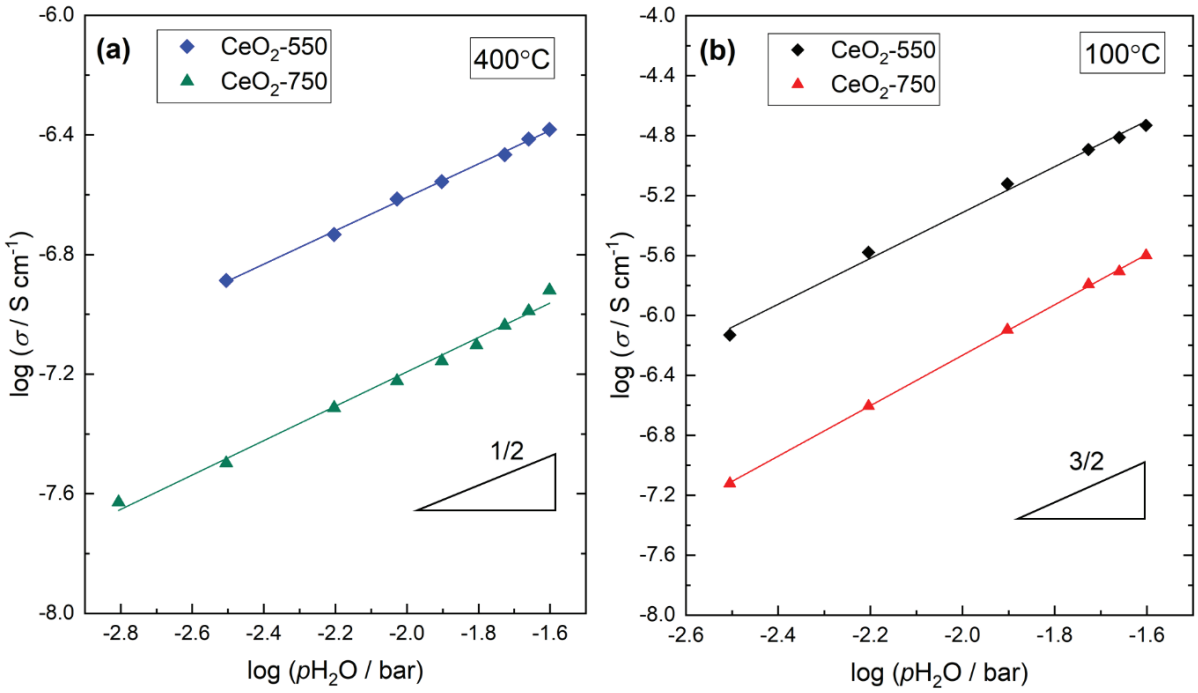

Figure 37 Plots of log σ (surface protonic conductivity) *vs* log p_{H_2O} of both sintered samples in N_2 at 400°C (a) and 100°C (b).

5.4 Modelling the surface protonic conductivity

5.4.1 From sample conductivity to surface conductance using the brick layer model (BLM)

Figure 38 shows the geometry-corrected surface protonic conductances G_{s,H^+} according to the brick layer model (BLM, Eq. 106). For our samples, ψ is calculated to be $2.5 \cdot 10^5$/cm for CeO_2-550 and $1.0 \cdot 10^5$/cm for CeO_2-750. As can be seen, they become roughly identical for the two samples over the entire temperature range, demonstrating that the level of the surface protonic conductivity in Figure 36 is largely determined by the grain size and porosity that enter into the BLM. The surface conductance in wet atmosphere at the highest temperatures (above 500°C in

Figure 38) cannot be reasonably modelled with transport in chemisorbed water and we attribute it as said before to transport of protons and/or electrons in the surface and/or subsurface caused by hydrogenation to protons in OH^- groups and electrons as Ce^{3+} in the CeOOH-like layer. An interpretation of its basis including temperature dependence deserves dedicated studies beyond the scope of the present work.

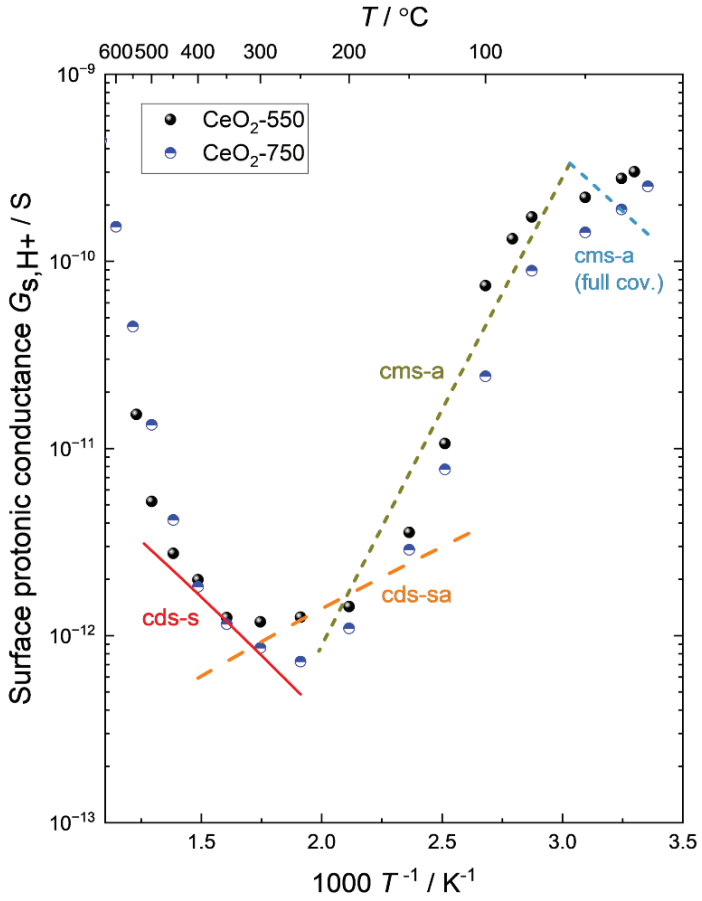

Figure 38 Surface protonic conductance of the CeO_2 samples at p_{H_2O} = 0.025 bar *vs* $1/T$ in N_2, obtained from the sample conductivities via the BLM. The lines are drawn using preexponentials derived for models *cds-s*, *cds-ca*, and *cms-a* in the cases of low coverage, the latter with an extension also to full coverage, as derived in **Section 2.6.3**. The enthalpies are chosen to fit the experimental data reasonably in different regions as discussed for each model, see below in Table 9.

5.4.2 Parameterisation of surface conductance in chemisorbed water

In the approach used previously for ZrO_2 (**Chapter 4**), I dealt with relatively well-defined temperature dependencies and used them in combination with selected thermodynamic values from literature to obtain activation enthalpies for proton diffusivities. In the case of CeO_2, the transitions are shallower. Different from the case of ZrO_2, all mechanisms proposed in **Section 2.6.3** have been evaluated for CeO_2. Derived p_{H_2O} dependences and estimated preexponentials and activation enthalpies of surface conductance for all models are listed in Table 9.

Moreover, I will go further in suggesting enthalpies not only for thermodynamics but also for migration of protons in order to get a comprehensible treatment. In the following, I use excerpts to describe and parameterise models that fit the experimental data of Figure 38.

Nonetheless, it must be emphasised that the derivation at this stage neglects the possible effects of the surface being more like CeOOH than CeO_2. We treat the mean surface as having 2 oxide ions per Ce ion. The effect of having just one available unprotonated oxide ion for protonation and migration per cerium ion will for the most part be minor, but the parameterisation of models may unavoidably reflect CeOOH-like rather than CeO_2 surfaces in our work like in any other. We see our work hence not as the final, but an important step towards a complete description of protonic conduction over CeO_2 surfaces in wet and other hydrogen-containing atmospheres.

Table 9 Derived p_{H_2O} dependences and predicted preexponentials and activation enthalpies of surface protonic conductance within the chemisorbed water layer at p_{H_2O} = 0.025 bar according to four models of dissociation and transport in cases of low coverage, for which molecular or dissociated chemisorption have the same parameters. Also included are predictions for full coverage, where there are no p_{H_2O} dependences, but differences between molecular or dissociated dominance. Lines in Figure 38 are based on the predicted preexponentials and empirical enthalpies in parenthesis.

Model **Parameter**	**cms-s** **cds-s**	**cms-sa** **cds-sa**	**cms-a** **cds-a**	**cma-a**	**cms-s**	**cds-s**	**cms-sa**	**cds-sa**	**cms-a**	**cds-a**	**cma-a**
n in $G_{s,H^+0} \propto p_{H_2O}^n$	1/2	1	3/2	2	0 (Full coverage)						
G_{s,H^+0} (SK), p_{H_2O} = 0.025 bar	$2\cdot10^{-7}$	$8\cdot10^{-11}$	$1\cdot10^{-14}$	$4\cdot10^{-18}$	$1\cdot10^{-3}$	$4\cdot10^{-4}$	$1.5\cdot10^{-3}$	$8\cdot10^{-4}$	$1\cdot10^{-3}$	$8\cdot10^{-4}$	$1.5\cdot10^{-3}$
ΔH_c (kJ/mol) (plotted in Figure 38)	+30 (+29)	0 (-10)	-60 (-45)	-70	+60	+50	+60	+40	+30 (+25)	0	+40

5.4.2.1 *cds-s model for the high temperature region*

TG data suggested that the adsorption is not complete (low coverage) and that dissociation prevails at the highest temperatures. Given that the protons migrate between surface hydroxide and oxide ions (Eq. 31), it is identical to the "*cds-s*" model schematically shown in Figure 11 (c) – from *c*hemisorption *d*issociative to *s*urface – with migration on the *s*urface.

The surface protonic conductance is in this case represented by Eq. 36 to Eq. 38, with preexponential $G_{s,H^+_{cds\text{-}s}0}$ following Eq. 38. Assuming $\Delta S^0_{a_{cm}}$ = -109 J/molK as measured for the entropy of condensation of water at 100°C [196] as before, $\Delta S^0_{d_{cs}}$ = 0 J/molK, $\gamma_{M_s} \approx 5$ /nm^2 = $8\cdot10^{-10}$ mol/cm^2, and $u_{H^+0} \approx 10$ cm^{2}K/Vs, we get $G_{s,H^+_{cds\text{-}s}0} \approx 2\cdot10^{-7}$ SK at p_{H_2O} = 0.025 bar.

In order to make a first estimate of the activation enthalpy of conductance, we take $\Delta H^0_{a_{cm}}$ = -60 kJ/mol as measured on nano-CeO_2 at 25°C by water adsorption calorimetry.[96] This is of the same order as that of water molecules bound directly to Ce ions.[197] We further assume $\Delta H^0_{d_{cs}}$ = 20 kJ/mol based on the 22 kJ/mol measured for YSZ.[169] If we take $\Delta H_{m,H^+_s} \approx 50$ kJ/mol as a round value first guess based on the enthalpy of bulk mobility of protons in 50 mol% La-substituted CeO_2 reported as 43 kJ/mol,[165] we obtain $\Delta H_{c_{cds\text{-}s}} = \frac{1}{2}\Delta H^0_{a_{cm}} + \frac{1}{2}\Delta H^0_{d_{cs}} + \Delta H_{m,H^+_s} \approx +30$ kJ/mol. The line for this "*cds-s*" model in Figure 38 is drawn to rationalise surface conductance in the region 400-300°C using the derived preexponential and $\Delta H_{c_{cds\text{-}s}} = +29$ kJ/mol. Moreover, the $p^{1/2}_{H_2O}$ dependence of the "*cds-s*" model is confirmed by the data for 400°C in Figure 37 (a).

5.4.2.2 cds-sa model for the intermediate temperature region

At the highest p_{H_2O} at 400°C, the p_{H_2O} dependences in Figure 37 (a) start to increase and as temperature decreases, the conductance levels out at intermediate temperatures in Figure 38. Both indicate that as *RH* and coverage increases, there is an increasing role of adsorbed species in the conduction process, leading to the next mechanism, where protons jump between *s*urface oxide ions and dissociated *a*dsorbed OH^- groups, hence abbreviated "*cds-sa*" model (schematic in Figure 12 c) and representing the reverse of the dissociation to surface oxide ions, *i.e.,* reverse Eq. 16.

The surface protonic conductance along this model is expressed by Eq. 46 to Eq. 48. With assumptions like before, we obtain $G_{s,H^+_{cms\text{-}sa}0} \approx 8{\cdot}10^{-11}$ SK at $p_{H_2O} = 0.025$ bar. We assume that migration of protons is easier between these species than solely along the surface (previous case), and with the choice of a lower enthalpy of migration of this mechanism of $\Delta H_{m,H^+_{sa}} = 40$ kJ/mol, we obtain $\Delta H_{c_{cms\text{-}sa}} = \Delta H^0_{a_{cm}} + \Delta H^0_{d_{cs}} + \Delta H_{m,H^+_{sa}} \approx 0$ kJ/mol. This conductance is plotted with -10 kJ/mol in Figure 38 to represent the shallow minimum level at 300–200°C. The model proposes a proportionality to $p^1_{H_2O}$ of surface protonic conduction, which is approached for the highest p_{H_2O} at 400°C in our measurements shown in Figure 37 (a), and in particular in those of Manabe *et al.* [83] measured at even higher p_{H_2O}.

5.4.2.3 cms-a model for temperatures below 200°C

As we go lower in temperature, the conductance starts to increase more steeply in Figure 38, and the p_{H_2O} dependence increases further, see Figure 37 (b) measured at 100°C. This suggests even more involvement of adsorbed species for migration: We consider that dissociation still goes to surface oxide ions, but may be weaker as its enthalpy is positive and

temperature is now lower. Migration now takes place in the adsorbed layer between the remaining water molecules and dissociated hydroxide ions according to Eq. 33. The mechanism is abbreviated "*cds-a*" or "*cms-a*" depending on the degree of dissociation, as schematically illustrated in Figure 13 (a) and (c). For this mechanism to occur, dissociation is needed, but also some undissociated water needs to remain.

The surface protonic conductance is given by Eq. 56 to Eq. 58. As indicated above, the adsorption comes in at full play, while the dissociation has a two-sided effect and comes in to a lesser extent. With assumptions as before, we obtain $G_{s,H^+_{chm\text{-}a}0} \approx 1{\cdot}10^{-14}$ SK at $p_{H_2O} = 0.025$ bar. If we now take the mobility in the molecular layer to be lower, say $\Delta H_{m,H^+_a} = 20$ kJ/mol, the enthalpy of conduction may be estimated to be $\Delta H_{c_{cms\text{-}a}} = \frac{3}{2}\Delta H^0_{a_{cm}} + \frac{1}{2}\Delta H^0_{d_{cs}} + \Delta H_{m,H^+_a} \approx$ -60 kJ/mol, meaning that conductance increases strongly with decreasing temperature, describing roughly the conductivity in the range 200-100°C in Figure 38, there plotted with $\Delta H_{c_{cms\text{-}a}} =$ -45 kJ/mol. This behaviour of transport in the chemisorbed layer hence fits the conductivity in the region where it earlier has traditionally been assigned to transport in the physisorbed layer. Moreover, the predicted $p_{H_2O}^{3/2}$ dependence fits well with the data for 100°C in Figure 37 (b), further supporting the assigned mechanism.

As before, it does not matter mathematically whether we consider a mainly undissociated (*cms-a*) or dissociated (*cds-a*) case as long as low coverage predominates. The difference becomes evident, however, if we consider the full coverage cases.

As we pass below 100°C, the conductivities in Figure 38 level off with decreasing temperature, which is only rational if we approach full coverage. These behaviours must follow one of the models for full coverage introduced in **Chapter 2**. In the "*cds-a*" case at full coverage and fully dissociation (Figure 13 d), we predict an enthalpy of conduction close to 0 kJ/mol, which with the predicted preexponential cannot fit the levelling off at low temperatures in Figure 38. However, low dissociation and full coverage ("*cms-a*" case in Figure 13 b) seems to rationalize the results.

In this case, the conductance follows Eq. 59 to Eq. 61, with preexponential coming out as $G_{s,H^+_{cms\text{-}a}0} = 1.1{\cdot}10^{-3}$ SK. Assuming the enthalpy of mobility $\Delta H_{m,H^+_a}$ is still around 20 kJ/mol, the enthalpy of conduction may be estimated to be $\Delta H_{c_{cms\text{-}a}} = \frac{1}{2}\Delta H^0_{d_{cs}} + \Delta H_{m,H^+_a} \approx +30$ kJ/mol. It is plotted in Figure 38 with $\Delta H_{c_{cms\text{-}a}} = +25$ kJ/mol as a continuation to lower temperatures where it takes over for the low coverage model.

As summarized in Table 9, we have also evaluated dissociation within the chemisorbed layer itself, to form adsorbed OH^- and H_3O^+ ions, *i.e.,* "*cma-a*" mechanism (Figure 14) corresponds to one proposed by Raz *et al.* [136], and predicts conductance and temperature behaviours similar to those of the "*cms-a*" and "*cds-a*" models above. However, we must expect that dissociation

to the surface is stronger (has a lower enthalpy) than within the adsorbed water layer, and by that the H_3O^+ ions will be minority defects in the overall electroneutrality and play little role.

For completeness, we mention that CeO_2 due to its hydrophobicity does not lend itself to analysis of models for conduction in the physisorbed water layers beyond those provided in our previous work on ZrO_2.

5.5 Protonic conduction in physisorbed water

For most samples, including the ones in Figure 38, the continuing increase in conductivity at the lowest temperatures suggests the onset of conduction in the physisorbed layers that are filling up under these conditions. Indeed, a conductivity decrease with decreasing temperature near room temperature was observed for one sample (not shown here).

Figure 39 shows examples of p_{H_2O} dependences of conductivity at 25°C (RT), where we believe that physisorbed water starts to contribute. The CeO_2-550 sample lost all conductivity at $RH < 30\%$, but otherwise, both samples showed conductivities approximately proportional to p_{H_2O} at $RH < 60\%$, while the p_{H_2O} dependences increased to at least $p_{H_2O}^2$ at $RH > 60\%$. We cannot attribute these behaviours to quantitative models like we did above for the chemisorbed water on CeO_2 and for physisorbed water in our previous work on ZrO_2. Qualitatively, it may reflect hysteresis in the contact angle and wettability of liquid-like physisorbed water and that the activation enthalpy of the mobility of protons decreases with increasing thickness and decreasing viscosity of the liquid-like physisorbed water layer.

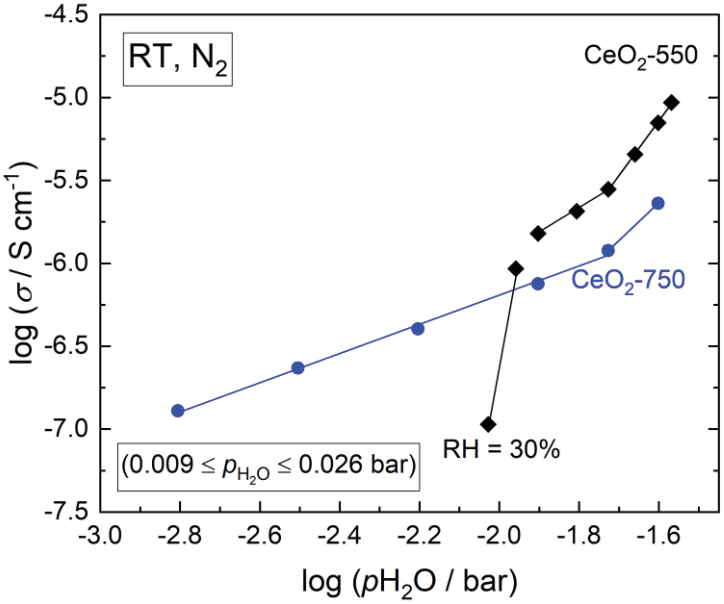

Figure 39 p_{H_2O} dependence of surface protonic conductivity at 25°C (RT) for both CeO_2 samples.

For a CeO_2-550 sample that was heated to 540°C in dry N_2 and then cooled straight to RT, the conductivity was initially immeasurably small in dry atmosphere. It remained so upon small

steps towards wetter conditions, and became measurable only above *RH* ≈ 30%, and took several days to equilibrate, and consequent behaviours of conductivity at high *RH* were variable. We suggest that this relates to a restructuring of the CeO_2 surface upon beginning adsorption of water in order to lower the surface energy. After completion of this process, changes in humidity were equilibrated faster, within a couple of hours. Combined ^{17}O and ^{1}H solid-state NMR spectroscopy with DFT calculations indicate that reconstructions occur on CeO_2(100) nanotube surfaces upon adsorption of water.[198] Yang *et al.* [199] provided direct spectroscopic evidence for the extensive restructuring of rod-shaped ceria nanoparticles, they further showed that (111) nanofacets is an intrinsic property of the catalytically most active CeO_2(110) surface. For the CeO_2-750 sample, long equilibration times of the order of 24 h were required to reach steady-state conditions at each *RH* level at RT. We may also anticipate that competing impurity adsorbents such as CO_2 and hydrocarbons may play a role.[200] Similarly, Simons *et al.* [99] reported that hydration of ceria took up to three days for thin films at RT.

One the other hand, it is well known that water condenses more easily in the presence of pores in the nanometer regime due to capillary condensation at low temperatures. This is evaluated by the Kelvin equation at contact angle of 0°, 64° and 112°, representing CeO_2 surface with spreading, wetting (hydrophilic), and non-wetting (hydrophobic) character, respectively.[185] As shown in Figure 40, capillary condensation of water may play a role near room temperature, based on mesopore sizes of 14 and 20 nm from the BET analysis (Table 8). However, this may still not be reflected in the measured conductivity of CeO_2 because the hydrophobicity and surface reorganization prevent connection of the narrowest parts of the pores. Furthermore, wedge-shaped porosity due to low-temperature sintering of nanocrystalline materials can also add favourable water adsorption sites.[73]

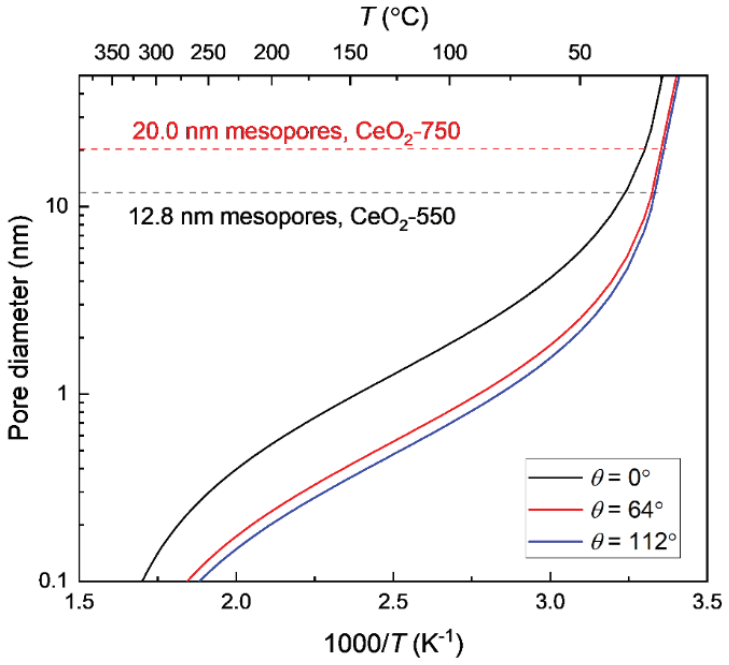

Figure 40 Pore diameter required for water condensation at different temperatures at p_{H_2O} = 0.025 bar, calculated for three characteristic contact angles based on the Kelvin equation.

5.6 Conclusions on CeO_2

Water adsorption and surface protonic conductivity measurements on nominally pure porous sintered CeO_2 samples confirm the expectancy that adsorption relates to specific surface area, while surface conductivity relates to grain size and porosity, quantifiable through a brick layer model. TG supports indications from EELS that the surface and/or subsurface of CeO_2 in the presence of water vapour is hydrogenated to Ce^{3+} ions and protons H^+, and that the following chemisorption is dissociative at high temperatures. Physisorption sets in only at the highest relative humidities, typical of hydrophobic behaviour, different from other, more hydrophilic oxides like TiO_2 and ZrO_2.

For CeO_2, the native conductivity in dry atmospheres is likely due to surface electronic conductivity, possibly a result of the hydrogenated subsurface layer. The conductivity in wet atmospheres below 500°C is dominated entirely by surface protonic conduction.

The interpretation of the preexponentials and p_{H_2O} dependence of surface protonic conductivity is for the case of CeO_2 restricted to chemisorbed water only due to the absence of physisorbed water except for the near room temperature region.

In this work, we have further expanded the models for transport from and in chemisorbed water to comprise migration of protons between surface oxide ions, migration between surface oxide ions and adsorbed hydroxide ions, and migration between adsorbed water molecules and hydroxide ions, with predicted positive, near-zero, and negative apparent activation enthalpies of conduction, respectively, and $p_{H_2O}^{1/2}$, $p_{H_2O}^{1}$, and $p_{H_2O}^{3/2}$ dependences. With predicted preexponentials and estimates of enthalpies for adsorption, dissociation, and proton diffusion, these matches observed surface protonic conductances at high, intermediate, and low temperatures, respectively.

At the lowest temperatures and highest *RH*s, the surface protonic conductivity of CeO_2 levels off, as expected from saturation to full coverage of the chemisorbed layer. A contribution from physisorbed water sets in, but remains modest and variable because of hysteresis of wetting and possible restructuring of the surface and surface-oxide interface, and changes in surface composition.

The TG data of dissociative chemisorption fit literature suggestions of a standard molecular adsorption enthalpy of -60 kJ/mol H_2O and dissociation of a proton to a surface oxide ion of the order of +20 kJ/mol H_2O. With these, conductivity data further suggest that migration of protons between surface oxide ions have activation energies as high as 50 kJ/mol, while they decrease towards values around 20 kJ/mol in the adsorbed layer.

It is believed that the findings have consequences for understanding and controlling the surface properties of ceria-based nanomaterials. This study further suggests that incomplete and weak yet dissociative chemisorption of water may plays an important role for ceria as a catalyst in

that much of the surface is left available for reactant molecules, while dissociated mobile protons are available on the surface along with electrons from the Ce^{3+} in the surface.

6 Further results, summarising discussions and outlook

Until now, the surface protonic conduction of porous ZrO_2 (**Chapter 4**) and CeO_2 (**Chapter 5**) has been discussed on the basis of models presented in **Chapters 2 and 3**. The present chapter serves to complement what is already discussed previously, based on additional measurements performed on ZrO_2, CeO_2 and TiO_2, also being a critical assessment to the results obtained so far. The thermodynamic parameters of water adsorption on oxide surfaces are estimated from their thermogravimetric data modelled in terms of the Langmuir and the BET expressions introduced in **Chapter 2** and discussed with respect to their limitations. Enthalpies of proton mobility in water layers are extracted on the basis of available literature and my experimental data. Finally, I will discuss how surface protonics and the models developed may play a role for various applications mentioned in **Chapter 1**, and how this thesis can contribute to fundamental and applied studies in these directions.

6.1 Specific surface area and pore size

The water uptake kinetics of samples and possibly also thermodynamics can be affected by their specific surface area.[201] To gain a better understanding of the adsorption behaviour on oxide surfaces in general, N_2 sorption measurements have been performed on the representative ZrO_2 samples studied in **Chapter 4**, and on two types of commercial TiO_2 powders in addition to the CeO_2 samples investigated in **Chapter 5**. One of the two TiO_2 powders was of anatase type (< 25 nm particle size, CAS No.1317-70-0, Sigma-Aldrich), and the other of TiO_2 P25 type containing anatase and rutile phases in a ratio of about 3:1 (21 nm by TEM, CAS No.13463-67-7, Sigma-Aldrich). Samples (0.4 – 1 g) were degassed for 2 h at 150°C in vacuum prior to analysis. The N_2 sorption isotherms of CeO_2, ZrO_2 and TiO_2 are depicted in Figure 41 (a-c), respectively, and their corresponding pore size distribution curves in Figure 41 (d-f). The microstructural features of the samples determined from these data are summarized in Table 10.

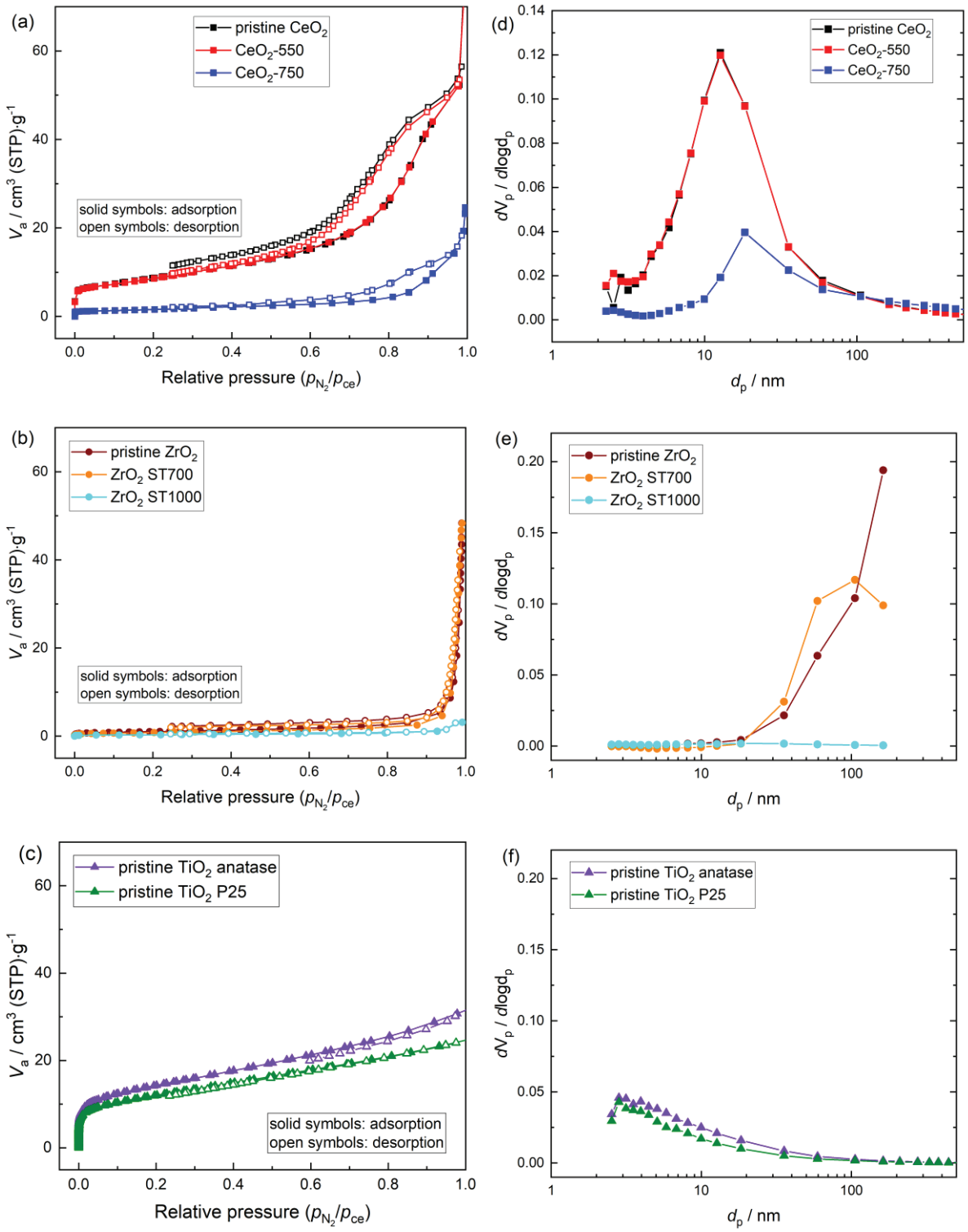

Figure 41 (a-c) N_2 adsorption isotherms of the CeO_2, ZrO_2 and TiO_2 samples, (d-f) the corresponding BJH pore size distribution.

As mentioned in **Section 5.3.3**, increasing the sintering temperature of CeO_2 from 550 to 750°C slightly shifted the average pore size from 14 to 20 nm. The filling and emptying of such mesopores (2-50 nm [202]) by capillary condensation of N_2 is evidenced by the hysteresis loop. A significant N_2 adsorption is observed for the pristine and ZrO_2 ST700 sample only at the highest relative pressure, which disappeared in the case of ZrO_2 ST1000. As compared to the other

ZrO_2 samples, ZrO_2 ST1000 is accompanied by a significant reduction in specific surface area, total volume of open pores and average pore diameter. Such an effect may be a consequence of condensation in macropores (> 80 nm) due to particle agglomeration. The pristine TiO_2 powders obtained their pore volume from mesopores in range of 3-4 nm. It should be noted that facet-engineered anatase porous TiO_2 with a similar BET surface area show considerable larger mesopores of 25-44 nm (see SI, Table S1 in ref. [118]).

Table 10 Specific surface area and pore structure properties of CeO_2, ZrO_2 and TiO_2 samples determined by N_2 sorption isotherms at 77 K.

Samples	CeO_2			ZrO_2			TiO_2	
	Pristine	CeO_2-550	CeO_2-750	Pristine	ST700	ST1000	Anatase	P25
BET A_g [cm^2/g]	$3.2\cdot10^5$	$3.1\cdot10^5$	$5.9\cdot10^4$	$3.7\cdot10^4$	$2.9\cdot10^4$	$1.1\cdot10^4$	$5.0\cdot10^5$	$4.2\cdot10^5$
Pore volume [cm^3/g]	$1.1\cdot10^{-1}$	$1.0\cdot10^{-1}$	$3.5\cdot10^{-2}$	$7.4\cdot10^{-2}$	$7.3\cdot10^{-2}$	$4.8\cdot10^{-3}$	$4.8\cdot10^{-2}$	$3.8\cdot10^{-2}$
Mean pore diameter [nm]	13	14	20	81	101	-	4	3

6.1.1 Pore condensation

As briefly discussed in **Section 5.5**, condensation of water can take place in the presence of nanoporosity, and the amount of condensed water further depends on the available pore sizes and their distribution. According to the Kelvin equation assuming non-slit-shaped pores and at a given p_{H_2O} = 0.025 bar, this is hardly the case for our ZrO_2 samples at any temperatures owing to their large macropore sizes of 80 nm and above. It might contribute to the protonic conductivity near room temperature for the CeO_2 samples, yet suppressed by their hydrophobic nature. On the other hand, it is expected that the surface curvature from the small pore size of 3-4 nm as in the case of the commercial nanoscopic TiO_2 materials enhances adsorption and induces pore condensation of water at temperatures typically below 60°C. This phenomenon and the presence of open nanoporosity is considered crucial for applications as polymer electrolyte membranes (PEMs) and humidity sensors, where the proton conductivity rely on transport through a continuous percolation path formed by the physisorbed water inside the pore network at low temperatures.[203, 204]

In **Section 1.3.**, it was said that PEMs exhibit noticeably higher protonic conductivity than that of bulk water ($\sigma_{bulk,H2O} \approx 10^{-4}$ S/m, assuming that the diffusion coefficient and concentration of H_3O^+ for bulk water are $3.5\cdot10^{-9}$ m^2/s and $1.1\cdot10^{22}$ $/m^3$, respectively [205]), ascribed to the conduction via water confined in the nanoporosity of the polymers. Ryzhkin *et al.* [205] demonstrated a model explaining the high protonic conductivity of PEMs (e.g. Nafion). In the model, it is assumed that: 1) a liquid-like surface layer of ice with an ordered oxygen lattice and

destroyed proton lattice applies, 2) molecules are ordered with protons towards the channel walls, and that the walls can release some protons to dangling bonds of water molecules. The authors further suggest that increasing the concentration of proton complex on the surface of channel walls and decreasing the channel diameter during polymerization of PEMs can retain their protonic conductivity at higher temperatures. However, when the channel diameters are of the order of intermolecular distances, the model becomes inapplicable.

In an extended model developed by the same group,[206] the proton transport of water confined in nanochannels of porous materials is explained by the inconsistency of the ice rules with ordering of interface molecules as compared to bulk water. Consequently, additional charge carriers are generated in proximity of the interface, giving rise to higher protonic conductivity. The model considers two types of carriers (ionic and bond defects) allowing interpretation of proton transport in nanoporous materials of various types. For silica-based highly ordered nanoporous materials such as MCM-41 and SBA-15 with dissociative adsorption of water, *i.e.,* "*cds*" model in our nomenclature, enhanced protonic conductivity can be achieved through the incorporation of sulfonic acid groups (SO_3H). Assuming the relative surface concentration of the Si-SO_3H sulfonic acid group is about 0.1, the relative concentration of doped positive ionic defects will follow

$$x_+ \simeq 0.1\frac{S/a^2}{V/a^3} = 0.1\frac{\pi d/a^2}{\pi d^2/4a^3} = \frac{0.4a}{d} \qquad \text{Eq. 120}$$

where a is the distance between water molecules, d is the diameter of the nanochannels, S is the internal surface area, and V is the free volume of the porous material. Applying a = 0.28 nm, d = 2 nm, and a diffusion coefficient $D_+ = 4\cdot10^{-9}$ m^2/s as in bulk water, the conductivity is estimated as $\sigma = e_1^2 D_+ x_+ N_0 / kT$ = 16 S/m, where N_0 is the volume concentration of water molecules. The results were in qualitative agreement with preciously reported experimental values.[207, 208]

6.2 Evaluation of specific surface area: BET vs BLM

As mentioned in **Section 3.2.1**, the brick layer model (BLM) allows estimates of the volumetric specific surface area (A_v) based on the same parameters – grain size and relative density or porosity. And from this, we may calculate gravimetric specific surface area (A_g) and molar specific surface area (A_m) following Eq. 112 and Eq. 113, respectively. This is verified by the three types of oxides introduced in the preceding section, which allows us to compare with that of the BET analyses. As shown in Table 11, the results show good agreement between the experimental and presumed gravimetric specific surface area (A_g), suggesting that the BLM can be used as an order-of-magnitude estimate of the specific surface area.

Table 11 Comparison of the specific surface area of ZrO_2, CeO_2 and TiO_2 based on the brick layer model and the BET analyses. For the pristine oxide powder, the specific surface areas were obtained assuming 50% relative density in the BLM.

Sample	BET	BLM		
	A_g [cm^2/g]	A_v [cm^2/cm^3]	A_g [cm^2/g]	A_m [cm^2/mol]
pristine CeO_2	$3.2 \cdot 10^5$	$7.1 \cdot 10^5$	$2.0 \cdot 10^5$	$3.4 \cdot 10^7$
CeO_2-550	$3.1 \cdot 10^5$	$3.8 \cdot 10^5$	$1.0 \cdot 10^5$	$1.8 \cdot 10^7$
CeO_2-750	$5.9 \cdot 10^4$	$1.6 \cdot 10^5$	$3.5 \cdot 10^4$	$6.0 \cdot 10^6$
pristine ZrO_2	$3.7 \cdot 10^4$	$1.1 \cdot 10^5$	$3.2 \cdot 10^4$	$3.9 \cdot 10^6$
ZrO_2-ST700	$2.9 \cdot 10^4$	$9.6 \cdot 10^4$	$2.7 \cdot 10^4$	$3.4 \cdot 10^6$
ZrO_2-ST800	-	$9.6 \cdot 10^4$	$2.7 \cdot 10^4$	$3.4 \cdot 10^6$
ZrO_2-ST900	-	$9.0 \cdot 10^4$	$2.6 \cdot 10^4$	$3.2 \cdot 10^6$
ZrO_2-ST1000	$1.1 \cdot 10^4$	$8.1 \cdot 10^4$	$2.1 \cdot 10^4$	$2.6 \cdot 10^6$
ZrO_2-ST1100	-	$6.6 \cdot 10^4$	$1.6 \cdot 10^4$	$2.0 \cdot 10^6$
pristine TiO_2 anatase	$5.0 \cdot 10^5$	$7.5 \cdot 10^5$	$3.9 \cdot 10^5$	$3.1 \cdot 10^7$
pristine TiO_2 P25	$4.2 \cdot 10^5$	$7.1 \cdot 10^5$	$3.4 \cdot 10^5$	$2.7 \cdot 10^7$

6.3 Concentration of adsorbed water by thermogravimetry

TG analysis has been conducted on the ZrO_2, CeO_2 and TiO_2 samples as a function of temperature in N_2 atmosphere to determine the coverage of the oxides by adsorbed water. All TG measurements were performed well below the sintering temperature of ZrO_2 and CeO_2 to maintain their microstructures, and for TiO_2 the temperatures were limited to 400°C and below to refrain the anatase-rutile phase transformation.[209] After dehydrating the samples at the highest measurement temperature for at least 2 h, the samples were equilibrated at $p_{H_2O} = 0.02$ bar and measured upon stepwise cooling to RT. As temperature decreases, the stabilization time was extended accordingly to ensure equilibrium measurements. The weight change after subtraction from an equivalent measurement in bottle-dry atmospheres reflects the amount of water adsorbed on the oxides. Figure 42 depicts the temperature dependence of the surface concentration of water for all considered oxides interpreted as number of H_2O per nm^2 by using the BET surface area given in Table 11.

Traditionally, protonic conduction in water adsorbed on oxide surfaces can be characterized by their distinct temperature regions: above 200°C, between 200 and 50°C, and below 50°C, where transport of protons takes place in the chemisorbed, the first ice-like physisorbed, and the liquid-like physisorbed water layers, respectively. As Figure 42 demonstrates, water adsorbed on the ZrO_2 samples (half-filled circles) saturates towards 200°C with a coverage going from 4 H_2O/nm^2 for ST700 towards 7 H_2O/nm^2 for ST1000, corresponding to transport of protonic

species in the chemisorbed water layer. Further increase in water uptake can be attributed to physisorbed water, in line with conclusions in **Chapter 4**. For the CeO_2 samples, observations from TEM (Figure 30) and the measured $p_{H_2O}^{1/4}$ dependence of water adsorption (Figure 33 a) as seen from **Chapter 5** led us to suggest that the plateau from TG around 250°C (filled squares) with a low coverage of 0.8-2 H_2O/nm^2 reflect saturation of the hydrogenated CeOOH-type subsurface layer. Consequently, chemisorption comes into play only below 200°C, while physisorption only starts to appear near RT. The pristine TiO_2 powders (open triangles) show less apparent transition from chemisorbed to physisorbed water, probably a result of their more amorphous nature (low fraction of crystallite material) as compared to the other, more well-sintered samples.

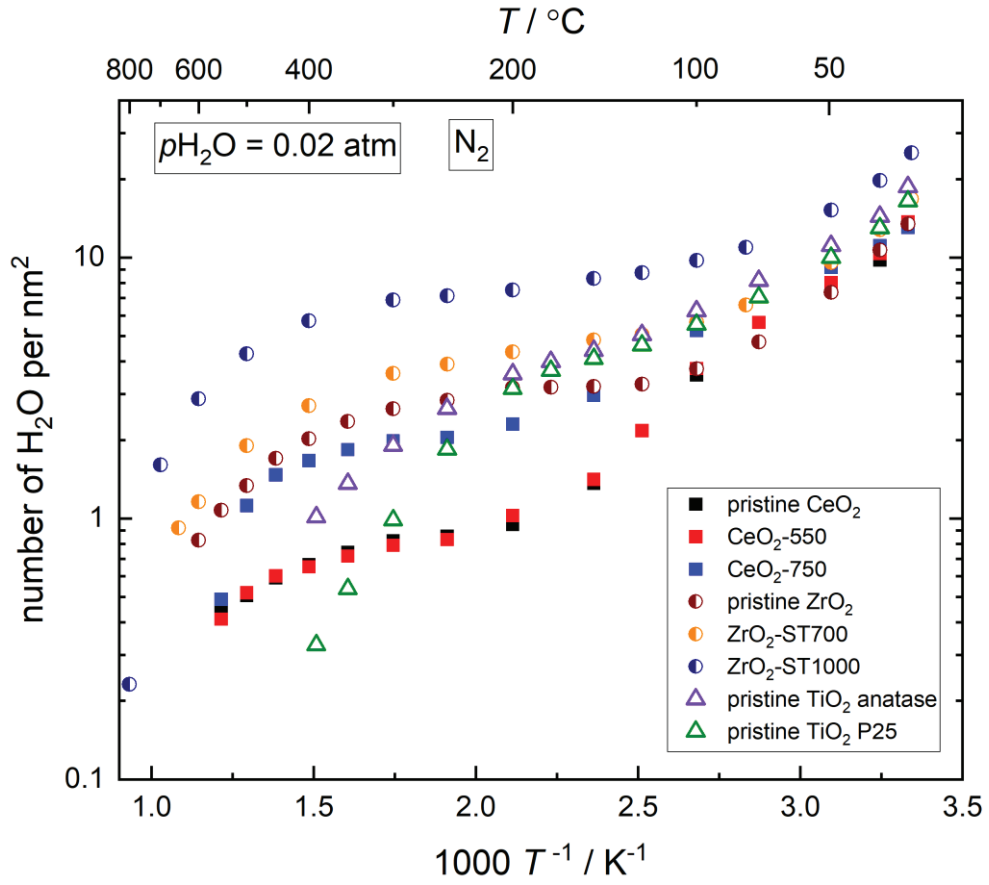

Figure 42 Surface concentration of water measured for CeO_2, ZrO_2 and TiO_2 samples in wet (p_{H_2O} = 0.02 bar) N_2 atmosphere and plotted as number of H_2O per nm^2 *vs* 1/*T*.

6.3.1 Evaluating ΔH^0 and ΔS^0 of chemisorption by TG

Attempts to obtain the thermodynamic parameters have been made by modelling the water uptake data in Figure 42 to the simple limiting cases, namely, Langmuir equations for molecular chemisorption (*cm* model) according to Eq. 13, and for fully dissociative chemisorption (*cds* model) as described by Eq. 22. The former yields equilibrium coefficients $K_{a_{cm}}$, which in turn

allows determination of $\Delta S^0_{a_{cm}}$ and $\Delta H^0_{a_{cm}}$ through Eq. 12. Likewise, $\Delta S^0_{a_{cds}}$ and $\Delta H^0_{a_{cds}}$ can be derived from $K_{a_{cds}}$ through Eq. 19. We also note that TG only measures amount of water, not the degree of dissociation, hence we cannot model the intermediate cases (expressed by Eq. 16 and Eq. 25). Moreover, the assignment to an equilibrium coefficient *K* depends on a model for the reaction, so that the obtained standard entropy and enthalpy changes of water adsorption depend on the appropriateness of the model and its assumptions. Accordingly, the results here serve only as a first approximation. On the other hand, thermodynamic parameters existing among earlier reports in literature sometimes scatter significantly. This is especially true when dealing with nanomaterials, since the number of variables increases, hence the error sources. For instance, the total integral adsorption enthalpy studied by means of water adsorption calorimetry cannot distinguish contributions of different surfaces, while theoretical approaches usually consider dominant surfaces with lowest energies and disregard contributions from surface heterogeneity (e.g. step sites and kink sites). All in all, the actual accuracy of the results from different methods is hard to evaluate.

It must be said that the Langmuir isotherms assume homogeneous (perfect) surfaces with all adsorption sites of equal shape and size. Such isotherms may not correctly reflect faceted samples with presumably curved surfaces as in the case of CeO_2 and ZrO_2, yet sufficient to distinguish between the models.

Figure 43 and Figure 44 illustrate filling up of the monolayer for the three oxides based on the TG results fitted to molecular and dissociative chemisorption, respectively, with their numerical parameters indicated in each plot, and further gathered at the end of the section in Table 12. The fitting to the CeO_2 data was done after subtraction of the mass gain due to the CeOOH-like subsurface layer as described above. The accuracy of the fitting strongly depends on the quality of the experimental data, it is thus crucial to obtain data over sufficient temperature ranges to allow accurate deconvolution of the standard entropy and enthalpy values from TG. Most data points in the case of ZrO_2 within the temperature range examined here are close to saturation of the chemisorbed monolayer at the intermediate temperatures. Therefore, the saturation as such is fairly well modelled, while the ΔS^0 and ΔH^0 values are effectively evaluated from a limited dataset and must be expected to be of relatively low confidence. Deviations from previous calorimetry and DFT studies should thus not be overinterpreted.

The standard enthalpy change of adsorption can be directly measured from a combined thermogravimetry and differential scanning calorimetry (TG-DSC) method. This technique allows simultaneous measurements of heat exchange and the corresponding weight change, hence, recommended for further study.[210, 211]

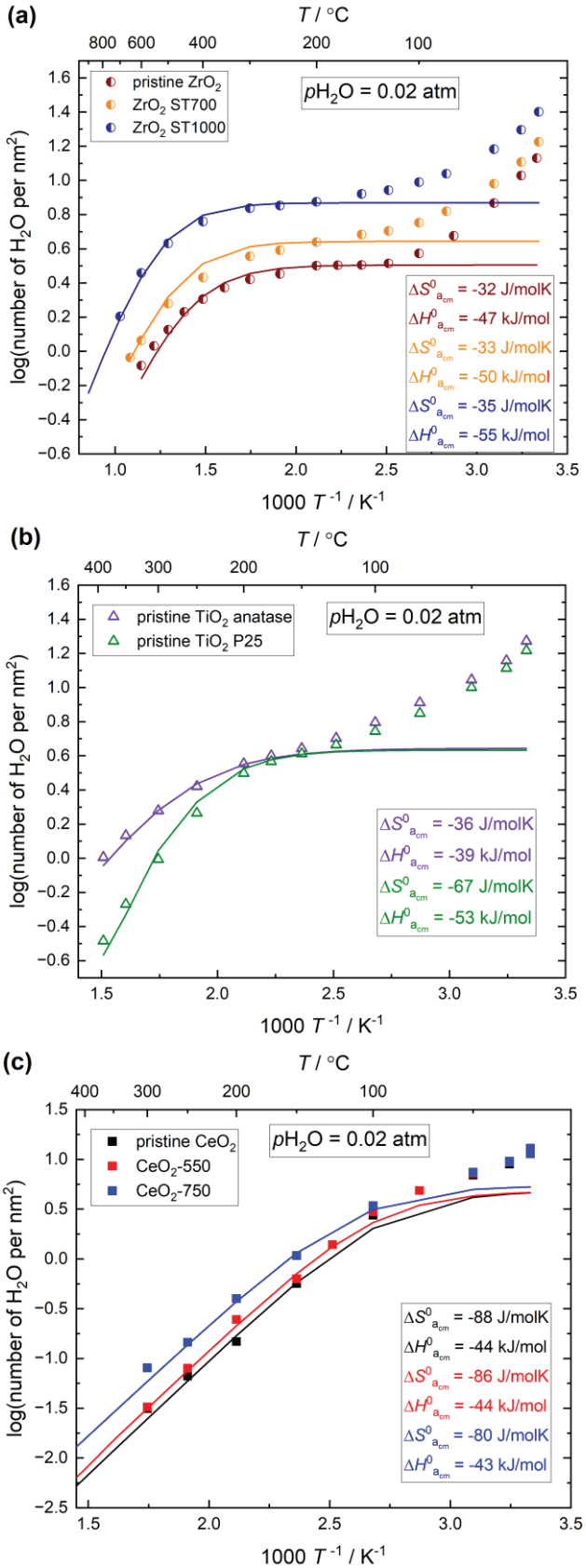

Figure 43 Concentration of adsorbed water for (a) ZrO_2, (b) TiO_2 and (c) CeO_2 in wet (p_{H_2O} = 0.02 bar) N_2 atmosphere. $\Delta S^0_{a_{cm}}$ and $\Delta H^0_{a_{cm}}$ (indicated in each plot) were extracted from fitting the data to the Langmuir equation (solid lines) for molecular chemisorption (*cm* model) given in Eq. 13.

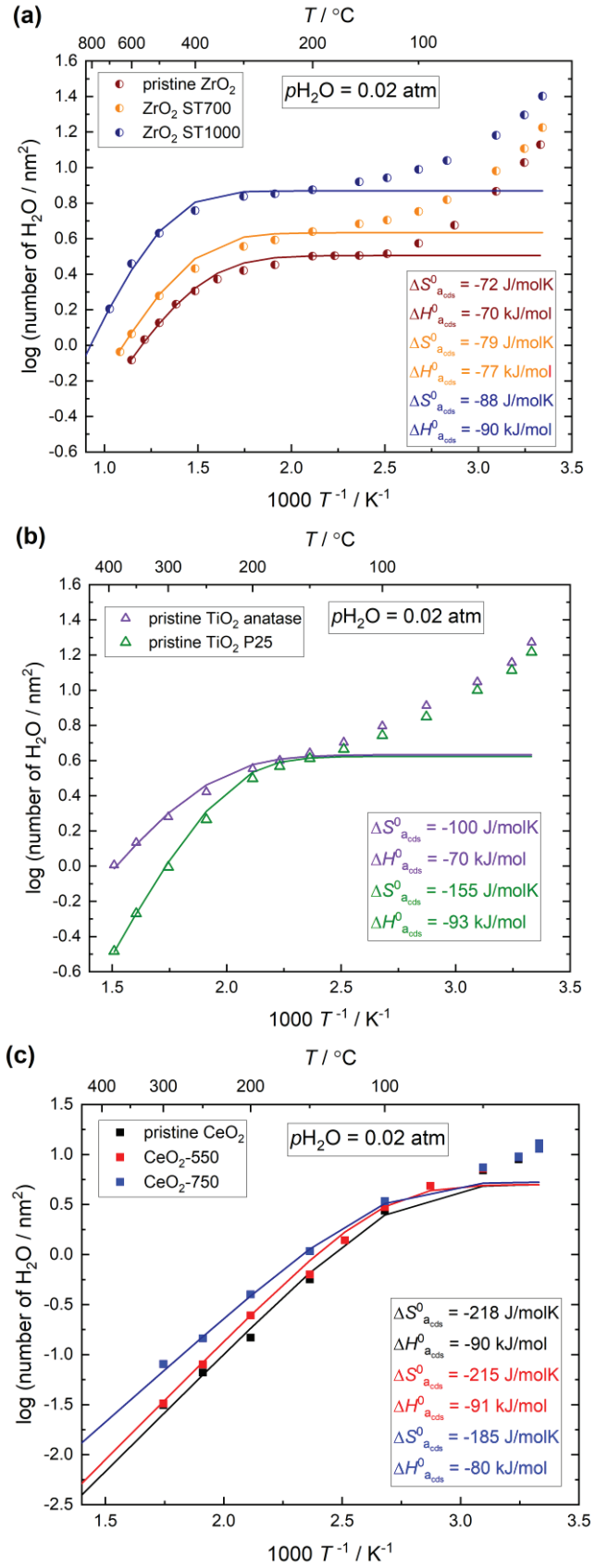

Figure 44 Concentration of adsorbed water for (a) ZrO_2, (b) TiO_2 and (c) CeO_2 in wet (p_{H_2O} = 0.02 bar) N_2 atmosphere. The data were further modelled to the Langmuir isotherm for dissociative chemisorption (*cds* model) given in Eq. 22. The fitted $\Delta S^0_{a_{cds}}$ and $\Delta H^0_{a_{cds}}$ are indicated in the plots.

If molecular chemisorption dominates, as evident from Figure 43 and Table 12, the fitting of ZrO_2 data to Eq. 13 yields $\Delta H^0_{a_{cm}}$ of -50 kJ/mol for ST700 and -55 kJ/mol for ST1000, with corresponding $\Delta S^0_{a_{cm}}$ of around -34 J/molK. First-principles calculations reported that the enthalpy of molecular chemisorption for the (001) surface of monoclinic ZrO_2 is expected to be more exothermic, -90 kJ/mol at 50% coverage and -65 kJ/mol at full coverage.[212] Moreover, the obtained $\Delta S^0_{a_{cm}}$ is too low (e.g. compared to the entropy of condensation to liquid water at 100°C, specifically, -109 J/molK) and cannot be rationalized. Similar values of $\Delta S^0_{a_{cm}}$ are revealed for anatase TiO_2 (Figure 43 b), associated with an even lower $\Delta H^0_{a_{cm}}$ of -39 kJ/mol. In comparison, TiO_2 P25 shows somewhat more exothermic $\Delta S^0_{a_{cm}}$ of -67 J/molK, and $\Delta H^0_{a_{cm}}$ of -53 kJ/mol. The extracted $\Delta H^0_{a_{cm}}$ is still low compared to the value of around -70 kJ/mol estimated for water adsorbed on the (101) surface of TiO_2 anatase showing favourable molecular chemisorption up to monolayer coverage.[120, 213, 214] Nevertheless, the data are not sufficient for deeper analysis.

In contrast, $\Delta S^0_{a_{cm}}$ and $\Delta H^0_{a_{cm}}$ values for CeO_2 (Figure 43 c) turn out to be around -85 J/molK and -44 kJ/mol, respectively. This $\Delta S^0_{a_{cm}}$ is more reasonable in terms of the entropy of condensation of water suggesting that molecular chemisorption may apply on CeO_2 surfaces. However, $\Delta H^0_{a_{cm}}$ is lower than previously published values for nanoceria, which have been demonstrated as -94 kJ/mol at 1 H_2O/nm^2, going towards -60 kJ/mol at full monolayer coverage of 8 H_2O/nm^2.[96] Prin *et al.* [215] reported values in the range -55 to -59 kJ/mol from TG measurements on CeO_2 powder. DFT studies show values between -47 to -54 kJ/mol.[190, 191] The obtained values are within acceptable agreement with those from other techniques, considering the several assumptions employed. Nevertheless, the measured $p^{1/2}_{H_2O}$ dependence of water adsorption at 100°C (Eq. 21 and Figure 33 b) indicates that strong dissociative chemisorption may still prevail during filling up of the incomplete (weak) chemisorbed layer, so that the *cds* model better describes water adsorption on CeO_2. If this is the case, $\Delta H^0_{a_{cds}}$ = -44 kJ/mol can be understood as the sum of those for molecular chemisorption ($\Delta H^0_{a_{cm}}$ = -60 kJ/mol) and dissociation ($\Delta H^0_{d_{cs}}$ = +20 kJ/mol [169]), given by Eq. 19. The standard enthalpy value is small, which might be related to the hydrophobic nature of CeO_2.[216]

For dissociative chemisorption, as shown in Figure 44 and Table 12, ZrO_2 revealed $\Delta S^0_{a_{cds}}$ = -79 J/molK and $\Delta H^0_{a_{cds}}$ = -77 kJ/mol for ST700, which evolves into -88 J/molK and -90 kJ/mol with increasing sintering temperature (ST1000), substantially more negative than that of molecular chemisorption. DFT calculations show that the standard enthalpy changes of water adsorbed on ZrO_2 generally decrease with increasing surface coverage, ending up at $\Delta H^0_{a_{cds}}$ of

-109 and -91 kJ/mol on the (001) surface of monoclinic and tetragonal ZrO_2, respectively, at monolayer coverage.[152, 212]

This is further compared with the results obtained from calorimetry, which showed $\Delta H^0_{a_{cds}}$ of -142 kJ/mol at half-monolayer coverage of 2.2 H_2O/nm^2, and -119 kJ/mol at full coverage of 5 H_2O/nm^2.[126] $\Delta H^0_{a_{cds}}$ according to our fitting are in general low, however, the well-developed ZrO_2 ST1000 sample indeed show $\Delta H^0_{a_{cds}}$ (-90 kJ/mol) in reasonably agreement with the reported values. The present results are furthermore comparable to what have been reported on YSZ. Specifically, Raz *et al.* [136] based on the assumption of two parallel chemisorption processes yields enthalpies of -94 ± 19 kJ/mol and -70 ± 14 kJ/mol for YSZ by fitting the water adsorption data from TG. The two enthalpies of chemisorption can be taken to represent different crystallographic planes, adsorption on smooth surfaces *vs* corners, etc. In the case of TiO_2, $\Delta S^0_{a_{cds}}$ values are in overall agreement with that of the condensation to liquid water at 100°C. The extracted $\Delta H^0_{a_{cds}}$ of -70 kJ/mol for anatase TiO_2 and -93 kJ/mol for TiO_2 P25 (Figure 44 b) are to be compared with the -120 kJ/mol calculated for the anatase (001) surface where water shows a strong preference to dissociate.[217]

All in all, the results so far have demonstrated that dissociative chemisorption of water is likely prevalent on ZrO_2 and TiO_2 surfaces. This further supports what has been proposed previously that the proton transport in ZrO_2 follows the *cds-s* model (*c*hemisorption *d*issociative to *s*urface and migrate between *s*urface oxide ions) by going from low towards full coverage upon increased sintering temperature. In contrast, the chemisorbed water is predominantly bound to the surface of CeO_2 in a molecular state, because fitting of the data to the dissociative model (Figure 44 c) result in $\Delta S^0_{a_{cds}}$ (-200 ± 20 J/molK) far above the reasonable level, hence can be ruled out. As discussed before, the adsorption entropy ΔS^0 is far less explored and reported in literature and represents the biggest uncertainty. Our fitting to both models suggests that $\Delta S^0_{a_{cm}}$ and $\Delta S^0_{a_{cds}}$ are less exothermic than what we assumed and used (-109 J/molK). This will influence the calculated preexponentials of surface protonic conductance for ZrO_2 and CeO_2, but still allow differentiation between the conduction models.

Table 12 Standard entropies and enthalpies of water adsorption on ZrO_2, TiO_2 and CeO_2 extracted from TG and modelled with the Langmuir expressions for molecular chemisorption (*cm* model) and dissociative chemisorption (*cds* model).

Samples	*cm* model		*cds* model	
	$\Delta S^0_{a_{cm}}$ [J/molK]	$\Delta H^0_{a_{cm}}$ [kJ/mol]	$\Delta S^0_{a_{cds}}$ [J/molK]	$\Delta H^0_{a_{cds}}$ [kJ/mol]
pristine ZrO_2	-32	-47	-72	-70
ZrO_2-ST700	-33	-50	-79	-77
ZrO_2-ST1000	-35	-55	-88	-90
pristine TiO_2 anatase	-36	-39	-100	-70
pristine TiO_2 P25	-67	-53	-155	-93
Pristine CeO_2	-88	-44	-218	-90
CeO_2-550	-86	-44	-215	-91
CeO_2-750	-80	-43	-185	-80

6.3.2 Evaluating ΔH^0 and ΔS^0 of physisorption by TG

To estimate the thermodynamic parameters of physisorbed water in a similar way as we did for the chemisorbed water alone, we further added the concentration of physisorbed water given by the BET expression (Eq. 75) to the concentration modelled for the chemisorbed layer. As discussed in **Section 2.7.1**, the BET equation holds for the first ice-like physisorbed layer and subsequent liquid-like physisorbed layers. For the fitting of the experimental data in Figure 42, the concentration of a monolayer, $\gamma_{H_2O_{ph1}}$, is assumed the same as for chemisorption, namely, $\gamma_{H_2O_{ph1}} = \gamma_{M_s}$. The condensation equilibrium water partial pressure, p_{ce}, is expressed by the thermodynamics of condensation given in Eq. 77, with $\Delta S^0_{ce,298.15}$ ≈ -118 J/molK, and $\Delta H^0_{ce,298.15}$ ≈ -44 kJ/mol. The estimation is done by adjusting the difference in binding energy, E_1 - E_L, for the three oxides. The solid lines in Figure 45 (a-c) displays the results modelled as the sum of $\gamma_{M_{M_s}OH_2^x}$ (molecular chemisorption, *cm* model, Eq. 13) and $\gamma_{H_2O_{H_2O_{ph1}}}$ (BET, Eq. 75), considering $|E_1|$ - $|E_L|$ = 5, 6 and 4 kJ/mol for ZrO_2, TiO_2 and CeO_2, respectively. The fitting is done similarly with $\gamma_{M_{M_s}OH'}$ (dissociative chemisorption, *cds* model, Eq. 22) and $\gamma_{H_2O_{H_2O_{ph1}}}$ (BET, Eq. 75), and the results are shown accordingly in Figure 45 (d-f). With the relatively small E_1 - E_L, the fitting to the experimental values is considered satisfactory.

For comparison purpose, the alternative BET equation in the Langmuir form (ph1 equation) given in Eq. 78 with K_{ph1} defined by Eq. 74 was applied to model the concentration of water up to the first ice-like physisorbed monolayer. We consider here that the standard entropy for

physisorption for the first layer, ΔS^0_{ph1}, is roughly that for condensation, $\Delta S^0_{ce,373.15}$, *i.e.,* -109 J/molK, and that the standard enthalpy for physisorption, ΔH^0_{ph1}, is given by $\Delta H^0_{ce,373.15}$ (-40.7 kJ/mol) plus a few kJ/mol of exothermic enthalpy because of the hydrogen-bonded water molecules attached to the chemisorbed layer underneath. This is sufficient to fit the data, as revealed by the dashed lines in Figure 45. The fitting to the ph1 equation yields ΔH^0_{ph1} = -48 kJ/mol for ZrO_2, -49 kJ/mol for TiO_2, and -46 kJ/mol for CeO_2. The fitted values are all within the expected range. It further agrees with the results demonstrated by Raz *et al.* [136] showing ΔH^0_{ph1} = -47.6 kJ/mol for YSZ at $|E_1| - |E_L| = 7 \pm 1.4$ kJ/mol.

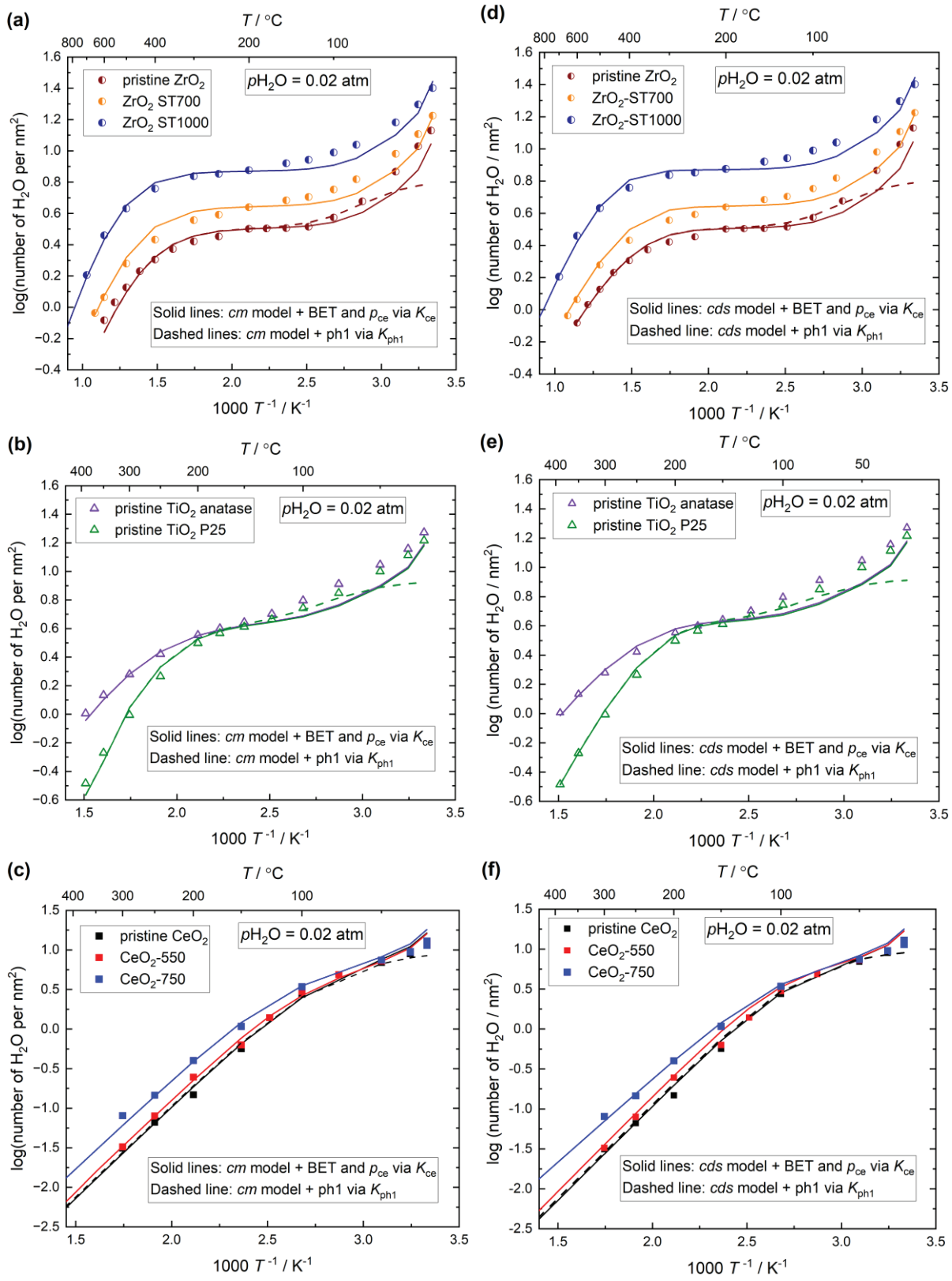

Figure 45 Concentration of adsorbed water on the surface of (a, d) ZrO_2, (b, e) TiO_2, (c, f) CeO_2 *vs* $1/T$ in wet (p_{H_2O} = 0.02 bar) N_2 atmosphere. The data were fitted as the sum of (a-c) the Langmuir isotherm for molecular chemisorption (*cm* model) and physisorption, (d-f) the Langmuir isotherm for dissociative chemisorption (*cds* model) and physisorption. The concentration of physisorbed water was modelled with the BET equation given in Eq. 75 (solid lines) and the ph1 equation given in Eq. 78 (dashed lines).

6.4 Migration and conductivity

The work for this thesis and in particular CeO_2 has encountered protons in the subsurface arising from hydrogenation of CeO_2 surfaces, and protons dissociated from and in chemisorbed and physisorbed water layers. The migration of subsurface protons has been left beyond the scope of this thesis. It has – together with the enhanced transport of electrons also presumably in the subsurface – been subject of several papers in the literature.[91-93, 218] However, in light of the novel approaches in this thesis, mixed proton-electron conduction in the subsurface of CeO_2 and many other oxides deserves renewed dedicated interest, as they are the consequences for details of the models presented in the thesis for transport in the adsorbed water layers.

In this part, I will briefly recapitulate, compare, and discuss proton migration in the chemisorbed and physisorbed water layers based on the results achieved so far.

As introduced in **Section 2.5** (and **Appendix I** – list of symbols and abbreviations), the transport mechanisms for protons (denoted by an abbreviation following a dash) have been classified into jumps between oxide ions on the surface (denoted the -s mechanism), between the surface and adsorbed (chemisorbed) oxide ions (-sa), between adsorbed oxide species (-a), between water molecules in the first physisorbed layer (-ph1), and in the liquid-like physisorbed layer (-ph2). As shown by isotope effect studies,[81, 118] the latter (-ph2) occurs to a large extent by vehicular transport and is not quantified, while all the formers are free proton jump (Grotthuss) mechanisms.

For the different proton jump mechanisms, it was assumed that all jumps take place essentially between two neighbouring oxide ions, so that parameters are of the same magnitude, and that the preexponentials of the diffusivity (D_{H^+0}) and hence charge mobility (u_{H^+0}) are the same for all mechanisms, namely $1 \cdot 10^{-3}$ cm^2/s and 10 cm^2K/Vs, respectively (see **Section 2.4.2** for details). The nomenclature for defect surface species allows us to operate with standard states, statistical thermodynamics, and configurational entropies through equilibrium coefficients, and by next applying qualified estimates of vibrational entropy changes, we have arrived at preexponentials for the protonic surface conductance in the adsorbed water layers, G_{s,H^+0}. See for instance Table 9 for a summary of G_{s,H^+0} for CeO_2 predicted from the different conduction models within the chemisorbed water layer.

The brick layer model (e.g. Eq. 117) further allows us to link these preexponentials to those of the measured conductivities of the porous ceramic samples. As discussed in **Chapter 4** (ZrO_2) and **5** (CeO_2), within order of magnitude, the match and predictive power are in our opinion satisfactory. Kang *et al.* [118] in the preceding work on porous TiO_2 obtained σ_{M,s,H^+0} of 10^{-2}–10^{0} SK/cm for conduction in chemisorbed water at relatively high temperatures from samples with different predominant crystal facets. Using the provided microstructure data, we obtain G_{M,s,H^+0} of 10^{-7}–10^{-5} SK via the BLM, which fits with the model for surface conductance by protons from chemisorbed water transported in the surface oxide layer (*cds-s*). The (101)-dominated

TiO_2 showed considerable conductivity at intermediate temperatures, which can now plausibly be interpreted in terms of proton transport between surface and adsorbed oxide ions (*cds-sa*) based on the predicted G_{M,s,H^+0} of $1 \cdot 10^{-11}$ SK. In physisorbed water, all samples show estimated G_{s,H^+0} of the order of 10^{-20} SK, in agreement with the *ph*1 model reflecting dissociation in the physisorbed layer. For the first time, the widely differing behaviours of surface protonic conductivity from chemisorbed and physisorbed water layers on porous oxides of different microstructures have been fully mapped over large ranges of temperature, p_{H_2O}, and *RH*.

However, one empirical parameter remains; the enthalpy. I have above discussed the standard enthalpies of molecular chemi- and physisorption ($\Delta H^0_{a_{cm}}$, ΔH^0_{ph1}) and dissociative chemisorption ($\Delta H^0_{a_{cds}}$) in view of the TG results, now I will turn attention to the enthalpies of the proton jumps in the different mechanisms proposed in this thesis.

Some of the mechanisms require input of the enthalpies of adsorption and dissociation separately. As said, TG cannot be used to model the degree of dissociation, but since the reaction for dissociative chemisorption (*cds* model, Eq. 18) is the sum of the reaction for molecular chemisorption (*cm* model, Eq. 11) and that of opthe reaction for dissociation of a proton to a surface oxide ion (Eq. 16), the standard enthalpy change for the latter is predictable through $\Delta H^0_{a_{cds}} = \Delta H^0_{a_{cm}} + \Delta H^0_{d_{cs}}$ if one of the values is known independently, e.g. from calorimetry or DFT calculations.

In the case of CeO_2, assuming -44 kJ/mol from fitting the TG curve represents the standard enthalpy for dissociative chemisorption, $\Delta H^0_{a_{cds}}$ (supported by the observed $p^{1/2}_{H_2O}$ dependence of chemisorption), taking $\Delta H^0_{a_{cm}}$ = -60 kJ/mol from literature,[96] $\Delta H^0_{d_{cs}}$ is predicted as 16 kJ/mol, which is close to the value of 22 kJ/mol reported for YSZ.[169] With the apparent activation enthalpies of conductance ΔH_c extracted from fitting the surface protonic conductance plot in Figure 38, it is possible to predict the enthalpies of proton mobility within the chemisorbed water by assigning appropriate equations for the enthalpy for each conduction mechanism. The surface protonic conductance of CeO_2 from high to low temperatures have been rationalized with *cds-s*, *cds-sa*, *cms-a* (low coverage) and *cms-a* (full coverage) models, respectively, with corresponding enthalpy of proton mobility estimated as $\Delta H_{m,H^+_s}$ = 51 kJ/mol for surface migration (Eq. 37), $\Delta H_{m,H^+_{sa}}$ = 34 kJ/mol for migration between surface and adsorbed species (Eq. 47), and $\Delta H_{m,H^+_a}$ = 37 kJ/mol for migration in the adsorbed layer (Eq. 57), while $\Delta H_{m,H^+_a}$ = 17 kJ/mol for the adsorbed layer in the case of full coverage (Eq. 60). For CeO_2 in particular, physisorbed water appeared only close to room temperature due to its hydrophobic nature, therefore we do not attempt to estimate the enthalpy of proton mobility in the physisorbed water layers.

The surface protonic conductivity of the monoclinic ZrO_2 samples sintered at the lowest temperatures is expected to have proton migration between surface oxide ions (*cds-s*) at high temperatures (supported by the observed $p_{H_2O}^{1/2}$ dependence of conductivity), and migration within physisorbed water with protons arising from a weak chemisorbed water layer underneath (*chm-ph1*) at low temperatures (supported by the $p_{H_2O}^{3/2}$ dependence of conductivity). Using experimental activation enthalpies of $\Delta H_{c_{cds\text{-}s}}$ = +27 kJ/mol and $\Delta H_{c_{chm\text{-}ph1}}$ = -30 kJ/mol for conductivity (from Table 4) and literature values for thermodynamics as discussed before, we get $\Delta H_{m,H^+_s}$ = 54 kJ/mol (according to Eq. 37), and $\Delta H_{m,H^+_{chm\text{-}ph1}}$ = 17 kJ/mol (according to Eq. 86) as a first estimate. Likewise, the more faceted ZrO_2 samples show apparent activation enthalpy of $\Delta H_{c_{cds\text{-}s}}$ of +57 kJ/mol at high temperatures, which is also attributed to the *cds-s* model. At low temperatures, the preexponentials show good fit with the model for dissociation from the physisorbed water (*ph1*), with $\Delta H_{c_{ph1}}$ of -50 kJ/mol and hence a predicted $\Delta H_{m,H^+_{ph1}}$ of +19 kJ/mol (Eq. 93). The enthalpies of proton jumps extracted from this study are summarized in Table 13.

The extended and more mature models of proton transport mechanisms – especially for the chemisorbed layer – were developed for the CeO_2 results, after the time of publication of the ZrO_2 paper. It is hence interesting at this stage to attempt a new look at the ZrO_2 data. Figure 46 shows the geometry-corrected surface protonic conductance of ZrO_2 converted from its conductivity via the BLM. The lines and empirical enthalpies ΔH_c indicated in the figure are chosen to fit the experimental data in different regions based on the predicted preexponentials G_{s,H^+0}. This includes the possibility of an additional process at intermediate temperatures.

The less-faceted ZrO_2 samples yield empirical enthalpies of $\Delta H_{c_{cds\text{-}s}}$ = +36 kJ/mol, $\Delta H_{c_{cds\text{-}sa}}$ = +5 kJ/mol, and $\Delta H_{c_{chm\text{-}ph1}}$ = -30 kJ/mol at high, intermediate and low temperatures, respectively. Inserting into equations for enthalpy of conductance of the appropriate processes reveals $\Delta H_{m,H^+_s}$ = 63 kJ/mol, $\Delta H_{m,H^+_{sa}}$ = 59 kJ/mol, and $\Delta H_{m,H^+_{chm\text{-}ph1}}$ = 21 kJ/mol as a first estimate. These numbers are further included in Table 13 (in parenthesis) for comparison purpose. The fitting of conductances for the well-sintered samples yield $\Delta H_{c_{cds\text{-}s}}$ = +43 kJ/mol, $\Delta H_{c_{cds\text{-}sa}}$ = +13 kJ/mol, and $\Delta H_{c_{ph1}}$ = -50 kJ/mol from high to low temperatures, with corresponding enthalpies of $\Delta H_{m,H^+_s}$ = 70 kJ/mol, $\Delta H_{m,H^+_{sa}}$ = 67 kJ/mol, and $\Delta H_{m,H^+_{ph1}}$ = 25 kJ/mol, based on own measurements of ΔH^0_{ph1} = -48 kJ/mol from TG for ZrO_2 and literature values.

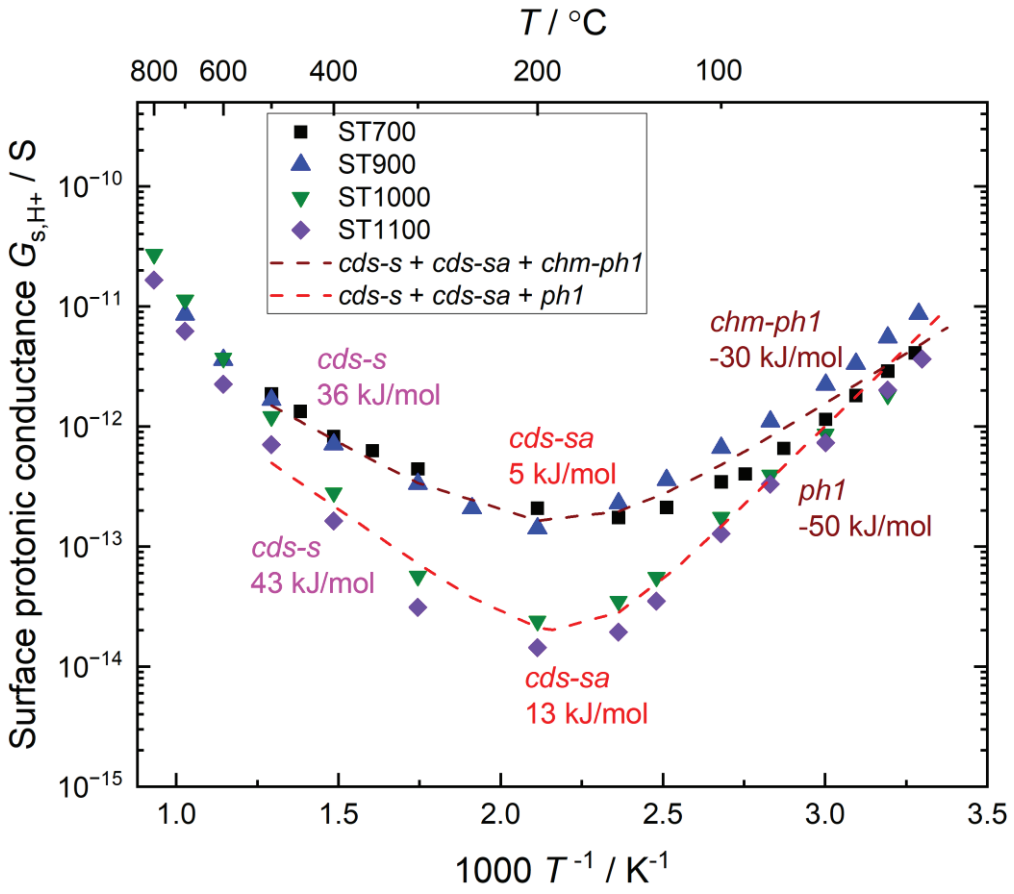

Figure 46 Surface protonic conductance of ZrO_2 at p_{H_2O} = 0.03 bar *vs* 1/*T*. The enthalpies indicated in the plot are chosen to fit the experimental data given the predicted preexponentials for the various models in the different temperature regions.

From Table 13 below, we see that the enthalpies of proton mobility for both ZrO_2 and CeO_2 decrease systematically as we move from jumps between the rigidly bonded surface oxide ions (-s) with values around 50 kJ/mol for CeO_2 and considerably larger for ZrO_2, via those involving more loosely bonded adsorbed species (-sa) where the enthalpies group around 35 kJ/mol for CeO_2, to those jumping only between the loosely bonded adsorbed water molecules (-a) within chemisorbed layer, at 17 kJ/mol for CeO_2. The enthalpies attributed to migration in physisorbed water for ZrO_2 also end up at similar values (17-25 kJ/mol, reasonably just a bit larger than that of bulk liquid water (12 kJ/mol).

All in all, we may – based on the values in Table 13 – conclude that enthalpies for protonic surface mobility for ZrO_2 are higher than for CeO_2 within each of the mechanisms. This may be due to the enhanced lattice dynamics by the higher mass and interatomic distances as well as a more symmetric structure of CeO_2 *vs* ZrO_2.

Table 13 Estimated enthalpies of proton mobility $\Delta H_{m,H^+}$ within the chemisorbed and first physisorbed water layers based on the proposed proton transport mechanisms, with derived p_{H_2O} dependence of surface protonic conductance at low coverage or full coverage (no p_{H_2O} dependence). Enthalpies in parenthesis are calculated from the new extractions of enthalpies for conductance for ZrO_2 samples shown in Figure 46 and the extended set of appropriate equations for the enthalpy of surface protonic protonic conductance.

	High *T*	**Intermediate *T***	**Low *T* (below 200°C)**			
Model Parameter	cms-s cds-s	cms-sa cds-sa	cms-a cds-a	cms-a full coverage	chm-ph1	ph1
n in $G_{s,H^+0} \propto p_{H_2O}^n$	1/2	1	3/2	0	3/2	2
CeO_2 $\Delta H_{m,H^+}$ (kJ/mol)	51	34	37	17	-	-
ZrO_2 (ST700) $\Delta H_{m,H^+}$ (kJ/mol)	54 (63)	(59)	-	-	17 (21)	-
ZrO_2 (ST1100) $\Delta H_{m,H^+}$ (kJ/mol)	84 (70)	(67)	-	-	-	19 (25)

6.5 Implications for applications and future research

Surface protonics plays a central role in a range of applications, where some of them have already been mentioned in **Section 1.4**. With the understanding achieved at this stage, I will now revisit some of their applications, seeing from a new perspective with the models developed through this thesis that allow parameterization and prediction of surface protonic conductivities in porous oxide ceramics.

Electrolyte in electrochemical devices: As a potential electrolyte material, porous oxide ceramics are cheap and robust and permit a wider range of operating temperatures as compared to polymer materials. An ideal nanoporous oxide should display high mechanical, thermal and checmical stability, fulfil the requirement of being highly hydrophilic, having a high surface area and fraction of crystalline material for water adsorption, and suitable pore size in the nanometer regime to optimize the effect of capillary condensation (to retain water) under high *RH*, and thereby possibly close a porous membrane gas tight by liquid water (impermeable to H_2 and O_2) during operation. The percolation path formed by the physisorbed water inside the pore network allows transport of proton with relatively high mobility, which enhances the overall proton conductivity.

Let us calculate a couple of examples, assuming a film of 10 μm thickness of a nanoporous ceramic with grain size of 100 nm and relative density of 50%: With data for the well-sintered

ZrO_2, the surface protonic conductivity in chemisorbed water at 400°C and p_{H_2O} = 0.03 bar is predicted as $2 \cdot 10^{-7}$ S/cm in case of low water coverage (*cds-s*), yielding a corresponding area-specific resistance (ASR) of $5 \cdot 10^3$ Ωcm^2 for the thin membrane, or $9 \cdot 10^2$ Ωcm^2 at 1 bar steam. Alternatively, if strong dissociative chemisorption prevails, we get $\sigma \approx 3 \cdot 10^{-4}$ S/cm and ASR ≈ 4 Ωcm^2 under the same conditions. In physisorbed water at 100°C (*RH* ≈ 3%), the predicted conductivity and ASR according to the *ph*1 model would be $\sigma \approx 4 \cdot 10^{-7}$ S/cm and ASR ≈ $3 \cdot 10^3$ Ωcm^2, respectively. At 1 bar steam, the conductivity and ASR will be significantly higher, with expected values of $4 \cdot 10^{-4}$ S/cm and 2 Ωcm^2, respectively.

We conducted similar calculations for TiO_2 for comparison. TiO_2 with 50% porosity and grain size of around 50 nm displays surface protonic conductivities of around $5 \cdot 10^{-7}$ S/cm, $2 \cdot 10^{-7}$ S/cm and $2 \cdot 10^{-6}$ S/cm for samples with a predominance of the (001), (100) and (101) facet, respectively, at 400°C and p_{H_2O} = 0.026 bar.[118] Taking these values, and assuming the thin membrane with thickness of 10 μm and area of 1 cm^2, the ASR would be $2 \cdot 10^3$ Ωcm^2 for TiO_2(001), $5 \cdot 10^3$ Ωcm^2 for TiO_2(100), and $6 \cdot 10^2$ Ωcm^2 for TiO_2(101). At 100°C, TiO_2(001), (100) and (101) samples yield measured surface protonic conducitivties of $3 \cdot 10^{-7}$ S/cm, $5 \cdot 10^{-7}$ S/cm and $9 \cdot 10^{-8}$ S/cm, respectively, with predicted ASRs of $3 \cdot 10^3$ Ωcm^2, $2 \cdot 10^3$ Ωcm^2, and $1 \cdot 10^4$ Ωcm^2 for a thin film of 10 μm thickness. At 25°C with *RH* of around 80%, the values are much higher for TiO_2 due to the presence of liquid-like physisorbed water, reaching conductivities in the range 10^{-5} – 10^{-3} S/cm and ASRs of 10^1 – 10^{-1} Ωcm^2, respectively. Protonic conductivity showed a strong dependence on *RH* and would hence be even higher at 100% *RH*.

The surface protonic conductivity is considerably lower for CeO_2 than for TiO_2 and ZrO_2 owing to its hydrophobic nature.

The promising protonic conductivity of nanoscopic oxides may find usage in new types of low-temperature energy-harvesting devices such as fuel cells (e.g. single chamber fuel cells using a porous electrolyte and selectively catalytic electrodes for biogas-air mixtures) and photoelectrochemical cells (for hydrogen production) as well as electrochemical pumps and potentiometric sensors.

The predicted conductivity of nanoporous TiO_2 membranes at RT - especially for the sample grown with predominantly (100) facet – is not much lower than that of the traditional PEMs, which has also been demonstrated by others.[100, 101, 219] A protonic conductivity of $3.8 \cdot 10^{-2}$ S/cm at 80°C and 81% *RH* has been reported for anatase TiO_2. Other thicknesses and grain sizes can be accounted for by simple proportionalities. Specifically, the conductivity can be improved further by reducing the thickness of the membranes,[105] or by decreasing the grain size of the samples [78] following the BLM. The functioning of such nanoporous thin films as electrolyte would require a separation layer with nanopores that are filled with water to keep H_2 and O_2 from mixing. As mentioned in **Section 1.4**, CeO_2 films of less than 400 nm in both dense and "rough" form can be used as the electrolyte, which is appealing for miniaturuzed implantable microdevices.[105] A recently demonstrated CeO_2-based glucose fuel cell device revealed a total through-plane protonic conductivity of $5.4 \cdot 10^{-10}$ S/cm at 23.5°C. Furthermore, the fuel cell with

"rough" electroyte microstructure exhibited an average open circuit voltage (OCV) of 44.7 mV, and peak power density of 11.4 $\mu W/cm^2$.

The functioning of a full assembly of an all-porous electrochemical cell based on surface protonic conduction in adsorbed water layers with nanoporous ceramic electroyte also relies on the development of compatible catalytically active and selective electrode materials. This may enable a low-cost single chamber fuel cell for dilute fuel-oxidant mixtures (e.g. biogas and air).

Humidity sensors: Relative humidity sensors based on protonic ceramic materials are widely used in industry and research laboratories. The new models allow better prediction of the use of the p_{H_2O} dependent surface protonic conductivities in humidity sensors for a range of temperatures. The applicability to a variety of oxides should enable us to find suitable ones for harsh chemical and physical environments (corrosive, radioactive, etc.).

Electrodes: Surface protonic diffusion is believed to play a decisive role for electrodes on proton ceramic electrochemical cells, as one of the means to transport protons between the electrolyte and the active surface catalytic site, notably for oxygen redox reactions. Since electrode materials are electronic conductors, it is notoriously difficult to assess their minority protonic conductivity, and our models may help to predict the order of magnitude involved. Attempts to measure surface protonic transport on electronically conducting oxides is underway and will be required to very our models for this class of oxides.

Heterogeneous catalysis: As said, surface protonic conduction is already well documented to play a role in the activity of certain systems of catalysts on oxide carriers when enhanced by electrical field and/or current.[91, 92, 95, 220, 221] Our models will allow more quantitative interpretations of these effects. The hydrogenation of the CeO_2 surface provides rationalization of its hydrophobic character: the surface is reduced, hence less acidic. It is protonated, therefore less hydrophilic. We have furthermore suggested how its hydrogenated surface weakens its chemi- and physisorption, and, in turn, enhances its catalytic activity by more availability of surface sites and presence of mixed valence of Ce, which is of great benefit for the design of catalysts. All in all, we believe that a more integrated understanding of adsorption of both hydrogen and water and resulting protonic and electronic conduction on oxide surfaces will be major focus of future research in heterogeneous catalysis.

Photocatalysis: The invention of using adsorbed water not only as a proton transport pathway, but also as the very source of the water to split in hydrogen production and other artificial photosynthesis is now adding interest to surface protonics. New energy generation and conversion devices such as the solid-state photoelectrochemical (SSPEC) cells have been demonstrated, where TiO_2 played a dual functionality, acting both as a photocatalyst and as a surface protonic conductor.[109] Moreover, the long-term operation of the device rely on the presence of physisorbed water layers on the oxide surface, which can be retained by intermittent illumination.[108]

Role as filler in proton exchange membrane (PEM) electrolytes: To close the circle, we end with a brief look at what role surface protonics of oxides can have when they are dispersed as nanoscopic fillers in various types of PEM electrolytes. For low-temperature composite PEMs based on Nafion® and Aquivion® relying on swelling of self-organised proton conducting water channels between sulfonated polymer strands, it is natural to relate the role of oxide nanoparticles to their hydrophilicity (e.g. for ZrO_2) versus hydrophobicity (e.g. for CeO_2). Such PEMs typically operate at around 40% *RH*, and under such conditions we have seen that ZrO_2 may hold on to physisorbed water better than CeO_2. Based on the high conductivity of TiO_2 at high *RH*s,[118] we expect that also TiO_2 holds on to physisorbed water well, although our brief TG study above suggested that pristine anatase TiO_2 nanoparticles has limited adsorptivity. The latter point brings us to another important lesson from the present work: Contrary to what one might expect, water appears to adsorb better on the more faceted surfaces of well-annealed powders than on pristine and probably more defective or amorphous ones. Indeed, Simons *et al.* [99] showed higher proton conductivity from a post-annealed CeO_2 film as compared to an as-deposited film, which can be explained by a higher degree of crystallinity of the proton conducting surfaces. So, all in all, if water retaining capacity is the prime function of the filler, we would predict that nanoscopic but still annealed TiO_2 is best, followed by ZrO_2, better than CeO_2. Moreover, hydrophilic SiO_2 and TiO_2 nanofillers in Nafion have been shown to form additional ionic water phase clusters around the particls in the composite membranes, which in turn reduces the tortuosity of the overall proton transport pathways.[222]

The hydrophobicity and mixed Ce^{3+}/Ce^{4+} valence character of hydrogenated CeO_2 surfaces may on the other hand have advantages for the electrode structures of PEM cell. The hydrophobicity may help keep the microstructure partly open for gas and hence be helpful both in the gas diffusion and electrocatalytic layers. The redox activity may make CeO_2 assist the carbon backbone also as a catalyst, catalyst support, and conveyor of protons and electrons. It may – as already suggested by others – help to destroy oxidising radicals before they consume carbon backbone in oxygen-side electrodes while the cell is idle open circuit.[223-225] The protons and electrons in the hydrogenated surface may play role as sacrificial reactants here, regenerated by water.

For high-temperature PEMs, as well as for normal PEMs attempted operated above 100°C – the role as filler can be to retain a water and/or acid content as well as structural integrity, but also to contribute proton conductivity. Interestingly, fast surface proton conduction has been reported from phytic acid doped PBI nanofibers (Phy-PBINfs) embedded in Nafion, and later in sulfonated polyimide (SPI).[226, 227] It was found that phytic acid mainly locates near the surface of PBI nanofibers, forming an acid-condensed region at the interface between Phy-PBINfs and the polymer matrix. Furthermore, the difference in proton conductivity measured in parallel and perpendicular directions to the aligned PBI nanofiber axis, especially at low *RH* suggests that effective proton conductive pathways were constructed due to the acid aggregation at the nanofiber/polymer matrix interface, which are faster than the conventional pathways in the polymer matrix.

Unfortunately, surface protonic conduction in porous oxides swindles as fast as it does in the acid-doped polymers when we surpass 100°C and physisorbed water disappears, leaving conduction to the more tightly bonded protons in the chemisorbed layer. We have however seen that the surface protonic conduction in the temperature region 100–200°C varies by orders of magnitude between oxides and by different microstructures and thermal histories. This thesis project has not investigated effects of doping of the oxides and/or their surfaces, but the work of Stub *et al.* [144] on doped TiO_2 materials suggests that large effects are attainable from aliovalent dopants (ranging from conductivity-killing Fe to conductivity-boosting Cr in that particular case). The main impact of the present work is to provide a fundamental as well as methodological framework for parameterisation of the thermodynamics and kinetics involved in surface protonic conduction. This will make future studies over a larger span of materials and conditions – and with a wider range of methods – more systematic, efficient, and targeted.

Research focus and methodology: As shown above, surface protonics finds applications in a variety of technologies where surface chemistry is critical to success. Surface science is invaluable for understanding the interaction of water with oxide surfaces, including the adsorbed species and possible conduction pathways and mechanisms, and has been subject of intense investigation. As demonstrated in **Section 2.3.2**, *in situ* FT-IR can precisely evaluate the strength of the hydroxyl groups that are responsible for Brønsted acidity under controlled temperature and atmosphere. X-ray photoelectron spectroscopy (XPS) would help to distinguish the metal-oxygen bond from hydroxyl bonding. Solid-state NMR spectroscopy allows one to study the nature (Brønsted or Lewis), type, and location of acid sites. By adsorbing probe molecules (e.g. water), it is possible to determine the type of interactions between the probe molecules and the active sites on the surface. Calorimetric techniques enable precision gas dosing, volumetric detection of amount of adsorbed gas, and simultaneous measurement of adsorption enthalpy. As suggested, TG-DSC is an ideal technique for direct measurement of the standard adsorption enthalpy. Theoretical and modelling approaches are useful for predicting the structure and properties of a surface, the stability, the adsorption sites of the adsorbates on the surfaces at different coverage, but it depends on the model for the reaction and calculation method. Each of these above-mentioned techniques have its advantage, but also present drawbacks, therefore the use of combined techniques appears most suitable.

7 Conclusions

This thesis reports a study of water adsorption and surface protonic conduction on porous undoped oxide ceramics with well-defined, reproducible microstructure.

For the first time, the surface protonic conductivity of porous ceramic samples has been quantitatively estimated by credible models derived on the basis of thermodynamics of water adsorption and dissociation, and various proton transport mechanisms.

Molecular chemisorption can be discriminated against the dissociative case from measurements of p_{H_2O} dependence of water adsorption, with predicted $p_{H_2O}^{1/2}$ and $p_{H_2O}^{1}$ dependences in the case of dissociative and molecular adsorption at low coverage, respectively, and independent of p_{H_2O} at full coverage. The thermodynamic parameters derived from the Langmuir isotherms in the case of molecular and dissociative chemisorption, and BET isotherms for physisorption differ considerably between ZrO_2, TiO_2, and CeO_2, and also depend on coverage, while the properties of the physisorbed layers are more similar for the different oxides. The proton migration mechanisms in the chemisorbed water represent Grotthuss hopping, and have in this thesis been expanded to comprise jumps between the surface oxide ions (-*s*), between the surface and adsorbed species (-*sa*), and between the adsorbed species (-*a*). Migration of protons in the first physisorbed layer takes place by hopping between water molecules with dissociated protons either originated from the molecular chemisorbed layer underneath, or from the physisorbed layer itself.

A brick layer model (BLM) is developed, which can be used as an order-of-magnitude estimate of the specific surface area of porous oxides, on top of that, it allows conversion between measured preexponentials of macroscopic surface protonic conductivity and the predicted values from conduction models of surface protonic conductance. It is further discussed in the context of the available experimental results of nanoscopic porous ZrO_2 and CeO_2. The BLM enables order-of-magnitude discrimination between distinct types of adsorption and surface transport in the different water layers, supported by p_{H_2O} dependencies of adsorption and conductivity and enthalpies.

The two opposite temperature dependences of surface protonic conductivity of ZrO_2 have been interpreted in terms of proton migration in the chemisorbed layer and the ice-like physisorbed layer. At 200°C and above, the measured preexponentials of surface protonic conductivities increase with increasing sintering temperature, reflecting a transition from low coverage of chemisorbed water with weak dissociation and migration between surface oxide ions towards a more dissociated chemisorbed water. Below 200°C, samples sintered at low temperatures have dissociated protons stem from the weak chemisorbed layer underneath. The preexponentials

decrease with increasing sintering temperature, suggesting that the conduction can only arise from dissociation within the physisorbed layer itself as the chemisorbed layer underneath is fully dissociated.

For CeO_2, the isothermal TG results led to the suggestion of surface hydrogenation into proton and electron defects in the surface, and formation of oxyhydroxide layer like CeOOH, in common with other rare-earth oxides. From the weight increase, the hydrogenation goes several layers deep, in agreement with TEM observations. Accordingly, the conduction in wet atmospheres at the highest temperatures (>500°C) can presumably be attributed mostly to electrons in this hydrogenated layer. The surface protonic conductivity from 500°C down to room temperature is rationalized for the first time in terms of the extended models of proton transport mechanisms within the chemisorbed layer alone, which fit well with the observed positive, near zero and negative enthalpies of conduction. For hydrophobic CeO_2, the low-temperature mechanism of proton transport between adsorbed species behaves similarly as what is traditionally assigned to transport in the ice-like physisorbed layer in other more hydrophilic oxides such as TiO_2 and ZrO_2, where probably the two contribute together. The levelling off in conductivity at the highest *RH* near RT was ascribed to saturation to full coverage of the chemisorbed layer.

The enthalpies of surface proton mobility in the different proton transport mechanisms were discussed in light of the experimental results for ZrO_2 and CeO_2 and the thermodynamic parameters reported earlier. Despite the variation in enthalpies within chemisorbed water between oxides, a general trend is realized: the enthalpies decrease systematically from jumping between the rigidly bonded surface oxide ions, via those involving more loosely bonded chemisorbed species, to jump between loosely bonded adsorbed water molecules within the chemsisorbed layer, ending up at values comparable to that of proton migration in the ice-like physisorbed water layer, reasonably slightly larger than that of bulk liquid water.

More dedicated p_{H_2O} dependencies of water adsorption, preexponentials and isothermal p_{H_2O} dependencies of conductivity for other porous oxide ceramics, and the effects of doping of the oxides we have explored here will help discriminate mechanisms and allow more reliable comparative parameterisation.

References

1. Energy Transitions Commission: Making the Hydrogen Economy Possible: Accelerating clean hydrogen in an electrified economy. **April 2021**.
2. Bockris, J. O. M., The origin of ideas on a Hydrogen Economy and its solution to the decay of the environment. *Int J Hydrogen Energ* **2002,** *27* (7-8), 731-740.
3. Norby, T.; Jensen, E. H.; Sartori, S., Deep decarbonization efforts in Norway for energy sustainability. *MRS Energy & Sustainability* **2019,** *6*, 1-7.
4. Wang, F.; Harindintwali, J. D.; Yuan, Z.; Wang, M.; Wang, F.; Li, S.; Yin, Z.; Huang, L.; Fu, Y.; Li, L., Technologies and perspectives for achieving carbon neutrality. *The Innovation* **2021,** *2* (4), 100180.
5. Zhang, H.; Maijenburg, A. W.; Li, X.; Schweizer, S. L.; Wehrspohn, R. B., Bifunctional heterostructured transition metal phosphides for efficient electrochemical water splitting. *Adv Funct Mater* **2020,** *30* (34), 2003261.
6. Cipriani, G.; Di Dio, V.; Genduso, F.; La Cascia, D.; Liga, R.; Miceli, R.; Galluzzo, G. R., Perspective on hydrogen energy carrier and its automotive applications. *Int J Hydrogen Energ* **2014,** *39* (16), 8482-8494.
7. Nikolaidis, P.; Poullikkas, A., A comparative overview of hydrogen production processes. *Renew Sust Energ Rev* **2017,** *67*, 597-611.
8. Acar, C.; Dincer, I., Comparative assessment of hydrogen production methods from renewable and non-renewable sources. *Int J Hydrogen Energ* **2014,** *39* (1), 1-12.
9. IEA (2022), Hydrogen Supply, IEA, Paris https://www.iea.org/reports/hydrogen-supply. **Accessed on 02. Dec 2022**.
10. Schmidt, O.; Gambhir, A.; Staffell, I.; Hawkes, A.; Nelson, J.; Few, S., Future cost and performance of water electrolysis: An expert elicitation study. *Int J Hydrogen Energ* **2017,** *42* (52), 30470-30492.
11. Zeng, K.; Zhang, D. K., Recent progress in alkaline water electrolysis for hydrogen production and applications. *Prog Energ Combust* **2010,** *36* (3), 307-326.
12. Kuckshinrichs, W.; Ketelaer, T.; Koj, J. C., Economic analysis of improved alkaline water electrolysis. *Front Energy Res* **2017,** *5*, 1.
13. IEA (2022), Electrolysers, IEA, Paris https://www.iea.org/reports/electrolysers, License: CC BY 4.0.
14. Barbir, F., PEM electrolysis for production of hydrogen from renewable energy sources. *Sol Energy* **2005,** *78* (5), 661-669.
15. Carmo, M.; Fritz, D. L.; Merge, J.; Stolten, D., A comprehensive review on PEM water electrolysis. *Int J Hydrogen Energ* **2013,** *38* (12), 4901-4934.
16. Arico, A. S.; Siracusano, S.; Briguglio, N.; Baglio, V.; Di Blasi, A.; Antonucci, V., Polymer electrolyte membrane water electrolysis: status of technologies and potential applications in combination with renewable power sources. *J Appl Electrochem* **2013,** *43* (2), 107-118.
17. Sapountzi, F. M.; Gracia, J. M.; Weststrate, C. J.; Fredriksson, H. O. A.; Niemantsverdriet, J. W., Electrocatalysts for the generation of hydrogen, oxygen and synthesis gas. *Prog Energ Combust* **2017,** *58*, 1-35.

18. Staffell, I.; Scamman, D.; Abad, A. V.; Balcombe, P.; Dodds, P. E.; Ekins, P.; Shah, N.; Ward, K. R., The role of hydrogen and fuel cells in the global energy system. *Energ Environ Sci* **2019,** *12* (2), 463-491.
19. Sharaf, O. Z.; Orhan, M. F., An overview of fuel cell technology: Fundamentals and applications. *Renew Sust Energ Rev* **2014,** *32*, 810-853.
20. Alaswad, A.; Baroutaji, A.; Achour, H.; Carton, J.; Al Makky, A.; Olabi, A. G., Developments in fuel cell technologies in the transport sector. *Int J Hydrogen Energ* **2016,** *41* (37), 16499-16508.
21. Wang, S. Y.; Jiang, S. P., Prospects of fuel cell technologies. *Natl Sci Rev* **2017,** *4* (2), 163-166.
22. Singla, M. K.; Nijhawan, P.; Oberoi, A. S., Hydrogen fuel and fuel cell technology for cleaner future: a review. *Environmental Science and Pollution Research* **2021,** *28* (13), 15607-15626.
23. Fan, L.; Tu, Z.; Chan, S. H., Recent development of hydrogen and fuel cell technologies: A review. *Energy Reports* **2021,** *7*, 8421-8446.
24. Marques, F. M. B.; Kharton, V. V.; Naumovich, E. N.; Shaula, A. L.; Kovalevsky, A. V.; Yaremchenko, A. A., Oxygen ion conductors for fuel cells and membranes: selected developments. *Solid State Ionics* **2006,** *177* (19-25), 1697-1703.
25. Steele, B. C. H.; Heinzel, A., Materials for fuel-cell technologies. *Nature* **2001,** *414* (6861), 345-352.
26. Butz, B.; Kruse, P.; Stormer, H.; Gerthsen, D.; Muller, A.; Weber, A.; Ivers-Tiffee, E., Correlation between microstructure and degradation in conductivity for cubic Y_2O_3-doped ZrO_2. *Solid State Ionics* **2006,** *177* (37-38), 3275-3284.
27. Ni, M.; Shao, Z. P., Fuel cells that operate at 300 degrees to 500 degrees C. *Science* **2020,** *369* (6500), 138-139.
28. Katahira, K.; Kohchi, Y.; Shimura, T.; Iwahara, H., Protonic conduction in Zr-substituted $BaCeO_3$. *Solid State Ionics* **2000,** *138* (1-2), 91-98.
29. Kreuer, K. D., Proton-conducting oxides. *Annu Rev Mater Res* **2003,** *33*, 333-359.
30. Kochetova, N.; Animitsa, I.; Medvedev, D.; Demin, A.; Tsiakaras, P., Recent activity in the development of proton-conducting oxides for high-temperature applications. *Rsc Adv* **2016,** *6* (77), 73222-73268.
31. Cao, J. F.; Ji, Y. X.; Shao, Z. P., Perovskites for protonic ceramic fuel cells: a review. *Energ Environ Sci* **2022,** *15* (6), 2200-2232.
32. Seong, A.; Kim, J.; Jeong, D.; Sengodan, S.; Liu, M.; Choi, S.; Kim, G., Electrokinetic Proton Transport in Triple ($H^+/O^{2-}/e^-$) Conducting Oxides as a Key Descriptor for Highly Efficient Protonic Ceramic Fuel Cells. *Adv Sci* **2021,** *8* (11), 2004099.
33. Fabbri, E.; Pergolesi, D.; Traversa, E., Materials challenges toward proton-conducting oxide fuel cells: a critical review. *Chem Soc Rev* **2010,** *39* (11), 4355-4369.
34. Stevenson, D. A.; Jiang, N.; Buchanan, R. M.; Henn, F. E. G., Characterization of Gd, Yb and Nd Doped Barium Cerates as Proton Conductors. *Solid State Ionics* **1993,** *62* (3-4), 279-285.
35. D'Epifanio, A.; Fabbri, E.; Di Bartolomeo, E.; Licoccia, S.; Traversa, E., Design of $BaZr_{0.8}Y_{0.2}O_{3-\delta}$ Protonic Conductor to Improve the Electrochemical Performance in Intermediate Temperature Solid Oxide Fuel Cells (IT‐SOFCs). *Fuel Cells* **2008,** *8* (1), 69-76.
36. Wachsman, E. D.; Lee, K. T., Lowering the Temperature of Solid Oxide Fuel Cells. *Science* **2011,** *334* (6058), 935-939.
37. Haile, S. M.; Boysen, D. A.; Chisholm, C. R. I.; Merle, R. B., Solid acids as fuel cell electrolytes. *Nature* **2001,** *410* (6831), 910-913.

38. Matsui, T.; Kukino, T.; Kikuchi, R.; Eguchi, K., An intermediate temperature proton-conducting electrolyte based on a CsH_2PO_4 / SiP_2O_7 composite. *Electrochemical and Solid-State Letters* **2005,** *8* (5), A256.
39. Alberti, G.; Casciola, M., Layered metal(IV) phosphonates, a large class of inorgano-organic proton conductors. *Solid State Ionics* **1997,** *97* (1-4), 177-186.
40. Alberti, G.; Casciola, M.; Cavalaglio, S.; Vivani, R., Proton conductivity of mesoporous zirconium phosphate pyrophosphate. *Solid State Ionics* **1999,** *125* (1-4), 91-97.
41. Meng, Y. Q.; Gao, J.; Zhao, Z. Y.; Amoroso, J.; Tong, J. H.; Brinkman, K. S., Review: recent progress in low-temperature proton-conducting ceramics. *J Mater Sci* **2019,** *54* (13), 9291-9312.
42. Wieser, C., Novel Polymer Electrolyte Membranes for Automotive Applications - Requirements and Benefits. *Fuel Cells* **2004,** *4* (4), 245-250.
43. DOE technical targets for polymer electrolyte membrane fuel cell components. *https://www.energy.gov/eere/fuelcells/doe-technical-targets-polymer-electrolyte-membrane-fuel-cell-components#membrane* **Accessed on 13. Nov 2022**.
44. Pollet, B. G.; Staffell, I.; Shang, J. L., Current status of hybrid, battery and fuel cell electric vehicles: From electrochemistry to market prospects. *Electrochim Acta* **2012,** *84*, 235-249.
45. Cunanan, C.; Tran, M.-K.; Lee, Y.; Kwok, S.; Leung, V.; Fowler, M., A review of heavy-duty vehicle powertrain technologies: Diesel engine vehicles, battery electric vehicles, and hydrogen fuel cell electric vehicles. *Clean Technologies* **2021,** *3* (2), 474-489.
46. Sun, X.; Simonsen, S. C.; Norby, T.; Chatzitakis, A., Composite membranes for high temperature PEM fuel cells and electrolysers: a critical review. *Membranes-Basel* **2019,** *9* (7), 83.
47. Zou, X. X.; Zhang, Y., Noble metal-free hydrogen evolution catalysts for water splitting. *Chem Soc Rev* **2015,** *44* (15), 5148-5180.
48. Sun, X.; Xu, K.; Fleischer, C.; Liu, X.; Grandcolas, M.; Strandbakke, R.; Bjørheim, T. S.; Norby, T.; Chatzitakis, A., Earth-abundant electrocatalysts in proton exchange membrane electrolyzers. *Catalysts* **2018,** *8* (12), 657.
49. Banerjee, S.; Curtin, D. E., Nafion perfluorinated membranes in fuel cells. *J Fluorine Chem* **2004,** *125* (8), 1211-1216.
50. Aili, D.; Henkensmeier, D.; Martin, S.; Singh, B.; Hu, Y.; Jensen, J. O.; Cleemann, L. N.; Li, Q., Polybenzimidazole-based high-temperature polymer electrolyte membrane fuel cells: new insights and recent progress. *Electrochem Energy R* **2020,** *3* (4), 793-845.
51. Escorihuela, J.; Olvera-Mancilla, J.; Alexandrova, L.; Del Castillo, L. F.; Compañ, V., Recent progress in the development of composite membranes based on polybenzimidazole for high temperature proton exchange membrane (PEM) fuel cell applications. *Polymers-Basel* **2020,** *12* (9), 1861.
52. Grigoriev, S.; Kuleshov, N.; Grigoriev, A.; Millet, P., Electrochemical Characterization of a High-Temperature Proton Exchange Membrane Fuel Cell Using Doped-Poly Benzimidazole as Solid Polymer Electrolyte. *J Fuel Cell Sci Tech* **2015,** *12* (3).
53. Gil, M.; Ji, X.; Li, X.; Na, H.; Hampsey, J. E.; Lu, Y., Direct synthesis of sulfonated aromatic poly (ether ether ketone) proton exchange membranes for fuel cell applications. *J Membrane Sci* **2004,** *234* (1-2), 75-81.
54. Wu, X.; He, G.; Li, X.; Nie, F.; Yan, X.; Yu, L.; Benziger, J., Improving proton conductivity of sulfonated poly (ether ether ketone) proton exchange membranes at low humidity by semi-interpenetrating polymer networks preparation. *J Power Sources* **2014,** *246*, 482-490.
55. https://www.advent.energy/products-high-temperature-meas/, **accessed November 10, 2022**.

56. Chuang, S.-W.; Hsu, S. L.-C.; Hsu, C.-L., Synthesis and properties of fluorine-containing polybenzimidazole/montmorillonite nanocomposite membranes for direct methanol fuel cell applications. *J Power Sources* **2007,** *168* (1), 172-177.
57. Li, X.; Ma, H.; Wang, P.; Liu, Z.; Peng, J.; Hu, W.; Jiang, Z.; Liu, B.; Guiver, M. D., Highly conductive and mechanically stable imidazole-rich cross-linked networks for high-temperature proton exchange membrane fuel cells. *Chem Mater* **2020,** *32* (3), 1182-1191.
58. Chandan, A.; Hattenberger, M.; El-Kharouf, A.; Du, S. F.; Dhir, A.; Self, V.; Pollet, B. G.; Ingram, A.; Bujalski, W., High temperature (HT) polymer electrolyte membrane fuel cells (PEMFC) - A review. *J Power Sources* **2013,** *231*, 264-278.
59. https://www.energy.gov/eere/fuelcells/doe-technical-targets-polymer-electrolyte-membrane-fuel-cell-components **Accessed February 23, 2021**.
60. Bakangura, E.; Wu, L.; Ge, L.; Yang, Z. J.; Xu, T. W., Mixed matrix proton exchange membranes for fuel cells: State of the art and perspectives. *Prog Polym Sci* **2016,** *57*, 103-152.
61. Laberty-Robert, C.; Valle, K.; Pereira, F.; Sanchez, C., Design and properties of functional hybrid organic–inorganic membranes for fuel cells. *Chem Soc Rev* **2011,** *40* (2), 961-1005.
62. Miyake, N.; Wainright, J. S.; Savinell, R. F., Evaluation of a sol-gel derived Nafion/silica hybrid membrane for polymer electrolyte membrane fuel cell applications - II. Methanol uptake and methanol permeability. *J Electrochem Soc* **2001,** *148* (8), A905-A909.
63. Rao, Z.; Tang, B. B.; Wu, P. Y., Proton Conductivity of Proton Exchange Membrane Synergistically Promoted by Different Functionalized Metal Organic Frameworks. *Acs Appl Mater Inter* **2017,** *9* (27), 22597-22603.
64. Patel, H. A.; Mansor, N.; Gadipelli, S.; Brett, D. J.; Guo, Z., Superacidity in Nafion/MOF hybrid membranes retains water at low humidity to enhance proton conduction for fuel cells. *Acs Appl Mater Inter* **2016,** *8* (45), 30687-30691.
65. Boysen, D. A., *Superprotonic solid acids: structure, properties, and applications*. California Institute of Technology: 2004.
66. Anselmi-Tamburini, U.; Maglia, F.; Chiodelli, G.; Riello, P.; Bucella, S.; Munir, Z. A., Enhanced low-temperature protonic conductivity in fully dense nanometric cubic zirconia. *Appl Phys Lett* **2006,** *89* (16), 163116.
67. Avila-Paredes, H. J.; Barrera-Calva, E.; Anderson, H. U.; De Souza, R. A.; Martin, M.; Munir, Z. A.; Kim, S., Room-temperature protonic conduction in nanocrystalline films of yttria-stabilized zirconia. *J Mater Chem* **2010,** *20* (30), 6235-6238.
68. Kim, S.; Avila-Paredes, H. J.; Wang, S. Z.; Chen, C. T.; De Souza, R. A.; Martin, M.; Munir, Z. A., On the conduction pathway for protons in nanocrystalline yttria-stabilized zirconia. *Phys Chem Chem Phys* **2009,** *11* (17), 3035-3038.
69. Avila-Paredes, H. J.; Chen, C. T.; Wang, S. Z.; De Souza, R. A.; Martin, M.; Munir, Z.; Kim, S., Grain boundaries in dense nanocrystalline ceria ceramics: exclusive pathways for proton conduction at room temperature. *J Mater Chem* **2010,** *20* (45), 10110-10112.
70. Park, H. J.; Shin, J. S.; Choa, Y. H.; Song, H. B.; Lee, K. M.; Lee, K. H., Protonic Conduction Properties of Nanostructured Gd-doped CeO_2 at Low Temperatures. *J Korean Ceram Soc* **2015,** *52* (6), 527-530.
71. Park, H. J.; Roh, J. W., Protonic Conduction of Nanostructured Y-Doped $BaZrO_3$. *J Nanomater* **2016,** *2016*.
72. Kim, S.; Maier, J., On the conductivity mechanism of nanocrystalline ceria. *J Electrochem Soc* **2002,** *149* (10), J73-J83.
73. Shirpour, M.; Gregori, G.; Merkle, R.; Maier, J., On the proton conductivity in pure and gadolinium doped nanocrystalline cerium oxide. *Phys Chem Chem Phys* **2011,** *13* (3), 937-940.

74. Tande, C.; Perez-Coll, D.; Mather, G. C., Surface proton conductivity of dense nanocrystalline YSZ. *J Mater Chem* **2012,** *22* (22), 11208-11213.
75. Scherrer, B.; Schlupp, M. V. F.; Stender, D.; Martynczuk, J.; Grolig, J. G.; Ma, H.; Kocher, P.; Lippert, T.; Prestat, M.; Gauckler, L. J., On Proton Conductivity in Porous and Dense Yttria Stabilized Zirconia at Low Temperature. *Adv Funct Mater* **2013,** *23* (15), 1957-1964.
76. Gregori, G.; Shirpour, M.; Maier, J., Proton Conduction in Dense and Porous Nanocrystalline Ceria Thin Films. *Adv Funct Mater* **2013,** *23* (47), 5861-5867.
77. Takamura, H.; Takahashi, N., Electrical conductivity of dense nanocrystalline ceria under humidified atmosphere. *Solid State Ionics* **2010,** *181* (3-4), 100-103.
78. Tredici, I. G.; Maglia, F.; Ferrara, C.; Mustarelli, P.; Anselmi-Tamburini, U., Mechanism of Low-Temperature Protonic Conductivity in Bulk, High-Density, Nanometric Titanium Oxide. *Adv Funct Mater* **2014,** *24* (32), 5137-5146.
79. Kreuer, K. D., Proton conductivity: Materials and applications. *Chem Mater* **1996,** *8* (3), 610-641.
80. Kreuer, K. D.; Rabenau, A.; Weppner, W., Vehicle Mechanism, a New Model for the Interpretation of the Conductivity of Fast Proton Conductors. *Angewandte Chemie-International Edition in English* **1982,** *21* (3), 208-209.
81. Stub., S. Ø.; Vøllestad, E.; Norby, T., Mechanisms of Protonic Surface Transport in Porous Oxides: Example of YSZ. *J Phys Chem C* **2017,** *121* (23), 12817-12825.
82. Stub, S. Ø.; Vøllestad, E.; Norby, T., Protonic surface conduction controlled by space charge of intersecting grain boundaries in porous ceramics. *J Mater Chem A* **2018,** *6* (18), 8265-8270.
83. Manabe, R.; Stub, S. O.; Norby, T.; Sekine, Y., Evaluating surface protonic transport on cerium oxide via electrochemical impedance spectroscopy measurement. *Solid State Commun* **2018,** *270*, 45-49.
84. Miyoshi, S.; Akao, Y.; Kuwata, N.; Kawamura, J.; Oyama, Y.; Yagi, T.; Yamaguchi, S., Water uptake and conduction property of nano-grained yttria-doped zirconia fabricated by ultra-high pressure compaction at room temperature. *Solid State Ionics* **2012,** *207*, 21-28.
85. Miyoshi, S.; Akao, Y.; Kuwata, N.; Kawamura, J.; Oyama, Y.; Yagi, T.; Yamaguchi, S., Low-Temperature Protonic Conduction Based on Surface Protonics: An Example of Nanostructured Yttria-Doped Zirconia. *Chem Mater* **2014,** *26* (18), 5194-5200.
86. Almar, L.; Tarancon, A.; Andreu, T.; Torrell, M.; Hu, Y.; Dezanneau, G.; Morata, A., Mesoporous ceramic oxides as humidity sensors: A case study for gadolinium-doped ceria. *Sensor Actuat B-Chem* **2015,** *216*, 41-48.
87. Wang, J.; Su, M. Y.; Qi, J. Q.; Chang, L. Q., Sensitivity and complex impedance of nanometer zirconia thick film humidity sensors. *Sensor Actuat B-Chem* **2009,** *139* (2), 418-424.
88. Chen, Z.; Lu, C., Humidity sensors: A review of materials and mechanisms. *Sens Lett* **2005,** *3* (4), 274-295.
89. Anisimov, Y. A.; Evitts, R. W.; Cree, D. E.; Wilson, L. D., Polyaniline/Biopolymer Composite Systems for Humidity Sensor Applications: A Review. *Polymers-Basel* **2021,** *13* (16).
90. Li, J. Y.; Sun, C. X.; Sebo, S. A., Humidity and contamination severity impact on the leakage currents of porcelain insulators. *Generation, Transmission & Distribution, IET* **2011,** *5*, 19-28.
91. Hisai, Y.; Ma, Q. B.; Qureishy, T.; Watanabe, T.; Higo, T.; Norby, T.; Sekine, Y., Enhanced activity of catalysts on substrates with surface protonic current in an electrical field - a review. *Chem Commun* **2021,** *57* (47), 5737-5749.
92. Manabe, R.; Okada, S.; Inagaki, R.; Oshima, K.; Ogo, S.; Sekine, Y., Surface protonics promotes catalysis. *Sci Rep-Uk* **2016,** *6* (1), 1-7.

93. Torimoto, M.; Murakami, K.; Sekine, Y., Low-Temperature Heterogeneous Catalytic Reaction by Surface Protonics. *B Chem Soc Jpn* **2019,** *92* (10), 1785-1792.
94. Sekine, Y.; Haraguchi, M.; Tomioka, M.; Matsukata, M.; Kikuchi, E., Low-Temperature Hydrogen Production by Highly Efficient Catalytic System Assisted by an Electric Field. *J Phys Chem A* **2010,** *114* (11), 3824-3833.
95. Murakami, K.; Manabe, R.; Nakatsubo, H.; Yabe, T.; Ogo, S.; Sekine, Y., Elucidation of the role of electric field on low temperature ammonia synthesis using isotopes. *Catal Today* **2018,** *303*, 271-275.
96. Hayun, S.; Shvareva, T. Y.; Navrotsky, A., Nanoceria - Energetics of Surfaces, Interfaces and Water Adsorption. *J Am Ceram Soc* **2011,** *94* (11), 3992-3999.
97. Ruiz-Trejo, E.; Kilner, J. A., Possible proton conduction in $Ce_{0.9}Gd_{0.1}O_{2-delta}$ nanoceramics. *J Appl Electrochem* **2009,** *39* (4), 523-528.
98. Mullins, D. R., The surface chemistry of cerium oxide. *Surf Sci Rep* **2015,** *70* (1), 42-85.
99. Simons, P.; Torres, K. P.; Rupp, J. L., Careful choices in low temperature ceramic processing and slow hydration kinetics can affect proton conduction in ceria. *Adv Funct Mater* **2021,** *31* (31), 2009630.
100. Colomer, M. T., Nanoporous anatase ceramic membranes as fast-proton-conducting materials. *J Eur Ceram Soc* **2006,** *26* (7), 1231-1236.
101. Colomer, M. T., Nanoporous Anatase Thin Films as Fast Proton‐Conducting Materials. *Adv Mater* **2006,** *18* (3), 371-374.
102. Shabanikia, A.; Javanbakht, M.; Amoli, H. S.; Hooshyari, K.; Enhessari, M., Effect of $La_2Ce_2O_7$ on the physicochemical properties of phosphoric acid doped polybenzimidazole nanocomposite membranes for high temperature proton exchange membrane fuel cells applications. *J Electrochem Soc* **2014,** *161* (14), F1403.
103. Oh, T. S.; Boyd, D. A.; Goodwin, D. G.; Haile, S. M., Proton conductivity of columnar ceria thin-films grown by chemical vapor deposition. *Phys Chem Chem Phys* **2013,** *15* (7), 2466-2472.
104. Kim, S.; Anselmi-Tambtirini, U.; Park, H. J.; Martin, M.; Munir, Z. A., Unprecedented room-temperature electrical power generation using nanoscale fluorite-structured oxide electrolytes. *Adv Mater* **2008,** *20* (3), 556-559.
105. Simons, P.; Schenk, S. A.; Gysel, M. A.; Olbrich, L. F.; Rupp, J. L., A Ceramic-Electrolyte Glucose Fuel Cell for Implantable Electronics. *Adv Mater* **2022**, 2109075.
106. Xu, K.; Chatzitakis, A.; Vollestad, E.; Ruan, Q.; Tang, J.; Norby, T., Hydrogen from wet air and sunlight in a tandem photoelectrochemical cell. *Int J Hydrogen Energ* **2019,** *44* (2), 587-593.
107. Nosaka, A. Y.; Fujiwara, T.; Yagi, H.; Akutsu, H.; Nosaka, Y., Characteristics of water adsorbed on TiO_2 photocatalytic systems with increasing temperature as studied by solid-state ^1H NMR spectroscopy. *J Phys Chem B* **2004,** *108* (26), 9121-9125.
108. Sun, X.; Xu, K.; Chatzitakis, A.; Norby, T., Photocatalytic generation of gas phase reactive oxygen species from adsorbed water: Remote action and electrochemical detection. *J Environ Chem Eng* **2021,** *9* (2), 104809.
109. Kang, X. L.; Chaperman, L.; Galeckas, A.; Ammar, S.; Mammeri, F.; Norby, T.; Chatzitakis, A., Water Vapor Photoelectrolysis in a Solid-State Photoelectrochemical Cell with TiO_2 Nanotubes Loaded with CdS and CdSe Nanoparticles. *Acs Appl Mater Inter* **2021,** *13* (39), 46875-46885.
110. Wang, Y.; Zhou, Q.; Kang, L.; Yang, L.; Wu, H.; Zhou, Z.; Xiao, C.; Guo, J.; Yang, F.; Zhang, S., Oxide-water interaction and wetting property of ceria surfaces tuned by high-temperature thermal aging. *Appl Surf Sci* **2021,** *554*, 149658.

111. Chorkendorff, I.; Niemantsverdriet, J. W., *Concepts of modern catalysis and kinetics*. John Wiley & Sons, page 185-186: 2017.
112. Puigdollers, A. R.; Illas, F.; Pacchioni, G., Reduction of Hydrogenated ZrO_2 Nanoparticles by Water Desorption. *Acs Omega* **2017,** *2* (7), 3878-3885.
113. Komarewsky, V. I.; Miller, D., Hydrogenation with Metal Oxide Catalysts. *Adv Catal* **1957,** *9*, 707-715.
114. Thøgersen, A.; Sun, X.; Jensen, I. T.; Prytz, Ø.; Norby, T., In-situ electron loss spectroscopy reveals surface dehydrogenation of hydrated ceria nanoparticles at elevated temperatures. *Journal of Physics and Chemistry of Solids* **2022,** *170*, 110955.
115. Young, T., III. An essay on the cohesion of fluids. *Philosophical transactions of the royal society of London* **1805,** (95), 65-87.
116. Law, K. Y., Definitions for Hydrophilicity, Hydrophobicity, and Superhydrophobicity: Getting the Basics Right. *J Phys Chem Lett* **2014,** *5* (4), 686-688.
117. Barteau, M. A., Organic reactions at well-defined oxide surfaces. *Chem Rev* **1996,** *96* (4), 1413-1430.
118. Kang, X. L.; Chatzitakis, A.; Aarholt, T.; Sun, X. W.; Negri, C.; Norby, T., Facet-engineered TiO_2 nanomaterials reveal the role of water-oxide interactions in surface protonic conduction. *J Mater Chem A* **2022,** *10* (1), 218-227.
119. Ignatchenko, A.; Nealon, D. G.; Dushane, R.; Humphries, K., Interaction of water with titania and zirconia surfaces. *J Mol Catal a-Chem* **2006,** *256* (1-2), 57-74.
120. Vittadini, A.; Selloni, A.; Rotzinger, F. P.; Gratzel, M., Structure and energetics of water adsorbed at TiO2 anatase (101) and (001) surfaces. *Phys Rev Lett* **1998,** *81* (14), 2954-2957.
121. Diebold, U.; Li, S. C.; Schmid, M., Oxide Surface Science. *Annu Rev Phys Chem* **2010,** *61*, 129-148.
122. Tilocca, A.; Selloni, A., Structure and reactivity of water layers on defect-free and defective anatase TiO2(101) surfaces. *J Phys Chem B* **2004,** *108* (15), 4743-4751.
123. Bomati-Miguel, O.; Mazeina, L.; Navrotsky, A.; Veintemillas-Verdaguer, S., Calorimetric study of maghemite nanoparticles synthesized by laser-induced pyrolysis. *Chem Mater* **2008,** *20* (2), 591-598.
124. McHale, J. M.; Auroux, A.; Perrotta, A. J.; Navrotsky, A., Surface energies and thermodynamic phase stability in nanocrystalline aluminas. *Science* **1997,** *277* (5327), 788-791.
125. Pitcher, M. W.; Ushakov, S. V.; Navrotsky, A.; Woodfield, B. F.; Li, G. S.; Boerio-Goates, J.; Tissue, B. M., Energy crossovers in nanocrystalline zirconia. *J Am Ceram Soc* **2005,** *88* (1), 160-167.
126. Radha, A. V.; Bomati-Miguel, O.; Ushakov, S. V.; Navrotsky, A.; Tartaj, P., Surface Enthalpy, Enthalpy of Water Adsorption, and Phase Stability in Nanocrystalline Monoclinic Zirconia. *J Am Ceram Soc* **2009,** *92* (1), 133-140.
127. Costa, G. C. C.; Ushakov, S. V.; Castro, R. H. R.; Navrotsky, A.; Muccillo, R., Calorimetric Measurement of Surface and Interface Enthalpies of Yttria-Stabilized Zirconia (YSZ). *Chem Mater* **2010,** *22* (9), 2937-2945.
128. Norby, T.; Wideroe, M.; Glockner, R.; Larring, Y., Hydrogen in oxides. *Dalton T* **2004,** (19), 3012-3018.
129. Harvey, A. H., *Thermodynamic properties of water: Tabulation from the IAPWS Formulation 1995 for the thermodynamic properties of ordinary water substance for general and scientific use*. US Department of Commerce, Technology Administration, National Institute of …: 1998.
130. McCafferty, E.; Zettlemoyer, A., Entropy of adsorption and the mobility of water vapor on α-Fe_2O_3. *J Colloid Interf Sci* **1970,** *34* (3), 452-460.

131. McCafferty, E.; Zettlemoyer, A., Adsorption of water vapour on α-Fe_2O_3. *Discuss Faraday Soc* **1971,** *52*, 239-254.
132. Tojo, T.; Atake, T.; Mori, T.; Yamamura, H., Excess heat capacity in yttria stabilized zirconia. *J Therm Anal Calorim* **1999,** *57* (2), 447-458.
133. Tojo, T.; Atake, T.; Mori, T.; Yamamura, H., Heat capacity and thermodynamic functions of zirconia and yttria-stabilized zirconia. *J Chem Thermodyn* **1999,** *31* (7), 831-845.
134. Atkins, P., *Physical chemistry, 3rd Ed . pp .770-780*. Oxford University Press: 1987.
135. Langmuir, I., The constitution and fundamental properties of solids and liquids Part I Solids. *J Am Chem Soc* **1916,** *38*, 2221-2295.
136. Raz, S.; Sasaki, K.; Maier, J.; Riess, I., Characterization of adsorbed water layers on Y_2O_3-doped ZrO_2. *Solid State Ionics* **2001,** *143* (2), 181-204.
137. Stub, S. Ø. Protonic Conduction in Porous Oxides. University of Oslo, 2017.
138. Brunauer, S.; Emmett, P. H.; Teller, E., Adsorption of gases in multimolecular layers. *J Am Chem Soc* **1938,** *60*, 309-319.
139. Sun, X. W.; Gu, J.; Han, D. L.; Norby, T., Quantifiable models for surface protonic conductivity in porous oxides - case of monoclinic ZrO_2. *Phys Chem Chem Phys* **2022,** (24), 11856 - 11871.
140. Buck, A. L., New Equations for Computing Vapor-Pressure and Enhancement Factor. *J Appl Meteorol* **1981,** *20* (12), 1527-1532.
141. Egashira, M.; Nakashima, M.; Kawasumi, S.; Seiyama, T., Temperature Programmed Desorption Study of Water Adsorbed on Metal-Oxides .2. Tin Oxide Surfaces. *J Phys Chem-Us* **1981,** *85* (26), 4125-4130.
142. Hair, M. L.; Hertl, W., Adsorption on hydroxylated silica surfaces. *The Journal of Physical Chemistry* **1969,** *73* (12), 4269-4276.
143. Nowick, A. S.; Vaysleyb, A. V., Isotope effect and proton hopping in high-temperature protonic conductors. *Solid State Ionics* **1997,** *97* (1-4), 17-26.
144. Stub, S. Ø.; Thorshaug, K.; Rørvik, P. M.; Norby, T.; Vøllestad, E., The influence of acceptor and donor doping on the protonic surface conduction of TiO_2. *Phys Chem Chem Phys* **2018,** *20* (23), 15653-15660.
145. Peckham, T. J.; Holdcroft, S., Structure-Morphology-Property Relationships of Non-Perfluorinated Proton-Conducting Membranes. *Adv Mater* **2010,** *22* (42), 4667-4690.
146. Lapid, H.; Agmon, N.; Petersen, M. K.; Voth, G. A., A bond-order analysis of the mechanism for hydrated proton mobility in liquid water. *The Journal of chemical physics* **2005,** *122* (1), 014506.
147. Haile, S. M.; West, D. L.; Campbell, J., The role of microstructure and processing on the proton conducting properties of gadolinium-doped barium cerate. *Journal of Materials Research* **1998,** *13* (6), 1576-1595.
148. Maier, J., Ionic conduction in space charge regions. *Progress in Solid State Chemistry* **1995,** *23* (3), 171-263.
149. Kidner, N. J.; Homrighaus, Z. J.; Ingram, B. J.; Mason, T. O.; Garboczi, E. J., Impedance/Dielectric Spectroscopy of Electroceramics–Part 1: Evaluation of Composite Models for Polycrystalline Ceramics. *Journal of Electroceramics* **2005,** *14* (3), 283-291.
150. Sato, R.; Ohkuma, S.; Shibuta, Y.; Shimojo, F.; Yamaguchi, S., Proton Migration on Hydrated Surface of Cubic ZrO_2: Ab initio Molecular Dynamics Simulation. *J Phys Chem C* **2015,** *119* (52), 28925-28933.
151. Sato, R.; Shibuta, Y.; Shimojo, F.; Yamaguchi, S., Effects of CO_2 adsorption on proton migration on a hydrated ZrO_2 surface: an ab initio molecular dynamics study. *Phys Chem Chem Phys* **2017,** *19* (30), 20198-20205.

152. Korhonen, S. T.; Calatayud, M.; Krause, A. O. I., Stability of hydroxylated (111) and (101) surfaces of monoclinic zirconia: A combined study by DFT and infrared spectroscopy. *J Phys Chem C* **2008,** *112* (16), 6469-6476.
153. Piskorz, W.; Grybos, J.; Zasada, F.; Cristol, S.; Paul, J. F.; Adamski, A.; Sojka, Z., Periodic DFT and Atomistic Thermodynamic Modeling of the Surface Hydration Equilibria and Morphology of Monoclinic ZrO_2 Nanocrystals. *J Phys Chem C* **2011,** *115* (49), 24274-24286.
154. Kock, E. M.; Kogler, M.; Klotzer, B.; Noisternig, M. F.; Penner, S., Structural and Electrochemical Properties of Physisorbed and Chemisorbed Water Layers on the Ceramic Oxides Y_2O_3, YSZ, and ZrO_2. *Acs Appl Mater Inter* **2016,** *8* (25), 16428-16443.
155. Ma, Z. Y.; Cheng, Y.; Wei, W.; Li, W. H.; Sun, Y. H., Surface properties and CO adsorption on zirconia polymorphs. *J Mol Catal a-Chem* **2005,** *227* (1-2), 119-124.
156. Jung, K. T.; Bell, A. T., The effects of synthesis and pretreatment conditions on the bulk structure and surface properties of zirconia. *J Mol Catal a-Chem* **2000,** *163* (1-2), 27-42.
157. Suresh, A.; Mayo, M. J.; Porter, W. D., Thermodynamics of the tetragonal-to-monoclinic phase transformation in fine and nanocrystalline yttria-stabilized zirconia powders. *J Mater Res* **2003,** *18* (12), 2912-2921.
158. Cerrato, G.; Bordiga, S.; Barbera, S.; Morterra, C., A surface study of monoclinic zirconia (m-ZrO_2). *Surf Sci* **1997,** *377* (1-3), 50-55.
159. Kwon, O. H.; Jang, C.; Lee, J.; Jeong, H. Y.; Kwon, Y.-i.; Joo, J. H.; Kim, H., Investigation of the electrical conductivity of sintered monoclinic zirconia (ZrO_2). *Ceramics International* **2017,** *43* (11), 8236-8245.
160. Weibel, A.; Bouchet, R.; Boulc'h, F.; Knauth, P., The big problem of small particles: A comparison of methods for determination of particle size in nanocrystalline anatase powders. *Chem Mater* **2005,** *17* (9), 2378-2385.
161. Mamontov, E., Dynamics of surface water in ZrO_2 studied by quasielastic neutron scattering. *J Chem Phys* **2004,** *121* (18), 9087-9097.
162. Zhao, X.; Vanderbilt, D., Phonons and lattice dielectric properties of zirconia. *Physical Review B* **2002,** *65* (7), 075105.
163. Muccillo, E. N. S.; Kleitz, M., Impedance spectroscopy of Mg-partially stabilized zirconia and cubic phase decomposition. *J Eur Ceram Soc* **1996,** *16* (4), 453-465.
164. Erdal, S.; Kongshaug, C.; Bjorheim, T. S.; Jalarvo, N.; Haugsrud, R.; Norby, T., Hydration of Rutile TiO_2: Thermodynamics and Effects on n- and p-Type Electronic Conduction. *J Phys Chem C* **2010,** *114* (19), 9139-9145.
165. Kalland, L.-E.; Løken, A.; Bjørheim, T. S.; Haugsrud, R.; Norby, T., Structure, hydration, and proton conductivity in 50% La and Nd doped CeO_2–$La_2Ce_2O_7$ and $Nd_2Ce_2O_7$– and their solid solutions. *Solid State Ionics* **2020,** *354*, 115401.
166. Sun, X.; Vøllestad, E.; Rørvik, P. M.; Prodinger, S.; Kalantzopoulos, G. N.; Chatzitakis, A.; Norby, T., Surface protonic conductivity in chemisorbed water in porous nanoscopic CeO_2. *Appl Surf Sci* **2023,** *611*, 155590.
167. Anez, R.; Sierraalta, A.; Martorell, G.; Sautet, P., Stabilization of the (110) tetragonal zirconia surface by hydroxyl chemical transformation. *Surf Sci* **2009,** *603* (16), 2526-2531.
168. Li, Y.; Hibino, M.; Miyayania, M.; Kudo, T., Proton conductivity of tungsten trioxide hydrates at intermediate temperature. *Solid State Ionics* **2000,** *134* (3-4), 271-279.
169. Blesa, M. A.; Maroto, A. J. G.; Regazzoni, A. E., Surface-Acidity of Metal-Oxides Immersed in Water - a Critical Analysis of Thermodynamic Data. *J Colloid Interf Sci* **1990,** *140* (1), 287-290.
170. Jaiswal, N.; Tanwar, K.; Suman, R.; Kumar, D.; Upadhyay, S.; Parkash, O., A brief review on ceria based solid electrolytes for solid oxide fuel cells. *J Alloy Compd* **2019,** *781*, 984-1005.

171. Liu, M.; Ding, D.; Bai, Y.; He, T.; Liu, M., An efficient SOFC based on samaria-doped ceria (SDC) electrolyte. *J Electrochem Soc* **2012,** *159* (6), B661.
172. Nigara, Y.; Yashiro, K.; Kawada, I.; Mizusaki, J., Hydrogen permeability in $(CeO_2)_{0.9}(GdO_{1.5})_{0.1}$ at high temperatures. *Solid State Ionics* **2003,** *159* (1-2), 135-141.
173. Perez-Coll, D.; Sanchez-Lopez, E.; Mather, G. C., Influence of porosity on the bulk and grain-boundary electrical properties of Gd-doped ceria. *Solid State Ionics* **2010,** *181* (21-22), 1033-1042.
174. Runnerstrom, E. L.; Ong, G. K.; Gregori, G.; Maier, J.; Milliron, D. J., Colloidal Nanocrystal Films Reveal the Mechanism for Intermediate Temperature Proton Conductivity in Porous Ceramics. *J Phys Chem C* **2018,** *122* (25), 13624-13635.
175. Melchionna, M.; Fornasiero, P., The role of ceria-based nanostructured materials in energy applications. *Mater Today* **2014,** *17* (7), 349-357.
176. Zhou, K. B.; Wang, X.; Sun, X. M.; Peng, Q.; Li, Y. D., Enhanced catalytic activity of ceria nanorods from well-defined reactive crystal planes. *J Catal* **2005,** *229* (1), 206-212.
177. Trovarelli, A.; Llorca, J., Ceria Catalysts at Nanoscale: How Do Crystal Shapes Shape Catalysis? *Acs Catal* **2017,** *7* (7), 4716-4735.
178. Paier, J.; Penschke, C.; Sauer, J., Oxygen Defects and Surface Chemistry of Ceria: Quantum Chemical Studies Compared to Experiment. *Chem Rev* **2013,** *113* (6), 3949-3985.
179. Ganduglia-Pirovano, M. V.; Hofmann, A.; Sauer, J., Oxygen vacancies in transition metal and rare earth oxides: Current state of understanding and remaining challenges. *Surf Sci Rep* **2007,** *62* (6), 219-270.
180. Mogensen, M.; Sammes, N. M.; Tompsett, G. A., Physical, chemical and electrochemical properties of pure and doped ceria. *Solid State Ionics* **2000,** *129* (1-4), 63-94.
181. Shearer, G. C.; Chavan, S.; Bordiga, S.; Svelle, S.; Olsbye, U.; Lillerud, K. P., Defect Engineering: Tuning the Porosity and Composition of the Metal-Organic Framework UiO-66 via Modulated Synthesis. *Chem Mater* **2016,** *28* (11), 3749-3761.
182. Kalantzopoulos, G. N.; Lundvall, F.; Thorshaug, K.; Lind, A.; Vajeeston, P.; Dovgaliuk, I.; Arstad, B.; Wragg, D. S.; Fjellvag, H., Factors Determining Microporous Material Stability in Water: The Curious Case of SAPO-37. *Chem Mater* **2020,** *32* (4), 1495-1505.
183. Sing, K. S. W.; Everett, D. H.; Haul, R. A. W.; Moscou, L.; Pierotti, R. A.; Rouquerol, J.; Siemieniewska, T., Reporting Physisorption Data for Gas Solid Systems with Special Reference to the Determination of Surface-Area and Porosity (Recommendations 1984). *Pure Appl Chem* **1985,** *57* (4), 603-619.
184. Canivet, J.; Bonnefoy, J.; Daniel, C.; Legrand, A.; Coasne, B.; Farrusseng, D., Structure-property relationships of water adsorption in metal-organic frameworks. *New J Chem* **2014,** *38* (7), 3102-3111.
185. Fronzi, M.; Assadi, M. H. N.; Hanaor, D. A. H., Theoretical insights into the hydrophobicity of low index CeO_2 surfaces. *Appl Surf Sci* **2019,** *478*, 68-74.
186. Azimi, G.; Dhiman, R.; Kwon, H. M.; Paxson, A. T.; Varanasi, K. K., Hydrophobicity of rare-earth oxide ceramics. *Nat Mater* **2013,** *12* (4), 315-320.
187. Wachowski, S. L.; Szpunar, I.; Sørby, M. H.; Mielewczyk–Gryń, A.; Balaguer, M.; Ghica, C.; Istrate, M. C.; Gazda, M.; Gunnæs, A. E.; Serra, J. M., Structure and water uptake in $BaLnCo_2O_{6-\delta}$ (Ln= La, Pr, Nd, Sm, Gd, Tb and Dy). *Acta Materialia* **2020,** *199*, 297-310.
188. Schuster. P, Z. G., Sandorfy. C, The Hydrogen Bond: Recent Developments in Theory and Experiments III: Dynamics, thermodynamics and special systems. Chapter 27: Hydrogen Bonds in Systems of Adsorbed Molecules, p. 1263. . Knözinger, H., Ed. North-Holland Publishing Company - Amsterdam, New York, Oxford: 1976.

189. Kuchibhatla, S. V. N. T.; Karakoti, A. S.; Vasdekis, A. E.; Windisch, C. F.; Seal, S.; Thevuthasan, S.; Baer, D. R., An unexpected phase transformation of ceria nanoparticles in aqueous media. *J Mater Res* **2019,** *34* (3), 465-473.
190. Fronzi, M.; Piccinin, S.; Delley, B.; Traversa, E.; Stampfl, C., Water adsorption on the stoichiometric and reduced CeO2(111) surface: a first-principles investigation. *Phys Chem Chem Phys* **2009,** *11* (40), 9188-9199.
191. Kumar, S.; Schelling, P. K., Density functional theory study of water adsorption at reduced and stoichiometric ceria (111) surfaces. *J Chem Phys* **2006,** *125* (20), 204704.
192. Tschope, A.; Sommer, E.; Birringer, R., Grain size-dependent electrical conductivity of polycrystalline cerium oxide I. Experiments. *Solid State Ionics* **2001,** *139* (3-4), 255-265.
193. Knauth, P.; Engel, J.; Bishop, S.; Tuller, H., Study of compaction and sintering of nanosized oxide powders by in situ electrical measurements and dilatometry: Nano CeO_2—case study. *Journal of Electroceramics* **2015,** *34* (1), 82-90.
194. Gobel, M. C.; Gregori, G.; Guo, X. X.; Maier, J., Boundary effects on the electrical conductivity of pure and doped cerium oxide thin films. *Phys Chem Chem Phys* **2010,** *12* (42), 14351-14361.
195. Sun, W.; Fang, S.; Yan, L.; Liu, W., Investigation on Proton Conductivity of $La_2Ce_2O_7$ in Wet Atmosphere: Dependence on Water Vapor Partial Pressure. *Fuel Cells* **2012,** *12* (3), 457-463.
196. Wagner, W.; Pruß, A., The IAPWS formulation 1995 for the thermodynamic properties of ordinary water substance for general and scientific use. *Journal of physical and chemical reference data* **2002,** *31* (2), 387-535.
197. Thiel, P. A.; Madey, T. E., The Interaction of Water with Solid-Surfaces - Fundamental-Aspects. *Surf Sci Rep* **1987,** *7* (6-8), 211-385.
198. Chen, J.; Wu, X.-P.; Hope, M. A.; Qian, K.; Halat, D. M.; Liu, T.; Li, Y.; Shen, L.; Ke, X.; Wen, Y., Polar surface structure of oxide nanocrystals revealed with solid-state NMR spectroscopy. *Nat Commun* **2019,** *10* (1), 1-10.
199. Yang, C. W.; Yu, X. J.; Heissler, S.; Nefedov, A.; Colussi, S.; Llorca, J.; Trovarelli, A.; Wang, Y. M.; Woll, C., Surface Faceting and Reconstruction of Ceria Nanoparticles. *Angew Chem Int Edit* **2017,** *56* (1), 375-379.
200. Külah, E.; Marot, L.; Steiner, R.; Romanyuk, A.; Jung, T. A.; Wäckerlin, A.; Meyer, E., Surface chemistry of rare-earth oxide surfaces at ambient conditions: reactions with water and hydrocarbons. *Sci Rep-Uk* **2017,** *7* (1), 1-10.
201. Yamazaki, Y.; Babilo, P.; Haile, S. M., Defect Chemistry of Yttrium-Doped Barium Zirconate: A Thermodynamic Analysis of Water Uptake. *Chem Mater* **2008,** *20* (20), 6352-6357.
202. Lowell, S.; Shields, J. E.; Thomas, M. A.; Thommes, M., *Characterization of porous solids and powders: surface area, pore size and density*. Springer Science & Business Media: 2006; Vol. 16.
203. Garcia-Belmonte, G.; Kytin, V.; Dittrich, T.; Bisquert, J., Effect of humidity on the ac conductivity of nanoporous TiO_2. *J Appl Phys* **2003,** *94* (8), 5261-5264.
204. Ekstrom, H.; Wickman, B.; Gustavsson, M.; Hanarp, P.; Eurenius, L.; Olsson, E.; Lindbergh, G., Nanometer-thick films of titanium oxide acting as electrolyte in the polymer electrolyte fuel cell. *Electrochim Acta* **2007,** *52* (12), 4239-4245.
205. Ryzhkin, M. I.; Ryzhkin, I. A.; Kashin, A.; Galitskaya, E. A.; Sinitsyn, V., Proton conductivity of water in mesoporous materials. *Jetp Lett+* **2018,** *108* (9), 596-600.
206. Ryzhkin, I.; Ryzhkin, M.; Kashin, A.; Galitskaya, E.; Sinitsyn, V., High proton conductivity state of water in nanoporous materials. *EPL (Europhysics Letters)* **2019,** *126* (3), 36003.

207. Fujita, S.; Koiwai, A.; Kawasumi, M.; Inagaki, S., Enhancement of Proton Transport by High Densification of Sulfonic Acid Groups in Highly Ordered Mesoporous Silica. *Chem Mater* **2013,** *25* (9), 1584-1591.
208. Colomer, M. T.; Rubio, F., Textural characteristics, degree of protonation, water uptake and proton transport properties relationships in colloidal sol-gel derived micro- and mesoporous silica membranes. *Int J Hydrogen Energ* **2016,** *41* (13), 5748-5757.
209. Hanaor, D. A. H.; Sorrell, C. C., Review of the anatase to rutile phase transformation. *J Mater Sci* **2011,** *46* (4), 855-874.
210. Kjølseth, C.; Wang, L. Y.; Haugsrud, R.; Norby, T., Determination of the enthalpy of hydration of oxygen vacancies in Y-doped $BaZrO_3$ and $BaCeO_3$ by TG-DSC. *Solid State Ionics* **2010,** *181* (39-40), 1740-1745.
211. Løken, A.; Kjølseth, C.; Haugsrud, R., Electrical conductivity and TG-DSC study of hydration of Sc-doped $CaSnO_3$ and $CaZrO_3$. *Solid State Ionics* **2014,** *267*, 61-67.
212. Iskandarova, I. M.; Knizhnik, A. A.; Rykova, E. A.; Bagatur'yants, A. A.; Potapkin, B. V.; Korkin, A. A., First-principle investigation of the hydroxylation of zirconia and hafnia surfaces. *Microelectron Eng* **2003,** *69* (2-4), 587-593.
213. Selloni, A.; Vittadini, A.; Gratzel, M., The adsorption of small molecules on the TiO_2 anatase(101) surface by first-principles molecular dynamics. *Surf Sci* **1998,** *402* (1-3), 219-222.
214. Herman, G. S.; Dohnalek, Z.; Ruzycki, N.; Diebold, U., Experimental investigation of the interaction of water and methanol with anatase-TiO_2(101). *J Phys Chem B* **2003,** *107* (12), 2788-2795.
215. Prin, M.; Pijolat, M.; Soustelle, M.; Touret, O., Characterization of a Cerium Dioxide Powder from Its Equilibrium with Water-Vapor. *Thermochim Acta* **1991,** *186* (2), 273-283.
216. Kim, J.; Qian, W.; Al-Saigh, Z. Y., Measurements of water sorption enthalpy on polymer surfaces and its effect on protein adsorption. *Surf Sci* **2011,** *605* (3-4), 419-423.
217. Fahmi, A.; Minot, C., A Theoretical Investigation of Water-Adsorption on Titanium-Dioxide Surfaces. *Surf Sci* **1994,** *304* (3), 343-359.
218. Matsuda, T.; Ishibashi, R.; Koshizuka, Y.; Tsuneki, H.; Sekine, Y., Quantitative investigation of CeO_2 surface proton conduction in H_2 atmosphere. *Chem Commun* **2022,** *58* (77), 10789-10792.
219. Colomer, M. T.; Rubio, F.; Jurado, J. R., Transport properties of fast proton conducting mesoporous silica xerogels. *J Power Sources* **2007,** *167* (1), 53-57.
220. Murakami, K.; Tanaka, Y.; Sakai, R.; Hisai, Y.; Hayashi, S.; Mizutani, Y.; Higo, T.; Ogo, S.; Seo, J. G.; Tsuneki, H.; Sekine, Y., Key factor for the anti-Arrhenius low-temperature heterogeneous catalysis induced by H^+ migration: H^+ coverage over support. *Chem Commun* **2020,** *56* (23), 3365-3368.
221. Takahashi, A.; Inagaki, R.; Torimoto, M.; Hisai, Y.; Matsuda, T.; Ma, Q. B.; Seo, J. G.; Higo, T.; Tsuneki, H.; Ogo, S.; Norby, T.; Sekine, Y., Effects of metal cation doping in CeO_2 support on catalytic methane steam reforming at low temperature in an electric field. *Rsc Adv* **2020,** *10* (25), 14487-14492.
222. Yin, C. S.; Li, J. J.; Zhou, Y. W.; Zhang, H. N.; Fang, P. F.; He, C. Q., Phase Separation and Development of Proton Transport Pathways in Metal Oxide Nanoparticle/Nafion Composite Membranes during Water Uptake. *J Phys Chem C* **2018,** *122* (17), 9710-9717.
223. Wang, L.; Advani, S. G.; Prasad, A. K., Degradation reduction of polymer electrolyte membranes using CeO_2 as a free-radical scavenger in catalyst layer. *Electrochim Acta* **2013,** *109*, 775-780.
224. Lei, M.; Yang, T. Z.; Wang, W. J.; Huang, K.; Zhang, R.; Fu, X. L.; Yang, H. J.; Wang, Y. G.; Tang, W. H., Self-assembled mesoporous carbon sensitized with ceria

nanoparticles as durable catalyst support for PEM fuel cell. *Int J Hydrogen Energ* **2013,** *38* (1), 205-211.
225. Baker, A. M.; Williams, S. T. D.; Mukundan, R.; Spernjak, D.; Advani, S. G.; Prasad, A. K.; Borup, R. L., Zr-doped ceria additives for enhanced PEM fuel cell durability and radical scavenger stability. *J Mater Chem A* **2017,** *5* (29), 15073-15079.
226. Tanaka, M.; Takeda, Y.; Wakiya, T.; Wakamoto, Y.; Harigaya, K.; Ito, T.; Tarao, T.; Kawakami, H., Acid-doped polymer nanofiber framework: Three-dimensional proton conductive network for high-performance fuel cells. *J Power Sources* **2017,** *342*, 125-134.
227. Ibaraki, T.; Tanaka, M.; Kawakami, H., Fast surface proton conduction on acid-doped polymer nanofibers in polymer electrolyte composite membranes. *Electrochim Acta* **2019,** *296*, 1042-1048.

Appendices

Appendix I

List of symbols for variables and constants and abbreviations for sub- and subscripts

Appendix II

Quantifiable models for surface protonic conductivity in porous oxides – case of monoclinic ZrO_2

Xinwei Sun, Jie Gu, Donglin Han, Truls Norby
Phys. Chem. Chem. Phys., 2022, *24*, 11856-11871.

Appendix III

Surface protonic conductivity in chemisorbed water in porous nanoscopic CeO_2

Xinwei Sun, Einar Vøllestad, Per Martin Rørvik, Sebastian Prodinger, Georgios N. Kalantzopoulos, Athanasios Chatzitakis, and Truls Norby
Applied Surface Science (2022), *611*, 155590.

Appendix IV

In-situ electron loss spectroscopy reveals surface dehydrogenation of hydrated ceria nanoparticles at elevated temperatures

Annett Thøgersen, Xinwei Sun, Ingvild Thue Jensen, Øystein Prytz, Truls Norby
Journal of Physics and Chemistry of Solids 170 (2022), *170*, 110955.

Appendix V

Composite Membranes for High Temperature PEM Fuel Cells and Electrolysers: A Critical Review (MDPI *Membranes* 2021 Best paper award)

Xinwei Sun, Stian Christopher Simonsen, Truls Norby, Athanasios Chatzitakis
Membranes 2019, *9*, 83.

Contributions to other publications and manuscripts during the PhD period but not included in the thesis

Facet-engineered TiO_2 nanomaterials reveal the role of water-oxide interactions in surface protonic conduction
Kang, X., Chatzitakis, A., Aarholt, T., Sun, X., Negri, C. and Norby, T.
J. Mater. Chem. A, 2022, *10*, 218-227.

Earth-abundant electrocatalysts in proton exchange membrane electrolyzers
Sun, X., Xu, K., Fleischer, C., Liu, X., Grandcolas, M., Strandbakke, R., Bjørheim, T.S., Norby, T. and Chatzitakis, A.
Catalysts 8(12), 2018: 657.

Photocatalytic generation of gas phase oxygen species from adsorbed water: Remote action and electrochemical detection
Sun, X., Xu, K., Chatzitakis, A. and Norby, T.
Journal of Environmental Chemical Engineering 9 (2), 2021: 104809.

Appendix I

List of symbols and abbreviations

List of symbols for variables and constants and abbreviations for sub- and subscripts

Variables, constants	Unit	Description	Comment
a	(dimensionless)	Activity	
A	(dimensionless)	Geometric factor	
c_{BET}	(dimensionless)	BET constant	
c	mol/cm^3	Volume concentration	
C	F	Capacitance	
D	cm^2/s	Random diffusion coefficient	
d_g	cm	Grain and pore size	
E	kJ/mol	Heat of adsorption	Enters in c_{BET}
F	C/mol	Faraday constant	96485 C/mol
G	S	Conductance	
ΔH	kJ/mol	Enthalpy change	
K	(dimensionless)	Equilibrium coefficient	like in $K_{a_{cm}}$
l	cm	Length of surface layer sheet	
M	(dimensionless)	Metal	M = Ti, Zr,Ce…
M_m	g/mol	Molar mass	
p	bar	Partial pressure	
R	J/molK	Gas constant	8.3144 J/molK
R	ohm	Resistance	
RH	(dimensionless)	Relative humidity	$= p_{H_2O} / p_{ce}$
s	cm	Jump distance	
ΔS	J/molK	Entropy change	
SSA_g	cm^2/g	Specific surface area, gravimetric	
SSA_v	cm^2/cm^3	Specific surface area, volumetric	
SSA_m	cm^2/mol	Specific surface area, molar	
T	K	Absolute temperature	
t	cm	Thickness of surface layer	
u	cm^{2}K/Vs	Charge mobility	
w	cm	Width of surface layer sheet	
X	(dimensionless)	Site fraction	
Z	ohm	Impedance	
γ	mol/cm^2	Surface concentration	Gamma
ε_0	F/cm	Vacuum permittivity	8.854·10^{-14} F/cm
ε_e	F/cm	Effective dielectric constant	Epsilon
ε_r	(dimensionless)	Relative dielectric constant	Epsilon
θ	(dimensionless)	Surface coverage	Theta, $= \nu / \nu_m$
ν	mol/cm^2	Molar concentration of physisorbed water	Nu
ν_m	mol/cm^2	Molar concentration of a monolayer of water	Nu
ξ	(dimensionless)	Percolation power	Xi
ρ	g/cm^3	Density	Actual material
ρ_r	(dimensionless)	Relative density	Rho
ρ_t	g/cm^3	Theoretical density	Dense material
σ	S/cm	Conductivity	Sigma

ψ	1/cm				BLM porosity surface factor	Psi, = $\sigma_{M,s}$ / G_s
ω_0	1/s = Hz				Vibrational attempt frequency	Omega
Subscripts						
1st level	2nd level (no. of letter)					
	1st	2nd	3rd	-4th		
a					adsorption	
c					conduction	
	c				chemisorbed	
	p				physisorbed	
		m			molecular	
		d			dissociative	
d					dissociation	
			s		to surface oxide ion	
			a		to adsorbed water molecule	
	chm-ph1				from chemisorbed to 1st physisorbed layer	pcp
	ph1				in 1st physisorbed layer	ppp
m					migration	= diffusion
m,H^+					migration of H^+	Grotthuss
				–s	between surface oxide	
				–sa	between surface oxide and adsorbed hydroxide	
				–a	between adsorbed water molecule and ionised species	
0					preexponential	like in u_0 and G_0
M					Macroscopic	like in σ_M
L and Lp					One layer and one layer with effect of percolation	in $G_{s,L}$ and $G_{s,Lp}$
ce					condensation equilibrium	in p_{ce} and K_{ce}
r					relative	like in ρ_r and ε_r
geom					geometric	
cvex					convex	
cave					concave	
Superscript						
0					standard	like in p^0 and G^0

Appendix II

Quantifiable models for surface protonic conductivity in porous oxides – case of monoclinic ZrO_2

Xinwei Sun,[a] ‡ Jie Gu,[b] ‡ Donglin Han,[b] * Truls Norby[a,b] *

[a] Department of Chemistry, University of Oslo, Centre for Materials Science and Nanotechnology (SMN), FERMiO, Gaustadalléen 21, NO-0349 Oslo, Norway

[b] College of Energy, Soochow University, No 1 Shizi Street, Gusu District, Suzhou, 215006, China

‡ Equal first authors

* Corresponding authors: dlhan@suda.edu.cn , truls.norby@kjemi.uio.no

Phys. Chem. Chem. Phys., 2022, *24*, 11856-11871.

II

PCCP

ROYAL SOCIETY OF CHEMISTRY

PAPER

View Article Online
View Journal | View Issue

Cite this: *Phys. Chem. Chem. Phys.*, 2022, **24**, 11856

Quantifiable models for surface protonic conductivity in porous oxides – case of monoclinic ZrO_2†

Xinwei Sun, ‡[a] Jie Gu,‡[b] Donglin Han *[b] and Truls Norby*[ab]

The surface protonic conductivity of porous monoclinic ZrO_2 sintered at temperatures in the range 700–1100 °C yielding relative densities of around 60% and grain sizes of approximately 160 nm has been studied using impedance spectroscopy as a function of temperature well below the sintering temperature in wet atmospheres (p_{H_2O} = 0.03 bar). The sum of two high-frequency impedance responses is argued to represent surface conductance according to a new model of impedance over curved surfaces. A simple brick layer model is applied to compare the measured macroscopic conductivities with predicted surface conductances. The well-faceted samples sintered at the highest temperatures exhibited activation enthalpies up to 58 kJ mol^{-1} of surface protonic conduction in wet atmospheres at temperatures above 300 °C. We attribute this to the mobility of dissociated protons over surface oxide ions, and the high pre-exponential is in good agreement with a model comprising relatively strong dissociative chemisorption. With decreasing sintering temperature, the particles appear more rounded, with less developed facets, and we obtain activation enthalpies of surface protonic conduction in the chemisorbed layer down to around 30 kJ mol^{-1}, with correspondingly smaller preexponentials and an observed $p_{H_2O}^{1/2}$ dependency. Supported by the thermogravimetry of adsorption, we attribute this to weaker and more molecular chemisorption on the more randomly terminated less faceted surfaces, providing water layers with fewer dissociated charge carrying protons, but also smaller activation enthalpies of mobility. Below 200 °C, all samples exhibit a strongly inverse temperature dependency characteristic of conduction in the 1st physisorbed layer with increasing coverage. The preexponentials correspond well to the models of physisorption, with dissociation to and proton migration between physisorbed water molecules. The enthalpies fit well to physisorption and with enthalpies of dissociation and proton mobility close to those of liquid water. We have by this introduced models for proton conduction in chemisorbed and physisorbed water on ZrO_2, applicable to other oxides as well, and shown that preexponentials are quantitatively assessable in the order-of-magnitude level to discriminate models *via* a simple brick layer model based topographical analysis of the ceramic microstructure.

Received 12th December 2021,
Accepted 8th April 2022

DOI: 10.1039/d1cp05668a

rsc.li/pccp

1 Introduction

Adsorption of water on the outer and inner surfaces of dense and porous ceramics is well known and studied, which enables humidity sensors (see *e.g.* ref. 1 and references therein) and gives rise to protonic conduction that in combination with various airborne contamination decreases the performance of electrical insulators.[2] Surface protonic conduction in water adsorbed in porous nano-grained ceramics has more recently received renewed interest as potential electrolytes for fuel cells,[3–5] while it is also realised that it plays significant roles in kinetics of catalysts, photocatalysts, and electrocatalysts.[6,7]

Surface protonics is particularly well studied for pure and doped dioxides of tetravalent cations. Much of our present knowledge on the adsorption of water and surface protonics in porous nano-grained ceramic oxides stems from studies of undoped monoclinic and cubic ZrO_2,[8–11] and cubic Y-stabilised ZrO_2 (YSZ).[12–18] Miyoshi *et al.*[19,20] showed that the room temperature (RT) protonic conductivity of YSZ increased by 3 orders of magnitude when the grain size was reduced from 100 to 13 nm, while the concentration of Y_2O_3 did not have a significant effect on the surface protonic conductivity.

[a] *Department of Chemistry, University of Oslo, Centre for Materials Science and Nanotechnology (SMN), FERMiO, Gaustadalléen 21, NO-0349 Oslo, Norway. E-mail: truls.norby@kjemi.uio.no*
[b] *College of Energy, Soochow University, No. 1 Shizi Street, Gusu District, Suzhou, 215006, China. E-mail: dlhan@suda.edu.cn*

† Electronic supplementary information (ESI) available. See DOI: https://doi.org/10.1039/d1cp05668a

‡ Equal first authors.

They attributed the proton conductivity to water adsorbed at grain boundaries and surfaces. CeO_2 is of particular importance in catalysis; the water adsorption has been well characterised,[21,22] and surface protonic conduction has been measured,[23,24] but it exhibits a complex surface chemistry with slow equilibria and considerable hysteresis.[25–27] TiO_2 has also been well studied[28–30] lately because protonic migration in adsorbed water appears to be central for the use of TiO_2 photocatalysts.[31,32] Recently, Kang *et al.*[33] investigated the role of surface orientation on water adsorption and surface protonic conduction in anatase TiO_2 materials synthesised under conditions that favour different surface facets. They found by *in situ* FT-IR and conductivity measurements that simple {100} and {001} surfaces with accessible cations and anions favour dissociative chemisorption and the conductivity suggested that the subsequent physisorbed water layer was rigidly bonded and solid (ice-like). In comparison, the {101} surface favours molecular (associative) chemisorption, with a more loosely bonded subsequent physisorbed layer. The two types of surfaces have characteristic differences in surface protonic conductivity – especially its temperature dependency.

Gregori *et al.*[23] proposed a brick layer model that qualitatively estimates the surface protonic conductivity of porous oxides based on the pore size, volume fraction of the open porosity, and thickness and bulk conductivity of the adsorbed water layer. They further assumed that dissociation into charge carriers follows autoprotolysis of water. Stub *et al.*[15,16] suggested that proton transport can occur over grain surfaces (intra) and over grain boundary intersects (inter). They treated surface protonic conduction quantitatively based on their own measurements, standard models for adsorption, and transport terms for YSZ developed by Raz *et al.*[12]

These recent studies and the growing understanding of the phenomena involved have led us to propose a quantitative approach to parameterise models of adsorption, dissociation, and migration, which can also be applied to other porous materials. This in turn leads to prediction and interpretation of the macroscopic surface protonic conductivity of the porous sample, employing both enthalpies and, unlike non-quantitative approaches, the preexponentials. To do this, we define and employ a defect chemical notation for surface species, merge adsorption theory and defect equilibrium thermodynamics, apply normal theory of proton diffusion and migration, and link the surface conductance through the macroscopic sample conductivity by a simple topographical analysis – a brick layer model (BLM) – of the microstructure.

The surfaces of monoclinic ZrO_2 show a preferred termination along the {111} plane after sintering at high temperatures.[34] The literature on adsorption is limited to a review and study of CO adsorption[35] in addition to the aforementioned studies on the adsorption of water and stability of hydroxylated ZrO_2 surfaces.[8,11] Surface protonic conductivity has not been reported for porous monoclinic ZrO_2 and only scarcely from the perspective of volume conduction in undoped ZrO_2 with a relatively high density ($>80\%$) and a coarse microstructure.[36] We herein report the surface protonic conductivity in adsorbed water layers in nano-grained porous monoclinic ZrO_2, with focus on the effect of sintering temperature and hence small differences in the microstructure and degree of faceting of the surfaces. Samples are characterised by X-ray diffraction (XRD), scanning electron microscopy (SEM), thermogravimetry (TG) and electrochemical impedance spectroscopy (EIS). Results are interpreted according to the model for activation enthalpies and preexponentials of protonic conduction in chemisorbed and physisorbed water layers, supported by the observed isothermal p_{H_2O} dependence of conductivity, and the effect of faceting is considered. A discussion on the appearance of two high-frequency time responses in the impedance spectra is provided, which our samples have in common with most porous materials with surface protonic conduction.

2 Experimental

In order to prepare ZrO_2 ceramic pellets, ZrO_2 powder (99.99% metal basis except Hf, CAS no. 1314-23-4, Aladdin Industrial Corporation, China) and a binder (a mixture of polyvinyl, glycerol, ethanol and DI water) were mixed in the weight ratio of 7 : 1 and pressed into disks with a diameter of 12.7 mm and a thickness of approx. 2.0 mm under a pressure of 760 MPa. They were sintered for 24 h at 600, 700, 800, 900, 1000, or 1100 °C, with a heating and cooling ramp rate of 5 °C min^{-1}. Samples sintered at 600 °C were of insufficient mechanical strength for conductivity measurements, and only samples sintered at 700–1100 °C were characterised further and were denoted as ST700-ST1100 accordingly, see Table 1.

Table 1 Sample notation with sintering and microstructural parameters. Factor ψ is the ratio between the macroscopic conductivity of the porous sample and the grain surface conductance according to the brick layer model (BLM) that we will come back to later in eqn (3) with a percolation power $\xi = 1$. Also, volumetric, gravimetric, and molar specific surface areas are estimated to first approximation based on the BLM (see ESI 5, ESI)

Sample	ST700	ST800	ST900	ST1000	ST1100
Sintering temperature, °C	700	800	900	1000	1100
FWHM, °	0.175	0.178	0.177	0.181	0.177
Relative density, %	60	60	60	65	70
Average grain size from SEM, nm	150	150	160	170	190
ψ, cm^{-1} (eqn (3) with $\xi = 1$)	6.4×10^4	6.4×10^4	6.0×10^4	5.4×10^4	4.4×10^4
SSA_v, $cm^2\ cm^{-3}$	9.6×10^4	9.6×10^4	9.0×10^4	8.1×10^4	6.6×10^4
SSA_g, $cm^2\ g^{-1}$	2.7×10^4	2.7×10^4	2.6×10^4	2.1×10^4	1.6×10^4
SSA_M, $cm^2\ mol^{-1}$	3.4×10^6	3.4×10^6	3.2×10^6	2.6×10^6	2.0×10^6

Powder XRD patterns were collected using a Bruker D8 Advance Diffractometer (Laguna Hills, CA, USA) with Cu Kα radiation (λ = 1.5418 Å). Microstructures were observed by SEM using a Hitachi SU 8010 Boerne (Hitachi, Tokyo, Japan).

Thermogravimetric data were acquired using a Netzsch 449 F1 Jupiter® thermal analyser (GmbH, Germany) on ST700 and ST1000, representing samples sintered at low and high temperatures, respectively. Samples were first degassed during heating to 650 °C (ST700) or 900 °C (ST1000) at 3 K min^{-1} using bottle-dry 99.999% N_2 as both the carrier and protective gas, and further held at the given temperature for 2 h. (In our experience, even very dry gases typically end up with 30 ppm H_2O in high-temperature apparatus.[37]) Then, the uptake of water was measured by flowing wet (p_{H_2O} = 0.026 bar) N_2 over the samples during stepwise cooling to 26 °C. The water uptake was obtained by subtracting the background measurements in dry N_2 gas carried out under otherwise identical conditions.

For electrical measurements, silver paste (SOFCMAN, China) was painted on both sides of the pellets, and heat-treated at 800 °C in an ambient atmosphere for 2 h, except for the sample sintered at 700 °C for which the heat-treatment was made at 600 °C. The pellets were mounted in a ProboStat™ (NORECS, Norway) sample holder with a 4-wire 2-electrode configuration. AC impedance spectra were collected in the range 1 MHz–1 Hz at 0.7 V rms applied voltage with a CHI604E electrochemical workstation (Shanghai Chenhua Instruments Ltd, Shanghai, China) or at 3 V rms using a Solartron SI 1260 frequency response analyser (Solartron Analytical, Farnborough, UK). For both, the ProboStat™ base unit chassis was connected to instrument ground to reduce noise and eliminate parasitic parallel conduction, and it was controlled that both instruments yielded equivalent spectra. The atmosphere was flowing Ar (99.999%) either bottle-dry or wetted to $p_{H_2O} \approx 0.03$ bar by bubbling through de-ionized water at room temperature or using a HumiStat gas-mixer and humidifier (NORECS, Norway). The impedance spectra were collected after keeping the sample at each temperature for at least 1 h during cooling and analysed with ZView software (Scribner Associates, Inc. NC, USA). The electrical conductivity of each porous sample is calculated from its resistance, thickness, and electrode area.

3 Results

3.1 Microstructure characterisation

The geometrical dimensions after sintering were close to those of green bodies, *i.e.*, little sintering takes place. From the dimensions and weight, the relative densities were calculated to vary only between 60% and 70% for the samples sintered at 700 and 1100 °C, respectively, see Table 1.

Fig. 1 shows the XRD results for the precursor powder and powder ground off the sintered samples. They all correspond to the monoclinic polymorph of ZrO_2. Analyses of the main peaks shows that the full width at half maximum (FWHM) values are close, at about 0.180° for the samples annealed at 700–1100 °C, see Table 1, indicating from the Debye–Scherrer formula average crystallite sizes around 50 nm.[38]

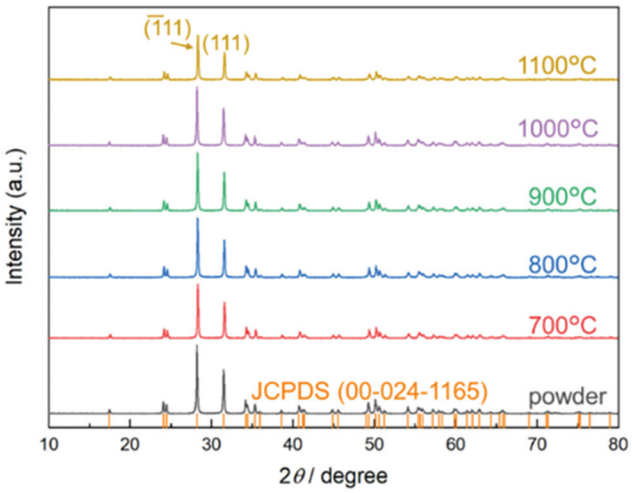

Fig. 1 X-ray diffractograms collected at RT for the ZrO_2 powder and samples sintered at the given temperatures, compared with peak locations of the monoclinic ZrO_2 structure (JCPDS).

Fig. 2 shows the SEM images of the precursor powder and sintered samples, revealing the openly porous microstructure in agreement with the densities from geometry and weight. From the statistical analyses of the images, we estimate average grain sizes of 150 nm for the precursor powder and 150–190 nm for the ST700–ST1100 samples. Hence, both sintering and grain growth are modest at the sintering temperatures applied here.

Closer inspection of the grains suggests no differences in the aspect ratio and modest differences in connectivity (necks). However, while the mostly spherical shape of the precursor particles has been retained in the samples sintered at low temperatures (below 900 °C), the particles of samples sintered at higher temperatures show more faceted surfaces, apparently a distribution over normal {100}, {110}, and {111} surfaces (in cubic framework) as the regular aspect of the crystallite is maintained.

3.2 Thermogravimetry (TG)

Fig. 3 shows the TG result in terms of the amount of water (chemisorbed and physisorbed) adsorbed on ZrO_2 ST700 and ST1000, with area specific coverage calculated based on the estimates of specific surface areas listed in Table 1. The uptake of chemisorbed water saturates towards 200 °C at around 4–5 H_2O molecules per nm^2, which is considered a monolayer.[8] We note that the coverage is not yet complete at 400 °C for the ST700 sample, suggesting relatively weak and hence molecular chemisorption, while the ST1000 sample achieves coverage at somewhat higher temperatures, indicating stronger chemisorption on its more developed (facetted) surfaces, as observed also for CeO_2.[39]

Physisorption sets in below 200 °C, and a first physisorbed layer is complete around 80 °C. Qualitatively, the water uptake modelled as the sum of a completed chemisorbed layer and physisorbed layers yields adsorption enthalpies similar to that of condensation to liquid water,[12] as expected. The total water

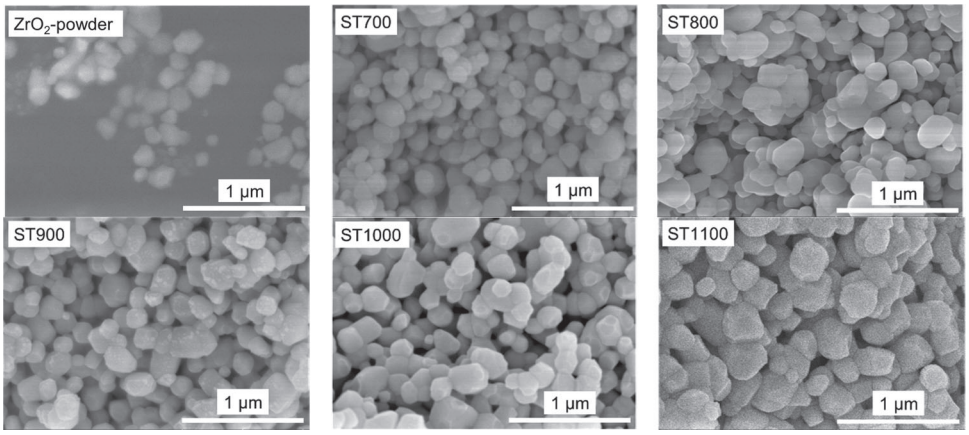

Fig. 2 SEM images of the precursor powder and fracture surfaces of the samples sintered at the given temperatures.

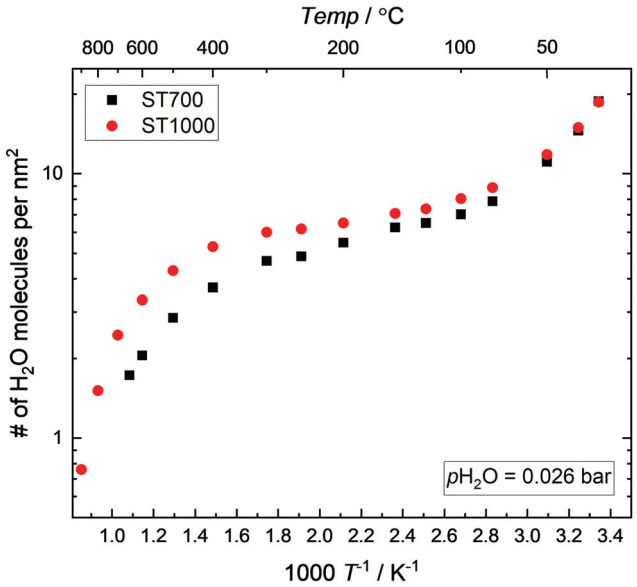

Fig. 3 The area specific uptake of water obtained from TG analysis for ST700 and ST1000 in wet (p_{H_2O} = 0.026 bar) N_2 *vs.* $1/T$.

uptake corresponds well to one reported in the literature, when its surface area of 80 $m^2\ g^{-1}$, a factor of 4 higher than in our samples is taken into account.[40]

3.3 Electrical properties

3.3.1 Electrochemical impedance spectroscopy (EIS). Representative impedance spectra are displayed in ESI 2 and Fig. S1 (ESI†). All samples exhibited two overlapping semicircles in the high frequency domain, with capacitances in the lower and higher end of the 10^{-11} F range, irrespective of sintering and measurement temperature or atmosphere (dry or wet). The literature does not provide a consistent rationalisation of this, but in our present understanding, it reflects surface conduction over the curved surface of the porous microstructure, namely concave regions with small capacitance of the gas phase over the gap and convex regions with higher capacitance due to the dielectric solid phase. We provide a more detailed discussion of the origin and capacitances of the two responses in ESI 3 (ESI†), but here take it that the sum of the two resistances represents the total resistance of the surface transport.

The two responses are present also in dry atmospheres at the highest measurement temperatures. This suggests that also the native, non-protonic conduction is dominated by surface transport, which is reasonable in these fine-grained porous samples.

At the highest measurement temperatures, there is an additional response at the lowest frequencies, with characteristic capacitances of the order of magnitude of 10^{-8} F, both in wet and dry atmospheres. This may be a grain boundary impedance as reported by Stub *et al.*[16] for YSZ, but it may also be an electrode response. The contact area between the adsorbed water layer and the metal electrode is small compared with a normal solid electrolyte, hence the normal capacitance of 10^{-6} F for samples of this size attributed to the double layer in parallel with charge transfer may be reduced by orders of magnitude and be what we observe.

3.3.2 Surface protonic conductivities. An Arrhenius plot of the electrical conductivity of all samples under wet and dry Ar (separated) is provided in ESI 4 and Fig. S2 (ESI†). The conductivities in wet atmosphere generally behave like typical surface protonic isobars with considerable conductivities at high temperatures, a minimum at around 200 °C, and conductivities increasing with decreasing temperature towards room temperature. In bottle-dry atmospheres, the measured conductivities were similar for all samples, with activation energies of around 100 kJ mol^{-1} at the highest temperatures, typical of oxide vacancy mobility in ZrO_2 materials.[36,41] We attribute this to native conductivity of the sample, apparently dominated by surface transport based on the above-mentioned interpretation of the impedance spectra in dry atmospheres.

Fig. 4 shows the surface protonic conductivities obtained in wet atmospheres after subtraction of native conductivity, plotted as $\log(\sigma T)$ *vs.* $1/T$ as we shall use that for extracting enthalpies and preexponentials, listed in Table 2.

The surface protonic conductivities in wet atmospheres above 200 °C are typical of conduction in the chemisorbed

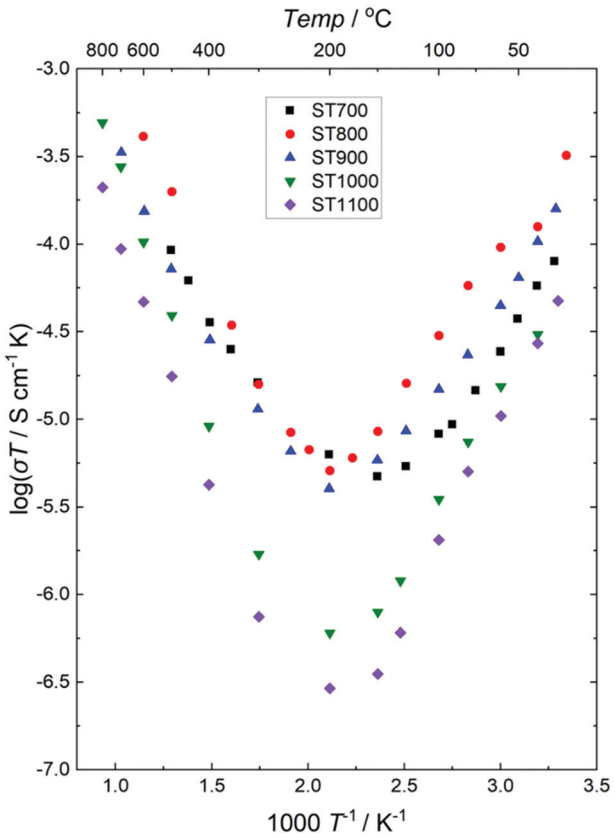

Fig. 4 Plot of log(σT) *vs.* 1/T measured in wet (p_{H_2O} = 0.03 bar) Ar, after subtraction of the dry atmosphere native conductivities, as explained in the text.

water layer, which according to adsorption thermodynamics of ZrO_2[8] should approach full coverage below 400 °C at p_{H_2O} = 0.03 bar. The enthalpies in this region are approaching 60 kJ mol^{-1} for ST1000 and ST1100, which we for now note is comparable to the enthalpy of mobility of protons in the lattices of MO_2 oxides, *e.g.* 58 kJ mol^{-1} for polycrystalline rutile TiO_2[42], and 43 kJ mol^{-1} as an estimate for 50% La-doped CeO_2.[43] With lower sintering temperatures, the enthalpies decrease, to around 30 kJ mol^{-1} for ST700, and conductivities are higher suggesting that the enthalpy of migration is lower and/or the exothermic adsorption is at play, *i.e.*, the layer is not complete and still filling up with decreasing temperature for these samples, in agreement with the TG results, and to be discussed further later.

Below 150 °C, we have a strong increase in conductivity, as a first molecular physisorbed water layer starts to build on top of the chemisorbed layer, providing easier transfer of protons. The activation enthalpies are now found to be in the range of −40 to −20 kJ mol^{-1}. This is qualitatively dominated by the exothermic enthalpy of the condensation of water vapour, and we shall quantify it when we discuss models for transport in this layer later.

As the physisorbed layer builds, it expectedly gets more liquid-like and the physisorption enthalpy approaches that of pure liquid water. This gives rise to an additional strong increase in the surface protonic conductivity in many porous ceramics,[15,28] including some facets of TiO_2[33] as we approach RT and relative humidity (RH) surpasses 60%. For our monoclinic ZrO_2 samples, however, there is no such secondary increase in conductivity. This is similar to the {101} facet of TiO_2[33] and our on-going work on undoped CeO_2[39] where it even increases less steeply above RHs of 60%. As our data do not extensively explore the region at RH > 60%, we refrain from analysing that region further and it is not part of Table 2.

3.3.3 Isothermal p_{H_2O} dependencies. Fig. 5 shows the p_{H_2O} dependence of surface protonic conductivity obtained for the ST700 sample recorded at 400 and 100 °C, reflecting the chemisorbed and first physisorbed water layer, respectively. A close to $p_{H_2O}^{1/2}$ dependency is revealed at 400 °C, in agreement with the results for 4 mol% Y_2O_3-stabilised ZrO_2 (4YSZ) at 250–400 °C[19] and more recently for undoped CeO_2 at 400 °C.[39] This may be interpreted to reflect a weak molecular and hence incomplete chemisorbed layer with only partial dissociation to conductive protons. At 100 °C, we obtained close to $p_{H_2O}^{3/2}$ dependency, same as that of undoped nanoscopic CeO_2 sintered at 550 °C and measured at 100 °C.[39] We will discuss models that may rationalise it below.

4 Models and quantitative interpretation

In the following, we provide a deeper theoretical analysis of the preexponentials and activation enthalpies of surface conduction in porous oxides, with focus on MO_2 type oxides and ZrO_2 and the actual samples and data presented here. For this, we will go through some definitions and clarifications of conductivity contributions, considerations of geometrical factors for surface conduction in porous materials, estimation of charge mobility of protonic species, nomenclature for surface species, and

Table 2 Preexponentials and activation enthalpies of the macroscopic conductivity of the porous sample material fitted from log(σT) *vs.* 1/T plots

			Sample				
Conditions	Type of conduction	Parameter	ST700	ST800	ST900	ST1000	ST1100
High T, dry	Native conductivity	$\sigma_{M\,0}$, SK cm^{-1}	2×10^{1}	1×10^{1}	1×10^{2}	1×10^{2}	7×10^{1}
		ΔH, kJ mol^{-1}	95	92	109	105	104
High T, wet	Surface protonic, chemisorbed	$\sigma_{M\,0}$, SK cm^{-1}	5×10^{-3}	1×10^{-1}	2×10^{-2}	4×10^{-1}	1×10^{-1}
		ΔH, kJ mol^{-1}	27	41	34	58	57
Low T, wet	Surface protonic, 1st physisorbed	$\sigma_{M\,0}$, SK cm^{-1}	6×10^{-9}	1×10^{-9}	5×10^{-9}	7×10^{-12}	4×10^{-13}
		ΔH, kJ mol^{-1}	−22	−32	−25	−40	−47

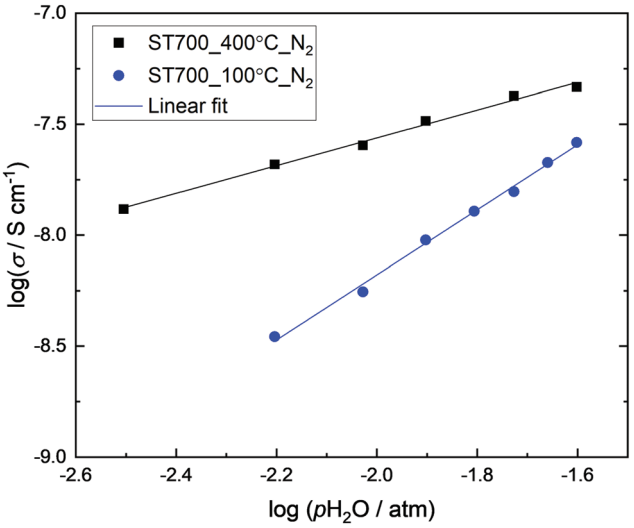

Fig. 5 p_{H_2O} dependence of surface protonic conductivity for ST700 at 400 and 100 °C recorded in N_2 gas, representing the chemisorbed and physisorbed regions, respectively.

thermodynamics of adsorption and dissociation, leading up to expressions for surface conduction and sample macroscopic conductivity. A list of symbols and subscripts is provided in the ESI† (ESI 1 and Table S1).

4.1 Conductivity and geometry

The total macroscopic conductivity of a porous material σ_M can be taken to have bulk and surface contributions. Under our experimental conditions, we take it that the bulk conductivity of ZrO_2 is due to native oxide ion transport, and while it appears that this is negligible, the surface conductivity also has a contribution from oxide ions in addition to protonic conduction. The latter may be taken to arise from migration in chemisorbed, first rigid physisorbed, and second liquid-like physisorbed water layers:

$$\begin{aligned}\sigma_M &= \sigma_{M,b} + \sigma_{M,s} \approx \sigma_{M,s,O^{2-}} + \sigma_{M,s,H^+} \\ \sigma_{M,s,H^+} &= \sigma_{M,ch,H^+} + \sigma_{M,ph1,H^+} + \sigma_{M,ph2,H^+}\end{aligned} \quad (1)$$

We will treat the three water layers as one, dominated by the outermost one, in the sense that the layers adsorb one by one, to a first approximation, and that the conductivity of the outermost layer for the purpose of modelling totally outcompetes that of any layers underneath.

The conductivities in dry atmospheres at high temperatures exhibit activation energies of around 100 kJ mol^{-1}, attributable to inherent conduction by oxide ions in gross agreement with literature data for bulk conductivity of monoclinic ZrO_2.[36,41] If it is a bulk conduction process, the measured conductivity is empirically proportional to the square of the relative density, making factors such as $0.65^2 = 0.42$, but this does not change the comparison significantly. As mentioned earlier, impedance spectra suggest that the inherent conduction is also a surface process due to the presence of the overlapping high-frequency semicircles with capacitances of the order of 10^{-11} F (see ESI 2 and Fig. S1(e, f), ESI†). Dual time constants have also been reported for YSZ, suggested to reflect *intra-* and *inter-grain* surface protonic resistances.[16] It is anyway not of our interest here, and we subtract it where it is significant at high temperatures and can neglect it at lower temperatures, so that Fig. 4 represents $\sigma_M = \sigma_{M,s,H^+}$.

The macroscopic protonic surface conductivity σ_{M,s,H^+} of the sample material must be related to the adsorbed water surface layer volume conductivity σ_{s,H^+} along an appropriate geometric model. For this, we need the protonic surface layer conductance, G_{s,H^+}. It has unit S (Siemens) and is the in-plane conductance of a square of a surface layer with thickness t. It is independent of the width w and the length l of the square, since they are equal and cancel. The surface protonic conductance G_{s,H^+} with average volume concentration c_{H^+} and charge mobility u_{H^+} in the water layer is then related to the protonic surface layer volume conductivity σ_{s,H^+} by

$$G_{s,H^+} = \sigma_{s,H^+}\frac{w}{l}t \overset{w=l}{=} \sigma_{s,H^+}t = Fu_{H^+}c_{H^+}t = Fu_{H^+}\gamma_{H^+} \quad (2)$$

where we have also replaced the protonic surface layer volume concentration c_{H^+} (in mol cm^{-3}) with surface concentration γ_{H^+} (in mol cm^{-2}) and layer thickness t in $c_{H^+} = \gamma_{H^+}/t$. As stated above, we here treat the surface layer as one, and we have deliberately used subscript s to distinguish conductance and conductivity of the surface layer from other geometries, while we have omitted the superscript s for concentration and mobility terms to avoid build-up of too many subscripts later on.

From a simple brick layer model (BLM, see ESI 5, ESI†), we may make an order-of-magnitude approximation to the macroscopic conductivity contribution $\sigma_{M,s}$ of a porous material from the surface conductance G_s, the relative density ρ_r, and assumed equal grain and pore size d_g:

$$\sigma_{M,s} \approx \frac{4\rho_r^{\xi}(1-\rho_r)^{\xi}}{d_g}G_s = \psi G_s \quad (3)$$

The exponent ξ adjusts for percolation. For materials of regular and equal shapes of grains and pores, and densities around 50%, it will be ξ = 1–2 and we here use ξ = 1. The effect is still less than half an order of magnitude for densities around 50%. The factor $\psi = \sigma_{M,s}/G_s$ in eqn (3) calculated on this basis is listed for our samples in Table 1. In this work, we hence calculate the predicted macroscopic sample surface protonic conductivity from $\sigma_{M,s,H^+} = \psi G_{s,H^+}$.

4.2 Charge mobility of protonic species

We now consider the diffusivity and charge mobility of protons, which we will need to couple thermodynamics and concentrations with conductance and conductivity. Since the proton is a defect on oxide surfaces, its random diffusivity is in the classic approximation we will use here a simple activated function, multiplied by the chance X_O that the oxide ion it jumps to is available to accept the proton:

$$D_{H^+} = X_O D_{H^+0}\exp\left(\frac{-\Delta H_{m,H^+}}{RT}\right) \quad (4)$$

X_O is the fractional occupancy of any oxide-ion containing species, O^{2-}, OH^-, or H_2O, that can accept a proton, depending on the mechanism. The charge mobility is *via* the Nernst–Einstein relation then:

$$u_{H^+} = \frac{F}{RT} D_{H^+} = X_O \frac{F}{RT} D_{H^+0} \exp\left(\frac{-\Delta H_{m,H^+}}{RT}\right) = X_O \frac{1}{T} u_{H^+0} \exp\left(\frac{-\Delta H_{m,H^+}}{RT}\right) \quad (5)$$

Generally, the preexponential of diffusivity is given by $D_0 = As^2\omega_0 \cdot \exp\left(\frac{\Delta S_m}{R}\right)$ where A is a geometrical factor of the order of unity, s is the jump distance, ω_0 is the vibrational attempt frequency, and ΔS_m is the entropy part of the energy barrier. The proton always jumps from its host oxide ion to a nearest one, so we may take the effective jump distance to be $2.8 \approx 3$ Å. The vibrational attempt frequency is in practice that of the oxide ion host, of the order of 10^{12} s^{-1} (not the 10^{13} s^{-1} of the proton itself). With this, we get $D_{H^+0} \approx 1 \times 10^{-3}$ cm^2 s^{-1} as an order of magnitude estimate, irrespective of the mechanism or host system, and in turn, $u_{H^+0} = \frac{F}{R} D_{H^+0} \approx 10$ cm^2 K V^{-1} s^{-1}.

4.3 Nomenclature for surface species

Now that we start our thermodynamic analysis with the aim to combine it with charge mobility to get conductivity, we choose to use a Kröger–Vink compatible notation for surface chemistry in which superscripts $^\times$, $'$, and $^\bullet$ denote, respectively, neutral, negative, and positive effective charges compared to the charge of the clean, "perfect" surface. For compatibility with other binary oxides, we furthermore choose to denote cations by the general symbol M, so that here M = Zr and surface cation and oxide ion sites are hence denoted as M_s and O_s.

4.4 The chemisorbed layer

We start by attempting to predict the level and behaviour of surface protonic conductivity in the chemisorbed layer, which dominates typically in wet atmospheres at high temperatures down to around 200 °C. The samples behave differently in terms of activation enthalpy and preexponentials, and we will derive two models that can rationalise the two. One is based on weak, molecular chemisorption, and it divides further into two sub-models with different dissociation and migration behaviours, of which one will be shown to be applicable to sample sintered at the lowest temperatures. The other model is based on strong, dissociative chemisorption, which appears to apply to the samples sintered at higher temperatures. The models are schematically depicted in Fig. 6.

4.4.1 Weak, molecular chemisorption. A previous *in situ* FTIR study shows that a high surface concentration of hydroxyl groups is missing from water chemisorption on monoclinic ZrO_2 between RT and 1173 K over a pressure range of 10^{-5}–24 mbar, in contrast to highly hydroxylated YSZ and Y_2O_3.[18] Room temperature IR measurements on high surface area ZrO_2 after annealing at 873 K reveal a single broad peak at 3690 cm^{-1}, attributed to the O–H stretch mode of H_2O molecules, in addition to a characteristic molecular water band at ~1630 cm^{-1} due to H–O–H bending.[40] *Ab initio* molecular dynamics calculations suggest that while only dissociative adsorption is observed on tetragonal ZrO_2{110} surfaces,[44] both undissociated and dissociated water species coexist on the two most stable surfaces of monoclinic ZrO_2, *i.e.* {101} and {111}.[11]

These experimental and computational studies lead us to propose that H_2O adsorbs on a surface M^{4+} cation but does not easily dissociate protons H^+ onto surface oxide ions O^{2-} or to other water molecules. The lack of dissociation, *i.e.*, an endothermic dissociation enthalpy, leaves the overall chemisorption weak (only modestly exothermic adsorption enthalpy, dominated by unfavourable entropy) and makes an only partly

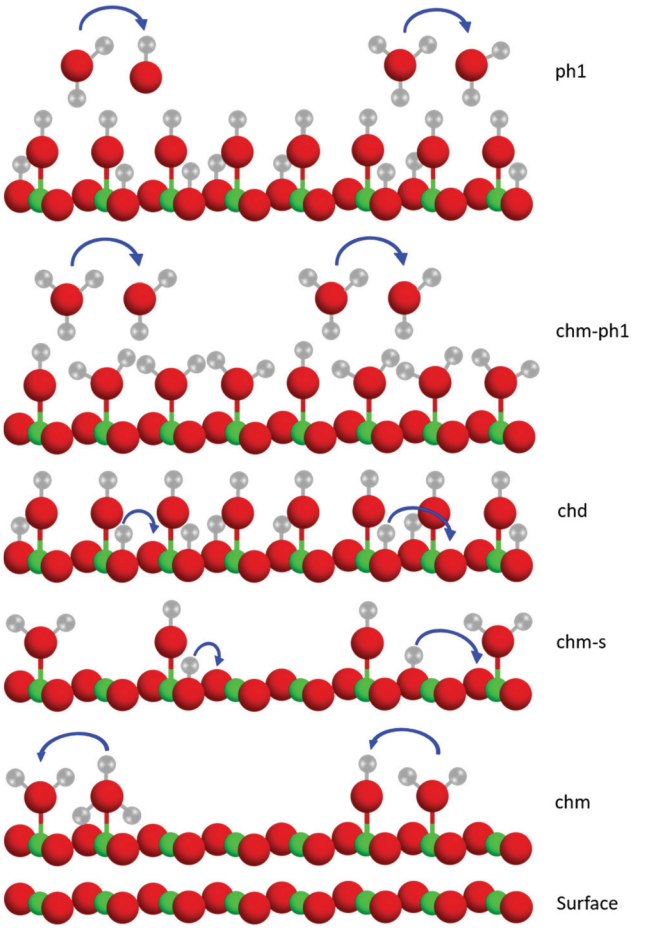

Fig. 6 Schematic illustration of the five models derived for adsorption, dissociation and protonic migration in this work. "Surface" shows the bare MO_2 surface. "chm" shows weak molecular chemisorption and dissociation (for reasons of space limitations shown as half covered and half dissociated) with resulting protonic migration (arrows) in the molecular dissociated layer. "chm-s" is similar, but protons are dissociated to and migrate with the help of surface oxide ions. "chd" shows strong dissociative chemisorption with proton migration on surface oxide ions. "chm-ph1" shows partial coverage of the 1st physisorbed layer with protons dissociated from a molecular chemisorbed layer underneath. "ph1" shows partial coverage of the 1st physisorbed layer with weak dissociation over a strongly adsorbed and dissociated chemisorbed layer underneath.

covered and largely molecular layer (''chm'' and ''chm-s'' in Fig. 6). The molecular chemisorption is in our nomenclature written as follows:

$$M^{\times}_{M_s} + H_2O(g) \rightleftharpoons M_{M_s}OH^{\times}_2 \quad (6)$$

with equilibrium coefficient

$$K_{a_{chm}} = \frac{X_{M_{M_s}OH^{\times}_2}}{X_{M^{\times}_{M_s}} \frac{p_{H_2O(g)}}{p^0}} = \frac{\gamma_{M_{M_s}OH^{\times}_2}}{\gamma_{M^{\times}_{M_s}} \frac{p_{H_2O}}{p^0}} = \exp\left(\frac{\Delta S^0_{a_{chm}}}{R}\right)\exp\left(\frac{-\Delta H^0_{a_{chm}}}{RT}\right) \quad (7)$$

Here, X represents the fractional occupancy (which ideally corresponds to activity and also to surface site coverage), p is the partial pressure, and γ is the surface concentration *e.g.* in mol cm^{-2}. The concentration of adsorbed molecular water according to this model follows simple adsorption isotherm treatments. We are interested in partial dissociation, either protonating other adsorbed molecules (''chm'') or surface oxide ions (''chm-s'') and thereby providing protonic conductivity. We shall derive expressions for both, and compare with the experimental data.

Dissociation within molecular water

As suggested by *e.g.* Raz *et al.*,[12] chemisorbed water molecules may dissociate into adsorbed OH^- ions and H_3O^+ ions, in our nomenclature according to

$$2M_{M_s}OH^{\times}_2 \rightleftharpoons M_{M_s}OH' + M_{M_s}OH^{\bullet}_3 \quad (8)$$

and the equilibrium constant can then be written as follows:

$$K_{d_{chm}} = \frac{X_{M_{M_s}OH'} X_{M_{M_s}OH^{\bullet}_3}}{X^2_{M_{M_s}OH^{\times}_2}} = \frac{\gamma_{M_{M_s}OH'}\gamma_{M_{M_s}OH^{\bullet}_3}}{\gamma^2_{M_{M_s}OH^{\times}_2}} = \exp\left(\frac{\Delta S^0_{d_{chm}}}{R}\right)\exp\left(\frac{-\Delta H^0_{d_{chm}}}{RT}\right) \quad (9)$$

If this dominates, we have the following simple electroneutrality:

$$\gamma_{M_{M_s}OH'} = \gamma_{M_{M_s}OH^{\bullet}_3} \quad (10)$$

Moreover, cation surface site balance requires $\gamma_{M^{\times}_{M_s}} + \gamma_{M_{M_s}OH^{\times}_2} + \gamma_{M_{M_s}OH'} + \gamma_{M_{M_s}OH^{\bullet}_3} = \gamma_{M_s}$, but under the assumption of weak molecular adsorption (low coverage and limited dissociation), we have $\gamma_{M^{\times}_{M_s}} \approx \gamma_{M_s} \gg \gamma_{M_{M_s}OH^{\times}_2} \gg \gamma_{M_{M_s}OH'} + \gamma_{M_{M_s}OH^{\bullet}_3}$, and we can insert and simplify to get

$$K_{d_{chm}} = \frac{\gamma^2_{M_{M_s}OH'}}{\left(K_{a_{chm}}\gamma_{M_s}\frac{p_{H_2O}}{p^0}\right)^2} \Rightarrow \gamma_{M_{M_s}OH'} = \gamma_{M_{M_s}OH^{\bullet}_3} = K_{a_{chm}}\sqrt{K_{d_{chm}}}\gamma_{M_s}\frac{p_{H_2O}}{p^0} \quad (11)$$

In estimating the surface conductance based on this dissociation model, we assume that jumps of protons from dissociated protons H_3O^+ to H_2O and jumps from H_2O to dissociated OH^- contribute equally, and from the electroneutrality the surface protonic conductance in the chemisorbed layer according to eqn (2) can be expressed as the product of charge, surface concentration, and charge mobility:

$$G_{s,H^+_{chm}} = F\left(\gamma_{M_{M_s}OH^{\bullet}_3} + \gamma_{M_{M_s}OH'}\right)u_{H^+_{chm}} = 2F\gamma_{M_{M_s}OH^{\bullet}_3}u_{H^+_{chm}} \quad (12)$$

The charge mobility of the charged defects contains the chance that a proton in an H_3O^+ group finds an adjacent water molecule to jump to, or that a water molecule is there to offer a proton to jump to OH^-. Hence, we get

$$G_{s,H^+_{chm}} = 2F\gamma_{M_{M_s}OH^{\bullet}_3}\frac{\gamma_{M_{M_s}OH^{\times}_2}}{\gamma_{M_s}}u_{H^+0}\frac{1}{T}\exp\left(\frac{-\Delta H_{m,H^+_{chm}}}{RT}\right) \quad (13)$$

which, by combination with eqn (7) and (11), yields

$$G_{s,H^+_{chm}} = 2FK^2_{a_{chm}}\sqrt{K_{d_{chm}}}\gamma_{M_s}\left(\frac{p_{H_2O}}{p^0}\right)^2 u_{H^+0}\frac{1}{T}\exp\left(\frac{-\Delta H_{m,H^+_{chm}}}{RT}\right) \quad (14)$$

We rewrite this as

$$G_{s,H^+_{chm}} = G_{s,H^+_{chm}0}\frac{1}{T}\exp\left(\frac{-\Delta H}{RT}\right) = G_{s,H^+_{chm}0}\frac{1}{T}\exp\left(\frac{-\left(2\Delta H^0_{a_{chm}} + \frac{1}{2}\Delta H^0_{d_{chm}} + \Delta H_{m,H^+_{chm}}\right)}{RT}\right) \quad (15)$$

with

$$G_{s,H^+_{chm}0} = G^0_{s,H^+_{chm}0}\left(\frac{p_{H_2O}}{p^0}\right)^2 = 2F\gamma_{M_s}\exp\left(\frac{2\Delta S^0_{a_{chm}} + \frac{1}{2}\Delta S^0_{d_{chm}}}{R}\right)u_{H^+0}\left(\frac{p_{H_2O}}{p^0}\right)^2 \quad (16)$$

where $G^0_{s,H^+_{chm}0}$ is the standard preexponential of surface protonic conductance at $p_{H_2O} = 1$ bar. We emphasize that $G^0_{s,H^+_{chm}0}$ is hence the most fundamental parameter specific for a surface and a particular adsorption and transport model, in this case weak molecular adsorption with dissociation and transport in the molecular layer. To derive such a fundamental parameter is only meaningful once a model is chosen, so that the p_{H_2O} dependency is clear.

Now, we attempt to estimate $G^0_{s,H^+_{chm}0}$, $G_{s,H^+_{chm}0}$, and eventually $\sigma_{M,s,H^+_{chm}0}$. The standard entropy change $\Delta S^0_{a_{chm}}$ plays a major role and represents the biggest uncertainty. Condensation of water vapour to liquid water has a standard entropy change of -109 J mol^{-1} K^{-1} at 100 °C.[45] It decreases strongly with temperature, *e.g.*, to -44 J mol^{-1} K^{-1} at 300 °C which is relevant for our chemisorption temperature range. On the other hand, the entropy of condensation to ice is larger than that to water (-144 *vs.* -118 J mol^{-1} K^{-1} at RT) and the entropy of molecular adsorption to hydroxylated α-Fe_2O_3, *i.e.*, physisorption, has been reported to be -138 J mol^{-1} K^{-1}.[46] We will hence in this

work for the most part use -109 J mol^{-1} K^{-1} from the entropy of condensation to water at 100 °C[45] as our value for the standard entropy of molecular adsorption $\Delta S^0_{a_{chm}}$, both here for chemisorption and later for physisorption. This implies uncertainties of several orders of magnitude in our calculations for conductances, but helps to emphasise differences between different models.

We next assume $\Delta S^0_{d_{chm}} = 0$ J mol^{-1} K^{-1} for dissociation (since it does not involve gas species or solvation of ions). Using furthermore an adsorption site surface concentration $\gamma_{M_s} \approx 5$ nm^{-2} = 8×10^{-10} mol cm^{-2}, and $u_{H^+0} \approx 10$ cm^2 K V^{-1} s^{-1} as derived earlier, we get $G^0_{s,H^+_{chm}0} \approx 7 \times 10^{-15}$ S K for $p_{H_2O} = 1$ bar and $G_{s,H^+_{chm}0} \approx 6 \times 10^{-18}$ S K at $p_{H_2O} = 0.03$ bar. By applying $\sigma_{M,s,H^+_{chm}0} = \psi G_{s,H^+_{chm}0}$ from eqn (3) and values of ψ from Table 1, we get predicted preexponentials for macroscopic conductivity of around $\sigma_{M,s,H^+_{chm}0} \approx 4 \times 10^{-13}$ S K cm^{-1} for our samples at p_{H_2O} = 0.03 bar. This low value, dominated by the variable and uncertain but grossly negative entropy of adsorption, is several orders of magnitude below the experimental ones for the surface protonic conductivity in the chemisorbed layer at higher temperatures (Table 2) and the "chm" model can be ruled out.

Dissociation to surface oxide ions

In the other possibility of dissociation, the molecule dissociates into an adsorbed hydroxide ion and a surface hydroxide ion, *i.e.*, it protonates a surface oxide ion ("chm-s" in Fig. 6), as suggested by AIMD simulations on cubic ZrO_2{110} surfaces[9]:

$$M_{M_s}OH_2^\times + O^\times_{O_s} \rightleftharpoons M_{M_s}OH' + OH^\bullet_{O_s} \tag{17}$$

$$\begin{aligned} K_{d_{chs}} &= \frac{X_{M_{M_s}OH'} X_{OH^\bullet_{O_s}}}{X_{M_{M_s}OH_2^\times} X_{O^\times_{O_s}}} = \frac{\gamma_{M_{M_s}OH'} \gamma_{OH^\bullet_{O_s}}}{\gamma_{M_{M_s}OH_2^\times} \gamma_{O^\times_{O_s}}} \\ &= \exp\left(\frac{\Delta S^0_{d_{chs}}}{R}\right) \exp\left(\frac{-\Delta H^0_{d_{chs}}}{RT}\right) \end{aligned} \tag{18}$$

The same analysis as above now yields

$$K_{d_{chs}} = \frac{\gamma^2_{OH^\bullet_{O_s}}}{K_{a_{ch,m}} \gamma_{M_s} \gamma_{O_s} \frac{p_{H_2O}}{p^0}} \Rightarrow \gamma_{OH^\bullet_{O_s}} = \sqrt{K_{a_{chm}} K_{d_{chs}} \gamma_{M_s} \gamma_{O_s} \frac{p_{H_2O}}{p^0}} \tag{19}$$

We may further assume that the proton on surface oxide in the $OH^\bullet_{O_s}$ defect may migrate by jumping to other surface oxide ions, since $M_{M_s}OH'$ it left behind from the dissociation is rare to find. The surface protonic conductance will then be

$$\begin{aligned} G_{s,H^+_{chm-s}} &= F \gamma_{OH^\bullet_{O_s}} u_{H^+_{chm-s}} \\ &= F \gamma_{OH^\bullet_{O_s}} X_{O^\times_{O_s}} u_{H^+0} \frac{1}{T} \exp\left(\frac{-\Delta H_{m,H^+_{chm-s}}}{RT}\right) \end{aligned} \tag{20}$$

Since we have little adsorption and little dissociation, surface oxide ions are generally available, $X_{O^\times_{O_s}} \approx 1$, so that we by inserting eqn (19) get

$$G_{s,H^+_{chm-s}} = F \sqrt{K_{a_{chm}} K_{d_{chs}} \gamma_{M_s} \gamma_{O_s} \frac{p_{H_2O}}{p^0}} u_{H^+0} \frac{1}{T} \exp\left(\frac{-\Delta H_{m,H^+_{chm-s}}}{RT}\right) \tag{21}$$

and hence

$$G_{s,H^+_{chm-s}} = G_{s,H^+_{chm-s}0} \frac{1}{T} \exp\left(\frac{-\left(\frac{1}{2}\Delta H^0_{a_{chm}} + \frac{1}{2}\Delta H^0_{d_{chs}} + \Delta H_{m,H^+_{chm-s}}\right)}{RT}\right) \tag{22}$$

with

$$\begin{aligned} G_{s,H^+_{chm-s}0} &= G^0_{s,H^+_{chm-s}0} \sqrt{\frac{p_{H_2O}}{p^0}} \\ &= F \sqrt{\gamma_{M_s} \gamma_{O_s}} \exp\left(\frac{\frac{1}{2}\Delta S^0_{a_{chm}} + \frac{1}{2}\Delta S^0_{d_{chs}}}{R}\right) u_{H^+0} \sqrt{\frac{p_{H_2O}}{p^0}} \end{aligned} \tag{23}$$

Considering that the concentration of surface oxide adsorption sites in ZrO_2 is twice that of cation sites, *i.e.*, $\gamma_{Os} = 2\gamma_{Ms}$, and other parameters are the same as before, we predict now $G^0_{s,H^+_{chm-s}0} \approx 2 \times 10^{-6}$ S K, $G_{s,H^+_{chm-s}0} \approx 3 \times 10^{-7}$ S K, and $\sigma_{M,s,H^+_{chm-s}0} \approx 2 \times 10^{-2}$ S K cm^{-1}. Sample ST700 has a preexponential of macroscopic conductivity of around 5×10^{-3} S K cm^{-1} (Table 2), *i.e.*, within an order of magnitude of prediction, suggesting that weak molecular adsorption and dissociation to protons transported along surface oxide ions may apply. In this case, the experimental enthalpy should be interpreted according to $\Delta H = \frac{1}{2}\Delta H^0_{a_{chm}} + \frac{1}{2}\Delta H^0_{d_{chs}} + \Delta H_{m,H^+_{chm-s}} \approx 27$ kJ mol^{-1}. The standard enthalpy of molecular chemisorption has been determined calorimetrically as $\Delta H^0_{a_{chm}} = -76 \pm 5$ kJ mol^{-1} for YSZ relatively independent of the Y content.[13] If we adopt a dissociation enthalpy of 22.1 kJ mol^{-1} from ref. 47 used by Raz *et al.*[12] for YSZ, we get an enthalpy for surface mobility of protons of $\Delta H_{m,H^+_{chm-s}} = 54$ kJ mol^{-1}.

The model proposes a proportionality to $p^{1/2}_{H_2O}$ of surface protonic conduction for weakly adsorbed and dissociated chemisorbed water according to eqn (21). This is in line with the experimental results obtained for the ST700 sample at 400 °C (Fig. 5).

All in all, partial coverage of molecularly chemisorbed water, partially dissociated into mobile protonic species, forms a credible model for the surface protonic conductivity at temperatures above 200 °C for samples sintered at the lowest temperatures. Involvement of surface hydroxide as a dissociation product and mobile species fits much better with the observed preexponentials than transport between adsorbed water species. We suggest that this may apply also to other oxides where a similar behaviour is observed, and is a result of surfaces that are relatively amorphous or rounded (*vs.* faceted) or have

terminations where dissociation is unfavourable. While the transfer of a proton to a surface oxide ion is not very favourable, the transfer between oxide ions may be correspondingly easier.

4.4.2 Strong, dissociative chemisorption. Next, we assume as before that H_2O adsorbs on a surface M^{4+} cation (here Zr^{4+}) and dissociates one proton H^+ onto a surface oxide ion O^{2-}. However, now this dissociation step is favourable (exothermic) and strengthens the overall chemisorption (making it more exothermic) and makes a fully covered and dissociated layer at relatively high temperatures (low RH). Dissociative chemisorption ("chd" in Fig. 6) is then a combination of eqn (6) and (17):

$$M_{M_s}^{\times} + O_{O_s}^{\times} + H_2O(g) \rightleftharpoons M_{M_s}OH' + OH_{O_s}^{\bullet} \tag{24}$$

with equilibrium coefficient being the product of eqn (7) and (9):

$$\begin{aligned} K_{a_{chd}} &= K_{a_{chm}} K_{d_{chs}} = \frac{X_{M_{M_s}OH'} X_{OH_{O_s}^{\bullet}}}{X_{M_{M_s}} X_{O_{O_s}^{\times}} \frac{p_{H_2O}}{p_0}} \\ &= \frac{\gamma_{M_{M_s}OH'} \gamma_{OH_{O_s}^{\bullet}}}{\gamma_{M_{M_s}} \gamma_{O_{O_s}^{\times}} \frac{p_{H_2O}}{p^0}} = \exp\left(\frac{\Delta S^0_{a_{chd}}}{R}\right) \exp\left(\frac{-\Delta H^0_{a_{chd}}}{RT}\right) \end{aligned} \tag{25}$$

While we earlier used data for weak molecular chemisorption on ZrO_2, there exist data also for strong dissociative adsorption. From first principles calculations, the enthalpy of dissociative chemisorption on the {001} surface of monoclinic ZrO_2 has been reported to be −165 kJ mol^{-1} for half-monolayer coverage, and −109 kJ mol^{-1} for full-monolayer coverage[48]. Radha *et al.*[8] measured the amount of chemisorbed water on monoclinic ZrO_2 and found that full coverage corresponds to 3.8–5 H_2O per nm^2. From high-temperature oxide melt solution calorimetry on samples annealed at 600 and 800 °C, they found integral enthalpies of dissociative chemisorption at half monolayer coverage (2.2 H_2O per nm^2) and full monolayer coverage of −142 kJ mol^{-1} and −119.5 ± 1.7 kJ mol^{-1}, respectively. With this and aforementioned estimates of the entropy, eqn (25) and the electroneutrality and site balances yield the coverage of cation adsorption sites at p_{H_2O} = 0.03 bar varying from above 90% at the lower end of the temperature range considered for strong dissociative chemisorption here to 50% at higher temperatures. For the interpretation of the exponential changes in conductivity with temperature, these variations are minor (of the order of a factor of 2) in the range where we assign conductivity to transport in the chemisorbed layer. The Arrhenius plots of the surface protonic conductivity for the samples sintered at higher temperatures are indeed linear in the range above 300 °C (Fig. 4). The electroneutrality and assumption of full coverage leads directly to

$$\gamma_{M_{M_s}OH'} = \gamma_{OH_{O_s}^{\bullet}} \approx \gamma_{M_s} \tag{26}$$

indicating that the concentration of dissociated protons is independent of temperature as well as RH and p_{H_2O}, and that the temperature dependence is attributable solely to the mobility of dissociated protons. We assume that the dominating transport mechanism for dissociated protons on ZrO_2 surfaces within the chemisorbed water layer is their jump between their surface oxide host sites, and that these have an average occupancy of $X_{O_{O_s}^{\times}} = 0.5$ since half of them are occupied with dissociated protons. The surface protonic conductance then becomes

$$\begin{aligned} G_{s,H^+_{chd}} &= \frac{F}{2} \gamma_{M_s} u_{H^+0} \frac{1}{T} \exp\left(\frac{-\Delta H_{m,H^+_{chd}}}{RT}\right) \\ &= G_{s,H^+_{chd}0} \frac{1}{T} \exp\left(\frac{-\Delta H_{m,H^+_{chd}}}{RT}\right) \end{aligned} \tag{27}$$

with

$$G_{s,H^+_{chd}0} = G^0_{s,H^+_{chd}0} = \frac{F}{2} \gamma_{M_s} u_{H^+0} \tag{28}$$

With the same assumptions as before, this yields $G_{s,H^+_{chd}0} = G^0_{s,H^+_{chd}0} \approx 4 \times 10^{-4}$ S K, and $\sigma_{M,s,H^+_{chd}0} \approx 20$ S K cm^{-1}, to be compared with the corresponding experimental preexponentials (Table 2) for the chemisorbed layer of 0.1–0.4 S K cm^{-1} for the samples sintered at the highest temperatures. The two orders of magnitude difference may be ascribed to the many approximations along the way, but may also mean that the assumptions of the model comprising fully covered and dissociated chemisorbed water are not fully met. However, we may assign the activation enthalpies of up to 60 kJ mol^{-1} to the diffusion barrier for protons migrating between oxide ions on the faceted surfaces of monoclinic ZrO_2 covered with dissociatively chemisorbed water. The aforementioned comparison to the enthalpy of mobility of protons of 58 kJ mol^{-1} for polycrystalline rutile TiO_2[42] and 43 kJ mol^{-1} as an estimate for 50% La-doped CeO_2[43] is reasonable if the concentration of carriers is constant as in a fully covered chemisorbed layer, which based on the TG result seems reasonable for the samples sintered at the highest temperatures.

The samples sintered at intermediate temperatures show preexponentials and enthalpies between those sintered at the lowest and highest temperatures, and we may expect that they (or in fact all samples) have mixed presence of surface areas with weak molecular and strong dissociated chemisorption.

4.5 Physisorbed layers

4.5.1 Physisorption. Below 150 °C, the conductivities of the samples show a steep increase. This is attributed to the effect of water molecules physisorbed on top of its complete chemisorbed layer. It starts with a structured, relatively rigid (ice-like) first physisorbed layer:

$$v_{H_2O_{ph1}} + H_2O(g) = H_2O_{H_2O_{ph1}} \tag{29}$$

with equilibrium coefficient

$$\begin{aligned} K_{ph1} &= \frac{\gamma_{H_2O_{H_2O_{ph1}}}}{\left(\gamma_{H_2O_{ph1}} - \gamma_{H_2O_{H_2O_{ph1}}}\right) \frac{p_{H_2O}}{p^0}} \\ &= \exp\left(\frac{\Delta S^0_{ph1}}{R}\right) \exp\left(\frac{-\Delta H^0_{ph1}}{RT}\right) \end{aligned} \tag{30}$$

and in a second step builds further, increasingly liquid-like layers:

$$H_2O(g) = H_2O_{ph2} \quad (31)$$

The enthalpy of physisorption starts out a bit more exothermic than condensation into liquid water due to the stronger hydrogen bonds to the chemisorbed layer, and becomes less exothermic and eventually reaches the heat of condensation of water, which is −44.0 kJ mol^{-1} at RT and decreases with increasing temperature, *e.g.* −40.7 kJ mol^{-1} at 100 °C. The number of monolayers of physisorbed water is given by the BET isotherm[49]

$$\frac{v}{v_m} = \frac{c_{BET}\frac{p_{H_2O}}{p_{ce}}}{\left(1-\frac{p_{H_2O}}{p_{ce}}\right)\left(1+(c_{BET}-1)\frac{p_{H_2O}}{p_{ce}}\right)} = \frac{c_{BET}\cdot RH}{(1-RH)(1+(c_{BET}-1)RH)} \quad (32)$$

where v is the volume of adsorbed water, v_m is the volume of one monolayer such that v/v_m gives the surface coverage in number of monolayers, c_{BET} is the so-called BET constant, p_{H_2O} is the partial pressure of water, p_{ce} is the temperature-dependent condensation–evaporation equilibrium partial pressure, and $RH = \frac{p_{H_2O}}{p_{ce}}$. The BET constant is approximated by

$$c_{BET} \cong \exp\left(\frac{E_1 - E_L}{RT}\right) \quad (33)$$

where E_1 is the heat of adsorption for the first layer and E_L for the second and higher layers. E_L is usually more or less equal to the heat of condensation, −44 kJ mol^{-1} at RT and −40.7 kJ mol^{-1} at 100 °C. Here, when the chemisorbed layer is treated separately and we deal only with the physisorbed layers, the energy difference between the first and second physisorbed water layer is expected to be small, but still non-zero; a typical estimate is $E_1 - E_L$ = −4 kJ mol^{-1}.

The equilibrium pressure p_e is a strong function of temperature, which can be expressed by the thermodynamics of vaporisation or condensation as

$$\frac{p_{ce}}{p^0} = \frac{1}{K_{ce}} = \frac{1}{\exp\left(\frac{\Delta S^0_{ce}}{R}\right)\exp\left(\frac{-\Delta H^0_{ce}}{RT}\right)} \quad (34)$$

At RT we have approximate thermodynamic parameters of condensation of $\Delta S^0_{ce,298.15} = -118.9$ J mol^{-1} K^{-1} and $\Delta H^0_{ce,298.15} = -44.0$ kJ mol^{-1}, while at 100 °C, we have $\Delta S^0_{ce,373.15} = -109.0$ J mol^{-1} K^{-1} and $\Delta H^0_{ce,373.15} = -40.7$ kJ mol^{-1}.[45] In the low coverage region of the first physisorbed layer, eqn (30) can be simplified to yield the coverage as

$$X_{H_2O_{H_2O_{ph1}}} = \frac{\gamma_{H_2O_{H_2O_{ph1}}}}{\gamma_{H_2O_{ph1}}} = \frac{v}{v_m} = c_{BET}\frac{p_{H_2O}}{p_{ce}} = c_{BET}RH = \frac{p_{H_2O}}{p^0}K_{ph1} = \frac{p_{H_2O}}{p^0}\exp\left(\frac{\Delta S^0_{ph1}}{R}\right)\exp\left(\frac{-\Delta H^0_{ph1}}{RT}\right) \quad (35)$$

We express this in many ways and using many parameters to stress its significance and simplicity. Here, ΔS^0_{ph1} and ΔH^0_{ph1} are temperature dependent parameters for the first physisorbed layer, expressing the temperature dependency of c_{BET}/p_{ce}. They are close to those of condensation to bulk water, enhanced by the extra few kJ mol^{-1} of exothermic enthalpy because of the extra hydrogen bonds in the first layer bonding to the chemisorbed layer underneath. Eqn (35) is an alternative representation of eqn (32) and (33), more useful for our purpose. From this, we will later on use an estimate that the enthalpy of physisorption for the first physisorbed layer around 100 °C will be $\Delta H^0_{ph1} \approx -(40.7 + 4)$ kJ mol^{-1} ≈ −45 kJ mol^{-1}.

4.5.2 Dissociation and conduction in the first physisorbed water layer. Dissociation of physisorbed water has different possibilities; we will consider and evaluate two of them here.

Dissociation from chemisorbed to physisorbed water

In the first, we assume that chemisorbed molecular water dissociate protons into the physisorbed layer forming H_3O^+ (“chm-ph1” in Fig. 6) so that we have

$$M_{M_s}OH_2^{\times} + H_2O_{H_2O_{ph1}} \rightleftharpoons M_{M_s}OH' + H_3O^{\bullet}_{H_2O_{ph1}} \quad (36)$$

with equilibrium constant

$$K_{d_{chm-ph1}} = \frac{X_{M_{M_s}OH'}X_{H_3O^{\bullet}_{H_2O_{ph1}}}}{X_{M_{M_s}OH_2^{\times}}X_{H_2O_{H_2O_{ph1}}}} = \frac{\gamma_{M_{M_s}OH'}\gamma_{H_3O^{\bullet}_{H_2O_{ph1}}}}{\gamma_{M_{M_s}OH_2^{\times}}\gamma_{H_2O_{H_2O_{ph1}}}} = \exp\left(\frac{\Delta S^0_{d_{chm-ph1}}}{R}\right)\exp\left(\frac{-\Delta H^0_{d_{chm-ph1}}}{RT}\right) \quad (37)$$

If this dominates, we have the following simple electroneutrality:

$$\gamma_{M_{M_s}OH'} = \gamma_{H_3O^{\bullet}_{H_2O_{ph1}}} \quad (38)$$

Moreover, the cation surface site balance assuming full coverage in the chemisorbed layer and low dissociation $\gamma_{M_{M_s}OH_2^{\times}} \approx \gamma_{M_s}$ allows us to insert and combine with physisorption thermodynamics, and get

$$K_{d_{chm-ph1}} = \frac{\gamma_{M_{M_s}OH'}\gamma_{H_3O^{\bullet}_{H_2O_{ph1}}}}{\gamma_{M_s}\gamma_{H_2O_{H_2O_{ph1}}}} = \frac{\gamma^2_{H_3O^{\bullet}_{H_2O_{ph1}}}}{\gamma_{M_s}\gamma_{H_2O_{ph1}}\frac{p_{H_2O}}{p^0}K_{ph1}} \quad (39)$$

which is rearranged into

$$\gamma_{H_3O^{\bullet}_{H_2O_{ph1}}} = \sqrt{K_{d_{chm-ph1}}\gamma_{M_s}\gamma_{H_2O_{ph1}}\frac{p_{H_2O}}{p^0}K_{ph1}} \quad (40)$$

The surface protonic conductance in the 1st physisorbed layer will by this model be

$$G_{s,H^+_{chm-ph1}} = F\gamma_{H_3O^{\bullet}_{H_2O_{ph1}}}u_{H_3O^{\bullet}_{H_2O_{ph1}}} = F\sqrt{K_{d_{chm-ph1}}\gamma_{M_s}\gamma_{H_2O_{ph1}}}\left(\frac{p_{H_2O}}{p^0}K_{ph1}\right)^{3/2} \times u_{H^+0}\frac{1}{T}\exp\left(\frac{-\Delta H_{m,H^+_{chm-ph1}}}{RT}\right) \quad (41)$$

which we may write as follows:

$$G_{s,H^+_{chm-ph1}} = G_{s,H^+_{chm-ph1}0}\frac{1}{T} \times \exp\left(\frac{-\left(\frac{3}{2}\Delta H^0_{ph1} + \frac{1}{2}\Delta H^0_{d_{chm-ph1}} + \Delta H_{m,H^+_{chm-ph1}}\right)}{RT}\right) \quad (42)$$

with

$$G_{s,H^+_{chm-ph1}0} = G^0_{s,H^+_{chm-ph1}0}\left(\frac{p_{H_2O}}{p^0}\right)^{3/2} = F\sqrt{\gamma_{M_s}\gamma_{H_2O_{ph1}}}\exp\left(\frac{\frac{3}{2}\Delta S^0_{ph1} + \frac{1}{2}\Delta S^0_{d_{chm-ph1}}}{R}\right) \times u_{H^+0}\left(\frac{p_{H_2O}}{p^0}\right)^{3/2} \quad (43)$$

If we assume that u_{H^+0} is still of the order of magnitude of 10 $cm^2\ K\ V^{-1}\ s^{-1}$, and that the standard entropy of physisorption is -109 J $mol^{-1}\ K^{-1}$, and that of dissociation is negligible, we obtain $G^0_{s,H^+_{chm-ph1}0} \approx 2.3 \times 10^{-12}$ S K, $G_{s,H^+_{chm-ph1}0} \approx 1.2 \times 10^{-14}$ S K, and $\sigma_{M,s,H^+_{chm-ph1}0} \approx 7 \times 10^{-10}$ S K cm^{-1}. If we assign a negative standard entropy to dissociation, like a small part of what it is in liquid water, the preexponentials decrease further. This is in rough agreement with the experimentally observed preexponentials of conductivity in the 1st physisorbed layer for the samples sintered at the lowest temperatures ($\sim 10^{-9}$ SK cm^{-1}, see Table 2). The corresponding apparent activation enthalpies of around -30 kJ mol^{-1} contain in this case 3/2 times the standard adsorption enthalpy estimated at -45 kJ mol^{-1} as explained earlier, plus half the dissociation enthalpy, which as a first estimate now may be taken as that in water at 100 °C of +42 kJ mol^{-1}, leaving the activation enthalpy of proton mobility at around +17 kJ mol^{-1}, credible in being just somewhat higher than that in liquid water of 12 kJ mol^{-1}.

Furthermore, ST700 revealed an approximate $p^{3/2}_{H_2O}$ dependence of conductivity in the physisorbed region (Fig. 5), in agreement with the predicted results from the current model, suggesting that dissociated protons come from the chemisorbed water layer underneath.

Dissociation within physisorbed water

In a second model, we assume instead that the chemisorbed water is already fully dissociated into surface protons, and that dissociation into the physisorbed layer must originate from physisorbed water molecules themselves ("ph1" in Fig. 6):

$$2H_2O_{H_2O_{ph1}} \rightleftharpoons OH'_{H_2O_{ph1}} + H_3O^\bullet_{H_2O_{ph1}} \quad (44)$$

with equilibrium constant

$$K_{d_{ph1}} = \frac{X_{OH'_{H_2O_{ph1}}} X_{H_3O^\bullet_{H_2O_{ph1}}}}{X^2_{H_2O_{H_2O_{ph1}}}} = \frac{\gamma_{OH'_{H_2O_{ph1}}}\gamma_{H_3O^\bullet_{H_2O_{ph1}}}}{\gamma^2_{H_2O_{H_2O_{ph1}}}} = \exp\left(\frac{\Delta S^0_{d_{ph1}}}{R}\right)\exp\left(\frac{-\Delta H^0_{d_{ph1}}}{RT}\right) \quad (45)$$

If this dominates, we have the following simple electroneutrality:

$$\gamma_{OH'_{H_2O_{ph1}}} = \gamma_{H_3O^\bullet_{H_2O_{ph1}}} \quad (46)$$

Assuming low coverage and low degree of dissociation and that the surface concentration of physisorption sites is the same as that for chemisorption, $\gamma_{H_2O_{ph1}} \approx \gamma_{M_s}$, we may insert and combine with physisorption thermodynamics to get

$$K_{d_{ph1}} = \frac{\gamma^2_{H_3O^\bullet_{H_2O_{ph1}}}}{\gamma^2_{H_2O_{H_2O_{ph1}}}} = \frac{\gamma^2_{H_3O^\bullet_{H_2O_{ph1}}}}{\left(\gamma_{M_s}\frac{p_{H_2O}}{p^0}K_{ph1}\right)^2} \Rightarrow \gamma_{H_3O^\bullet_{H_2O_{ph1}}} = \sqrt{K_{d_{ph1}}}\gamma_{M_s}\frac{p_{H_2O}}{p^0}K_{ph1} \quad (47)$$

The surface protonic conductance in the 1st physisorbed layer will by this model, assuming contributions of jumps from both H_3O^+ and to OH^-, be

$$G_{s,H^+_{ph1}} = 2F\gamma_{H_3O^\bullet_{H_2O_{ph1}}}u_{H_3O^\bullet_{H_2O_{ph1}}} = 2F\sqrt{K_{d_{ph1}}}\gamma_{M_s}\left(\frac{p_{H_2O}}{p^0}K_{ph1}\right)^2 \times u_{H^+0}\frac{1}{T}\exp\left(\frac{-\Delta H_{m,H^+_{ph1}}}{RT}\right) \quad (48)$$

The surface protonic conductance from this process is then

$$G_{s,H^+_{ph1}} = 2G_{s,H^+_{ph1}0}\frac{1}{T}\exp\left(\frac{-\left(2\Delta H^0_{ph1} + \frac{1}{2}\Delta H^0_{d_{ph1}} + \Delta H_{m,H^+_{ph1}}\right)}{RT}\right) \quad (49)$$

where the preexponential of surface protonic conductance is

$$G_{s,H^+_{ph1}0} = G^0_{s,H^+_{ph1}0}\left(\frac{p_{H_2O}}{p^0}\right)^2 = 2F\gamma_{M_s}\exp\left(\frac{2\Delta S^0_{ph1} + \frac{1}{2}\Delta S^0_{d_{ph1}}}{R}\right)u_{H^+0}\left(\frac{p_{H_2O}}{p^0}\right)^2 \quad (50)$$

Under the same assumptions as above, we obtain $G^0_{s,H^+_{ph1}0} \approx 6 \times 10^{-15}$ S K, $G_{s,H^+_{ph1}0} \approx 6 \times 10^{-18}$ S K, and $\sigma_{M,s,H^+_{ph1}0} \approx 3.4 \times 10^{-13}$ S K cm^{-1}, possibly somewhat lower if the entropy of

dissociation is negative like in liquid water. This corresponds well with the experimentally observed preexponentials for the samples sintered at the highest temperatures, see Table 2. The corresponding apparent activation enthalpies approaching -50 kJ mol^{-1} are to compare with twice the estimated standard adsorption enthalpy of -45 kJ mol^{-1} plus half the dissociation enthalpy, which as a first estimate may be taken as that in liquid water at 100 °C of +42 kJ mol^{-1}, leaving the activation enthalpy of proton mobility at 19 kJ mol^{-1}, again a credible assessment. The difference to the preceding model is the expected effect of half the adsorption enthalpy.

There is a $p^2_{H_2O}$-dependency of this latter model *vs.* a $p^{3/2}_{H_2O}$-dependency of the preceding one. Sun *et al.*[39] report $p^2_{H_2O}$-dependency for surface conduction in the 1st physisorbed layer on undoped more facetted CeO_2, supporting our assumption that ZrO_2 samples sintered at high temperatures take place by this last model, *i.e.*, by dissociation and migration in the physisorbed layer.

4.6 Summarising discussion

Table 3 summarises the derived p_{H_2O} dependencies along with the predicted estimates of preexponentials we have arrived at in this work for surface protonic conduction in the chemisorbed and 1st physisorbed layer of water of porous oxides. The experimental values for ST700 and ST1100, representing samples sintered at low and high temperatures, representatively, are included in the same table for easier comparison.

For the sake of completion, we mention here again that as RH surpasses 60%, *i.e.*, below 50 °C at p_{H_2O} = 0.03 bar, a 2nd liquid-like physisorbed layer is expected with strong increase in conductivity as temperature decreases further, as observed for, *e.g.*, porous YSZ[15] and TiO_2,[33] but this was not evidenced in this study of monoclinic ZrO_2.

The temperature dependency of the conductivity can be measured and modelled at constant RH instead of constant p_{H_2O}. With the exception of the modest effect of c_{BET}, a constant RH yields a constant coverage, as one may see in the mathematics derived here. All models, except strong dissociative chemisorption, then come out with an activation enthalpy given by half the dissociation enthalpy plus the migration enthalpy: $\Delta H_{RH} \approx \frac{1}{2}\Delta H^0_d + \Delta H_{m,H^+}$. Stub *et al.*[15] did this for YSZ in the region of physisorption, and for constant RHs in the range of 20–60% obtained enthalpies of 43–34 kJ mol^{-1}. Colomer[50] studied the proton conductivity of nanoporous anatase TiO_2 thin films as a function of temperature (from 25 to 80 °C) at different RH values, and found the activation enthalpies to be 36 kJ mol^{-1} at RH of 33%, and 33 kJ mol^{-1} at RH of 58%. These results are in agreement with our assessment for ZrO_2 of 38–40 kJ mol^{-1} measured at constant p_{H_2O} after subtraction of the estimated enthalpies of adsorption according to the two models applied for surface protonic conduction in the 1st physisorbed layer.

It appears that the surface protonic conductivity in the porous samples of ZrO_2 sintered at low and high temperatures can be rationalised with simple models of adsorption, dissociation, and transport. But why do well-sintered and presumably well-faceted surfaces show a stronger more dissociative chemisorption, while the less developed surfaces show weaker, molecular chemisorption? During annealing at high temperatures, the system lowers its excess surface and grain boundary energies by sintering and grain growth, but the type of surface and hence area-specific surface energy and adsorption behaviour may still be the same. In faceting, on the other hand, random surfaces from particle growth during synthesis, or from milling, transform into more stable, usually low-index surfaces. However, the lower-energy facets should adsorb water less strongly, so this explanation seems not to hold. But if the low-sintered samples have a large amount of amorphous surfaces, not yet faceted at all, they are believed from general adsorption theory to have low surface energies by the freedom to arrange terminations variably along the surface, with less gain in adsorbing gases like water. This would explain our

Table 3 Derived p_{H_2O} dependencies and predicted preexponentials for the five models of protonic surface transport in the chemisorbed layer and 1st physisorbed layer, for porous MO_2 oxides in general, and in the case of conditions and microstructures employed in this study, compared with the experimental values of the same parameters for ST700 and ST1100. The preexponentials are rounded off to one significant digit, but the realistic predictive power is much less accurate, rather within 1–2 orders of magnitude due to the many assumptions mainly in adsorption thermodynamics and transport parameters

Derived values according to the five models					
Layer of adsorption	Chemisorbed layer			1st physisorbed layer	
Model notation	chm	chm-s	chd	chm-ph1	ph1
p_{H_2O} dependency, n in $p^n_{H_2O}$	2	1/2	0	3/2	2
G^0_{s,H^+0} (S K), p_{H_2O} = 1 bar	7×10^{-15}	2×10^{-6}	4×10^{-4}	2×10^{-12}	6×10^{-15}
G_{s,H^+0} (S K), p_{H_2O} = 0.03 bar	6×10^{-18}	3×10^{-7}	4×10^{-4}	1×10^{-14}	6×10^{-18}
σ_{M,s,H^+0} (S K cm^{-1}), p_{H_2O} = 0.03 bar, $\psi = 6 \times 10^4$ cm^{-1}	4×10^{-13}	2×10^{-2}	2×10^{1}	7×10^{-10}	3×10^{-13}

Experimental values (p_{H_2O} = 0.03 bar)		
Layer of adsorption	Chemisorbed layer	1st physisorbed layer
$\sigma_{M\ 0}$ (S K cm^{-1}), ST700	5×10^{-3}	6×10^{-9}
$\sigma_{M\ 0}$ (S K cm^{-1}), ST1100	1×10^{-1}	4×10^{-13}
n in $p^n_{H_2O}$ for ST700	0.6	1.5

observations. But why do amorphous surfaces crystallise and facet if they already have low energies? This would be because the subsurface lattice decreases its energy in crystallisation, while the surface itself may increase in energy.

If our interpretations hold, the samples sintered at low temperatures, exhibiting weak molecular chemisorption, have physisorbed water that dissociates protons from the chemisorbed water underneath ("chm-ph1" in Fig. 6). In comparison, the samples sintered at high temperatures have dissociation from the physisorbed water itself ("ph1" in Fig. 6), because the strongly dissociated chemisorbed water on the high temperature sintered samples has no more protons to offer; they have all gone to the oxide surface, where they are immobile due to their high activation energy and the now low temperature. Hence, the conduction in the physisorbed layer can now only arise from dissociation within the physisorbed layer itself. It appears intuitive that the steep increase in conductivity with increasing coverage of this layer then must imply that mobility has less activation enthalpy here than on the oxide surface, and indeed the derived enthalpies of mobility go from those typical of solid-state proton mobility towards those typical of liquid water. We note that both still reflect Grotthuss proton jumps.

5 Conclusions

Our impedance spectrometric study of the surface protonic conductivity *vs.* temperature in wet atmospheres of porous undoped monoclinic ZrO_2 sintered at five different temperatures has allowed us to forward models for interpretation and parameterisation of surface protonic conduction that may be applied to porous oxides in general. The dual time constants in the high frequency part of the impedance spectra with capacitances in the geometric (bulk) range are omnipresent and attributable to different capacitances over concave and convex surface paths of porous microstructures. A simple brick layer model (BLM) connects measured preexponentials of macroscopic surface protonic conductivity σ_{M,s,H^+0} to the predicted values from credible models of preexponentials G_{s,H^+0} of surface protonic conductance. Along with p_{H_2O} dependencies and credible enthalpies, this enables discrimination between models.

The surface protonic conductivity in wet atmospheres above 200 °C is attributed to the chemisorbed water monolayer. Samples sintered at low temperatures have activation enthalpies as low as 30 kJ mol^{-1}, along with an observed $p_{H_2O}^{1/2}$ dependency, and preexponentials expected for water weakly chemisorbed to surface cations and weakly dissociated into protons on and migrating between surface oxide ions. (Dissociation to and migration between adsorbed water molecules have a predicted preexponential orders of magnitude away from experimental values, and can be ruled out.) Samples sintered at higher temperatures display higher activation energies and preexponentials, expected for strong, near complete dissociative chemisorption, driven by a more exothermic dissociation to surface oxide ions. The activation enthalpy of conductivity of up to 58 kJ mol^{-1} can then be interpreted as that of mobility of protons on surface oxide ions. The smaller enthalpy for the samples sintered at low temperatures can be understood as a combination of incomplete exothermic molecular adsorption, unfavourable endothermic dissociation, and easier mobility of protons on surface oxide ions than in the case of the surface with strong dissociative chemisorption. In other words, the well-faceted surfaces are relaxed by protons that bond strongly and are hard to move, while the random surfaces have less affinity for protons, allowing those that are there to move more easily.

The surface protonic conductivity in wet atmospheres below around 150 °C and down to around 50 °C can be attributed to the first physisorbed water monolayer. The apparent negative enthalpies are readily attributed to a lower activation energy of mobility now overtaken by the negative enthalpy of physisorption contributing strongly because more than one water molecule is now involved to dissociate and migrate a proton. The samples sintered at low temperatures have preexponentials and $p_{H_2O}^{3/2}$ dependency suggesting that the dissociated protons come from the chemisorbed layer, while for the samples sintered at high temperatures, they seem to come from the physisorbed layer itself (autoprotolysis), supported by the difference in enthalpies. The measured enthalpies fit to the models if physisorption is assumed to have an enthalpy of −45 kJ mol^{-1}, dissociation has +42 kJ mol^{-1} like in water, and mobility has around 17 kJ mol^{-1}, close to that in liquid water. To our understanding, the difference between samples of ZrO_2 sintered at low and high temperatures must be related to crystallisation and faceting from a more amorphous state of the surface.

All in all, surface protonic conductivity data can be credibly modelled with simple thermodynamics and transport. It is noteworthy how all thermodynamics of adsorption and dissociation and proton mobility terms change completely from the chemisorbed to the physisorbed layers, giving them their widely different temperature dependencies. In the chemisorbed layer, we have favourable adsorption, weakly or strongly favourable dissociation, and difficult migration. In the physisorbed layer, adsorption is weak and dissociation is hard, but migration is easy. We point out how preexponentials and isothermal p_{H_2O} dependencies of conductivity can discriminate between models.

Author contributions

JG and XS fabricated the samples and performed characterisation and electrical measurements. XS and JG interpreted and plotted the results and fitted them to the models. XS performed and interpreted TG. DH and TN conceived and supervised the experimental study. XS and TN developed the models and wrote the first manuscript draft. All authors contributed to revision and checking of the final manuscript.

Conflicts of interest

There are no conflicts to declare.

Acknowledgements

JG and DH acknowledge support from the Natural Science Foundation of Jiangsu Province (Grant No. BK20211071) and the Key Technology Initiative of Suzhou Municipal Science and Technology Bureau (Grant No. SYG202011). XS and TN acknowledge support from The Research Council of Norway (RCN) through projects MoZEES (257653) and SUPROX (280868). The authors acknowledge valuable experimental support from MSc. Lulu Jiang, Soochow University.

References

1 L. Almar, *et al.*, Mesoporous ceramic oxides as humidity sensors: A case study for gadolinium-doped ceria, *Sens. Actuators, B*, 2015, **216**, 41–48.
2 J. Y. Li, C. X. Sun and S. A. Sebo, Humidity and contamination severity impact on the leakage currents of porcelain insulators, *Gener. Transm. Distrib. IET*, 2011, **5**, 19–28.
3 M. T. Colomer, Nanoporous anatase ceramic membranes as fast-proton-conducting materials, *J. Eur. Ceram. Soc.*, 2006, **26**(7), 1231–1236.
4 S. Kim, *et al.*, Unprecedented room-temperature electrical power generation using nanoscale fluorite-structured oxide electrolytes, *Adv. Mater.*, 2008, **20**(3), 556–559.
5 L. Malavasi, C. A. Fisher and M. S. Islam, Oxide-ion and proton conducting electrolyte materials for clean energy applications: Structural and mechanistic features, *Chem. Soc. Rev.*, 2010, **39**(11), 4370–4387.
6 D. Poetzsch, R. Merkle and J. Maier, Proton uptake in the H^+-SOFC cathode material $Ba_{0.5}Sr_{0.5}Fe_{0.8}Zn_{0.2}O_3$-delta: Transition from hydration to hydrogenation with increasing oxygen partial pressure, *Faraday Discuss.*, 2015, **182**, 129–143.
7 Y. Hisai, *et al.*, Enhanced activity of catalysts on substrates with surface protonic current in an electrical field – A review, *Chem. Commun.*, 2021, **57**(47), 5737–5749.
8 A. V. Radha, *et al.*, Surface enthalpy, enthalpy of water adsorption, and phase stability in nanocrystalline monoclinic zirconia, *J. Am. Ceram. Soc.*, 2009, **92**(1), 133–140.
9 R. Sato, *et al.*, Proton migration on hydrated surface of cubic ZrO_2: Ab initio molecular dynamics simulation, *J. Phys. Chem. C*, 2015, **119**(52), 28925–28933.
10 R. Sato, *et al.*, Effects of CO_2 adsorption on proton migration on a hydrated ZrO_2 surface: An ab initio molecular dynamics study., *Phys. Chem. Chem. Phys.*, 2017, **19**(30), 20198–20205.
11 S. T. Korhonen, M. Calatayud and A. O. I. Krause, Stability of hydroxylated (111) and (101) surfaces of monoclinic zirconia: A combined study by DFT and infrared spectroscopy, *J. Phys. Chem. C*, 2008, **112**(16), 6469–6476.
12 S. Raz, *et al.*, Characterization of adsorbed water layers on Y_2O_3-doped ZrO_2, *Solid State Ionics*, 2001, **143**(2), 181–204.
13 G. C. C. Costa, *et al.*, Calorimetric measurement of surface and interface enthalpies of yttria-stabilized zirconia (YSZ), *Chem. Mater.*, 2010, **22**(9), 2937–2945.
14 B. Scherrer, *et al.*, On proton conductivity in porous and dense yttria stabilized zirconia at low temperature, *Adv. Funct. Mater.*, 2013, **23**(15), 1957–1964.
15 S. Ø. Stub, E. Vøllestad and T. Norby, Mechanisms of protonic surface transport in porous oxides: Example of YSZ, *J. Phys. Chem. C*, 2017, **121**(23), 12817–12825.
16 S. Ø. Stub, E. Vøllestad and T. Norby, Protonic surface conduction controlled by space charge of intersecting grain boundaries in porous ceramics, *J. Mater. Chem. A*, 2018, **6**(18), 8265–8270.
17 S. Kim, *et al.*, On the conduction pathway for protons in nanocrystalline yttria-stabilized zirconia, *Phys. Chem. Chem. Phys.*, 2009, **11**(17), 3035–3038.
18 E. M. Kock, *et al.*, Structural and electrochemical properties of physisorbed and chemisorbed water layers on the ceramic oxides Y_2O_3, YSZ, and ZrO_2, *ACS Appl. Mater. Interfaces*, 2016, **8**(25), 16428–16443.
19 S. Miyoshi, *et al.*, Water uptake and conduction property of nano-grained yttria-doped zirconia fabricated by ultra-high pressure compaction at room temperature, *Solid State Ionics*, 2012, **207**, 21–28.
20 S. Miyoshi, *et al.*, Low-temperature protonic conduction based on surface protonics: An example of nanostructured yttria-doped zirconia, *Chem. Mater.*, 2014, **26**(18), 5194–5200.
21 S. Hayun, T. Y. Shvareva and A. Navrotsky, Nanoceria – Energetics of surfaces, interfaces and water adsorption, *J. Am. Ceram. Soc.*, 2011, **94**(11), 3992–3999.
22 P. A. Thiel and T. E. Madey, The interaction of water with solid-surfaces – Fundamental-aspects, *Surf. Sci. Rep.*, 1987, **7**(6–8), 211–385.
23 G. Gregori, M. Shirpour and J. Maier, Proton conduction in dense and porous nanocrystalline ceria thin films, *Adv. Funct. Mater.*, 2013, **23**(47), 5861–5867.
24 M. Shirpour, *et al.*, On the proton conductivity in pure and gadolinium doped nanocrystalline cerium oxide, *Phys. Chem. Chem. Phys.*, 2011, **13**(3), 937–940.
25 K. Murakami, *et al.*, Key factor for the anti-Arrhenius low-temperature heterogeneous catalysis induced by H^+ migration: H^+ coverage over support, *Chem. Commun.*, 2020, **56**(23), 3365–3368.
26 P. Simons, K. P. Torres and J. L. M. Rupp, Careful choices in low temperature ceramic processing and slow hydration kinetics can affect proton conduction in ceria, *Adv. Funct. Mater.*, 2021, **31**(31), 2009630.
27 D. R. Mullins, The surface chemistry of cerium oxide, *Surf. Sci. Rep.*, 2015, **70**(1), 42–85.
28 S. Ø. Stub, *et al.*, The influence of acceptor and donor doping on the protonic surface conduction of TiO_2, *Phys. Chem. Chem. Phys.*, 2018, **20**(23), 15653–15660.
29 I. G. Tredici, *et al.*, Mechanism of low-temperature protonic conductivity in bulk, high-density, nanometric titanium oxide, *Adv. Funct. Mater.*, 2014, **24**(32), 5137–5146.
30 J. Gao, *et al.*, Insights into the proton transport mechanism in TiO_2 simple oxides by in situ Raman spectroscopy, *ACS Appl. Mater. Interfaces*, 2020, **12**(34), 38012–38018.

31 A. Y. Nosaka, *et al.*, Characteristics of water adsorbed on TiO_2 photocatalytic systems with increasing temperature as studied by solid-state ^{1}H NMR spectroscopy, *J. Phys. Chem. B*, 2004, **108**(26), 9121–9125.
32 X. W. Sun, *et al.*, Photocatalytic generation of gas phase reactive oxygen species from adsorbed water: Remote action and electrochemical detection, *J. Environ. Chem. Eng.*, 2021, **9**(2), 104809.
33 X. L. Kang, *et al.*, Facet-engineered TiO_2 nanomaterials reveal the role of water-oxide interactions in surface protonic conduction., *J. Mater. Chem. A*, 2022, **10**(1), 218–227.
34 G. Cerrato, *et al.*, A surface study of monoclinic zirconia (m-ZrO_2), *Surf. Sci.*, 1997, **377**(1–3), 50–55.
35 S. Kouva, *et al.*, Review: Monoclinic zirconia, its surface sites and their interaction with carbon monoxide, *Catal. Sci. Technol.*, 2015, **5**(7), 3473–3490.
36 O. H. Kwon, *et al.*, Investigation of the electrical conductivity of sintered monoclinic zirconia (ZrO_2), *Ceram. Int.*, 2017, **43**(11), 8236–8245.
37 T. Norby, Direct-current conductivity of Y_2O_3 as a function of water vapor pressure, *J. Am. Ceram. Soc.*, 1986, **69**(11), 780–783.
38 A. Weibel, *et al.*, The big problem of small particles: A comparison of methods for determination of particle size in nanocrystalline anatase powders, *Chem. Mater.*, 2005, **17**(9), 2378–2385.
39 X. Sun, N. G. Kalantzopoulos, E. Vøllestad, A. Chatzitakis and T. Norby, Surface protonic conductivity in chemisorbed and physisorbed water layers in porous nanoscopic CeO_2, to be submitted.
40 E. Mamontov, Dynamics of surface water in ZrO_2 studied by quasielastic neutron scattering, *J. Chem. Phys.*, 2004, **121**(18), 9087–9097.
41 E. N. S. Muccillo and M. Kleitz, Impedance spectroscopy of Mg-partially stabilized zirconia and cubic phase decomposition, *J. Eur. Ceram. Soc.*, 1996, **16**(4), 453–465.
42 S. Erdal, *et al.*, Hydration of rutile TiO_2: Thermodynamics and effects on n- and p-type electronic conduction, *J. Phys. Chem. C*, 2010, **114**(19), 9139–9145.
43 L. E. Kalland, *et al.*, Structure, hydration, and proton conductivity in 50% La and Nd doped CeO_2–$La_2Ce_2O_7$ and $Nd_2Ce_2O_7$ – and their solid solutions, *Solid State Ionics*, 2020, **354**, 115401.
44 R. Anez, *et al.*, Stabilization of the (110) tetragonal zirconia surface by hydroxyl chemical transformation, *Surf. Sci.*, 2009, **603**(16), 2526–2531.
45 A. H. Harvey, Thermodynamic Properties of Water: Tabulation from the lAPWS Formulation 1995 for the Thermodynamic Properties of Ordinary Water Substance for General and Scientific Use, U.S.D.o. Commerce, Editor. 1998, National Institute of Standards and Technology: Technology Administration.
46 E. McCafferty and A. Zettlemoyer, Entropy of adsorption and the mobility of water vapor on α-Fe_2O_3, *J. Colloid Interface Sci.*, 1970, **34**(3), 452–460.
47 M. A. Blesa, A. J. G. Maroto and A. E. Regazzoni, Surface acidity of metal oxides immersed in water: A critical analysis of thermodynamic data, *J. Colloid Interface Sci.*, 1990, **140**(1), 287–290.
48 I. M. Iskandarova, *et al.*, First-principle investigation of the hydroxylation of zirconia and hafnia surfaces, *Microelectron. Eng.*, 2003, **69**(2), 587–593.
49 S. Brunauer, P. H. Emmett and E. Teller, Adsorption of gases in multimolecular layers, *J. Am. Chem. Soc.*, 1938, **60**(2), 309–319.
50 M. T. Colomer, Nanoporous anatase thin films as fast proton-conducting materials, *Adv. Mater.*, 2006, **18**(3), 371–374.

Supplementary information (SI)

Quantifiable models for surface protonic conductivity in porous oxides – case of monoclinic ZrO_2

Xinwei Sun,[a] ‡ Jie Gu,[b] ‡ Donglin Han,[b] * Truls Norby[a,b] *

[a] Department of Chemistry, University of Oslo, Centre for Materials Science and Nanotechnology (SMN), FERMiO, Gaustadalléen 21, NO-0349 Oslo, Norway

[b] College of Energy, Soochow University, No 1 Shizi Street, Gusu District, Suzhou, 215006, China

‡ Equal first authors

* Corresponding authors: dlhan@suda.edu.cn , truls.norby@kjemi.uio.no

SI 1 List of symbols and abbreviations

Table S1 Lists of symbols for variables and constants and abbreviations for sub- and subscripts.

Variables, constants	Unit	Description	Comment
a		Activity	
A		Geometric factor	
c_{BET}		BET constant	
c	mol/cm^3	Volume concentration	
C	F	Capacitance	
D	cm^2/s	Random diffusion coefficient	
d_g	cm	Grain and pore size	
E	kJ/mol	Heat of adsorption	Enters in c_{BET}
F	C/mol	Faraday constant	96485 C/mol
G	S	Conductance	
ΔH	kJ/mol	Enthalpy change	
K		Equilibrium coefficient	
l	cm	Length of surface layer sheet	
M		Metal	M = Ti, Zr, Ce…
M_m	g/mol	Molar mass	
p	bar	Partial pressure	
R	J/molK	Gas constant	8.3144 J/molK
R	ohm	Resistance	
RH		Relative humidity	$= p_{H_2O} / p_{ce}$
s	cm	Jump distance	
ΔS	J/molK	Entropy change	
SSA_g	cm^2/g	Specific surface area, gravimetric	
SSA_v	cm^2/cm^3	Specific surface area, volumetric	
SSA_m	cm^2/mol	Specific surface area, molar	

T	K	Absolute temperature	
t	cm	Thickness of surface layer	
u	cm^2K/Vs	Charge mobility	
w	cm	Width of surface layer sheet	
X		Site fraction	
Z	ohm	Impedance	
γ	mol/cm^2	Surface concentration	Gamma
ε_0	F/cm	Vacuum permittivity	$8.854 \cdot 10^{-14}$ F/cm
ε_e	F/cm	Effective dielectric constant	Epsilon
ε_r		Relative dielectric constant	Epsilon
θ		Surface coverage	Theta, $= \nu / \nu_m$
ν	mol/cm^2	Molar concentration of physisorbed water	Nu
ν_m	mol/cm^2	Molar concentration of a monolayer of water	Nu
ξ		Percolation power	Xi
ρ	g/cm^3	Density	Actual material
ρ_r		Relative density	Rho
ρ_t	g/cm^3	Theoretical density	Dense material
σ	S/cm	Conductivity	Sigma
ψ	1/cm	BLM porosity surface factor	Psi, $= \sigma_{M,s} / G_s$
ω_0	1/s = Hz	Vibrational attempt frequency	Omega
Subscripts			
1st level	2nd level		
a		adsorption	
	chm	chemisorbed molecular	
	chd	chemisorbed dissociative	
	ph1	1st physisorbed	
	ph2	2nd physisorbed	
d		dissociation	
	chm	in chemisorbed molecular layer	
	chm-s	from chemisorbed molecular layer to surface	
	chm-ph1	from chemisorbed molecular to 1st physisorbed	
	ph1	in 1st physisorbed layer	
m		migration	= diffusion
m,H^+		migration of H^+	Grotthuss
m,H_3O^+		migration of H_3O^+	vehicular in ph2
0		preexponential	like in u_0 and G_0
M		Macroscopic	like in σ_M
s		surface	like in G_s
L and Lp		One layer and one layer with effect of percolation	in $G_{s,L}$ and $G_{s,Lp}$
ce		condensation equilibrium	in p_{ce} and K_{ce}
r		relative	like in ρ_r and ε_r
geom		geometric	
cvex		convex	
cave		concave	
Superscript			
0		standard	like in p^0 and G^0

SI 2 Impedance spectra

Representative impedance spectra of samples sintered at low and high temperatures, measured at low and high temperatures, and in wet or dry atmosphere, are shown in Figure S1. The main

features are described in the main text, while we in SI 3 provide a more detailed assessment of the origin and parameters of the two high-frequency responses.

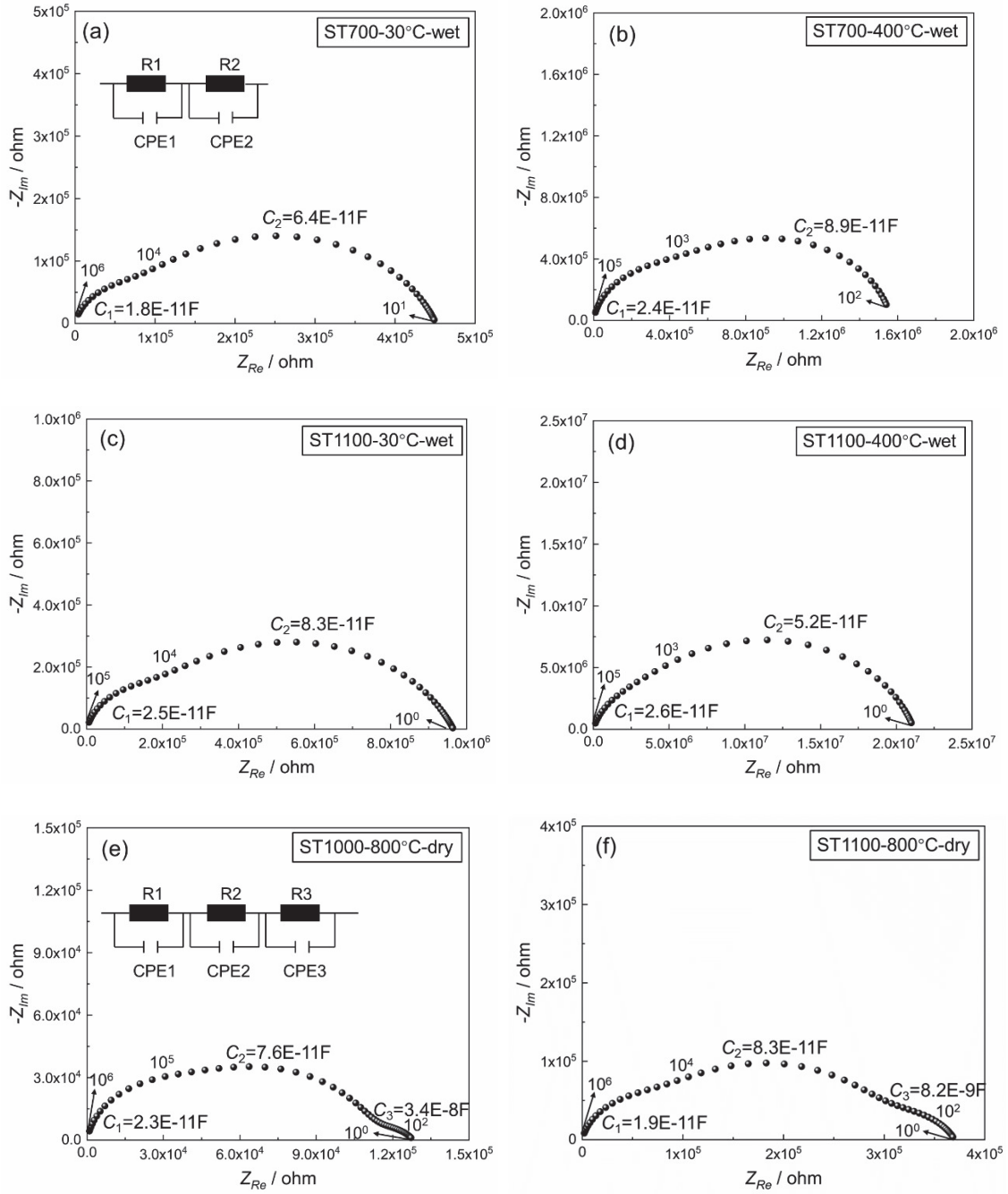

Figure S1. Impedance spectra ($-Z_{im}$ vs Z_{Re} in ohms) as measured at 30°C (a and c), 400°C (b and d) in wet (p_{H_2O} = 0.03 bar) Ar and at 800°C (e and f) in dry Ar for the samples sintered at 700°C (a and b), 1000°C (e), and 1100°C (c, d, f). The equivalent circuit used to model the data was either $(R_1Q_1)(R_2Q_2)$ in wet (exemplified in (a)) or $(R_1Q_1)(R_2Q_2)(R_3Q_3)$ in dry (exemplified in (e)). Numbers along the curve show the AC frequencies. Characteristic capacitances for the two or three responses are indicated (these include the parasitic capacitance of the ProboStat™ cell, which in the configuration used amounts to a few pF).

SI 3 Origin of the two high-frequency responses

The presence of two time constants associated with high frequencies and small bulk-like capacitances in these samples as well as in other porous ceramics with surface protonic

conduction could be attempted rationalised as due to intersecting grain boundaries or part of the electrode impedance. However, the high-temperature spectra in this study shows that the two high-frequency responses are well separated from the third response at lower frequencies that may be grain boundaries or electrodes. Moreover, the omnipresence of these dual time constants for all samples and conditions in this work and other studies of surface conduction in porous ceramics suggests that a more intrinsic phenomenon is at play.

Consider first two electrodes connected to a porous sample with no conductivity. It will have a dielectric response corresponding to the effective dielectric constant $\varepsilon_e = \varepsilon_{re}\varepsilon_0$ given by those of the gas phase (approximated by that of vacuum) and the ceramic phase, to a first approximation weighted by the relative density:

$$\varepsilon_{re} = 1 + (\varepsilon_r - 1)\rho_r \quad \text{and} \quad \varepsilon_e = \varepsilon_0(1 + (\varepsilon_r - 1)\rho_r) \qquad \textbf{Eq. 1}$$

For bulk monoclinic ZrO_2, the relative dielectric constant is approximately 20 [1], so that with 60% relative density, we will have $\varepsilon_{re} \approx 12$ and $\varepsilon_e \approx 10^{-10}$ F/m = 10^{-12} F/cm. Our samples with thickness 0.20 cm and electrode area 1.27 cm^2 would be expected to exhibit a geometric capacitance of $C_{geom} \approx 6 \cdot 10^{-12}$ F. With the addition of parasitic cell capacitance, this corresponds acceptably to the smallest capacitance responses in Figure SI 1.

If conduction would take place in the bulk of the grains, or along parallel surfaces, the response will be given by a simple circuit of the conductance and the capacitance in parallel, yielding a single bulk-like semicircle in a Nyquist plot. However, if the surface is curved, it will have convex features, like rounded and edged grains, and concave features, like grain necks. When the current passes over a convex feature, it will have a longer way to go in the conductive surface layer, but the parallel capacitance through the dielectric material of the grain gives this part of the transport a higher ratio between the parallel capacitance and the conductance compared to the average sample. In contrast, passing a concave part offers little capacitance from the gas phase there. Hence, the sample response would break up into a $(R_{cave}C_{cave})(R_{cvex}C_{cvex})$ type circuit, where the first part attributed to the concave features has low capacitance and high-frequency response, and the second one attributed to convex features has higher capacitance and a lower-frequency response. As an alternative, one may assign the geometric capacitance C_{geom} in parallel over a series connection of the concave part resistance and the parallel $(R_{cvex}C_{cvex})$ element: $(C_{geom}(R_{cave}(R_{cvex}C_{cvex})))$.

Deriving parameters from a simple 3D model microstructure is a mathematical exercise beyond the scope of this work. In reality, parameters are even more complicated to predict and analyse and may be expected to be dispersed due to variations in real microstructures. Hence, a very first step in this direction is to assign constant phase elements Q_{cvex} instead of C_{cvex} and use circuits $(R_{cave}C_{cave})(R_{cvex}Q_{cvex})$ or $(C_{geom}(R_{cave}(R_{cvex}Q_{cvex})))$.

Regardless of the difficulty to apply a geometrically correct model, the total surface resistance is $R_{tot} = R_{cave} + R_{cvex}$. We may furthermore predict that $R_{cvex}/R_{cave} > 1$ due to the long path around convex features compared with the short path across concave features like grain necks. In this work, the ratio is indeed typically 2-4. Somewhat larger ratios are being reported for porous

nanoscopic CeO_2 [2] while TiO_2 [3] with oriented grains have indications of larger ratios, that may reflect the sharper transitions between grains for materials crystallised rather than sintered.

The ratio between capacitances should be $C_{cvex}/C_{cave} > 1$, and predicted to reflect to a first approximation the ratio between the dielectric constant of the ceramic and the gas phase. The ratio of 2-4 in this work is considerably smaller, and we note that it is remarkably similar to the ratio of the resistances.

SI 4 Temperature dependence of conductivities

The temperature dependencies of the electrical conductivity extracted from the sum of resistances of the two high-frequency responses (as explained above) for all samples are shown in Figure S2.

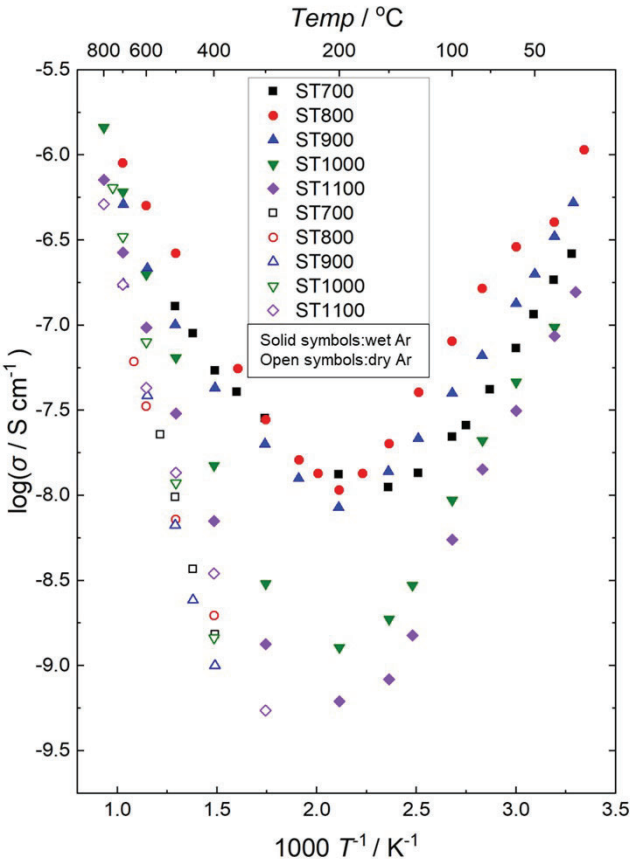

Figure S2 Plot of logσ vs 1/T in wet (p_{H_2O} = 0.03 bar) or bottle-dry Ar for samples sintered at different temperatures shown in the legend.

The results comprise samples manufactured and measured in the collaborating laboratories in China and Norway over a time span of several months, underlining the robustness of the temperature dependencies of the data.

Another sample ST800 was measured in wet O_2, and showed qualitatively the same conductivities and temperature dependencies as ST800 and the other samples measured in wet

Ar, suggesting that the oxygen partial pressure plays no significant role for ZrO_2, unlike what it does in CeO_2. [2, 4]

SI 5 Brick layer model (BLM) for surface conduction and SSA

Here, we first introduce briefly a simple brick layer model (BLM) for surface conduction in porous materials. Let us divide the volume of a porous material with equal grain diameters and pore diameters d_g into cubic bricks of the same size d_g so that there are $1/d_g$ bricks in each unit length direction and $1/d_g^2$ per unit area. The bricks are statistically grains or pores. We may count surfaces as belonging to grains or pores; we choose to count surfaces as belonging to grains. The chance that a brick is a grain is proportional to the relative density ρ_r.

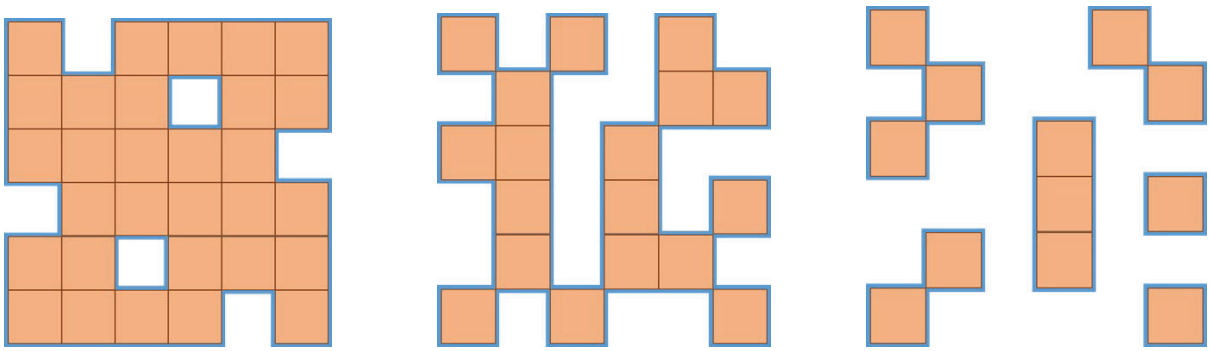

Figure S3. Schematic single layers of 6 x 6 brick "random" porous microstructures viewed from above, into the direction of conduction. Coloured bricks are grains, grain boundaries are thin black lines, surfaces with adsorbed water are thick blue lines. Densities are 5/6 (≈83%, left), ½ (50%, middle), and 2/3 (≈33%, right). Statistical numbers of conducting surfaces according to the model are, respectively, 20, 36, and 32 while actual numbers in a repeating matrix (counting only half the side surfaces) of these "random" examples of a small number of bricks are, respectively, 22, 45, and 36. Their overestimation of surfaces stems from the human rather than statistical selection of the microstructure.

In the direction of conduction, only 4 of the 6 sides (2/3) of a grain can contribute a conducting surface, and only if the neighbouring brick is a pore. For unit area of one layer of bricks, the number of grain side surfaces is thus $4\rho_r(1-\rho_r)/d_g^2$. This is a simple function that goes through a maximum of $1/d_g^2$ at 50% relative density $\rho_r = 0.5$. The surface conductance $G_{s,L}$ through one layer of bricks is obtained by multiplying with the side sheet surface conductance:

$$G_{s,L} = \frac{4\rho_r(1-\rho_r)}{d_g^2} G_s \qquad \text{Eq. 2}$$

Now, we consider the chance of percolation, i.e., the chance that a surface meets a new surface in the next layer. We take this to be the same that an interface is a surface, namely $\rho_r(1-\rho_r)$. Hence, the area specific number of connected conducting surfaces through one layer that percolates to the next is $4\rho_r^2(1-\rho_r)^2/d_g^2$. This is still a simple function with maximum at a relative density of 50%, now down at 0.25 conducting surfaces per brick, 0.5 per grain.

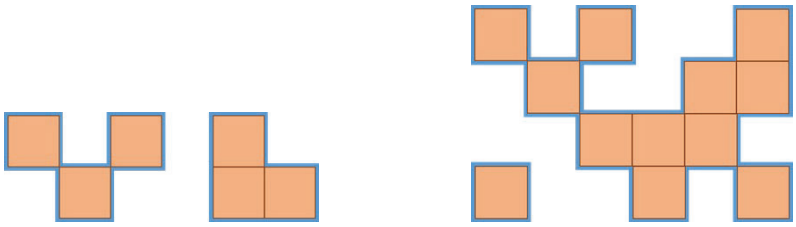

Figure S4. Schematic side views of the now vertical direction of conduction for examples of 2-layer (left) and 4-layer (right) brick structures both with 50% density. The 2-layer example shows that the top layer has 5 internal and one shared conducting surface, totalling at 5½, while the simple vertical percolation to the next layer restricts them to only 3. Statistically the model predicts a lowering by a factor of 4 for a case of 50% density in 2-dimesional brick planes, while for this 1-dimensional side-view case of only one brick thickness, the factor is expectedly 2. The 4-layer example (right) may help the reader evaluate how vertical percolation continues to restrict pathways, until there in this case is no vertical percolating paths, while horizontal surfaces continue to uphold conducting although longer paths.

We might continue like this, making the conduction path ever rarer, but orthogonal surfaces will immediately start to connect the ones we consider, and increase the conducting pathways. A numerical simulation of this could be useful, but the brick model is anyway crude. Generally, the power that the density and porosity are raised to, 1 and 2 in the above cases, can be a variable ξ in the surface conductance per layer of bricks taking percolation into account, $G_{s,Lp}$:

$$G_{s,Lp} = \frac{4\rho_r^{\xi}(1-\rho_r)^{\xi}}{d_g^2} G_s \qquad \textbf{Eq. 3}$$

In reality, an isotropic microstructure of high porosity such as for powder compacts or poorly sintered ceramics will have well-connected pores and ξ probably between 1 and 2, while low porosities and certain non-isotropic pore structures may be expected have ξ above 2.

A unit volume will have a conductance divided by the number of layers of grains, i.e., $1/d_g$, so that we get a macroscopic specific surface conductivity $\sigma_{M,s}$ for the porous material of

$$\sigma_{M,s} = \frac{G_{s,Lp}}{\frac{1}{d_g}} = d_g G_{s,Lp} = \frac{4\rho_r^{\xi}(1-\rho_r)^{\xi}}{d_g} G_s = \psi G_s \qquad \textbf{Eq. 4}$$

In this formula we recognise that the essential parameters are the conductance G_s of the surface layer (given by its volume specific conductivity and thickness), the relative density, and the grain (brick) size d_g.

The surface protonic conductivity of a simple porous material according to this model is inversely proportional to the grain size and has a maximum at 50% relative density of $\sigma_{M,s} = G_s/d_g$ for $\xi=1$ and $\sigma_{M,s} = 0.25 \cdot G_s/d_g$ for $\xi=2$.

The BLM handles in principle densities from 0 to 1 and to some extent closed porosity if $\xi>1$. In considering square bricks it underestimates conductivity by not allowing conduction along facets connecting otherwise unconnected grain sides. The BLM and the model proposed by Gregori *et al.* [5] model coincide well for $\xi=1$ (full percolation) at low porosities, while the BLM continues to handle the situation also as the porosity gets high.

From the geometry of porous ceramics, we may expect macroscopic conductivities to have shallow peaks around 50% density at values corresponding to order of magnitude of $\sigma_M = G_s/d_g$, i.e., the layer resistance in Siemens (S) divided by the grain size.

We next use the same BLM to make first approximation estimates of the specific surface area (*SSA*) of a porous material of the category we deal with here. In each layer of bricks there are 6 sides to each cube provided that the cube is a grain and its neighbour (in all 6 directions) is a pore. The number of surface sides per unit area of a layer is then

$$n_{6sL} = \frac{6\rho_r p_r}{d_g^2} = \frac{6\rho_r(1-\rho_r)}{d_g^2} \quad \textbf{Eq. 5}$$

The number of sides in a unit volume will be that of one layer have a surface area multiplied with the number of layers of grains, i.e., $1/d_g$;

$$n_{vs} = \frac{n_{6sL}}{d_g} = \frac{6\rho_r(1-\rho_r)}{d_g^3} \quad \textbf{Eq. 6}$$

The volumetric specific surface area SSA_v is then obtained by multiplying with the area of each side:

$$SSA_v = n_{vs} d_g^2 = \frac{6\rho_r(1-\rho_r)}{d_g} \quad \textbf{Eq. 7}$$

We may convert volumetric specific surface area SSA_v to gravimetric specific surface area SSA_g by

$$SSA_g = \frac{SSA_v}{\rho} = \frac{SSA_v}{\rho_r \rho_s} \quad \textbf{Eq. 8}$$

where ρ and ρ_r are, respectively, the density and relative density of the (porous) material, and ρ_s is the theoretical density of the dense material. We may also convert to molar specific surface area SSA_m by

$$SSA_m = \frac{SSA_g}{M_m} = \frac{SSA_v}{\rho_r \rho_s M_m} \quad \textbf{Eq. 9}$$

where M_m is the molar mass of the material.

References

1. Zhao, X. and D. Vanderbilt, *Phonons and lattice dielectric properties of zirconia.* Physical Review B, 2002. **65**(7): p. 075105.
2. Sun, X., Kalantzopoulos. N.G., Vøllestad. E., Chatzitakis, A, and Norby, T, *Surface protonic conductivity in chemisorbed and physisorbed water layers in porous nanoscopic CeO_2.* To be submitted.
3. Kang, X.L., et al., *Facet-engineered TiO_2 nanomaterials reveal the role of water-oxide interactions in surface protonic conduction.* Journal of Materials Chemistry A, 2022. **10**(1): p. 218-227.
4. Runnerstrom, E.L., et al., *Colloidal Nanocrystal Films Reveal the Mechanism for Intermediate Temperature Proton Conductivity in Porous Ceramics.* Journal of Physical Chemistry C, 2018. **122**(25): p. 13624-13635.

5. Gregori, G., M. Shirpour, and J. Maier, *Proton Conduction in Dense and Porous Nanocrystalline Ceria Thin Films.* Advanced Functional Materials, 2013. **23**(47): p. 5861-5867.

Appendix III

Surface protonic conductivity in chemisorbed water in porous nanoscopic CeO_2

Xinwei Sun,[a] Einar Vøllestad,[b] Per Martin Rørvik,[b] Sebastian Prodinger,[a] Georgios N. Kalantzopoulos,[a] Athanasios Chatzitakis,[a] and Truls Norby [a *]

[a] Department of Chemistry, University of Oslo, Centre for Materials Science and Nanotechnology (SMN), NO-0318 Oslo, Norway

[b] Sustainable Energy Technology, SINTEF Industry, Forskningsveien 1, NO-0373 Oslo, Norway

[*] Corresponding author: truls.norby@kjemi.uio.no

Applied Surface Science (2022), *611*, 155590.

III

Applied Surface Science 611 (2023) 155590

Contents lists available at ScienceDirect

Applied Surface Science

journal homepage: www.elsevier.com/locate/apsusc

Full length article

Surface protonic conductivity in chemisorbed water in porous nanoscopic CeO_2

Xinwei Sun [a], Einar Vøllestad [b], Per Martin Rørvik [b], Sebastian Prodinger [a], Georgios N. Kalantzopoulos [a], Athanasios Chatzitakis [a], Truls Norby [a,*]

[a] Department of Chemistry, University of Oslo, Centre for Materials Science and Nanotechnology (SMN), POB 1126 Blindern, NO-0318 Oslo, Norway
[b] Sustainable Energy Technology, SINTEF Industry, Forskningsveien 1, NO-0373 Oslo, Norway

ARTICLE INFO

Keywords:
Ceria
CeO_2
Porous
Hydrogenation
Water adsorption
Chemisorption
Conductivity
Protonic
Surface
Brick layer model

ABSTRACT

CeO_2 surfaces play decisive roles in heterogeneous catalysis of important processes. Here, we investigate adsorption and dissociation of water and migration of protons on internal surfaces of nanoscopic porous CeO_2. Sorption and thermogravimetry confirm literature suggestions that the surface is hydrogenated to Ce^{3+} ions and protons H^+. The following chemisorption is dissociative, yet weak, and physisorption sets in only at the very highest relative humidities, reflecting hydrophobic behaviour. We link sample conductivities to surface protonic conductances via a brick layer model and show that behaviours at high, intermediate, and low temperatures with, respectively, positive, close to zero, and negative apparent activation energies and $p_{H_2O}^{1/2}$, $p_{H_2O}^{1}$, and $p_{H_2O}^{3/2}$ dependences, can be attributed to different models of migration all within the chemisorbed layer, without contribution from physisorbed water. While CeO_2 may special in this respect due to the effect of the hydrogenated surface, we believe the extended models of transport in the chemisorbed layer may apply also to other oxides. Unsaturated chemisorption may play an important role for CeO_2 as catalyst in that the surface is left available for reactant molecules, still with availability of dissociated and mobile protons in the chemisorbed layer and electronic defects by Ce^{3+} in the surface.

1. Introduction

Ceria (CeO_2) takes on a cubic fluorite structure irrespective of temperature, and is remarkably unreactive with bases and acids such as H_2O and CO_2 and most acidic metal oxides. It has a well-understood defect structure dominated by understoichiometry ($CeO_{2-\delta}$; oxygen vacancies and charge compensating electrons representing Ce^{3+}). Lower-valent acceptor impurities or deliberate doping with for instance Gd^{3+} or Sm^{3+} to form gadolinia- or samaria-doped ceria (GDC, SDC) enhance the concentration of oxygen vacancies and suppress electrons, making the material a good oxide ion conductor for use as a solid-state electrolyte in solid oxide fuel cells (SOFCs). [1,2] The oxygen vacancies in bulk ceria have unfavourable hydration thermodynamics and there is hence no reliable report of significant hydration or proton conductivity in regularly acceptor-doped bulk ceria, and only a hardly measurable hydrogen permeability. [3] It has recently been shown that doping with 50% La^{3+} to form $Ce_{0.5}La_{0.5}O_{1.75}$ (or "$Ce_2La_2O_7$") leads to some hydration, but this is attributed to the affinity of protons to oxide ions fully coordinated by basic La^{3+} ions. [4]

Following discovery of surface protonic conductivity in other MO_2 oxides like undoped ZrO_2 and yttria-stabilized zirconia (YSZ), [5–10] TiO_2, [11–13] and SiO_2, [14] CeO_2 was found to behave similarly. Early reports on nanocrystalline samples attributed the protonic conduction to grain boundary transport, [15–17] but it is now accepted that the triple-grain junctions in some studies were open enough that it can be treated as surface transport in a porous material, and that fully dense materials do not exhibit appreciable protonic conductivity. Porous undoped and acceptor doped CeO_2 exhibits surface protonic conductivity in chemisorbed water down to around 200 °C. Below this, an increase with decreasing temperature is traditionally attributed to conduction in physisorbed water, [18–20] but we shall in the present paper see that it for a large part arises from chemisorbed water alone.

Runnerstrom et al. [21] found that CeO_2 and TiO_2 thin films with grain sizes well below 10 nm exhibit more pronounced protonic conductivity across the minimum at intermediate temperatures (100–350 °C) than more well-crystallised samples. This tendency is observed also

* Corresponding author.
E-mail address: truls.norby@kjemi.uio.no (T. Norby).

https://doi.org/10.1016/j.apsusc.2022.155590
Received 22 June 2022; Received in revised form 15 October 2022; Accepted 2 November 2022
Available online 8 November 2022

for certain facets of surfaces on TiO_2 [22] and for poorly crystallised ZrO_2. [23] Dependences on oxygen activity and morphology led the authors to suggest that oxygen vacancies promote dissociative adsorption of water and resulting higher protonic conductivity. Simons et al. [24] studied CeO_2 thin films and concluded that hydration is a slow process, while adsorption along surfaces and through open pores is fast. This may explain the inconsistency on the protonic conductivity of porous and dense ceria in literature.

Based on measurements of conductivity of dense films and porous ceramic samples of CeO_2 under wet and dry atmospheres, Gregori et al. [20] considered that protons from adsorbed water may dissociate and migrate in the subsurface region as well as in the layer of adsorbed water. They proposed a brick-layer model (BLM) for a qualitative estimate of the conductivity of oxides with small amounts of open porosity based on the conductivity and thickness of the water layer and the size and volume fraction of pores. In their assessment, they assume that the dissociation into charge carriers follows autoprotolysis of water, and based on the measured sample conductivity and their BLM, they found that mobilities of protons in the adsorbed water layers are within order of magnitude of that in bulk water at 200 °C.

An important application of nano- or microcrystalline ceria is as catalyst or support for noble metal nanoparticles in chemical industry and combustion engine exhaust catalyst systems. [25] Its catalytic activity suggests that CeO_2 surfaces deviate from the simplicity of bulk cubic CeO_2. [26,27] This may comprise enhanced understoichiometry and n-type conductivity as well as hydration. On-going density functional theory (DFT) calculations show strong tendency of hydration of reduced CeO_2 surfaces, meaning that the surfaces may be seen as reduced oxyhydroxides, formed according to schematic hydrogenation reactions like

$$CeO_2 + \frac{1}{2}H_2O(g) \rightleftarrows CeOOH + \frac{1}{4}O_2(g) \quad (1)$$

$$CeO_2 + \frac{1}{2}H_2(g) \rightleftarrows CeOOH \quad (2)$$

This is supported by in situ electron energy loss spectroscopy (EELS) of CeO_2 nanoparticles in transition electron microscopy (TEM) showing that Ce^{3+} in a surface layer oxidises to Ce^{4+} during heating in vacuum, which we may assign to dehydrogenation (Eq. (2) reversed). [28]

While the surface chemistry of CeO_2 is important and much studied, [29,30] the adsorption of water and resulting surface protonic transport are far from well understood. Here we contribute a study of adsorption of water and dissociation and migration of protons in chemisorbed and physisorbed water on the internal surfaces of nanoscopic porous CeO_2 ceramics. The results are interpreted in terms of a theoretical framework that relates adsorption thermodynamics via transport theory to surface conductance, and a brick layer model that quantitatively relates surface conductance with the measured conductivity of highly porous materials. [23] The combined used of thermogravimetry and conductivity vs T and p_{H_2O} suggests that hydrogenation of the surface must be taken into account and that transport in the chemisorbed layer covers a wider range of temperature than hitherto realised, with an extended set of models for this. Physisorption is suppressed due to the hydrophobicity of CeO_2 that, in turn, arises from the hydrogenated surface.

2. Experimental

2.1. Materials and preparation

Ceria nanopowder (< 50 nm particle size, 99.95% trace rare earth metals basis, SKU no. 700290, Sigma Aldrich) was cold-pressed at ~65 MPa, followed by sintering at 550 or 750 °C in air with a dwell time of 8 h into disks with approximate dimensions of 20 mm diameter and 2 mm thickness. The sintered samples are hereafter denoted CeO_2–550 and CeO_2–750. The resulting relative densities of the disks were about 50% (CeO_2–550) and 62% (CeO_2–750), calculated from their mass and geometry and nominal density of stoichiometric CeO_2 of 7.22 g cm^{-3}. [31]

2.2. Characterization

The microstructure and porosity of the samples were analysed by scanning electron microscopy (SEM, Hitachi SU8230). Powder X-ray diffraction with a Bruker D8 Discover diffractometer with CuKα_1 radiation (λ = 1.5406 Å, Bragg-Brentano mode) was used to verify the structure and examine the crystallite size.

Nitrogen sorption measurements were performed on a BELSORP mini II instrument (MicrotracBEL Corp., Japan) at 77 K to determine the specific surface area (*SSA*), and the pore size distribution of the materials. In each experiment, approximately 200 mg of material was weighed into a quartz cell. The samples were pre-treated by annealing under dynamic vacuum for 2 h at 150 °C. The total *SSA* was extracted from the nitrogen adsorption isotherms via the Brunauer–Emmett–Teller (BET) method. [32] Non-local density functional theory (NLDFT) calculations of the pore size distribution were performed using the commercial BELMaster software (MicrotracBEL Corp., Japan). The Grand Canonical Monte Carlo (GCMC) calculation method was applied on the adsorption branch using the nitrogen physisorption data collected at 77 K, assuming a slit pore model.

Water sorption measurements were performed at 25 °C using a BELSORP Max physisorption instrument (MicrotracBEL Corp., Japan) to determine the maximum water capacity. [33] The measurements took place in the relative humidity (*RH*) range: $0 < RH = \frac{p_{H_2O}}{p_{ce}} < 0.9$, with p_{ce} being the condensation equilibrium partial pressure of H_2O at 25 °C. In each experiment, approximately 200 mg of material was weighed into a quartz cell and pre-treated with annealing under dynamic vacuum for 2 h at 150 °C in situ to avoid exposure to atmospheric humidity. The number of physisorbed H_2O molecules per unit surface is calculated from Eq. (3), where wt% is the gravimetric adsorption, N_A is Avogadro's number, MW_{gas} is the molecular weight of the adsorbed gas (H_2O), and SSA_g is the gravimetric specific surface area from BET analysis.

$$\frac{N_{molecule}}{nm^2} = \frac{N_A \cdot wt.\%}{10^{20} \cdot MW_{gas} \cdot SSA_g} \quad (3)$$

Thermogravimetry (TG) was carried out using a 449 F1 Jupiter® thermal analyser (Netzsch GmbH, Germany) on the pristine CeO_2 powder and sintered samples under bottle-dry or wet N_2 (99.999%) purge gases. The sintered samples were crushed coarsely to fit into the sample holder, while retaining its microstructure. The samples were heated to 550 °C at 3 K min^{-1} in bottle-dry N_2 at a flow rate of 40 mL min^{-1}, thereafter held at the given temperature for at least 2 h to eliminate adsorbed water and organic residue from the sample surface. The p_{H_2O} dependence of water adsorption was measured at 400, 100, 50 and 30 °C, while the temperature dependence was conducted as follows: After fully dehydrating at 550 °C as described above, the samples were equilibrated at 550 °C at p_{H_2O}= 0.020 atm and measured during stepwise cooling to 25 °C – the weight increase reflects the total content of hydrogen as well as both chemisorbed and physisorbed water. Background measurements in bottle-dry N_2 were carried out under otherwise identical conditions and used for background subtraction, with the dry-to-wet step at 550 °C as a starting point, assuming that uptakes from water in dry atmosphere at 550 °C is zero.

For electrical characterization, symmetrical circular Ag paste electrodes of 10 mm diameter were painted on both faces of the sintered pellets. Electrical conductivity was measured via Pt mesh and four Pt wire contacts by electrochemical impedance spectroscopy (EIS) in a ProboStat™ sample holder cell (NORECS, Norway). The atmosphere was a flow of bottle-dry or wet (p_{H_2O}= 0.025 atm) N_2 (99.999%), O_2 (99.5% or 99.999%) or air, or N_2 with variable p_{H_2O} controlled by a HumiStat gas-mixer and humidifier (NORECS, Norway). Impedance spectra (10 MHz – 10 mHz, 100–500 mV RMS) were recorded using a

Novocontrol alpha-A spectrometer coupled with a ZG4 interface. Impedance data were analysed and modelled with ZView™ software (Scribner Associates Inc.). Specific conductivities of the porous samples were calculated based on their thickness and electrode area, without correction for the porosity.

3. Results and discussion

3.1. Microstructural characterization

Fig. 1 presents SEM images of the CeO_2–550 and CeO_2–750 samples, showing average grain sizes of approximately 40 and 90 nm, respectively. The shape of the particles of the CeO_2–550 sample remains rounded, similar to the pristine powder, but evolved to more faceted surfaces upon sintering at 750 °C. X-ray diffractograms (SI 2.1, Fig. S1) of the CeO_2 starting powder and the sintered samples show cubic fluorite structure with space group *Fm*-3*m* and lattice parameters $a = b = c =$ 5.411 Å (COD_9009008). The grain sizes obtained from Scherrer analysis were 21 and 62 nm for CeO_2–550 and CeO_2–750, respectively, while they were 20 and 80 nm from Rietveld analysis, in rough agreement with those from SEM images, which we have used in subsequent quantitative analyses. From weight and geometry, sintering at 550 and 750 °C resulted in relative densities of around 50 and 62%, respectively, in agreement with the SEM images.

3.2. Nitrogen and water sorption measurements

N_2 adsorption-desorption of all CeO_2 samples display characteristic type II isotherms (SI 2.2, Fig. S3a). [34] BET analyses of the pristine CeO_2, CeO_2–550, and CeO_2–750 provide gravimetric specific surface area (SSA_g) of $3.2\bullet10^5$, $3.1\bullet10^5$ and $5.9\bullet10^4$ $cm^2\ g^{-1}$, respectively, (Table 1) and average pore size of 13, 14, and 20 nm (SI 2.2, Fig. S3b), which is again characteristic of mesoporous structures. The volume specific surface area (SSA_v) is also included in Table 1, calculated as the product of the SSA_g and the density of the porous sample. The results reflect the modest increases in grain size and relative density by sintering at 750 °C vs 550 °C, while the surface area for adsorption varies by a factor of 5, probably due to elimination of sub-granular and surface defects.

Water sorption measurements were performed at 25 °C for all samples, exhibiting type II isotherms similar to the N_2 adsorption. The number of adsorbed H_2O molecules normalised for BET surface area via Eq. (3) is shown in Fig. 2 at $0 < RH < 0.9$ and is remarkably equal for all three samples. The surface coverage is also shown, on basis of 5 H_2O per nm^2 as monolayer coverage. [35] A first layer of chemisorbed water appears to be in place already at low *RH* in agreement with calorimetric adsorption measurements on various oxides. [35–37] However, saturation appears to be reached only at closer to two monolayers. As indicated by TG results later on, part of this may reflect subsurface hydrogenation that gives an overestimate of what is interpreted as chemisorbed water.

The double-logarithmic insert in Fig. 2 displays a slope around 1/3 at low *RH*. This shows that adsorption is far from molecular (slope of 1) and instead suggests that each water molecule dissociates into 2, 3, or 4 species (slopes of ½, 1/3, or ¼, respectively). Based on the TG results to follow, we believe this reflects a combination of subsurface hydrogenation to protons and electrons with a $p_{H_2O}^{1/4}$ dependence and dissociative chemisorption with a $p_{H_2O}^{1/2}$ dependence.

Fig. 2 further shows that major uptake of physisorbed water beyond the chemisorbed layer occurs in our material only at unusually high *RH*, reflecting stronger adsorbate-adsorbate (H_2O-H_2O) interaction than adsorbate-adsorbent (H_2O-CeO_2) interaction. The α parameter (*RH* at which we reach half of the total water capacity, taken here to be at $RH = 0.9$) is a qualitative indication of surface hydrophobicity. [38] It was extracted from the water sorption data and listed in Table 1 and show that all CeO_2 samples can be considered as hydrophobic by having high α values of 0.78–0.82. Hydrophobicity is demonstrated for low-index CeO_2 surfaces by DFT calculations. [39] The intrinsic hydrophobicity of CeO_2 surfaces is a property it has in common with other rare earth (*RE*) oxides RE_2O_3. [40] We note that this may be connected with the general stability of *RE*OOH oxyhydroxides and hence tendency of RE_2O_3 forming a *RE*OOH-like surface by hydration, like CeO_2 may form CeOOH by hydrogenation.

The total volume of water adsorbed at *RH* of 0.9, commonly taken as the water adsorption capacity, can serve as a measure of sample porosity. [41] As seen in Table 1, it is indeed proportional to the BET surface area. The results indicate that at a *RH* of 0.9 there will be around 10 monolayers of water with a total thickness of close to 3 nm based on a monolayer thickness of 2.82 Å. [42]

3.3. Thermogravimetry (TG)

Fig. 3 shows isothermal p_{H_2O} dependences of water uptake measured by TG. If in Fig. 3 (a) we attribute the weight increase at 400 °C to H_2O, the water layer is still far from being complete assuming a monolayer coverage as 5 H_2O per nm^2 as mentioned above. A close to a $p_{H_2O}^{1/4}$ dependence is observed for both samples at 400 °C. Our recent STEM-EELS study [28] suggests that CeO_2 surfaces have a CeOOH-like layer according to Eq. (1) or Eq. (2), in agreement with other findings of Ce^{3+} in CeO_2 nanoparticles. [36,43] The TG results at 400 °C may then be better interpreted in terms of weight of uptake of H_2 instead of H_2O. Although it is reasonable per se and from the TEM-EELS study that the hydrogen is dissolved in the subsurface, we may still express the uptake as a surface concentration, i.e., number of H_2 per nm^2 surface (filled symbols in the figure). In defect-chemical terms the hydrogenation of the subsurface CeO_2 can be written

$$Ce_{Ce}^{x} + O_O^x + \frac{1}{2}H_2O(g) \rightleftarrows Ce_{Ce}^{/} + OH_O^{\bullet} + \frac{1}{4}O_2(g) \quad (4)$$

where Ce_{Ce}^{x} and $Ce_{Ce}^{/}$ represent Ce^{4+} and Ce^{3+}, respectively, and O_O^x and $OH_O^{\bullet}$ represent oxide and hydroxide ions, respectively. If this reaction

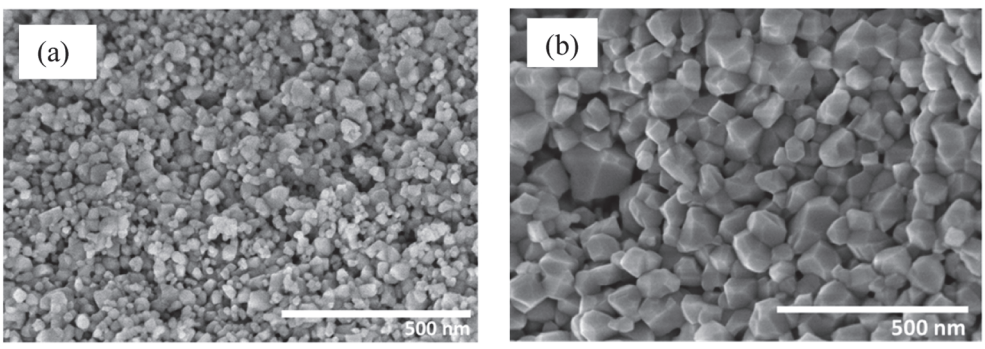

Fig. 1. SEM images of the (a) CeO_2–550 and (b) CeO_2–750 samples.

Table 1
Sorption parameters from N_2 adsorption isotherms at 77 K and water adsorption data at 298 K.

Samples	Specific surface area[§] (*SSA*)		Total pore volume[§] (cm^3 g^{-1})	Average pore size (BJH)[§] (nm)	α (*RH* at 50% of H_2O uptake at RH = 0.9)	Water capacity[§§] (cm^3 g^{-1})
	SSA_g (cm^2 g^{-1})	SSA_v (cm^2 cm^{-3})				
Pristine CeO_2	$3.2•10^5$	n.a.	$1.1•10^{-1}$	13	0.78	53
CeO_2–550	$3.1•10^5$	$1.1•10^6$	$1.0•10^{-1}$	14	0.79	55
CeO_2–750	$5.9•10^4$	$2.6•10^5$	$3.5•10^{-2}$	20	0.82	10

[§] Estimated from N_2 adsorption isotherms at 77 K.
[§§] From H_2O adsorption data at 298 K at *RH* = 0.9.

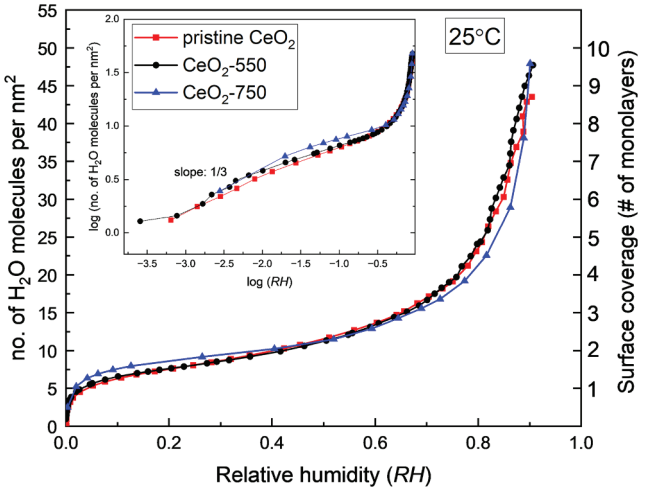

Fig. 2. Number of adsorbed water molecules per nm^2 as a function of relative humidity (*RH*) calculated from water sorption isotherms at 25 °C. The right-hand axis shows the same data in number of layers of water, assuming a monolayer coverage of 5 H_2O per nm^2. The inset shows a double-logarithmic plot of the data, suggesting approximately a $p_{H_2O}^{1/3}$ dependence in the low *RH* part.

provides the dominant charged defects, but at low concentrations, we obtain

$$\left[OH_O^•\right] = \left[Ce_{Ce}^{/}\right] = K_H^{1/4} p_{H_2O}^{1/4} p_{O_2}^{-1/8} \quad (5)$$

where K_H is the equilibrium coefficient of the reaction. The qualitative fit with the observed $p_{H_2O}^{1/4}$ dependence supports our suggestion that the weight increase at 400 °C is dominated by reduction of the subsurface, and not by adsorption of water.

Fig. 3 (b) shows the p_{H_2O} dependence of water uptake at 100, 50, and 30 °C, see also Fig. S4 in SI 3 for more detail on slopes and reversibility at 100 and 30 °C. At 100 °C, the weight change represents filling up of a yet far from complete chemisorbed water layer, with an overall $p_{H_2O}^{1/2}$ dependence – showing that the chemisorption is mainly dissociative. At 50 °C and 30 °C, the lower p_{H_2O} dependence may represent a beginning completion of the chemisorbed layer, while physisorbed water comes on at the highest p_{H_2O} at 30 °C (*RH* > 50%), giving rise to what appears to approach a $p_{H_2O}^{1}$ dependence (molecular physisorption).

As a thermodynamic basis for the p_{H_2O} dependences and later on enthalpies of TG data and models for conduction to follow, we apply an extension of a recently proposed framework and Kröger-Vink type notation for surface reactions and transport on ZrO_2 [23] (see SI for details). We first write the molecular chemisorption to a surface cation,

$$M_{M_s}^x + H_2O(g) \rightleftharpoons M_{M_s}OH_2^x \quad (6)$$

where *M* denotes the cation in binary oxides, in this case *M* = Ce and surface cation and oxide ion sites are denoted M_s and O_s. The

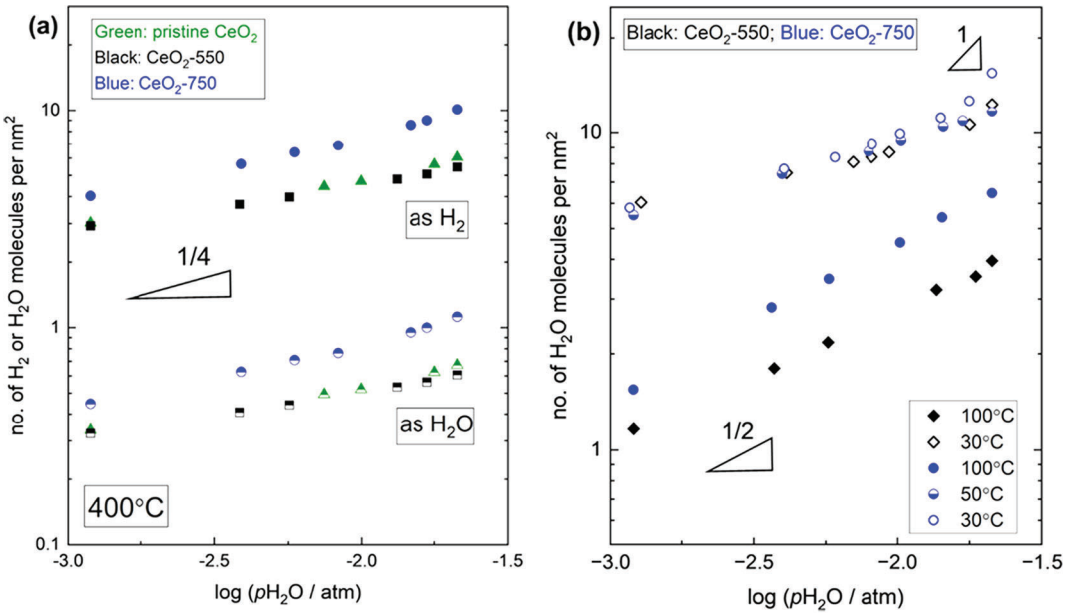

Fig. 3. Area specific adsorption in CeO_2 samples as a function ofp_{H_2O} in N_2 represented as number of H_2 or H_2O per nm^2 measured at (a) 400 °C and at (b) 100, 50, and 30 °C.

corresponding equilibrium coefficient $K_{a_{cm}}$ can be written

$$K_{a_{cm}} = \frac{X_{M_{M_s}OH_2^x}}{X_{M_{M_s}^x}\frac{p_{H_2O}}{p^0}} = \frac{\gamma_{M_{M_s}OH_2^x}}{\gamma_{M_{M_s}^x}\frac{p_{H_2O}}{p^0}} = exp\left(\frac{\Delta S^0_{a_{cm}}}{R}\right)exp\left(\frac{-\Delta H^0_{a_{cm}}}{RT}\right) \quad (7)$$

where X denotes site fraction and γ denotes surface concentration. For low coverage, this yields

$$\gamma_{M_{M_s}OH_2^x} = \gamma_{M_s}\frac{p_{H_2O}}{p^0}K_{a_{cm}} = \gamma_{M_s}\frac{p_{H_2O}}{p^0}exp\left(\frac{\Delta S^0_{a_{cm}}}{R}\right)exp\left(\frac{-\Delta H^0_{a_{cm}}}{RT}\right) \quad (8)$$

Dissociation of a proton to a surface oxide ion is similarly written

$$M_{M_s}OH_2^x + O_{O_s}^x \rightleftharpoons M_{M_s}OH^{/} + OH^{\bullet}_{O_s} \quad (9)$$

with equilibrium coefficient

$$K_{d_{cs}} = \frac{\gamma_{M_{M_s}OH^{/}}\gamma_{OH^{\bullet}_{O_s}}}{\gamma_{M_{M_s}OH_2^x}\gamma_{O_{O_s}^x}} = exp\left(\frac{\Delta S^0_{d_{cs}}}{R}\right)exp\left(\frac{-\Delta H^0_{d_{cs}}}{RT}\right) \quad (10)$$

The sum of both reactions describes dissociative chemisorption,

$$M_{M_s}^x + O_{O_s}^x + H_2O(g) \rightleftharpoons M_{M_s}OH^{/} + OH^{\bullet}_{O_s} \quad (11)$$

with equilibrium coefficient

$$K_{a_{cds}} = K_{a_{cm}}K_{d_{cs}} = \frac{\gamma_{M_{M_s}OH^{/}}\gamma_{OH^{\bullet}_{O_s}}}{\gamma_{M_{M_s}}\gamma_{O_{O_s}^x}\frac{p_{H_2O}}{p^0}} = exp\left(\frac{\Delta S^0_{a_{cds}}}{R}\right)exp\left(\frac{-\Delta H^0_{a_{cds}}}{RT}\right) \quad (12)$$

where the standard entropy and enthalpy changes $\Delta S_{a_{cds}}{}^0$ and $\Delta H_{a_{cds}}{}^0$ are sums of those for molecular chemisorption and dissociation. The electroneutrality is

$$\gamma_{M_{M_s}OH^{/}} = \gamma_{OH^{\bullet}_{O_s}} \quad (13)$$

and insertion into Eq. (12) yields the observed $p_{H_2O}^{1/2}$ dependence of the dissociated species:

$$\gamma_{OH^{\bullet}_{O_s}} = \gamma_{M_{M_s}OH^{/}} = \sqrt{K_{a_{cds}}\gamma_{M_{M_s}}\gamma_{O_{O_s}^x}\frac{p_{H_2O}}{p^0}} = \sqrt{\gamma_{M_{M_s}}\gamma_{O_{O_s}^x}\frac{p_{H_2O}}{p^0}}exp\left(\frac{\Delta S^0_{a_{cds}}}{2R}\right)exp\left(\frac{-\Delta H^0_{a_{cds}}}{2RT}\right) \quad (14)$$

If chemisorbed water remains undissociated, the mass gain would show a $p_{H_2O}^1$ dependence (Eq. (8)) while if it is predominantly dissociated, we obtain a $p_{H_2O}^{1/2}$ dependence (Eq. (14)). If the overall process saturates at complete coverage, the mass of the chemisorbed layer will become constant, independent of p_{H_2O}, irrespective of the degree of dissociation.

The mass gain as a function of temperature in wet atmosphere and interpreted as adsorption of water is shown in SI 3, Fig. S5. Fig. 4 displays the same data in area-specific terms, obtained by using the SSA_g from BET analysis. The mass gain upon cooling from 550 °C appears to level off towards 200 °C corresponding to around 0.8 H_2O per nm^2 for the pristine CeO_2 powder and the CeO_2–550 sample and around 2 H_2O per nm^2 for CeO_2–750. Such low coverage supports the finding that what we see in this region is not chemisorption of water, but saturation of the CeOOH-like subsurface layer as a result of hydrogenation of CeO_2 from water vapour. Recalculated, the apparent levels of 0.8 and 2 H_2O per nm^2 correspond then instead to 7 and 18 H_2 (or 14 and 36H) per nm^2, meaning that the layer of "CeOOH" with Ce^{3+} and H^+ goes 4–8 unit cells down if each Ce takes one electron.

The stronger increase in water adsorption below 200 °C then reflects chemisorbed water. After subtraction of the mass from the CeOOH-like layer, the data in the range 200–100 °C have enthalpies around −40 kJ mol^{-1}. If this is molecular chemisorption, we expect from Eq. (8) an enthalpy corresponding to $\Delta H_{a_{cm}}{}^0$. The p_{H_2O} dependences suggested predominantly dissociative chemisorption, and following Eq. (14) the

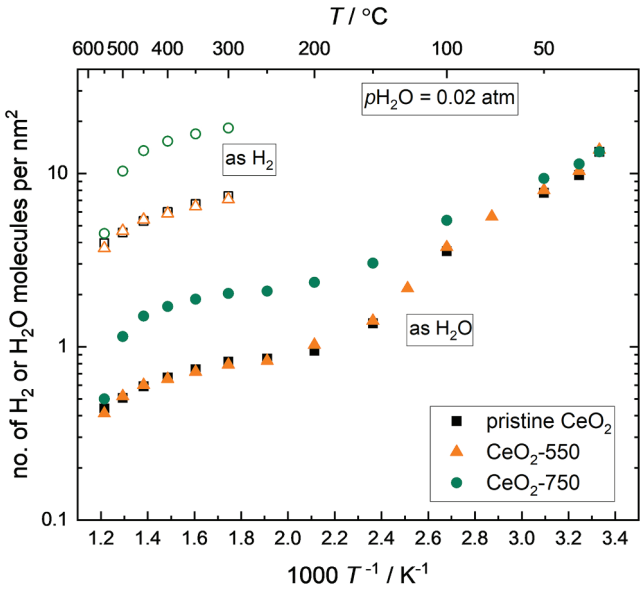

Fig. 4. Area-specific uptake from water by TG interpreted as number of H_2 or H_2O per nm^2 for the CeO_2 samples in the range 550–25 °C in wet (p_{H_2O}= 0.02 atm) N_2 atmosphere.

enthalpy is then instead $\frac{1}{2}\Delta H^0_{a_{cds}} = \frac{1}{2}\left(\Delta H^0_{a_{cm}} + \Delta H^0_{d_{cs}}\right)$. Existing literature suggests that $\Delta H_{a_{cm}}{}^0 = -60$ kJ mol^{-1} based on calorimetry [36] and first-principles calculations [44,45], and we may take $\Delta H_{d_{cs}}{}^0 \approx$ 20 kJ mol^{-1} as a round-off estimate based on the dissociation enthalpy 22 kJ mol^{-1} of water adsorbed on YSZ [46]. We hence expect enthalpies of $\Delta H_{a_{cds}}{}^0 \approx -20$ kJ mol^{-1} for the dissociated case, changing towards $\Delta H_{a_{cm}}{}^0 \approx -60$ kJ mol^{-1} as it turns molecular with decreasing T and increasing p_{H_2O}. For now we observe that the experimental enthalpies lie in a range in between, but they are not sufficient for deeper analysis.

Towards 50 °C, the curves in Fig. 4 display a tendency of levelling out at around 10 H_2O per nm^2, in agreement with the curve at the same temperature in Fig. 3 (b), which we attribute to saturation at full coverage of the chemisorbed layer. On further approach to RT and the highest RH, there is a new increase in mass gain as physisorbed water comes on, visible in both Fig. 3 (b) and Fig. 4.

3.4. Electrical conductivity

3.4.1. Impedance spectroscopy

Examples of impedance spectra are shown in SI 4.1 Fig. S6. Two overlapping arcs are revealed in the high-frequency range irrespective of sample, temperature and atmospheres (dry/wet), with capacitances in the range of geometric volume dielectrics. Similar duality has been reported for porous YSZ, but with bigger differences in capacitance, suggested to reflect *intra-grain* protonic transport over grain surfaces affiliated with low capacitance and *inter-grain* protonic transport over resistive grain boundaries affiliated with higher capacitance. [6] The present results for CeO_2 are instead similar to what is reported for porous undoped monoclinic ZrO_2, [23] and are suggested to reflect an inherent frequency response of porous ceramic materials with conduction over the concave (neck) and convex (grain) parts of the curved surfaces, now with the grain capacitance being the bigger because of its dielectric solid phase as compared to the concave neck having the smaller capacitance of the gas phase. In the following, we report the conductivity calculated from the sum of the two resistances extracted from the two high frequency responses.

3.4.2. Effects of atmosphere and temperature

The conductivities of CeO_2–550 and CeO_2–750 have been measured

vs temperature below their sintering temperatures. The main features of the electrical conductivity involve native non-protonic conductivity at the highest temperatures and surface protonic conductivity in adsorbed water with characteristic temperature dependences. Like most others studying surface protonics of CeO_2, we observe slow, and sometimes hysteretic changes and equilibria, the most important being irreversible effects of atmosphere (O_2 or air vs N_2), hysteretic adsorption and desorption of water, and what is believed to be surface restructuring and hydrophobicity of water adsorption at near ambient temperatures and high relative humidities. We note that some of these effects may be attributable to changes in the "CeOOH"-like subsurface layer, which only requires transport of protons and electrons and may take place at low temperatures. The observations are detailed in SI 4.2, while we here proceed to report and interpret results taken with long equilibration times under N_2 atmospheres, which represent the most reproducible and systematic behaviours.

3.4.3. Temperature dependences

Fig. 5 shows the Arrhenius plots of the conductivity (σ) of both CeO_2 samples, measured in bottle-dry and wet (p_{H_2O}= 0.025 atm) N_2. Under nominally dry conditions, the conductivity is significant and measurable only at the highest temperatures. It follows Arrhenius behaviour, with apparent activation enthalpies of around 80 kJ mol^{-1}. This is low compared to that of the conductivity of many bulk and porous nanoceria materials attributed to oxide ion conduction, [20,24,47] but comparable to what is expected for n-type electronic conduction of CeO_2 [19] (e.g. 0.77 eV for nanocrystalline CeO_2 thin film [21]). Knauth et al. [48] measured the p_{O_2} dependence of conductance of CeO_2 nanopowder and of coarsened powder, which gave rise to a $p_{O_2}{}^{-1/6}$dependence, similar to those of pulsed laser deposition (PLD) thin films. [49] In our work, the lack of an electrode impedance in impedance spectra at high temperatures in dry atmospheres correspondingly suggest that this conduction is electronic (assumingly n-type), and the presence of dual time constants in impedance spectra suggests that it is surface conduction.

The conductivity in wet atmospheres is higher than in dry. Fig. 6 shows the conductivity of our CeO_2 samples after subtraction of the native apparently electronic conductivity measured in dry atmosphere. At temperatures above 500 °C this may be attributed to electrons in the hydrogenated (CeOOH-like) layer, with a high activation energy. This deserves further study, but is beyond the scope of this article.

Below 500 °C, the impedance spectra show – as said above – that we have increasingly dominant surface protonic conduction, with a contribution with positive apparent activation enthalpy attributed to transport in the chemisorbed layer in the range 500–300 °C. In the temperature range 300–200 °C, the conductivity levels out, like in previous studies on nanocrystalline CeO_2 [19,50] formerly not having a plausible interpretation.

Below 200 °C, the conductivity increases with decreasing temperature, while as temperature passes below 100 °C and *RH* surpasses ~6%, the conductivity increases less steeply. These have commonly been attributed to solid- and liquid-like physisorbed water. The TG results showed however that the low-temperature (high *RH*) regions may need re-interpretation in the case of CeO_2: The region 200–100 °C is in fact mainly filling up with chemisorbed water, the first (solid-like) physisorbed water comes on only well below 100 °C, and liquid-like physisorbed water maybe never contributes much to conduction on CeO_2 surfaces due to their hydrophobicity. In the following, we evaluate these assessments by comparing their p_{H_2O} dependences, temperature dependences (enthalpies) and preexponentials with credible models. These partly coincide with and partly go beyond those presented in our preceding work on ZrO_2. [23]

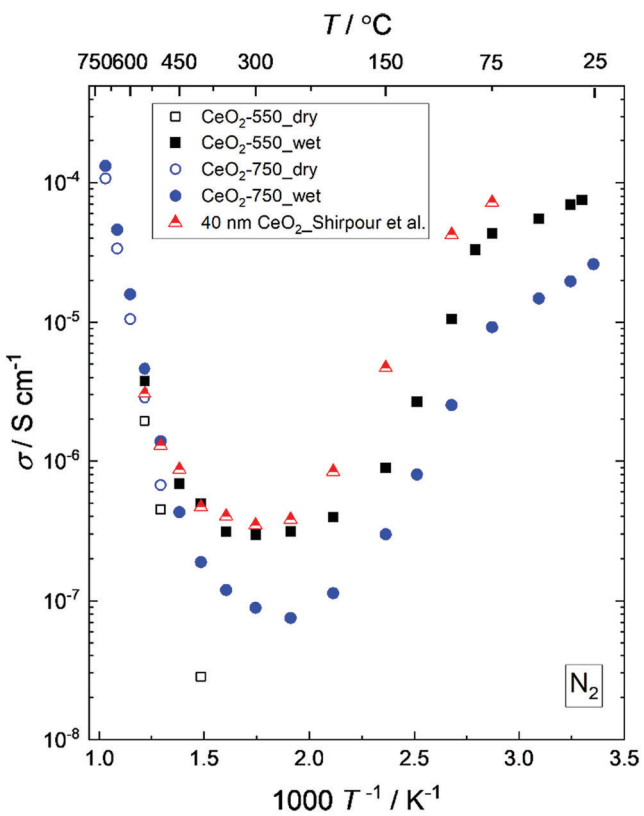

Fig. 5. Plot of σ vs $1/T$ for CeO_2–550 and CeO_2–750 in dry (open symbols) and wet (p_{H_2O} = 0.025 atm, solid symbols) N_2. Protonic conductivity reported by Shirpour et al. [19] for nanocrystalline undoped CeO_2 is shown for comparison.

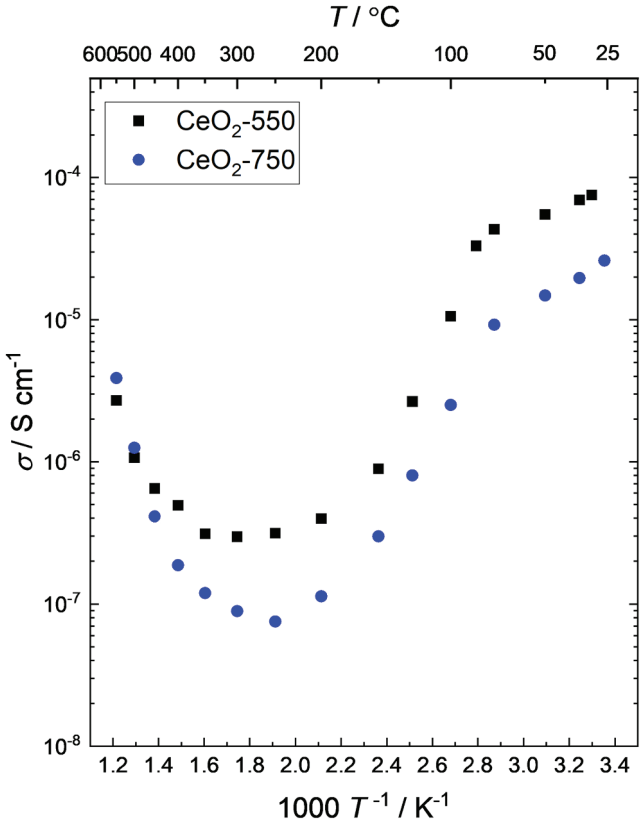

Fig. 6. Plot of σ vs $1/T$ for surface protonic conductivity of CeO_2–550 and CeO_2–750 obtained from wet N_2 atmosphere after subtraction of the dry conductivity.

3.4.4. Isothermal conductivity vs pH_2O

Fig. 7 shows the isothermal p_{H_2O} dependences of the surface protonic conductivity of the two CeO_2 samples. At 400 °C, we have close to a $p_{H_2O}^{1/2}$ dependence of surface protonic conductivity, steepening a bit towards a slope of 1 towards the highest pressure (0.025 atm), coinciding with a report by Manabe et al. [51] of a $p_{H_2O}^{1}$ dependence in the range p_{H_2O}= 0.026–0.2 atm of conductivity over grain surfaces (σ_{intra}) in porous CeO_2 at 400 °C. Studies of $Zr_{1-x}Y_xO_{2-x/2}$ (x = 0.04, 4YSZ) showed a $p_{H_2O}^{1/2}$ dependence of surface protonic conductivity at 400–250 °C, [52] and so did $Ce_{0.9}Gd_{0.1}O_{2-\delta}$ at 200 °C, [53] and $La_2Ce_2O_7$ at 550–250 °C. [54] The $p_{H_2O}^{1/2}$ dependence shows that each adsorbed H_2O molecule splits in two charged species to facilitate protonic transport in chemisorbed water.

At 100 °C, Fig. 7 (b) shows higher slopes reflecting close to $p_{H_2O}^{3/2}$ dependences of conductivity, suggesting involvement of multiple H_2O molecules in the protonic transport step. In our recent report on ZrO_2, [23] we proposed models for surface protonic conduction in the first physisorbed layer with $p_{H_2O}^{3/2}$ and $p_{H_2O}^{2}$ dependences, but based on the TG results for CeO_2 here, we have only chemisorption under these conditions, and we shall derive and parameterise extended models for conductance in the chemisorbed layer that yield similar predictions.

3.5. Modelling the surface protonic conductivity

3.5.1. General expressions of sample conductivity and surface conductance

We now move on to evaluate and parameterise the surface protonic conductivities according to the framework laid down in our work on ZrO_2, [23] expanded and detailed for the present results on CeO_2 in SI 5 (also containing an updated list of abbreviations in SI 1). For this purpose, we first relate the measured conductivity of the porous sample and the conductance of the adsorbed water layer via a brick layer model (BLM, see SI 5.2):

$$\sigma_{M,s,H^+} = \sigma_{M,s,H^+\,0}\frac{1}{T}exp\left(\frac{-\Delta H_c}{RT}\right) = \psi G_{s,H^+\,0}\frac{1}{T}exp\left(\frac{-\Delta H_c}{RT}\right)$$
$$= \psi G^0_{s,H^+0}\left(\frac{p_{H_2O}}{p_0}\right)^n\frac{1}{T}exp\left(\frac{-\Delta H_c}{RT}\right) \quad (15)$$

where $\sigma_{M,\,s,\,H^+}$ in S/cm is the measured surface protonic conductivity of the porous material, $\sigma_{M,\,s,\,H^+\,0}$ in SK/cm is its preexponential factor, ΔH_c is the enthalpy of conductivity, ψ in 1/cm is the factor derived from the BLM connecting $\sigma_{M,\,s,\,H^+}$ and $\sigma_{M,\,s,\,H^+\,0}$ to surface conductance $G_{s,\,H^+}$ in S and its preexponential factor $G_{s,\,H^+\,0}$ in SK. Furthermore, while $G_{s,\,H^+\,0}$ is usually proportional to $p_{H_2O}^{n}$ with n depending on predominant mechanism of adsorption, dissociation, and transport, the factor $G^0_{s,\,H^+\,0}$ standardises this to $p_{H_2O} = p^0 = 1$ bar.

Fig. 8 shows the geometry-corrected surface protonic conductances $G_{s,\,H^+}$ according to the BLM. They become roughly identical for the two samples over the entire temperature range (see also SI 5.2), demonstrating that the level of the surface protonic conductivity in Fig. 6 is largely determined by the grain size and porosity that enter into the BLM.

The surface conductance in wet atmosphere at the highest temperatures (above 500 °C in Fig. 8) cannot be reasonably modelled with transport in chemisorbed water and we attribute it as said before to transport of protons and/or electrons in the surface and/or subsurface caused by hydrogenation to protons in OH^- groups and electrons as Ce^{3+} in the CeOOH-like layer. An interpretation of its basis including temperature dependence deserves dedicated studies beyond the scope of this paper.

3.5.2. Models and parameterisation of surface conductance in chemisorbed water

The entire temperature dependence of surface protonic conductance can now be depicted by different models derived for adsorption, dissociation, and proton migration in chemisorbed water. A complete treatment of models is provided in SI section 5.3, which also provides schematic illustrations of all cases. Derived p_{H_2O} dependences and estimated preexponentials and activation enthalpies of surface conductance are collected in Table S4. Here we use excerpts to describe and parameterise models that fit the experimental data of Fig. 7 and Fig. 8.

It must be emphasised that the derivation at this stage neglects the possible effects of the surface being more like CeOOH than CeO_2. We treat the mean surface as having 2 oxide ions per Ce ion. The effect of having just one available unprotonated oxide ion for protonation and migration per cerium ion will for the most part be minor, but the parameterisation of models may unavoidably reflect CeOOH-like rather than CeO_2 surfaces in our work like in any other. We see our work hence not as the final, but an important step towards a complete description of

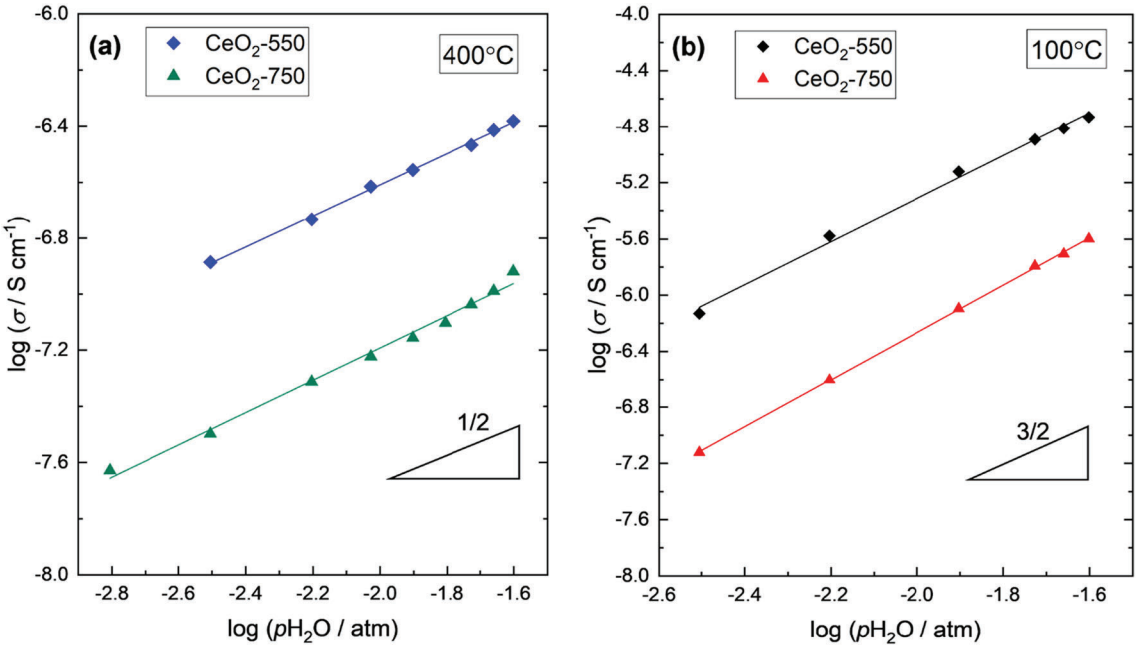

Fig. 7. Plots of log σ (surface protonic conductivity) vs log p_{H_2O} of both CeO_2 samples in N_2 at 400 °C (a) and 100 °C (b).

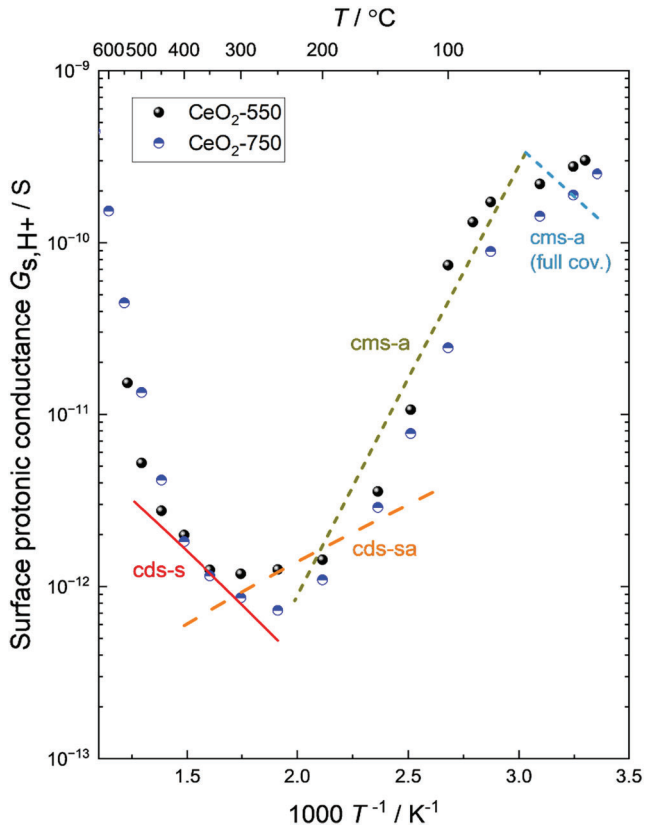

Fig. 8. Surface protonic conductance of the CeO_2 samples at $p_{H_2O} = 0.025$ atm vs $1/T$ in N_2, obtained from the sample conductivities via the BLM (see SI 5.2). The lines are drawn using preexponentials derived for models cds-s, cds-ca, and cms-a in the cases of low coverage, the latter with an extension also to full coverage, as derived below and in SI 5.3. The enthalpies are chosen to fit the experimental data reasonably in different regions as discussed for each model, see SI 5 Table S4.

protonic conduction over CeO_2 surfaces in wet and other hydrogen-containing atmospheres.

Molecular adsorption of water and dissociation of protons to surface oxide ions is described through Eqs. (6)–(14). TG data suggested that the adsorption is not complete (low coverage) and that dissociation prevails at the highest temperatures, but for the concentration of charged species, the mathematics remains the same irrespective of degree of dissociation.

We first consider migration of protons between surface oxide ions, which we may write mechanistically as

$$OH^{\bullet}_{O_s} + O^{x}_{O_s} \rightleftharpoons O^{x}_{O_s} + OH^{\bullet}_{O_s} \tag{16}$$

and which in our case gives rise to a model abbreviated **cds-s** (from **c**hemisorption **d**issociative to **s**urface – with migration on the **s**urface). It will have a relatively high activation energy and prevail at high temperatures with low coverages (few other options for migration). The surface conductance is given by the charge, surface concentration, and charge mobility of the chosen carrier (see ref. [23] and SI 4) and is for the cds-s model

$$G_{s,H^+_{cds\text{-}s}} = F\gamma_{OH^{\bullet}_{O_s}} u_{H^+} = F\gamma_{OH^{\bullet}_{O_s}} X_{O^{x}_{O_s}} u_{H^+0} \frac{1}{T} exp\left(\frac{-\Delta H_{m,H^+_s}}{RT}\right) \tag{17}$$

For low coverage, unprotonated surface oxide ions are generally available, $X_{O_{Os}}{}^{x} \approx 1$, and by inserting Eq. (14) we get

$$G_{s,H^+_{cds\text{-}s}} = F\gamma_{M_s}\sqrt{2K_{a_{cs}}\frac{p_{H_2O}}{p^0}}u_{H^+0}\frac{1}{T}exp\left(\frac{-\Delta H_{m,H^+_s}}{RT}\right) \tag{18}$$

which we may express as

$$G_{s,H^+_{cds\text{-}s}} = G_{s,H^+_{cds\text{-}s}0}\frac{1}{T}exp\left(\frac{-\left(\frac{1}{2}\Delta H^0_{a_{cm}} + \frac{1}{2}\Delta H^0_{d_{cs}} + \Delta H_{m,H^+_s}\right)}{RT}\right) \tag{19}$$

with preexponential

$$G_{s,H^+_{cds\text{-}s}0} = G^0_{s,H^+_{cds\text{-}s}0}\sqrt{\frac{p_{H_2O}}{p^0}} = \sqrt{2}F\gamma_{M_s}exp\left(\frac{\frac{1}{2}\Delta S^0_{a_{cm}} + \frac{1}{2}\Delta S^0_{d_{cs}}}{R}\right)u_{H^+0}\sqrt{\frac{p_{H_2O}}{p^0}} \tag{20}$$

As detailed in SI 5.3, we estimate preexponentials by assuming $\Delta S_{a_{cm}}{}^0 = -109$ J mol^{-1} K^{-1} as measured for the entropy of condensation of water at 100 °C, [55] $\Delta S_{d_{cs}}{}^0 = 0$ J mol^{-1} K^{-1}, $\gamma_{M_s} \approx 5$ /nm^2 $= 8\bullet10^{-10}$ mol cm^{-2}, and $u_{H^+0} \approx 10$ cm^{2}K V^{-1} s^{-1}, and get $G_{s,\,H^+_{cds\text{-}s}}{}^0 \approx 1.6\bullet10^{-6}$ SK for $p_{H_2O} = 1$ bar and $G_{s,H^+_{cds\text{-}s}0} \approx 2\bullet10^{-7}$ SK at $p_{H_2O} = 0.025$ atm, see entries for the cds-s model in Table S4. In order to make a first estimate of the activation enthalpy of conductance we assume as before $\Delta H_{a_{cm}}{}^0 = -60$ kJ mol^{-1} [36] and $\Delta H_{d_{cs}}{}^0 \approx 20$ kJ mol^{-1}, [46] and if we take $\Delta H_{m,H^+_s} \approx 50$ kJ mol^{-1} as a round value first guess based on the enthalpy of bulk mobility of protons in 50 mol% La-substituted CeO_2 ($La_2Ce_2O_7$) reported as 43 kJ mol^{-1}, [4] we obtain $\Delta H_{c_{cds\text{-}s}} = \frac{1}{2}\Delta H^0_{a_{cm}} + \frac{1}{2}\Delta H^0_{d_{cs}} + \Delta H_{m,H^+_s} \approx +30$ kJ mol^{-1}. The line for this cds-s model in Fig. 8 is drawn to rationalise surface conductance in the region 500–300 °C using the derived preexponential and $\Delta H_{c_{cds\text{-}s}} = +29$ kJ mol^{-1}. Moreover, the $p_{H_2O}^{1/2}$ dependence of the cds-s model is confirmed by the data for 400 °C in Fig. 7 (a).

At the highest p_{H_2O} at 400 °C, the p_{H_2O} dependences in Fig. 7(a) start to increase and as temperature decreases, the conductance levels out in Fig. 8. Both indicate that as *RH* and coverage increases, there is an increasing role of adsorbed species in the conduction process, leading to the next mechanism, where protons jump between **s**urface oxide ions and dissociated **a**dsorbed OH^- groups, hence abbreviated **cds-sa** and representing the reverse of the dissociation to the surface:

$$OH^{\bullet}_{O_s} + M_{M_s}OH^{/} \rightleftharpoons O^{x}_{O_s} + M_{M_s}OH^{x}_{2} \tag{21}$$

The surface protonic conductance along this mechanism can be expressed in terms of the surface protons and will then be proportional to the site fraction of available dissociated adsorbed hydroxide ions:

$$G_{s,H^+_{cds\text{-}sa}} = F\gamma_{OH^{\bullet}_{O_s}} u_{H^+_{sa}} = F\gamma_{OH^{\bullet}_{O_s}} X_{M_{M_s}OH^{/}} u_{H^+0}\frac{1}{T}exp\left(\frac{-\Delta H_{m,H^+_{sa}}}{RT}\right) \tag{22}$$

By assuming low coverage and inserting Eq. (14) we get

$$G_{s,H^+_{cms\text{-}sa}} = 2FK_{a_{cm}}K_{d_{cs}}\gamma_{M_s}\frac{p_{H_2O}}{p^0}u_{H^+0}\frac{1}{T}exp\left(\frac{-\Delta H_{m,H^+_{sa}}}{RT}\right) \tag{23}$$

and hence

$$G_{s,H^+_{cms\text{-}sa}} = G_{s,H^+_{cms\text{-}sa}0}\frac{1}{T}exp\left(\frac{-\left(\Delta H^0_{a_{cm}} + \Delta H^0_{d_{cs}} + \Delta H_{m,H^+_{sa}}\right)}{RT}\right) \tag{24}$$

with preexponential

$$G_{s,H^+_{cms\text{-}sa}0} = G^0_{s,H^+_{cms\text{-}sa}0}\frac{p_{H_2O}}{p^0} = 2F\gamma_{M_s}exp\left(\frac{\Delta S^0_{a_{cm}} + \Delta S^0_{d_{cs}}}{R}\right)u_{H^+0}\frac{p_{H_2O}}{p^0} \tag{25}$$

With assumptions like before we get $G_{s,\,H^+_{cms\text{-}sa}}{}^0 \approx 3\bullet10^{-9}$ SK and $G_{s,H^+_{cms\text{-}sa}0} \approx 8\bullet10^{-11}$ SK at $p_{H_2O} = 0.025$ bar. We assume that migration of protons is easier between these species than solely along the surface, and with the choice of a lower enthalpy of migration of this mechanism of 40 kJ mol^{-1}, we obtain $\Delta H_{c_{cms\text{-}sa}} = \Delta H^0_{a_{cm}} + \Delta H^0_{d_{cs}} + \Delta H_{m,H^+_{sa}}$ to be around 0 kJ mol^{-1}. This conductance is plotted with −10 kJ mol^{-1} in Fig. 8 to

represent the shallow minimum level at 300–200 °C. The model proposes a proportionality to $p_{H_2O}^{1}$ of surface protonic conduction, which is approached for high p_{H_2O} at 400 °C in our measurements (Fig. 7 a) and in those of Manabe et al. [51]

As we go lower in temperature, the conductance starts to increase more steeply in Fig. 8, and the p_{H_2O} dependence increases further, see Fig. 7 (b). This suggests even more involvement of adsorbed species for migration: We consider that dissociation still goes to surface oxide ions, but may be weaker as its enthalpy is positive and temperature is now lower. Migration now takes place between the remaining adsorbed water molecules and dissociated hydroxide ions, hence the mechanism is abbreviated **cds-a** or **cms-a** depending on degree of dissociation, and migration proceeds according to

$$M_{M_s}OH_2^x + M_{M_s}OH^{/} \rightleftharpoons M_{M_s}OH^{/} + M_{M_s}OH_2^x \quad (26)$$

For this mechanism we realise that dissociation is needed, but that also some undissociated water needs to remain. We will see how it comes out in the thermodynamics. The surface conductance can in this case be written

$$G_{s,H^+_{cds\text{-}a}} = G_{s,H^+_{cms\text{-}a}} = F\gamma_{M_{M_s}OH_2^x} u_{H^+_a} = F\gamma_{M_{M_s}OH_2^x}\frac{\gamma_{M_{M_s}OH^{/}}}{\gamma_{M_s}} u_{H^+0}\frac{1}{T} exp\left(\frac{-\Delta H_{m,H^+_a}}{RT}\right) \quad (27)$$

which, under assumption of **low coverage** by combination with Eq. (7) and Eq. (12) yields

$$G_{s,H^+_{cms\text{-}a}} = F\gamma_{M_s} K_{a_{cm}}\sqrt{2K_{a_{cds}}}\left(\frac{p_{H_2O}}{p^0}\right)^{3/2} u_{H^+0}\frac{1}{T} exp\left(\frac{-\Delta H_{m,H^+_a}}{RT}\right) \quad (28)$$

We rewrite this as

$$G_{s,H^+_{cms\text{-}a}} = G_{s,H^+_{cms\text{-}a}0}\frac{1}{T} exp\left(\frac{-\Delta H_{c_{cms\text{-}a}}}{RT}\right) = G_{s,H^+_{cms\text{-}a}0}\frac{1}{T} exp\left(\frac{-\left(\Delta H^0_{a_{cm}} + \frac{1}{2}\Delta H^0_{a_{cds}} + \Delta H_{m,H^+_a}\right)}{RT}\right) \quad (29)$$

with $\Delta H_{c_{cms\text{-}a}} = \Delta H^0_{a_{cm}} + \frac{1}{2}\Delta H^0_{a_{cds}} + \Delta H_{m,H^+_a} = \frac{3}{2}\Delta H^0_{a_{cm}} + \frac{1}{2}\Delta H^0_{d_{cs}} + \Delta H_{m,H^+_a}$, and preexponential

$$G_{s,H^+_{cms\text{-}a}0} = G^0_{s,H^+_{cms\text{-}a}0}\left(\frac{p_{H_2O}}{p^0}\right)^{3/2} = \sqrt{2}F\gamma_{M_s} exp\left(\frac{\frac{3}{2}\Delta S^0_{a_{cm}} + \frac{1}{2}\Delta S^0_{d_{cs}}}{R}\right) u_{H^+0}\left(\frac{p_{H_2O}}{p^0}\right)^{3/2} \quad (30)$$

As indicated above, the adsorption comes in at full play, while the dissociation has a two-sided effect and comes in to a lesser extent. With assumptions as before, we obtain $G_{s,\,H^+_{chm\text{-}a}}{}^{0} \approx 3\bullet10^{-12}$ SK and $G_{s,H^+_{chm\text{-}a}0} \approx 1\bullet10^{-14}$ SK at p_{H_2O}= 0.025 bar. If we now take the mobility in the molecular layer to be lower, at 20 kJ mol^{-1}, the enthalpy of conduction may be estimated to be $\Delta H_{c_{cms\text{-}a}} = \frac{3}{2}\Delta H^0_{a_{cm}} + \frac{1}{2}\Delta H^0_{d_{cs}} + \Delta H_{m,H^+_a} \approx -60$ kJ mol^{-1}, meaning that conductance increases strongly with decreasing temperature, describing roughly the conductivity in the range 200–100 °C in Fig. 8, there plotted with $\Delta H_{c_{cms\text{-}a}} = -45$ kJ mol^{-1}. This behaviour of transport in the chemisorbed layer hence fits the conductivity in the region where it earlier has traditionally been assigned to transport in the physisorbed layer. Moreover, the predicted $p_{H_2O}^{3/2}$ dependence fits well with the data for 100 °C in Fig. 7 (b), further supporting the assigned mechanism.

As before, it does not matter mathematically whether we consider a mainly undissociated (cms-a) or dissociated (cds-a) case as long as we have low coverage. The difference becomes evident, however, if we consider the full coverage cases. As we pass below 100 °C, the conductivities in Fig. 8 level off with decreasing temperature, which is only rational if we approach full coverage. We did indeed see a conductivity decreasing with decreasing temperature near room temperature for one sample (see SI 4.2, Fig. S7). These behaviours must follow one of the models for full coverage derived in SI 5.3. In the dissociated cds-a case, we predict an enthalpy of conduction close to 0 kJ mol^{-1}, which with the predicted preexponential cannot fit the levelling off at low temperatures in Fig. 8. However, the case of low dissociation and full coverage can: At full coverage, $\gamma_{M_{Ms}OH_2^x} \approx \gamma_{M_s}$, and low dissociation ($\gamma_{O_s} \approx 2\gamma_{M_s}$), the conductance becomes

$$G_{s,H^+_{cms\text{-}a}} = F\gamma_{M_{M_s}OH_2^x} u_{H^+_a} = F\gamma_{M_s}\sqrt{2K_{d_{cs}}} u_{H^+0}\frac{1}{T} exp\left(\frac{-\Delta H_{m,H^+_a}}{RT}\right) \quad (31)$$

which we rewrite as

$$G_{s,H^+_{cms\text{-}a}} = G_{s,H^+_{cms\text{-}a}0}\frac{1}{T} exp\left(\frac{-\Delta H_{cms\text{-}a}}{RT}\right) = G_{s,H^+_{cms\text{-}a}0}\frac{1}{T} exp\left(\frac{-\left(\frac{1}{2}\Delta H^0_{d_{cs}} + \Delta H_{m,H^+_a}\right)}{RT}\right) \quad (32)$$

with preexponential

$$G_{s,H^+_{cms\text{-}a}0} = G^0_{s,H^+_{cms\text{-}a}0} = \sqrt{2}F\gamma_{M_s} exp\left(\frac{\frac{1}{2}\Delta S^0_{d_{cs}}}{R}\right) u_{H^+0} \quad (33)$$

coming out as $G_{s,H^+_{cms\text{-}a}0} = G^0_{s,H^+_{cms\text{-}a}0} = 1.1\bullet10^{-3}$ SK. If the activation enthalpy of mobility is still 20 kJ mol^{-1}, the enthalpy of conduction may be estimated to be around +30 kJ mol^{-1}. It is plotted in Fig. 8 with $\Delta H_{c_{cms\text{-}a}}$ = + 25 kJ mol^{-1} as a continuation to lower temperatures where it takes over for the low coverage model.

The SI 5.3 also evaluates dissociation within the chemisorbed layer itself, to form adsorbed OH^- and H_3O^+ ions. This corresponding cma-a mechanism corresponds to one proposed by Raz et al. [9] and predicts conductances and temperature behaviours similar to those of the cms-a and cds-a models above. However, we must expect that dissociation to the surface is stronger (has a lower enthalpy) than within the adsorbed water layer, and by that the H_3O^+ ions will be minority defects in the overall electroneutrality and play little role.

3.5.3. Conduction in physisorbed water

For most samples, including the ones in Fig. 8, the continuing increase in conductivity at the lowest temperatures suggests the onset of conduction in the physisorbed layers that are filling up under these conditions. Fig. 9 shows examples of p_{H_2O}dependences of conductivity at 25 °C (RT), where we believe that physisorbed water starts to contribute. The CeO_2–550 sample lost all conductivity at $RH < 30\%$, but otherwise, both samples showed conductivities approximately proportional to p_{H_2O} at $RH < 60\%$, while the p_{H_2O} dependences increased to at least $p_{H_2O}^2$ at $RH > 60\%$. We cannot attribute these behaviours to quantitative models like we did above for the chemisorbed water and for physisorbed water in our previous work on ZrO_2. Qualitatively, it may reflect hysteresis in the contact angle and wettability of liquid-like physisorbed water and that the activation enthalpy of the mobility of protons decreases with increasing thickness and decreasing viscosity of the liquid-like physisorbed water layer.

For a CeO_2–550 sample that was heated to 540 °C in dry N_2 and then cooled straight to RT, the conductivity was initially immeasurably small in dry atmosphere. It remained so upon small steps towards wetter conditions, and became measurable only above $RH \approx 30\%$, and took several days to equilibrate. We suggest that this relates to a restructuring of the CeO_2 surface upon beginning adsorption of water in order to lower the surface energy. After completion of this process, changes in humidity were equilibrated faster, within a couple of hours. Combined ^{17}O and ^{1}H

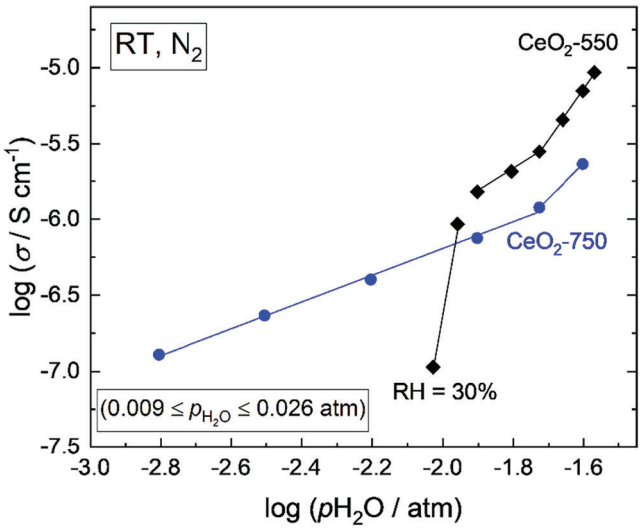

Fig. 9. p_{H_2O}dependence of surface protonic conductivity at 25 °C (RT) for both CeO_2 samples.

solid-state NMR spectroscopy with DFT calculations indicate that reconstructions occur on CeO_2{100}nanotube surfaces upon adsorption of water. [56] Yang et al. [57] provided direct spectroscopic evidence for the extensive restructuring of rod-shaped ceria nanoparticles, and they further showed that {111} nanofacets is an intrinsic property of the catalytically most active CeO_2{110} surface. For the CeO_2–750 sample, long equilibration times of the order of 24 h were required to reach steady-state conditions at each *RH* level at RT. Similarly, Simons et al. [24] reported that hydration of ceria took up to three days for thin films at RT.

All in all, the behaviours of adsorption and conduction in physisorbed water layers on nano-ceria at high *RH* appear to be a result of hydrophobicity and restructuring of the surface, maybe involving changes in surface composition (degree of hydrogenation). We may also anticipate that competing impurity adsorbents such as CO_2 and hydrocarbons may play a role. [58] Moreover, the average pore diameters of ~12 nm for CeO_2–550 and ~ 20 nm for CeO_2–750 from BET analysis (SI 6, Fig. S13) suggest capillary condensation of water close to RT, which still may not be reflected in the measured conductivity of CeO_2 because the hydrophobicity prevents connection of the narrowest parts of the pores. Furthermore, wedge-shaped porosity due to low-temperature sintering of nanocrystalline materials can also add favourable water adsorption sites. [19]

3.6. Comparison with recent studies of ZrO_2 and TiO_2

Recent literature on surface protonics of monoclinic ZrO_2 by Sun et al. [23] and anatase TiO_2 by Kang et al. [22] with similar microstructures and methodologies invites comparisons in view of the new developments in the present paper on CeO_2. The surface conductance by protons from chemisorbed water over surface oxide ions (cds-s) that dominates at 300–400 °C appears comparable for these oxides when microstructure is taken into account via the BLM. The enthalpies are similar, and delineation of adsorption and proton mobility is difficult because of insufficient literature data and unreliable subtraction of the competing native (dry) conduction.

At intermediate temperatures (200–300 °C), poorly faceted ZrO_2 and {101}-dominated TiO_2 have considerable conduction across a shallow minimum in common with CeO_2, which we here for the first time has given a possible interpretation in terms of proton transport between surface oxide and adsorbed hydroxide species (cds-sa). Future studies must validate this and investigate whether and why certain oxides and surfaces promote this mechanism.

Kang et al. [22] found by in situ FTIR that anatase TiO_2 had physisorbed water below 200 °C, and the conductance especially of samples grown with predominantly {100} and {001} facets had more negative enthalpies and higher levels of surface protonic conductivity than in our CeO_2. Below 100 °C the conduction in TiO_2 increased even more strongly with decreasing temperature, assigned to liquid-like physisorbed water, in stark contrast to the behaviour of the hydrophobic CeO_2. All in all, TiO_2 appears to have stronger adsorption of water and to be hydrophilic contrary to the hydrophobic CeO_2. It seems that ZrO_2 behaves somewhere between TiO_2 and CeO_2 in terms of activation enthalpy and hydrophilicity and the contribution from liquid-like physisorbed water, depending on the degree of faceting of the surfaces.

More dedicated p_{H_2O} dependences of TG and conductivity data for other oxides like we have taken here will help discriminate mechanisms and allow more reliable comparative parameterisation.

4. Conclusions

Water adsorption and surface protonic conductivity measurements on nominally pure porous sintered CeO_2 samples confirm the expectancy that adsorption relates to specific surface area, while surface conductivity relates to grain size and porosity, quantifiable through a brick layer model. Thermogravimetry supports indications in the literature that the surface and/or subsurface of CeO_2 in presence of water vapour is hydrogenated to Ce^{3+} ions and protons H^+, that the following chemisorption is dissociative at high temperatures, and that physisorption sets in only at the highest relative humidities, typical of hydrophobic behaviour.

The observed dual time constants in the high frequency part of the impedance spectra represent according to our interpretation conduction over the concave and the convex part of curved surfaces. This together with the absence of an electrode impedance under dry atmospheres suggests that the native conductivity is surface electronic, likely from the hydrogenated layer. The conductivity under wet atmosphere below 500 °C is dominated entirely by surface protonic conduction.

The preexponentials and p_{H_2O} dependences of surface protonic conductivity are discussed on the basis of models for adsorption and dissociation of water and migration of protons, which connect the predicted surface protonic conductances to measured conductivity of the sample via the brick layer model. In the absence of physisorbed water, we have expanded models for transport from and in chemisorbed water to comprise migration of protons between surface oxide ions, migration between surface oxide ions and adsorbed hydroxide ions, and migration between adsorbed water molecules and hydroxide ions, with predicted positive, near-zero, and apparent negative activation enthalpies of conduction, respectively, and $p_{H_2O}^{1/2}$, $p_{H_2O}^{1}$, and $p_{H_2O}^{3/2}$ dependences. With predicted pre-exponentials and estimates of enthalpies for adsorption, dissociation, and proton diffusion, these match observed surface protonic conductances at high, intermediate, and low temperatures. For hydrophobic CeO_2, the low temperature mechanism of proton transport between adsorbed species behaves similarly as what is traditionally concluded to reflect physisorbed water in other, hydrophilic oxides, where probably the two contribute together.

At the highest *RH*s, the surface protonic conductivity of CeO_2 levels off, as expected from saturation to full coverage of the chemisorbed layer. A contribution from physisorbed water sets in, but remains modest and suffers from hysteresis of wetting and maybe restructuring of the surface and surface-oxide interface.

The TG data of dissociative chemisorption fit literature suggestions of a standard molecular adsorption enthalpy of −60 kJ mol^{-1} H_2O and dissociation of a proton to a surface oxide ion of the order of +20 kJ mol^{-1} H_2O. With these, conductivity data further suggest that migration of protons between surface oxide ions have activation energies as high as 50 kJ mol^{-1}, while they decrease towards values around 20 kJ mol^{-1} in the adsorbed layer.

It is believed that the findings have consequences for understanding

and controlling the surface properties of ceria-based nanomaterials. This study further suggests that incomplete and weak yet dissociative chemisorption of water may plays an important role for ceria as a catalyst in that much of the surface is left available for reactant molecules, while dissociated mobile protons are available on the surface along with electrons from the Ce^{3+} in the surface.

The deeper analysis of hydrogenation of the surface, and of the properties of the hydrogenated layer is suggested for future studies, as are the consequences for details of the models presented here for transport in the chemisorbed water layer.

CRediT authorship contribution statement

Xinwei Sun: Investigation, Methodology, Validation, Visualization, Writing – original draft, Writing – review & editing. **Einar Vøllestad:** Validation, Writing – review & editing. **Per Martin Rørvik:** Funding acquisition, Project administration, Validation, Writing – review & editing. **Sebastian Prodinger:** Investigation, Validation, Writing – review & editing. **Georgios N. Kalantzopoulos:** Investigation, Validation, Writing – review & editing. **Athanasios Chatzitakis:** Supervision, Validation, Writing – review & editing. **Truls Norby:** Conceptualization, Funding acquisition, Methodology, Project administration, Resources, Supervision, Writing – original draft, Writing – review & editing.

Declaration of Competing Interest

The authors declare no existing conflict of interest.

Data availability

Data will be made available on request.

Acknowledgements

X.S., A.C, and T.N. acknowledge MoZEES, a Norwegian Centre for Environment-Friendly Energy Research (FME), co-sponsored by The Research Council of Norway (project #257653) and 40 partners from research, industry and public sector. X.S., E.V., P.M.R., and T.N. acknowledge the SUPROX project (#280868) financed by the Research Council of Norway. S.P. acknowledges the iCSI project (#237922) financed by the Research Council of Norway. The authors thank Dr. David S. Wragg (University of Oslo) for HT-XRD measurements.

Appendix A. Supplementary data

Supplementary data to this article can be found online at https://doi.org/10.1016/j.apsusc.2022.155590.

References

[1] M.F. Liu, et al., An efficient SOFC based on Samaria-doped ceria (SDC) electrolyte, J. Electrochem. Soc. 159 (6) (2012) B661–B665.
[2] N. Jaiswal, et al., A brief review on ceria based solid electrolytes for solid oxide fuel cells, J. Alloys Compd. 781 (2019) 984–1005.
[3] Y. Nigara, et al., Hydrogen permeability in $(CeO_2)_{0.9}(GdO_{1.5})_{0.1}$ at high temperatures, Solid State Ionics 159 (1–2) (2003) 135–141.
[4] L.E. Kalland, et al., Structure, hydration, and proton conductivity in 50% La and Nd doped CeO_2 - $La_2Ce_2O_7$ and $Nd_2Ce_2O_7$ - and their solid solutions, Solid State Ionics 354 (2020).
[5] R. Sato, et al., Proton migration on hydrated surface of cubic ZrO_2: ab initio molecular dynamics simulation, J. Phys. Chem. C 119 (52) (2015) 28925–28933.
[6] S.Ø. Stub, E. Vøllestad, T. Norby, Mechanisms of protonic surface transport in porous oxides: example of YSZ, J. Phys. Chem. C 121 (23) (2017) 12817–12825.
[7] S.Ø. Stub, E. Vøllestad, T. Norby, Protonic surface conduction controlled by space charge of intersecting grain boundaries in porous ceramics, J. Mater. Chem. A 6 (18) (2018) 8265–8270.
[8] B. Scherrer, et al., On proton conductivity in porous and dense Yttria stabilized zirconia at low temperature, Adv. Funct. Mater. 23 (15) (2013) 1957–1964.
[9] S. Raz, et al., Characterization of adsorbed water layers on Y_2O_3-doped ZrO_2, Solid State Ionics 143 (2) (2001) 181–204.
[10] E.M. Kock, et al., Structural and electrochemical properties of Physisorbed and chemisorbed water layers on the ceramic oxides Y_2O_3, YSZ, and ZrO_2, ACS Appl. Mater. Interfaces 8 (25) (2016) 16428–16443.
[11] J. Gao, et al., Insights into the proton transport mechanism in TiO_2 simple oxides by in situ Raman spectroscopy, ACS Appl. Mater. Interfaces 12 (34) (2020) 38012–38018.
[12] S.Ø. Stub, et al., The influence of acceptor and donor doping on the protonic surface conduction of TiO_2, Phys. Chem. Chem. Phys. 20 (23) (2018) 15653–15660.
[13] F. Maglia, et al., Low temperature proton conduction in bulk nanometric TiO_2 prepared by high-pressure field assisted sintering, J. Mater. Res. 27 (15) (2012) 1975–1981.
[14] M.T. Colomer, F. Rubio, J.R. Jurado, Transport properties of fast proton conducting mesoporous silica xerogels, J. Power Sources 167 (1) (2007) 53–57.
[15] S. Kim, et al., On the conduction pathway for protons in nanocrystalline yttria-stabilized zirconia, Phys. Chem. Chem. Phys. 11 (17) (2009) 3035–3038.
[16] H.J. Avila-Paredes, et al., Grain boundaries in dense nanocrystalline ceria ceramics: exclusive pathways for proton conduction at room temperature, J. Mater. Chem. 20 (45) (2010) 10110–10112.
[17] S. Kim, et al., Unprecedented room-temperature electrical power generation using nanoscale fluorite-structured oxide electrolytes, Adv. Mater. 20 (3) (2008) 556–559.
[18] D. Perez-Coll, E. Sanchez-Lopez, G.C. Mather, Influence of porosity on the bulk and grain-boundary electrical properties of Gd-doped ceria, Solid State Ionics 181 (21−22) (2010) 1033–1042.
[19] M. Shirpour, et al., On the proton conductivity in pure and gadolinium doped nanocrystalline cerium oxide, Phys. Chem. Chem. Phys. 13 (3) (2011) 937–940.
[20] G. Gregori, M. Shirpour, J. Maier, Proton conduction in dense and porous Nanocrystalline ceria thin films, Adv. Funct. Mater. 23 (47) (2013) 5861–5867.
[21] E.L. Runnerstrom, et al., Colloidal nanocrystal films reveal the mechanism for intermediate temperature proton conductivity in porous ceramics, J. Phys. Chem. C 122 (25) (2018) 13624–13635.
[22] X.L. Kang, et al., Facet-engineered TiO_2 nanomaterials reveal the role of water-oxide interactions in surface protonic conduction, J. Mater. Chem. A 10 (1) (2022) 218–227.
[23] X.W. Sun, et al., Quantifiable models for surface protonic conductivity in porous oxides - case of monoclinic ZrO_2, Phys. Chem. Chem. Phys. 24 (2022) 11856–11871.
[24] P. Simons, K.P. Torres, J.L.M. Rupp, Careful choices in low temperature ceramic processing and slow hydration kinetics can affect proton conduction in ceria, Adv. Funct. Mater. 31 (31) (2021) 2009630.
[25] Y. Hisai, et al., Enhanced activity of catalysts on substrates with surface protonic current in an electrical field - a review, Chem. Commun. 57 (47) (2021) 5737–5749.
[26] K.B. Zhou, et al., Enhanced catalytic activity of ceria nanorods from well-defined reactive crystal planes, J. Catal. 229 (1) (2005) 206–212.
[27] A. Trovarelli, J. Llorca, Ceria catalysts at nanoscale: how do crystal shapes shape catalysis? ACS Catal. 7 (7) (2017) 4716–4735.
[28] A. Thøgersen, et al., In-situ electron loss spectroscopy reveals surface dehydrogenation of hydrated ceria nanoparticles at elevated temperatures, J. Phys. Chem. Solids 170 (2022), 110955.
[29] J. Paier, C. Penschke, J. Sauer, Oxygen defects and surface chemistry of ceria: quantum chemical studies compared to experiment, Chem. Rev. 113 (6) (2013) 3949–3985.
[30] D.R. Mullins, The surface chemistry of cerium oxide, Surf. Sci. Rep. 70 (1) (2015) 42–85.
[31] M. Mogensen, N.M. Sammes, G.A. Tompsett, Physical, chemical and electrochemical properties of pure and doped ceria, Solid State Ionics 129 (1–4) (2000) 63–94.
[32] G.C. Shearer, et al., Defect engineering: tuning the porosity and composition of the metal-organic framework UiO-66 via modulated synthesis, Chem. Mater. 28 (11) (2016) 3749–3761.
[33] G.N. Kalantzopoulos, et al., Factors determining microporous material stability in water: the curious case of SAPO-37, Chem. Mater. 32 (4) (2020) 1495–1505.
[34] K.S.W. Sing, et al., Reporting Physisorption data for gas solid systems with special reference to the determination of surface-area and porosity (recommendations 1984), Pure Appl. Chem. 57 (4) (1985) 603–619.
[35] A.V. Radha, et al., Surface enthalpy, enthalpy of water adsorption, and phase stability in Nanocrystalline monoclinic zirconia, J. Am. Ceram. Soc. 92 (1) (2009) 133–140.
[36] S. Hayun, T.Y. Shvareva, A. Navrotsky, Nanoceria - energetics of surfaces, interfaces and water adsorption, J. Am. Ceram. Soc. 94 (11) (2011) 3992–3999.
[37] G.C.C. Costa, et al., Calorimetric measurement of surface and Interface enthalpies of Yttria-stabilized zirconia (YSZ), Chem. Mater. 22 (9) (2010) 2937–2945.
[38] J. Canivet, et al., Structure-property relationships of water adsorption in metal-organic frameworks, New J. Chem. 38 (7) (2014) 3102–3111.
[39] M. Fronzi, M.H.N. Assadi, D.A.H. Hanaor, Theoretical insights into the hydrophobicity of low index CeO_2 surfaces, Appl. Surf. Sci. 478 (2019) 68–74.
[40] G. Azimi, et al., Hydrophobicity of rare-earth oxide ceramics, Nat. Mater. 12 (4) (2013) 315–320.
[41] S.L. Wachowski, et al., Structure and water uptake in BaLnCo2O6− δ (ln= La, Pr, Nd, Sm, Gd, Tb and Dy), Acta Mater. 199 (2020) 297–310.
[42] P.Z.G. Schuster, C. Sandorfy, The Hydrogen Bond: Recent Developments in Theory and Experiments III: Dynamics, thermodynamics and special systems. Chapter 27: Hydrogen Bonds in Systems of Adsorbed Molecules, North-Holland Publishing Company, Amsterdam, New York, Oxford, 1976, p. 1263. H. Knözinger, Editor.

[43] S.V.N.T. Kuchibhatla, et al., An unexpected phase transformation of ceria nanoparticles in aqueous media, J. Mater. Res. 34 (3) (2019) 465–473.
[44] M. Fronzi, et al., Water adsorption on the stoichiometric and reduced CeO2(111) surface: a first-principles investigation, Phys. Chem. Chem. Phys. 11 (40) (2009) 9188–9199.
[45] S. Kumar, P.K. Schelling, Density functional theory study of water adsorption at reduced and stoichiometric ceria (111) surfaces, J. Chem. Phys. 125 (20) (2006) 204704.
[46] M.A. Blesa, A.J.G. Maroto, A.E. Regazzoni, Surface-acidity of metal-oxides immersed in water - a critical analysis of thermodynamic data, J. Colloid Interface Sci. 140 (1) (1990) 287–290.
[47] A. Tschope, E. Sommer, R. Birringer, Grain size-dependent electrical conductivity of polycrystalline cerium oxide I. Experiments, Solid State Ionics 139 (3–4) (2001) 255–265.
[48] P. Knauth, et al., Study of compaction and sintering of nanosized oxide powders by in situ electrical measurements and dilatometry: Nano CeO_2—case study, J. Electroceram. 34 (1) (2015) 82–90.
[49] M.C. Gobel, et al., Boundary effects on the electrical conductivity of pure and doped cerium oxide thin films, Phys. Chem. Chem. Phys. 12 (42) (2010) 14351–14361.
[50] T.S. Oh, et al., Proton conductivity of columnar ceria thin-films grown by chemical vapor deposition, Phys. Chem. Chem. Phys. 15 (7) (2013) 2466–2472.
[51] R. Manabe, et al., Evaluating surface protonic transport on cerium oxide via electrochemical impedance spectroscopy measurement, Solid State Commun. 270 (2018) 45–49.
[52] S. Miyoshi, et al., Water uptake and conduction property of nano-grained yttria-doped zirconia fabricated by ultra-high pressure compaction at room temperature, Solid State Ionics 207 (2012) 21–28.
[53] E. Ruiz-Trejo, J.A. Kilner, Possible proton conduction in $Ce_{0.9}Gd_{0.1}O_{2\text{-delta}}$ nanoceramics, J. Appl. Electrochem. 39 (4) (2009) 523–528.
[54] W. Sun, et al., Investigation on proton conductivity of $La_2Ce_2O_7$ in wet atmosphere: dependence on water vapor partial pressure, Fuel Cells 12 (3) (2012) 457–463.
[55] W. Wagner, A. Pruß, The IAPWS formulation 1995 for the thermodynamic properties of ordinary water substance for general and scientific use, J. Phys. Chem. Ref. Data 31 (2) (2002) 387–535.
[56] J.C. Chen, et al., Polar surface structure of oxide nanocrystals revealed with solid-state NMR spectroscopy, Nat. Commun. 10 (2019), 5420.
[57] C.W. Yang, et al., Surface faceting and reconstruction of ceria nanoparticles, Angewandte Chemie-International Edition 56 (1) (2017) 375–379.
[58] E. Kulah, et al., Surface chemistry of rare-earth oxide surfaces at ambient conditions: reactions with water and hydrocarbons, Sci. Rep. 7 (2017) 43369.

Supplementary Information (SI)

Surface protonic conductivity in chemisorbed water in porous nanoscopic CeO_2

Xinwei Sun,[a] Einar Vøllestad,[b] Per Martin Rørvik,[b] Sebastian Prodinger,[a] Georgios N. Kalantzopoulos,[a] Athanasios Chatzitakis,[a] and Truls Norby [a *]

[a] Department of Chemistry, University of Oslo, Centre for Materials Science and Nanotechnology (SMN), NO-0318 Oslo, Norway

[b] Sustainable Energy Technology, SINTEF Industry, Forskningsveien 1, NO-0373 Oslo, Norway

[*] Corresponding author: truls.norby@kjemi.uio.no

SI 1 List of symbols and abbreviations

Table S1 List of symbols for variables and constants and abbreviations for sub- and subscripts

Variables, constants	Unit	Description	Comment
a	(dimensionless)	Activity	
A	(dimensionless)	Geometric factor	
c_{BET}	(dimensionless)	BET constant	
c	mol/cm^3	Volume concentration	
C	F	Capacitance	
D	cm^2/s	Random diffusion coefficient	
d_g	cm	Grain and pore size	
E	kJ mol^{-1}	Heat of adsorption	Enters in c_{BET}
F	C/mol	Faraday constant	96485 C/mol
G	S	Conductance	
ΔH	kJ mol^{-1}	Enthalpy change	
K	(dimensionless)	Equilibrium coefficient	like in $K_{a_{cm}}$
l	cm	Length of surface layer sheet	
M	(dimensionless)	Metal	M = Ti, Zr, Ce…
M_m	g/mol	Molar mass	
p	bar	Partial pressure	
R	J/molK	Gas constant	8.3144 J/molK
R	ohm	Resistance	
RH	(dimensionless)	Relative humidity	$= p_{H_2O} / p_{ce}$
s	cm	Jump distance	
ΔS	J/molK	Entropy change	
SSA_g	cm^2/g	Specific surface area, gravimetric	
SSA_v	cm^2/cm^3	Specific surface area, volumetric	
SSA_m	cm^2/mol	Specific surface area, molar	

T	K				Absolute temperature	
t	cm				Thickness of surface layer	
u	cm^2K/Vs				Charge mobility	
w	cm				Width of surface layer sheet	
X	(dimensionless)				Site fraction	
Z	ohm				Impedance	
γ	mol/cm^2				Surface concentration	Gamma
ε_0	F/cm				Vacuum permittivity	$8.854 \cdot 10^{-14}$ F/cm
ε_e	F/cm				Effective dielectric constant	Epsilon
ε_r	(dimensionless)				Relative dielectric constant	Epsilon
θ	(dimensionless)				Surface coverage	Theta, $= \nu / \nu_m$
ν	mol/cm^2				Molar concentration of physisorbed water	Nu
ν_m	mol/cm^2				Molar concentration of a monolayer of water	Nu
ξ	(dimensionless)				Percolation power	Xi
ρ	g/cm^3				Density	Actual material
ρ_r	(dimensionless)				Relative density	Rho
ρ_t	g/cm^3				Theoretical density	Dense material
σ	S/cm				Conductivity	Sigma
ψ	1/cm				BLM porosity surface factor	Psi, $= \sigma_{M,s} / G_s$
ω_0	1/s = Hz				Vibrational attempt frequency	Omega
Subscripts						
1st level	2nd level (no. of letter)					
	1st	2nd	3rd	-4th		
a					adsorption	
c					conduction	
	c				chemisorbed	
	p				physisorbed	
		m			molecular	
		d			dissociative	
d					dissociation	
			s		to surface oxide ion	
			a		to adsorbed water molecule	
	chm-ph1				from chemisorbed to 1st physisorbed layer	pcp
	ph1				in 1st physisorbed layer	ppp
m					migration	= diffusion
m,H^+					migration of H^+	Grotthuss
				–s	between surface oxide	
				–sa	between surface oxide and adsorbed hydroxide	
				–a	between adsorbed water molecule and ionised species	
0					preexponential	like in u_0 and G_0
M					Macroscopic	like in σ_M
L and Lp					One layer and one layer with effect of percolation	in $G_{s,L}$ and $G_{s,Lp}$
ce					condensation equilibrium	in p_{ce} and K_{ce}
r					relative	like in ρ_r and ε_r
geom					geometric	
cvex					convex	
cave					concave	
Superscript						
0					standard	like in p^0 and G^0

SI2 Structure of the CeO_2 samples

2.1 X-ray diffractograms

Figure S1 shows the X-ray diffractograms of the CeO_2 starting power and the sintered samples. CeO_2-750 clearly reveal more intense diffraction peaks and narrower full width at half

maximum (FWHM) as compared to CeO_2-550. Scherrer analyses on the main XRD peaks indicate average grain sizes of roughly 20, 21 and 62 nm for the pristine powder, CeO_2-550 and CeO_2-750, respectively. Fitting results from Rietveld analysis using TOPAS software reveal crystallite size of 20, 20, and 80 nm, respectively, with a low R_{wp} value (5-8%).

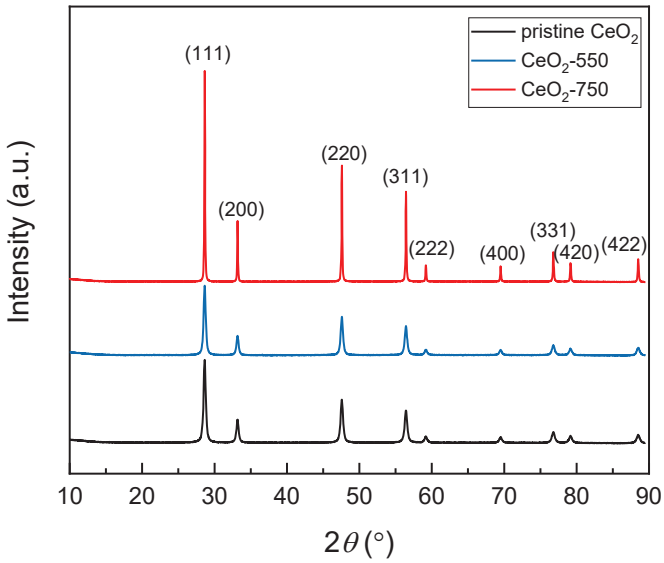

Figure S1 X-ray diffractograms of the CeO_2 starting powder and the corresponding sintered samples.

In situ X-ray diffractograms of the CeO_2 collected at room temperature (RT) showed no difference between wet (p_{H_2O} = 0.03 atm) and dry atmospheres. High-temperature XRD during heating-cooling cycle in wet atmosphere in the range 550-25°C showed symmetrical thermal change in the lattice parameter (Figure S2 a), but no structural change. A slight jump in lattice parameter was observed at 430°C upon switching to dry atmosphere (Figure S2 b). All in all, XRD did not capture the anticipated changes in the surface structure of the nanograined materials upon changes in p_{H_2O} or temperature, or give insights to indications from electrical measurements of slow hysteretic structural changes in the surface induced by adsorbed water.

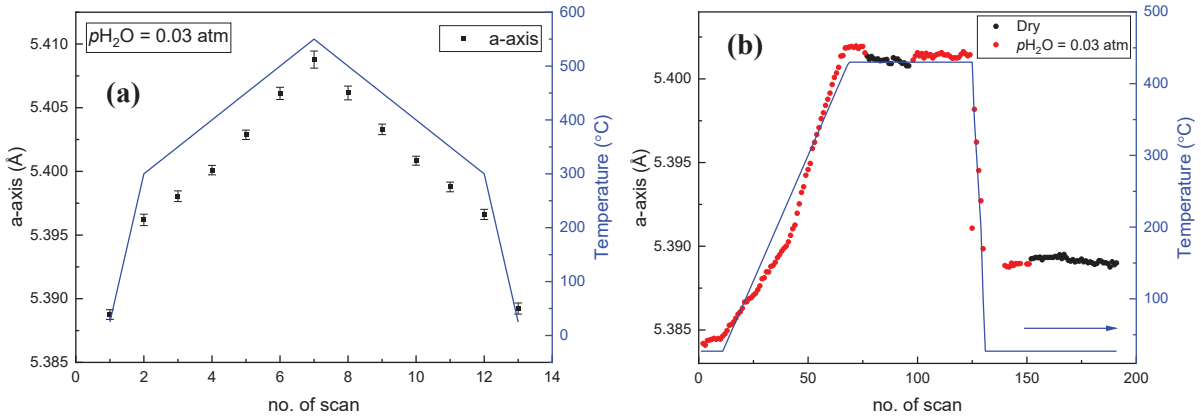

Figure S2 (a) Isobaric XRD recorded between 25-550°C, (b) isothermal measurement at 430°C and RT by switching between dry and wet (p_{H_2O} = 0.03 atm) N_2 atmospheres. The blue lines represent the temperature changes (right y-axis).

2.2 N_2 sorption isotherms

Figure S3 (a) shows the N_2 adsorption-desorption isotherms of the pristine and the sintered CeO_2 samples performed at 77 K. All the isotherms indicate type II isotherm according to the IUPAC classification.[1] The hysteresis loops are associated with capillary condensation of N_2 in mesopore structures. The volume adsorption of CeO_2-750 is significantly lower than that for the other two samples, which is attributed to its lower BET surface area. Sintering at 750°C reduced the number of mesopores as shown from the pore size distributions (Barrett-Joyner-Halenda (BJH) analyses) of the BET analyses (Figure S3 b), shifting the average pore size from 10 to around 20 nm for the CeO_2-750 sample.

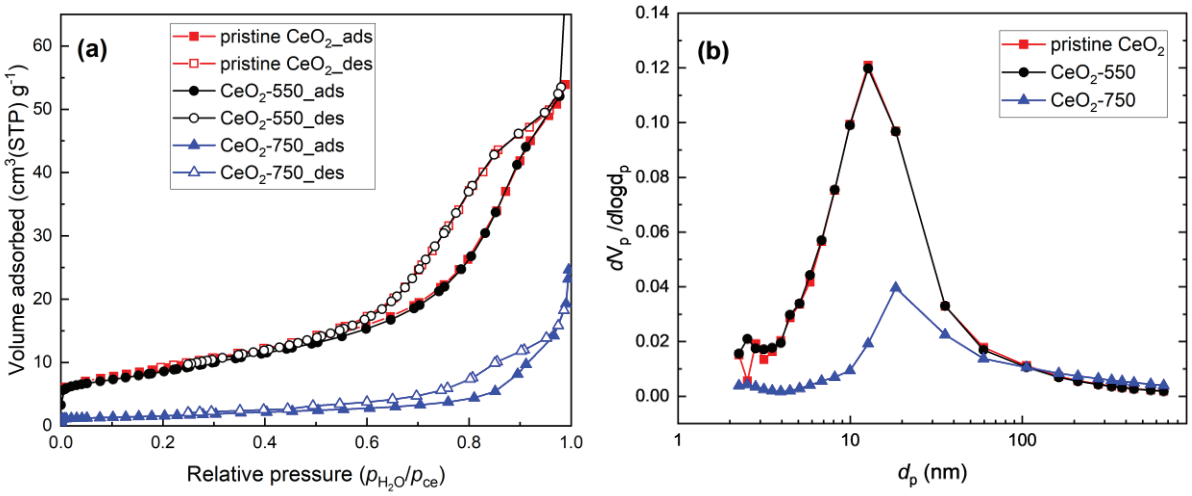

Figure S3 (a) N_2 adsorption-desorption isotherms of the CeO_2 samples, (b) the corresponding pore size distribution (BJH method).

SI 3 Thermogravimetry (TG)

Figure S4 presents the water uptake of the sintered samples as a function of p_{H_2O} at selected temperatures.

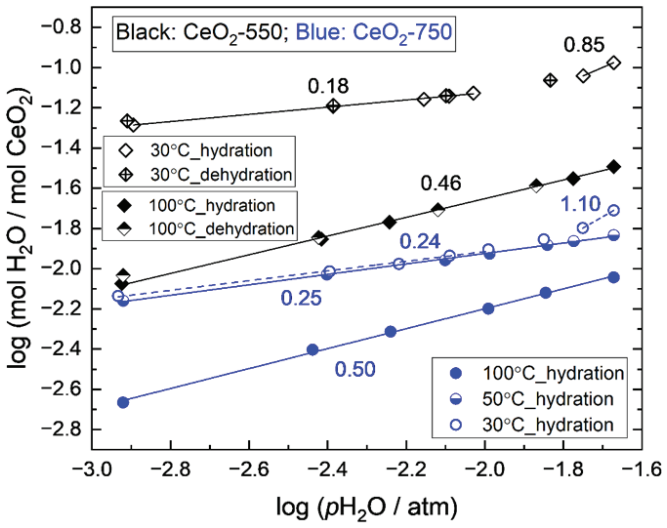

Figure S4 Water uptake on the sintered CeO_2 samples measured as a function of p_{H_2O} at 100, 50 and 30°C in N_2 atmosphere. Numbers along the curve show the slope from curve fitting.

Figure S5 further shows the uptake of water on all CeO_2 samples on going stepwise from high to low temperature in wet (p_{H_2O} = 0.02 atm) N_2, corrected for non-stoichiometry and buoyancy from an equivalent run in dry N_2. The results reveal that the water uptake at 550°C and at room temperature is proportional to the BET surface area, as the CeO_2-750 sample with lower SSA_g show correspondingly lower adsorption of water. The pristine powder, CeO_2-550 and CeO_2-750 take up 0.13, 0.12 and 0.017 mol H_2O per mol CeO_2, respectively, in the range 550–25°C.

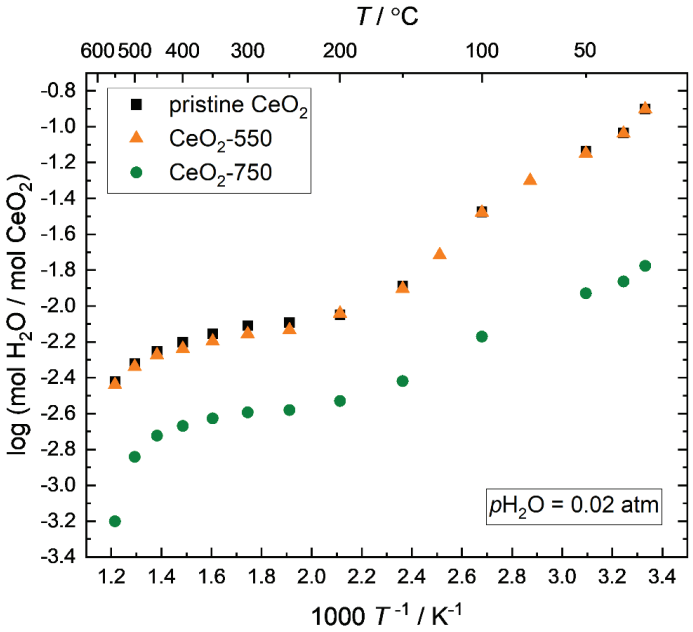

Figure S5 Adsorption on the pristine CeO_2 and the two sintered samples CeO_2-550 and CeO_2-750 in wet (p_{H_2O} = 0.020 atm) N_2 *vs* $1/T$ in response to stepwise cooling after dry curve subtraction, interpreted as weight of H_2O. The dwell time was increased with decreasing temperature to ensure equilibrium.

SI 4 Electrical properties

4.1 Exemplary impedance spectra from measurements under N_2 atmosphere

Figure S6 shows representative impedance spectra for the CeO_2-550 sample in the different temperature regions under N_2 atmosphere. The two time constants at the highest frequencies are attributed to conduction over low capacitance necks and higher capacitance grains of the curved surfaces in the porous ceramic. Generally, the resistance over the necks is an order of magnitude smaller than that over the grains.

For the highest temperatures (Figure S6 a), the presence of the dual responses in both dry and wet atmospheres suggest that we have mainly surface conductivity. The absence of an electrode response suggests a large contribution of electronic conduction, but the lower resistance in wet than in dry atmosphere is typical of protonic contribution. At intermediate temperatures (Figure S6 b), three distinct processes were recognized. At the lowest temperatures (Figure S6 c, d), the three responses remain, but become increasingly overlapping. Figure S6 (e) shows the geometry-corrected capacitances for the three responses. C_1 and C_2 are of the order of 10^{-12} and 10^{-11} F cm^{-1}, both in the range of geometric volume dielectrics. C_3 observed below 400°C under wet conditions is of the order of 10^{-7}-10^{-6} F cm^{-2}, typical of an electrode contribution, which becomes blocking at the lowest temperatures.

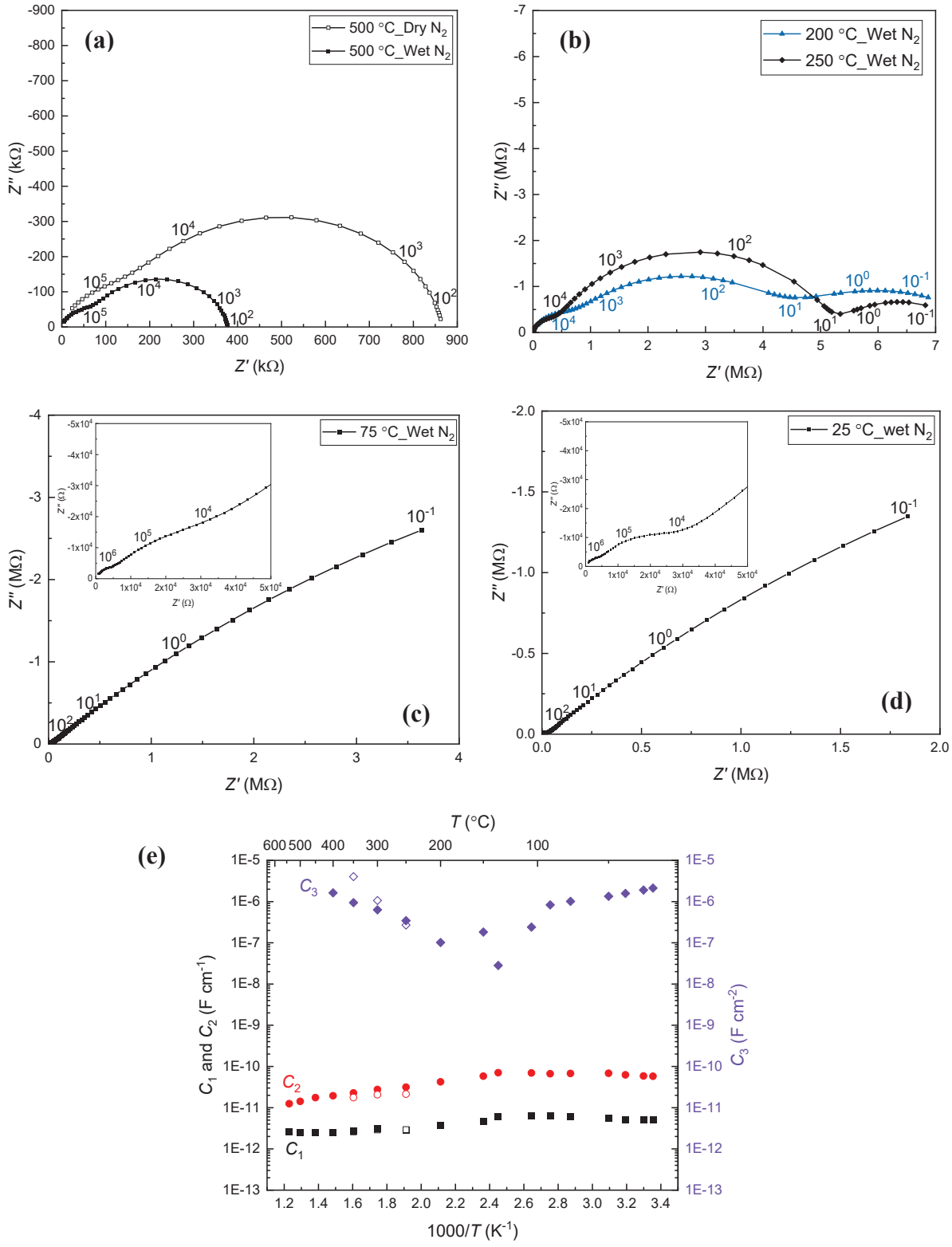

Figure S6 (a-d) Representative Nyquist impedance plots for the porous CeO_2-550 sample recorded in bottle-dry (open symbols) and wet (solid symbols, p_{H_2O} = 0.025 atm) N_2. The data were modelled by three parallel RQ in series except for the highest temperatures (> 400°C) where two parallel RQ in series were used. Numerical labels show the AC frequencies. The insets of (c) and (d) show close-ups of the high-frequency part of the spectra. (e) Geometry-corrected capacitance in dry (open symbols) and wet (solid symbols) N_2. C_3 is attributed to an electrode contribution.

4.2 Slow, hysteretic, and irreversible effects of atmosphere and temperature

The surface protonic conductivity of CeO_2 reveals in our experience more complex behaviours than for other oxides, such as pure and doped TiO_2 and ZrO_2, comprising slow, hysteretic, or seemingly irreversible effects of temperature and p_{H_2O} (i.e., *RH*) or p_{O_2} (*i.e.*, reduction or oxidation). In the following we provide selected examples of the most prominent effects.

4.2.1 General variations in conductivity level

It is our experience that samples sintered at nominally the same temperature for equal timespans can show variations in conductivity within an order of magnitude. It is uncertain what this relates to, but we suspect that variations in *RH* during pressing and sintering (e.g. due to different weather and times of the year) and varying exposure to air and *RH* during first heating cycles may be involved. We experience that samples made and sintered more simultaneously are in better correspondence, allowing correlation of the conductivity level with the microstructure of the sample via e.g. the brick layer model, as shown in the main text.

4.2.2 Effects of hydration and dehydration

Figure S7 shows the isobaric temperature dependencies of the conductivity of CeO_2-550, illustrating how the loss of water at around 250-350°C is sometimes affiliated with hysteresis. We tentatively attribute this to slow reorganisation of the CeO_2 surface in interaction with adsorbed water, although we could not verify structural changes by HT-XRD (SI 2.1, Figure S2), which is a bulk method probably too insensitive to the surfaces even in our nanomaterials.

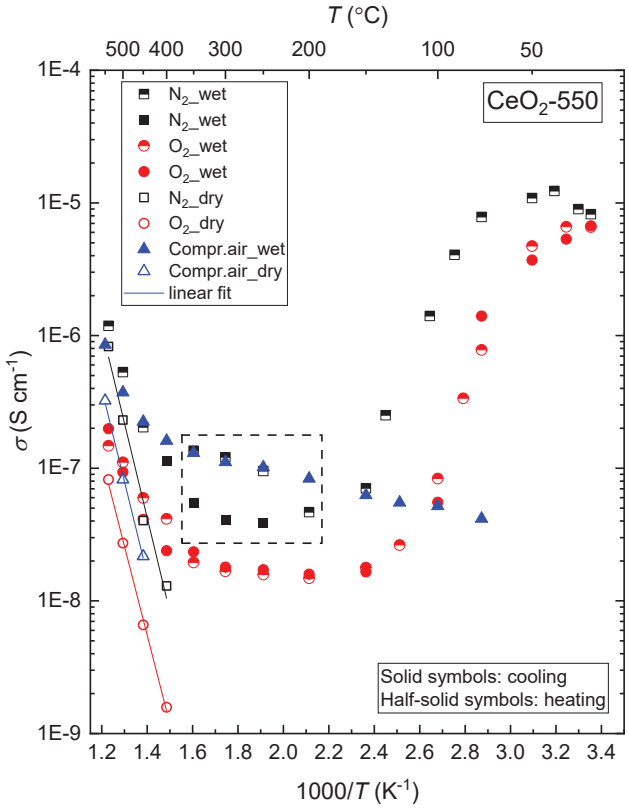

Figure S7 Plot of σ *vs* $1/T$ for CeO_2-550 in dry (open symbols) and wet (solid symbols, p_{H_2O} = 0.025 atm) N_2, O_2 and compressed air atmospheres. A hysteresis is observed in the range 250-350°C in N_2 during heating and cooling, indicated by the dashed rectangle.

One CeO_2-550 sample was heated to 540°C in dry N_2 gas, and then cooled straight to room temperature for p_{H_2O} dependence measurements. As discussed also in the main text, hydration and dehydration as a function of *RH* thereafter was slow – to regain conductivity during hydration of that dry sample required RH > 30% and took of the order of days, and consequent behaviours of conductivity at high *RH* were variable.

4.2.3 Effects of oxygen (O_2 or air) *vs* inert (N_2) atmospheres

The CeO_2-550 sample was first measured in N_2 and thereafter in O_2. As seen in Figure S7, the conductivity level for that sample was about an order of magnitude lower in O_2 than it had been in inert (N_2). This has been observed by others and suggested to be related to oxidative loss of oxygen vacancies which may be beneficial for water adsorption.[2] If the surface is dominated by Ce^{3+} and protons in OH^- ions as predicted by DFT calculations and supported by ETEM/EELS,[3] alternative relations to oxygen activity changes may be at play. Wang *et al*.[4] pointed out that annealing $CeO_2\{111\}$ thin films in O_2 reduces the concentration of adsorbed hydrocarbon and/or carbonate species, and facilitates water dissociation, an opposite effect of what O_2 is said above to have on oxygen vacancies.

After measurements in N_2 and the decrease in conductivity level in O_2, the same CeO_2-550 sample was subjected to *in situ* annealing (and sintering) at 750°C in N_2 for 24 h and is hereafter denoted CeO_2-750*. Figure S8 (a) shows the Arrhenius plot of the conductivity of the sample recorded at p_{H_2O} = 0.025 atm. The conductivities of CeO_2-750* in N_2 and thereafter O_2 were almost identical, especially in the intermediate region, and low compared to the two CeO_2 samples (CeO_2-550 and CeO_2-750) that were sintered in air. SEM image taken after the conductivity measurements (Figure S8 b) showed grains with sizes widely varying in the range of 40–110 nm, agglomeration of particles, as well as development of faceted grains. In this sense, the sample generally took on the same microstructure as the one originally sintered at 750°C (CeO_2-750). We conclude that annealing in N_2 does not revert to the higher conductivity observed initially in N_2, neither at 550°C nor during prolonged annealing at 750°C. In conclusion, exposure to O_2 decreases the conductivity at high temperatures attributed to the lowering of the n-type surface conduction (as discussed in the main text), but in addition has a variable tendency of lowering the level of conductivity irreversibly, as if it induces a further sintering (which we have not been able to verify) and/or reduces the number of adsorption sites, suggested by others to reflect annihilation of oxygen vacancies by oxidation (but not convincingly related to adsorption theory or irreversibility).

Furthermore, one may also expect that minor gas phase components may compete with water. Indeed, high purity N_2 and O_2 (99.999%) tend to yield somewhat higher conductivity than less pure gases, such as 99.5% O_2 and compressed ambient air. In particular, wet compressed air in one occasion suppressed the onset of conductivity below 200°C (Figure S7), possibly attributable to the affinity CeO_2 is known to have for the CO_2 in air.

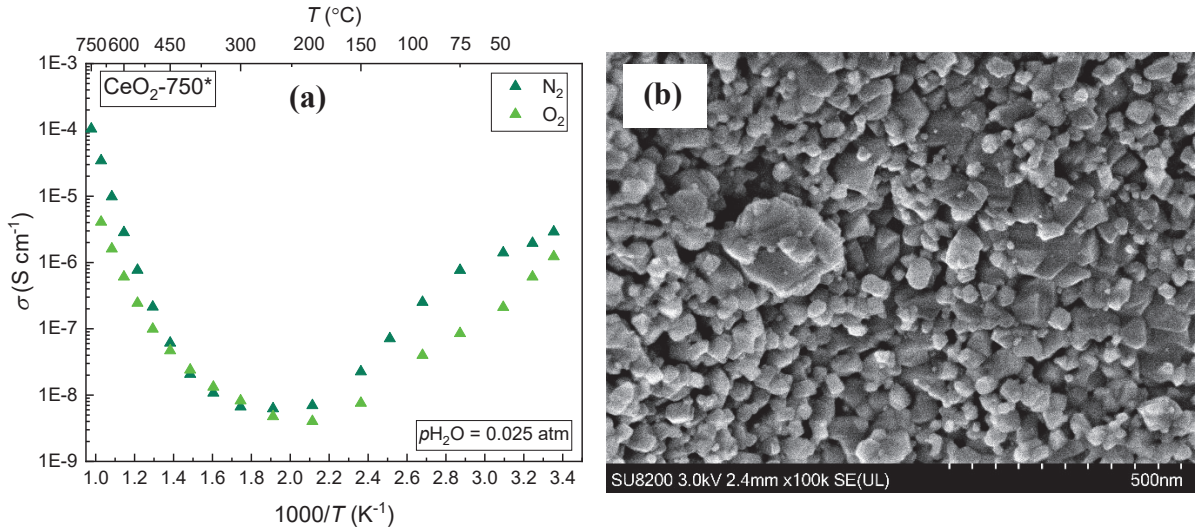

Figure S8 (a) Temperature dependence of the conductivity of the CeO_2-750* sample recorded in wet (p_{H_2O} = 0.025 atm) N_2 and O_2 atmospheres, (b) SEM image of CeO_2-750* after conductivity measurements.

SI 5 Models and interpretation

5.1 Surface conductance and conductivity

The total macroscopic conductivity σ_M of a porous material can be taken to have bulk ($\sigma_{M,b}$) and surface ($\sigma_{M,s}$) contributions. For our porous CeO_2 samples, the surface conductivity gets contributions from electronic conduction (as suggested by impedance spectra) and protonic conduction. As suggested in a recent study,[5] the measured surface protonic conductivity σ_{M,s,H^+} of porous ceramics like our CeO_2 samples (Figure 6 in the main manuscript) may be related to the volume conductivity σ_{s,H^+} of the adsorbed water layer along an appropriate geometric model. Assuming a square of a surface layer with thickness *t* and width *w* equal to length *l*, its surface protonic conductance G_{s,H^+} is proportional to σ_{s,H^+} via

$$G_{s,H^+} = \sigma_{s,H^+} \frac{w}{l} t \overset{w=l}{=} \sigma_{s,H^+} t = F u_{H^+} c_{H^+} t = F u_{H^+} \gamma_{H^+} \quad , \qquad \text{Eq. 1}$$

where c_{H^+} (in mol/cm^3) is the average volume concentration of protons that can be further expressed in terms of surface concentration γ_{H^+} (in mol/cm^2) and u_{H^+} is the charge mobility of protons that is related to its random diffusivity D_{H^+} via the Nernst-Einstein relation

$$u_{H^+} = \frac{F}{RT} D_{H^+} = X_O \frac{F}{RT} D_{H^+0} \exp\left(\frac{-\Delta H_{m,H^+}}{RT}\right) = X_O \frac{1}{T} u_{H^+0} \exp\left(\frac{-\Delta H_{m,H^+}}{RT}\right) \qquad \text{Eq. 2}$$

Here, X_O denotes the fractional occupancy of any oxide-ion containing species, O^{2-}, OH^-, or H_2O, that can accept a proton, depending on the mechanism. The preexponential of charge mobility of protons u_{H^+0} is estimated as 10 cm^2 K/Vs taking the assumption that the

preexponential of diffusivity $D_{H^+0} \approx 1 \cdot 10^{-3}$ cm^2/s, irrespective of mechanism or host system. $\Delta H_{m,H^+}$ is the enthalpy of proton mobility. For details, refer to ref.[5].

5.2 The brick layer model (BLM) for surface conduction

The macroscopic surface protonic conductivity σ_{M,s,H^+} of a porous material can be estimated from its surface protonic conductance G_{s,H^+} according to a brick layer model (BLM, see SI 5 in ref. [5])

$$\sigma_{M,s,H^+} \approx \frac{4\rho_r^{\xi}(1-\rho_r)^{\xi}}{d_g} G_{s,H^+} = \psi G_{s,H^+} \quad \text{Eq. 3}$$

where ψ is the microstructure factor that involves the relative density of the sample ρ_r, the grain/pore size d_g, and an exponent ξ that adjusts for percolation. For materials of regular and equal shapes of grains and pores and densities around 50%, ξ =1-2 is suggested, and here we will use $\xi = 1$. For our samples, ψ is on this basis calculated to be $2.5 \cdot 10^5$/cm for CeO_2-550 and $1.0 \cdot 10^5$/cm for CeO_2-750. With this, the surface protonic conductance G_{s,H^+} can be determined from the measured macroscopic sample conductivity. As shown in Figure 8 in the main manuscript, G_{s,H^+} of the two samples become roughly identical, as expected.

The BLM also allows estimates of the volumetric specific surface area (SSA_v) based on the same parameters – grain size and relative density or porosity, and from this, we may calculate gravimetric specific surface area (SSA_g) and molar specific surface area (SSA_m) via density and molar weight. Table S2 summarizes the SSA estimated from the brick layer model and converted to ψ, which allows us to compare with that of the BET analyses (Table 1 in the main manuscript, also included here in Table S2 for easy comparison). The SSA_g estimated from the BLM show a factor 3 in difference between CeO_2-550 and CeO_2-750, while the BET indicates a factor 5. The experimental and predicted SSA_g is similar for the CeO_2-750 sample, which may be related to its more faceted grains, while much of the surfaces remaining inside the crystallites of CeO_2-550 is unavailable for surface conduction, resulting in larger discrepancy.

Table S2 Specific surface area (SSA) of the porous CeO_2 estimated from the brick layer model (BLM) compared to the experimental BET surface area.

	Sample	Volumetric specific surface area (SSA_v) cm^2/cm^3	Gravimetric specific surface area (SSA_g) cm^2/g	Molar specific surface area (SSA_m) cm^2/mol
BLM	CeO_2-550	$3.7 \cdot 10^5$	$1.1 \cdot 10^5$	$1.9 \cdot 10^7$
	CeO_2-750	$1.6 \cdot 10^5$	$3.5 \cdot 10^4$	$6.0 \cdot 10^6$
BET	CeO_2-550	$1.1 \cdot 10^6$	$3.1 \cdot 10^5$	$5.3 \cdot 10^7$
	CeO_2-750	$2.6 \cdot 10^5$	$5.9 \cdot 10^4$	$1.0 \cdot 10^7$

5.3 Chemisorbed water layer

We next derive the mathematics of adsorption, dissociation, and transport according to discernible mechanisms in the chemisorbed layer. For CeO_2 and maybe other oxides we find reason to believe that more mechanisms for the chemisorbed layer than was suggested for ZrO_2 [5] are at play and contribute depending on conditions, and we here need to develop the nomenclature further to accommodate this. First level subscripts contain a letter denoting **a**dsorption, **d**issociation, and **m**igration, while second level subscripts have a first letter denoting **c**hemisorbed (*vs*. **p**hysisorbed), a second letter denoting **m**olecular *vs.* **d**issociative, a third letter denoting whether the dissociated proton goes to the **s**urface oxide ion or the **a**dsorbed water molecule, and – following a dash – one or two letters stating that protons migrate between oxide ions in the surface layer (**–s**), between a surface oxide ion and an adsorbed hydroxide ion (**–sa**), or between water and an ionised species in the adsorbed layer (**–a**).

In the approach used previously for ZrO_2 [5] we dealt with relatively well-defined temperature dependencies and used them in combination with selected thermodynamic values from literature to obtain activation enthalpies for proton diffusivities. Here now for CeO_2 we have shallower transitions and evaluate more mechanisms, and we will go further in suggesting enthalpies not only for thermodynamics but also for migration in order to get a comprehensible treatment.

5.3.1 Adsorption and dissociation in the chemisorbed layer

Using a Kröger-Vink-type notation for surface chemistry, [5] molecular chemisorption ("cm") is written as

$$M_{M_s}^{x} + \mathrm{H_2O}(g) \rightleftharpoons M_{M_s}\mathrm{OH}_2^{x} \ , \qquad \text{Eq. 4}$$

where M denotes the cation in binary oxides, in this case M = Ce. Surface cation and oxide ion sites are denoted M_s and O_s. Following ref. [5] and its SI 1, the equilibrium coefficient can be expressed

$$K_{a_{cm}} = \frac{X_{M_{M_s}\mathrm{OH}_2^{x}}}{X_{M_{M_s}^{x}} \dfrac{p_{\mathrm{H_2O}(g)}}{p^0}} = \frac{\gamma_{M_{M_s}\mathrm{OH}_2^{x}}}{\gamma_{M_{M_s}^{x}} \dfrac{p_{H_2O}}{p^0}} = \exp\left(\frac{\Delta S^0_{a_{cm}}}{R}\right)\exp\left(\frac{-\Delta H^0_{a_{cm}}}{RT}\right) \cdot \qquad \text{Eq. 5}$$

Here, p is partial pressure, X denotes fractional occupancy (which ideally corresponds to activity and also to surface site coverage), and γ is surface concentration, e.g., in mol/cm^2. Such molecular chemisorption has predictable negative standard entropy given by loss of one mole of gas, empirically within -120±20 J/molK. For CeO_2 surfaces values are not known, and we will here use -109 J/molK as measured for the entropy of condensation of water at 100°C [6] as an estimate of $\Delta S^0_{a_{cm}}$. Chemisorption is exothermic and the standard enthalpy hence predictably negative. Hayun *et al.* [7] carried out water adsorption calorimetry on nano-CeO_2 at 25°C and found the adsorption enthalpy to be -59.82 ± 0.74 kJ mol^{-1} at a coverage of 8.79 ± 0.39 H_2O/nm^2, which is of the same order as that of water molecules bound directly to Ce ions.[8] Hence, we will here take $\Delta H^0_{a_{cm}}$ = -60 kJ mol^{-1}.

The concentration of adsorbed water according to this molecular chemisorption model follows normal adsorption isotherms (i.e., Langmuir isotherms), and at low coverage (high T, low p_{H_2O} and RH) we have $\gamma_{M_{M_s}OH_2^x} << \gamma_{M_{M_s}^x} \approx \gamma_{M_s}$ and obtain simply

$$\gamma_{M_{M_s}OH_2^x} \approx \gamma_{M_s} K_{a_{cm}} \frac{p_{H_2O}}{p^0} \ , \qquad \text{Eq. 6}$$

so that the coverage – as measured by sorption or thermogravimetry – would be proportional to p_{H_2O} (and hence RH at constant T), but involve the enthalpy of adsorption as a function of temperature at constant p_{H_2O}.

At relatively high RH, the molecular chemisorbed layer may reach complete coverage

$$\gamma_{M_{M_s}OH_2^x} = \gamma_{M_s} = \text{constant} \ , \qquad \text{Eq. 7}$$

hence independent of both T and p_{H_2O} (RH). As an estimate of average cation surface concentration and hence adsorption sites we use 5 H_2O per nm^2 as an ideal monolayer coverage,[9] i.e., γ_{M_s} = 5 /nm^2 = $8 \cdot 10^{-10}$ mol/cm^2.

Molecular chemisorption with dissociation to surface oxide ions

The adsorbed H_2O may dissociate into an adsorbed OH^- and a proton on a surface oxide ion forming surface OH^- according to

$$M_{M_s}OH_2^x + O_{O_s}^x \rightleftharpoons M_{M_s}OH^{/} + OH_{O_s}^{\bullet} \ , \qquad \text{Eq. 8}$$

with equilibrium coefficient

$$K_{d_{cs}} = \frac{X_{M_{M_s}OH^{/}} X_{OH_{O_s}^{\bullet}}}{X_{M_{M_s}OH_2^x} X_{O_{O_s}^x}} = \frac{\gamma_{M_{M_s}OH^{/}} \gamma_{OH_{O_s}^{\bullet}}}{\gamma_{M_{M_s}OH_2^x} \gamma_{O_{O_s}^x}} = \exp\left(\frac{\Delta S_{d_{cs}}^0}{R}\right) \exp\left(\frac{-\Delta H_{d_{cs}}^0}{RT}\right) . \qquad \text{Eq. 9}$$

The standard entropy change is unknown, but should be modest since no gas molecules are involved. The large negative dissociation entropy of liquid water – caused by hydration of ions - need not apply here, since there is no hydration. We will hence assume $\Delta S_{d_{cs}}^0$ = 0 J/molK. The enthalpy of dissociation is expectedly positive, and while the value for dissociations reactions in adsorbed water on CeO_2 are unknown, we will assume a round value for $\Delta H_{d_{cs}}^0$ =20 kJ mol^{-1} based on the 22 kJ mol^{-1} measured for YSZ. [10] These values are much lower than in liquid water, which is reasonable as we here protonate an O^{2-} ion instead of a H_2O molecule.

Dissociative chemisorption

Dissociation of protons onto surface oxide ions may be sufficiently favourable to dissociate all adsorbed molecules in what is termed dissociative chemisorption ("cds"), which we may write without the molecular intermediate directly as the sum of the reactions in Eq. 4 and Eq. 8:

$$M_{M_s}^x + O_{O_s}^x + H_2O(g) \rightleftharpoons M_{M_s}OH^{/} + OH_{O_s}^{\bullet} \qquad \text{Eq. 10}$$

The equilibrium coefficient is then (from now on omitting the stage of site fractions)

$$K_{a_{cds}} = K_{a_{cm}} K_{d_{cs}} = \frac{\gamma_{M_{M_s}OH^{/}} \gamma_{OH^{\bullet}_{O_s}}}{\gamma_{M^{x}_{M_s}} \gamma_{O^{x}_{O_s}} \frac{p_{H_2O}}{p^0}} = \exp\left(\frac{\Delta S^0_{a_{cds}}}{R}\right) \exp\left(\frac{-\Delta H^0_{a_{cds}}}{RT}\right), \quad \text{Eq. 11}$$

where the standard entropy and enthalpy changes are sums of those for molecular chemisorption and dissociation: $\Delta S^0_{a_{cds}} = \Delta S^0_{a_{cm}} + \Delta S^0_{d_{cs}}$ and $\Delta H^0_{a_{cds}} = \Delta H^0_{a_{cm}} + \Delta H^0_{d_{cs}}$, here taken to be -109 + 0 = -109 J/molK and -60 + 20 = -40 kJ mol^{-1}, respectively.

Regardless of whether we have weak dissociation and hence molecular chemisorption ("cm") or dissociative chemisorption ("cd"), the simplified electroneutrality condition is

$$\gamma_{OH^{\bullet}_{O_s}} = \gamma_{M_{M_s}OH^{/}}, \quad \text{Eq. 12}$$

and insertion into Eq. 11 yields

$$\gamma_{OH^{\bullet}_{O_s}} = \gamma_{M_{M_s}OH^{/}} = \sqrt{K_{a_{cds}} \gamma_{M^{x}_{M_s}} \gamma_{O^{x}_{O_s}} \frac{p_{H_2O}}{p^0}}, \quad \text{Eq. 13}$$

At low coverage, we have $\gamma_{M^{x}_{M_s}} \approx \gamma_{M_s}$ and in MO_2 oxides $\gamma_{O^{x}_{O_s}} \approx \gamma_{O_s} = 2\gamma_{M_s}$, and we may then simplify further to

$$\gamma_{OH^{\bullet}_{O_s}} = \gamma_{M_{M_s}OH^{/}} = \gamma_{M_s} \sqrt{2K_{a_{cds}} \frac{p_{H_2O}}{p^0}}. \quad \text{Eq. 14}$$

We may consider the strongly dissociative chemisorption by Eq. 10 as a case where we may reach full coverage and obtain

$$\gamma_{OH^{\bullet}_{O_s}} = \gamma_{M_{M_s}OH^{/}} = \gamma_{M_s} = \text{constant}. \quad \text{Eq. 15}$$

Molecular chemisorption with dissociation to adsorbed water molecules

Chemisorbed H_2O may also dissociate within the molecular layer into adsorbed OH^- ions and adsorbed H_3O^+ ions as treated by Raz *et al.* [11] In our nomenclature it is written

$$2M_{M_s}OH^{x}_2 \rightleftharpoons M_{M_s}OH^{/} + M_{M_s}OH^{\bullet}_3, \quad \text{Eq. 16}$$

with equilibrium coefficient

$$K_{d_{ca}} = \frac{\gamma_{M_{M_s}OH^{/}} \gamma_{M_{M_s}OH^{\bullet}_3}}{\gamma^2_{M_{M_s}OH^{x}_2}} = \exp\left(\frac{\Delta S^0_{d_{ca}}}{R}\right) \exp\left(\frac{-\Delta H^0_{d_{ca}}}{RT}\right). \quad \text{Eq. 17}$$

We will assume that this dissociation has again a negligible standard entropy $\Delta S^0_{d_{ca}} = 0$ J/molK, while the enthalpy should be higher than for dissociation to surface oxygen. We will assume a round value of $\Delta H^0_{d_{ca}} = 40$ kJ mol^{-1}.

The total electroneutrality condition now becomes

$$\gamma_{OH^{\bullet}_{O_s}} + \gamma_{M_{M_s}OH^{\bullet}_3} = \gamma_{M_{M_s}OH^{/}}. \quad \text{Eq. 18}$$

If dissociation to the surface oxide ions dominates and Eq. 14 applies, insertion into Eq. 17 yields the concentration of minority hydronium ions, but this plays no role, as proton transport in the chemisorbed layer then will take place mainly between the majority adsorbed hydroxide ions and water molecules.

If instead dissociation within the chemisorbed layer dominates, electroneutrality simplifies to

$$\gamma_{M_{M_s}\mathrm{OH}_3^{\bullet}} = \gamma_{M_{M_s}\mathrm{OH}^{/}} \quad . \qquad \text{Eq. 19}$$

Cation surface site balance requires $\gamma_{M_{M_s}^{x}} + \gamma_{M_{M_s}\mathrm{OH}_2^{x}} + \gamma_{M_{M_s}\mathrm{OH}^{/}} + \gamma_{M_{M_s}\mathrm{OH}_3^{\bullet}} = \gamma_{M_s}$.

In the following, we assume that dissociation in the molecular layer must remain incomplete (weak). With low coverage and limited dissociation, we have $\gamma_{M_{M_s}^{x}} \approx \gamma_{M_s} >> \gamma_{M_{M_s}\mathrm{OH}_2^{x}} >> \gamma_{M_{M_s}\mathrm{OH}^{/}} + \gamma_{M_{M_s}\mathrm{OH}_3^{\bullet}}$, and we can insert and simplify to get the concentration of the dissociated species,

$$K_{\mathrm{d_{ca}}} = \frac{\gamma_{M_{M_s}\mathrm{OH}^{/}}^2}{\left(K_{\mathrm{a_{cm}}}\gamma_{M_s}\frac{p_{\mathrm{H_2O}}}{p^0}\right)^2} \quad \Rightarrow \quad \gamma_{M_{M_s}\mathrm{OH}_3^{\bullet}} = \gamma_{M_{M_s}\mathrm{OH}^{/}} = \gamma_{M_s} K_{\mathrm{a_{cm}}} \sqrt{K_{\mathrm{d_{ca}}}} \frac{p_{\mathrm{H_2O}}}{p^0} \quad . \qquad \text{Eq. 20}$$

If we reach full coverage within the molecular chemisorbed layer and dissociation within this layer is still weak, the cation surface site balance becomes $\gamma_{M_{M_s}\mathrm{OH}_2^{x}} \approx \gamma_{M_s}$, and we can insert and simplify to get the temperature dependence of the dissociated species,

$$K_{\mathrm{d_{ca}}} = \frac{\gamma_{M_{M_s}\mathrm{OH}^{/}}^2}{\gamma_{M_s}^2} \quad \Rightarrow \quad \gamma_{M_{M_s}\mathrm{OH}_3^{\bullet}} = \gamma_{M_{M_s}\mathrm{OH}^{/}} = \gamma_{M_s} \sqrt{K_{\mathrm{d_{ca}}}} \quad . \qquad \text{Eq. 21}$$

As summarized in Table S3, in all the cases of molecular chemisorption following Eq. 4 and Eq. 5, measurements of water adsorption and coverage by sorption and TG will reflect the amount of molecular water given by Eq. 6 in the low coverage region with a $p_{\mathrm{H_2O}}^1$ dependence and Eq. 7 in the high coverage cases (i.e., independent of $p_{\mathrm{H_2O}}$). In the case of dissociative adsorption, on the other hand, following Eq. 10, adsorption and coverage are determined by the dissociated charged species and have a $p_{\mathrm{H_2O}}^{1/2}$ dependence (Eq. 14). As we shall see later, conduction always follows the dissociated species and may have the same or other $p_{\mathrm{H_2O}}$ dependences. When the models reach full coverage, the $p_{\mathrm{H_2O}}$ dependences always disappear, both for total water contents from sorption and TG, and for dissociated species from conductance.

Table S3 Derived $p_{\mathrm{H_2O}}$ dependences of water adsorption and coverage based on the thermodynamics of adsorption and dissociation in cases of low and full coverage.

n in $p_{\mathrm{H_2O}}^n$	Low coverage	Full coverage
Molecular chemisorption, "**cm**"	1	0
Strong dissociative chemisorption, "**cds**"	1/2	0

5.3.2 Protonic conduction in chemisorbed water

Migration mechanisms

In order to evaluate conduction, we take on some simplified cases of proton migration. In the following reactions, the proton jumps from the first to the second species (see also schematic illustrations below):

Migration of protons between surface hydroxide and oxide ions, with charge mobility $u_{H^+_s}$:

$$OH^{\bullet}_{O_s} + O^{x}_{O_s} \rightleftharpoons O^{x}_{O_s} + OH^{\bullet}_{O_s} \qquad \text{Eq. 22}$$

Migration between surface and adsorbed hydroxide ions (reverse and forward dissociation), with charge mobility $u_{H^+_{sa}}$:

$$OH^{\bullet}_{O_s} + M_{M_s}OH^{/} \rightleftharpoons O^{x}_{O_s} + M_{M_s}OH^{x}_{2} \qquad \text{Eq. 23}$$

Migration in the adsorbed layer between water molecules and hydroxide ions, with charge mobility $u_{H^+_a}$:

$$M_{M_s}OH^{x}_{2} + M_{M_s}OH^{/} \rightleftharpoons M_{M_s}OH^{/} + M_{M_s}OH^{x}_{2} \qquad \text{Eq. 24}$$

Migration between hydroxonium ions and water molecules, assumed to have numerically the same charge mobility $u_{H^+_a}$:

$$M_{M_s}OH^{\bullet}_{3} + M_{M_s}OH^{x}_{2} \rightleftharpoons M_{M_s}OH^{x}_{2} + M_{M_s}OH^{\bullet}_{3} \qquad \text{Eq. 25}$$

It should be noted that we will treat all these mobilities according to analysis of $u_{H^+_s}$ introduced in Section 5.1. They hence have the same preexponentials, $u_{H^+_s 0}$, but different activation energies. Generally speaking, the activation energies decrease, and mobilities hence increase, as we go from the protons on the rigid surface, via jumps between the surface and the adsorbed layer, to jumps between adsorbed and hence more vibrant species.

In the following, the mechanisms are schematically depicted as they are coupled with the thermodynamics that determines carrier and jump site concentrations to obtain surface conductances.

Proton migration between surface oxide ions: cms-s and cds-s

A schematic illustration of the cms-s and cds-s models for adsorption, dissociation and proton migration at various water coverage is provided in Figure S9.

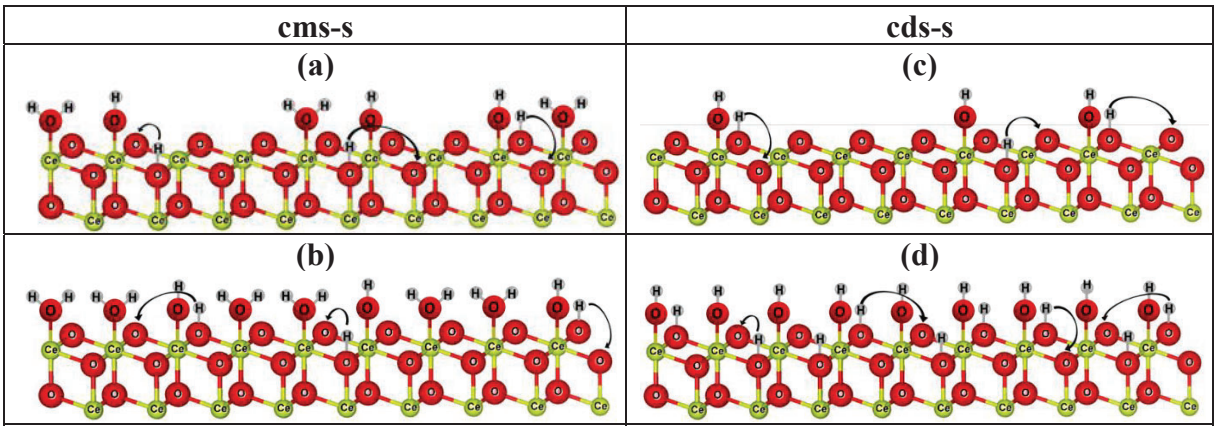

Figure S9 Schematic illustration of the "cms-s" model on the (111) surface of CeO_2 at low coverage (a) and at full coverage of molecular water with low dissociation (b), "cds-s" model at low coverage (c) and at full coverage of dissociatively chemisorbed water (d). The arrows show the protonic migration.

The proton on surface oxide in the $OH^{\bullet}_{O_s}$ defect may migrate by jumping to other surface oxide ions. The surface protonic conductance will then be

$$G_{s,H^+_{cds\text{-}s}} = G_{s,H^+_{cms\text{-}s}} = F\gamma_{OH^{\bullet}_{O_s}} u_{H^+_s} = F\gamma_{OH^{\bullet}_{O_s}} X_{O^x_{O_s}} u_{H^+0} \frac{1}{T} \exp\left(\frac{-\Delta H_{m,H^+_s}}{RT}\right). \qquad \text{Eq. 26}$$

In the case of **low coverage** (Figure S9 a and c), unprotonated surface oxide ions are generally available, $X_{O^x_{O_s}} \approx 1$, so that we by inserting Eq. 14 get

$$G_{s,H^+_{cms\text{-}s}} = F\gamma_{M_s}\sqrt{2K_{a_{cds}}\frac{p_{H_2O}}{p^0}}u_{H^+0}\frac{1}{T}\exp\left(\frac{-\Delta H_{m,H^+_s}}{RT}\right), \qquad \text{Eq. 27}$$

which we may express as

$$G_{s,H^+_{cms\text{-}s}} = G_{s,H^+_{cms\text{-}s}0}\frac{1}{T}\exp\left(\frac{-\left(\frac{1}{2}\Delta H^0_{a_{cm}} + \frac{1}{2}\Delta H^0_{d_{cs}} + \Delta H_{m,H^+_s}\right)}{RT}\right), \qquad \text{Eq. 28}$$

with

$$G_{s,H^+_{cms\text{-}s}0} = G^0_{s,H^+_{cms\text{-}s}0}\sqrt{\frac{p_{H_2O}}{p^0}} = \sqrt{2}F\gamma_{M_s}\exp\left(\frac{\frac{1}{2}\Delta S^0_{a_{cm}} + \frac{1}{2}\Delta S^0_{d_{cs}}}{R}\right)u_{H^+0}\sqrt{\frac{p_{H_2O}}{p^0}}. \qquad \text{Eq. 29}$$

With the estimates made above of $\Delta S^0_{a_{cm}}$ = -109 J/molK, $\Delta S^0_{d_{cm}}$ = 0 J/molK, $\gamma_{M_s} \approx 5$ /nm^2 = 8·10^{-10} mol/cm^2, and $u_{H^+0} \approx 10$ cm^{2}K/Vs, we get $G^0_{s,H^+_{cms\text{-}s}0} \approx 1.6\cdot10^{-6}$ SK for p_{H_2O} = 1 bar and $G_{s,H^+_{cms\text{-}s}0}$ ≈ 2·10^{-7} SK at p_{H_2O} = 0.025 atm, see entries for cds-s and cms-s in Table S4. The $p^{1/2}_{H_2O}$ dependence of the model is also entered along with a first estimate of the magnitude of the activation enthalpy of conductance being $\Delta H_{c_{cms\text{-}s}} = \Delta H_{c_{cds\text{-}s}} = \frac{1}{2}\Delta H^0_{a_{cm}} + \frac{1}{2}\Delta H^0_{d_{cs}} + \Delta H_{m,H^+_s} \approx +30$ kJ mol^{-1} from the values discussed above of $\Delta H^0_{a_{cm}} \approx$ -60 kJ mol^{-1}, $\Delta H^0_{d_{cs}} \approx +20$ kJ mol^{-1}, and taking a high migration barrier of $\Delta H_{m,H^+_s} \approx 50$ kJ mol^{-1} between surface oxide ions.

We note that for low coverage and proton migration on surface oxide ions, the above applies to surface protonic conduction regardless of whether the chemisorbed water remains mainly molecular or mainly dissociated, applying to models cms-s and cds-s. However, the measurement of the amount of adsorbed water by sorption or TG follows either the dominant molecular species H_2O with a $p_{H_2O}^{1}$ dependence (different from the conductance) or the dominant dissociated species with a $p_{H_2O}^{1/2}$ dependence (same as conductance), see p_{H_2O} dependences for total concentration of adsorbed water in Table S3 *vs* those for conductance in Table S4.

At **full coverage** of **molecularly chemisorbed** water (Figure S9 b), by sufficiently low T and high p_{H_2O} and RH, we have instead

$$\gamma_{M_{M_s}OH_2^x} = \gamma_{M_s} >> \gamma_{M_{M_s}OH'} = \gamma_{OH_{O_s}^{\bullet}} = \sqrt{\gamma_{M_s}\gamma_{O_{O_s}^x}K_{d_{cs}}} \quad . \qquad \text{Eq. 30}$$

We may assume $\gamma_{O_{O_s}^x} = \gamma_{O_s} = 2\gamma_{M_s}$ so that the surface protonic conductance becomes

$$G_{s,H^+_{cms\text{-}s}} = F\gamma_{M_s}\sqrt{2K_{d_{cms}}}u_{H^+0}\frac{1}{T}\exp\left(\frac{-\Delta H_{m,H^+_s}}{RT}\right) = G_{s,H^+_{cms\text{-}s}0}\frac{1}{T}\exp\left(\frac{-\left(\frac{1}{2}\Delta H^0_{d_{cs}} + \Delta H_{m,H^+_s}\right)}{RT}\right) \qquad \text{Eq. 31}$$

with

$$G_{s,H^+_{cms\text{-}s}0} = G^0_{s,H^+_{cms\text{-}s}0} = \sqrt{2}\gamma_{M_s}\exp\left(\frac{\Delta S^0_{d_{cs}}}{2R}\right)u_{H^+0} \quad . \qquad \text{Eq. 32}$$

In this case, the concentration of dissociated protons is independent of p_{H_2O}, and the temperature dependence is attributable to the enthalpies of dissociation and mobility, an estimate being ($1/2 \cdot 20 + 50 = 60$ kJ mol^{-1}) hence considerably more positive than for the low-coverage case. With parameters as before, we now get $G_{s,H^+_{cms\text{-}s}0} = G^0_{s,H^+_{cms\text{-}s}0} \approx 1{\cdot}10^{-3}$ SK, see Table S4.

At **full coverage** of **dissociatively chemisorbed** water (Figure S9 d), we will have

$$\gamma_{M_{M_s}OH'} = \gamma_{OH_{O_s}^{\bullet}} = \gamma_{M_s} \quad . \qquad \text{Eq. 33}$$

If migration of dissociated protons takes place by jumps between surface oxide host sites on a CeO_2 surface, we may now assume an average occupancy of $X_{O_{O_s}^x} = 0.5$, since half of them are occupied with dissociated protons. The surface protonic conductance then becomes

$$G_{s,H^+_{cds\text{-}s}} = \frac{F}{2}\gamma_{M_s}u_{H^+0}\frac{1}{T}\exp\left(\frac{-\Delta H_{m,H^+_s}}{RT}\right) = G_{s,H^+_{cds\text{-}s}0}\frac{1}{T}\exp\left(\frac{-\Delta H_{m,H^+_s}}{RT}\right), \qquad \text{Eq. 34}$$

with

$$G_{s,H^+_{cds\text{-}s}0} = G^0_{s,H^+_{cds\text{-}s}0} = \frac{F}{2}\gamma_{M_s}u_{H^+0} \quad . \qquad \text{Eq. 35}$$

In this case, the concentration of dissociated protons is independent of temperature and p_{H_2O}, and the temperature dependence is attributable to the mobility of protons alone. With the same assumptions as before, we get $G_{s,H^+_{cds\text{-}s}0} = G^0_{s,H^+_{cds\text{-}s}0} \approx 4{\cdot}10^{-4}$ SK. The enthalpy will reflect proton mobility only, e.g. around 50 kJ mol^{-1}.

Conduction via surface oxide ions by protons dissociated from chemisorbed water has for MO_2 oxides in general enough oxide ions, even at full coverage, from the 2:1 ratio of oxide ions to cations. However, the hydrogenation leading to CeOOH-like surface and subsurface layers introduces surface hydroxide ions, i.e. already pre-protonated surface oxide ions. This may limit the availability of proton jump sites in the case of strong dissociative chemisorption to full coverage – a theme beyond the scope of this paper.

Proton migration between surface oxide ions and adsorbed hydroxide ions: cms-sa and cds-sa

Let us now analyse the contribution from protons jumping between the $OH^{\bullet}_{O_s}$ and $M_{M_s}OH^{/}$ defects formed in the dissociation, schematically depicted in Figure S10.

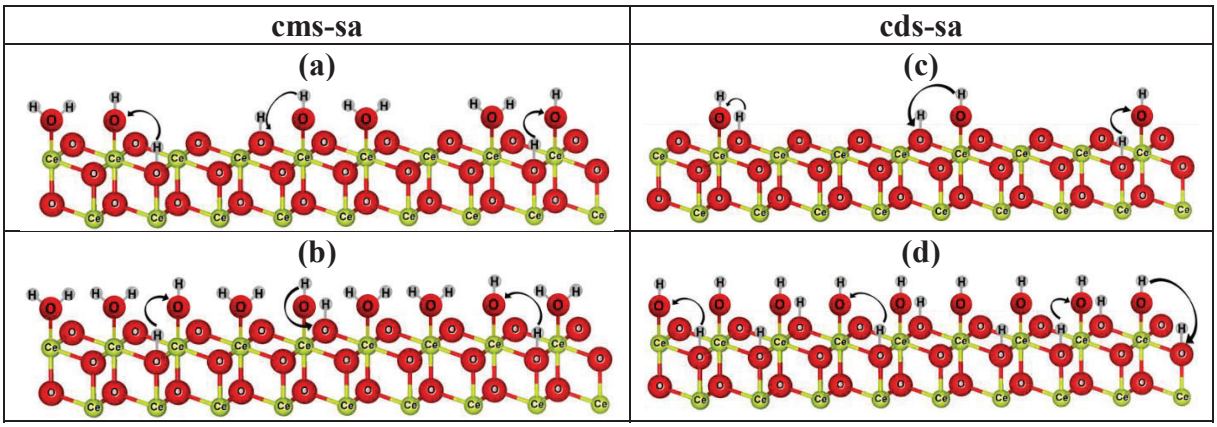

Figure S10 Schematic illustration of the "cms-sa" model on the (111) surface of CeO_2 at low coverage (a) and full coverage of molecular water with low dissociation (b), "cds-sa" model at low coverage (c) and at full coverage of dissociatively chemisorbed water (d). The arrows show the protonic migration.

The surface protonic conductance along this can be expressed in terms of the surface protons and will then be proportional to the site fraction of available dissociated adsorbed hydroxide ions:

$$G_{s,H^+_{cds\text{-}sa}} = G_{s,H^+_{cms\text{-}sa}} = F\gamma_{OH^{\bullet}_{O_s}} u_{H^+_{sa}} = F\gamma_{OH^{\bullet}_{O_s}} X_{M_{M_s}OH^{/}} u_{H^+0} \frac{1}{T} \exp\left(\frac{-\Delta H_{m,H^+_{sa}}}{RT}\right) \qquad \text{Eq. 36}$$

By assuming **low coverage** (Figure S10 a and c) and inserting Eq. 14 we get

$$G_{s,H^+_{cms\text{-}sa}} = 2FK_{a_{cm}} K_{d_{cs}} \gamma_{M_s} \frac{p_{H_2O}}{p^0} u_{H^+0} \frac{1}{T} \exp\left(\frac{-\Delta H_{m,H^+_{sa}}}{RT}\right), \qquad \text{Eq. 37}$$

and hence

$$G_{s,H^+_{cms\text{-}sa}} = G_{s,H^+_{cms\text{-}sa}0} \frac{1}{T} \exp\left(\frac{-\left(\Delta H^0_{a_{cm}} + \Delta H^0_{d_{cs}} + \Delta H_{m,H^+_{sa}}\right)}{RT}\right), \qquad \text{Eq. 38}$$

with

$$G_{\mathrm{s,H^+_{cms\text{-}sa}}0} = G^0_{\mathrm{s,H^+_{cms\text{-}sa}}0}\frac{p_{\mathrm{H_2O}}}{p^0} = 2F\gamma_{M_\mathrm{s}}\exp\left(\frac{\Delta S^0_{\mathrm{a_{cm}}}+\Delta S^0_{\mathrm{d_{cs}}}}{R}\right)u_{\mathrm{H^+}0}\frac{p_{\mathrm{H_2O}}}{p^0}\ . \qquad \text{Eq. 39}$$

With assumptions like before we get $G^0_{\mathrm{s,H^+_{cms\text{-}sa}}0} \approx 3\cdot10^{-9}$ SK and $G_{\mathrm{s,H^+_{cms\text{-}sa}}0} \approx 8\cdot10^{-11}$ SK at $p_{\mathrm{H_2O}} =$ 0.025 bar. With an assumed enthalpy of migration of 40 kJ mol^{-1}, we estimate $\Delta H_{\mathrm{c_{cms\text{-}sa}}} = \Delta H^0_{\mathrm{a_{cm}}} + \Delta H^0_{\mathrm{d_{cs}}} + \Delta H_{\mathrm{m,H^+_{sa}}}$ to be around 0 kJ mol^{-1}. It is intriguing that CeO_2 displays a conductance contribution with small temperature dependency in the shallow conductance minimum at intermediate temperatures, where the predictions here of preexponential and enthalpy fit well.

The model proposes a proportionality to $p^1_{\mathrm{H_2O}}$ of surface protonic conduction. This appears to be approached for high $p_{\mathrm{H_2O}}$ at 400°C in our measurements and in those of Manabe *et al.* [12]

At **full coverage**, $\gamma_{M_{M_\mathrm{s}}\mathrm{OH}^\mathrm{x}_2} \approx \gamma_{M_\mathrm{s}}$, but still **low dissociation** ($\gamma_{\mathrm{O}^\mathrm{x}_{\mathrm{O_s}}} \approx \gamma_{\mathrm{O_s}} = 2\gamma_{M_\mathrm{s}}$), i.e., following Figure S10 b, combination with Eq. 9 yields for the conductance

$$G_{\mathrm{s,H^+_{cms\text{-}sa}}} = F\gamma_{\mathrm{OH^\bullet_{O_s}}}\frac{\gamma_{M_{M_\mathrm{s}}\mathrm{OH}^/}}{\gamma_{M_\mathrm{s}}}u_{\mathrm{H^+}0}\frac{1}{T}\exp\left(\frac{-\Delta H_{\mathrm{m,H^+_{sa}}}}{RT}\right) = 2F\gamma_{M_\mathrm{s}}K_{\mathrm{d_{cs}}}u_{\mathrm{H^+}0}\frac{1}{T}\exp\left(\frac{-\Delta H_{\mathrm{m,H^+_{sa}}}}{RT}\right), \qquad \text{Eq. 40}$$

and hence

$$G_{\mathrm{s,H^+_{cms\text{-}sa}}} = G_{\mathrm{s,H^+_{cms\text{-}sa}}0}\frac{1}{T}\exp\left(\frac{-\left(\Delta H^0_{\mathrm{d_{cs}}}+\Delta H_{\mathrm{m,H^+_{sa}}}\right)}{RT}\right), \qquad \text{Eq. 41}$$

with

$$G_{\mathrm{s,H^+_{cms\text{-}sa}}0} = G^0_{\mathrm{s,H^+_{cms\text{-}sa}}0} = 2F\gamma_{M_\mathrm{s}}\exp\left(\frac{\Delta S^0_{\mathrm{d_{cs}}}}{R}\right)u_{\mathrm{H^+}0}\ . \qquad \text{Eq. 42}$$

Here, we estimate $G_{\mathrm{s,H^+_{cms\text{-}sa}}0} = G^0_{\mathrm{s,H^+_{cms\text{-}sa}}0} \approx 1.5\cdot10^{-3}$ SK and the enthalpy may be estimated to be in the range +60 kJ mol^{-1}.

At **full coverage** but now **high dissociation** (Figure S10 d), we have $\gamma_{\mathrm{OH^\bullet_{O_s}}} = \gamma_{M_{M_\mathrm{s}}\mathrm{OH}^/} \approx \gamma_{M_\mathrm{s}}$ which yields for the conductance

$$G_{\mathrm{s,H^+_{cds\text{-}sa}}} = F\gamma_{\mathrm{OH^\bullet_{O_s}}}\frac{\gamma_{M_{M_\mathrm{s}}\mathrm{OH}^/}}{\gamma_{M_\mathrm{s}}}u_{\mathrm{H^+}0}\frac{1}{T}\exp\left(\frac{-\Delta H_{\mathrm{m,H^+_{sa}}}}{RT}\right) = F\gamma_{M_\mathrm{s}}u_{\mathrm{H^+}0}\frac{1}{T}\exp\left(\frac{-\Delta H_{\mathrm{m,H^+_{sa}}}}{RT}\right), \qquad \text{Eq. 43}$$

and hence

$$G_{\mathrm{s,H^+_{cds\text{-}sa}}} = G_{\mathrm{s,H^+_{cds\text{-}sa}}0}\frac{1}{T}\exp\left(\frac{-\Delta H_{\mathrm{m,H^+_{sa}}}}{RT}\right), \qquad \text{Eq. 44}$$

with

$$G_{\mathrm{s,H^+_{cds\text{-}sa}}0} = G^0_{\mathrm{s,H^+_{cds\text{-}sa}}0} = F\gamma_{M_\mathrm{s}}u_{\mathrm{H^+}0}\ . \qquad \text{Eq. 45}$$

Here, we estimate $G_{s,H^+_{cds\text{-}sa}0} = G^0_{s,H^+_{cds\text{-}sa}0} \approx 8\cdot10^{-4}$ SK and the enthalpy will be that of mobility only, e.g., +40 kJ mol^{-1}.

Proton migration between adsorbed water molecules and hydroxide ions: cms-a and cds-a

Schematic illustrations of the cms-a and cds-a models at low and full coverage are displayed in Figure S11.

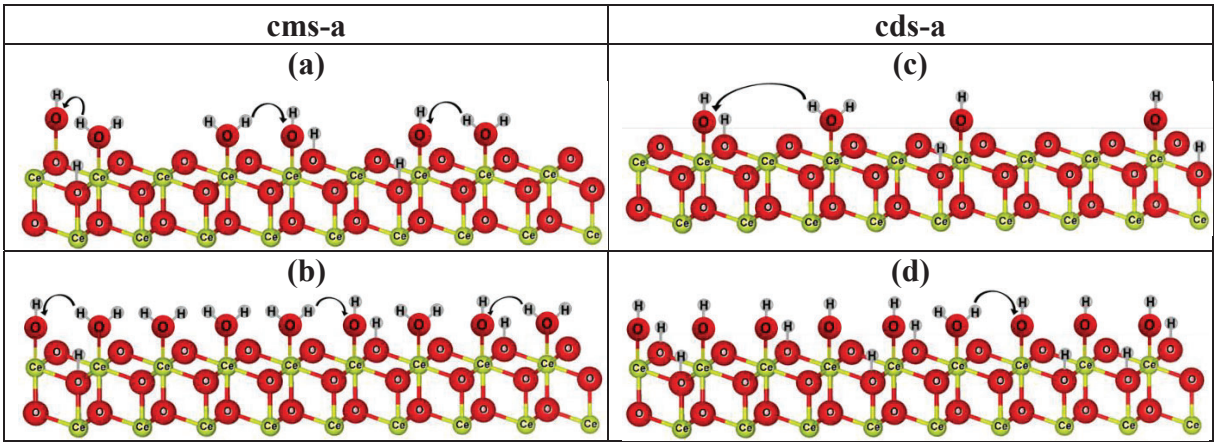

Figure S11 Schematic illustration of the "cms-a" model on the (111) surface of CeO_2 at low coverage (a) and full coverage of molecular water and low dissociation (b), "cds-a" model at low coverage (c) and full coverage with high dissociation of chemisorbed water (d). The arrows show the protonic migration.

The surface conductance based on Eq. 24 can be written

$$G_{s,H^+_{cds\text{-}a}} = G_{s,H^+_{cms\text{-}a}} = F\gamma_{M_{M_s}OH^x_2} u_{H^+_a} = F\gamma_{M_{M_s}OH^x_2} \frac{\gamma_{M_{M_s}OH'}}{\gamma_{M_s}} u_{H^+0} \frac{1}{T} \exp\left(\frac{-\Delta H_{m,H^+_a}}{RT}\right), \qquad \text{Eq. 46}$$

which, under assumption of **low coverage** (Figure S11 a and c), by combination with Eq. 5 and Eq. 14, yields

$$G_{s,H^+_{cms\text{-}a}} = F\gamma_{M_s} K_{a_{cm}} \sqrt{2K_{a_{cs}}} \left(\frac{p_{H_2O}}{p^0}\right)^{3/2} u_{H^+0} \frac{1}{T} \exp\left(\frac{-\Delta H_{m,H^+_a}}{RT}\right). \qquad \text{Eq. 47}$$

We rewrite this as

$$G_{s,H^+_{cms\text{-}a}} = G_{s,H^+_{cms\text{-}a}0} \frac{1}{T} \exp\left(\frac{-\Delta H_{cms\text{-}a}}{RT}\right) = G_{s,H^+_{cms\text{-}a}0} \frac{1}{T} \exp\left(\frac{-\left(\Delta H^0_{a_{cm}} + \frac{1}{2}\Delta H^0_{a_{cs}} + \Delta H_{m,H^+_a}\right)}{RT}\right) \qquad \text{Eq. 48}$$

with $\Delta H_{c_{cms\text{-}a}} = \Delta H^0_{a_{cm}} + \frac{1}{2}\Delta H^0_{a_{cds}} + \Delta H_{m,H^+_a} = \frac{3}{2}\Delta H^0_{a_{cm}} + \frac{1}{2}\Delta H^0_{d_{cs}} + \Delta H_{m,H^+_a}$, and preexponential of surface protonic conductance given by

$$G_{s,H^+_{cms\text{-}a}0} = G^0_{s,H^+_{cms\text{-}a}0} \left(\frac{p_{H_2O}}{p^0}\right)^{3/2} = \sqrt{2}F\gamma_{M_s} \exp\left(\frac{\frac{3}{2}\Delta S^0_{a_{cm}} + \frac{1}{2}\Delta S^0_{d_{cs}}}{R}\right) u_{H^+0} \left(\frac{p_{H_2O}}{p^0}\right)^{3/2} \qquad \text{Eq. 49}$$

With assumptions as before, we obtain $G^0_{s,H^+_{chm\text{-}a}0} \approx 3\cdot10^{-12}$ SK and $G_{s,H^+_{chm\text{-}a}0} \approx 1\cdot10^{-14}$ SK at p_{H_2O} = 0.025 bar. With an enthalpy of mobility in the adsorbed layer of 20 kJ mol^{-1}, the enthalpy of

conduction may be estimated to be $\Delta H_{\mathrm{c_{cms\text{-}a}}} = \frac{3}{2}\Delta H^0_{\mathrm{a_{cm}}} + \frac{1}{2}\Delta H^0_{\mathrm{d_{cs}}} + \Delta H_{\mathrm{m,H^+_a}} \approx$ -60 kJ mol^{-1}, meaning that conductance increases strongly with decreasing temperature. This behaviour hence appears to fit with the conductivity in the region where it has traditionally been assigned to transport in the physisorbed layer.

At **full coverage**, $\gamma_{M_{M_s}\mathrm{OH}^{\mathrm{x}}_2} \approx \gamma_{M_s}$, and **low dissociation** ($\gamma_{\mathrm{O_s}} \approx 2\gamma_{M_s}$), Figure S11 b, combination with Eq. 9 yields for the conductance

$$G_{\mathrm{s,H^+_{cms\text{-}a}}} = F\gamma_{M_{M_s}\mathrm{OH}^{\mathrm{x}}_2} u_{\mathrm{H^+_a}} = F\gamma_{M_s}\sqrt{2K_{\mathrm{d_{cs}}}}\,u_{\mathrm{H^+0}}\frac{1}{T}\exp\left(\frac{-\Delta H_{\mathrm{m,H^+_a}}}{RT}\right), \qquad \text{Eq. 50}$$

which we rewrite as

$$G_{\mathrm{s,H^+_{cms\text{-}a}}} = G_{\mathrm{s,H^+_{cms\text{-}a}0}}\frac{1}{T}\exp\left(\frac{-\Delta H_{\mathrm{cms\text{-}a}}}{RT}\right) = G_{\mathrm{s,H^+_{cms\text{-}a}0}}\frac{1}{T}\exp\left(\frac{-\left(\frac{1}{2}\Delta H^0_{\mathrm{d_{cs}}} + \Delta H_{\mathrm{m,H^+_a}}\right)}{RT}\right), \qquad \text{Eq. 51}$$

with the preexponential

$$G_{\mathrm{s,H^+_{cms\text{-}a}0}} = G^0_{\mathrm{s,H^+_{cms\text{-}a}0}} = \sqrt{2}F\gamma_{M_s}\exp\left(\frac{\frac{1}{2}\Delta S^0_{\mathrm{d_{cs}}}}{R}\right)u_{\mathrm{H^+0}}, \qquad \text{Eq. 52}$$

coming out as $G_{\mathrm{s,H^+_{cms\text{-}a}0}} = G^0_{\mathrm{s,H^+_{cms\text{-}a}0}} =$ 1.1·10^{-3} SK. The enthalpy may be estimated to be around +30 kJ mol^{-1}.

At **full coverage** and **high dissociation** (Figure S11 d), we have $\gamma_{\mathrm{OH^{\bullet}_O}} = \gamma_{M_{M_s}\mathrm{OH^{/}}} \approx \gamma_{M_s}$ and combination with Eq. 9 yields for the conductance in the adsorbed layer

$$G_{\mathrm{s,H^+_{cds\text{-}a}}} = \frac{F\gamma_{M_s}}{K_{\mathrm{d_{cs}}}}u_{\mathrm{H^+0}}\frac{1}{T}\exp\left(\frac{-\Delta H_{\mathrm{m,H^+_a}}}{RT}\right), \qquad \text{Eq. 53}$$

which we rewrite as

$$G_{\mathrm{s,H^+_{cds\text{-}a}}} = G_{\mathrm{s,H^+_{cds\text{-}a}0}}\frac{1}{T}\exp\left(\frac{-\Delta H_{\mathrm{c_{cms\text{-}a}}}}{RT}\right) = G_{\mathrm{s,H^+_{cms\text{-}a}0}}\frac{1}{T}\exp\left(\frac{-\left(-\Delta H^0_{\mathrm{d_{cs}}} + \Delta H_{\mathrm{m,H^+_a}}\right)}{RT}\right), \qquad \text{Eq. 54}$$

with the preexponential

$$G_{\mathrm{s,H^+_{cds\text{-}a}0}} = G^0_{\mathrm{s,H^+_{cds\text{-}a}0}} = F\gamma_{M_s}\exp\left(\frac{-\Delta S^0_{\mathrm{d_{cs}}}}{R}\right)u_{\mathrm{H^+0}}, \qquad \text{Eq. 55}$$

coming out as $G_{\mathrm{s,H^+_{cds\text{-}a}0}} = G^0_{\mathrm{s,H^+_{cds\text{-}a}0}} =$ 8·10^{-4} SK. The enthalpy may be estimated to be around 0 kJ mol^{-1} as the negative of the dissociation enthalpy and the migration enthalpy cancel.

Proton migration between dissociated species within the chemisorbed layer: cma-a

The cma-a model is shown in Figure S12.

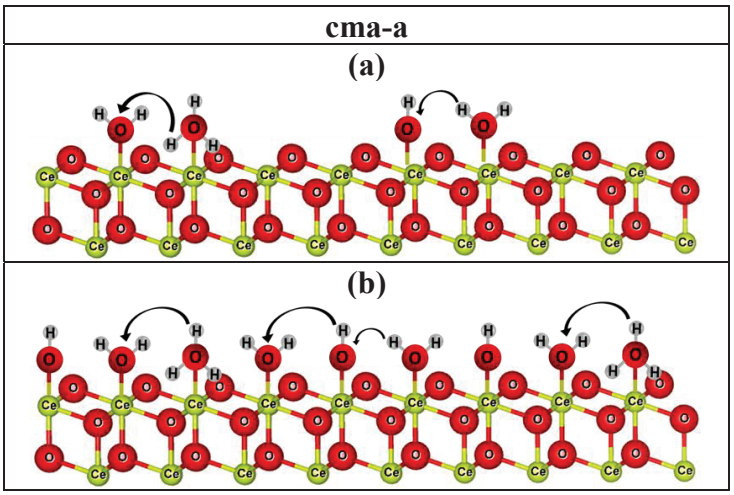

Figure S12 Schematic illustration of the "cma-a" model on the (111) surface of CeO_2 at low (a) and full coverage (b). The arrows show the protonic migration.

If dissociation within the chemisorbed layer (Eq. 16) dominates, we have the electroneutrality and concentrations determined by Eq. 19 and Eq. 20, respectively. This corresponds to the model suggested by Raz *et al.* [11] but as stated above, it cannot prevail because dissociation in the water layer should be weaker than to the surface oxide ions. We nevertheless provide a derivation of conductance under molecular and dissociative dominance, for reference. In estimating the surface conductance based on this model, we assume that jumps of protons from dissociated protons H_3O^+ to H_2O and jumps from H_2O to dissociated OH^- contribute equally:

$$G_{\mathrm{s,H^+_{cma\text{-}a}}} = F(\gamma_{M_{M_s}\mathrm{OH_3^{\bullet}}} u_{\mathrm{H^+_a}} + \gamma_{M_{M_s}\mathrm{OH'}} u_{\mathrm{H^+_a}}) = 2F\gamma_{M_{M_s}\mathrm{OH_3^{\bullet}}} u_{\mathrm{H^+_a}} \qquad \text{Eq. 56}$$

The charge mobility of the charged defects contains the chance that a proton in an H_3O^+ group finds an adjacent water molecule to jump to, or that a water molecule is there to offer a proton to jump to OH^-. Hence, we get

$$G_{\mathrm{s,H^+_{cma\text{-}a}}} = 2F\gamma_{M_{M_s}\mathrm{OH_3^{\bullet}}} \frac{\gamma_{M_{M_s}\mathrm{OH_2^x}}}{\gamma_{M_s}} u_{\mathrm{H^+0}} \frac{1}{T} \exp\left(\frac{-\Delta H_{\mathrm{m,H^+_a}}}{RT}\right), \qquad \text{Eq. 57}$$

which, for **low coverage** (Figure S12 a) and by combination with Eq. 5 and Eq. 20, yields

$$G_{\mathrm{s,H^+_{cma\text{-}a}}} = 2F\gamma_{M_s} K^2_{\mathrm{a_{cm}}} \sqrt{K_{\mathrm{d_{ca}}}} \left(\frac{p_{\mathrm{H_2O}}}{p^0}\right)^2 u_{\mathrm{H^+0}} \frac{1}{T} \exp\left(\frac{-\Delta H_{\mathrm{m,H^+_a}}}{RT}\right). \qquad \text{Eq. 58}$$

We rewrite this as

$$G_{\mathrm{s,H^+_{cma\text{-}a}}} = G_{\mathrm{s,H^+_{cma\text{-}a}0}} \frac{1}{T} \exp\left(\frac{-\Delta H}{RT}\right) = G_{\mathrm{s,H^+_{cma\text{-}a}0}} \frac{1}{T} \exp\left(\frac{-\left(2\Delta H^0_{\mathrm{a_{cm}}} + \frac{1}{2}\Delta H^0_{\mathrm{d_{ca}}} + \Delta H_{\mathrm{m,H^+_a}}\right)}{RT}\right), \qquad \text{Eq. 59}$$

with preexponential

$$G_{\mathrm{s,H^+_{cma\text{-}a}0}} = G^0_{\mathrm{s,H^+_{cma\text{-}a}0}} \left(\frac{p_{\mathrm{H_2O}}}{p^0}\right)^2 = 2F\gamma_{M_s} \exp\left(\frac{2\Delta S^0_{\mathrm{a_{cm}}} + \frac{1}{2}\Delta S^0_{\mathrm{d_{ca}}}}{R}\right) u_{\mathrm{H^+0}} \left(\frac{p_{\mathrm{H_2O}}}{p^0}\right)^2. \qquad \text{Eq. 60}$$

By using assumptions as above, with the standard entropy change of dissociation in the

chemisorbed layer $\Delta S^0_{d_{cma}}$ negligible, we get $G^0_{s,H^+_{cma\text{-}a}0} \approx 6\cdot10^{-15}$ SK and $G_{s,H^+_{cha\text{-}a}0} \approx 4\cdot10^{-18}$ SK at p_{H_2O} = 0.025 atm. Taking $\Delta H^0_{a_{cm}}$ = -60 kJ mol^{-1} [8] as before, but the dissociation enthalpy in adsorbed to be $\Delta H^0_{d_{ca}}$ = 40 kJ mol^{-1} and assuming an enthalpy of migration of 20 kJ mol^{-1}, the conductance will from Eq. 59 have a very negative enthalpy of -80 kJ mol^{-1}. It hence displays a sharp increase with decreasing temperature, hard to distinguish from conduction in physisorbed water, which is reasonable, as the two mechanisms are physically similar.

At **full coverage** (Figure S12 b), the cma-a model gives

$$G_{s,H^+_{cma\text{-}a}} = 2F\gamma_{M_{M_s}OH^\bullet_3}\frac{\gamma_{M_{M_s}OH^x_2}}{\gamma_{M_s}}u_{H^+0}\frac{1}{T}\exp\left(\frac{-\Delta H_{m,H^+_a}}{RT}\right) = 2F\gamma_{M_s}\sqrt{K_{d_{ca}}}u_{H^+0}\frac{1}{T}\exp\left(\frac{-\Delta H_{m,H^+_a}}{RT}\right) \quad \text{Eq. 61}$$

We rewrite this as

$$G_{s,H^+_{cma\text{-}a}} = G_{s,H^+_{cma\text{-}a}0}\frac{1}{T}\exp\left(\frac{-\Delta H}{RT}\right) = G_{s,H^+_{cma\text{-}a}0}\frac{1}{T}\exp\left(\frac{-\left(\frac{1}{2}\Delta H^0_{d_{ca}} + \Delta H_{m,H^+_a}\right)}{RT}\right), \quad \text{Eq. 62}$$

with preexponential of surface protonic conductance given by

$$G_{s,H^+_{cma\text{-}a}0} = G^0_{s,H^+_{cma\text{-}a}0} = 2F\gamma_{M_s}\exp\left(\frac{\frac{1}{2}\Delta S^0_{d_{ca}}}{R}\right)u_{H^+0}\,. \quad \text{Eq. 63}$$

With the same assumptions as before, we obtain $G^0_{s,H^+_{cma\text{-}a}0} = G_{s,H^+_{cha\text{-}a}0} \approx 1.5\cdot10^{-3}$ SK, with an estimate of the enthalpy of conduction of +40 kJ mol^{-1}.

We do not consider the possibility of full dissociation in the adsorbed layer (no cda-a model).

Table S4 Derived p_{H_2O} dependences and predicted preexponentials and activation enthalpies of surface protonic conductance within the chemisorbed water layer at p_{H_2O} = 1 and 0.025 atm according to four models of dissociation and transport in cases of low coverage, for which molecular or dissociated chemisorption have the same parameters. Also included are predictions for full coverage, where there are no p_{H_2O} dependences, but differences between molecular or dissociated dominance. Lines in manuscript Figure 8 are based on the predicted preexponentials and empirical enthalpies in parenthesis.

Model / Parameter	cms-s cds-s	cms-sa cds-sa	cms-a cds-a	cma-a	cms-s	cds-s	cms-sa	cds-sa	cms-a	cds-a	cma-a
n in $G_{s,H^+0} \propto p^n_{H_2O}$	1/2	1	3/2	2	0 (Full coverage)						
G^0_{s,H^+0} (SK), p_{H_2O} = 1 bar	$2\cdot10^{-6}$	$3\cdot10^{-9}$	$3\cdot10^{-12}$	$6\cdot10^{-15}$	$1\cdot10^{-3}$	$4\cdot10^{-4}$	$1.5\cdot10^{-3}$	$8\cdot10^{-4}$	$1\cdot10^{-3}$	$8\cdot10^{-4}$	$1.5\cdot10^{-3}$
G_{s,H^+0} (SK), p_{H_2O} = 0.025 bar	$2\cdot10^{-7}$	$8\cdot10^{-11}$	$1\cdot10^{-14}$	$4\cdot10^{-18}$	$1\cdot10^{-3}$	$4\cdot10^{-4}$	$1.5\cdot10^{-3}$	$8\cdot10^{-4}$	$1\cdot10^{-3}$	$8\cdot10^{-4}$	$1.5\cdot10^{-3}$
ΔH_c (kJ mol^{-1}) (plotted in Fig. 8)	+30 (+29)	0 (-10)	-60 (-45)	-70	+60	+50	+60	+40	+30 (+25)	0	+40

For completeness, we mention that CeO_2 due to it hydrophobicity does not lend itself to analysis of models for conduction in the physisorbed water layers beyond those provided in our previous work on ZrO_2. [5]

SI 6 Evaluation of capillary condensation

Water condenses more easily in the presence of pores in the nanometer regime due to capillary condensation at low temperatures. This is evaluated by the Kelvin equation:

$$r = \left| \frac{2\gamma v_m \cos\theta}{RT \ln\left(\frac{p_{H_2O}}{p_{ce}}\right)} \right| \qquad \text{Eq. 64}$$

where θ is the contact angle, r is the pore radius, R is the gas constant, T is the temperature, γ is the surface tension of bulk water ($\gamma_L = 72.8$ mN m^{-1} at 20°C, and decreasing to zero at the critical point of 374°C), v_m is the molar volume of water, p_{ce} is the condensation-evaporation equilibrium partial pressure, and $p_{H_2O} = 0.025$ atm in this case.

Figure S13 shows the limiting pore diameter required for condensation of water *vs* $1/T$ at contact angle of 0°, 64° and 112°, representing CeO_2 surface with spreading, wetting (hydrophilic), and non-wetting (hydrophobic) character, respectively.[13] The results show that capillary condensation of water may play a role near room temperature, based on mesopore sizes of 13-20 nm from the BET analysis.

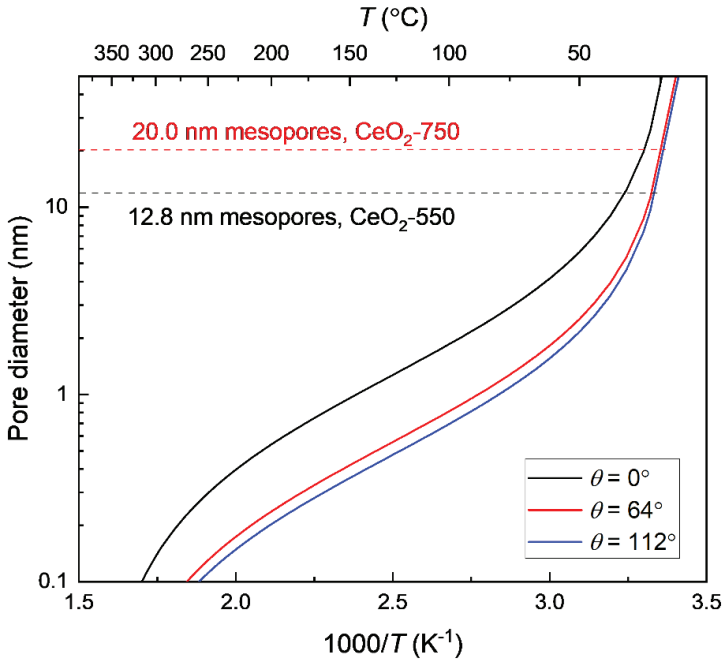

Figure S13 Pore diameter required for water condensation at different temperatures, calculated for three characteristic contact angles based on the Kelvin equation.

References

1. Thommes, M., et al., *Physisorption of gases, with special reference to the evaluation of surface area and pore size distribution (IUPAC Technical Report).* Pure and Applied Chemistry, 2015. **87**(9-10): p. 1051-1069.
2. Runnerstrom, E.L., et al., *Colloidal Nanocrystal Films Reveal the Mechanism for Intermediate Temperature Proton Conductivity in Porous Ceramics.* Journal of Physical Chemistry C, 2018. **122**(25): p. 13624-13635.
3. Thøgersen, A., et al., *In-situ electron loss spectroscopy reveals surface dehydrogenation of hydrated ceria nanoparticles at elevated temperatures.* Journal of Physics and Chemistry of Solids, 2022. **170**: p. 110955.
4. Wang, Y.L., et al., *Oxide-water interaction and wetting property of ceria surfaces tuned by high-temperature thermal aging.* Applied Surface Science, 2021. **554:** 149658.
5. Sun, X.W., et al., *Quantifiable models for surface protonic conductivity in porous oxides - case of monoclinic ZrO_2.* Physical Chemistry Chemical Physics, 2022(24): p. 11856 - 11871.
6. Wagner, W. and A. Pruß, *The IAPWS formulation 1995 for the thermodynamic properties of ordinary water substance for general and scientific use.* Journal of physical and chemical reference data, 2002. **31**(2): p. 387-535.
7. Hayun, S., T.Y. Shvareva, and A. Navrotsky, *Nanoceria - Energetics of Surfaces, Interfaces and Water Adsorption.* Journal of the American Ceramic Society, 2011. **94**(11): p. 3992-3999.
8. Thiel, P.A. and T.E. Madey, *The Interaction of Water with Solid-Surfaces - Fundamental-Aspects.* Surface Science Reports, 1987. **7**(6-8): p. 211-385.
9. Radha, A.V., et al., *Surface Enthalpy, Enthalpy of Water Adsorption, and Phase Stability in Nanocrystalline Monoclinic Zirconia.* Journal of the American Ceramic Society, 2009. **92**(1): p. 133-140.
10. Blesa, M.A., A.J.G. Maroto, and A.E. Regazzoni, *Surface-Acidity of Metal-Oxides Immersed in Water - a Critical Analysis of Thermodynamic Data.* Journal of Colloid and Interface Science, 1990. **140**(1): p. 287-290.
11. Raz, S., et al., *Characterization of adsorbed water layers on Y_2O_3-doped ZrO_2.* Solid State Ionics, 2001. **143**(2): p. 181-204.
12. Manabe, R., et al., *Evaluating surface protonic transport on cerium oxide via electrochemical impedance spectroscopy measurement.* Solid State Communications, 2018. **270**: p. 45-49.
13. Fronzi, M., M.H.N. Assadi, and D.A.H. Hanaor, *Theoretical insights into the hydrophobicity of low index CeO_2 surfaces.* Applied Surface Science, 2019. **478**: p. 68-74.

Appendix IV

In-situ electron loss spectroscopy reveals surface dehydrogenation of hydrated ceria nanoparticles at elevated temperatures

Annett Thøgersen, [a] * Xinwei Sun,[b] Ingvild Thue Jensen,[a] Øystein Prytz,[c] Truls Norby[b]

[a] SINTEF Materials Physics, Forskningsveien 1, NO-0373 Oslo, Norway

[b] Department of Chemistry, University of Oslo, Centre for Materials Science and Nanotechnology (SMN), NO-0318 Oslo, Norway

[c] Department of Physics, University of Oslo, Centre for Materials Science and Nanotechnology (SMN), NO-0318 Oslo, Norway

* Corresponding author: annett.thogersen@sintef.no

Journal of Physics and Chemistry of Solids 170 (2022), *170*, 110955.

IV

Journal of Physics and Chemistry of Solids 170 (2022) 110955

Contents lists available at ScienceDirect

Journal of Physics and Chemistry of Solids

journal homepage: www.elsevier.com/locate/jpcs

FLA

In-situ electron loss spectroscopy reveals surface dehydrogenation of hydrated ceria nanoparticles at elevated temperatures

Annett Thøgersen [a,*], Xinwei Sun [b], Ingvild Thue Jensen [a], Øystein Prytz [c], Truls Norby [b]

[a] SINTEF, Materials Physics, Forskningsveien 1, Oslo, NO-0373, Norway
[b] University of Oslo, Department of Chemistry, Centre for Materials Science and Nanotechnology, FERMIO, Gaustadalléen 21, Oslo, NO-0349, Norway
[c] University of Oslo, Department of Physics, Centre for Materials Science and Nanotechnology, Box 1048 Blindern, Oslo, NO-0316, Norway

ARTICLE INFO

Keywords:
ETEM
EELS
Ceria
Microscopy
Nanopowder
Hydrogen

ABSTRACT

Ceria (CeO_2) exhibits high reversible oxygen storage capacity at intermediate temperatures (500–800 °C) related to an extraordinary and not fully understood reduction of its surfaces. We have investigated pristine and alcohol-dispersed commercially available ceria nanoparticles by in-situ scanning transmission electron microscopy with electron energy loss spectroscopy (STEM-EELS) to examine the dynamic changes during the initial redox reaction process of ceria nanoparticles in an ultra-high vacuum atmosphere using an in-situ heating holder. High spatially resolved EELS was used to estimate the amounts of Ce^{3+} and Ce^{4+} in the nanoparticles as a function of temperature, based on the white-line ratios M_5/M_4 of the EELS spectra. The results show a nm-range thick surface layer rich in Ce^{3+} on pristine particles prior to heating. During heating, this oxidises to Ce^{4+}. Heating in high vacuum should normally not lead to oxidation, but the observed results can be understood if the surface layer has an oxyhydroxide composition such as CeOOH, which by heating in the vacuum dehydrogenates and hence oxidises to CeO_2, a process that requires diffusion of hydrogen only. This process occurred for all samples, but was more pronounced for the particles that were previously dispersed in ethanol. Thermogravimetric analysis (TGA) by heating the pristine powder in dry atmosphere yielded a considerable weight loss confirming the content of hydroxide and probably water in and on the CeO_2 particles. The results suggest that CeO_2 surfaces are reduced to a layer of oxyhydroxide by hydrogen-containing molecules like water vapour or alcohols.

1. Introduction

Ceria (CeO_2) nanoparticles find use in applications such as oxygen sensors, solid oxide fuel cells, and three-way catalysts to remove NOx and CO from combustion exhausts [1–3], owing to the oxide ion conductivity, electronic structure, and variable stoichiometry.

Ceria particles exhibit high and reversible oxygen storage capacities by changing the valence state of Ce between +4 and +3 in the surface at intermediate temperatures (500–800 °C). The reduced state involves oxygen vacancies and electrons (representing Ce^{3+}) introducing oxide ion and electronic conductivity in the surface [4,5]. The separation of the Ce^{3+} and Ce^{4+} components can be carried out by peak fitting the electron energy loss spectra (EELS) $M_{4,5}$ peak using transmission electron microscopy (TEM), as well as measuring the white line intensity ratio [4,5]. For pure ceria, the reduction from +4 to +3 was found to occur by heating above 730 °C, in a hydrogen rich atmosphere [4]. Most studies on the temperature evolution of ceria particles have therefore been made at high temperatures. Previous TEM investigations of the surface of ceria have shown a thin layer of Ce^{3+} [4,6–8]. Studies have also shown that investigating the particles under high vacuum produces more Ce^{3+} on the surface than if investigating the particles in an oxygen atmosphere [9,10]. Baalousha et al. [11] and Wu et al. [11] found that ceria nanoparticles have more Ce^{3+} than larger particles and bulk ceria. It is important to map the compositional variations on the nanoparticle surface in-situ at low temperatures, as reduced ceria nanoparticles may be unstable and small changes may have a big influence in the catalytic functionality of the particles [4]. We have therefore investigated the composition of pristine ceria nanoparticles as well as the composition of ceria dispersed in alcohols prior to analysis, which is the most common way of preparing and dispersing nanoparticles for TEM analysis.

2. Methodology

Ceria nanoparticles from Sigma-Aldrich Co. were used for the ex-

* Corresponding author.
E-mail address: annett.thogersen@sintef.no (A. Thøgersen).

https://doi.org/10.1016/j.jpcs.2022.110955
Received 27 April 2022; Received in revised form 6 August 2022; Accepted 8 August 2022
Available online 27 August 2022

periments (Cerium (IV) Oxide nanopowder, Pcode: 1001924131, <25 nm particle size). For the in-situ heating measurements, a *Protochips* Fusion holder was used. TEM samples were prepared by dispersing dry ceria powder or a drop of ceria mixed with either isopropanol or ethanol on a Protochips in-situ heating chip. The samples were analysed by a probe corrected and monochromated FEI Titan G2 60–300 microscope operated at 300 kV, using high resolution scanning TEM (STEM), electron energy loss spectroscopy (EELS) with a Gatan imaging filter and detector, and Super-X energy dispersive spectroscopy (EDS). In order to reduce beam damage, electron beam current of less than 0.1 nA was used. In some of our experiments we also performed a double analysis of each particle in the heating test to see if there were any changes in our results after the spectral image EELS acquisition. No damage was observed in our extra tests. The EELS spectra were acquired using dual EELS spectrum image (SI), in order to avoid referencing issues. This means that we acquire a low loss EELS spectrum with the zero-loss peak together with the core-loss EELS spectrum of the Ce-$M_{4,5}$ peak, and using the zero-loss peak as the referencing peak. The post acquisition data processing was performed using Digital Micrograph from Gatan Inc. and CasaXPS for peak fitting analysis. More details on the peak fitting is given in the Results chapter.

In-situ heating was performed with temperature steps of 0.05 °C per second, for then to wait about 10 min (before taking EELS spectra) to avoid drift due to heating. EELS spectra were acquired with either a 0.25 eV/ch dispersion (collection semi-angle 12 mrad and convergence semi-angle 21 mrad), or with a 0.1 eV/ch dispersion (collection semi-angle 100 mrad and convergence semi-angle 30 mrad), with some variations in spectrum image pixel size.

Thermogravimetric analysis (TGA) was made with a Netzsch 449 F1 Jupiter® thermal analyser (Netzsch GmbH, Germany) on the as-received CeO_2 nanopowder, uniaxially pressed at 3 MPa into a pellet. The sample was first dried at 26 °C in N_2 gas for 3 h. It was further dried and degassed during stepwise heating to 400 °C at 3 K/min, and then held at 400 °C for 6 h to ensure complete removal of water and hydrogen and any organic residue from the surface. The weight increase was then measured by flowing wet (pH_2O = 0.026 atm) N_2 over the sample at 400, 125 and 26 °C during cooling. The relative increase in weight and corresponding uptake of water is calculated on the basis that the content of adsorbed water and other gases in dry N_2 at 400 °C was zero.

3. Results

The shape and sizes of the ceria nanoparticles studied in this work are shown in the STEM images in Fig. 1 A and E, with the corresponding electron diffraction images in B and D. The diffraction pattern in Fig. 1B is consistent with the CeO_2 crystal structure with a space group of Fm-3m (225) in the [110] zone axis. Diffraction of several particles in (E) shows ring patterns resulting from many crystal orientations, all corresponding well to the CeO_2 structure. A 1:2 compositional relationship between Ce and O was also confirmed by EDS.

The content of Ce^{3+} in the samples may be affected by the treatment of the ceria nanoparticles prior to the analysis. We have therefore investigated ceria treated in three different ways common to the TEM-sample preparation process namely, as-received (pristine) ceria powder and ceria dispersed in ethanol or isopropanol. EELS spectra in Fig. 2 shows spectra taken from bulk and surface of our caria nanopowder, with a clear Ce^{3+} and Ce^{4+} signature. Even though there may be minor Ce^{4+} and Ce^{3+} present in the spectra as well, these spectra shows the signature shapes we are analyzing in this paper. The spectra are composed of the two peaks, due to spin-orbit splitting, (white lines) $M_{4,5}$. These lines are caused by excitations from the $M_{4,5}$ (3d) to the unoccupied states in the N(4f) band, reflecting changes in the occupancy of the 4f band and thereby also the oxidation state [4]. The EELS Ce-$M_{4,5}$ peaks have been peak-fitted with Gaussian-Lorentzian peaks corresponding to Ce-M_5 and Ce-M_4, where the Ce-M_5 and Ce-M_4 peaks of Ce^{3+} are located at energy losses of 880.1 eV and 898 eV respectively, with an energy separation of about 17.9 ± 0.2 eV. For the Ce^{4+} component, the Ce-M_5 peak is located at 881.4 eV and Ce-M_4 peak at 899.6 eV, with an energy separation of about 18.2 ± 0.2 eV. Intensity ratios of the M_5 to M_4 white lines of Ce^{3+} was found to be 1.3 (I_{M_5}/I_{M_4} = 1.3.), while for Ce^{4+} the intensity difference is I_{M_5}/I_{M_4} = 0.8. A variation in-between these two numbers can be related to a change in oxidation state.

We have used the zero-loss peak (from dual EELS) for initial energy referencing. However, due to some misalignment of the drift tube or the image filter, we also experienced a shift in the peaks between samples dispersed in ethanol and isopropanol. In order to more easily compare the peaks we aligned the 3+ peaks for the samples at room temperature. The analysis has been carried out for eight different particles, and the results of some of them are presented in the following sections.

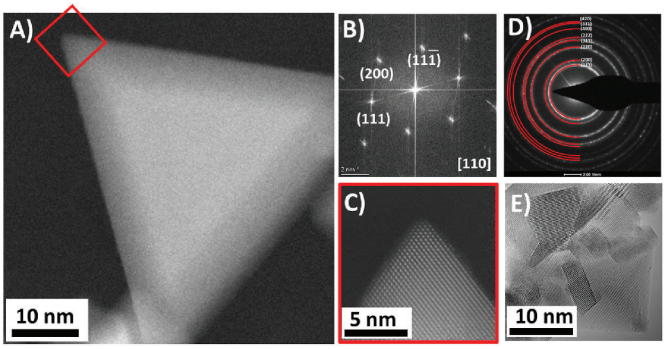

Fig. 1. A) HAADF STEM image of a CeO_2 nanoparticle, B) corresponding electron diffraction pattern, C) high resolution HAADF STEM image, D) electron diffraction pattern from E), and E) STEM image of many CeO_2 particles.

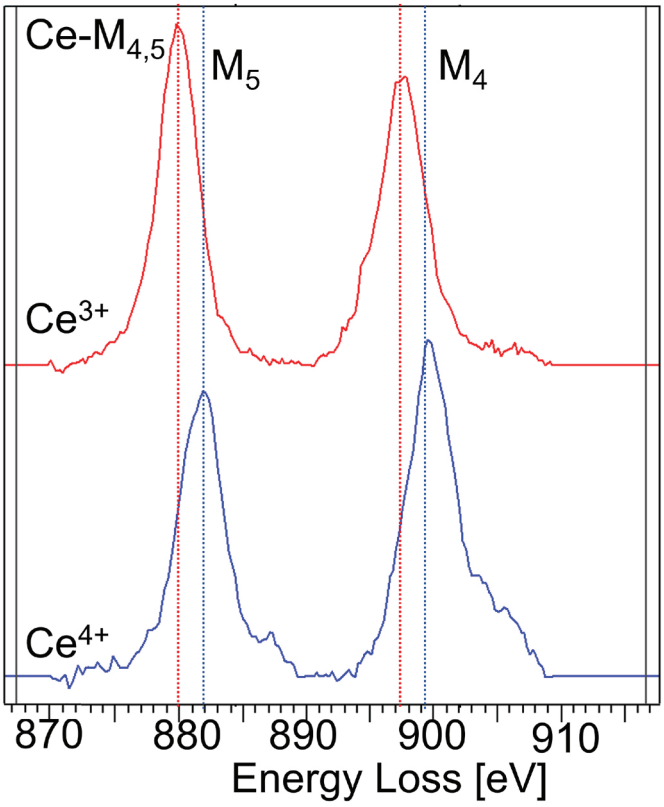

Fig. 2. EELS spectra of the Ce-$M_{4,5}$ peak, in an area with mainly Ce^{3+} and Ce^{4+} showing the different spectral signatures.

3.1. Pristine CeO_2-powder

We examined four pristine particles at 25 °C, 200 °C, and 400 °C, where most of the changes in composition were found to occur. Only the spectra and images of one of the particles will be presented, while the data of the other three nanoparticles are plotted in Section 3.4.

EELS spectra of the pristine ceria particle is shown in Fig. 3A and B, from the whole particle and from the surface layer respectively. The percentages of Ce^{3+} at the corresponding temperature, as well as the estimated oxidation state based on the white line ratio are presented in Table 1. The pristine particle contains 53% Ce^{3+} in the whole particle at room temperature (estimated oxidation state of +3.3), and 80% Ce^{3+} at the surface, as shown in Fig. 3B. During heating in high vacuum, the Ce-$M_{4,5}$ peak moves to higher energy loss, and the white line intensity ratio shifts to a clear Ce^{4+} signature. At 400 °C, the particle contains only 13% Ce^{3+}, and we can observe 31% Ce^{3+} at the surface layer. Energy loss mapping of the integrated EELS signal of the Ce^{4+} and Ce^{3+} peaks presented in Fig. 4 shows that at room temperature the particle contains a mix of both Ce^{3+} and Ce^{4+}. During heating, most of the Ce^{3+} in the bulk particle transform into Ce^{4+}, while the transformation at the surface is not as quick, resulting in a layer of Ce^{3+} at the surface. This evolution profile was also found for the three other samples we have examined.

3.2. CeO_2-powder in ethanol solution

EELS spectra of ceria particles dispersed in ethanol prior to analysis are shown in Fig. 3C and D. At room temperature, the particle contains 71% Ce^{3+} (estimated oxidation state +3.3). The white line intensity ratio also shows a clear Ce^{3+} signature. During heating in high vacuum, we observe a clear shift in the Ce-$M_{4,5}$ peak to higher energy loss, as well as a shift in the white line intensity ratio to a pronounced Ce^{4+} signature. At 700 °C, the particle contains only 16% of Ce^{3+}. This can also be observed in the spectra from the surface (in Fig. 3D) where Ce^{4+} dominates at higher temperatures. Fig. 5 shows energy filtered images of the particle at the different temperatures. The result reveals that the Ce^{3+} is mainly found at the surface of the particle. There is also a clear decrease in Ce^{3+} at 400 °C.

3.3. CeO_2-powder in isopropanol solution

EELS spectra of ceria dispersed in isopropanol prior to analysis are shown in Fig. 3E and F. Ce^{3+} is observed at both the whole nanoparticle and the surface at room temperature, with 64% and 100% Ce^{3+}, respectively. Increasing the temperature shows a significant reduction in Ce^{3+} content of the whole particle, resulting in more Ce^{4+}. However, no significant decrease in Ce^{3+} is observed at the surface. The corresponding energy filtered image are shown in Fig. 6. The images show that at room temperature, Ce^{3+} is pronounced at the surface. During heating, Ce^{3+} is reduced overall in the particle.

3.4. Temperature evolution of the ceria samples

The composition of Ce^{3+} in the four samples as a function of temperature is shown in Fig. 7, for the whole particle (A) and for the surface (B). The error bars are estimated uncertainty/errors in the calculated oxidation state (y-axis, ± 0.1), and calculated composition from EELS data (y-axis, ± 4%), found by varying the fitting parameters and measurements of the spectra. All samples start with a relatively high amount of Ce^{3+} in the whole particle, which decreases with increasing temperature (Fig. 7A). The sample dispersed in isopropanol shows a small initial increase in the amount of Ce^{3+}, with a slight increase at 200 °C, before it decreases further.

The calculated oxidation state based on the white line ratio as a function of Ce^{3+} content is shown in Fig. 8, using data from all samples investigated. A linear thread-line is fitted to the data points and shows a near-linear evolution of the oxidation state, with a R^2 value of about 0.86 (a measurement of how good the line fits the data points, where 1 is the best). However, some of the data points are not connected to the

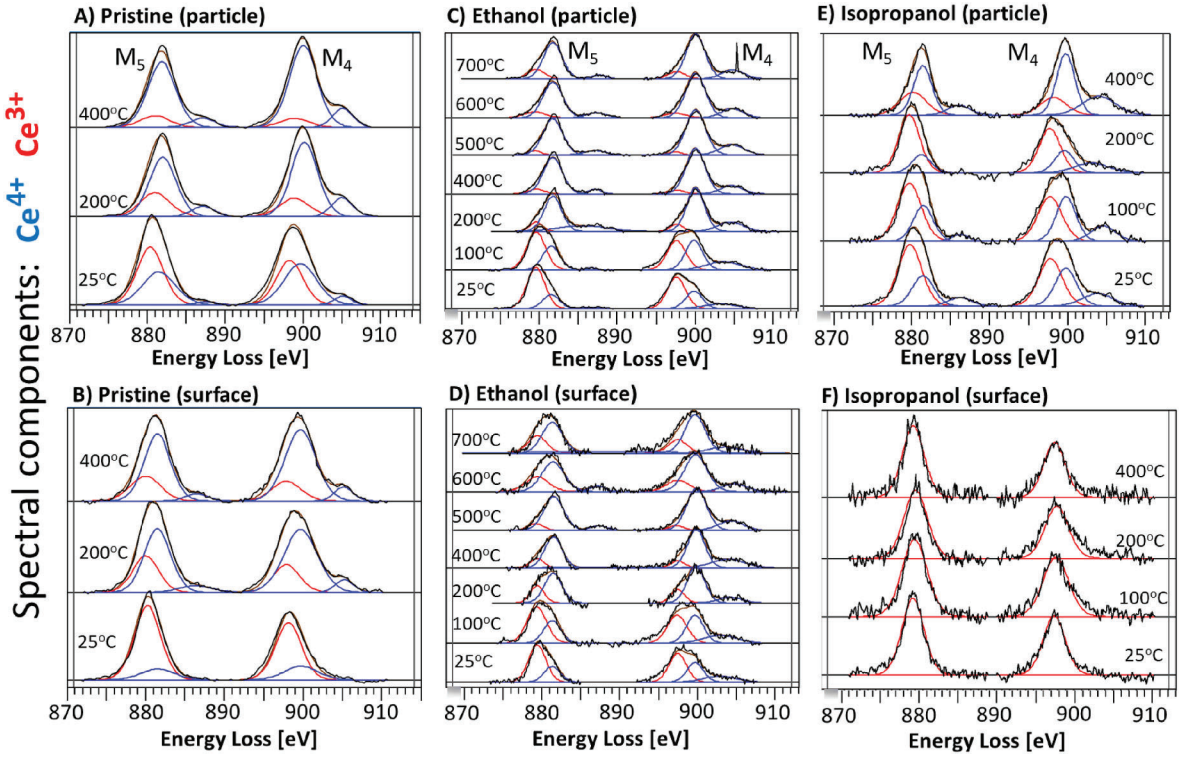

Fig. 3. EELS spectra of the Ce-$M_{4,5}$ peaks, both from the whole particle (A,C,E) and the surface (B,D,F), of pristine ceria particle (A and B), ceria first dispersed in ethanol (C and D), and ceria first dispersed in isopropanol (E and F), at 25 °C–700 °C. The component Ce^{4+} is shown in blue, $Ce^{3+}$is shown in red, and the black is the experimental spectra.

Table 1
Amount of Ce^{3+} present in pristine ceria, ceria dispersed in ethanol, and ceria dispersed in isopropanol, with the mean oxidation state (ox. state) calculated based on the white line ratio.

	Particle						Surface					
	Pristine		Ethanol		Isopropanol		Pristine		Ethanol		Isopropanol	
Temp.	Ce^{3+}	ox.	Ce^{3+}	ox.	Ce^{3+}	ox.	Ce^{3+}	ox.	Ce^{3+}	ox.	Ce^{3+}	ox.
(°C)	(%)	state	(%)	state	(%)	state	(%)	state	(%)	state	(%)	state
25	53	+3.3	71	+3.3	64	+3.3	80	+3.0	54	+3.4	100	+3.0
100			58	+3.5	61	+3.4			59	+3.6	100	+3.0
200	26	+3.6	13	+3.8	74	+3.1	24	+3.4	26	+3.7	100	+3.1
400	13	+3.8	8	+3.7	35	+3.8	31	+3.6	16	+3.9	100	+3.0
500			6	+3.7					11	+3.7		
600			13	+3.8					29	+3.7		
700			16	+3.7					29	+3.6		

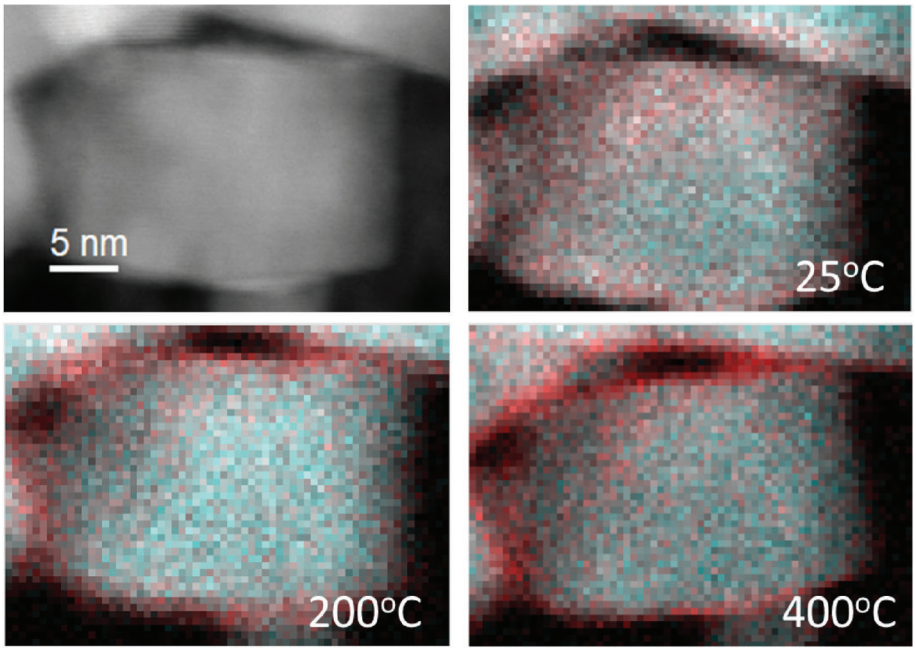

Fig. 4. STEM image of a pristine ceria particle, and EELS-mapping of the Ce^{3+} (red) and Ce^{4+} (blue) peaks at 25 °C, 200 °C, and 400 °C.

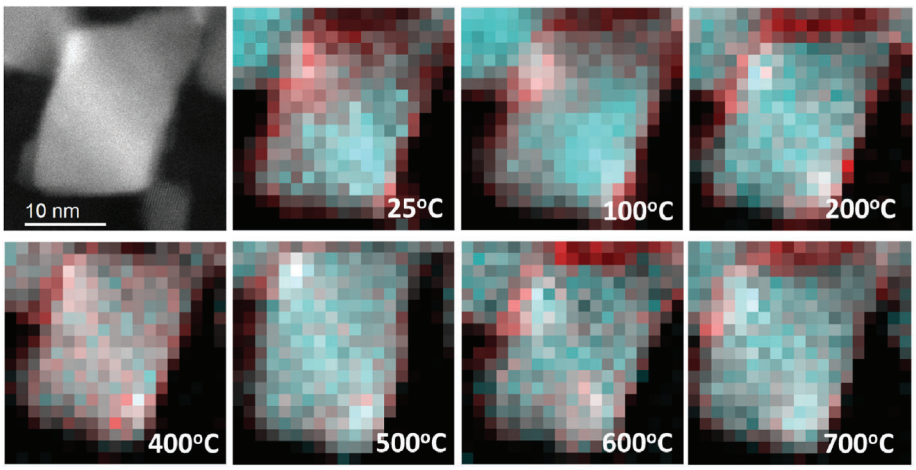

Fig. 5. STEM image of a ceria particle dispersed in ethanol, and EELS-mapping of the Ce^{3+} (red) and Ce^{4+} (blue) peaks at room temperature 25 °C, 100 °C, 200 °C, 400 °C, 500 °C, 600 °C, and 700 °C.

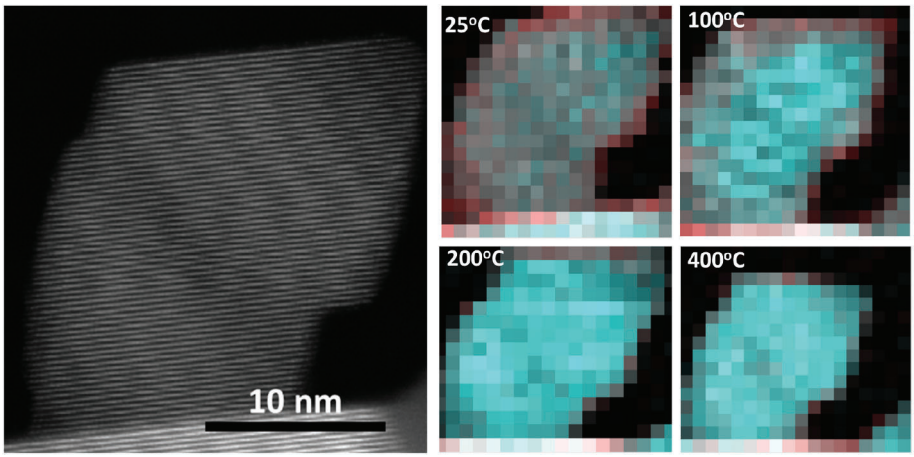

Fig. 6. A) STEM image of a ceria particle dispersed in isopropanol, and EELS-mapping of the Ce^{3+} (red) and Ce^{4+} (blue) peaks at room temperature (25°), 100 °C, 200 °C, and 400 °C.

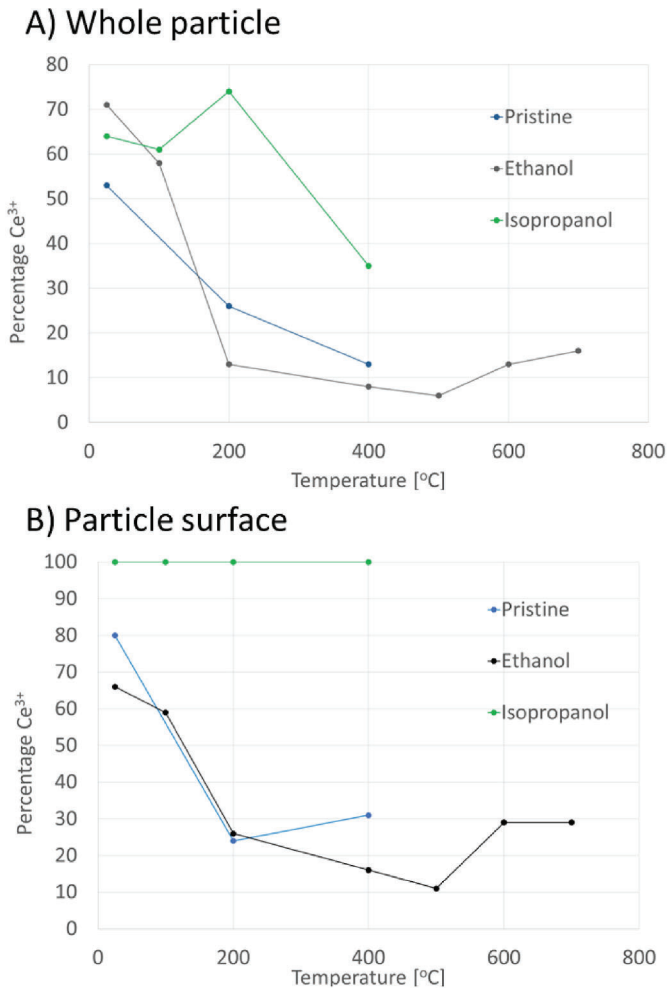

Fig. 7. Plot showing the fraction of Ce^{3+} present in A) the entire ceria particle, and B) ceria particle surface, with increasing temperature.

thread-line. From our experience, a combination of the oxidation state based on the white line ratio together with the fitted peaks is necessary to correctly determine the compositional profile of the samples.

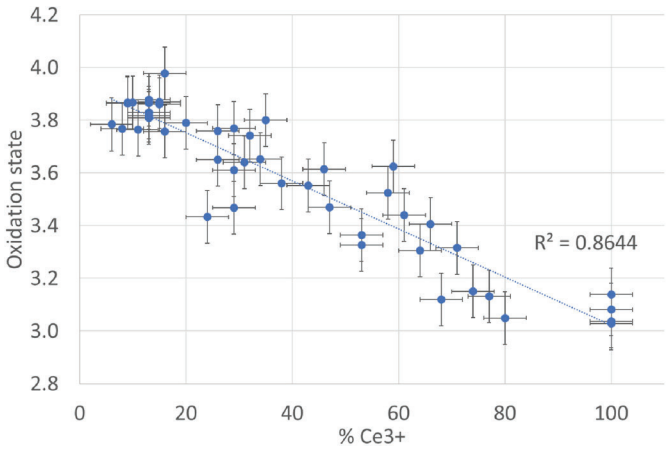

Fig. 8. A graph showing the average oxidation state found from using the white line ratio of the EELS Ce-$M_{4,5}$ spectra of the entire particle, as a function of the fraction of Ce^{3+} present in the sample found by peak fitting the EELS spectra of the different particles.

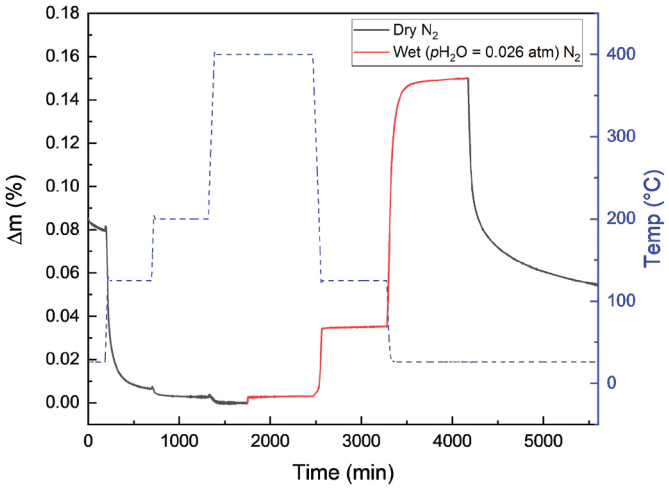

Fig. 9. Time-dependent mass change of CeO_2 under dry and wet (pH_2O = 0.026 atm) N_2 (left y-axis) in response to temperature change (right y-axis).

3.5. Thermogravimetry (TG)

The TG results for the temperature range 26–400 °C during heating in dry N_2 and cooling in wet N_2 are shown in Fig. 9. During heating under dry conditions, a significant amount of water is desorbed from the oxide upon heating to 125–200 °C, normally taken to reflect physisorbed water [12]. Further heating to 400 °C represents the removal of chemisorbed water, possibly also any water in the structure. In total, the water lost, supposedly present in and on the pristine CeO_2, amounts to around 0.092 mol H_2O per mol CeO_2. The amount of water adsorbed in the bulk of CeO_2 may be assumed to be negligible due to its unfavourable hydration thermodynamics. Therefore, the mass change may reflect adsorbed water. There may also be water or hydrogen left inside the crystallites from their synthesis. The following water uptakes in wet N_2 at 400, 125 and 26 °C correspond to approx. 0.003, 0.03 and 0.12 mol H_2O per mol CeO_2, respectively, in rough agreement with a previous report on CeO_2 powder with a specific surface area of 55 m^2/g [13].

4. Discussion

EELS results show that both pristine ceria as well as ceria dispersed in alcohols prior to analysis start with high amounts of Ce^{3+} at the surface of the particles. When heating in vacuum, this partly transforms into Ce^{4+}, where it is stable up to 700 °C. Johnston-Peck et al. [14] studied dose-rate-dependent damage of cerium dioxide by STEM-EELS. They found that when ceria is exposed to high beam damage, oxygen vacancies will form, and ceria will be reduced from +4 to +3 oxidation state. Since the particles in our study mainly experience a shift from +3 to +4 oxidation state, this process cannot be due to beam damage. The amount of Ce^{3+} and the evolution process during heating in the three types of samples are not significantly different, only a small increase in Ce^{3+} was found in the samples dispersed in ethanol. However, the amount of Ce^{3+} in the pristine samples is surprising. Heating in high vacuum should normally not lead to further oxidation. If the reoxidation to Ce^{4+} was due to annihilation of oxygen vacancies, it would require uptake of oxygen (which is not available in high vacuum) and lower temperatures (due to the negative entropy change of gas uptake). However, the results can be rationalized if the surface layer is an oxyhydroxide (based on the known stability of rare earth (III) oxyhydroxides) that we for simplicity represent as CeOOH, not oxide like Ce_2O_3 (both being Ce^{3+}). Dehydrogenation of a hydroxide yields hydrogen release, which is natural in the TEM vacuum, and it increases with temperature due to the positive entropy change of gas release. Thereby, when heating the particles in high vacuum, the surface layer dehydrogenates (oxidises) to CeO_2, a process that requires diffusion of protons only:

$$CeOOH \longrightarrow CeO_2 + \frac{1}{2}H_2(g)$$

The formation of the CeOOH layer is expected to happen under ambient conditions according to a reducing hydrogenation from water vapour:

$$CeO_2 + \frac{1}{2}H_2O(g) \longrightarrow CeOOH + \frac{1}{4}O_2(g)$$

Wang et al. [15] found the presence of hydroxyl groups (O–H) after water exposure of ceria surfaces. They suggest that these groups as well as hydrocarbons may also be absorbed from ambient environments. This will have a large effect on the wettability of the surface of ceria. The formation of a layer and not a complete hydrogenation of bulk CeO_2 suggests that the formation of a surface of CeOOH and the interface between CeO_2 and CeOOH, along with the associated charge separation and space charge layers, lowers the energy compared to a single CeO_2 surface. The growth of the layer then stops as soon as the surface attains bulk properties and/or the two space charge layers in the CeOOH layer meet.

This shows that H in CeO_2 is indeed present as H^+ compensated by Ce^{3+} in what may be termed CeOOH-like structures in a surface layer. If the TG results showing a loss of water from the pristine oxide of 0.092 mol H_2O/mol CeO_2 is interpreted as loss of H_2, this corresponds to as much as 0.83 mol H_2/mol CeO_2, or 1.66 H/CeO_2. It is hence likely that pristine CeO_2 nanoparticles have a mixture of H inside or on the surface, e.g. like regions or a layer of CeOOH, and H_2O adsorbed on the surface.

The existence of a layer of CeOOH on CeO_2 surfaces explains many observations, behaviours, and properties of CeO_2, e.g. redox and catalytic behaviour as well as protons found on the surface, but not bulk. The reasons why the surface phase has not been observed earlier may stem from the fact that it has the same oxygen content and a similar structure as the host CeO_2, and is very thin, requiring the use of TEM and the understanding gained by in-situ heating experiments.

We observed different evolution of the oxidation process for the different particles. Such differences have also been observed in the redox activity level [4,16]. Crozier et al. [4] reported that some particles were found to be inactive at room temperature and that heating till 700 °C in hydrogen resulted in no significant changes. Wang et al. [16] found that CeO_2–ZrO_2 solid solution nanoparticles with a large variation in concentrations through the particle were more active than homogeneous ones. They identified types of ceria nanoparticle behaviour depending on their redox activity level. In our case, with samples dispersed in alcohols, the evolution of the oxidation process may be dependent on the thickness of the CeOOH layer at the surface. The surface of ceria dispersed in isopropanol showed predominately Ce^{3+} with very little changes after heating. For particles dispersed in ethanol we observed both Ce^{3+} and Ce^{4+} at the surface, with a clear reduction upon heating. The ethanol sample has overall more Ce^{3+} in the whole particle at room temperature compare to the isopropanol sample, and it experiences a more abrupt decrease in Ce^{3+} content. The isopropanol sample on the other hand has still a large amount of Ce^{3+} left in the particle at 200 °C, located mostly at the surface. To our knowledge, such results have not been reported, and we recommend future studies on a larger set of particles to fully understand the difference between ceria dispersed in ethanol vs isopropanol.

5. Conclusion

We have found that during low temperature heating of ceria nanoparticles in vacuum, the oxidation state changes from +3 to +4 in a surface layer. There are small differences in the oxidation process between different particles, but at 400 °C and higher, they all have about the same compositional structure with mainly Ce^{4+}. This process occurs for both pristine sample and samples dispersed in alcohols. However, the Ce^{3+} content is much higher in the latter. Heating in vacuum should normally not lead to further oxidation, and our observations indicate that a layer of oxyhydroxide like CeOOH dehydrogenates to CeO_2, a process that only requires diffusion of H. This means that much of the Ce^{3+} we see on the surface is not a reduced oxide such as Ce_2O_3 but a reduced oxyhydroxide like CeOOH, i.e. the Ce^{3+} is not compensated by oxygen vacancies but by protons. These results are supported by TG results showing that the pristine CeO_2 powder contains a considerable amount of water and possibly hydrogen, probably partly adsorbed from ambient humidity and partly left from the synthesis of the powder. The use of in-situ TEM and EELS to map the evolution process of Ce^{3+} to Ce^{4+} in ceria nanoparticles has hence provided new insight to understand their properties, utilizing that the $M_{4,5}$ white line ratio gives good indication on the oxidation state of the particles.

Author statement

This is the individual author's contributions to the paper:

Annett Thøgersen: Data curation; Formal analysis; Funding acquisition; Investigation; Methodology (TEM/EELS work); Project administration; Main writer of manuscript/Review and editing.

Xinwei Sun: Data curation; Formal analysis; Investigation; Methodology (TG + samples), Writing part of manuscript and help with edit.

Ingvild Thue Jensen: Formal analysis; Investigation;

Øystein Prytz: Formal analysis; Funding acquisition; Project administration;

Truls Norby: Formal analysis; Funding acquisition; Supervision; Writing part of manuscript and help with edit.

Declaration of competing interest

The authors declare that they have no known competing financial interests or personal relationships that could have appeared to influence the work reported in this paper.

Data availability

Data will be made available on reasonable request.

Acknowledgement

Acknowledgement to Kathrin Michel, at Institute of Physical Chemistry, Justus Liebig University Giessen, for her contributions to this project. The Research Council of Norway (RCN) is acknowledged for the support to The Norwegian Center for Transmission Electron Microscopy [197405], and for support through projects “MoZEES” (257653) and “SUPROX” (280868).”

References

[1] J. Kašpar, P. Fornasiero, M. Graziani, Use of ceo2-based oxides in the three-way catalysis, Catal. Today 50 (2) (1999) 285–298, https://doi.org/10.1016/S0920-5861(98)00510-0. URL, http://www.sciencedirect.com/science/article/pii/S0920586198005100.

[2] A. Alinezhadchamazketi, A.A. Khodadadi, Y. Mortazavi, A. Nemati, Catalytic evaluation of promoted ceo2-zro2 by transition, alkali, and alkaline-earth metal oxides for diesel soot oxidation, J. Environ. Sci. 25 (12) (2013) 2498–2506, https://doi.org/10.1016/S1001-0742(12)60334-9. URL, http://www.sciencedirect.com/science/article/pii/S1001074212603349.

[3] A. Trovarelli, C. de Leitenburg, M. Boaro, G. Dolcetti, The utilization of ceria in industrial catalysis, Catal. Today 50 (2) (1999) 353–367, https://doi.org/10.1016/S0920-5861(98)00515-X. URL, http://www.sciencedirect.com/science/article/pii/S092058619800515X.

[4] P.A. Crozier, R. Wang, R. Sharma, In situ environmental tem studies of dynamic changes in cerium-based oxides nanoparticles during redox processes, Ultramicroscopy 108 (11) (2008) 1432–1440, https://doi.org/10.1016/j.ultramic.2008.05.015. URL, http://www.sciencedirect.com/science/article/pii/S0304399108001782.

[5] S. Turner, S. Lazar, B. Freitag, R. Egoavil, J. Verbeeck, S. Put, Y. Strauven, G. Van Tendeloo, High resolution mapping of surface reduction in ceria nanoparticles, Nanoscale 3 (2011) 3385–3390, https://doi.org/10.1039/C1NR10510H. URL.

[6] U.M. Graham, M.T. Tseng, J.B. Jasinski, R.A. Yokel, J.M. Unrine, B.H. Davis, A. K. Dozier, S.S. Hardas, R. Sultana, E.A. Grulke, D.A. Butterfield, Invivo processing of ceria nanoparticles inside liver: impact on free-radical scavenging activity and oxidative stress, arXiv:https://chemistry-europe.onlinelibrary.wiley.com/doi/pdf/10.1002/cplu.201402080, Chem Plus Chem. 79 (8) (2014) 1083–1088, https://doi.org/10.1002/cplu.201402080. URL, https://chemistry-europe.onlinelibrary.wiley.com/doi/abs/10.1002/cplu.201402080.

[7] B. Goris, S. Turner, S. Bals, G. Van Tendeloo, Three-dimensional valency mapping in ceria nanocrystals, ACS Nano 8 (10) (2014) 10878–10884, pMID: 25286190. arXiv:10.1021/nn5047053.

[8] J.M. Perkins, S. Fearn, S.N. Cook, R. Srinivasan, C.M. Rouleau, H.M. Christen, G. D. West, R.J.H. Morris, H.L. Fraser, S.J. Skinner, J.A. Kilner, D.W. McComb, Anomalous oxidation states in multilayers for fuel cell applications, arXiv:https://onlinelibrary.wiley.com/doi/pdf/10.1002/adfm.201000279, Adv. Funct. Mater. 20 (16) (2010) 2664–2674, https://doi.org/10.1002/adfm.201000279. URL, https://onlinelibrary.wiley.com/doi/abs/10.1002/adfm.201000279.

[9] A.C. Johnston-Peck, W.-C.D. Yang, J.P. Winterstein, R. Sharma, A.A. Herzing, In situ oxidation and reduction of cerium dioxide nanoparticles studied by scanning transmission electron microscopy, Micron 115 (2018) 54–63, https://doi.org/10.1016/j.micron.2018.08.008. URL, https://www.sciencedirect.com/science/article/pii/S0968432818302361.

[10] F. Zhang, P. Wang, J. Koberstein, S. Khalid, S.-W. Chan, Cerium oxidation state in ceria nanoparticles studied with x-ray photoelectron spectroscopy and absorption near edge spectroscopy, Surf. Sci. 563 (1) (2004) 74–82, https://doi.org/10.1016/j.susc.2004.05.138. URL, https://www.sciencedirect.com/science/article/pii/S003960280400812X.

[11] J. I, J.R. L, M. Baalousha, P. Le Coustumer, Characterisation of structural and surface speciation of representative commercially available cerium oxide nanoparticles, Environ. Chem. 7 (2010) 377–385.

[12] S. Raz, K. Sasaki, J. Maier, I. Riess, Characterization of adsorbed water layers on y2o3-doped zro2, Solid State Ionics 143 (2) (2001) 181–204, https://doi.org/10.1016/S0167-2738(01)00826-8. URL, https://www.sciencedirect.com/science/article/pii/S0167273801008268.

[13] E. Mamontov, Observation of fragile-to-strong liquid transition in surface water in ceo2, J. Chem. Phys. 123 (17) (2005), 171101 arXiv:10.1063/1.2125729.

[14] A.C. Johnston-Peck, J.S. DuChene, A.D. Roberts, W.D. Wei, A.A. Herzing, Dose-rate-dependent damage of cerium dioxide in the scanning transmission electron microscope, Ultramicroscopy 170 (2016) 1–9, https://doi.org/10.1016/j.ultramic.2016.07.002. URL, https://www.sciencedirect.com/science/article/pii/S0304399116300936.

[15] Y. Wang, Q. Zhou, L. Kang, L. Yang, H. Wu, Z. Zhou, C. Xiao, J. Guo, F. Yang, S. Zhang, G. Li, Y. Jin, Oxide-water interaction and wetting property of ceria surfaces tuned by high-temperature thermal aging, Appl. Surf. Sci. 554 (2021), 149658, https://doi.org/10.1016/j.apsusc.2021.149658. URL, https://www.sciencedirect.com/science/article/pii/S0169433221007340.

[16] R. Wang, P.A. Crozier, R. Sharma, J.B. Adams, Measuring the redox activity of individual catalytic nanoparticles in cerium-based oxides, Nano Lett. 8 (3) (2008) 962–967, pMID: 18251517. arXiv:10.1021/nl073135c.

Appendix V

Composite Membranes for High Temperature PEM Fuel Cells and Electrolysers: A Critical Review

MDPI *Membranes* 2021 Best paper award

Xinwei Sun, Stian Christopher Simonsen, Truls Norby, Athanasios Chatzitakis[*]

[a] Department of Chemistry, University of Oslo, Centre for Materials Science and Nanotechnology (SMN), NO-0318 Oslo, Norway

[*] Corresponding author: athanasios.chatzitakis@smn.uio.no

Membranes 2019, *9*, 83.

V

membranes

an Open Access Journal by MDPI

CERTIFICATE

2021 BEST PAPER AWARDS

This certificate is given to

Xinwei Sun, Stian Christopher Simonsen, Truls Norby and Athanasios Chatzitakis

Composite Membranes for High Temperature PEM Fuel Cells and Electrolysers: A Critical Review
Membranes **2019**, *9*(7), 83; doi:10.3390/membranes9070083

MDPI Academic Open Access Publishing since 1996

Basel, May 2021

Dr. Shu-Kun Lin
President & Publisher
MDPI

membranes

MDPI

Review

Composite Membranes for High Temperature PEM Fuel Cells and Electrolysers: A Critical Review

Xinwei Sun, Stian Christopher Simonsen, Truls Norby and Athanasios Chatzitakis *

Centre for Materials Science and Nanotechnology, Department of Chemistry, University of Oslo, FERMiO, Gaustadalléen 21, NO-0349 Oslo, Norway

* Correspondence: a.e.chatzitakis@smn.uio.no; Tel.: +47-2284-0693

Received: 6 June 2019; Accepted: 8 July 2019; Published: 11 July 2019

Abstract: Polymer electrolyte membrane (PEM) fuel cells and electrolysers offer efficient use and production of hydrogen for emission-free transport and sustainable energy systems. Perfluorosulfonic acid (PFSA) membranes like Nafion® and Aquivion® are the state-of-the-art PEMs, but there is a need to increase the operating temperature to improve mass transport, avoid catalyst poisoning and electrode flooding, increase efficiency, and reduce the cost and complexity of the system. However, PSFAs-based membranes exhibit lower mechanical and chemical stability, as well as proton conductivity at lower relative humidities and temperatures above 80 °C. One approach to sustain performance is to introduce inorganic fillers and improve water retention due to their hydrophilicity. Alternatively, polymers where protons are not conducted as hydrated H_3O^+ ions through liquid-like water channels as in the PSFAs, but as free protons (H^+) via Brønsted acid sites on the polymer backbone, can be developed. Polybenzimidazole (PBI) and sulfonated polyetheretherketone (SPEEK) are such materials, but need considerable acid doping. Different composites are being investigated to solve some of the accompanying problems and reach sufficient conductivities. Herein, we critically discuss a few representative investigations of composite PEMs and evaluate their significance. Moreover, we present advances in introducing electronic conductivity in the polymer binder in the catalyst layers.

Keywords: proton exchange membrane; composite membrane; inorganic fillers; proton conductivity; mixed proton electron conducting membranes; positrode; negatrode; fuel cells; electrolysers

1. Introduction

Molecular hydrogen, or hydrogen gas is one of our most important chemicals, and the technologies to produce, transport, store, and use it are mature and safe [1]. Today, it is mainly produced with little energy cost, but large CO_2 emissions from fossil resources. As the world must move towards renewable energy, electrolysis (in addition to use of biomass) will become of increasing importance, and it is imperative to optimise performance and reduce the cost and environmental impact (e.g., use of rare elements) of electrolysis [2–4]. Alkaline (KOH-based) electrolysis (AEs) is the leading industrial technology [5], but solid-electrolyte electrolysers, notably polymer electrolyte membrane electrolysers (PEMEs), are catching up, offering many advantages. For the use of hydrogen gas as intermittent storage of electricity and in transport, the fuel cell is an essential component, and while phosphoric acid and alkaline electrolysers have been leading industrially, solid-electrolyte fuel cells are considered safer and more efficient. In particular, polymer electrolyte membrane fuel cells (PEMFCs) are becoming industry leaders for hydrogen-driven fuel cell electrical vehicles (FCEVs; cars and trucks), trains and ships, and small- and intermediate-sized autonomous and grid-balancing energy systems [6–8].

The advantages of using a stationary solid polymer electrolyte comprise high power density, rapid start-up, and system simplicity. Nevertheless, durability and cost remain primary challenges for

PEMFCs to become commercially competitive with conventional vehicle technologies. According to a cost-analysis from 2015, the cost of an 80/kW_{net} automotive PEMFC operated on direct hydrogen gas is projected to be \$53/kW_{net} when manufactured at a volume of 500,000 units/year (Figure 1), whereas the cost of the membrane accounts for ca. 5.6% (\$2.95/kW) [9]. The target cost of automotive PEMFC systems for 2020 based on current technology is approximately \$40/kW_{net} [10]. This implies a reduction in the cost of the membrane by \$0.8/kW. Further system cost reduction to \$30/kW_{net} must be achieved for long-term competitiveness with the current technologies, which corresponds to \$1.44/kW cost reduction for the membrane for a market with high volume production. More specifically, PEM materials must possess the required characteristics as listed in Table 1.

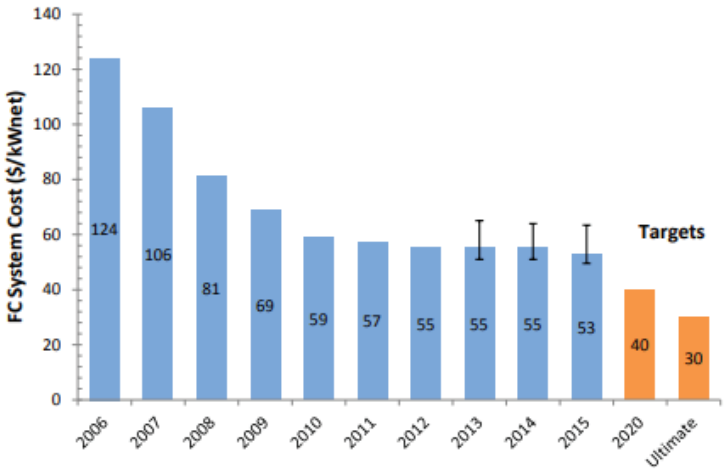

Figure 1. Cost-analysis of an 80 kW_{net} automotive PEMFC-based on projection to a volume of 500,000 units/year [10].

Table 1. US DOE technical targets for PEMs for transportation applications, adapted from Refs. [11–13].

Characteristics	2013 Status	2020 Targets
Maximum oxygen/hydrogen crossover *	<1.8 mA/cm^2	2 mA/cm^2
Maximum operating temperature	120 °C	120 °C
Membrane conductivity	0.002–0.04 S/cm	0.1 S/cm (120 °C) 0.07 S/cm (Ambient) 0.01 S/cm (−20 °C)
Area specific proton resistance at maximum Operating temperature and water partial pressures from 40 to 80 kPa	40 kPa: 0.023 Ω cm^2 80 kPa: 0.012 Ω cm^2	0.02 Ω cm^2
Minimum electronic area specific resistance		1000 Ω cm^2
Cost	\$18/m^2	\$20/m^2
Durability (mechanical & chemical)	>20,000 cycles w/<10 sccm crossover, >2300 h	20,000 cycles w/<10 sccm crossover, 500 h

* Tested in MEA at 1 atm O_2 or H_2 at nominal stack operating temperature, humidified.

The core of traditional PEM electrochemical cells (PEMECs)—treated in many articles and reviews, e.g., Refs. [14,15]—is the membrane electrode assembly (MEA) consisting of a solid-state proton-conductive polymer electrolyte sandwiched between two porous, electronically-conductive

and catalytically-active electrodes. The solid proton-conductive electrolyte ensures the conduction of protonic charge carriers (hydrated H_3O^+ ions) between the electrodes, and is electronically insulating.

One electrode operates under reducing conditions, exposed to hydrogen gas and water vapour. It is always negative, whether run as an anode in the fuel cell or a cathode in an electrolyser, and we will here refer to it as a negatrode. Similarly, the other electrode is always positive, operating under oxidising conditions in oxygen and water vapour as a cathode in the fuel cell or anode in the electrolyser, and we will here refer to it as a positrode, see Figure 2.

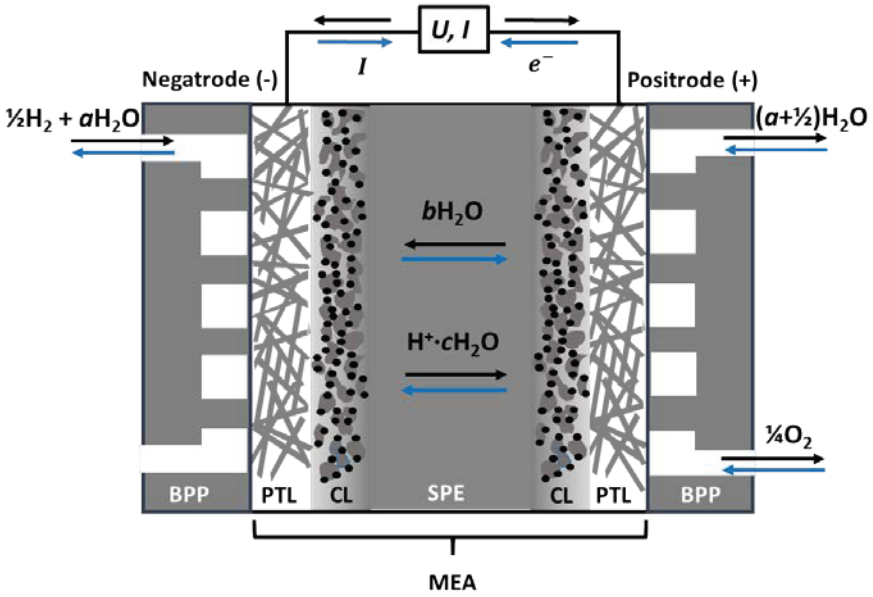

Figure 2. Schematic of PEM electrochemical cells (PEMECs)—fuel cells (PEMFC, black upper arrows) and electrolysers (PEMEs, blue lower arrows). Protons hydrated with c bonded and electro-osmotically dragged H_2O molecules migrate through the solid polymer electrolyte (SPE), the water supplied by b back-diffusing water, and a water supplied in a feed gas, so that $a + b = c$. BPP: bipolar plate gas manifold, PTL: Porous transport layer, CL: catalyst layer, SPE: solid polymer electrolyte, MEA: membrane electrode assembly.

Each of the electrodes comprises a catalyst layer (CL), where the electrocatalysts are dispersed on a nanoporous support to promote charge transfer kinetics by lowering the activation energy. Next comes the more openly porous transport layer (PTL), also acting as a current collector alone or by the help of additional metallic meshes or sinters. The MEA is encased by gas manifold bipolar plates (BPPs) on each side, which direct and distribute gases in flow channels and connect the positrode electronically to the negatrode of the adjacent cell in the case of a PEMEC stack [16].

When PEMECs are operated in fuel cell (PEMFC) mode, humidified hydrogen gas is supplied to the negatrode, where it oxidises to protons and electrons, see Figure 2. The protons migrate to the positrode through the electrolyte and react with oxygen to produce water vapour, while the electrons travel through the external circuit and deliver electrical work. In electrolyser (PEME) mode, the current and all processes are reversed.

It is common to consider the transport of single free protons and to write the negatrode, positrode, and overall reactions forward (fuel cell mode) and backward (electrolyser mode) as:

$$\text{Negatrode}: \quad \frac{1}{2}H_2 \rightleftharpoons H^+ + e^- \quad |2 \tag{1}$$

$$\text{Positrode}: \quad H^+ + e^- + \frac{1}{4}O_2 \rightleftharpoons \frac{1}{2}H_2O \quad |2 \tag{2}$$

$$\text{Overall}: \ H_2 + \frac{1}{2}O_2 \rightleftharpoons H_2O \tag{3}$$

In reality, however, the protonic transport in traditional PEMs takes place by hydrated protons, namely H_3O^+ ions solvated by a number c of additional H_2O molecules, which are pulled along in an electroosmotic drag, so that one may consider the charge carrier as $H^+{\cdot}cH_2O$, and write the reactions more generally like

$$\text{Negatrode}: \ \frac{1}{2}H_2 + cH_2O \ \rightleftharpoons \ H^+{\cdot}cH_2O + e^- \quad |2 \tag{4}$$

$$\text{Positrode}: \ H^+{\cdot}cH_2O + e^- + \frac{1}{4}O_2 \ \rightleftharpoons \ (c + \frac{1}{2})H_2O \quad |2 \tag{5}$$

$$\text{Overall}: \ H_2 + \frac{1}{2}O_2 \rightleftharpoons H_2O \tag{6}$$

The case of $c = 0$ represents the simplified case from above and also free proton transport in high-temperature water-free proton conductors, while increasing c describes systems at lower temperatures, higher relative humidities, and higher contents of adsorbed water or liquid-like condensed water. High c is also accompanied with high mobility of protonic charge carriers in the liquid-like water.

As schematically illustrated in Figure 2, the dragged water may partly back-diffuse in the direction opposite to the protonic current, and partly be supplied to the reactant gas and be recirculated from the outlet. On the other hand, as the membrane becomes dehydrated by the electro-osmotic drag, the pores shrink. It is then possible that the back diffusion of water is not enough to avoid dehydration of the membrane, leading to a decrease of efficiency of the fuel cell [17].

Ionic transport in PEMs is a complex matter, with several types of mobile protonic species and pathways. The two classifications used above are the Grotthuss (free proton) and vehicle mechanisms, while surface (or interface) transport is sometimes mentioned as a third type [15,18]. In the Grotthuss mechanism, a proton jumps from one anion, normally the oxide ion in a solvated H_3O^+ or stationary -OH^-, to another. The vehicle mechanism, on the other hand, comprises transport of H_3O^+ ions solvated in liquid-like aqueous media. Generally, the breaking and making of bonds in the Grotthuss mechanism involves a higher activation energy than the fluidic diffusion of vehicular species. Moreover, the amount of hydration—the volume of the water phase—decreases with lower relative humidity, usually a result of increasing temperature. Hence, all in all, Grotthuss-type free proton transport tends to become more dominating at higher temperatures and lower relative humidities, while vehicle transport dominates at low temperatures and higher relative humidities. In a fully-hydrated polymer, or at constant relative humidity, the temperature dependencies may appear different, as the state (viscosity) of the water phase changes, while its volume may remain constant. Surface and interface transport of protonic species takes place by protons jumping between neighbouring acidic donor/acceptor sites on the polymer backbone, facing gas or water, respectively, in dry or hydrated membranes, and does as such represent Grotthuss type transport. On the basis of the above, the total protonic conductivity of a polymer membrane depends on its backbone morphology and dynamics, the concentration and acidity of proton donor/acceptor sites, and the resulting hydrophilicity and water content. We may translate this into volume of the conducting phase and concentration and charge mobility of protonic species. For a given polymer, the conductivity becomes a complex function of temperature and water activity (partial pressure) or relative humidity.

Traditional PEMECs are based on perfluorinated polyethylene polymer membranes, which are grafted (branched), sulfonated with concentrated sulphuric acid, neutralised with an alkali such as NaOH, and proton exchanged (hence the use of the name proton exchange membrane (PEM)) to replace Na^+ with H^+ (or H_3O^+). In contact with water, they swell and form hydrophilic water-filled proton-conducting channels and hydrophobic backbones. They operate typically at 80 °C at high

relative humidity (RH, >40%), and cannot withstand much increased temperatures as they dehydrate, causing a drop in proton conductivity, and eventually degrade irreversibly [19].

Nafion® developed by DuPont in the late 60s is still the state-of-the-art PEM. Initially, Nafion was developed for the chloralkali electrolysers as a permselective separator, but Nafion had oxidative stability, and after proton exchange, also the proton conductivity required for PEMFCs [14,20]. Nafion is composed of a hydrophobic tetrafluoroethylene (TFE) backbone sequence together with a co-monomer that contains pendant side chains of perfluorinated vinyl ethers, which are terminated by perfluorosulfonic acid groups (Figure 3a). The synthetic route of TFE-carrying branches of pendant sulfonic acid groups is given in Figure 3b.

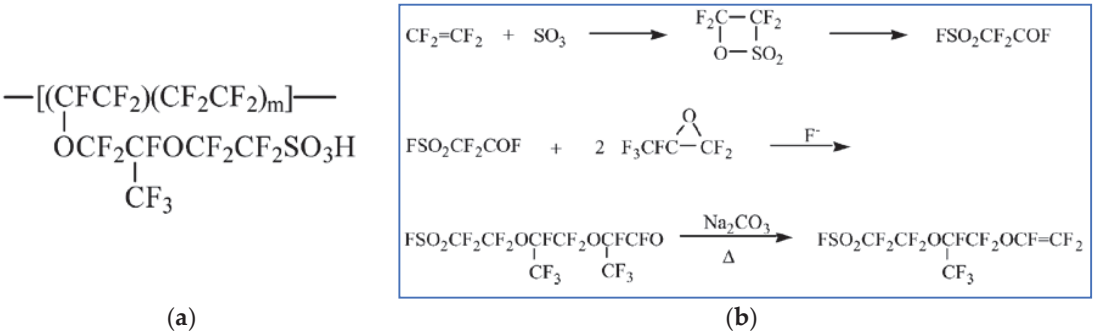

(**a**) (**b**)

Figure 3. The chemical structure of Nafion (**a**) and the synthesis process for the vinyl ether monomers, the starting point for Nafion (**b**). (**b**) is reprinted with permission from Ref. [20]. Copyright 2004 Elsevier.

The polytetrafluoroethylene (PTFE) hydrophobic matrix contains well-connected hydrophilic ionic clusters that despite their low ion exchange capacity (IEC) show high proton conductivity below 90 °C. Moreover, this unique fluorocarbon polymer structure is responsible for the good mechanical and chemical stability [21,22].

The performance of low-temperature PEMFCs (LT-PEMFC ≤ 80 °C) is in general limited by fuel crossover, CO poisoning on the anode Pt catalyst, slow electrode reaction kinetics, complex water management, inefficient cooling heat exchange, and little usage of waste heat [23,24]. As mentioned, Nafion as the state-of-the-art LT-PEM material relies on a high level of hydration in order to accommodate the proton transport and reach sufficient proton conductivity (100 mS/cm) at temperatures up to 80 °C. At higher temperatures, the chemical and mechanical stability of Nafion is compromised because of the low glass transition temperatures of the perfluoroaliphatic polymer chains of PFSAs. Moreover, at these temperatures, the ionic clusters dehydrate and the protonic conductivity is heavily reduced, leading to a significant decrease in the PEMFC performance. Another concern is the high cost of Nafion, which is holding back mass production and full commercialization [25,26]. Ideally, the operating temperature of a PEMFC should be above 100 °C, and this has stimulated efforts to develop proton conductors for higher temperature operation in the last two decades. However, also PEM electrolysers would benefit from higher operating temperatures for many of the same reasons. In addition, one may supply waste heat or steam and increase the electrical efficiency by operating at high temperatures (e.g., above 100 °C).

Strategies to increase the operating temperatures of PEMs involve the use of heterocyclic polymers like the thermoplastic polybenzimidazole (PBI); its structure can be seen in Figure 4a.

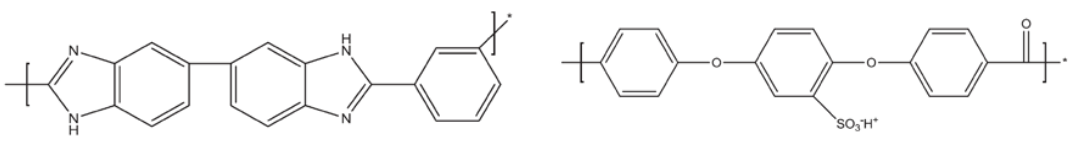

(**a**) (**b**)

Figure 4. Structures of PBI (**a**) and SPEEK (**b**).

The original idea is that the N atoms of PBI will bond protons weaker than fully covalent carbon or oxide ions would in other polymers and hence act as suitable proton donors and acceptors for free proton transport at elevated temperatures. However, acid-doping has turned out necessary to achieve considerable proton conductivity in PBI.

Another route has been the high-temperature thermoplastic polyether-ether-ketone (PEEK), where again acid-doping in order to form sulfonated PEEK (SPEEK) is necessary to achieve appreciable proton conductivity (Figure 4b) [27]. The mobility of protons from or in the acid increases with temperature, and generally one needs well above 120 °C, typically 160 °C, to yield a sufficient proton conductivity. However, at these temperatures, the long term stability of these polymers is compromised and the acid doping can sip out and corrode metal interconnections [13].

As nicely depicted by Wieser (Figure 5), a "conductivity-gap" exists at intermediate temperatures and especially around 120 °C which is the target temperature as given in Table 1 [28].

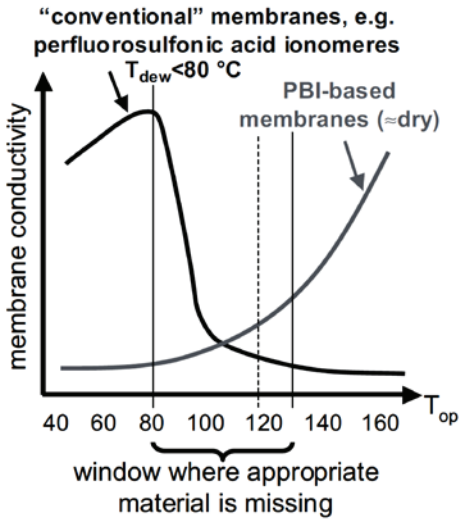

Figure 5. Membrane conductivity based on perfluorosulfonic acid (PFSA) ionomers and PBI, displaying the conductivity gap from 80 °C to 130 °C. Reprinted with permission from Ref. [28]. Copyright John Wiley & Sons, Ltd.

A number of studies attempt to improve the conductivity and stability at temperatures in the conductivity-gap by dispersing a secondary ceramic phase (filler) so as to make a polymer-ceramic (pemcer) composite. Ceramics are added to both LT polymers like Nafion, as well as to PBI and SPEEK. The fillers are intended to increase the water retention due to their hygroscopicity, reduce fuel and oxygen cross-over, induce fast proton mobility at the interfaces, scavenge harmful radicals, and finally, improve the mechanical properties [29]. Here, we review these materials, their principles of operation and their performances. It is appropriate to ask how sound the principles are and if the materials work as claimed.

For instance, hygroscopic ceramic fillers may "save" the polymer by retaining water during a critical overheating, but one rarely finds a well-founded thermodynamic or physicochemical argument for the effect of the ceramic. The use of inert particles in order to avoid gas crossover can eventually impede proton transport, and one might just as well increase the thickness of the membrane. Fast transport in polymer–ceramic interfaces is possible, but to beat the highly conducting liquid aqueous phase is hard, and little is put forward e.g., in terms of charge separation or space charge effects to rationalise why and how it would work. Scavenging harmful oxidising radicals like OH* or catalyst poisons like CO will be highly beneficial, but could possibly be applied better in the electrode matrix than in the membrane, although Macauley et al. [30] recently showed that a CeO_2-scavenger-modified PFSA has the potential to achieve a 25,000 h of heavy-duty fuel cell durability. Ceramic dispersions may increase the hardness and temporarily the thermal stability of the membrane, but they also increase the

brittleness; hence, we may ask if they are really of help, or whether the toughness of the pure polymer is a better choice. A few important studies highlighting several approaches to increase the mechanical and chemical properties of PEMs can be found in Refs. [31,32].

The next section reviews and discusses composite membranes based on PFSAs with Nafion as the prominent example, while the following two sections cover composite membranes based on PBI and SPEEK. After that, we introduce briefly the progress on mixed electron–proton-conducting polymers, which are particularly interesting for the efficient utilization of the electrocatalysts in the CL. By the end of this review, we hope to advocate and foster deeper physicochemical analysis for better founded strategies on how composites may help develop high-temperature proton-conducting polymer electrolyte membranes.

2. Long Side Chain PFSA Polymer: Nafion-Based Composite Membranes

Protonic conductivity of Nafion membranes depends heavily on the degree of hydration and the availability of the sulfonic acid sites, which attract water and form solvated hydronium ions (H_3O^+) as the protonic transport vehicle. The conductivity of fully-humidified Nafion reaches 0.12 S/cm at 80 °C and atmospheric pressure, and decreases by several orders of magnitude with decreasing relative humidity [33,34]. As mentioned earlier, one common approach to alleviate membrane dehydration at elevated temperatures is by introducing ceramic fillers. Possible mechanisms are still under debate, but there are indications that the improved proton conduction is due to the water retention properties resulting from an increased tortuosity induced by the fillers inside the membrane, and enhanced crystallinity especially for elevated pressure operation [35,36]. In the following section, we review in more detail some promising Nafion-based composite membranes for high-temperature fuel cells or electrolysers.

2.1. Hydrophilic Inorganic Material

Dispersed "hygroscopic" oxides, such as SiO_2 [37,38], TiO_2 [39,40], ZrO_2 [41,42] and Al_2O_3 [36], have been reported to form dynamic cross-links with sulfonic acid groups of Nafion, thereby increasing the porosity and improving water retention. They also decrease the gas crossover with respect to bare Nafion. Minimum cell resistance is achieved at around 140 °C, where physisorbed water is reported to be desorbed from the investigated inorganic fillers [36]. Up to 10 wt.% of the oxide can be added to Nafion without a significant decrease in the protonic conductivity [43]. Even better protonic conductivity can be achieved by sulfonating the oxides [44–46].

An in-situ sol-gel process was used to make Nafion membranes containing ZrO_2, SiO_2 and TiO_2. This process used pre-cast membranes that were cleaned in hydrogen peroxide solution and underwent an ion exchange from H^+ to Na^+ by reacting the membrane with NaOH solution. The membranes were then heat-treated in a vacuum furnace before being immersed in a 90% ethanol-solution to hydrate and swell the membrane. The swelled membrane was then placed in the metal-precursor solution that decomposed to the metal oxide when reacted with water. The idea behind this method is that the membranes will serve as the template that directs the morphology, particle size and growth rate of the metal oxide [47]. Results from this study showed that the composite membrane either retained or increased the water uptake. The membranes with ZrO_2 increased the water retention capacity by 33% and 45% at 90 °C and 120 °C, respectively, TiO_2 by 20–25%, and SiO_2 had a 15% increase at 120 °C. The conductivity measurements, however, showed that neither TiO_2 nor SiO_2 gave any increase in conductivity compared to the recast Nafion, and the ZrO_2 had an increase of merely 8–10% compared to pure Nafion (Figure 6). The authors concluded that the increase in water uptake does not necessarily result in a higher conductivity [47].

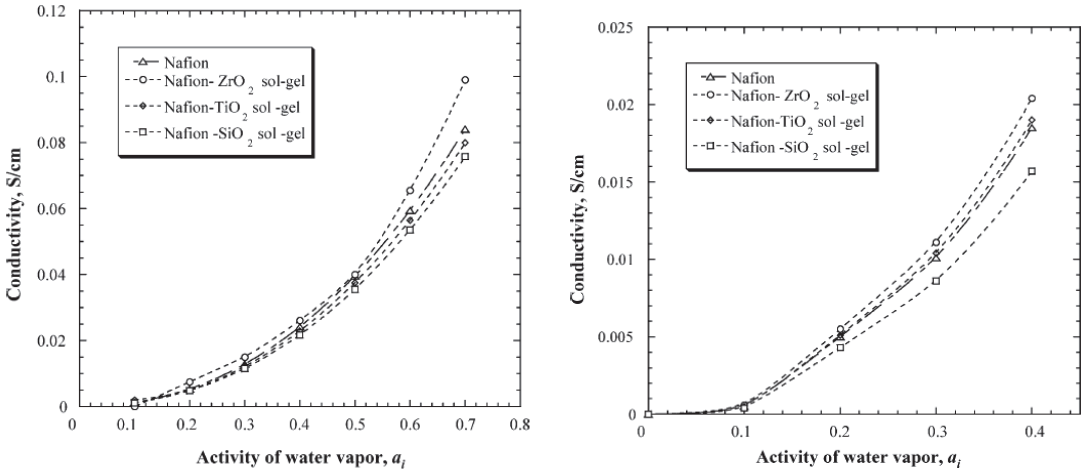

Figure 6. The conductivity of the measured membranes at different water activities at 90 °C (**a**) and 120 °C (**b**). Reprinted with permission from Ref. [47]. Copyright 2005 Elsevier.

Another synthesis method comprised pre-made nanoparticles of SiO_2, Al_2O_3, TiO_2 and ZrO_2. These particles were mixed in a 5% Nafion solution mixed with double its volume of isopropyl acid. The total mass of the inorganic particles was 3 wt.%, and the membranes were standardized to a thickness of 125 μm [24]. The membranes were tested at 130 °C at relative humilities between 100% and 75% (Figure 7). A 68% reduction of resistance was observed for the membrane with SiO_2 particle sizes of 0.2–0.3 μm and a surface area of 90 g/m^2, compared to the plain Nafion at 75% RH. The closer to 100% RH, the smaller the differences in proton transport resistances. For the TiO_2, the same trend was observed with a smaller difference in resistance to the higher the relative humidity, and at 75% RH there was a 61% decrease in the resistance. The particle size in this membrane was 1–2 μm. For the alumina composite (Figure 7c), the membrane with particle size of 25 μm showed better results than 1 μm, where the resistance at 75% RH decreased by 22%, but at 100% RH the composite membrane showed a higher resistance than the plain Nafion. The membrane with 6 μm ZrO_2 particles showed a decrease of 40% in resistance at 75% RH compared to the recast Nafion membrane [24].

Another study used a self-assembly process by mixing a Nafion-solution with M-methyl-2-pyrrolidone and all other solvents were removed by heat treatment. The mixing in the metal precursor solution and the subsequent hydrolysing reaction produced metal oxide nanoparticles that are stabilized by the Nafion matrix. The solution was then heat treated to produce the final membrane [48]. This study used composite membranes made with zirconia and silica particles, and based on the water uptake measurements, the composite membranes showed a higher water content at 100 °C, where below 20% RH the improvement is minimal. At higher than 40% RH levels, a water uptake between 2 to 3 times higher for the composite membranes compared to plain Nafion was observed. The conductivity of the membranes was tested without external humidification in order to assess the water retention capacity of the membranes. The results indicated that the zirconia-doped membrane had the best conductivity that can come from the water retention compared to the Nafion, and the conductivity at 100 °C was six times higher, reaching ca. 0.01 S/cm (Figure 8). The silica-doped membrane also showed a higher conductivity but less than the zirconia-doped membrane [48].

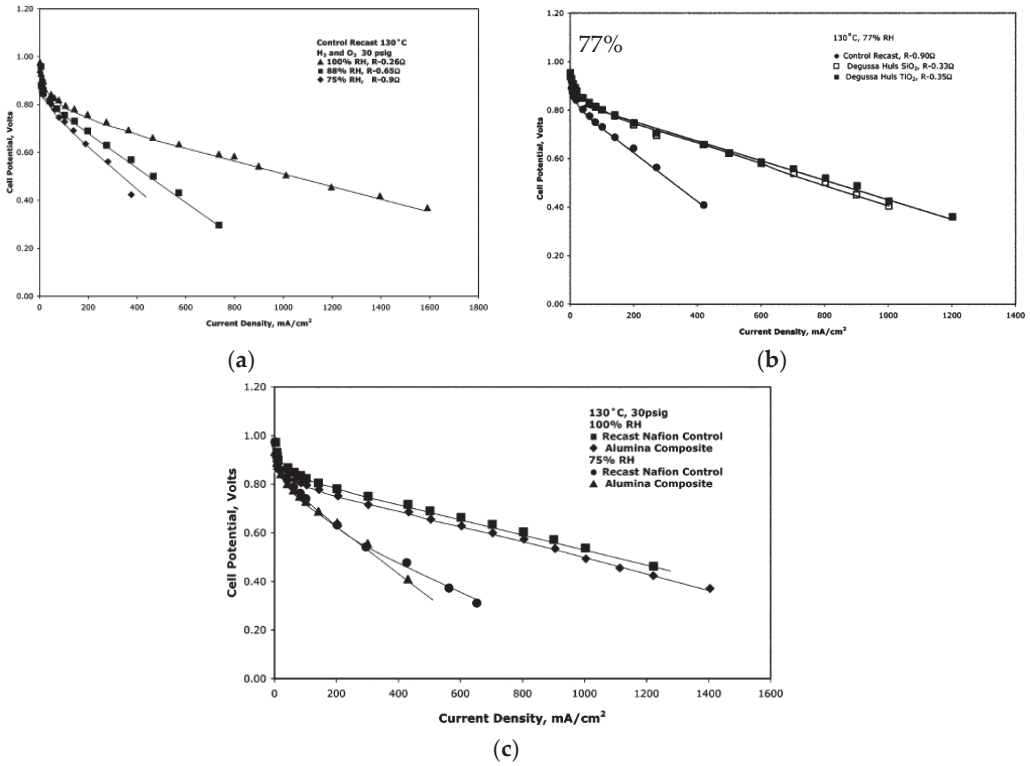

Figure 7. The current density plot for recast Nafion at 130 °C, 30 psig and using H_2/O_2 as reagent gases (**a**). The current density plots for membranes containing SiO_2 and TiO_2 at 130 °C at 77% RH using a pressure of 30 psig and H_2/O_2 as reagent gases (**b**). The current density plot for Nafion membrane and an Al_2O_3 composite membrane at 130 °C, 30 psig and using H_2/O_2 as reagent gases (**c**). Reprinted with permission from Ref. [24]. Copyright 2006 American Chemistry Society.

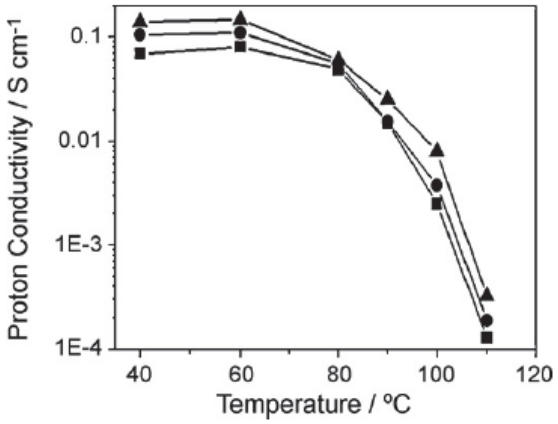

Figure 8. The proton conductivity of membranes without external humidification. Triangle is zirconia-doped, circle is silica-doped membrane and square is recast Nafion. Reprinted with permission from Ref. [48]. Copyright 2010 Elsevier.

In a similar work, silica, zirconia and their combinations were used as inorganic "dopants" to Nafion membranes. The membranes were made by mixing premade surfactant-free particles into a Nafion solution and then heat treated. The membranes were made with 10 wt.% inorganic fillers [49]. The results from this study showed that the silica-doped membrane had a lower water uptake than the recast Nafion and the commercial Nafion 112. The highest water uptake was in the zirconia-modified membrane, where the water uptake increased merely from 38.3% to 39%. All the other combinations of the binary oxide particles followed a linear trend depending on the zirconia concentration. The

conductivity of the membranes at 80 °C showed that the zirconia-modified membrane had the highest conductivity of 0.1 S/cm at 90% RH. The recast Nafion, commercial Nafion 112 and the silica-doped membrane, all had a conductivity of 0.07 S/cm (Figure 9a). At 120 °C and 50% RH, the recast Nafion and commercial Nafion 112 had a conductivity of 0.0175 S/cm, while the membrane with two parts silica and one part zirconia as the inorganic dopant had a conductivity of ca. 0.03 S/cm (Figure 9b). This is a slight improvement from the pure silica and zirconia-doped membranes, that showed conductivity values of 0.024 and 0.026 S/cm, respectively [49].

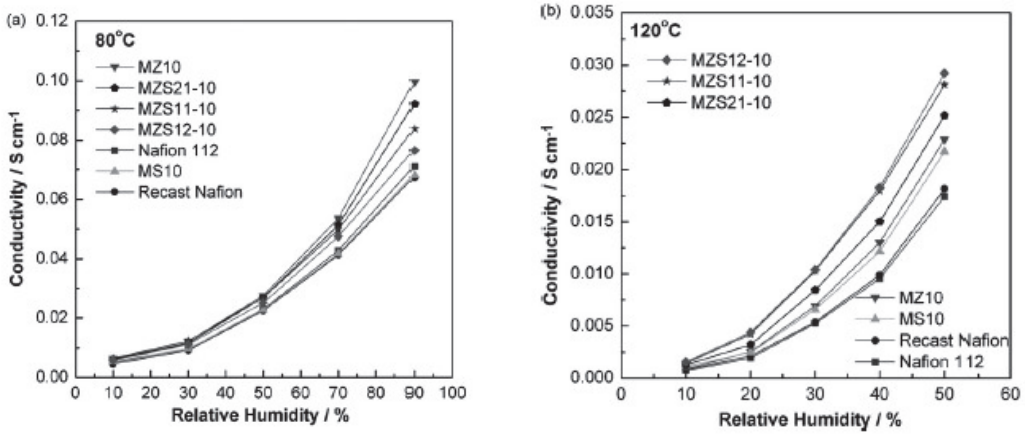

Figure 9. The measured conductivity of the membranes over different RH levels, where the membranes are labeled MZSxy-10 and x:y is Zr:Si, at 80 °C (**a**) and at 120 °C (**b**). Reprinted with permission from Ref. [49]. Copyright 2008 Elsevier.

Chalkova et al. used titania powders with particle sizes of 0.1–1 μm and 0.2–0.3 μm, which were mixed into 5% Nafion solution and heat treated to obtain 10 wt.% TiO_2 Nafion membranes with a thickness of 80 μm [50]. The current density of the membranes with titania showed a significant improvement compared with the recast Nafion membrane over all RH values, at temperatures of 80 °C and 120 °C. Comparing the composite membranes at a cell voltage of 0.6 V, the one with particles size of 0.2—0.3 μm performed 1.2 to 1.7 times better at 26% and 50% RH at 80 °C and 1.4 to 4 times better at 26% and 50% RH compared to the membrane with a particle size of 0.1–1 μm. It is also noted that the membrane with particles size of 0.2–0.3 μm was less affected by the change in relative humidity. These results suggest that the surface properties of TiO_2 somehow can decrease the resistance of the proton diffusion. The surface properties are dependent on the morphology, surface area, and the electric double layer created by the charged surface [50].

Finally, the outstanding mechanical properties of carbon nanotubes (CNTs) make them an interesting filler material for composite reinforcement [51]. Nafion filled with sulfonic acid functionalized single-walled carbon nanotubes (S-SWCNTs) exhibits almost one order of magnitude higher ionic conductivity than that of Nafion1135 even above 100 °C, as well as enhanced mechanical stability [52]. The composite membrane gives a maximum power density of 260 mW/cm^2 at 0.42 V, whereas the Nafion 1135 membrane gives 210 mW/cm^2 at 0.39 V.

2.2. Metal Organic Frameworks (MOFs)

Another category of inorganic fillers recently reported to increase the conductivity of Nafion for operation at low RH is metal organic frameworks (MOFs). Some MOFs become proton conducting after the incorporation of protonic charge carriers, such as water, acids and heterocycles into their pores [53]. In general, increased proton conductivity can be achieved from polymer/MOF composites through two ways, either drenching the pores of MOFs with proton carriers (e.g., phytic@MIL [54], PIL@MIL [55], acids@MIL-101 [56], ZIF-8 and ZIF-67 [57], sulfonated MIL [58], ZIF-8/CNT network [59], Fe-MIL-101-NH_2 [60]), or through modification of their organic ligand with functional groups (-SO_3H, -NH_2) to increase the acidity and hydrophilicity (e.g., sulfonated Zr-MOF-808 [61], S-UiO-66@GO [62]).

Nevertheless, very few of them have actually been tested for PEMFC operation [56,63,64]. In this chapter, we will briefly touch upon a few recent developments reported in the literature regarding fillers based on MOFs.

Sadakiyo et al. controlled the hydrophilicity of a class of MOF materials based on $(NR_3(CH_2COOH))(MCr(ox)_3)\cdot nH_2O$, where R = methyl, ethyl or n-butyl and M = Mn or Fe [65]. The MOFs are simply named as R-MCr, and the most hydrophilic sample was the Me-FeCr, which at room temperature showed a proton conductivity of 0.1 mS/cm at 65% RH. The performance and the effect of this MOF have not been investigated in a mixed conducting membrane or at higher temperatures and even lower RH levels.

Li et al. immobilized phytic acid, which can be obtained from plants and contains a high concentration of phosphate groups, onto MIL101 via vacuum-assisted impregnation [54]. Composite Nafion/phytic@MIL101 membranes were synthesized by the solution casting method with varying amounts of MIL101 and phytic@MIL101. The proton conductivities were measured at 80 °C in different RH levels, showing conductivities of the best performing composite (which had 12 wt.% of phytic@MIL101) of 61 mS/cm and 0.7 mS/cm at 57% and 11% RH, values that are 2.8 and 11 times higher than pure Nafion. The improved proton conductivity is assigned to the continuous channels formed by the MIL101 and the phosphate groups available from the phytic acid. It is worth mentioning that the authors measured the conductivity of the pure Nafion at 80 °C and 100% RH, and it was found to be of the order of 100 mS/cm, giving confidence in their methodology. On the other hand, in their schematic representation of the mechanism for the improved proton conduction, the MOFs appear to be smaller than the Nafion channels. This is questionable, as the MOF appears to be hundreds-of-nanometers-big particles. It is not clear if a percolating network is formed between the modified MOFs, and in fact the Nafion/MIL101 composite performed worse than the pure Nafion. So, is it possible that phosphate groups are leaking from the phytic acid "dope" Nafion? The leakage test was performed in water, but can it accurately simulate the conditions in Nafion?

A high-performing Nafion/MOF composite membrane was developed by Yang et al. [66]. In this work, the porous framework ZIF-8 is grown on graphene oxide (GO) and the ZIF-8@GO composite is introduced into Nafion. The authors reported a proton conductivity of 280 mS/cm at 120 °C, at 40% RH, a performance that is 55 times higher than that of Nafion (5 mS/cm). This high performance is attributed to the high water retention capability of the composite, as well as to the unique monolayer structure of ZIF-8@GO. Unfortunately, the authors did not test this membrane in an actual PEMFC or PEMWE in order to verify the positive effects of such a composite membrane under realistic conditions.

One of the first studies of a Nafion/MOF composite membrane employed in a PEMFC is described by Tsai et al. [67]. Herein, the authors mixed MOFs with 1D microporous channels (CPO-27(Mg) and MIL-53(Al)) with Nafion through a simple solution recast protocol. The filler content was kept at 3 wt.% as this was the maximum amount of filler that a homogeneous membrane could obtain. The composite with CPO-27(Mg) had the higher water uptake and protonic conductivity, which was measured at 50 °C and 100% RH. The PEMFC performance of the composite membranes against the pure Nafion one was compared at 100% RH and at different operating temperatures. The Nafion/CPO-27(Mg) composite showed the highest power densities across all temperatures and for example at 50 °C the performance was 74% higher than that of Nafion. Unfortunately, the authors tested only this composite at lower RH, 15%, therefore a comparison with the other membranes cannot be made for low RH values. Nevertheless, the Nafion/CPO-27(Mg) showed exceptional performance at low RH values compared to the high one, and at some temperatures, the power densities were even higher, e.g., at 50 °C and 15% RH, the power density was 853 mW/cm^2 and 818 mW/cm^2 at 100% RH. The performance of such a composite should also be tested at high temperatures and both low and high RH.

Recently, Rao et al. incorporated the UiO-66-NH_2 tethered on GO into Nafion [68]. The composite membrane operated at 90 °C both in 95% RH and reportedly under anhydrous conditions with conductivities of 303 and 3.4 mS/cm, respectively. These values were approx. 1.57 and 1.88 times higher than the conductivities measured for recast Nafion, assigned to a synergy between the vehicle

and Grotthuss mechanisms. Another UiO-66-based MOF employed in composite Nafion membranes was presented by Donnadio et al. [69]. In this work, a set of composites with the UiO MOF that was either sulfonated or not was tested under different temperatures and RH. The results showed a slight improvement of the proton conductivity at 110 °C; at 50% RH for the composite membranes, either the MOF was sulfonated or not. The optimum filler content was 2 wt.% and independent of the presence of sulfonic groups. It was speculated that the improvement is due to the filler modifying the ionomer's structural features. The authors conclude and imply that sulfonation of this particular MOF does not improve the performance, and other functional groups, such as phosphates, are suggested for further research. Patel et al. synthesized a composite membrane based on Nafion and superacid sulfonated Zr-MOF (SZM) [61]. The water uptake of the composite membrane was constantly higher at different RH compared to the pure Nafion ones. Therefore, the performance of a PEMFC operated at 80 °C and 35% RH was also improved, showing also increased proton conductivity, as seen from EIS measurements (Figure 10).

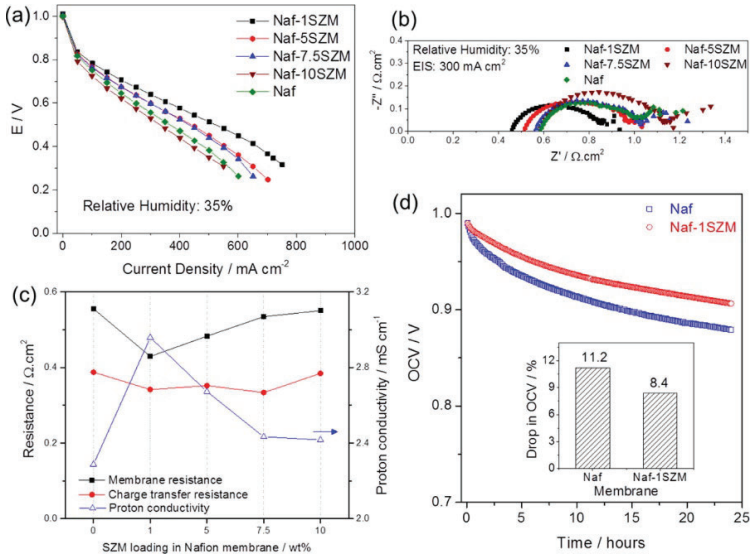

Figure 10. Polarization curves (**a**). Nyquist plots obtained with EIS (**b**), membrane resistances, proton conductivities and charge transfer resistances as a function of the SZM content in the composite (**c**). Stability runs as obtained for 24 h at 35% RH, at 80 °C (**d**). The inset shows the OCP drop in percentage (%). Reprinted with permission from Ref. [61] under a Creative Commons Attribution (CC-BY) License. Copyright 2016 American Chemical Society.

The composite with 1 wt.% SZM improved by 34% the voltage of the PEMFC at 0.5 A/cm^2, while the proton conductivity was increased by 23%.

2.3. Solid Acids

The materials referred to in the following, classified as solid acids in the literature and therefore used as fillers for polymer membranes, are in fact not bulk proton conductors, but mainly conduct protons in adsorbed water. This is worth taking into account when their potential and reported effects on hydration and proton conductivity of composites are evaluated.

Shao et al. compared the performance of a composite Nafion membrane with phosphotungstic acid ($H_3PW_{12}O_{40}{\cdot}nH_2O$, PWA) supported on silica gel against Nafion 115 [70]. It was found that the Nafion\$SiO_2$\PWA had the highest water uptake, as well as the highest proton conductivity at 100 °C under a wide range of RH values. The authors assembled a single PEMFC, which was operated at 110 °C and 70% RH. They found that the composite membrane delivered a current density of 540 mA/cm^2 at 0.4 V, while the pure Nafion delivered only 95 mA/cm^2. One should notice however that the proton conductivity of the composite membrane at 110 °C and 70% RH was as low as 27 mS/cm.

Layer-structured zirconium hydrogen phosphate ($Zr(HPO_4)_2 \cdot H_2O$) ("ZrP") has a protonic conductivity of the order of 10^{-7}–10^{-3} S/cm depending on the phase composition, structure and hydration state [71,72]. A remarkable proton conductivity of 218 mS/cm at 80 °C with 100% RH has been reported for Nafion/ZrP composite as a consequence of enhanced water uptake, which could be explained by the hydrophilicity of ZrP particles, providing additional proton-conducting moieties in the membrane [73]. Yang et al. [72] further suggested that ZrP forms an internal rigid scaffold within the membrane that permits increased water uptake.

The permeation of hydrogen can be substantially reduced by adding layered silicates such as montmorillonite (MMT) or laponite (Lp). Although the proton conductivities of the nanocomposite membranes were lower than that of pure PBI membranes, the performance of the MEAs was higher than the commercial Nafion [74,75].

Heteropolyacids (HPAs) including phosphotungstic acid (PWA) and silicotungstic acid (SiWA) ($H_4SiW_{12}O_{40} \cdot nH_2O$) etc. are known to have high intrinsic proton conductivity as the humidity increases, thus HPAs as inorganic additives have been extensively studied for intermediate-temperature and low-humidity PEMFC applications. However, the proton conductivity of these composite membranes is in general low reportedly because not all protons are available for protonic conduction at higher temperatures even though they move more rapidly [35]. In fact, this protonic conductivity is as stated above probably attributable mainly to adsorbed surface water.

A comparison of the proton conductivities obtained from Nafion-based composite membranes and their PEMFC performance are summarized in Table 2.

Table 2. Comparison of proton conductivities of Nafion-based composite membranes and their PEMFC performance.

Membrane	Conductivity/ Activation Energy	Temperature (°C)	RH (%)	Maximum Power Density in PEMFC	Ref.
Nafion/12 wt.%Phytic@MIL101	228 mS/cm and 15.14 kJ/mol	80	100	Not reported	[54]
Nafion/10 wt.% SAFHSS	100 mS/cm	100	100	Not reported	[45]
Nafion/4 wt.% GO	170 mS/cm and 12.98 kJ/mol	80	100	100 °C and RH = 25% 212 mW/cm^2	[76]
Nafion/0.05 wt.%s-SWCNTs	15.5 mS/cm	100	100	65 °C 650 mW/cm^2	[77]
Nafion/5 wt.% sPPSQ	157 mS/cm	120	100	Not reported	[46]
Recast Nafion/20 wt.% ZrSPP	50 mS/cm	110	98	100 °C 700 mA/cm^2 @0.4 V *	[78]
Nafion/15 wt.% Analcime	437.3 mS/cm	80	100	Not reported	[79]
Nafion/1 wt.% ZIF-8@GO	280 mS/cm and 13.2 kJ/mol	120	40	Not reported	[66]
Nafion-0.6/UiO-66-NH_2 + UiO-66-SO_3H	256 mS/cm	90	95	Not reported	[80]
Nafion-0.6/GO@UiO-66-NH_2	303 mS/cm	90	95	Not reported	[68]
Nafion/3 wt.% CPO-27(Mg)	11 mS/cm	50	99.9	50 °C and RH = 100% 818 mW/cm^2 80 °C and RH = 100% 591 mW/cm^2	[67]
Nafion/1 wt.% SZM	2.96 mS/cm	80	35	80 °C and RH = 35% 550 mA/cm^2 @0.3 V	[61]
Nafion/1 wt.% F-GO	17 mS/cm	70	20	70 °C and RH = 20% 300 mW/cm^2	[81]
Nafion/3 wt.% Fe_3O_4-SGO	11.62 mS/cm and 21.41 kJ/mol	120	20	120 °C and RH = 25% 258.82 mW/cm^2	[82]
Recast Nafion/14.3 wt.% SiO_2-PWA	26.7 mS/cm and 11.2 kJ/mol	110	70	110 °C and RH = 70% 540 mA/cm^2 @0.4 V *	[70]
meso-Nafion/ 19 wt.% $H_3PW_{12}O_{40}$	72 mS/cm	80	40	80 °C and RH = 50% 541 mW/cm^2	[83]

* Power density not reported, but we give the current density at the respective applied voltage.

3. PBI-Based Composite Membranes

Polybenzimidazole (PBI) provides exceptional chemical resistance, high thermo-oxidative stability, and good thermal and mechanical properties at temperatures above 80 °C [84]. The earlier-reported inherent protonic conductivities of PBI are low and contradicting; values such as 10^{-12} S/cm [85], 10^{-7} S/cm [86] and 2×10^{-4}–8×10^{-4} S/cm [87] at RH from 0 to 100% were published, all suggesting that PBI is an insulator without potential use as solid electrolyte in fuel cell applications. Nevertheless, due to the basic character of PBI (pK_a = 5.23 for 2-phenyl benzimidazole in the salt form [88]), the N–H sites of the imidazole ring associated with PBI can readily combine with strong acids to form a single-phase polymer electrolyte for use as proton conductors [89–91]. The proton transport is essentially through proton hopping between two molecules via rearrangement of the hydrogen bonds [92]. Water produced from the cathode can further promote the dissociation of the acid and facilitate proton transport [93]. The type of acids, acid doping level and immersion time, RH and temperature were found to be of special importance for the proton conductivity of the acid-doped PBI membranes. Sulfuric acid (H_2SO_4)-doped PBI has been shown to generate the highest conductivity [85,94], however, it has a significant vapour pressure. Besides, the high performance also requires RH of above 50% under H_2SO_4 doping level of 9.65 to achieve conductivities of 0.2 S/cm at 150 °C [95]. In the literature, the acid doping level (ADL) is often expressed as the number of H_3PO_4 mols per PBI unit. In comparison, it was much easier to dope PBI with phosphoric acid (H_3PO_4), forming a dynamic hydrogen bond network so that protons can transport through [96]. A breakthrough was reported by Wainright et al., where they measured a proton conductivity of 22 mS/cm from H_3PO_4 doped PBI membrane with a doping level of 5.01 at 190 °C [90].

Since then, H_3PO_4 doped PBI type membranes have been studied extensively and seem so far the most successful membranes for application in fuel cells at temperatures up to 200 °C under ambient pressure. For this reason, we will in the present review limit ourselves to H_3PO_4-doped PBI composite membranes only. Thermoplastic polymers other than PBI, e.g., poly(vinylalcohol) (PVA), poly(ethyleneimine) (PEI), polyimide (PI), poly(ethyleneoxide) (PEO), poly(ethersulfone) (PES) doped with other types of acids are beyond the scope of this review [19,97–99].

3.1. H_3PO_4 Doped PBI Membrane

As mentioned before, the intrinsic proton conductivity of PBI is negligible and it requires acid doping to facilitate proton transport. After doping with H_3PO_4, the associated anions are linked to the PBI polymer, which acts as both a donor and acceptor in proton transfers, allowing protons to move along the anionic chain. As seen from Figure 11a, an immersing time of 50 h is necessary before the weight and volume of the membrane reaches a stable level at ambient temperature. This is due to both water uptake and acid doping. In order to differentiate the contribution of each, the membrane was dried at 110 °C in vacuum for about 5 h until a constant weight was reached. It was assumed that all absorbed water was removed in this way and the gain in volume was due to acid doping alone. Moreover, the amount of absorbed water was very much influenced by the acid concentration (Figure 11b). At low acid concentrations (<5 M), no significant difference in water uptake was observed because the active sites of the imidazole ring are preferably occupied by the doping acid molecules. However, the amount of absorbed water increased significantly at higher acid concentrations (>8 M). In this case, the water uptake is predominated by the excess of hygroscopic acid [93,100]. Li et al. [100] proposed that the H_3PO_4 can be classified into "bonded acid" and "free acid", depending on the acid doping level. Moreover, the water uptake is accompanied by a volume swelling of 20–25 vol%. Figure 11c further shows that when the total acid concentration increases from 2 to 11 M, the "bonded acid" remains more or less constant. In this case, the proton migration takes place via the H^+ hopping between the N-H site and the phosphate anion. By increasing the acid amount, the amount of "free acid" increases, which is responsible for the increase in protonic conductivity [93]. The protonic conductivity increased from 25 mS/cm to 68 mS/cm at 200 °C and RH of 5% as the acid doping level

increases from 2 to 5.6 due to the presence of "free acid". In brief, the acid doping level related to free acid is the most important parameter that determines the membrane proton conductivity.

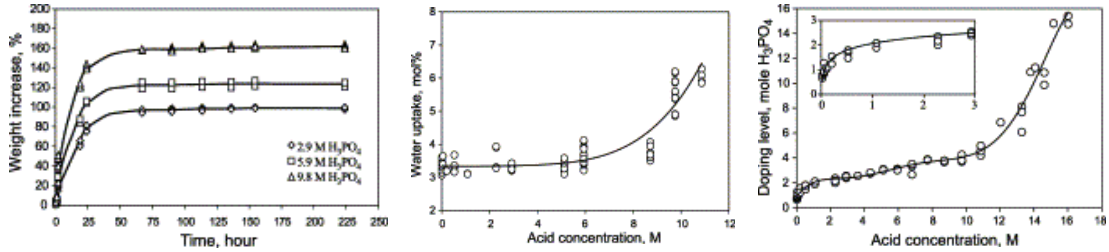

Figure 11. Weight increase as a function of time (**a**); water uptake (**b**); acid doping level of acid-doped PBI membranes at room temperature (**c**). Reprinted with permission from Ref. [100]. Copyright 2004 Elsevier.

In general, a high acid doping level results in high proton conductivity, but excessive acid sometimes leads to the formation of a soft paste, which cannot be processed into a membrane [101,102]. Another disadvantage is acid leaching from the membrane after certain operation time, which decreases the mechanical strength, and reduces the lifetime of PEMFCs severely. Therefore, a balance between acid doping level and membrane stability is required.

Brooks et al. [103] claimed that the absorbed water greatly affects the mechanical properties of PBI. PBI loses its compressive strength at increased water content, which could be due to weakened van der Waals forces and hydrogen bonding interactions as a consequence of polymer swelling. Iwamoto et al. [104] investigated the relationship between the tensile strength of PBI as a function of water content. They found that 10% water absorption resulted in a 25–30% decrease in the tensile strength.

3.2. Metal Oxides

Most filler particles used for Nafion-based membranes have also been added into the PBI polymer matrix, which is expected to improve the mechanical strength of the membrane, and also to increase the acid retention capability of the membrane. Herein, we summarize the recent developments around metal oxide-based PBI composite membranes.

Quartarone et al. [105] investigated the role of SiO_2 with three different morphologies. An acidic silica (HiSilTM T700), a mesoporous SiO_2 (SBA-15) and an imidazole-functionalised SiO_2 (SiO_2-Im) with filler loading ranging between 0–20 wt.% were studied with respect to the physicochemical properties of the H_3PO_4-doped PBI composites. SiO_2-Im fillers were synthesized by means of a standard basic hydrolysis/condensation process, using tetraethoxysilaine (TEOS) and N-(3-triethoxysilylpropyl)-4,5-dihydroimidazole in molar ratio 2:1 as starting materials [106]. The composite membrane increased the acid retention capabilities and facilitated the proton transport across the polymer matrix. In terms of conductivity, the as-prepared PBI/SiO_2-Im composite membrane was almost independent on the filler concentration, and close to the free acid conductivity [93]. Acid leaching test was performed by washing the as-doped membrane in hot water (80 °C) to remove the free acid. An increase in conductivity is obtained even at relatively small amount of SiO_2-Im (2 wt.%) at 120 °C and 50% RH [106]. In comparison, an initial conductivity increase was observed for the PBI/HiSilTM SiO_2 up to 8 wt.%, which is attributed to the acid-base interactions and/or the formation of space charge layers. This is followed by a decrease that could be due to a dilution effect and/or plasticizing effect promoted by an excess of H_3PO_4 adsorbed by the fillers [107,108]. Furthermore, the influence of SiO_2-Im fillers on the MEA performance was studied by Kurdakova et al. [109]. The incorporation of 20 wt.% SiO_2-Im gave a maximum power density of 83 mW/cm^2 at 300 mA/cm^2, which is 20% higher than that of the MEA using pristine PBI polymer. In addition, a reduced charge transfer resistance of the cathode side was observed from electrochemical impedance spectroscopy (EIS).

Devrim et al. [110] prepared H_3PO_4-doped PBI with 5 wt.% SiO_2 by a solid-casting method and reached a high proton conductivity of 102.7 mS/cm at 180 °C and 0% RH. They further fabricated gas diffusion electrodes by an ultrasonic coating technique with 1 mg Pt/cm^2 catalyst loading for both the anode and cathode in order to test the performance of the membrane in a single HT-PEMFC of a 5 cm^2 active area at the temperature range of 140–180 °C. A current density of 240 mA/cm^2 was observed at 165 °C and a cell voltage of 0.6 V. This gave a maximum power density of 250 mW/cm^2, whereas the pristine-doped PBI measured at the same condition yielded only 185 mW/cm^2. The application of this composite membrane was not only restricted to PEMFCs and DMFCs, but also for gas separation applications [111].

Suryani et al. [112] synthesized PBI-functionalized SiO_2 nanoparticles (SNP-PBI) by a previously reported ozone-mediated process [113] using N-(p-carboxyphenyl)maleimide functionalized SNPs (SNP-Pcpm) as precursors to make the PBI chemical bond to the SNP surface (Figure 12a). The synthesized nanofillers were then used for the preparation of the PBI/SNP–PBI nanocomposite membranes for PEMFC application. Interaction between the maleimide groups of SNP-Pcpm and PBI matrix lead to a cross-linked structure of the nanocomposite membrane, which slightly enhanced the membrane's thermal properties. The addition of the fillers reinforces the membrane due to the enhanced interfacial compatibility between the SNP-PBI and PBI matrix, notified by the increases in their Young's modulus and the tensile strength. Moreover, it is observed that the acid uptake decreased from 420% to 360% as the filler content increases from 0–20 wt.%. They suggested that the crosslinked structure might depress the swelling effect of the composite membranes as well as acid uptake. This is however in contrast with what has been observed from nanocomposite membranes containing imidazole-functionalised SiO_2 [106]. Moreover, the membrane with 10 wt.% SNP-PBI fillers showed the highest proton conductivity at 160 °C compared to that of the pristine membrane (Figure 12b). It further showed a maximum power density of 650 mW/cm^2 in a single H_2/O_2 fuel cell test, higher than the 530 mW/cm^2 obtained from the corresponding pristine PBI membrane (Figure 12c).

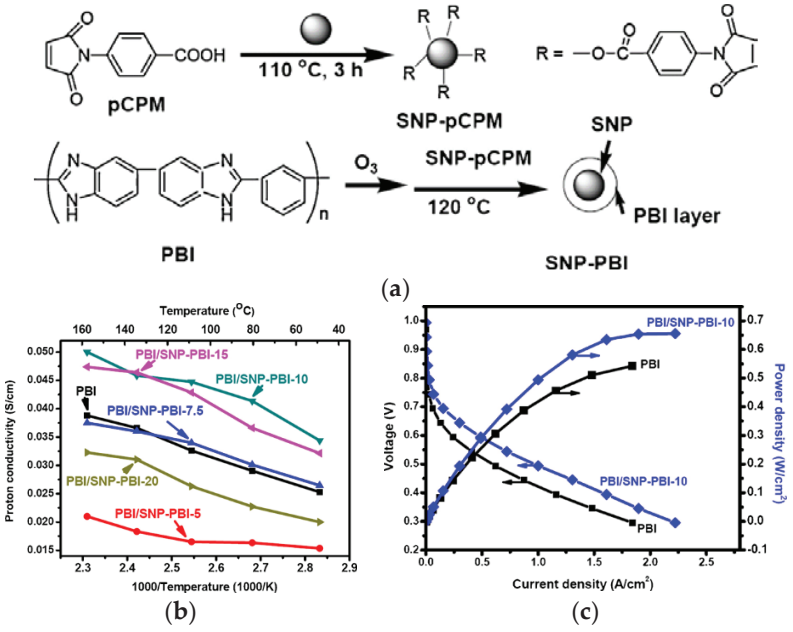

Figure 12. Ozone-mediated process for the synthesis of PBI/SNP–PBI nanocomposite membranes (**a**); proton conductivity of PBI/SNP–PBI membranes with different filler content (**b**); PEMFC polarization curve of PBI compared to PBI/SNP–PBI with 10 wt.% SiO_2 membranes at 150 °C using dry H_2/O_2 as reactant at a flow rate of 0.3 L/min (**c**). Reprinted with permission from Ref. [112]. Copyright 2012 Elsevier.

PBI–TiO_2 nanocomposite membranes have been prepared by mixing TiO_2 nanoparticles with PBI solutions in *N,N*-dimethylacetamide (DMAc) solvent [114,115]. Two wt.% TiO_2 in PBI reached the highest doping level at 15 mol H_3PO_4 per PBI repeat unit and water uptake compared with those obtained from other PBI-based membranes. It further showed high proton conductivity above 100 mS/cm between 125–175 °C and a promising power density of 800 mW/cm^2 at 150 °C. The influence of TiO_2 loading (2–16 wt.%) in the PBI membrane was studied by Pinar et al. [116]. They found that membranes containing 2–4 wt.% TiO_2 exhibited the best properties in terms of acid and water absorption capability and proton conductivity at all operation temperatures. Even larger amounts of fillers did not contribute to any further improvement. The long-term stability of the 2 wt.% TiO_2 composite PBI membrane was performed in a 150 cm^2 HT-PEM stack cell, which exhibited an irreversible voltage loss of less than 2% after 1100 h continuously operation [117]. Moreover, the acid leaching from the stack reduced from 2% to 0.6% compared to the standard PBI membrane, indicating that the introduction of fillers enhanced both the durability and stability of the membrane.

Moradi et al. [108] synthesized Fe_2TiO_5 nanoparticles through a sol-gel process [118], and prepared H_3PO_4-doped PBI–Fe_2TiO_5 nanocomposite membranes by a solution-casting method for use in HT–PEMFCs. The cross-section SEM image of the nanocomposite membrane containing 4 wt.% and 16 wt.% of Fe_2TiO_5 (Figure 13a) showed that in the case of 4 wt.% Fe_2TiO_5, the nanoparticles were uniformly dispersed inside the PBI matrix, which is further confirmed by EDX. In the case of 16 wt.% Fe_2TiO_5, a significant agglomeration of the nanoparticles was observed. The proton conductivity of the membranes was enhanced by increasing the weight percentage up to 4 wt.% due to the increase of free acid adsorbed by the nanoparticles. Even higher Fe_2TiO_5 concentration led to a decrease in proton conductivity due to the agglomeration of nanoparticles as confirmed by SEM. The temperature effect on proton conductivity of the nanocomposites in dry conditions is shown in Figure 13b. A maximum proton conductivity of 78 mS/cm was attained with PBI membranes with a H_3PO_4 doping level of 12 and 4 wt.% of Fe_2TiO_5 at 180 °C under dry conditions. The good proton conductivity may be explained by the fact that Fe^{3+} cations are located near Ti^{4+} cations in the nanoparticles and increase the acidic properties of these ions. Consequently, the interaction between H_3PO_4 and Fe_2TiO_5 inside the structure is much stronger, resulting in higher proton conductivity. The 4 wt.% Fe_2TiO_5 PBI membrane was also used to prepare a MEA. The single PEMFC performance of the MEA at various temperatures is shown in Figure 13c. As it can be seen, the fuel cell performance increased considerably from 100 to 180 °C, which is due to the faster reaction kinetics and enhanced proton conductivity of the membrane. The highest values of power and current density at 180 °C were 430 mW/cm^2 and 850 mA/cm^2, respectively.

Recently, Ozdemir et al. [119] prepared composites of 5 wt.% TiO_2, SiO_2 and acidic zirconium phosphate (ZrP, see also next paragraph) nanoparticles in PBI polymer, followed by different H_3PO_4 doping levels. The membranes were characterized in terms of their thermal, morphological and mechanical properties. All membranes are thermally stable for temperatures between 130 and 550 °C, their conductivities little affected by the introduction of fillers, and they are reported suitable for use in HT–PEMFCs. The SEM images revealed that SiO_2 particles were uniformly dispersed in the polymer matrix without sedimentation, contrary to the case for PBI/TiO_2 composites. The observation is in agreement with Pinar et al., who found that agglomeration occurs for TiO_2 concentrations higher than 2 wt.% [116]. The effect of fillers on membrane proton conductivities was investigated by EIS. The PBI/SiO_2 and PBI/ZrP composites showed enhanced properties in terms of acid retention capability and proton conductivity owing to the good interaction between PBI and fillers. High conductivities of 113 mS/cm and 200 mS/cm were achieved for PBI/SiO_2 and PBI/ZrP, respectively, at 180 °C and non-humidified conditions. These values are much higher than the previously reported ones [106], and the corresponding activation energies were only 23.8 kJ/mol and 19.4 kJ/mol. As mentioned above, the conductivity of PBI membranes increases with acid doping level on one hand, but sacrifices the mechanical strength on the other hand. The tensile strength of the pristine PBI membrane was highest (127 MPa) among all as anticipated, while PBI/TiO_2 showed the lowest tensile strength (85.6 MPa) due

to the uneven distribution of TiO_2 particles. The specific interactions between SiO_2 and PBI generate a mechanism for reinforcement, consequently, the elongation at break increased significantly.

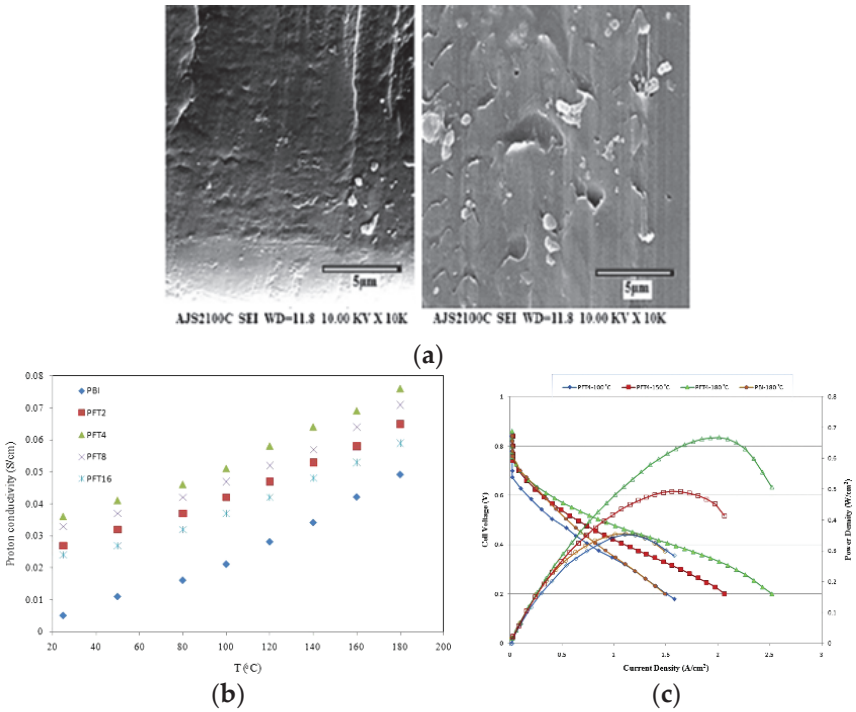

Figure 13. SEM cross-section image of H_3PO_4-doped PBI nanocomposite membrane with 4 wt.% and 16 wt.% Fe_2TiO_5 nanoparticles (**a**); proton conductivity at RH = 0% (**b**); polarization curves for the single PEMFC of H_3PO_4-doped PBI with 4 wt.% Fe_2TiO_5 nanocomposite membrane (**c**). Reprinted with permission from Ref. [108]. Copyright 2016 Elsevier.

3.3. Solid Acids—Heteropolyacids (HPA), Zirconium Phosphate (ZrP), and Caesium Salts of HPA

Hydrated heteropolyacids (HPAs) with the general formula of $H_xAM_{12}O_{40}{\cdot}H_2O$, where A stands for P or Si, and M indicates W or Mo, are called solid acids and display high conductivity and acidity. The proton conductivity, mainly by the Grotthuss mechanism [120], is mainly confined to adsorb surface water layers.

The use of PBI membranes with two different HPAs, namely phosphotungstic acid, $H_3PW_{12}O_{40}{\cdot}nH_2O$ (PWA) and silicotungstic acid, $H_4SiW_{12}O_{40}{\cdot}nH_2O$ (SiWA) for fuel cell application was first reported by Staiti et al. [121,122]. A maximum conductivity of 3 mS/cm was obtained under fully humid conditions at 100 °C with 60 wt.% PWA/SiO_2 in PBI, and the proton conductivity remained more or less constant as the temperature increased to 150°C. This conductivity is however too low for fuel cell applications. Inspired by this, Aili et al. developed a novel composite membrane based on an PWA-impregnated mesoporous SiO_2 functionalized H_3PO_4-doped PBI membrane, PBI/PWA-meso-SiO_2 [123]. The stability of the acid-doped PBI membrane-based fuel cell enhanced substantially after the addition of PWA-meso-SiO_2 fillers, most possibly due to the formation of the phosphosilicate phase between H_3PO_4 and mesoporous SiO_2.

He et al. [93] cast PBI composite membranes by dissolving commercial PWA and SiWA in DMAc, followed by mixing 5 wt.% PBI in DMAc, and immersion in H_3PO_4 of different concentrations in order to obtain sufficient proton conductivity. However, the conductivity after introducing 30 wt.% of PWA and SiWA in PBI was slightly lower than that of the H_3PO_4-PBI membrane under the same conditions. A possible explanation is that the HPAs diluted the density of the acid groups that provide transport for protons. Verma et al. emphasized in their paper that SiWA neutralized with NaOH prior to acid doping of PBI avoids agglomeration and leads to well-defined proton pathways, which

improved the proton conductivity [124]. The same group prepared zirconium hydrogen phosphate $Zr(HPO_4)_2{\cdot}nH_2O$ (ZrP) by mixing zirconyl chloride ($ZrOCl_2$) with orthophosphoric acid with a mole ratio of 1:2, following the procedure described by Staiti et al. [121]. A similar procedure was also employed by Qian et al. [125]. In both cases, a washing step was necessary to eliminate the remaining Cl^- and the excess acid inside the crystal. The composite membrane with 15 wt.% ZrP was found to exhibit slightly higher conductivity than that of the 20 wt.% ZrP at all temperatures, but the reasons for this behaviour are not clear. A conductivity of 96 mS/cm with corresponding activation energy of 11.9 kJ/mol was obtained at 200 °C and 5% RH, a conductivity value that is comparable to that of Nafion membrane at 80 °C and 100% RH. For composite PBI/ZrP membranes, different ionic species such as H_3O^+, H_2O, PO_4^{3-}, and P–O and P–OH species can exist by bonding with ZrP inside the structure or at the surface, which can aid the proton conductivity compared with that of PBI membranes [93,126].

Yamazaki et al. [127] prepared a zirconium tricarboybutylphosphonate Zr(PBTC) powder by using 2-phosphonobutane-1,2,4-tricarboxylic acid in place of orthophosphoric acid, and dispersed the powder in a PBI solution of DMAc. The presence of Zr(PBTC) grains were reported to inter-connect with each other, providing conduction paths via the PBI polymer. The proton conductivity of the composite membrane with 50 wt.% Zr(PBTC) increased with a factor of 2 after H_3PO_4 treatment and post-sulfonation thermal treatment, suggesting the possible use of the Zr(PBTC)/PBI as an electrolyte material for fuel cells.

Li et al. [128] prepared $Cs_{2.5}H_{0.5}PMo_{12}O_{40}$ (CsPOMo) by mixing phosphomolybdic acid with caesium carbonate (Cs_2CO_3), and blended it with PBI to form a PBI/CsPOMo composite membrane. A chemical bond between CsPOMo and PBI was formed, as indicated by ^{31}P NMR analysis. Good thermal stability and high proton conductivity of >150 mS/cm were achieved after doping the composite with H_3PO_4. It is noteworthy that the conductivity of the PBI/CsPOMo membrane without H_3PO_4 was only 0.04 mS/cm at 150 °C and 0% RH, implying an important role of H_3PO_4 and water.

A similar study was carried out by Xu et al. [129], where they synthesized four Cs salts of heteropolyacids, denoted as $Cs_XH_{3-X}PMo_{12}O_{40}$ (CsPOMo), $Cs_XH_{3-X}PW_{12}O_{40}$ (CsPOW), $Cs_XH_{4-X}SiMo_{12}O_{40}$ (CsSiOMo) and $Cs_XH_{4-X}SiW_{12}O_{40}$ (CsSiOW) to form composite membranes with PBI. All four Cs salts were nanoparticles of around 100 nm. Subsequently, acid loading was conducted by immersing the composite membrane in H_3PO_4 solution of different concentrations for a certain time. All the composite membranes showed conductivity values (e.g., 47 mS/cm at 150 °C and 0% RH) to be higher than H_3PO_4/PBI membranes. Membranes with CsPOMo and CsPOW achieved significantly higher conductivity than CsSiOMo and CsSiOW. On the contrary, lower mechanical strength was observed from CsHPA with P atoms. The reason for the difference in conductivities of the P and Si-based CsHPA when formed as acid-doped PBI composite is still unknown. One possible explanation is the smaller particle size with P atoms (observed from SEM images), which will provide a more active surface area and potentially adsorb more acid. Increasing the CsHPA content in the composites also led to an enhancement of the proton conductivity. Figure 14a shows the conductivity of the 30 wt.% CsHPA/PBI membranes at ADL of 4.5 as a function of temperature under anhydrous conditions. The highest conductivity of 120 mS/cm was achieved from CsPOMo at 150 °C, which is in good agreement with Li et al. [128]. The results imply that this membrane is a promising material for high-temperature fuel cells. The test of the composite membranes in an actual fuel cell is shown in Figure 14b. All membranes have low gas permeability as the open circuit voltages were all above 0.95 V. The enhancement of the cell performance from the composite membranes was attributed to the higher proton conductivity and stronger acid retention properties. CsPOMo gave a maximum power density of around 600 mW/cm^2 with H_2/O_2 gas feeds at atmospheric pressure.

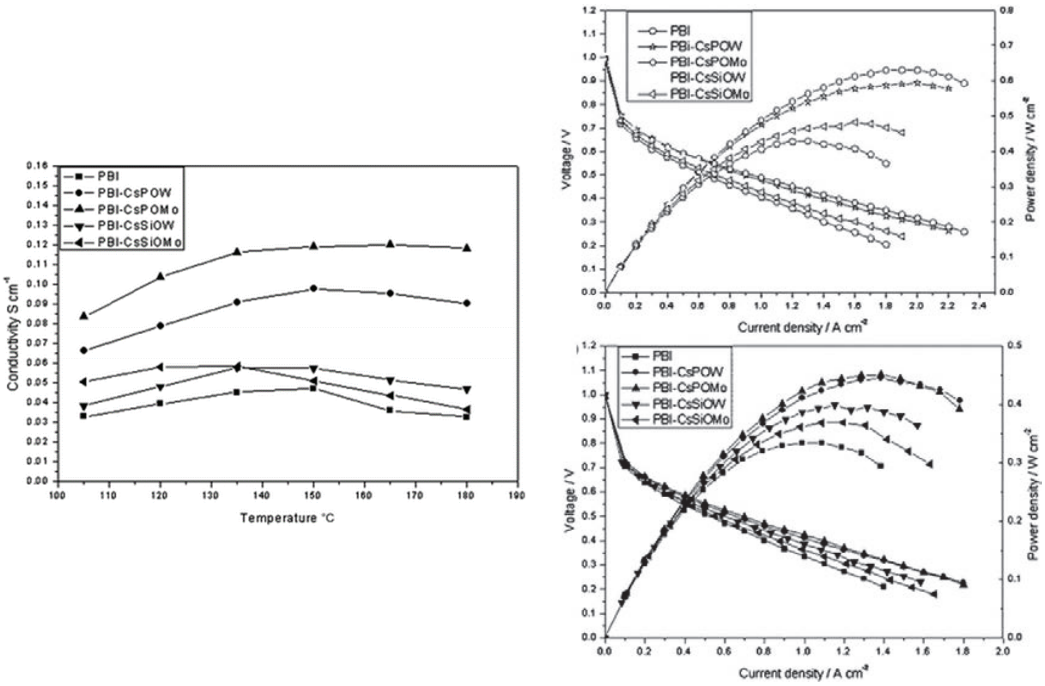

(**a**) (**b**)

Figure 14. Proton conductivities of PBI composite membrane containing 30 wt.% CsHPA at ADL = 4.5, RH < 1% (**a**); polarization and power density curves of a PEMFC operated at 150 °C with H_2/O_2 atmospheric pressure (upper plot) and H_2/air atmospheric pressure (lower plot) (**b**). Reprinted with permission from Ref. [129]. Copyright 2011 Royal Society of Chemistry.

3.4. Carbon-Based Materials

Both single-walled nanotubes (SWCNTs) and (MWCNTs) have been demonstrated to have superior mechanical, thermal and electronic properties, which make them attractive as advanced filler particles in composites [51]. The addition of CNTs to the polymer has shown improved tensile strength, Young's modules, and elongation at break, which was recently suggested to be attributed to the restriction of the polymer chain movements due to the effectual interfacial interactions such as H-bonding and π-π interactions [130]. Nevertheless, precautions must be taken when using CNTs in PEM, as the electronic conductivity may short circuit PEMFCs. Kannan et al. [131] demonstrated a dual functionalization strategy to incorporate phosphonic acid on the sidewalls of MWCNTs in order to make a composite with H_3PO_4-doped PBI membranes. The SEM image in Figure 15A (left) shows that the diameter of p-MWCNT is between 14–20 nm. The authors emphasized that the microwave treatment was critical for improved solubility hence the homogeneity of the membrane. Individual MWCNTs are observed instead of bundles, as seen from the TEM images. Composite PBI membranes with low levels of p-MWCNT (0.05–2.5 wt.%) have been prepared to avoid possible short circuit and agglomeration [132]. The composites were subsequently immersed in H_3PO_4. The TGA of the resulting membranes led to similar patterns under N_2 atmosphere between 50 and 700 °C, indicating the addition of CNTs did not cause any significant thermal degradation. The proton conductivity and the corresponding Arrhenius plots of the prepared membranes (PBpNT) were compared to a composite PBI with un-functionalized MWCNT (PBNT 1%), as shown in Figure 15B. The conductivity increased with increasing amounts of p-MWCNTs in the composite, except for the PBpNT 0.05 wt.%. The best composite membrane achieved almost half an order of improvement in the proton conductivity upon doping with H_3PO_4 (110 mS/cm for PBpNT 1%). The conductivity value was in good agreement with the value reported by Suryani et al. [133], where they prepared MWCNT through an ozone-mediated process and used it as a filler to make PBI/MWCNT composite membranes. The poor performance of PBNT 1% was due to the absence of phosphonate groups [132]. The drop in the activation energy further suggests

the synergistic role of the p-MWCNTs in facilitating proton conduction. With respect to the fuel cell performance (Figure 15C), a maximum power density of 780 mW/cm^2 was attained from composite PBI membrane with 1 wt.% p-MWCNT in comparison with 600 mW/cm^2 for the pristine PBI membrane under identical conditions.

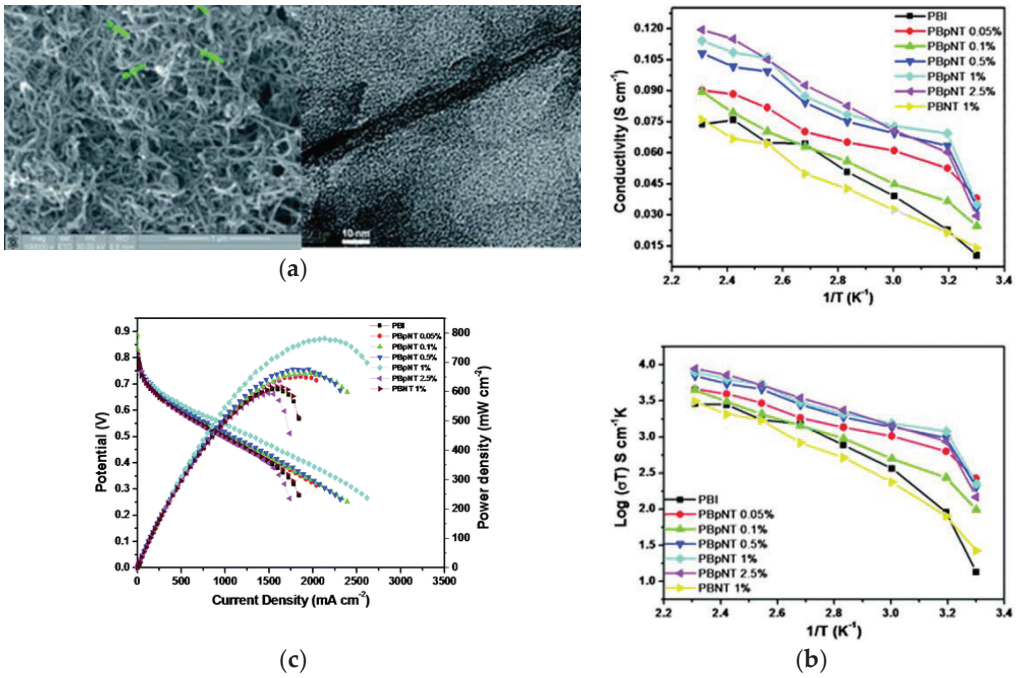

Figure 15. SEM image of p-MWCNTs and TEM image showing the distribution of p-MWCNTs inside the PBI matrix (**a**); proton conductivity and Arrhenius plots of the different composite membranes and pristine PBI (**b**); fuel cell polarization curves measured by supplying dry H_2/O_2 with a flow rate of 0.2 standard liter per minute (slpm) at 140 °C (**c**). Reprinted with permission from Ref. [132]. Copyright 2011 Royal Society of Chemistry.

The incorporation of small amounts of graphene oxide (GO) in the PBI membrane showed positive effects in terms of acid retention, proton conductivity, tensile strength and toughness. High-performance H_3PO_4-doped PBI/GO composite membranes have been prepared by Üregen et al., showing a high conductivity of 129.7 mS/cm at 165 °C at a GO content of 2 wt.% [134]. This is because hydrogen bonds in GO form acidic functional groups like carboxylic acid and epoxy oxygen, which provide pathways for proton hopping [135]. The GO in the PBI membrane is suggested to form well-connected channels that facilitate proton hopping through the membrane, thus improving the conductivity. Nonetheless, the formation of acidic functional groups in GO degrades the membrane and leads to reduced proton conductivity at temperatures above 165 °C. The maximum power density reached from a single PEMFC with a 5 cm^2 active area constructed with PBI/2 wt.% GO was 378 mW/cm^2 operated at ambient pressure and 165 °C. An open circuit voltage of 0.95 V implies that the membrane possessed low hydrogen crossover. At a constant current of 200 mA/cm^2, the composite membrane loss was about 3.8% after 500 h operation, while the H_3PO_4-doped PBI membrane showed 8.3% loss. This suggests that GO can trap more acid molecules and prevent acid leaching out of the membrane.

Phosphonated graphene oxide (PGO) embedded in 2,6-pyridine functionalized PBI (py-PBI) at different H_3PO_4 doping levels has been evaluated as HT-PEM material [136]. The pGO was prepared from graphite in a three-step procedure involving oxidation, exfoliation and phosphonation (Figure 16A), followed by a solution casting method to fabricate the composite membrane. After doping with H_3PO_4, the best proton conductivity was obtained from the py-PBI/1.5 wt.% PGO membrane, showing a conductivity value of 76.4 mS/cm at 140 °C under anhydrous condition, whereas the py-PBI membrane without filler showed a value of 19.6 mS/cm under similar conditions. The improvement

could be explained by the inherent strong hydrogen bonding between localized phosphonic acid groups of GO and imide groups of pyPBI that help to form a network for efficient proton transport. The proton conductivity measurement was further conducted for 20 h in order to investigate the durability of the composite membranes. As can be seen in Figure 16B, a significant drop in proton conductivity was evidenced from the one with 1.5 wt.% PGO during the first 5 h of operation, then remained more or less constant throughout the rest of the experiment. In comparison, the membrane with 1 wt.% PGO seems to be more stable. The highest performance in a fuel cell was also achieved from the same membrane, with a peak power density of >359 mW/cm^2 at 120 °C and 0% RH, which is 75% higher than the membrane without PGO.

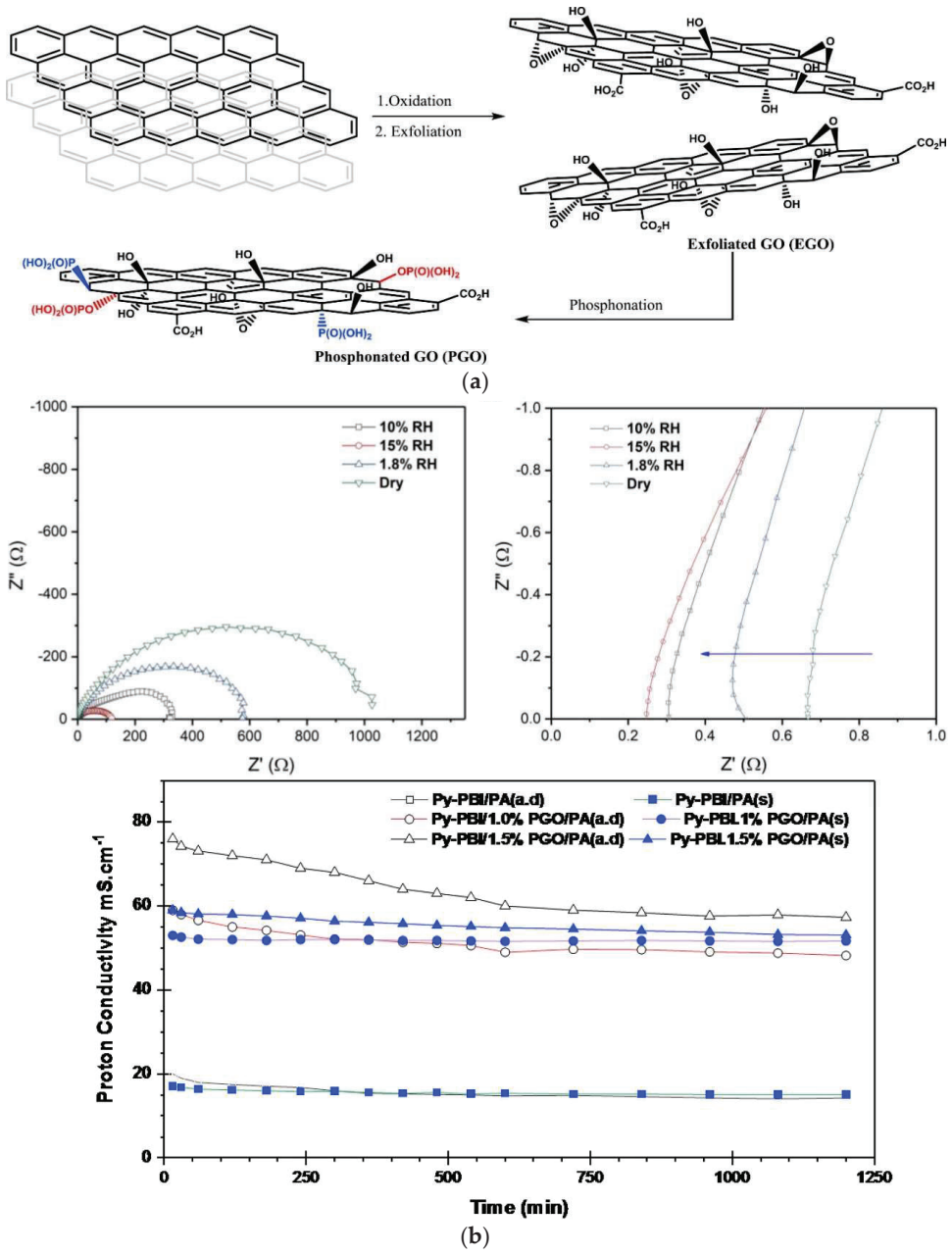

Figure 16. Preparation of functionalized graphene oxide (**a**); Nyquist plot of H_3PO_4-doped py-PBI/1.5 wt.% pGO under various RH at 120 °C; zoom-in in the high frequency intercept; and proton conductivity of the py-PBI composite membranes with different filler content as a function of testing time at 140 °C and 0% RH (**b**). Reprinted with permission from Ref. [136]. Copyright 2019 Elsevier.

Xue et al. [137] prepared graphite oxide/PBI from 3,3′-diaminobenzidine and 5-tert-butyl isophthalic aicd (GO/BuIPBI) and isocyanate modified GO/BuIPBI (iGO/BuIPBI) composite membranes, followed by H_3PO_4 loading for HT-PEMFCs. At 140 °C with no humidity, the proton conductivities of the H_3PO_4-doped BuIPBI, 5 wt.% iGO/BuIPBI and 5 wt.% GO/BuIPBI were 12, 16 and 27 mS/cm, respectively. Interestingly, the 10 wt.% iGO/BuIPBI demonstrated better proton conductivity than the 15 wt.% iGO/BuIPBI as an excessive amount of iGO might agglomerate and block the proton conduction paths.

OPBI/GO composite with only 0.3 wt.% GO was fabricated by a solvent-exchange method [138]. It showed a 17% increase in Young's modulus, 33% increase in tensile strength and 88% enhancement in toughness compared to pure OPBI membranes, which may find application in fuel cells.

3.5. Metal Organic Frameworks (MOFs)

In the past few years, the use of metal organic frameworks (MOFs) as fillers in PEMs has received massive attention. Zeolitic imidazolate frameworks (ZIFs) is a unique subgroup of MOFs that demonstrated high porosity in addition to being chemically and thermally stable [139]. Recently, Escorihuela et al. prepared a Zn-based ZIF-8, a Co-based ZIF-67, and a binary mixture of the two (represented as ZIF-mix), which have been embedded in the PBI matrix for the preparation of PBI composite membranes containing 5 wt.% of these fillers [57]. The as-prepared composites were characterized after immersing in H_3PO_4. The phosphonate anion seemed to attract Co more than Zn, as the acid uptake from PBI@ZIF-67 is higher (166%) after the same immersion time. Proton conductivity measurements of the membranes were performed at 0–200 °C under anhydrous conditions (Figure 17). Significantly enhanced proton conductivity was observed for the ZIF-67 and ZIF-mix with increasing temperature. A plateau around 140 °C was evidenced for the composite with ZIF-67, which may be due to the evaporation of H_3PO_4. The proton conductivity for acid-doped PBI@ZIF-67 reached 41 mS/cm at 200 °C, but an even higher proton conductivity of 91 mS/cm was achieved from the hybrid PBI@ZIF-mix membrane. This increase implies a synergistic effect between the two MOFs, resulting in more consecutive hydration channels, as observed with other PEM composites with fillers such as UiO–66–SO_3H/UiO–66–NH_2 [80]. The proton conductivities obtained in this work were among the highest reported for MOF-containing HT–PEMs measured under anhydrous conditions [140]. They further proposed that the proton conductivity in ZIF-containing PBI composites was mainly based on a Grotthuss mechanism, while the proton transfer from the surface of ZIF to the next ZIF by H_3PO_4 as proton carrier can be explained by the vehicle mechanism. A test of fuel cell performance based on ZIF-containing PBI composite membranes was however not conducted in their work.

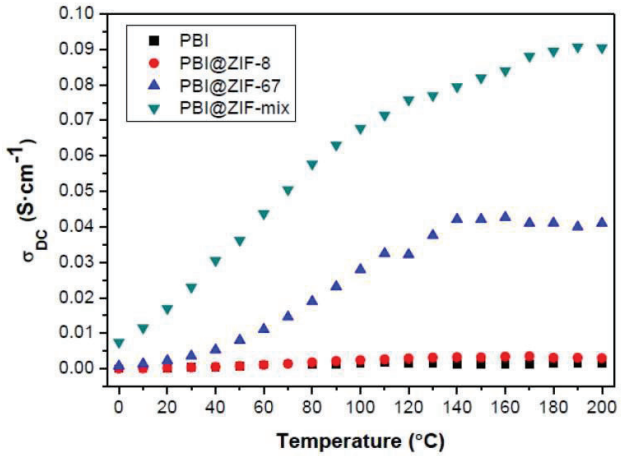

Figure 17. The temperature-dependent proton conductivity of H_3PO_4-doped PBI membrane and PBI composite membranes with 5 wt.% of ZIFs. Reprinted with permission from Ref. [57] under a Creative Commons Attribution (CC-BY) License. Copyright 2018 MDPI.

3.6. Clays

Two types of organically-modified nanoclays, imidazole salt-modified laponite RD (referred to as clay L) and dequalinium chloride salt-modified laponite RD (clay N) were synthesized by ion-exchange reactions with ammonium and pyridinium salts, and used for the preparation of PBI composite membranes [141]. Figure 18a shows the conductivity as a function of RH at different temperatures. At a clay content of 15 wt.%, it was clear that the conductivity depends on the H_3PO_4 doping level, RH and temperature. At ADL = 6, the PBI membrane without fillers exhibited a proton conductivity of about 30 mS/cm at 120 °C and 20% RH, which is in good agreement with previously reported results [93]. The highest proton conductivity was obtained from the PBI composite membrane with 12 wt.% clay N at ADL of 12 (120 mS/cm at 150 °C and 12% RH). The effect of the clay content on the proton conductivity of the PBI membranes was not investigated. They further showed that the hydrogen permeability of the composite membrane was five times lower than that of the unfilled PBI membrane at 150 °C. The fuel cell performance with the PBI-clay composite containing 5 wt.% clay L at different temperatures is presented in Figure 18b. At 175 °C with a catalyst loading of 0.66 mg Pt/cm^2 for each electrode, a current density of 210 mA/cm^2 was achieved at a cell voltage of 0.6 V.

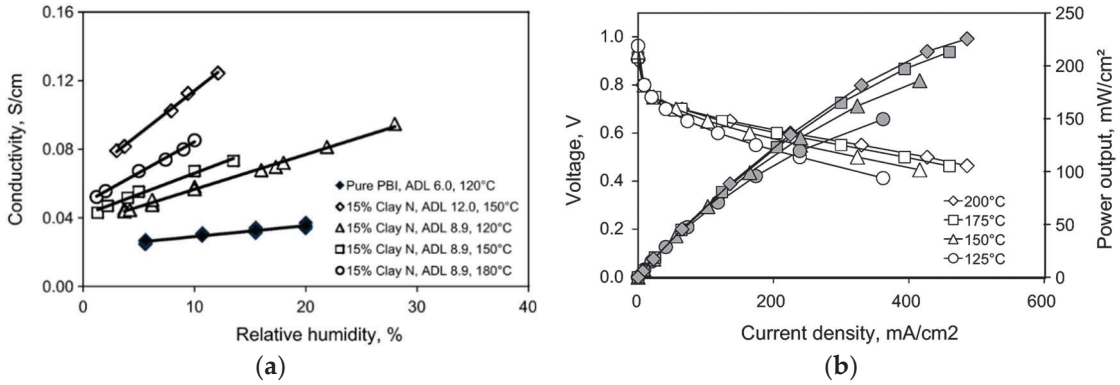

Figure 18. Conductivity of PBI membrane and PBI/clay N composites as a function of relative humidity at different temperatures (**a**); polarization curve for a fuel cell with PBI/5 wt.% clay L composite membranes (ADL = 8.2) obtained at different temperatures (**b**). Reprinted with permission from Ref. [141]. Copyright 2011 Elsevier.

Nanocomposite polymers consisting of two modified organoclays, namely, montmorillonite (OMMT) and kaolinite (OKao) in poly(4,4′-diphenylether-5,5′-bibenzimidazole) (OPBI) were prepared by dispersing the silicate layers in the OPBI matix by a solution blending method [142]. The morphology of the composites are dependent on the structure of the clays. In the case of OPBI/OMMT, an exfoliated structure is obtained, whereas intercalated morphology was achieved from OPBI/OKao. Loading of both organoclays enhanced the thermal stability of OPBI compared to the pristine one. The exfoliated structure for OMMT seemed more beneficial in terms of thermal stability due to the higher dispersion of the clay into the OPBI matrix. The nanoparticles in the OPBI polymer shielded the polymer chains from the attack of oxidative radicals (OH* and HOO*) and enhanced the oxidative stability of the membrane. At a high H_3PO_4 doping level, the proton conductivity increased with increasing temperature and clay content, and reached 72 mS/cm and 92 mS/cm at 160 °C, respectively, for OPBI/OKao and OPBI/OMMT with 7 wt.% fillers. The authors suggested that the proton conductivity was supported by a continuous "forming–breaking–forming" process of the hydrogen bonds of OPBI and the organoclays with the acid, which promotes the proton transfer in the composites. The very small activation energies (~8 kJ/mol) however suggest a faster (for instance liquid state) proton conduction process. The nanocomposite membranes have not been tested in HT-PEMFCs. Moreover, long-term stability tests are needed to evaluate the feasibility of this composite membrane.

Some characteristic parameters of different H_3PO_4–PBI-based composite membranes, in particular those that have been tested in PEMFCs at various conditions, are summarized in Table 3.

Table 3. Comparison of proton conductivities of H_3PO_4–PBI-based composite membranes and their PEMFC performance.

Membrane	Acid Doping Level (mol H_3PO_4 per r.u. PBI)	Conductivity/ Temp/%RH/	Maximum Power Density in PEMFC	Ref.
PBI/2 wt.% TiO_2	15.3	130 mS/cm at 150 °C and 10% RH	800 mW/cm^2@150 °C	[115]
PBI/2 wt.% TiO_2	Not provided	43 mS/cm at 150 °C	450 mW/cm2@175 °C	[116]
PBI/5 wt.% SiO_2	10	102.7 mS/cm at 180 °C and 0% RH	240 mW/cm^2@165 °C	[110]
PBI/5 wt.% SiO_2	13.4	113 mS/cm at 180 °C and 0% RH 23.8 kJ/mol	Not reported	[119]
PBI/5 wt.% ZrP	15.4	200 mS/cm at 180 °C and 0% RH 19.4 kJ/mol	Not reported	[119]
PBI/ 15 wt.% ZrP	5.6	96 mS/cm at 200 °C and 5% RH 16.65 kJ/mol	Not reported	[93]
OPBI/15 wt.% LAMS	23.4	181 mS/cm at 160 °C and 0% RH 16.65 kJ/mol	Not reported	[143]
PBI/4 wt.% Fe_2TiO_5	12	78 mS/cm at 180 °C and 0% RH	430 mW/cm^2@180 °C	[108]
PBI/10 wt.% SNP-PBI	Acid uptake 385 ± 15%	50 mS/cm at 160 °C and 0% RH	650 mW/cm^2@150 °C	[112]
PBI/$Cs_{2.5}H_{0.5}PMo_{12}O_{40}$	120%	150 mS/cm at 150 °C and 8.4% RH	700 mW/cm^2@150 °C	[128]
PBI/30 wt.% CsPOMo	4.5	120 mS/cm at 150 °C and 0% RH 6 kJ/mol	600 mW/cm^2@150 °C	[129]
PBI/PTFE	175% 300%	120 mS/cm at 180 °C and 8.5% RH 320 mS/cm at 180 °C and 8.4% RH	600 mW/cm^2@150 °C	[144]
PBI/15 wt.% laponite clay-N	8.2	120 mS/cm at 150 °C and 12% RH	220 mW/cm^2@150 °C	[141]
OPBI/20 wt.% AMS	31.25	125 mS/cm at 160 °C and 0% RH 16.15 kJ/mol	Not reported	[145]
Py-PBI/1.5 wt.% PGO	9.93	76.5 mS/cm at 140 °C and 0% RH 18 kJ/mol	360 mW/cm^2@120 °C	[136]
PBI/2 wt.% GO	13	129.7 mS/cm at 165 °C and 0% RH 24.7 kJ/mol	378 mW/cm^2@165 °C	[134]
PBI/5 wt.% ZIF-8+ZIF-67	Acid uptake 157%	91 mS/cm at 200 °C and 0% RH 19.6 kJ/mol	Not reported	[57]
OPBI/7 wt.% Okao	24.746	72 mS/cm at 160 °C 8.75 kJ/mol	Not reported	[142]
OPBI/7 wt.% OMMT	25.479	92 mS/cm at 160 °C 8.17 kJ/mol	Not reported	[142]
PBI/1 wt.% p-MWCNTs	12.4	110 mS/cm at 160 °C and 0% RH 25.1 kJ/mol	780 mW/cm^2@140 °C	[132]
PBI/10 wt.% nanoCaTiO$_3$	127.2%	28 mS/cm at 160 °C and 0% RH 21.32 kJ/mol	570 mW/cm^2@160 °C	[146]

4. Sulfonated PEEK-Based Composite Membranes

The use of sulfonated hydrocarbons as polymer backbones has also been widely studied in order to form effective water channels, with the most common one being the sulfonated aromatic hydrocarbon polyetheretherketone (SPEEK). SPEEK has certain advantages over Nafion as it is also commercially available (Victrex@PEEK) at a much lower cost. In addition, the SPEEK structure allows

the introduction of polar sites that help to increase water uptake [98]. In comparison to Nafion, the water channels in SPEEK are narrower, less separated and more branched with more dead-end channels. This leads to more hydrophilic/hydrophobic interfaces, which result in a larger average separation of neighbouring sulfonic acid functional groups [147].

The properties of SPEEK membranes synthesised directly from the sulfonated monomers are greatly improved in comparison to those of the post-sulfonated PEEK membranes [148]. SPEEK-based PEM with a long-term stability of at least 1000 h (in particular ≥3000 h) at a voltage range from 0.4 V to 1.1 V indicate that SPEEK-based membranes are durable enough under fuel cell operations [149]. Since the proton conductivity of SPEEK depends on several parameters, such as the choice of casting solvent, sulfonation procedure, degree of sulfonation, RH and temperature, large inconsistencies in proton conductivity are evidenced in the literature, especially at low temperatures (~80 °C). A summary of such data can be found in Ref. [150].

SPEEK composites containing 10% amorphous SiO_2, 30% ZrP or 40% amorphous zirconium phosphate sulfophenylphosphonate have been successfully prepared. All composites exhibited protonic conductivities in the range of 30–90 mS/cm at 100 °C under 100% RH, suggesting their potential as alternative PEM materials to Nafion for PEMFCs up to 120 °C [151].

Novel nanocomposite membranes based on SPEEK and iron titanate, Fe_2TiO_5, were prepared by the dispersion of Fe_2TiO_5 nanoparticles into SPEEK solution with the solution casting method [152]. Composite membranes with 1 wt.% Fe_2TiO_5 showed the highest proton conductivity of 96 mS/cm at 80 °C, which is 65.5% and 6.6% higher than that of pristine SPEEK membrane and Nafion 117 membrane, respectively. This composite membrane also showed a single fuel cell performance of peak power density of 188 mW/cm^2 at 80 °C under 90% RH.

The use of a natural zeolite in SPEEK, i.e., SPEEK/analcime composite membrane with 5, 10, 15, 25 and 35 wt.% analcime were synthesized for fuel cell applications [153]. Measurements performed under 100% RH showed that the proton conductivity of SPEEK increased with increasing temperature until 80 °C because of faster proton diffusion. However, a further increase in temperature led to a dramatic decrease in conductivity due to the membrane degradation. Such a decrease in proton conductivity was observed for SPEEK/10 wt.% analcime composite membrane at a temperature close to 100 °C. A maximum conductivity of 401.6 mS/cm was reached at 90 °C, with a corresponding activation energy of 15.1 kJ/mol. A similar trend and high conductivity have been reported for Nafion/15 wt.% analcime composite membrane [79]. They concluded that the hydrophilicity and protons inside the connected water channels of the zeolite are expected to be responsible for the superior conductivity. Nevertheless, these conductivity values are considerably higher than most of the previous published values obtained from SPEEK composite membranes, where some of them are summarized in Table 4. It would be interesting to know the performance of such a composite membrane in an actual PEMFC or PEME.

Sun et al. [59] synthesized two-dimensional ZIF-8/CNT hybrid cross-linked networks (ZCN) from ZIF-8. The ZCN was then introduced into SPEEK, and three SPEEK composite membranes were prepared, namely SPEEK/ZCN, SPEEK/CNT, and SPEEK/ZIF-8. Significant enhancement in the proton conductivity was observed from the SPEEK/ZCN membrane, which benefited from the 2D network. In particular, as shown in Figure 19, the composite with 2.5 wt.% ZCN achieved a proton conductivity of 50.24 mS/cm at 120 °C at 30% RH, which was 11.2 times better than the recast SPEEK membrane (4.5 mS/cm) and 2.1 times higher than the SPEEK/ZIF membrane (24.1 mS/cm). This study reveals that the proton conductivity of SPEEK-based composite membranes can be enhanced by creating superstructures of MOFs rather than modifying the chemical component, which may be applied to other types of MOFs as well.

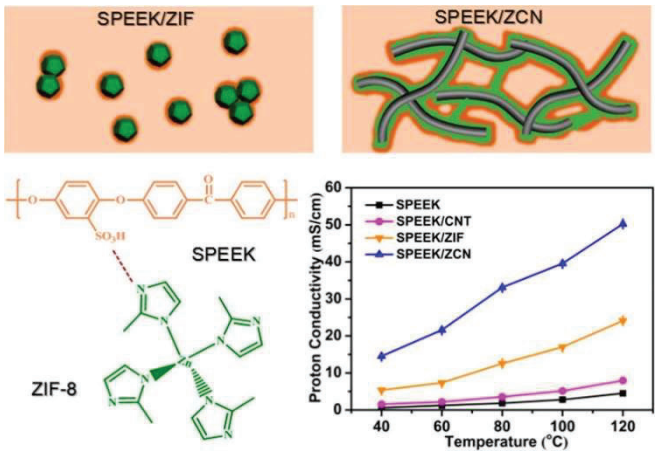

Figure 19. Interaction between SPEEK and ZIF-8, and the schematic illustration for the interface of SPEEK/ZIF and SPEEK/ZCN composite membranes. Reprinted with permission from Ref. [59]. Copyright 2017 American Chemical Society.

S–UiO–66 is another stable MOF with functional groups of $–SO_3H$ in its ligands that have been grown on graphene oxide (GO) hybrid nanosheets via a facile in-situ procedure, and then used for the fabrication of the SPEEK/S–UiO–66@GO composite membrane [62]. Taking the advantage of the tethering effect of GO surface and interconnection among S–UiO–66 grains, S–UiO–66 was well dispersed onto GO nanosheets, which effectively eliminated the agglomeration of S–UiO–66 in the SPEEK matrix [68]. The resulting composite membrane presented a significant increase in proton conductivity, 268 mS/cm at 70 °C and 95% RH and 16.57 mS/cm at 100 °C and 40% RH, which is 2.6 and 6 times than that of the recast SPEEK membrane under the same condition. The high proton conductivity indicates the great potential of this composite membrane for fuel cell application.

Zhang et al. presented a novel approach to in-situ synthesize and imbue phosphotungstic acid into the cavity of MIL-101 (Cr) using $Na_2WO_4{\cdot}2H_2O$ and Na_2HPO_4 as precursors (HPW@MIL101), which are then used for the preparation of SPEEK/HPW@MIL101 nanohybrid membranes [63]. In this way, nanochannels are formed both in the cavity of MIL101 and at the interface of HPW@MIL101 and SPEEK, increasing the chance for proton transport. At 9 wt.% HPW@MIL101, the composite membrane exhibited a proton conductivity of 272 mS/cm at 65 °C and 100% RH, which is 45.5% higher than the pristine SPEEK (187 mS/cm) (Figure 20a). When the relative humidity was decreased to 40%, the corresponding proton conductivity for the SPEEK/HPW@MIL101 membrane at 60 °C was 6.51 mS/cm, 7.25 times higher than the pristine (0.898 mS/cm). The pristine SPEEK membrane was very sensitive to changes of RH, while the introduction of phosphotungstic acid retained much of the conductivity, in particular under low relative humidities (Figure 20b). Furthermore, the single H_2/O_2 fuel cell performance tested at 60 °C was also improved after the introduction of fillers. As it can be seen in Figure 20c, a power density of 383 mW/cm^2 at 100% RH was achieved from the composites with 9 wt.% HPW@MIL101, which is 27% higher than that of pristine SPEEK (280 mW/cm^2).

Finally, composite membranes based on SPEEK/PEEK-BI displayed superiority in terms of oxidative stability due to the presence of benzimidazole groups, but the proton conductivity was lower than that of the corresponding pristine SPEEK at 80 °C under fully hydrated conditions, which was a result of reduced water uptake and swelling ratio [154].

A summary of the SPEEK-based composite membranes is given Table 4.

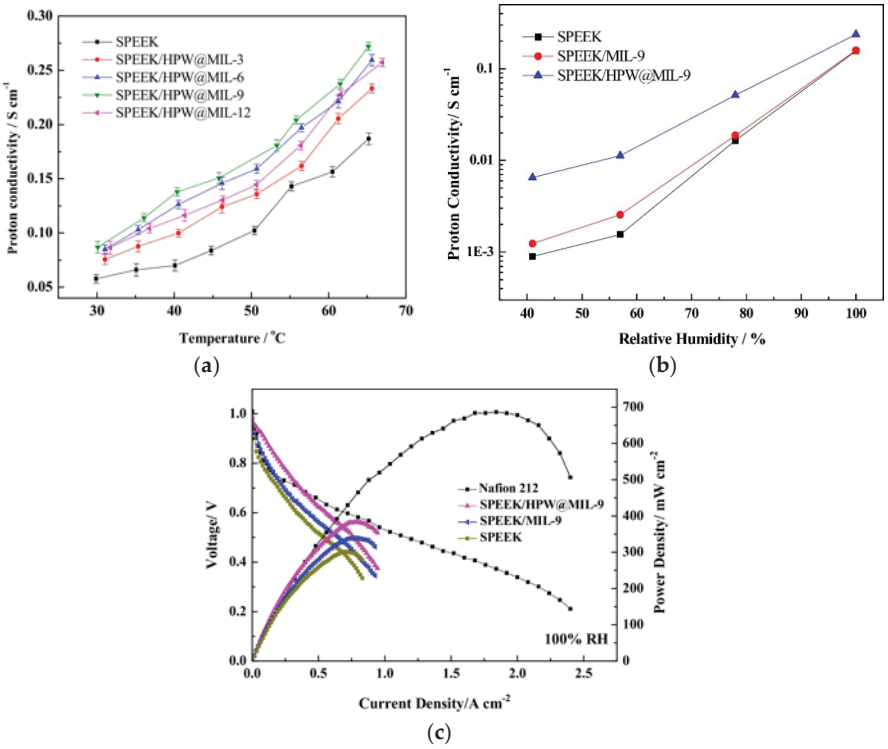

Figure 20. Proton conductivity of SPEEK/HPW@MIL101 membranes with different filler content at 100% RH under different temperatures (**a**); proton conductivity of the membranes with 9 wt.% HPW@MIL101 under different RHs (**b**); single H_2/O_2 fuel cell performance (**c**). Reprinted with permissions from Ref. [63]. Copyright 2017 Elsevier.

Table 4. Comparison of proton conductivities of sulfonated PEEK-based composite membranes and their PEMFC performance.

Membrane	Water Uptake	Conductivity/Temp/%RH/ Activation Energy	Maximum Power Density in PEMFC	Ref.
SPEEK/9.6 wt.% WC-SiW	6.95 ± 0.08@30 °C	50 mS/cm at 95 °C and 85% RH 11.2 kJ/mol	Not reported	[155]
SPEEK/2.5 wt.% ZCN	19.4%@30 °C	50.24 mS/cm at 100 °C and 100% RH 15.93 kJ/mol	Not reported	[59]
SPEEK/10 wt.% Analcime	31%@25 °C	401.6 mS/cm at 90 °C and 100% RH 15.1 kJ/mol	Not reported	[153]
SPEEK/10 wt.% S-UiO-66@GO	30 wt.%@100 °C	268 mS/cm at 70 °C and 95% RH 9 kJ/mol	Not reported	[62]
SPEEK/2.5 wt.% ZrO_2	20 wt.%@25 °C	40 mS/cm at 90 °C and 100% RH	Not reported	[156]
SPEEK/40 wt% polysilsesquioxane		142 mS/cm at 120 °C and 100% RH	Not reported	[157]
SPEEK/7.5 wt.% sul-MIL101	30%@25 °C	306 mS/cm at 75 °C and 100% RH	Not reported	[58]
SPEEK/1 wt% Fe_2TiO_5	61%@25 °C	96 mS/cm at 80 °C and 90% RH 10.8 kJ/mol	80 °C and RH = 90% 188 mW/cm^2	[152]
SPEEK/5 wt.% s-GO	60%@30 °C	55 mS/cm at 80 °C and 30% RH 22.21 kJ/mol	80 °C and RH = 30% 378 mW/cm^2	[64]
SPEEK/SFMC/5 wt.% GO	49.15@90 °C	111.9 mS/cm at 90 °C and 100% RH 21.31 kJ/mol	70 °C and RH = 100% 528.01 mW/cm^2	[158]
SPEEK/9 wt.% HPW@MIL101	29%@25 °C	272 mS/cm at 65 °C and 100% RH 6.51 mS/cm at 60 °C and 40% RH	60 °C and RH = 100% 383 mW/cm^2	[63]

5. Mixed Electron-Proton Conducting Composite Membranes for PEMFCs and Beyond

A critical parameter when designing PEMFC electrodes is the formation of a "three-phase" boundary among the substrate-supported catalyst, polymer and reactants. This requires that the gas/liquid, ion conduction and the electrocatalytically active and electronically-conducting phases must be present. If the Nafion content is low, then not all the catalyst particles are connected to the membrane, and therefore the catalyst utilization is reduced [159]. In the case where the Nafion content is too high, then the catalyst particles have poor electrical contact, resulting again in low catalyst utilization and cell efficiencies [160]. Nafion is an insulator so there is an optimal Nafion content that allows good ion conduction, but at the same time the catalyst particles have good electronic conduction too [161–164].

A promising alternative is to mix or replace Nafion in the catalyst ink with an electron-conducting polymer (ECP). In this way, electronic conductivity is introduced in parallel with the protonic one [165]. This is nicely depicted by Qi Z. et al. [166], who replaced Nafion by a mixture of poly(pyrrole)-polystyrenesulphonate (PPY/PSS), see Figure 21. In dry conditions, the electronic conductivity of the PPY/PSS composite membrane was 3 S/cm, which after deposition of the Pt particles was decreased to 0.3 S/cm. This decrease was attributed to the hydrogenation of the PPY during the Pt formation. The protonic conductivity of a 1-μm-thick film in 1 M H_2SO_4 at 0.15 V vs. SCE at room temperature and atmospheric pressure was 0.23 S/cm. The stability of the electrode was very good after 70 h of operation at +0.1 V vs. SCE and a current density of around 30 mA/cm^2. It should be noted that the authors did not assemble a full PEMFC, therefore one could expect a different performance of such an electrode.

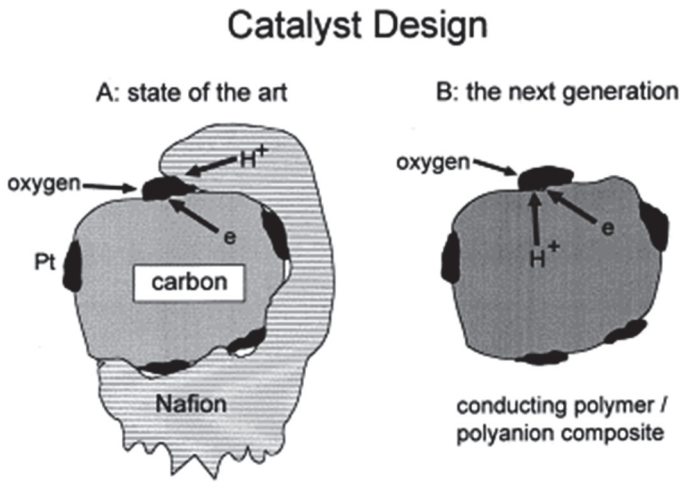

Figure 21. The commonly used electrode configuration (**A**) and the preferred design (**B**) in which the electronic conduction is added in parallel to the protonic one. Reprinted with permission from Ref. [166]. Copyright 1998 Elsevier.

Among the most studied ECPs are poly(pyrrole) (PPY), poly(aniline) (PANI) and poly(3,4-ethylenedioxythiophene) (PEDOT) [167]. The synthesis of these ECPs can be conducted by chemical, enzymatic and electrochemical methods. A comprehensive review article regarding the synthesis and applications of ECPs can be found in Ref. [168]. PPY in combination with Nafion has been used in PEMFCs [169–171], but the main disadvantages are the degradation PPY by H_2O_2, the unfavourable redox potentials and the low permeability of O_2 gas [165]. It should be noted though that PPY/Nafion composites have been extensively studied in direct methanol fuel cells (DMFCs), where the methanol crossover is heavily impeded by the addition of PPY in the Nafion matrix [172–179]. Although the mechanism behind the reduced methanol permeation is beyond the scope of this review, it is worth mentioning that this is related to the electrocatalytic activity of PPY for the oxidation of methanol [180].

On the other hand, Nafion/PANI composites seem to be the choice for mixed conduction in the catalyst layer of PEMFCs due to their high electronic and protonic conductivities [181,182]. In the very first reports, PANI is used as an electron-conducting matrix, where microparticles of the catalyst can be embedded and protected against particle loss and contamination from reactants [183]. The electrocatalytic activity of Pt microparticles, which were electrodeposited in PANI, showed excellent long-term stability for the electro-oxidation of methanol in acidic solutions [183]. PANI can be easily synthesized by electropolymerization of aniline with very good reproducibility and is stable in a wide potential window. PANI exists in four redox states, which are the leucoemeraldine base (reduced form), emeraldine base (half-oxidized form—EB), emeraldine salt (half-oxidized protonated form—ES) and pernigraniline base (oxidized form) [184]. Among these, only the half-oxidized form, ES, shows high conductivity, while the other forms show either low conductivity or act as dielectrics [185]. In addition, PANI exhibits high permeability to O_2 and is stable in oxygenated acidic solution. Coutanceau et al. and Croissant et al. have investigated the electrocatalytic activity of different mass loadings of Pt particles in PANI for both the oxidation of H_2 and the reduction of dioxygen for use in PEMFCs [186,187]. In their pioneering work, the authors concluded that the lowest Pt loading in a PEMFC for both negatrode and positrode electrodes equals to 0.35 mg/cm^2, which translates to 3 kW per gram of platinum. Such values are also realistic for PEMWEs as indicated by our extensive review on PEM water electrolyzers [188].

Lai et al. investigated two routes of depositing Pt particles in the matrix of a Nafion/PANI composite based on electrochemical and chemical reduction of K_2PtCl_6 [165]. With regards to the electrochemical reduction, although it showed a good dispersion of the Pt particles in the Nafion/PANI composite, the performance of the electrode showed inferior activity compared to the formation of Pt by chemical reduction. This was assigned to the nature of Pt growth in the polymer matrix. The stability of the electrode containing Pt particles grown with the chemical method for the ORR (positrode) was assessed over continuous cycling between 0.0 and +0.6 V at 5 mV/s in 0.5 M H_2SO_4. The electrode showed a 60% degradation over the first 300 h of operation, but then it stabilized. The authors acknowledge the importance of testing such an electrode under realistic PEM operation, since the oxygen flux is very different, and moreover, the stability of the polymer cannot be judged and it is not directly comparable to the RDE conditions. Barthet et al. prepared Nafion-doped PANI composites by two chemical methods, which differ essentially in the timing of the doping step [189]. The most effective method in terms of preparation of a polymer-based electrode for electrochemical processes, such as PEMFCs, was when polyemeraldine base dissolved in NMP was directly doped with acid-exchanged Nafion. The homogeneous composite polymer showed an electronic conductivity of 0.3 S/cm and an apparent diffusion coefficient for proton and Li ions between 10^{-6} and 10^{-8} cm^2/s. These values can be compared to the Li diffusion coefficients found for electrochemically synthesized Nafion/PPY composites [189].

Gharibi et al. synthesized PANI nanofibers by electropolymerization of aniline and trifluoromethanesulfonic acid on a Nafion-containing catalyst layer of a gas diffusion electrode (GDE) [190]. The introduction of PANI in the Nafion-containing catalyst (Pt) layer reduced the polarization resistance by minimizing the ohmic resistance, as well as the charge transfer and mass transport limitations. Moreover, the Pt utilization for the ORR was increased almost 30%, a fact that can eventually reduce the Pt amount [191]. A schematic diagram where the PANI nanofibers form a conducting network among the Pt particles is given in Figure 22. It should be noted though that the GDE was not tested in a PEMFC and the characterization was done as a half cell.

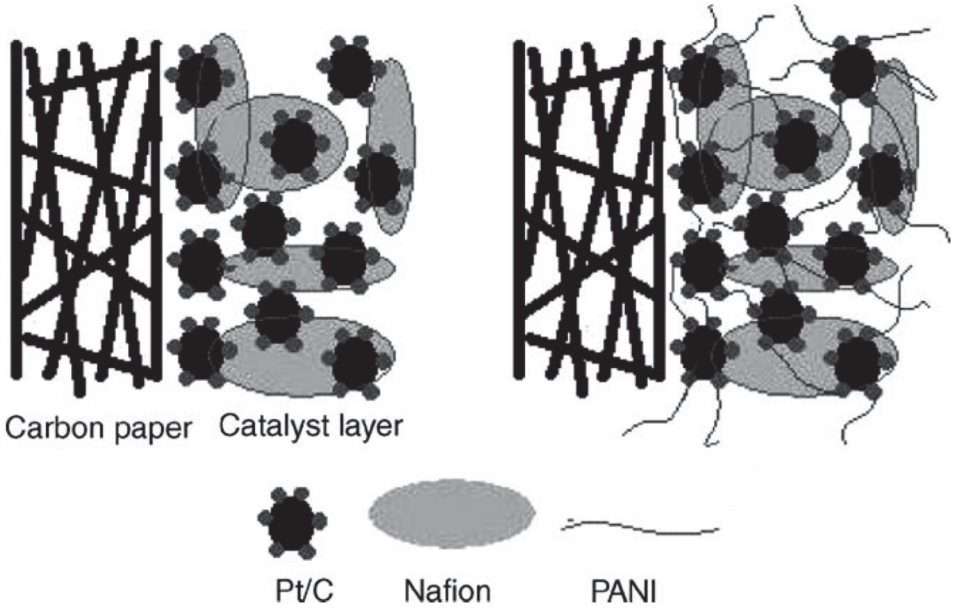

Figure 22. Schematic representation of the role of PANI nanofibers in connecting the catalyst particles embedded in the Nafion matrix. Reprinted with permission from Ref. [191]. Copyright 2006 Elsevier.

An interesting work, in which PANI did not induce electronic conductivity when mixed with Nafion, was presented by Yang et al. [192]. The reason for this behaviour was not investigated, but the authors did not experience any short-circuit when the membrane was mounted in a single cell PEMFC. A possible reason could be the fact that the amount of PANI did not reach the percolating threshold for electronic conduction. The composite membrane was synthesized by an in-situ chemical polymerization technique, where a pre-cleaned and pre-treated Nafion membrane was immersed in an aniline solution that was mixed with $(NH_4)_2S_2O_8$. The authors showed that the composite membrane had a superior performance compared to Nafion 112 at 60% RH at 30 °C. The conductivity was approx. 30 mS/cm, whilst for the Nafion 112, it was approx. 18 mS/cm. More interestingly, the composite membranes had lower water uptake capacity, and the improved proton conductivity was hypothesized to be due to the conjugated bonds in PANI. As expected, the single fuel cell testing showed a better performance with the composite membranes when operated with dry gas feed. On the other hand, Berezina et al. prepared composite membranes based on PANI and a Nafion-type (MF-4SC) membrane by a chemical template synthetic method [193]. The electronic conductivity of PANI alone was found in the range of 10^{-2} to 10^{3} S/m, while the composite PANI/MF-4SC had a total conductivity (electronic and protonic) of the order of 1.2 to 5.5 S/cm. The ion exchange membrane alone had a protonic conductivity of the range of 1 to 14 S/m. It can be seen that a synergistic effect in the conductivity values of the composite membrane did not occur and multiple factors may be responsible for this behaviour, such as morphological parameters and the redox inhomogeneity of the composite polymer.

Wolz et al. used the spray coating method to develop a layer-by-layer assembled electrode [194]. Pt nanoparticles were synthesized by the polyol method on PANI films and on single walled carbon nanotubes (SWCNTs). The multilayered electrode was applied on a Nafion membrane and its presence in the electrode was not necessary. This architecture improved the Pt utilization by a factor of three, yielding a performance of 2.7 W/mg_{Pt}.

One of the first studies where a Nafion/PANI composite was employed as a positrode for the ORR in a PEMFC was presented by Kakaei [195]. The cathode was prepared by mixing PANI, which was doped with trifluoromethane sulfonic acid, with Vulcan XC72 carbon. Then the mixture was impregnated with Pt particles by adding H_2PtCl_6, which was reduced by $NaBH_4$ solution. This electrode was compared with a standard Pt/C electrocatalyst in Nafion and the performance of the PANI modified electrode was improved by 1.82 times. PANI was in the form of fibres, which formed

an electron-conducting network along with the Vulcan XC72 carbon, improving the performance of the Pt particles due to improved electrical conduct of the particles.

Among other conducting polymers, poly(3,4-ethylenedioxythiophene) (PEDOT) has attracted interest due to its high electronic conductivity and optical transparency [196–198]. In combination with sulfonated poly(2,6-dimethyl 1,4-phenylene oxide) (sPPO), mixed conducting membranes can be prepared. Liu et al. developed a highly transparent, mixed conducting polymer composite of PEDOT:sPPO [199]. The synthesis was performed by mixing an aqueous solution of sPPO with EDOT and $Fe(SO_4)_3$ $9H_2O$, initiating the polymerization reaction. The ratio between PEDOT and sPPO was adjusted by the ratio of sPPO and EDOT. After DMSO treatment, an unprecedented enhancement of the electronic conductivity was observed, that reached as high as 10 S/cm, without compromising the proton conductivity. The latter reached up to 20 mS/cm and the increase in the electronic conductivity was attributed to the chain rearrangement and the improvement of the connectivity between the conducting grains of PEDOT. McFarlane et al. prepared Nafion/PEDOT:PSS mixed conducting membranes by simply mixing Nafion and PEDOT:PSS solutions and then drop-casting the dispersions on glass substrates [200]. The membranes were annealed in a vacuum oven, resulting in freestanding, semi-transparent (depending on the amount of PEDOT:PSS), water-insoluble and mechanically-robust membranes. The electronic conductivity was measured in ambient conditions with a four-probe set up, while the protonic in 4 M H_2SO_4 was measured in a special glass cell. Composite membranes containing 12% PEDOT:PSS exhibited an electronic conductivity of approx. 7 mS/cm and the ionic was of the order of 103 mS/cm, which is the same as a fully wetted Nafion at 80 °C and 100 RH. Although the purpose of these membranes is their use in systems of artificial photosynthesis for solar water splitting and hydrogen production, it will be very interesting to incorporate into PEMFCs and PEMWEs electrodes.

A few very interesting mixed electron proton-conducting membranes and standalone materials have been recently developed, but unfortunately have not been tested in PEMFCs or PEMWEs. They are worth presenting though for their innovation character as well as their possible applications beyond PEMFCs and PEMWEs, as in artificial photosynthesis, sensors and energy storage devices. In parallel though, we aim to inform and inspire the reader for potential use as electrodes in PEMFCs and PEMWEs.

Ijeri et al. combined Nafion with multi-walled carbon nanotubes (MWCNTs) beyond their percolation threshold with a very simple mix-and-cast method [201]. The authors tested the Nafion/MWCNTs under dry and wet conditions in ambient temperatures and found that the electronic conductivity increased with increasing MWCNTs content and reached approx. 0.37 mS/cm in dry conditions. After wetting, the electronic conductivity decreased by approx. 30% but as expected the protonic conductivity increased. The protonic conductivity reached the 5 mS/cm in the presence of 5% wt. of MWCNTs. In a follow-up work of the same group, the authors prepared the same type of composite membranes with the difference that the MWCNTs were now aligned forming distinct electron conduction paths [202]. The MWCNTs were grown with chemical vapor deposition (CVD) on Si substrates, which were patterned by optical lithography. The MWCNTs on Si were then flooded with Nafion solution and after evaporation the membrane was detached by immersion in HF. In this case, the electronic conductivity in dry conditions was improved to 0.57 mS/cm as opposed to 0.37 mS/cm in their previous work. The protonic conductivity was also improved from 5 to 9 mS/cm. Pilgrim et al. developed mixed conducting membranes made of vertically-aligned carbon nanotubes (VANT) [203]. The synthesis of the membrane was conducted through three basic steps: CNTs growth, epoxy coating and CNTs exposure (Figure 23).

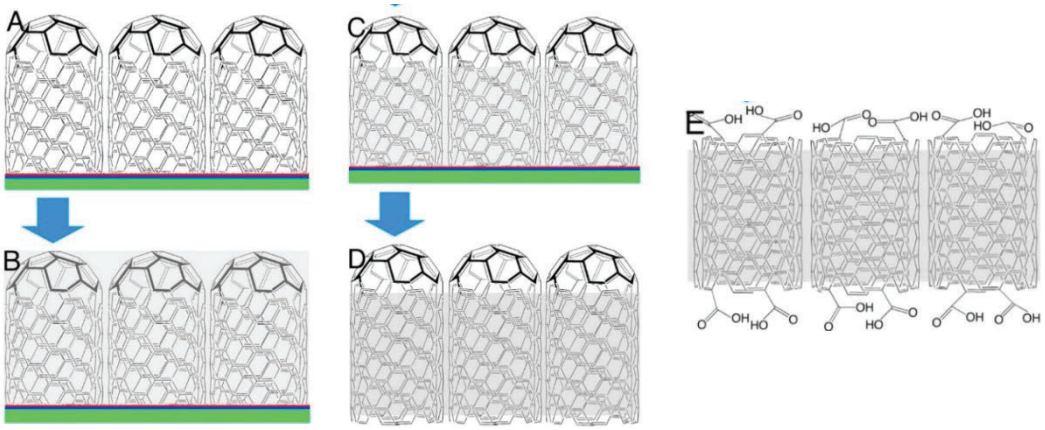

Figure 23. VANT membrane synthesis route. In green is the Si wafer, in blue an alumina support and in red an iron catalyst where the CNTs were grown (**A**); in grey the epoxy coating (**B**); tip exposure (**C**); removal of wafer and catalyst (**D**); tube opening via O_3 treatment (**E**). Reprinted with permission from Ref. [203]. Copyright 2014 American Chemical Society.

The electrical transport was ohmic with a conductivity of 495 mS/cm. After wetting the membrane, the proton conductivity was enabled through the bore of the CNTs and the authors hypothesize that the transport was due to the Grotthuss mechanism. The proton conductivity was measured by a peculiar set up in, where the proton transport was monitored by the absorption spectrum of bromophenol blue. The proton conductivity of the VANT membrane was found to be half of Nafion's, which was measured in the same experimental set up. The work lacks evidence on the transport mechanism and also conductivity dependencies over varying water levels and temperatures, parameters that will be very interesting to further investigate. Another single component, carbon-based mixed conductor was shown by Hatakeyama et al. [204]. In this work, the degree of GO reduction by photo and thermal methods can tune the mixed conductivity of the GO/rGO membrane. This is schematically illustrated in Figure 24.

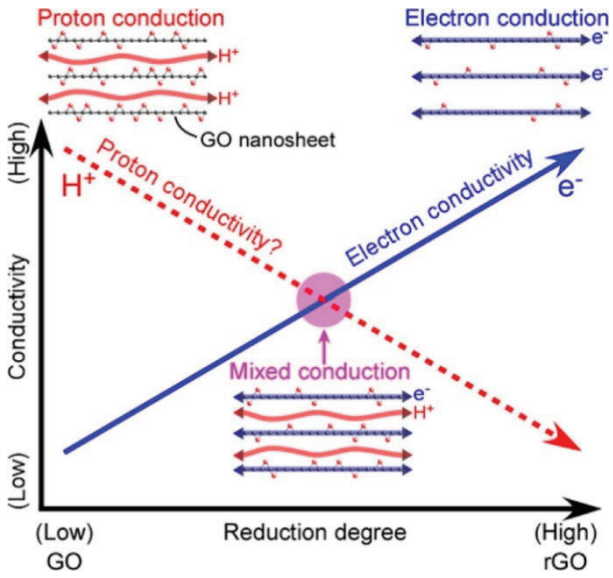

Figure 24. The concept behind the degree of GO reduction, which increases the electronic conductivity but decreases the protonic one. Reprinted with permission from Ref. [204]. Copyright 2014 American Chemical Society.

The protonic conductivity in this type of single component mixed conductor is attributed to the epoxide groups in between the GO sheets that facilitate the proton transport [205]. The authors found that the material with the optimum degree of reduction had the same electronic and protonic conductivity of approx. 10^{-4} S/cm at 90% RH at room temperature. In a follow up work of the same group, the rGO was modified with sulfate ions (r-sGO); the protonic conductivity at 90% RH in room temperature was increased to 3×10^{-2} S/cm and the electronic to 2×10^{-2} S/cm [206]. Finally, another single component mixed conductor is based on hierarchical nanostructured WO_3 [207]. The bioinspired hexagonal WO_3 nanorods (h-WO_3) were synthesized by the hydrothermal method. The proton conductivity of this material relies on the water content of the hydrous WO_3 (h–$WO_3 \cdot n H_2O$), which was determined by thermogravimetric analysis. On the other hand and in order to induce electronic conductivity, the h–$WO_3 \cdot n H_2O$ was reduced after annealing in reducing atmosphere (5% H_2 in N_2). At room temperature, the electronic conductivity was approx. 0.6 S/cm and decreased with increasing temperature, implying a metallic-like behaviour. The protonic conductivity reached the 1 mS/cm at room temperature at 50% RH, but it increased to 2.7 and 3.7 mS/cm at 60 and 90 °C, respectively. The material was assessed as a capacitor and showed good capacitance with fast charge/discharge capability and very good stability. It would be interesting to see if it can be employed as a mixed conducting component surface modified with Pt nanoparticles in the positrode of a PEMFC.

6. Summary, Challenges, Perspectives and Future Directions

In this review, we started with a brief account of the recent status, as well as the targets set for PEM-based energy systems in order to compete with the current energy technologies. There is surely a requirement and trend of reduced cost of PEM systems, but it looks like the rate is not as significant during the last few years as a decade or more ago. One of the main reasons is the cost of certain components, such as the PEM (e.g., Nafion) and the electrocatalysts (noble metals). We have recently reviewed the latter and it seems that PEM systems have a long way to go to escape from the use of noble metals as electrocatalysts [188]. There is an enormous amount of research on earth-abundant electrocatalysts, but the efforts to actually utilise them in operating PEM systems are few. This is definitely one of the main barriers the PEM world should realise and improve in order to further reduce the costs.

When it comes to the PEM, our review indicates that the "conductivity gap" still exists between the upper temperature limit for Nafion-based membranes and the lower temperatures of sufficient conductivity for the non-fluorinated systems based on acid-doped PBI and SPEEK. Apparently, metal oxide fillers do not significantly improve the proton conductivity at temperatures higher than 80 °C and low RH levels for PFSA polymers. At higher temperatures, when water evaporates from the polymer, the channels start to contract, breaking at the same time the connections among the filler particles. How can we then make percolating networks of the particles of the filler? Should such a self-standing network be synthesized first and then grow or infiltrate the polymer around it? On the other hand, the metal oxide fillers seem in some cases beneficial for temperatures below 80 °C, but are the results reproducible and is there a real gain considering the cost of that extra component, as well as the disadvantages of the increased brittleness and the of LT-PEMFC operation (catalyst poisoning, flooding etc.)? We have found a few promising materials, where Nafion is mixed with MOFs as well as graphene oxide (GO) that show quite high conductivity values even at 120 °C and low RH [61,68,80]. The main issue is that these membranes were not tested in full PEMFCs; their stability is not assessed and it could be that the costs of GO and the MOFs turn out to be prohibitive.

The acid-doped PBI-based membranes show very good conductivities at high temperature and low relative humidity, as well as good power densities, but the majority of the systems operate well above 150 °C and there are no reports at lower operating temperatures close to the US DOE target of 120 °C. Zirconium hydrogen phosphate has been shown to yield significant conductivity up to 200 °C, but the detailed interaction mechanism between this filler and the PBI matrix is not clear, and the stability with this composite membrane at such high temperature has hardly been studied. One must

suspect that this like many other phosphates more than anything else acts as a source of phosphoric acid upon decomposition at high temperature. Composite membranes containing heteropolyacids (HPA) exhibit high proton conductivity under anhydrous conditions at 150 °C attributed to HPAs providing additional surface functional sites through the composite membrane to promote the proton transport because protons are transferred on the surface of the HPA [208]. A balance between proton conductivity and mechanical strength of the membrane may be required for a promising PBI-based composite membrane. Recently, PEM with co-doped MOFs have demonstrated significant enhancement in proton conductivity, which is attributed to the synergistic effect between the two fillers leading to ionic channels with better connectivity. However, these composites have not found any practical applications in fuel cells yet. A further challenge is to make an electrocatalytic layer that would be compatible to both membrane and catalyst.

SPEEK is a cheaper alternative to Nafion, but its conductivity is in general lower. Moreover, the high degree of sulfonation leads to poor mechanical stability. As a consequence, inorganic fillers are, as we have seen, tried as remedy. Metal oxide composite membranes based on SPEEK show again lower conductivities than the analogues in Nafion, but certain composites with MOFs show improved conductivities [58,63,153]. Apparently, MOFs, as well as cavity-modified ones with acidic groups, improve the proton conduction, an effect observed also in the Nafion case. Again, full PEMFCs tests are missing and they are of paramount importance in order to assess the compatibility, stability and lifetime of such composite membranes. Another factor is also the cost of these structures, if proven to be successful. A technoeconomic analysis on the viability of MOFs-doped PEM should be conducted.

An interesting composite based on polysilsesquioxane was presented by Pezzin et al. [157]. This composite showed a proton conductivity of 142 mS/cm at 120 °C and 100% RH, but the performance and the stability of the composite membrane was not tested in a full PEMFC. Such hybrid membranes with Si–O networks look promising and may assist in the formation of percolating networks in the parent membrane during low RH conditions and temperatures around 120 °C. A similar study was conducted by Nam et al. where they also observed high proton conductivity of 157 mS/cm at 120 °C and 100% RH from a Nafion/sulfonated poly(phenylsilsesquioxaine) nanocomposite membrane, which is higher than that of Nafion [46]. A few follow-up works worth pursuing have been found [209–211].

We have introduced the definition of the negatrode and positrode electrodes, as used in proton ceramic fuel cells and electrolysers, and we are among the few to review developments on mixed electron proton-conducting polymer materials for use in the CL. Regarding the progress in mixed conducting polymers, we see a lack of measurements in full PEMFCs. Some of the reports are even performing the conductivity measurements in liquid electrolytes and in three-electrode configurations. This is useful as it is easier to set up such measurements, rather than full PEMFCs, and they can give immediate indications for the efficiency and performance as means of fast materials screening. On the other hand, the operational conditions are quite different, in terms of both temperature, but also concentration and mass transport of the reactants and products towards and from the active sites, respectively. The latter can also have a big impact on the stability and lifetime of the mixed conductor. Another important aspect that is missing in the literature is a more complete physicochemical and electrochemical characterization on different RH levels and temperatures, especially at elevated ones (above 100 °C). This is particularly important, as there are no synchronized efforts in the research for high temperature-tolerant mixed conductors that could follow up the developments on the high temperature membranes.

PEDOT is also a promising electronically-conducting polymer beyond PANI and it should be explored more, especially in full PEMFCs and also in terms of stability at high operating temperatures. The unprecedented increase in its electronic conduction after treatment with DMSO as presented by Liu et al. [199], should be studied further. The fundamental understanding behind this effect could lead to an increase in performance in other electron-conducting polymers and also to the discovery of other polymer systems that can turn into electron conductors.

The development of single-component mixed conductors based on oxides is an important approach, as oxides can tolerate high operating temperatures; however, certain aspects must be taken into account. For example, how is the electrocatalyst deposited and how efficient is the mixed conductor/electrocatalyst interface? It is important to investigate how the ions and electrons are transported and react on that interface. What is the impact of the morphology of the mixed conductor (e.g., tubes, rods, nanoparticles etc.) and its compatibility with the PEM?

At the very end, we would like to look back at the skepticism we expressed at the outset as to the effects of fillers of various kinds introduced to proton-conductive polymers. We have indeed seen some cases of remarkable improvements in conductivity, power density, stability and operation at higher temperatures and lower RH. However, the remarkable majority of them report improvements within limits that may well be statistical variation—a variation or reproducibility usually not reported. We may suspect underreporting of negative effects of fillers. The matrix of acid doping and fillers and their interactions is often not completely mapped. We have seen many cases of large improvements of protonic conductivity accompanied by a remarkable drop in activation energy to levels only associated with liquid phase transport, shedding doubt on the characterisation of the supposedly solid-state material. We have seen few credible rationalisations of why fillers work. For example, some refer to the use of particles of proton-conductive materials, all of which are recently understood to exhibit only protonic conduction in adsorbed water. This leads us to encourage that studies of PEM composites onwards emphasise well-characterised microstructures (bulk, grain boundaries, phase boundaries, internal surfaces) and a well-founded assignment of protonic conduction appropriate to bulk solid polymer and ceramic phases and liquid phases, adsorbed water layers (chemisorbed, physisorbed), and interfaces (e.g., through space charge effects).

Author Contributions: Writing-Original Draft Preparation, X.S., S.C.S., T.N. and A.C.; Writing-Review & Editing, X.S., T.N. and A.C.

Funding: The work has received financial support from the Research Council of Norway (RCN), grant number [257653].

Acknowledgments: X.S., A.C. and T.N. acknowledge MoZEES, a Norwegian Centre for Environment-friendly Energy Research (FME), co-sponsored by the Research Council of Norway (project number 257653) and 40 partners from research, industry and public sector. The authors would like to thank Magnus Thomassen from SINTEF for the valuable input on the introduction.

Conflicts of Interest: The authors declare no conflict of interest.

References

1. Kirubakaran, A.; Jain, S.; Nema, R. A review on fuel cell technologies and power electronic interface. *Renew. Sustain. Energy Rev.* **2009**, *13*, 2430–2440. [CrossRef]
2. Acar, C.; Dincer, I. Comparative assessment of hydrogen production methods from renewable and non-renewable sources. *Int. J. Hydrogen Energy* **2014**, *39*, 1–12. [CrossRef]
3. Balat, M.; Balat, M. Political, economic and environmental impacts of biomass-based hydrogen. *Int. J. Hydrogen Energy* **2009**, *34*, 3589–3603. [CrossRef]
4. Holladay, J.; Hu, J.; King, D.; Wang, Y. An overview of hydrogen production technologies. *Catal. Today* **2009**, *139*, 244–260. [CrossRef]
5. Zeng, K.; Zhang, D. Recent progress in alkaline water electrolysis for hydrogen production and applications. *Prog. Energy Combust. Sci.* **2010**, *36*, 307–326. [CrossRef]
6. Cipriani, G.; Di Dio, V.; Genduso, F.; La Cascia, D.; Liga, R.; Miceli, R.; Galluzzo, G.R. Perspective on hydrogen energy carrier and its automotive applications. *Int. J. Hydrogen Energy* **2014**, *39*, 8482–8494. [CrossRef]
7. Zhang, H.; Shen, P.K. Recent Development of Polymer Electrolyte Membranes for Fuel Cells. *Chem. Rev.* **2012**, *112*, 2780–2832. [CrossRef]
8. Wang, Y.-J.; Zhao, N.; Fang, B.; Li, H.; Bi, X.T.; Wang, H. Carbon-Supported Pt-Based Alloy Electrocatalysts for the Oxygen Reduction Reaction in Polymer Electrolyte Membrane Fuel Cells: Particle Size, Shape, and Composition Manipulation and Their Impact to Activity. *Chem. Rev.* **2015**, *115*, 3433–3467. [CrossRef]

9. Moreno, N.G.; Molina, M.C.; Gervasio, D.; Robles, J.F.P. Approaches to polymer electrolyte membrane fuel cells (PEMFCs) and their cost. *Renew. Sustain. Energy Rev.* **2015**, *52*, 897–906. [CrossRef]
10. Available online: https://www.hydrogen.energy.gov/pdfs/15015_fuel_cell_system_cost_2015.pdf (accessed on 1 May 2019).
11. DOE Technical Targets for Polymer Electrolyte Membrane Fuel Cell Components. Available online: https://www.energy.gov/eere/fuelcells/doe-technical-targets-polymer-electrolyte-membrane-fuel-cell-components (accessed on 1 May 2019).
12. Fuel Cell Technical Team Roadmap 2013. Available online: https://www.energy.gov/sites/prod/files/2014/02/f8/fctt_roadmap_june2013.pdf (accessed on 1 May 2019).
13. Chandan, A.; Hattenberger, M.; El-Kharouf, A.; Du, S.; Dhir, A.; Self, V.; Pollet, B.G.; Ingram, A.; Bujalski, W. High temperature (HT) polymer electrolyte membrane fuel cells (PEMFC)–A review. *J. Power Sources* **2013**, *231*, 264–278. [CrossRef]
14. Hickner, M.A.; Ghassemi, H.; Kim, Y.S.; Einsla, B.R.; McGrath, J.E. Alternative Polymer Systems for Proton Exchange Membranes (PEMs). *Chem. Rev.* **2004**, *35*, 4587–4612. [CrossRef]
15. Weber, A.Z.; Newman, J. Modeling Transport in Polymer-Electrolyte Fuel Cells. *Chem. Rev.* **2004**, *104*, 4679–4726. [CrossRef] [PubMed]
16. Bessarabov, D.; Wang, H.; Li, H.; Zhao, N. *PEM Electrolysis for Hydrogen Production: Principles and Applications*; Taylor & Francis: Boca Raton, FL, USA, 2015; p. 408.
17. Nguyen, T.V.; White, R.E. A Water and Heat Management Model for Proton-Exchange-Membrane Fuel Cells. *J. Electrochem. Soc.* **1993**, *140*, 2178. [CrossRef]
18. Kreuer, K.D.; Paddison, S.J.; Spohr, E.; Schuster, M. Transport in Proton Conductors for Fuel-Cell Applications: Simulations, Elementary Reactions, and Phenomenology. *Chem. Rev.* **2004**, *104*, 4637–4678. [CrossRef] [PubMed]
19. Shin, D.W.; Guiver, M.D.; Lee, Y.M. Hydrocarbon-Based Polymer Electrolyte Membranes: Importance of Morphology on Ion Transport and Membrane Stability. *Chem. Rev.* **2017**, *117*, 4759–4805. [CrossRef] [PubMed]
20. Banerjee, S.; Curtin, D.E. Nafion® perfluorinated membranes in fuel cells. *J. Fluor. Chem.* **2004**, *125*, 1211–1216. [CrossRef]
21. Mauritz, K.A.; Moore, R.B. State of Understanding of Nafion. *Chem. Rev.* **2004**, *104*, 4535–4586. [CrossRef] [PubMed]
22. Souzy, R.; Ameduri, B. Functional fluoropolymers for fuel cell membranes. *Fluorinated Mater. Energy Convers.* **2005**, *30*, 644–687.
23. Ji, M.; Wei, Z. A Review of Water Management in Polymer Electrolyte Membrane Fuel Cells. *Energies* **2009**, *2*, 1057–1106. [CrossRef]
24. Adjemian, K.T.; Dominey, R.; Krishnan, L.; Ota, H.; Majsztrik, P.; Zhang, T.; Mann, J.; Kirby, B.; Gatto, L.; Velo-Simpson, M.; et al. Function and Characterization of Metal Oxide−Nafion Composite Membranes for Elevated-Temperature H2/O2PEM Fuel Cells. *Chem. Mater.* **2006**, *18*, 2238–2248. [CrossRef]
25. RReed, D.; Thomsen, E.; Wang, W.; Nie, Z.; Li, B.; Wei, X.; Koeppel, B.; Sprenkle, V. Performance of Nafion® N115, Nafion® NR-212, and Nafion® NR-211 in a 1 kW class all vanadium mixed acid redox flow battery. *J. Power Sources* **2015**, *285*, 425–430. [CrossRef]
26. Yee, R.; Rozendal, R.; Zhang, K.; Ladewig, B.; Ladewig, B. Cost effective cation exchange membranes: A review. *Chem. Eng. Res. Des.* **2012**, *90*, 950–959. [CrossRef]
27. Iojoiu, C.; Chabert, F.; Maréchal, M.; Kissi, N.E.; Guindet, J.; Sanchez, J.Y. From polymer chemistry to membrane elaboration: A global approach of fuel cell polymeric electrolytes. *J. Power Sources* **2006**, *153*, 198–209. [CrossRef]
28. Wieser, C. Novel Polymer Electrolyte Membranes for Automotive Applications—Requirements and Benefits. *Fuel Cells* **2004**, *4*, 245–250. [CrossRef]
29. Bakangura, E.; Wu, L.; Ge, L.; Yang, Z.; Xu, T. Mixed matrix proton exchange membranes for fuel cells: State of the art and perspectives. *Prog. Polym. Sci.* **2016**, *57*, 103–152. [CrossRef]
30. Macauley, N.; Lauritzen, M.; Knights, S.; Kjeang, E. Predicting Membrane Lifetime with Cerium Oxide in Heavy Duty Fuel Cell Systems. *J. Electrochem. Soc.* **2018**, *165*, F780–F785. [CrossRef]

31. Subianto, S.; Pica, M.; Casciola, M.; Cojocaru, P.; Merlo, L.; Hards, G.; Jones, D.J. Physical and chemical modification routes leading to improved mechanical properties of perfluorosulfonic acid membranes for PEM fuel cells. *J. Power Sources* **2013**, *233*, 216–230. [CrossRef]
32. Devanathan, R. Recent developments in proton exchange membranes for fuel cells. *Energy Environ. Sci.* **2008**, *1*, 101–119. [CrossRef]
33. Carmo, M.; Fritz, D.L.; Mergel, J.; Stolten, D. A comprehensive review on PEM water electrolysis. *Int. J. Hydrogen Energy* **2013**, *38*, 4901–4934. [CrossRef]
34. Slade, S.; Campbell, S.A.; Ralph, T.R.; Walsh, F.C. Ionic Conductivity of an Extruded Nafion 1100 EW Series of Membranes. *J. Electrochem. Soc.* **2002**, *149*, A1556–A1564. [CrossRef]
35. Herring, A.M. Inorganic–Polymer Composite Membranes for Proton Exchange Membrane Fuel Cells. *J. Macromol. Sci. Part C* **2006**, *46*, 245–296. [CrossRef]
36. Aricò, A.S. Influence of the acid–base characteristics of inorganic fillers on the high temperature performance of composite membranes in direct methanol fuel cells. *Solid State Ion.* **2003**, *161*, 251–265. [CrossRef]
37. Antonucci, V.; Di Blasi, A.; Baglio, V.; Ornelas, R.; Matteucci, F.; Ledesma-García, J.; Arriaga, L.; Aricò, A.S. High temperature operation of a composite membrane-based solid polymer electrolyte water electrolyser. *Electrochim. Acta* **2008**, *53*, 7350–7356. [CrossRef]
38. Di Noto, V.; Gliubizzi, R.; Negro, E.; Pace, G. Effect of SiO_2 on Relaxation Phenomena and Mechanism of Ion Conductivity of [Nafion/(SiO_2)x] Composite Membranes. *J. Phys. Chem. B* **2006**, *110*, 24972–24986. [CrossRef] [PubMed]
39. Baglio, V.; Ornelas, R.; Matteucci, F.; Martina, F.; Ciccarella, G.; Zama, I.; Arriaga, L.G.; Antonucci, V.; Aricò, A.S. Solid Polymer Electrolyte Water Electrolyser Based on Nafion-TiO_2 Composite Membrane for High Temperature Operation. *Fuel Cells* **2009**, *9*, 247–252. [CrossRef]
40. Ye, G.; Li, K.; Xiao, C.; Chen, W.; Zhang, H.; Pan, M. Nafion (R)-Titania Nanocomposite Proton Exchange Membranes. *J. Appl. Polym. Sci.* **2011**, *120*, 1186–1192. [CrossRef]
41. Zhai, Y.; Zhang, H.; Hu, J.; Yi, B. Preparation and characterization of sulfated zirconia (SO_4^{2-}/ZrO_2)/Nafion composite membranes for PEMFC operation at high temperature/low humidity. *J. Membr. Sci.* **2006**, *280*, 148–155. [CrossRef]
42. Sacca, A.; Gatto, I.; Carbone, A.; Pedicini, R.; Passalacqua, E. ZrO_2–Nafion composite membranes for polymer electrolyte fuel cells (PEFCs) at intermediate temperature. *J. Power Sources* **2006**, *163*, 47–51. [CrossRef]
43. Dupuis, A.-C. Proton exchange membranes for fuel cells operated at medium temperatures: Materials and experimental techniques. *Prog. Mater. Sci.* **2011**, *56*, 289–327. [CrossRef]
44. Lónyi, F.; Valyon, J.; Engelhardt, J.; Mizukami, F. Characterization and Catalytic Properties of Sulfated ZrO_2–TiO_2Mixed Oxides. *J. Catal.* **1996**, *160*, 279–289. [CrossRef]
45. Yuan, J.J.; Pu, H.T.; Yang, Z.L. Studies on Sulfonic Acid Functionalized Hollow Silica Spheres/Nafion (R) Composite Proton Exchange Membranes. *J. Polym. Sci. Part a-Polym. Chem.* **2009**, *47*, 2647–2655. [CrossRef]
46. Nam, S.-E.; Kim, S.-O.; Kang, Y.; Lee, J.W.; Lee, K.-H. Preparation of Nafion/sulfonated poly(phenylsilsesquioxane) nanocomposite as high temperature proton exchange membranes. *J. Membr. Sci.* **2008**, *322*, 466–474. [CrossRef]
47. Jalani, N.H.; Dunn, K.; Datta, R. Synthesis and characterization of Nafion®-MO_2 (M=Zr, Si, Ti) nanocomposite membranes for higher temperature PEM fuel cells. *Electrochim. Acta* **2005**, *51*, 553–560. [CrossRef]
48. Li, K.; Ye, G.; Pan, J.; Zhang, H.; Pan, M. Self-assembled Nafion®/metal oxide nanoparticles hybrid proton exchange membranes. *J. Membr. Sci.* **2010**, *347*, 26–31. [CrossRef]
49. Park, K.T.; Jung, U.H.; Choi, D.W.; Chun, K.; Lee, H.M.; Kim, S.H. ZrO_2–SiO_2/Nafion® composite membrane for polymer electrolyte membrane fuel cells operation at high temperature and low humidity. *J. Power Sources* **2008**, *177*, 247–253. [CrossRef]
50. Chalkova, E.; Fedkin, M.V.; Wesolowski, D.J.; Lvov, S.N. Effect of TiO_2 Surface Properties on Performance of Nafion-Based Composite Membranes in High Temperature and Low Relative Humidity PEM Fuel Cells. *J. Electrochem. Soc.* **2005**, *152*, A1742–A1747. [CrossRef]
51. Coleman, J.N.; Khan, U.; Blau, W.J.; Gun'Ko, Y.K. Small but strong: A review of the mechanical properties of carbon nanotube–polymer composites. *Carbon* **2006**, *44*, 1624–1652. [CrossRef]
52. Kannan, R.; Kakade, B.A.; Pillai, V.K. Polymer Electrolyte Fuel Cells Using Nafion-Based Composite Membranes with Functionalized Carbon Nanotubes. *Angew. Chem.* **2008**, *120*, 2693–2696. [CrossRef]

53. Yoon, M.; Suh, K.; Natarajan, S.; Kim, K. Proton Conduction in Metal-Organic Frameworks and Related Modularly Built Porous Solids. *Angew. Chem. Int. Ed.* **2013**, *52*, 2688–2700. [CrossRef]
54. Li, Z.; He, G.; Zhang, B.; Cao, Y.; Wu, H.; Jiang, Z.; Tiantian, Z. Enhanced Proton Conductivity of Nafion Hybrid Membrane under Different Humidities by Incorporating Metal–Organic Frameworks With High Phytic Acid Loading. *ACS Appl. Mater. Interfaces* **2014**, *6*, 9799–9807. [CrossRef]
55. He, G.; Guiver, M.D.; Li, Z.; Wang, W.; Chen, Y.; Xiong, C.; Cao, Y.; Wu, H.; Jiang, Z. Constructing efficient ion nanochannels in alkaline anion exchange membranes by the in situ assembly of a poly(ionic liquid) in metal–organic frameworks. *J. Mater. Chem. A* **2016**, *4*, 2340–2348.
56. Dong, X.-Y.; Li, J.-J.; Han, Z.; Duan, P.-G.; Li, L.-K.; Zang, S.-Q. Tuning the functional substituent group and guest of metal–organic frameworks in hybrid membranes for improved interface compatibility and proton conduction. *J. Mater. Chem. A* **2017**, *5*, 3464–3474. [CrossRef]
57. Escorihuela, J.; Sahuquillo, Ó.; García-Bernabé, A.; Giménez, E.; Compañ, V. Phosphoric Acid Doped Polybenzimidazole (PBI)/Zeolitic Imidazolate Framework Composite Membranes with Significantly Enhanced Proton Conductivity under Low Humidity Conditions. *Nanomaterials* **2018**, *8*, 775. [CrossRef] [PubMed]
58. Li, Z.; He, G.; Zhao, Y.; Cao, Y.; Wu, H.; Li, Y.; Jiang, Z. Enhanced proton conductivity of proton exchange membranes by incorporating sulfonated metal-organic frameworks. *J. Power Sources* **2014**, *262*, 372–379. [CrossRef]
59. Sun, H.; Tang, B.; Wu, P. Two-Dimensional Zeolitic Imidazolate Framework/Carbon Nanotube Hybrid Networks Modified Proton Exchange Membranes for Improving Transport Properties. *ACS Appl. Mater. Interfaces* **2017**, *9*, 35075–35085. [CrossRef] [PubMed]
60. Wu, B.; Lin, X.; Ge, L.; Wu, L.; Xu, T. A novel route for preparing highly proton conductive membrane materials with metal-organic frameworks. *Chem. Commun.* **2013**, *49*, 143–145. [CrossRef] [PubMed]
61. Mansor, N.; Gadipelli, S.; Guo, Z.X.; Patel, H.A.; Brett, D.J.L. Superacidity in Nafion/MOF Hybrid Membranes Retains Water at Low Humidity to Enhance Proton Conduction for Fuel Cells. *ACS Appl. Mater. Interfaces* **2016**, *8*, 30687–30691.
62. Sun, H.Z.; Tang, B.B.; Wu, P.Y. Rational Design of S-UiO-66@GO Hybrid Nanosheets for Proton Exchange Membranes with Significantly Enhanced Transport Performance. *Acs Appl. Mater. Interfaces* **2017**, *9*, 26077–26087. [CrossRef] [PubMed]
63. Zhang, B.; Cao, Y.; Li, Z.; Wu, H.; Yin, Y.; Cao, L.; He, X.; Jiang, Z. Proton exchange nanohybrid membranes with high phosphotungstic acid loading within metal-organic frameworks for PEMFC applications. *Electrochim. Acta* **2017**, *240*, 186–194. [CrossRef]
64. Kumar, R.; Mamlouk, M.; Scott, K. Sulfonated polyether ether ketone–sulfonated graphene oxide composite membranes for polymer electrolyte fuel cells. *RSC Adv.* **2014**, *4*, 617–623. [CrossRef]
65. Sadakiyo, M.; Ōkawa, H.; Shigematsu, A.; Ohba, M.; Yamada, T.; Kitagawa, H. Promotion of Low-Humidity Proton Conduction by Controlling Hydrophilicity in Layered Metal–Organic Frameworks. *J. Am. Chem. Soc.* **2012**, *134*, 5472–5475. [CrossRef] [PubMed]
66. Yang, L.J.; Tang, B.B.; Wu, P.Y. Metal–organic framework–graphene oxide composites: a facile method to highly improve the proton conductivity of PEMs operated under low humidity. *J. Mater. Chem. A* **2015**, *3*, 15838–15842. [CrossRef]
67. Tsai, C.-H.; Wang, C.-C.; Chang, C.-Y.; Lin, C.-H.; Chen-Yang, Y.W. Enhancing performance of Nafion® -based PEMFC by 1-D channel metal-organic frameworks as PEM filler. *Int. J. Hydrogen Energy* **2014**, *39*, 15696–15705. [CrossRef]
68. Rao, Z.; Feng, K.; Tang, B.; Wu, P. Construction of well interconnected metal-organic framework structure for effectively promoting proton conductivity of proton exchange membrane. *J. Membr. Sci.* **2017**, *533*, 160–170. [CrossRef]
69. Donnadio, A.; Narducci, R.; Casciola, M.; Marmottini, F.; D'Amato, R.; Jazestani, M.; Chiniforoshan, H.; Costantino, F. Mixed Membrane Matrices Based on Nafion/UiO-66/SO_3H-UiO-66 Nano-MOFs: Revealing the Effect of Crystal Size, Sulfonation, and Filler Loading on the Mechanical and Conductivity Properties. *ACS Appl. Mater. Interfaces* **2017**, *9*, 42239–42246. [CrossRef] [PubMed]
70. Shao, Z.-G.; Xu, H.; Li, M.; Hsing, I.-M. Hybrid Nafion–inorganic oxides membrane doped with heteropolyacids for high temperature operation of proton exchange membrane fuel cell. *Solid State Ion.* **2006**, *177*, 779–785. [CrossRef]

71. Yang, C.; Srinivasan, S.; Aricò, A.S.; Cretí, P.; Baglio, V.; Antonucci, V. Composite Nafion/Zirconium Phosphate Membranes for Direct Methanol Fuel Cell Operation at High Temperature. *Electrochem. Solid State Lett.* **2001**, *4*, A31–A34. [CrossRef]
72. Yang, C.; Srinivasan, S.; Bocarsly, A.; Tulyani, S.; Benziger, J. A comparison of physical properties and fuel cell performance of Nafion and zirconium phosphate/Nafion composite membranes. *J. Membr. Sci.* **2004**, *237*, 145–161. [CrossRef]
73. Ozden, A.; Ercelik, M.; Ozdemir, Y.; Devrim, Y.; Colpan, C.O. Enhancement of direct methanol fuel cell performance through the inclusion of zirconium phosphate. *Int. J. Hydrogen Energy* **2017**, *42*, 21501–21517. [CrossRef]
74. Felice, C.; Ye, S.; Qu, D. Nafion−Montmorillonite Nanocomposite Membrane for the Effective Reduction of Fuel Crossover. *Ind. Eng. Chem. Res.* **2010**, *49*, 1514–1519. [CrossRef]
75. Jung, D.; Cho, S.; Peck, D.; Shin, D.; Kim, J. Preparation and performance of a Nafion®/montmorillonite nanocomposite membrane for direct methanol fuel cell. *J. Power Sources* **2003**, *118*, 205–211. [CrossRef]
76. Kumar, R.; Xu, C.; Scott, K. Graphite oxide/Nafion composite membranes for polymer electrolyte fuel cells. *RSC Adv.* **2012**, *2*, 8777–8782. [CrossRef]
77. Liu, Y.-L.; Su, Y.-H.; Chang, C.-M.; Suryani; Wang, D.-M.; Lai, J.-Y. Preparation and applications of Nafion-functionalized multiwalled carbon nanotubes for proton exchange membrane fuel cells. *J. Mater. Chem.* **2010**, *20*, 4409–4416. [CrossRef]
78. Kim, Y.-T.; Kim, K.-H.; Song, M.-K.; Rhee, H.-W. Nafion/ZrSPP composite membrane for high temperature operation of proton exchange membrane fuel cells. *Curr. Appl. Phys.* **2006**, *6*, 612–615. [CrossRef]
79. Kongkachuichay, P.; Pimprom, S. Nafion/Analcime and Nafion/Faujasite composite membranes for polymer electrolyte membrane fuel cells. *Chem. Eng. Res. Des.* **2010**, *88*, 496–500. [CrossRef]
80. Rao, Z.; Tang, B.; Wu, P. Proton Conductivity of Proton Exchange Membrane Synergistically Promoted by Different Functionalized Metal–Organic Frameworks. *ACS Appl. Mater. Interfaces* **2017**, *9*, 22597–22603. [CrossRef] [PubMed]
81. Sahu, A.K.; Ketpang, K.; Shanmugam, S.; Kwon, O.; Lee, S.C.; Kim, H. Sulfonated Graphene-Nafion Composite Membranes for Polymer Electrolyte Fuel Cells Operating under Reduced Relative Humidity. *J. Phys. Chem. C* **2016**, *120*, 15855–15866. [CrossRef]
82. Vinothkannan, M.; Kim, A.R.; Kumar, G.G.; Yoo, D.J. Sulfonated graphene oxide/Nafion composite membranes for high temperature and low humidity proton exchange membrane fuel cells. *RSC Adv.* **2018**, *8*, 7494–7508. [CrossRef]
83. Lu, J.L.; Fang, Q.H.; Li, S.L.; Jiang, S.P. A novel phosphotungstic acid impregnated meso-Nafion multilayer membrane for proton exchange membrane fuel cells. *J. Membr. Sci.* **2013**, *427*, 101–107. [CrossRef]
84. Chung, T.S. A critical review of polybenzimidazoles: Historical development and future R&D. *J. Macromol. Sci. Rev. Macromol. Chem. Phys.* **1997**, *C37*, 277–301.
85. Xing, B.Z.; Savadogo, O. The effect of acid doping on the conductivity of polybenzimidazole (PBI). *J. New Mater. Electrochem. Syst.* **1999**, *2*, 95–101.
86. Roziere, J.; Jones, D.J. Non-Fluorinated Polymer Materials for Proton Exchange Membrane Fuel Cells. *Annu. Rev. Mater. Res.* **2003**, *33*, 503–555. [CrossRef]
87. Hoel, D.; Grunwald, E. High protonic conduction of polybenzimidazole films. *J. Phys. Chem.* **1977**, *81*, 2135–2136. [CrossRef]
88. Litt, M.; Ameri, R.; Wang, Y.; Savinell, R.; Wainwright, J. Polybenzimidazoles/phosphoric acid solid polymer electrolytes: Mechanical and electrical properties. *Solid State Ion. V* **1999**, *548*, 313–323. [CrossRef]
89. Haque, M.A.; Sulong, A.; Loh, K.S.; Majlan, E.H.; Husaini, T.; Rosli, R.E. Acid doped polybenzimidazoles based membrane electrode assembly for high temperature proton exchange membrane fuel cell: A review. *Int. J. Hydrogen Energy* **2017**, *42*, 9156–9179. [CrossRef]
90. Wainright, J.S.; Wang, J.-T.; Weng, D.; Savinell, R.F.; Litt, M. Acid-Doped Polybenzimidazoles: A New Polymer Electrolyte. *J. Electrochem. Soc.* **1995**, *142*, L121–L123. [CrossRef]
91. Glipa, X.; Bonnet, B.; Mula, B.; Jones, D.J.; Rozière, J. Investigation of the conduction properties of phosphoric and sulfuric acid doped polybenzimidazole. *J. Mater. Chem.* **1999**, *9*, 3045–3049. [CrossRef]
92. Asensio, J.A.; Sánchez, E.M.; Gómez-Romero, P. Proton-conducting membranes based on benzimidazole polymers for high-temperature PEM fuel cells. A chemical quest. *Chem. Soc. Rev.* **2010**, *39*, 3210–3239. [CrossRef]

93. He, R.; Li, Q.; Xiao, G.; Bjerrum, N.J. Proton conductivity of phosphoric acid doped polybenzimidazole and its composites with inorganic proton conductors. *J. Membr. Sci.* **2003**, *226*, 169–184. [CrossRef]
94. Savadogo, O.; Xing, B. Hydrogen/oxygen polymer electrolyte membrane fuel cell (PEMFC) based on acid-doped polybenzimidazole (PBI). *J. New Mater. Electrochem. Syst.* **2000**, *3*, 343–347.
95. Iwu, K.O.; Galeckas, A.; Rauwel, P.; Kuznetsov, A.Y.; Norby, T. One-dimensional WO3 and its hydrate: One-step synthesis, structural and spectroscopic characterization. *J. Solid State Chem.* **2012**, *185*, 245–252. [CrossRef]
96. Schuster, M.; Rager, T.; Noda, A.; Kreuer, K.D.; Maier, J. About the Choice of the Protogenic Group in PEM Separator Materials for Intermediate Temperature, Low Humidity Operation: A Critical Comparison of Sulfonic Acid, Phosphonic Acid and Imidazole Functionalized Model Compounds. *Fuel Cells* **2005**, *5*, 355–365. [CrossRef]
97. Miyatake, K.; Bae, B.; Watanabe, M. Fluorene-containing cardo polymers as ion conductive membranes for fuel cells. *Polym. Chem.* **2011**, *2*, 1919–1929. [CrossRef]
98. Smitha, B.; Sridhar, S.; Khan, A. Solid polymer electrolyte membranes for fuel cell applications—A review. *J. Membr. Sci.* **2005**, *259*, 10–26. [CrossRef]
99. Kim, D.J.; Jo, M.J.; Nam, S.Y. A review of polymer–nanocomposite electrolyte membranes for fuel cell application. *J. Ind. Eng. Chem.* **2015**, *21*, 36–52. [CrossRef]
100. Li, Q.; He, R.; Berg, R.W.; Hjuler, H.A.; Bjerrum, N.J. Water uptake and acid doping of polybenzimidazoles as electrolyte membranes for fuel cells. *Solid State Ion.* **2004**, *168*, 177–185. [CrossRef]
101. Yu, S.; Xiao, L.; Benicewicz, B.C. Durability Studies of PBI-based High Temperature PEMFCs. *Fuel Cells* **2008**, *8*, 165–174. [CrossRef]
102. Li, Q.; Jensen, J.O.; Savinell, R.F.; Bjerrum, N.J. High temperature proton exchange membranes based on polybenzimidazoles for fuel cells. *Prog. Polym. Sci.* **2009**, *34*, 449–477. [CrossRef]
103. Brooks, N.W.; Duckett, R.A.; Rose, J.; Ward, I.M.; Clements, J. An Nmr-Study of Absorbed Water in Polybenzimidazole. *Polymer* **1993**, *34*, 4038–4042. [CrossRef]
104. Iwamoto, N. A property trend study of polybenzimidazole using molecular modeling. *Polym. Eng. Sci.* **1994**, *34*, 434–437. [CrossRef]
105. Quartarone, E.; Mustarelli, P.; Carollo, A.; Grandi, S.; Magistris, A.; Gerbaldi, A.C.; Gerbaldi, C. PBI Composite and Nanocomposite Membranes for PEMFCs: The Role of the Filler. *Fuel Cells* **2009**, *9*, 231–236. [CrossRef]
106. Mustarelli, P.; Quartarone, E.; Grandi, S.; Carollo, A.; Magistris, A. Polybenzimidazole-Based Membranes as a Real Alternative to Nafion for Fuel Cells Operating at Low Temperature. *Adv. Mater.* **2008**, *20*, 1339–1343. [CrossRef]
107. Croce, F.; Appetecchi, G.B.; Persi, L.; Scrosati, B. Nanocomposite polymer electrolytes for lithium batteries. *Nature* **1998**, *394*, 456–458. [CrossRef]
108. Moradi, M.; Moheb, A.; Javanbakht, M.; Hooshyari, K. Experimental study and modeling of proton conductivity of phosphoric acid doped PBI-Fe_2TiO_5 nanocomposite membranes for using in high temperature proton exchange membrane fuel cell (HT-PEMFC). *Int. J. Hydrogen Energy* **2016**, *41*, 2896–2910. [CrossRef]
109. Kurdakova, V.; Quartarone, E.; Mustarelli, P.; Magistris, A.; Caponetti, E.; Saladino, M.L. PBI-based composite membranes for polymer fuel cells. *J. Power Sources* **2010**, *195*, 7765–7769. [CrossRef]
110. Devrim, Y.; Devrim, H.; Eroğlu, I. Polybenzimidazole/SiO_2 hybrid membranes for high temperature proton exchange membrane fuel cells. *Int. J. Hydrogen Energy* **2016**, *41*, 10044–10052. [CrossRef]
111. Sadeghi, M.; Semsarzadeh, M.A.; Moadel, H. Enhancement of the gas separation properties of polybenzimidazole (PBI) membrane by incorporation of silica nano particles. *J. Membr. Sci.* **2009**, *331*, 21–30. [CrossRef]
112. Chang, Y.N.; Lai, J.Y.; Liu, Y.L. Polybenzimidazole (PBI)-functionalized silica nanoparticles modified PBI nanocomposite membranes for proton exchange membranes fuel cells. *J. Membr. Sci.* **2012**, *403*, 1–7.
113. Chang, C.-M.; Liu, Y.-L. Functionalization of multi-walled carbon nanotubes with non-reactive polymers through an ozone-mediated process for the preparation of a wide range of high performance polymer/carbon nanotube composites. *Carbon* **2010**, *48*, 1289–1297. [CrossRef]
114. Lobato, J.; Cañizares, P.; Rodrigo, M.A.; Úbeda, D.; Pinar, F.J. Enhancement of the fuel cell performance of a high temperature proton exchange membrane fuel cell running with titanium composite polybenzimidazole-based membranes. *J. Power Sources* **2011**, *196*, 8265–8271. [CrossRef]

115. Lobato, J.; Cañizares, P.; Rodrigo, M.A.; Úbeda, D.; Pinar, F.J. A novel titanium PBI-based composite membrane for high temperature PEMFCs. *J. Membr. Sci.* **2011**, *369*, 105–111. [CrossRef]
116. Pinar, F.J.; Cañizares, P.; Rodrigo, M.A.; Úbeda, D.; Lobato, J. Titanium composite PBI-based membranes for high temperature polymer electrolyte membrane fuel cells. Effect on titanium dioxide amount. *RSC Adv.* **2012**, *2*, 1547–1556. [CrossRef]
117. Pinar, F.J.; Cañizares, P.; Rodrigo, M.A.; Úbeda, D.; Lobato, J. Long-term testing of a high-temperature proton exchange membrane fuel cell short stack operated with improved polybenzimidazole-based composite membranes. *J. Power Sources* **2015**, *274*, 177–185. [CrossRef]
118. Enhessari, M.; Razi, M.K.; Etemad, L.; Parviz, A.; Sakhaei, M. Structural, optical and magnetic properties of the Fe_2TiO_5 nanopowders. *J. Exp. Nanosci.* **2014**, *9*, 167–176. [CrossRef]
119. Özdemir, Y.; Üregen, N.; Devrim, Y. Polybenzimidazole based nanocomposite membranes with enhanced proton conductivity for high temperature PEM fuel cells. *Int. J. Hydrogen Energy* **2017**, *42*, 2648–2657. [CrossRef]
120. Stenina, I.A.; Yaroslavtsev, A.B. Low- and intermediate-temperature proton-conducting electrolytes. *Inorg. Mater.* **2017**, *53*, 253–262. [CrossRef]
121. Staiti, P.; Minutoli, M.; Hocevar, S. Membranes based on phosphotungstic acid and polybenzimidazole for fuel cell application. *J. Power Sources* **2000**, *90*, 231–235. [CrossRef]
122. Staiti, P. Proton conductive membranes constituted of silicotungstic acid anchored to silica-polybenzimidazole matrices. *J. New Mater. Electrochem. Syst.* **2001**, *4*, 181–186.
123. Aili, D.; Zhang, J.; Jakobsen, M.T.D.; Zhu, H.; Yang, T.; Liu, J.; Forsyth, M.; Pan, C.; Jensen, J.O.; Cleemann, L.N.; et al. Exceptional durability enhancement of PA/PBI based polymer electrolyte membrane fuel cells for high temperature operation at 200 °C. *J. Mater. Chem. A* **2016**, *4*, 4019–4024. [CrossRef]
124. Verma, A.; Scott, K. Development of high-temperature PEMFC based on heteropolyacids and polybenzimidazole. *J. Solid State Electrochem.* **2010**, *14*, 213–219. [CrossRef]
125. Qian, W.; Shang, Y.; Fang, M.; Wang, S.; Xie, X.; Wang, J.; Wang, W.; Du, J.; Wang, Y.; Mao, Z. Sulfonated polybenzimidazole/zirconium phosphate composite membranes for high temperature applications. *Int. J. Hydrogen Energy* **2012**, *37*, 12919–12924. [CrossRef]
126. Clearfield, A. Structural concepts in inorganic proton conductors. *Solid State Ion.* **1991**, *46*, 35–43. [CrossRef]
127. Yamazaki, Y.; Jang, M.; Taniyama, T. Proton conductivity of zirconium tricarboxybutylphosphonate/PBI nanocomposite membrane. *Sci. Technol. Adv. Mater.* **2004**, *5*, 455–459. [CrossRef]
128. Li, M.Q.; Shao, Z.G.; Scott, K. A high conductivity $Cs_{2.5}H_{0.5}PMo1_2O_{40}$/polybenzimidazole (PBI)/H_3PO_4 composite membrane for proton-exchange membrane fuel cells OPE-rating at high temperature. *J. Power Sources* **2008**, *183*, 69–75. [CrossRef]
129. Xu, C.; Wu, X.; Wang, X.; Mamlouk, M.; Scott, K. Composite membranes of polybenzimidazole and caesium-salts-of-heteropolyacids for intermediate temperature fuel cells. *J. Mater. Chem.* **2011**, *21*, 6014–6019. [CrossRef]
130. Kim, A.R.; Gabunada, J.C.; Yoo, D.J. Amelioration in physicochemical properties and single cell performance of sulfonated poly(ether ether ketone) block copolymer composite membrane using sulfonated carbon nanotubes for intermediate humidity fuel cells. *Int. J. Energy Res.* **2019**, *43*, 2974–2989. [CrossRef]
131. Kannan, R.; Aher, P.P.; Palaniselvam, T.; Kurungot, S.; Kharul, U.K.; Pillai, V.K. Artificially Designed Membranes Using Phosphonated Multiwall Carbon Nanotube−Polybenzimidazole Composites for Polymer Electrolyte Fuel Cells. *J. Phys. Chem. Lett.* **2010**, *1*, 2109–2113. [CrossRef]
132. Kannan, R.; Kagalwala, H.N.; Chaudhari, H.D.; Kharul, U.K.; Kurungot, S.; Pillai, V.K. Improved performance of phosphonated carbon nanotube–polybenzimidazole composite membranes in proton exchange membrane fuel cells. *J. Mater. Chem.* **2011**, *21*, 7223–7231. [CrossRef]
133. Chang, C.M.; Liu, Y.L.; Lee, Y.M. Polybenzimidazole membranes modified with polyelectrolyte-functionalized multiwalled carbon nanotubes for proton exchange membrane fuel cells. *J. Mater. Chem.* **2011**, *21*, 7480–7486.
134. Üregen, N.; Pehlivanoğlu, K.; Özdemir, Y.; Devrim, Y. Development of polybenzimidazole/graphene oxide composite membranes for high temperature PEM fuel cells. *Int. J. Hydrogen Energy* **2017**, *42*, 2636–2647. [CrossRef]
135. Chen, D.; Tang, L.; Li, J. Graphene-based materials in electrochemistry. *Chem. Soc. Rev.* **2010**, *39*, 3157–3180. [CrossRef] [PubMed]

136. Abouzari-Lotf, E.; Zakeri, M.; Nasef, M.M.; Miyake, M.; Mozarmnia, P.; Bazilah, N.A.; Emelin, N.F.; Ahmad, A. Highly durable polybenzimidazole composite membranes with phosphonated graphene oxide for high temperature polymer electrolyte membrane fuel cells. *J. Power Sources* **2019**, *412*, 238–245. [CrossRef]
137. Xue, C.; Zou, J.; Sun, Z.; Wang, F.; Han, K.; Zhu, H. Graphite oxide/functionalized graphene oxide and polybenzimidazole composite membranes for high temperature proton exchange membrane fuel cells. *Int. J. Hydrogen Energy* **2014**, *39*, 7931–7939. [CrossRef]
138. Wang, Y.; Shi, Z.; Fang, J.; Xu, H.; Yin, J. Graphene oxide/polybenzimidazole composites fabricated by a solvent-exchange method. *Carbon* **2011**, *49*, 1199–1207. [CrossRef]
139. Park, K.S.; Ni, Z.; Côté, A.P.; Choi, J.Y.; Huang, R.; Uribe-Romo, F.J.; Chae, H.K.; O'Keeffe, M.; Yaghi, O.M. Exceptional chemical and thermal stability of zeolitic imidazolate frameworks. *Proc. Natl. Acad. Sci. USA* **2006**, *103*, 10186–10191. [CrossRef] [PubMed]
140. Vega, J.; Andrio, A.; Lemus, A.; Del Castillo, L.; Compañ, V. Conductivity study of Zeolitic Imidazolate Frameworks, Tetrabutylammonium hydroxide doped with Zeolitic Imidazolate Frameworks, and mixed matrix membranes of Polyetherimide/Tetrabutylammonium hydroxide doped with Zeolitic Imidazolate Frameworks for proton conducting applications. *Electrochim. Acta* **2017**, *258*, 153–166.
141. Plackett, D.; Siu, A.; Li, Q.; Pan, C.; Jensen, J.O.; Nielsen, S.F.; Permyakova, A.A.; Bjerrum, N.J. High-temperature proton exchange membranes based on polybenzimidazole and clay composites for fuel cells. *J. Membr. Sci.* **2011**, *383*, 78–87. [CrossRef]
142. Ghosh, S.; Sannigrahi, A.; Maity, S.; Jana, T. Role of Clays Structures on the Polybenzimidazole Nanocomposites: Potential Membranes for the Use in Polymer Electrolyte Membrane Fuel Cell. *J. Phys. Chem. C* **2011**, *115*, 11474–11483. [CrossRef]
143. Singha, S.; Jana, T. Structure and Properties of Polybenzimidazole/Silica Nanocomposite Electrolyte Membrane: Influence of Organic/Inorganic Interface. *ACS Appl. Mater. Interfaces* **2014**, *6*, 21286–21296. [CrossRef]
144. Li, M.; Scott, K. A polymer electrolyte membrane for high temperature fuel cells to fit vehicle applications. *Electrochim. Acta* **2010**, *55*, 2123–2128. [CrossRef]
145. Ghosh, S.; Maity, S.; Jana, T. Polybenzimidazole/silica nanocomposites: Organic-inorganic hybrid membranes for PEM fuel cell. *J. Mater. Chem.* **2011**, *21*, 14897–14906. [CrossRef]
146. Muthuraja, P.; Prakash, S.; Shanmugam, V.; Radhakrsihnan, S.; Manisankar, P. Novel perovskite structured calcium titanate-PBI composite membranes for high-temperature PEM fuel cells: Synthesis and characterizations. *Int. J. Hydrogen Energy* **2018**, *43*, 4763–4772. [CrossRef]
147. Kreuer, K. On the development of proton conducting polymer membranes for hydrogen and methanol fuel cells. *J. Membr. Sci.* **2001**, *185*, 29–39. [CrossRef]
148. Gil, M.; Ji, X.; Li, X.; Na, H.; Hampsey, J.E.; Lu, Y. Direct synthesis of sulfonated aromatic poly(ether ether ketone) proton exchange membranes for fuel cell applications. *J. Membr. Sci.* **2004**, *234*, 75–81. [CrossRef]
149. Available online: https://patents.google.com/patent/US6355149?oq=us-6355149 (accessed on 1 May 2019).
150. Iulianelli, A.; Basile, A. Sulfonated PEEK-based polymers in PEMFC and DMFC applications: A review. *Int. J. Hydrogen Energy* **2012**, *37*, 15241–15255. [CrossRef]
151. Bonnet, B.; Jones, D.J.; Roziere, J.; Tchicaya, L.; Alberti, G.; Casciola, M.; Massinelli, L.; Bauer, B.; Peraio, A.; Ramunni, E. Hybrid organic-inorganic membranes for a medium temperature fuel cell. *J. New Mater. Electrochem. Syst.* **2000**, *3*, 87–92.
152. Salarizadeh, P.; Javanbakht, M.; Pourmahdian, S. Fabrication and physico-chemical properties of iron titanate nanoparticles based sulfonated poly (ether ether ketone) membrane for proton exchange membrane fuel cell application. *Solid State Ion.* **2015**, *281*, 12–20. [CrossRef]
153. Intaraprasit, N.; Kongkachuichay, P. Preparation and properties of sulfonated poly(ether ether ketone)/Analcime composite membrane for a proton exchange membrane fuel cell (PEMFC). *J. Taiwan Inst. Chem. Eng.* **2011**, *42*, 190–195. [CrossRef]
154. Li, H.; Zhang, G.; Ma, W.; Zhao, C.; Zhang, Y.; Han, M.; Zhu, J.; Liu, Z.; Wu, J.; Na, H. Composite membranes based on a novel benzimidazole grafted PEEK and SPEEK for fuel cells. *Int. J. Hydrogen Energy* **2010**, *35*, 11172–11179. [CrossRef]
155. Fontananova, E.; Trotta, F.; Jansen, J.C.; Drioli, E. Preparation and characterization of new non-fluorinated polymeric and composite membranes for PEMFCs. *J. Membr. Sci.* **2010**, *348*, 326–336. [CrossRef]

156. Silva, V.S.; Ruffmann, B.; Silva, H.; Gallego, Y.A.; Mendes, A.; Madeira, L.M.; Nunes, S.P. Proton electrolyte membrane properties and direct methanol fuel cell performance I. Characterization of hybrid sulfonated poly(ether ether ketone)/zirconium oxide membranes. *J. Power Sources* **2005**, *140*, 34–40. [CrossRef]
157. Pezzin, S.; Stock, N.; Shishatskiy, S.; Nunes, S. Modification of proton conductive polymer membranes with phosphonated polysilsesquioxanes. *J. Membr. Sci.* **2008**, *325*, 559–569. [CrossRef]
158. Kim, A.R.; Vinothkannan, M.; Yoo, D.J. Sulfonated fluorinated multi-block copolymer hybrid containing sulfonated(poly ether ether ketone) and graphene oxide: A ternary hybrid membrane architecture for electrolyte applications in proton exchange membrane fuel cells. *J. Energy Chem.* **2018**, *27*, 1247–1260. [CrossRef]
159. Cheng, X.; Yi, B.; Han, M.; Zhang, J.; Qiao, Y.; Yu, J. Investigation of platinum utilization and morphology in catalyst layer of polymer electrolyte fuel cells. *J. Power Sources* **1999**, *79*, 75–81. [CrossRef]
160. Lee, S.; Mukerjee, S.; McBreen, J.; Rho, Y.; Kho, Y.; Lee, T. Effects of Nafion impregnation on performances of PEMFC electrodes. *Electrochim. Acta* **1998**, *43*, 3693–3701. [CrossRef]
161. Uchida, M.; Aoyama, Y.; Eda, N.; Ohta, A. Investigation of the Microstructure in the Catalyst Layer and Effects of Both Perfluorosulfonate Ionomer and PTFE-Loaded Carbon on the Catalyst Layer of Polymer Electrolyte Fuel Cells. *J. Electrochem. Soc.* **1995**, *142*, 4143–4149. [CrossRef]
162. Antolini, E.; Giorgi, L.; Pozio, A.; Passalacqua, E. Influence of Nafion loading in the catalyst layer of gas-diffusion electrodes for PEFC. *J. Power Sources* **1999**, *77*, 136–142. [CrossRef]
163. Paganin, V.; Ticianelli, E.; Gonzalez, E. Development and electrochemical studies of gas diffusion electrodes for polymer electrolyte fuel cells. *J. Appl. Electrochem.* **1996**, *26*, 297–304. [CrossRef]
164. Antolini, E. Recent developments in polymer electrolyte fuel cell electrodes. *J. Appl. Electrochem.* **2004**, *34*, 563–576. [CrossRef]
165. Lai, E.K.; Beattie, P.D.; Orfino, F.P.; Simon, E.; Holdcroft, S. Electrochemical oxygen reduction at composite films of Nafion®, polyaniline and Pt. *Electrochim. Acta* **1999**, *44*, 2559–2569. [CrossRef]
166. Qi, Z.; Lefebvre, M.C.; Pickup, P.G. Electron and proton transport in gas diffusion electrodes containing electronically conductive proton-exchange polymers1Presented at the Electrochemical Society Symposium: Processes in Polymers and Polymer|Metal Interfaces, Montreal, 4–9 May 1997.1. *J. Electroanal. Chem.* **1998**, *459*, 9–14. [CrossRef]
167. Holze, R.; Wu, Y. Intrinsically conducting polymers in electrochemical energy technology: Trends and progress. *Electrochim. Acta* **2014**, *122*, 93–107. [CrossRef]
168. Wolfart, F.; Hryniewicz, B.M.; Góes, M.S.; Torresi, R.; Minadeo, M.A.O.S.; Oliveira, R.D.; Vidotti, M.; Corrêa, C.M.; Marchesi, L.F. Conducting polymers revisited: applications in energy, electrochromism and molecular recognition. *J. Solid State Electrochem.* **2017**, *16*, 578–2515. [CrossRef]
169. Moravcova, S.; Cílová, Z.; Bouzek, K. Preparation of a Novel Composite Material Based on a Nafion® Membrane and Polypyrrole for Potential Application in a PEM Fuel Cell. *J. Appl. Electrochem.* **2005**, *35*, 991–997. [CrossRef]
170. Daş, E.; Yurtcan, A.B. Effect of carbon ratio in the polypyrrole/carbon composite catalyst support on PEM fuel cell performance. *Int. J. Hydrogen Energy* **2016**, *41*, 13171–13179. [CrossRef]
171. Oh, H.-S.; Oh, J.-G.; Roh, B.; Hwang, I.; Kim, H. Development of highly active and stable non-precious oxygen reduction catalysts for PEM fuel cells using polypyrrole and a chelating agent. *Electrochem. Commun.* **2011**, *13*, 879–881. [CrossRef]
172. Xu, F.; Innocent, C.; Bonnet, B.; Jones, D.J.; Rozière, J. Chemical Modification of Perfluorosulfo-nated Membranes with Pyrrole for Fuel Cell Application: Preparation, Characteri-sation and Methanol Transport. *Fuel Cells* **2005**, *5*, 398–405. [CrossRef]
173. Park, H.S.; Kim, Y.J.; Hong, W.H.; Lee, H.K. Physical and electrochemical properties of Nafion/polypyrrole composite membrane for DMFC. *J. Membr. Sci.* **2006**, *272*, 28–36. [CrossRef]
174. Easton, E.B.; Langsdorf, B.L.; Hughes, J.A.; Sultan, J.; Qi, Z.; Kaufman, A.; Pickup, P.G. Characteristics of Polypyrrole/Nafion Composite Membranes in a Direct Methanol Fuel Cell. *J. Electrochem. Soc.* **2003**, *150*, C735–C739. [CrossRef]
175. Sungpet, A. Reduction of alcohol permeation through Nafion® by polypyrrole. *J. Membr. Sci.* **2003**, *226*, 131–134. [CrossRef]
176. Bouzek, K.; Holzhauser, P.; Kodym, R.; Moravcova, S.; Paidar, M. Utilization of Nafion®/conducting polymer composite in the PEM type fuel cells. *J. Appl. Electrochem.* **2007**, *37*, 137–145. [CrossRef]

177. Lin, H.; Zhao, C.; Ma, W.; Li, H.; Na, H. Layer-by-layer self-assembly of in situ polymerized polypyrrole on sulfonated poly(arylene ether ketone) membrane with extremely low methanol crossover. *Int. J. Hydrogen Energy* **2009**, *34*, 9795–9801. [CrossRef]
178. Park, H.; Kim, Y.; Choi, Y.S.; Hong, W.H.; Jung, D. Surface chemistry and physical properties of Nafion/polypyrrole/Pt composite membrane prepared by chemical in situ polymerization for DMFC. *J. Power Sources* **2008**, *178*, 610–619. [CrossRef]
179. Li, L.; Zhang, Y.; Drillet, J.-F.; Dittmeyer, R.; Jüttner, K.-M. Preparation and characterization of Pt direct deposition on polypyrrole modified Nafion composite membranes for direct methanol fuel cell applications. *Chem. Eng. J.* **2007**, *133*, 113–119. [CrossRef]
180. Smit, M.; Ocampo, A.; Espinosa-Medina, M.; Sebastian, P.; Espinosa-Medina, M. A modified Nafion membrane with in situ polymerized polypyrrole for the direct methanol fuel cell. *J. Power Sources* **2003**, *124*, 59–64. [CrossRef]
181. Deslouis, C.; Musiani, M.M.; Tribollet, B. Ac Impedance Study of Transport Processes in Polyaniline Membranes. *J. Phys. Chem.* **1994**, *98*, 2936–2940. [CrossRef]
182. Chiang, J.-C.; MacDiarmid, A.G. 'Polyaniline': Protonic acid doping of the emeraldine form to the metallic regime. *Synth. Met.* **1986**, *13*, 193–205. [CrossRef]
183. Kost, K.M.; Bartak, D.E.; Kazee, B.; Kuwana, T. Electrodeposition of platinum microparticles into polyaniline films with electrocatalytic applications. *Anal. Chem.* **1988**, *60*, 2379–2384. [CrossRef]
184. Dale, S.E.; Day, T.M.; Wilson, N.R.; MacPherson, J.V.; Unwin, P.R.; O'Mullane, A.P.; O'Mullane, A. Formation of polyaniline/Pt nanoparticle composite films and their electrocatalytic properties. *J. Solid State Electrochem.* **2006**, *10*, 792–807.
185. Chartier, P.; Mattes, B.; Reiss, H. Donnan phenomena in the proton doping of emeraldine. *J. Phys. Chem.* **1992**, *96*, 3556–3560. [CrossRef]
186. Coutanceau, C.; Croissant, M.; Napporn, T.; Lamy, C. Electrocatalytic reduction of dioxygen at platinum particles dispersed in a polyaniline film. *Electrochim. Acta* **2000**, *46*, 579–588. [CrossRef]
187. Croissant, M.; Napporn, T.; Leger, J.-M.; Lamy, C. Electrocatalytic oxidation of hydrogen at platinum-modified polyaniline electrodes. *Electrochim. Acta* **1998**, *43*, 2447–2457. [CrossRef]
188. Sun, X.; Xu, K.; Fleischer, C.; Liu, X.; Grandcolas, M.; Strandbakke, R.; Bjørheim, T.S.; Norby, T.; Chatzitakis, A. Earth-Abundant Electrocatalysts in Proton Exchange Membrane Electrolyzers. *Catalysts* **2018**, *8*, 657. [CrossRef]
189. Barthet, C.; Guglielmi, M. Mixed electronic and ionic conductors: a new route to Nafion®-doped polyaniline. *J. Electroanal. Chem.* **1995**, *388*, 35–44. [CrossRef]
190. Gharibi, H.; Zhiani, M.; Mirzaie, R.A.; Kheirmand, M.; Entezami, A.A.; Kakaei, K.; Javaheri, M. Investigation of polyaniline impregnation on the performance of gas diffusion electrode (GDE) in PEMFC using binary of Nafion and polyaniline nanofiber. *J. Power Sources* **2006**, *157*, 703–708. [CrossRef]
191. Gharibi, H.; Zhiani, M.; Entezami, A.A.; Mirzaie, R.A.; Kheirmand, M.; Kakaei, K. Study of polyaniline doped with trifluoromethane sulfonic acid in gas-diffusion electrodes for proton-exchange membrane fuel cells. *J. Power Sources* **2006**, *155*, 138–144. [CrossRef]
192. Yang, J.; Shen, P.K.; Varcoe, J.; Wei, Z. Nafion/polyaniline composite membranes specifically designed to allow proton exchange membrane fuel cells operation at low humidity. *J. Power Sources* **2009**, *189*, 1016–1019. [CrossRef]
193. Berezina, N.P.; Kubaisy, A.A.; Timofeev, S.V.; Karpenko, L.V. Template synthesis and electrotransport behavior of polymer composites based on perfluorinated membranes incorporating polyaniline. *J. Solid State Electrochem.* **2007**, *11*, 378–389. [CrossRef]
194. Wolz, A.; Zils, S.; Michel, M.; Roth, C. Structured multilayered electrodes of proton/electron conducting polymer for polymer electrolyte membrane fuel cells assembled by spray coating. *J. Power Sources* **2010**, *195*, 8162–8167. [CrossRef]
195. Kakaei, K. Electrochemical Characteristics and Performance of Platinum Nanoparticles Supported by Vulcan/Polyaniline for Oxygen Reduction in PEMFC. *Fuel Cells* **2012**, *12*, 939–945. [CrossRef]
196. Heeger, A.J. Semiconducting and Metallic Polymers: The Fourth Generation of Polymeric Materials (Nobel Lecture). *Angew. Chem. Int. Ed.* **2001**, *40*, 2591–2611. [CrossRef]
197. Heywang, G.; Jonas, F. Poly(alkylenedioxythiophene)s—New, very stable conducting polymers. *Adv. Mater.* **1992**, *4*, 116–118. [CrossRef]

198. Dietrich, M.; Heinze, J.; Heywang, G.; Jonas, F. Electrochemical and spectroscopic characterization of polyalkylenedioxythiophenes. *J. Electroanal. Chem.* **1994**, *369*, 87–92. [CrossRef]
199. Liu, J.; Davis, N.R.; Liu, D.S.; Hammond, P.T. Highly transparent mixed electron and proton conducting polymer membranes. *J. Mater. Chem.* **2012**, *22*, 15534–15539. [CrossRef]
200. McFarlane, S.L.; Day, B.A.; McEleney, K.; Freund, M.; Lewis, N.S. Designing electronic/ionic conducting membranes for artificial photosynthesis. *Energy Environ. Sci.* **2011**, *4*, 1700–1703. [CrossRef]
201. Ijeri, V.; Cappelletto, L.; Bianco, S.; Tortello, M.; Spinelli, P.; Tresso, E. Nafion and carbon nanotube nanocomposites for mixed proton and electron conduction. *J. Membr. Sci.* **2010**, *363*, 265–270. [CrossRef]
202. Tortello, M.; Bianco, S.; Ijeri, V.; Spinelli, P.; Tresso, E. Nafion membranes with vertically-aligned CNTs for mixed proton and electron conduction. *J. Membr. Sci.* **2012**, *415*, 346–352. [CrossRef]
203. Pilgrim, G.A.; Leadbetter, J.W.; Qiu, F.; Siitonen, A.J.; Pilgrim, S.M.; Krauss, T.D. Electron Conductive and Proton Permeable Vertically Aligned Carbon Nanotube Membranes. *Nano Lett.* **2014**, *14*, 1728–1733. [CrossRef] [PubMed]
204. Hatakeyama, K.; Tateishi, H.; Taniguchi, T.; Koinuma, M.; Kida, T.; Hayami, S.; Yokoi, H.; Matsumoto, Y. Tunable Graphene Oxide Proton/Electron Mixed Conductor that Functions at Room Temperature. *Chem. Mater.* **2014**, *26*, 5598–5604. [CrossRef]
205. Hatakeyama, K.; Karim, M.R.; Ogata, C.; Tateishi, H.; Funatsu, A.; Taniguchi, T.; Koinuma, M.; Hayami, S.; Matsumoto, Y. Proton Conductivities of Graphene Oxide Nanosheets: Single, Multilayer, and Modified Nanosheets. *Angew. Chem.* **2014**, *126*, 7117–7120. [CrossRef]
206. Hatakeyama, K.; Islam, M.S.; Michio, K.; Ogata, C.; Taniguchi, T.; Funatsu, A.; Kida, T.; Hayami, S.; Matsumoto, Y. Super proton/electron mixed conduction in graphene oxide hybrids by intercalating sulfate ions. *J. Mater. Chem. A* **2015**, *3*, 20892–20895. [CrossRef]
207. Chen, Z.; Peng, Y.; Liu, F.; Le, Z.; Zhu, J.; Shen, G.; Zhang, D.; Wen, M.; Xiao, S.; Liu, C.-P.; et al. Hierarchical Nanostructured WO3 with Biomimetic Proton Channels and Mixed Ionic-Electronic Conductivity for Electrochemical Energy Storage. *Nano Lett.* **2015**, *15*, 6802–6808. [CrossRef]
208. Amirinejad, M.; Madaeni, S.S.; Lee, K.-S.; Ko, U.; Rafiee, E.; Lee, J.-S. Sulfonated poly(arylene ether)/heteropolyacids nanocomposite membranes for proton exchange membrane fuel cells. *Electrochimica Acta* **2012**, *62*, 227–233. [CrossRef]
209. Takemoto, M.; Hayashi, K.; Yamaura, S.-I.; Zhang, W.; Sakamoto, W.; Yogo, T. Synthesis of inorganic-organic hybrid membranes consisting of organotrisiloxane linkages and their fuel cell properties at intermediate temperatures. *Polymer* **2017**, *120*, 264–271. [CrossRef]
210. Hoshino, T.; Hayashi, K.; Sakamoto, W.; Yogo, T. One-pot synthesis of proton-conductive inorganic–organic hybrid membranes from organoalkoxysilane and phosphonic acid derivatives. *J. Membr. Sci.* **2016**, *502*, 133–140. [CrossRef]
211. Hattori, M.; Yamaura, S.-I.; Zhang, W.; Sakamoto, W.; Yogo, T. Proton-conductive inorganic–organic hybrid membranes synthesized from a trimethoxysilylmethylstyrene–fluorophenylvinyl acid copolymer. *J. Membr. Sci.* **2015**, *488*, 166–172. [CrossRef]